U.S. DEPARTMENT OF
ENERGY

Office of
**ENERGY EFFICIENCY &
RENEWABLE ENERGY**

Electrification

2022 Annual Progress Report

Vehicle Technologies Office

(This page intentionally left blank)

Disclaimer

This report was prepared as an account of work sponsored by an agency of the United States government. Neither the United States government nor any agency thereof, nor any of their employees, makes any warranty, express or implied, or assumes any legal liability or responsibility for the accuracy, completeness, or usefulness of any information, apparatus, product, or process disclosed or represents that its use would not infringe privately owned rights. Reference herein to any specific commercial product, process, or service by trade name, trademark, manufacturer, or otherwise does not necessarily constitute or imply its endorsement, recommendation, or favoring by the United States government or any agency thereof. The views and opinions of authors expressed herein do not necessarily state or reflect those of the United States government or any agency thereof.

Acronyms

A

AC	Alternating Current
ACC	Adaptive Cruise Control
accel	Acceleration
ACS	Advanced Combustion Systems
ACSforEVER	Advanced Climate Systems for EV Extended Range
AER	All-electric range
AFV	Alternative Fuel Vehicle
AMI	Advanced Metering Infrastructure
AMT	Automated Mechanical Transmission
ANL	Argonne National Laboratory
ANN	Artificial Neural Network
AOI	Areas of Interest
APEC	Asia Pacific Economic Council
APRF	Advanced Powertrain Research Facility
APT	Pressure Sensor
ASD	Aftermarket Safety Device
AVTA	Advanced Vehicle Testing Activity
AVTE	Advanced Vehicle Testing and Evaluation

B

BaSce	Baseline and Scenario
Batt	Battery
BEB	Battery Next-Generation Electric Transit Bus
BEC	Bussed Electrical Center
BEMS	Building Energy Management System
BET	Battery Electric Truck
BEV	Battery Electric Vehicle
BMW	Bayerische Motoren Werke AG
BSFC	Brake Specific Fuel Consumption
BTE	Brake Thermal Efficiency

C

CAC	Charge Air Cooler
CACC	Cooperative Adaptive Cruise Control
CAE	Computer-Aided Engineering
CAFE	Corporate Average Fuel Economy
CAN	Controller Area Network
CAV	Connected and automated vehicles
CARB	California Air Resources Board
CBD	Central Business District
CCS	Combined Charging System
CW, CCW	Clockwise, Counterclockwise

CD	Charge-Depleting
CERV	Conference on Electric Roads and Vehicles
CFD	Computational Fluid Dynamics
CFDC	Commercial Fleet Data Center
CFL	Combined Fluid Loop
CH4	Methane
CHTS	California Household Travel Survey
CIP	Common Integration Platform
Cm3	Cubic
CNG	Compressed Natural Gas
CO	Carbon monoxide
CO2	Carbon Dioxide
COMM	Commuter
Conv	Conventional Vehicle
COP	Coefficient of Performance
CPS	Cyber-Physical Security
CPSR	Constant Power Speed Ratio
CS	Charge Sustaining
Cs	Cold start
CV	Conventional vehicle

D

D3	Downloadable Dynamometer Database
DC	Direct current
DCFC	Direct Current Fast Charge
DCT	Dual-clutch transmission
decel	Deceleration
DER	Distributed energy resource
DFGM	Digital Flux Gate Magnetometer
DFMEA	Design of Failure Modes Analysis
DGE	Diesel Gallon Equivalent
DOE	U.S. Department of Energy
DOHC	Dual overhead cam
DS	Down speeding
DSM	Distributed Security Module
DSM	Diagnostic Security Module
DSP	Digital Signal Processor
DSRC	Dedicated Short Range Communications
dt	Change in time
dv	Change in velocity
Dyno	Dynamometer

E

EAVS	Electrically Assisted Variable Speed Supercharger
EC	European Commission
EDV	Electric Drive Vehicle

EDT	Electric Drive Technologies
EDX	Energy dispersive x-ray spectroscopy
EERE	Energy Efficiency and Renewable Energy
EGR	Exhaust Gas Recirculation
EG/W	Ethylene glycol/water
EOL	End of life
EPA	Environmental Protection Agency
ePATHS	Electrical PCM Assisted Thermal Heating System
EREV	Extended-Range Electric Vehicles
ESIF	Energy Systems Integration Facility
ESS	Energy Storage System
ETT	Electric Transportation Technologies
E-TREE	Electric Truck with Range Extending Engine
EUMD	End-Use Measurement Device
EV	Electric Vehicle
EV2G	Electric Vehicle-to-Grid
EVSE	Electric Vehicle Service Equipment
EXV	Electronic Expansion Valve

F

F	Force
FASTSim	Future Automotive Systems Technology Simulator
FC	Fuel cell
FC	Fast charge
FCons	Fuel consumption
FCTO	Fuel Cell Technologies Office
FE	Fuel Economy
FEA	Finite Element Analysis
FEX	Front-end Heat Exchanger
FHWA	Federal Highway Administration
FLNA	Frito-Lay North America
FM	Friction Modifier
FMEP	Friction Mean Effective Pressure
FOA	Funding Opportunity Announcement
FTIR	Fourier transform infrared spectroscopy
FTP	Federal Test Procedure
FWD	Four-wheel drive
FY	Fiscal year

G

g	gram
GB	Gigabyte
GCEDV	Grid Connected Electrical Drive Vehicles
GEM	Gas Emissions Model
GHG	Greenhouse Gas
GITT	Grid Interaction Tech Team

GMLC	Grid Modernization Lab Consortium
GnPs	graphene nanoplatelets
GO	Graphene Oxide
GPRA	Government Performance and Results Act
GPS	Global Positioning System
GREET	Greenhouse gases, Regulated Emissions, and Energy use in Transportation
GSF1	Generic Speed Form 1
GSU	Grid side unit
GUI	Graphic User Interface
GVW	Gross Vehicle Weight

H

h-APU	hybrid Auxiliary Power Unit
HATCI	Hyundai America Technical Center, Inc.
HC	Unburned hydrocarbons
HD	Heavy Duty
HEV	Hybrid-Electric Vehicle
H-GAC	Houston-Galveston Area Council
HHDDT	Heavy Heavy-Duty Diesel Truck
HHV	Hydraulic Hybrid Vehicle
HIL	Hardware-In-the-Loop
HP	Heat Pump
Hp	Horsepower
HTML	HyperText Markup Language
HV	High Voltage
HVAC	Heating Ventilating and Air Conditioning
HWFET	Highway Fuel Economy Test
HPMS	Highway Performance Monitoring System
HVTB	High Voltage Traction Battery
HWY	Highway Program or Highway Fuel Economy Test Cycle
HPC	High Performance Computing
HTR	Heater
Hz	Hertz

I

I	Inertia
IC	Internal Combustion
ICD	Interim Component Durability
ICDV	Internal Combustion Drive Vehicles
ICE	Internal Combustion Engine
ICTF	Intermodal Container Transfer Facility
ICU	Inverter-Charger Unit
IEB	Information Exchange Bus
IEC	International Electrotechnical Commission
IGBT	Insulated Gate Bipolar Transistors
IHX	Internal Heat Exchanger

INL	Idaho National Laboratory
INTEGRATE	Integrated Network Testbed for Energy Grid Research and Technology
IOT	Internet of Things
IR	Infrared Radiation
ISO	International Organization for Standardization
ITS	Intelligent Transportation Systems

J

| JIT | Just-in-Time |

K

kg	Kilogram
km	Kilometer
kW	Kilowatt
kWh	Kilowatt hour

L

L	litre
L1	Level 1 benchmark
L2	Level 2 benchmark
Lbf	Pounds force
LCC	Liquid-Cooled Condenser
LD	Light duty
LH	line haul
Li	Lithium
LIB	Lithium-ion battery
LLNL	Lawrence Livermore National Laboratory
LNG	Liquified natural gas
LTC	Lockport Technical Center
LV	Leading Vehicle

M

M	Mass
MBSE	Model Based System Engineering
MD	Medium Duty
mpg	Miles per gallon
MMTCE	Million Metric Tons of Carbon Equivalent
MIIT	Ministry of Industry and Information Technology
mi	Mile
MJ	Megajoules
MOSFET	Metal-Oxide Semiconductor Field-Effect Transistor
mph	Miles per hour
MPGe,	Miles per gallon equivalent, Miles per gallon gasoline equivalent
MTDC	Medium Truck Duty Cycle
MOVES	Motor Vehicle Emission Simulator
MRF	Moving Reference Frame
MURECP	Medium-Duty Urban Range Extended Connected Powertrain

MY	Model year
M2	Meters squared

N

NACFE	North American Council for Freight Efficiency
NDA	Non-Disclosure Agreement
NETL	National Energy Technology Laboratory
NHTS	National Household Travel Survey
NHTSA	National Highway Transportation Safety Administration
NM	Newton meters
NOx	Nitrogen oxides
NR	Natural Rubber
NRE	Non-Recurring Engineering
NREL	National Renewable Energy Laboratory
NRT	National Retail Trucking
NVH	Noise, vibration, and harshness
NVUSD	Napa Valley Unified School District
NYSERDA	New York State Energy Research Development Authority

O

OBC	On-board charger
OCBC	Orange County Bus Cycle
OEM	Original Equipment Manufacturer
OneSAF	One Semi-Automated Forces
ORNL	Oak Ridge National Laboratories

P

P	Active Power
PC	Polycarbonate
PCM	Phase-Change Material
PCU	Power Control Unit
PCU	Powertrain Control Unit
PEEM	Power Electronics and Electric Motor
PFC	Power factor correction
PFI	Port fuel injection
PGW	Pittsburgh Glass Works
PHEV	Plug-in Hybrid Electric Vehicle
PHEV##	Plug-in hybrid electric vehicle with ## miles of all-electric range
PI	Principal Investigator
PM	Permanent Magnet
PM	Particulate Matter
ppm	Parts per Million
PTC	Positive Temperature Coefficient (Electric Heater)
PTO	Power Take-Off
PVP	Polyvinylpyrrolidone
PWWMD	Public Works and Waste Management Department

λ	Power Factor
φ	Power Angle

Q

Q	Reactive power
QA	Quality assurance
QC	Quality control

R

R2	Coefficient of Determination
R/D	Receiver / Dryer
REV	New York State's Reforming the Energy Vision Initiative
REx	Range Extending Engine
rGO	reduced graphene oxide
RH	Relative Humidity
RMS	Root Mean Square
ROL	Ring-On-Liner
rpm	Revolutions Per Minute
RSU	Road Side Unit
RWDC	Real-World Drive-Cycle

S

S	Apparent power
SAE	Society of Automotive Engineers
SBR	Styrene-Butadiene Rubber
SC03	SC03 Supplemental Federal Test Procedure
SCAG	Southern California Association of Governments
SCAQMD	South Coast Air Quality Management District
SCIG	Southern California International Gateway
SCR	Silicon Controlled Rectifier
SCR	Selective Catalytic Reduction
SDO	Standards Definition Organizations
SI	Système International d'Unités
SI	Gasoline Spark Ignition
SNR	Sensor
SOC	State of Charge
SPL	Sound Pressure Level
SR	Speed Ratio
SS	Steady State
SPaT	Signal Phase and Timing
StAR	Storage-Assisted Recharging

T

T	Torque
TA	Technical Area
TA	Torque Assist
TC	Thermocouple

TE	Thermoelectric
TE	Transmission Error
TES	Thermal Energy Storage
TGA	thermogravimetric analysis
THC	Total hydrocarbon emissions
TIM	Thermal Interface Materials
TLRP	Thermal Load Reduction Package
TN	Testing Network
TOU	Time-Of-Use
TSDC	Transportation Secure Data Center
TSI	Turbocharged stratified injection
TUSD	Torrance Unified School District
TXVs	Thermal Expansion Valves

U

U.S. DRIVE	U.S. Driving Research and Innovation for Vehicle Efficiency and Energy Sustainability
UA	Transfer Coefficient
UC	Ultra-capacitor
UCR	University of California, Riverside
UDDS	Urban Dynamometer Driving Schedule
UN ECE	United Nations Economic Council for Europe
UPS	United Parcel Service
URL	Uniform Resource Locator
US06	Environmental Protection Agency US06 or Supplemental Federal Test Procedure
USABC	United States Advanced Battery Consortium
USCAR	U.S. Council for Automotive Research
Util	Battery capacity utilization

V

V	Voltage
V2G	Vehicle-to-Grid
VAr	Volt-Amp-reactive
VGI	Vehicle-Grid Integration
VGT	Variable Geometry Turbocharger
VIP	Vacuum Insulated Panels
VMT	Vehicle Miles Traveled
VS	Vehicle Systems
VSATT	Vehicle Systems Analysis Technical Team
VSI	Vehicle Systems Integration
VSST	Vehicle Systems Simulation and Testing
VTCab	Vehicle Thermal Cab Simulator
VTIF	Vehicle Testing and Integration Facility
VTO	Vehicle Technologies Office

W

| dw | Change in Angle W |

WCC	Water Cooled Condenser
WEC	World Endurance Championship
WEG	Water/Ethylene Glycol
Wh	Watt hour
WHR	Waste Heat Recovery
WPT	Wireless Power Transfer
WTW	Well-to-Wheels

X

XFC	Extreme Fast Charging
XPS	x-ray photoelectron spectroscopy

Z

ZECT	Zero-emissions cargo transport

Executive Summary

During fiscal year 2022 (FY 2022), the U.S. Department of Energy (DOE) Vehicle Technologies Office (VTO) funded early-stage research, development, demonstration, & deployment (RDD&D) projects that address Electrification of the U.S. transportation sector. The VTO Electrification Program is composed of Electric Drive Technologies, and Grid Integration activities. The Electric Drive Technologies group conducts R&D projects that advance electric motors and power electronics technologies. The Grid and Charging Infrastructure group conducts R&D projects that advance grid modernization and electric vehicle charging technologies. This document presents a brief overview of the Electrification Program and progress reports for its R&D projects. Each of the progress reports provide a project overview and highlights of the technical results that were accomplished in fiscal year (FY) 2022.

Table of Contents

List of Figures

List of Tables

Vehicle Technologies Office Overview

Vehicles move our national economy. Annually, vehicles transport 18 billion tons of freight—about $55 billion worth of goods each day[1]—and move people more than 3 trillion vehicle-miles.[2] Growing our economy requires transportation, and transportation requires energy. The transportation sector accounts for approximately 30% of total U.S. energy needs[3] and the average U.S. household spends over 15% of its total family expenditures on transportation,[4] making it, as a percentage of spending, the most costly personal expenditure after housing. Transportation is critical to the overall economy, from the movement of goods to providing access to jobs, education, and healthcare.

The transportation sector has historically relied heavily on petroleum, which supports over 90% of the sector's energy needs today,[5] and, as a result, surpassed electricity generation to become the largest source of CO_2 emissions in the country.[6] The Vehicle Technologies Office (VTO) will play a leading role to decarbonize the transportation sector and address the climate crisis by driving innovation within and deployment of clean transportation technologies.

VTO funds research, development, demonstration, and deployment (RDD&D) of new, efficient, and clean mobility options that are affordable for all Americans. VTO leverages the unique capabilities and world-class expertise of the National Laboratory system to develop new innovations in vehicle technologies, including: advanced battery technologies; advanced materials for lighter-weight vehicle structures and better powertrains; energy-efficient mobility technologies and systems (including automated and connected vehicles as well as innovations in connected infrastructure for significant systems-level energy efficiency improvement); combustion engines to reduce greenhouse gas and criteria emissions; and technology integration that helps demonstrate and deploy new technology at the community level. Across these technology areas and in partnership with industry, VTO has established aggressive technology targets to focus RDD&D efforts and ensure there are pathways for technology transfer of federally supported innovations into commercial applications.

VTO is uniquely positioned to accelerate sustainable transportation technologies due to strategic public–private research partnerships with industry (e.g., U.S. DRIVE, 21st Century Truck Partnership) that leverage relevant expertise. These partnerships prevent duplication of effort, focus DOE research on critical RDD&D barriers, and accelerate progress. VTO advances technologies that assure affordable, reliable mobility solutions for people and goods across all economic and social groups; enable and support competitiveness for industry and the economy/workforce; and address local air quality and use of water, land, and domestic resources.

Annual Progress Report

As shown in the organization chart (below), VTO is organized by technology area: Batteries R&D; Electrification R&D; Materials Technology R&D; Decarbonization of Offroad, Rail, Marine, and Aviation; Energy Efficient Mobility Systems; and Technology Integration. Each year, VTO's technology areas prepare an Annual Progress Report (APR) that details progress and accomplishments during the fiscal year. VTO is pleased to submit this APR for Fiscal Year (FY) 2022. The APR presents descriptions of each active project in FY 2022, including funding, objectives, approach, results, and conclusions.

---

[1] Bureau of Transportation Statistics, DOT, Transportation Statistics Annual Report 2020, Table 4-1, https://www.bts.gov/tsar.
[2] Davis, Stacy C., and Robert G. Boundy. Transportation Energy Data Book: Edition 39. Oak Ridge National Laboratory, 2021, https://doi.org/10.2172/1767864. Table 3.8 Shares of Highway Vehicle-Miles Traveled by Vehicle Type, 1970-2018.
[3] Ibid. Table 2.2 U.S. Consumption of Total Energy by End-use Sector, 1950-2018.
[4] Ibid. Table 11.1 Average Annual Expenditures of Households by Income, 2019.
[5] Ibid. Table 2.3 Distribution of Energy Consumption by Source and Sector, 1973 and 2019.
[6] Environmental Protection Agency, Draft U.S. Inventory of Greenhouse Gas Emissions and Sinks, 1990-2019, Table 2-11. Electric Power-Related Greenhouse Gas Emissions and Table 2-13. Transportation-Related Greenhouse Gas Emissions.

Organization Chart

Vehicle Technologies Office Federal Staff

September 2022

Deputy Director Vacant		Director Michael Berube (Acting)

Batteries R&D	Electrification R&D	Materials Technology R&D	Decarbonization of Offroad, Rail, Marine, & Aviation	Energy Efficient Mobility Systems	Technology Integration	Operations
Program Manager: Brian Cunningham	Program Manager: Mike Weismiller	Program Manager: Sarah Ollila	Program Manager: Gurpreet Singh	Program Manager: Jake Ward* (Acting)	Program Manager: Mark Smith	Operations Supervisor: Sarah Ollila (Acting)

*based at NETL-Pittsburgh

Electric Drive Technologies Program Overview

Introduction

The Electric Drive Technologies (EDT) program's mission is to conduct early-stage research and development on transportation electrification technologies that accelerate the development of cost-effective and compact electric traction drive systems that meet or exceed performance and reliability requirements of internal combustion engine (ICE)-based vehicles, thereby enabling electrification across all light-duty vehicle types.

Goals and Objectives

The goal of the EDT program is to develop an electric traction drive system at a cost of $6/kW for a 100-kW peak system by 2025. In addition, the program has a 2025 power density target of 33 kW/L for a 100-kW peak system. While achieving these targets will require transformational technology changes to current materials and processes, it is essential for enabling widespread electrification across all light-duty vehicle platforms.

Program Design and Execution

The EDT program provides support and guidance for many cutting-edge automotive technologies now under development. Researchers focus on developing revolutionary new power electronics (PE), electric motor (EM), and traction drive system (TDS) technologies that will leapfrog current on-the-road technologies. This will lead to lower cost and better efficiency in transforming battery energy to useful work. Research and development (R&D) is also aimed at achieving greater understanding of, and improvements in how the various components of tomorrow's automobiles will function as a unified system.

In supporting the development of advanced vehicle propulsion systems, the EDT program fosters the development of technologies that will significantly improve efficiency, costs, and fuel economy.

The EDT program directs early-stage research through a three-phase approach intended to

- Identify overall propulsion- and vehicle-related needs by analyzing programmatic goals and reviewing industry recommendations and requirements, and then develop and deliver the appropriate technical targets for systems, subsystems, and component R&D activities.

- Develop, test, and validate individual subsystems and components, including EMs and PE

- Estimate how well the components and subsystems work together in a vehicle environment or as a complete propulsion system and whether the efficiency and performance targets at the vehicle level have been achieved.

The research performed under this program addresses the technical and cost barriers that currently inhibit the introduction of advanced propulsion technologies into hybrid electric vehicles (HEVs), plug-in HEVs, battery electric vehicles (BEVs), and fuel cell powered automobiles that meet the DOE goals.

A key element in making these advanced vehicles practical is providing an affordable electric TDS. This will require attaining weight, volume, efficiency, and cost targets for the PE and EM subsystems of the TDS. Areas of development include:

- Novel traction motor designs that result in increased power density and lower cost

- Inverter technologies that incorporate advanced wide bandgap (WBG) semiconductor devices to achieve higher efficiency while accommodating higher-temperature environments and delivering higher reliability.

- Converter concepts that leverage higher-switching-frequency semiconductors, nanocomposite magnetics, higher-temperature capacitors, and novel packaging techniques that integrate more functionality into applications offering reduced size, weight, and cost.

- New onboard battery charging electronics that build from advances in converter architectures for decreased cost and size

- More compact and higher-performing thermal controls achieved through novel thermal materials and innovative packaging technologies

- Integrated motor-inverter TDS architectures that optimize the technical strengths of the underlying PE and electric machine subsystems.

VTO competitively awards funding through funding opportunity announcement (FOA) selections, and projects are fully funded through the duration of the project in the year that the funding is awarded. The future direction for direct-funded work at the National Laboratories is subject to change based on annual appropriations.

Electric Drive Technologies Lab Consortium

The multi-lab EDT Consortium will leverage U.S. research expertise and facilities at the national labs and universities to improve the power density of electric drives by 10X compared with the 2015 numbers while reducing the cost by 50% and doubling the lifetime miles within the next 5 years. The final objective of the consortium is to develop a 100-kW traction drive system that achieves a power density of 33 kW/L, has an operational life of 300,000 miles, and a cost of $6/kW. The system will be composed of a 100 kW/L inverter and a >20,000 rpm, 50 kW/L electric motor.

The EDT Consortium's research consists of a multi-disciplinary team that will plan, establish, conduct, and manage a portfolio of multi-lab and multi-university research efforts to advance the state-of-the-art in electric drive technologies.

The consortium is organized around three Keystone projects: (1) Power Electronics; (2) Electric Motors; and (3) Traction Drive System. The consortium will focus on early-stage research projects on advanced materials, high-density integration of dissimilar layers/materials, multifunctional subcomponents, and optimized and new thermal/electrical/magnetic architectures. New materials such as WBG semiconductors, soft magnetic materials, and ceramic dielectrics, merged using multi-objective co-optimization design techniques, will be utilized to achieve the program goals. Moreover, integration of components and subcomponents will further propel the research toward the goals of the consortium.

Consortium National Laboratory members include Ames National Laboratory, The National Renewable Energy Laboratory (NREL), Oak Ridge National Laboratory (ORNL), and Sandia National Laboratories (SNL). University consortium partners include North Carolina State University, The University of Arkansas, Virginia Polytechnic Institute, University of Wisconsin-Madison, Georgia Institute of Technology, University of California-Berkeley, Illinois Institute of Technology (IIT), Purdue University, The State University of New York (SUNY), and The Ohio State University.

Technical Targets & Status

Target Definition

The technical targets for the electric traction drive system (ETDS) are based upon what is needed for EDVs to be competitive in performance and economics with ICE vehicles. The targets recognize the need to provide solutions that enable all vehicle segments to be addressed by providing a better value proposition to consumers. Providing consumers with a better value proposition will ensure the market adoption will occur. Achieving these aggressive targets will require major technological breakthroughs through early-stage research. In order to establish U.S. industry as a leader in electrification, it is critical that this early-stage research can be translated into competitive advantages for industry in the U.S. The technical breakthroughs need to focus on those technologies that can be best taken advantage of by a highly skilled and capitalized industrial base. Consumers want to see vehicles that are more usable, functional, and cost effective to operate. This translates into high-density packaging of power electronics and electric motors, high drive cycle efficiency, reliability, and cost effectiveness. Accomplishing this will come from creating new materials and enabling higher orders of integration to occur from in-situ fabrication. The EDTT metrics focus on key issues related to component cost and size to enable widespread acceptance of these vehicles. The metrics are normalized based on a component or system peak power rating into cost per kilowatt ($/kW) and power density (kW/liter).

Cost

Ultimately, the purchase price of EDVs should be comparable ICE vehicles, but also be able to provide greater value to the consumer. The cost targets in this roadmap allow for a small initial price premium, but the cost difference should be no greater than 3 years of fuel cost savings. As part of the U.S. DRIVE 2025 target-setting process, vehicle-level modeling and simulation in Autonomie was carried out by the ISATT (Integrated Systems Analysis Technical Team), and for EDTT the result was $6/kW for a 100 kW peak power ETDS. While the 2025 target was derived based on consumer fuel savings payback expectations, EDV use in mobility as a service (maas) fleet applications will likely shift focus to lifetime cost and make the EDV business case more favorable.

Power Density

Power density is a very important target because of limited space "under the hood" and on the vehicle in general. Packaging constraints vary with the different vehicle types: for PHEV architectures, the ETDS must be added to a conventional ICE vehicle (i.e., a secondary drive train) as well as a high-voltage battery, DC/DC converter and on-board charger; for BEV applications, the space constraints are different, primarily driven by the large battery size and a small vehicle footprint to achieve acceptable driving range (200 miles for 2020 and more than 300 for 2025). For BEV applications, the design freedom enabled by the lack of requirements for the ICE compartment and driveline tunnel, which manufacturers typically use to expand the passenger and cargo space, further limit ETDS component packaging to around the battery, in the chassis alongside steering and suspension, and distant from vehicle crash zones. Increased power density is required to address these packaging constraints and to enable a skateboard-like chassis design that allows widespread electrification across all vehicle platforms.

Reliability

Previous EDTT's reliability targets were set to the traditional automotive life of 15 years or 150,000 miles. Longer range EVs (200+ miles) are starting to be tested in MaaS/fleet applications due to lower operating costs compared to ICE vehicles. HEVs and PHEVs are also gaining popularity in MaaS applications because they can run power accessories at "idle" without running the ICE, thereby saving on fuel costs. Some of the taxi-like MaaS applications (up to 20 hours per day of operation) can accumulate between 50,000 to 80,000 miles per year. Several automotive OEMs, including Ford, Stellantis, General Motors, Tesla and Volkswagen and a number of startups have indicated significant interest in EDV use for MaaS/Delivery, and recent literature and analysis reports see synergy between electrification and automation. Meeting the future EDTT targets by reducing the costs and size of ETDS components would accelerate market penetration of EDVs in

MaaS/Delivery applications and thereby significantly increasing energy efficiency and reducing emissions (greenhouse gas and criteria pollutants) per vehicle mile traveled. Mileage accumulation, and therefore vehicle turnover is a lot faster for MaaS/Fleet; hence, it presents an opportunity for much faster and greater impact of reducing petroleum use in the transportation sector. This is the driver for the EDV EDTT reliability requirement of 300,000 miles or 15 years.

Electric Traction Drive System Targets

The technical targets for 2025 shown in Table 1 are appropriate for all EDV applications. The targets are progressively increased starting at 100kW in 2025 and increasing until the year 2035. This is to accommodate the addition of new vehicle types and their associated requirements. The target includes high-voltage power electronics (one inverter and if needed a boost converter) and a single traction-drive electric motor.

Table 1. Technical Targets for Electric Traction Drive System

ETDS Targets			
Year	2025	2030	2035
Power Level kW (Peak)	100	150	225
Voltage	600	800	800
Cost ($/kW)	6	4	2.67
Power Density (kW/L)	33.3	50	75

High-Voltage Power Electronics Technical Targets

An approximate allocation of the targets for the high-voltage power electronics is shown in Table 2. The values estimate how much can be achieved with improvements to the high-voltage power electronics and are consistent with the system-level targets. The targets in Table 1 refer to a single power inverter and a boost converter if applicable; the DC/DC converter for powering the auxiliary loads and the on-board charger have their own targets, and are not included in the table.

Table 2. Technical Targets for High-Voltage Power Electronics

Power Electronics Targets			
Year	2025	2030	2035
Power Level kW	100	150	225
Voltage	600	800	800
Cost ($/kW)	2.70	1.80	1.20
Power Density (kW/L)	100	150	225

The 2025 power electronics cost, and volume targets are driven by the opportunity to replace silicon switches with WBG devices which can significantly reduce the size of the power modules while enabling operation at higher temperatures and frequencies. WBG devices are significantly costlier than silicon equivalents but enable overall power electronics cost to decrease due to the system cost reductions. Secondary-level targets or more appropriately technical guidelines for advanced integrated power module (AIPM) design are included in Appendix A.

Electric Traction Motor Technical Targets

Although the technical targets have been established at the system level, an approximate allocation of the targets between the electric traction motor and the high-voltage power electronics is useful as guidance for projects that address one or the other. The values in Table estimate how much can be achieved with improvements to the motor and, along with comparable numbers for the power electronics, are consistent with the system-level targets.

Table 3. Technical Targets for Electric Traction Motor

Electric Motor Targets			
Year	2025	2030	2035
Power Level kW	100	150	225
Voltage	600	800	800
Cost ($/kW)	3.30	2.20	1.47
Power Density (kW/L)7	50	75	112.5

Certain motor designs may have an impact on the weight, volume, and cost of other parts of the vehicle. Many hybrid vehicle architectures require two electrical machines to optimize for vehicle efficiency, one as a motor and another as a generator. Some of the architectures make use of a single machine for both purposes for cost and packaging reasons. The targets in Table 1 and Table refer to a single electric machine used for traction drive, specifically its rotor, rotor shaft, stator with end windings, housing and cooling, but not the reduction gearing.

The 2025 electric motor cost and volume targets are driven by the opportunity to reduce material use with better application of existing or use of new materials to improve motor performance.

Electric Drive Technologies Research Highlights

Edge Termination for Vertical Gallium Nitride Power Devices in Electric Drivetrains

Power Devices with Increased Efficiency and Power Density to Support Next-Generation Electric Drivetrains

Sandia National Laboratories

Next-generation power electronics are leveraging the advantages of wide-bandgap semiconductors to push for higher power densities and higher efficiency. In electric vehicle drivetrains, this translates to lighter-weight systems and more miles per charge. Vertical gallium nitride (GaN) power devices promise an advantage over silicon, or even silicon carbide, by leveraging a large breakdown electric field and, compared to lateral GaN, offer increased power densities for high-voltage and high-current applications.

---

[7] 2020 power density target was based on 55 kW peak power at a 325 V nominal DC and resulted in 9.6 L motor volume; 2025 target is based on 100 kW peak power at a 650 V nominal DC resulting in a 2L motor volume.
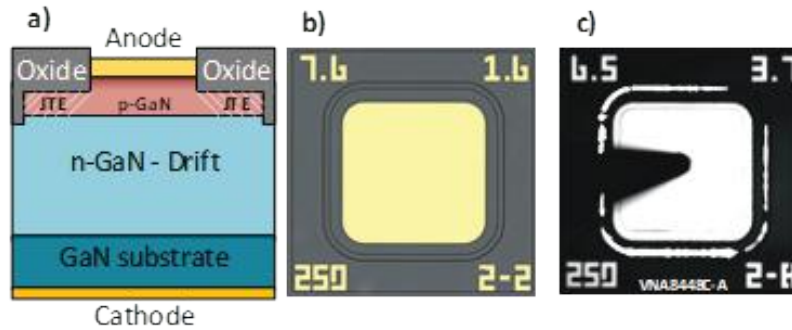
Figure 1 Representative structure (a) of the single-zone JTE vertical GaN on fabricated diodes, (b) an optical image of the fabricated device, and (c) electroluminescence of the diode under high reverse bias during avalanche showing emission at the oute

A key aspect of designing high-voltage vertical power devices is minimizing electric field crowding at the periphery of the device, which otherwise causes premature device breakdown. Because of limitations surrounding selective-area doping in GaN, many conventional methods for edge termination are not viable. The Sandia team has developed a process for edge termination in vertical GaN power devices and has reported a multipoint fit from theory to experiment, which marks a milestone of maturity for these devices.
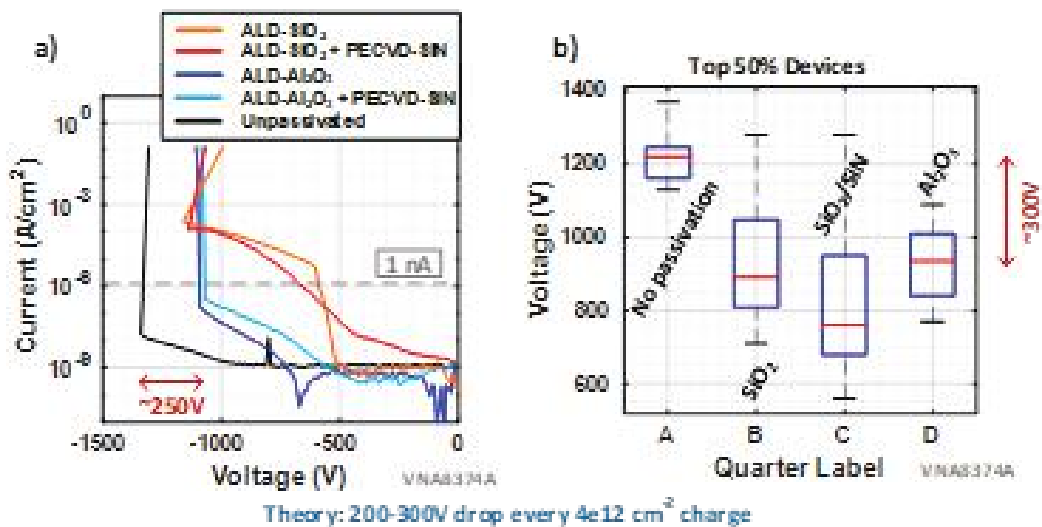
Figure 2 Results from a passivation study showing (a) reverse current-voltage characteristics comparing various passivation films against an unpassivated "baseline" device, and (b) the statistical breakdown data nominally demonstrating a ~300 V drop.

The Sandia edge termination strategy consists of a multi-zone junction termination extension (JTE) where the charge in the edge termination is proportional to the electric field at breakdown. To correctly design a multi-zone JTE, it is necessary to understand the optimal design point for a single-zone JTE and the sensitivity of breakdown voltage to JTE thickness, and to adjust for any offsets due to non-idealities.
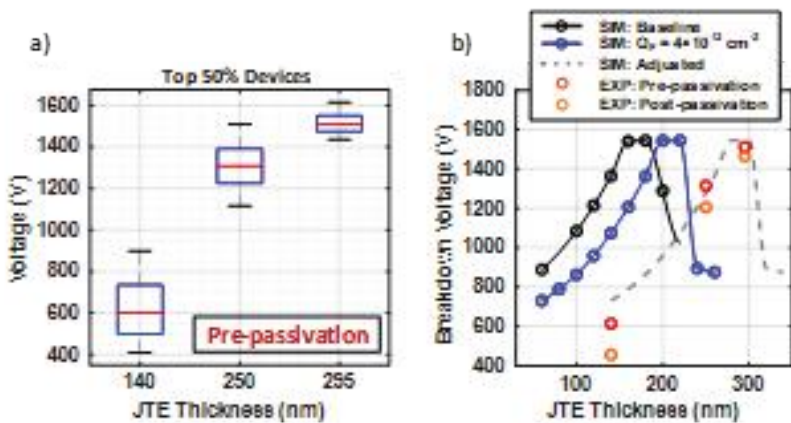
Figure 3 Results from the JTE study showing (a) statistical breakdown data versus JTE thickness (pre-passivation), and (b) a comparison between the theoretical model and experimental results.

This study (Figure 1) demonstrates the impact of charge in the passivation on edge termination design (Figure 2) and the impact of JTE thickness on breakdown voltage (Figure 3), allowing for an optimized JTE design that maximizes the potential of vertical GaN devices.

Power Block for Integrated Electric Drive

High-Power-Density Power Block for Integrated Drive

Oak Ridge National Laboratory

Researchers have designed a building block for power electronics (see Figure 4). The "power block" contains a silicon carbide (SiC) power module, gate driver, capacitor, and busbars—components needed for the technology to operate independently. Traditionally, these components are designed separately and integrated to form an inverter–converter system, but this approach can lead to voltage spikes. To achieve better performance, power electronic components must be co-optimized and co-designed. Oak Ridge is using multiple power blocks to develop an inverter–converter with little or no compromise on performance.
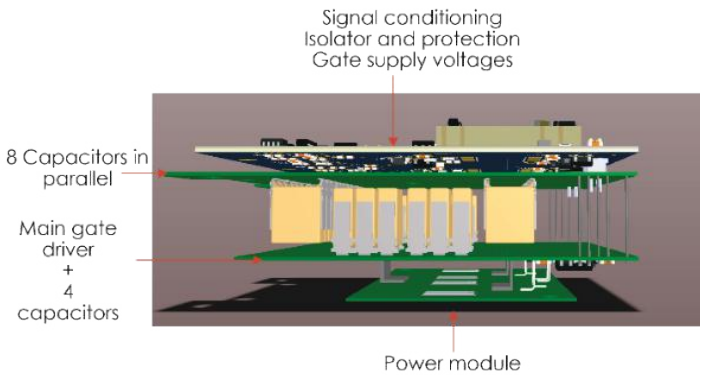
Figure 4 Assembled power block containing an SiC module, capacitor, gate driver, and protection circuitry

The power block components are shown in Figure 5. The module was designed to handle 800 V and 150 A currents. A gate driver board with decoupling capacitors was added on top of the module to reduce the gate loop and power loop inductance (a primary cause of voltage overshoot). A secondary capacitor board on the gate driver board handles higher currents and suppresses voltage oscillation. The entire capacitor board was designed to handle more than 80 A ripple current. The capacitors were also placed symmetrically from the termination to achieve low layout inductance and equal current-sharing among the parallel capacitor branches. Finally, a gate driver power supply board with protection circuitry is placed.
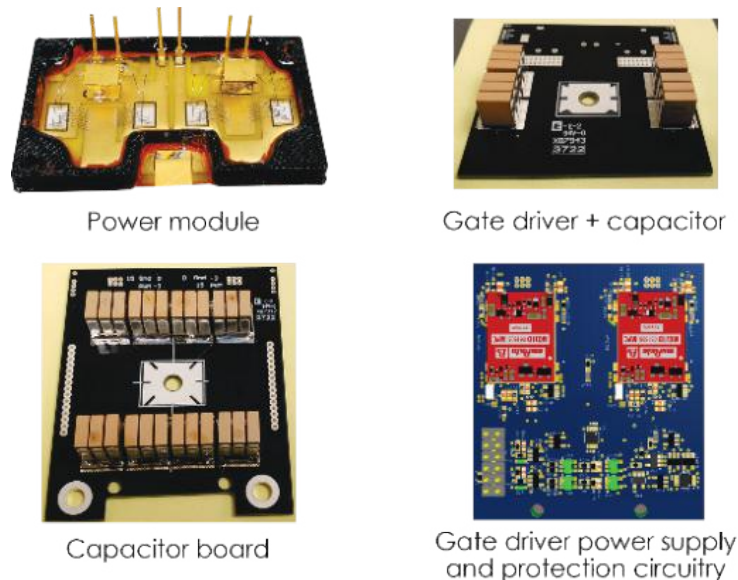
Figure 5 Power Block Components

The power board was then evaluated using a double pulse test setup where the DC bus was 800 V and the current was 150A, shown in Figure 6. The test measured output/inductor current, showing 250 V overshoot at 800 V (1050 V at the device terminal) and 150 A operation—well within the manufacturer voltage limit of 1200 V. Researchers calculated total power loop inductance ($\approx$ 27 nH) and power module inductance (20 nH) and estimated the layout inductance of the capacitor board and busbars (7 nH). The module inductance dominates the power loop inductance and can be further optimized.
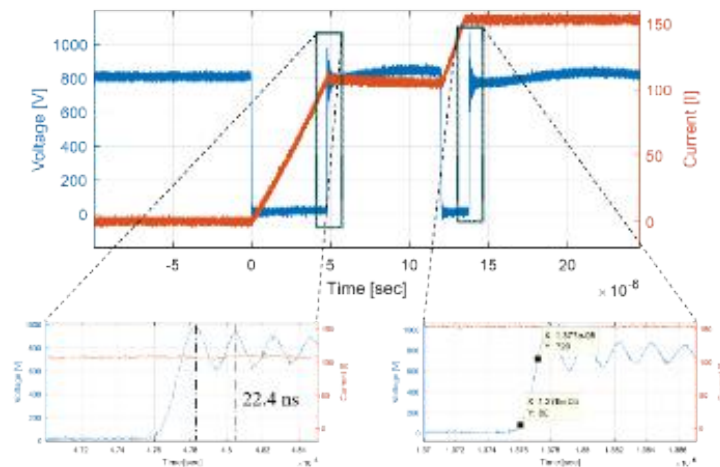
Figure 6 Double pulse test results showing 800 V up to 150 A operation with fast voltage rise to minimize switching loss.

Development of a Cost-Effective Manufacturing Process for High-Performance Soft Magnetic Materials

Scalable Processing of High-Silicon Steel Laminates and Stator Shapes

Ames National Laboratory

Ames National Laboratory (AMES) researchers have developed a highly simplified, cost-effective method of manufacturing 6.5% silicon (Si) steel for electric drive motor applications. The steel typically used today, which has 3.2% Si, gives rise to high core (power) losses, especially at higher motor speeds (Figure 7). Using steels with high Si content improves efficiency, thanks to the steels' higher capacity for magnetism and greater

electrical resistivity, which helps overcome core loss. However, steel with high Si content is brittle and hard to manufacture. The AMES approach is based on a method that solidifies steel at high rates of cooling, bypassing the transition that leads to brittleness. This 6.5% Si steel has higher electrical resistivity than 3.2% Si steel and higher saturation magnetization than other advanced/costly soft magnetic materials, e.g., nanocrystalline or amorphous alloys.
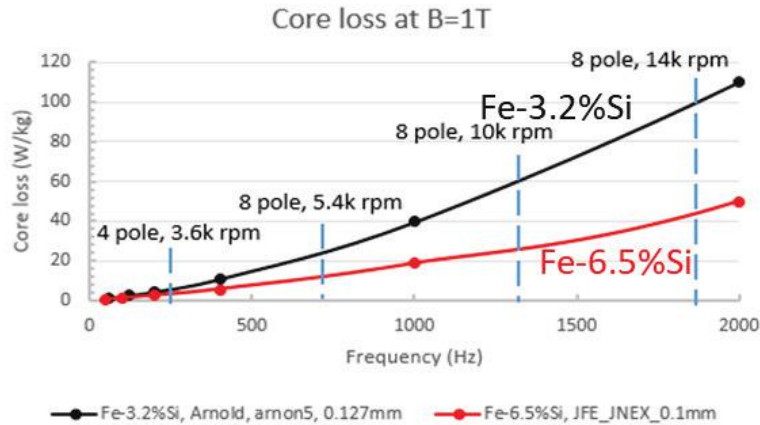
Figure 7 Comparison of motor core loss of commercially available Fe-3.2Si and Fe-6.5Si in a motor setting.

AMES researchers used rapid solidification to prepare thin ribbon made of an iron–silicon alloy with 6.5% Si (Fe-6.5%Si). They formulated and optimized a wire bundle concept for near-net-shape fabrication of stator segments (Figure 8) using the melt-spun 6.5% Si steel ribbon. Ribbons are insulated by a self-grown oxide, which the AMES team is currently optimizing.
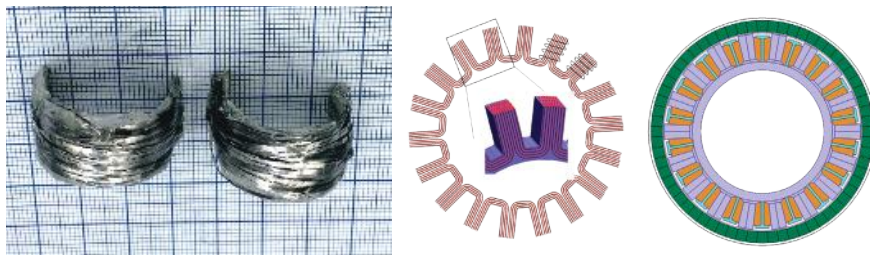
Figure 8 a) Demonstration of AMES wire bundle concept; b) wire bundle stator, c) stator and rotor assembly (Oak Ridge National Laboratory).

Regarding production challenges, the 6.5% Si steel sheet is a drop-in replacement for conventional 3.2% Si steel laminate production. The 6.5% Si steel can eliminate many heating and rolling steps typically used (Figure 9) and is likely to offer significant cost and energy savings.

Steps for Fe-3.2%Si

Casting, 200-250mm
Pre-heating + Pre-rolling
Reheating (up to 1400°C) +Rough rolling 40-80mm
Hot finishing rolling 2-3 mm
Hot strip annealing

+

Fist cold rolling
Intermediate annealing
cold rolling 0.23-0.35 mm
Decarburization
Anneal, separator coating

+

Anneal (up to 1200°C)
Insulation coating
Thermal flattening
Domain refinement

Steps for Fe-6.5%Si

Melt spinning to 0.02-0.01 mm
Anneal (up to 1100°C)
Insulation coating

Figure 9 Number of steps needed to make Fe-3.2%Si and Fe-6.5%Si, as well as their iron losses at various conditions.

This wire (ribbon) bundle concept not only simplifies the manufacturing process but also contributes to enhanced magnetic flux density and reduced core losses. However, making full-width Fe 6.5%Si laminate foil presents technical challenges. It has a high melting point and requires improved wetting on the quench wheel without lowering saturation magnetization.

Electric Motor Cooling Concept for Increased Power Density

Cooling End Windings of Electric Motors

National Renewable Energy Laboratory/Georgia Institute of Technology
The National Renewable Energy Laboratory (NREL) and Georgia Institute of Technology (Georgia Tech) have collaborated to develop an electric motor cooling concept to cool electric motor end windings directly. Advanced thermal management designs are needed to increase motor power density. Power density increases efficiency and reduces material costs, but it is often limited by the magnet wire used in electric motors because of the temperature limit of the magnet wire coating. The end windings of a motor produce considerable heat. They have irregular surfaces, making it difficult to incorporate a proximate thermal management strategy. End windings are a common hot spot and limiting factor in motor thermal management.

The NREL–Georgia Tech team retrofitted the cooling concept shown in Figure 10 to a commercial electric vehicle motor (Nissan Leaf). The concept included an end cap, separation wall, and channel cavity and was fitted into a commercial water jacket, as shown in Figure 10. A water–ethylene glycol (WEG) mixture (50–50 by volume) at 65°C temperature was circulated through the channel cavity to provide cooling. The channel cavity was filled with a high-performance potting compound to facilitate heat transfer from the end windings to the concept cooler. The concept appears sufficiently robust to work with different coolant temperatures that might be encountered within an automotive environment.
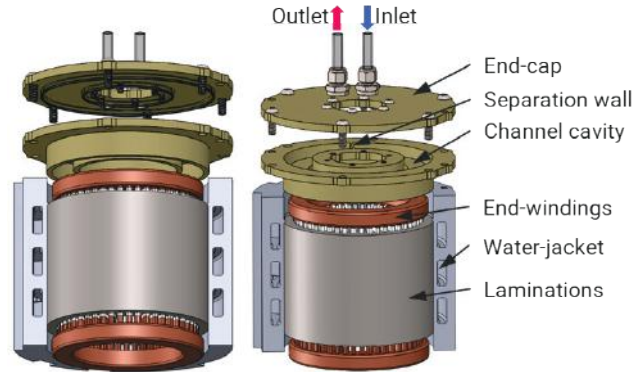
Figure 10 Section view of proposed motor end-winding cooling concept.

The cooling concept demonstrated a 30%–45% decrease in motor end-winding temperatures relative to the commercial baseline. This result should enable increased motor power density. Furthermore, the concept is straightforward to incorporate into the existing cooling loop and thus is scalable for commercial production. The concept might also enable integration of the electric motor and power electronics thermal management system utilizing the WEG coolant.
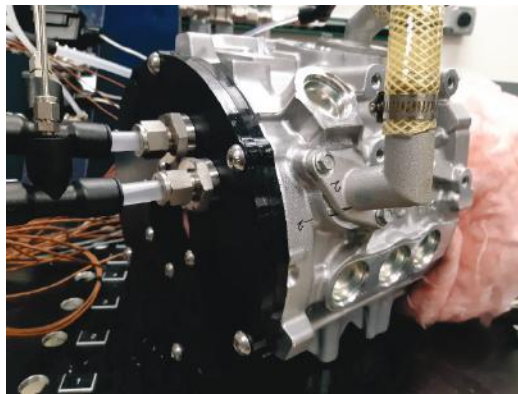
Figure 11 Assembled motor end-winding cooler at NREL. Photo Credit: Sebastien Sequeira, Georgia Tech/NREL.

With the cooling concept, the copper content (windings) in the motor can be reduced, and the separate oil pump and heat exchanger could potentially be eliminated. Future work could investigate the torque characteristics of the motor incorporating this concept. The channels could also be incorporated into the motor housing.

DC-Ripple-Energy Adaptive-Minimization (DREAM) Modulation for a High-Power Density Inverter

A New Modulation Scheme that Reduces Capacitor Current by up to 70%

Oak Ridge National Laboratory

Researchers have developed a method to reduce ripple current in an electric drive system: DC-ripple-energy adaptive-minimization (DREAM). DREAM addresses a major power-density and reliability hurdle of these systems: the direct current (DC) bus capacitor. Drive systems include a motor drive inverter with switches that regulate current and voltage, and these switches generate large ripple currents; the DC bus filter capacitor absorbs the currents for a constant flow into the battery. The capacitor takes up much space in the inverter but because it must be sized to meet the ripple current, is hard to shrink. A dual-inverter-based segmented drive can reduce the ripple current by 47% (vs. a non-segmented drive); DREAM can increase this reduction.

Figure 12 shows a segmented drive system with two inverters. The dual three-phase inverter system comprises six power switches (S1–S6) for each inverter and a DC bus filter capacitor. In one switching period, the motor

currents (i_a, i_b, i_c) are relatively constant, and the inverter DC side current i_{inv} is determined by the switching state of the six switches through modulation. Since the capacitor current iC_{bus} equals $i_{bat} - i_{inv}$, it is minimized when i_{bat} stays close to i_{inv}. The DREAM modulation can achieve this by selecting the optimal switching states of S1 to S6 adaptively across different motor operating conditions, so the DC ripple energy in the capacitor Cbus is always minimized.
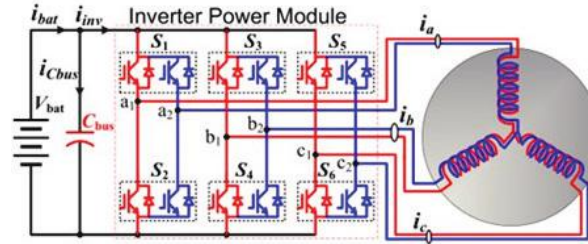
Figure 12 A segmented drive system and its possible inverter current values i_{inv} for a given battery current i_{bat}.
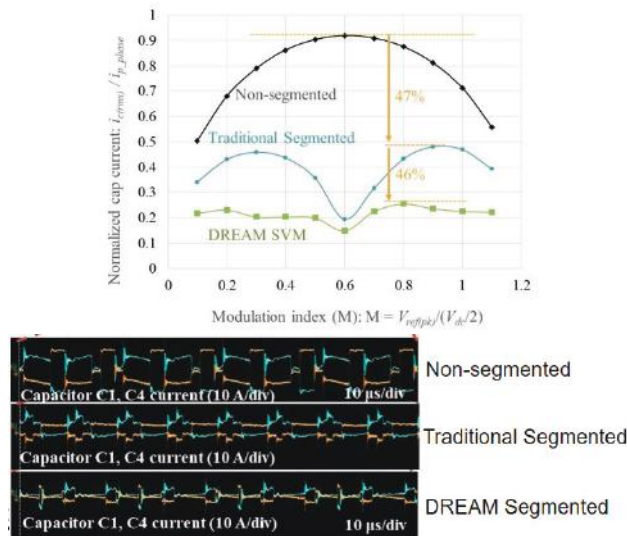
Figure 13 Simulated performance (top) and experimental waveforms (bottom).

Figure 13 (top) shows the normalized capacitor currents, comparing non-segmented, traditional segmented, and DREAM modulation. The DREAM modulation reduces the worst-case capacitor current by 46% more than the traditional segmented scheme. Experimental waveforms (bottom) show that DREAM reduces capacitor current magnitude by 38% against the traditional segmented scheme and by 70% against the non-segmented scheme.

The reduction in capacitor current ratings can lead to smaller capacitor size, which will improve the overall inverter power density. For example, film capacitor volume can be reduced by 77% when the rated current is cut by 70%.

Grid and Infrastructure Program Overview

Introduction

The Grid and Charging Infrastructure (G&I) program's mission is to conduct early-stage research and development on transportation electrification technologies that enable reduced petroleum consumption by light, medium, and heavy-duty vehicles. The program identifies and enables the role of vehicles in the future electrical grid.

Charging of EVs at scale creates an unpredictable and stochastic load demand on the electric grid. Newer EVs being introduced in the market can charge at low and high rates based on the need and availability of charging infrastructure. Additionally, charging profiles for EVs manufactured by different Original Equipment Manufacturers (OEMs) vary significantly which complicates meeting the aggregated charging loads. This creates difficulty in the prediction of magnitude, location, and timing of charging loads and could potentially have a detrimental grid impact.

To enable successful deployment of EVs at scale, a holistic approach is required across the vehicle, charging infrastructure, and electric grid. Figure 14 presents the key components of charging ecosystems that create challenges to be addressed. This includes controls, high voltage power electronics, interoperability, wireless and other advanced high power charging (HPC) technologies, and integration and optimization with the grid and Distributed Energy Resources (DERs) such as stationary storage and photovoltaics.

Figure 14 Key technologies and challenges addressed by the Grid and Infrastructure Program.

Hence, the effective control and optimization of the charging ecosystem is essential and is otherwise known as Smart Charge Management (SCM). SCM emphasizes the identification of pathways to reduce the potential grid impacts of EVs at scale, while providing enhanced value for EV/charging/grid systems including reduced costs and increased opportunities for grid services. If unmanaged, EVs at scale connecting to the grid would create numerous challenges for utilities, particularly at the distribution level, such as feeder voltage violations, system imbalances, flickers, equipment overloading, and large increases in daily peak loads. Interoperability and scalability, and high-speed communications and control are critical challenges facing SCM. Effective SCM will enable response to inappropriate energy management, malfunctioning equipment, and Cyber-Physical Security (CPS) breaches. SCM can also facilitate the provision of grid services from EV charging, including, but not limited to, peak load shaving, demand charge mitigation, voltage support, frequency regulation, and integration of renewable energy generation.

HPC of up to 400 kW for light-duty (LD) EVs, and 1+ MW for medium-duty (MD) and heavy-duty (HD) EVs, can enable greater vehicle utilization, extended range, and reduce recharging times. Technical advances are steadily being made with regards to HPC, but further progress is needed to facilitate the mass market adoption

of EVs. Specific technical challenges include the requirement for intelligent design and integration with the grid and DERs, to mitigate ramp rates and surge power demands, lower system cost of ownership, and interoperability of HPC infrastructure with MD and HD EVs. Additionally, as the charging power levels steadily increase, new challenges are manifested in ensuring HPC is effectively integrated with the grid in an efficient, flexible, and secure manner. High voltage power electronics and materials with better thermal and electrical properties are key enabling technologies for advancing HPC. Furthermore, improvements in wireless charging are required including the development of novel coils, advanced field shaping techniques, and control strategies.

Rapidly increasing numbers of EVs with advanced communication functionalities and networked chargers, as well as the trend towards HPC, dramatically increase cyber related risks and consequences. Coordinated cyber-attacks on chargers/charging stations can lead to serious local and potentially broader grid disruptions such as wide-scale blackouts and/or brownouts. A comprehensive understanding of the threat environment, including risks and consequences therein, is needed to identify, minimize, and/or eliminate critical cyber-physical vulnerabilities. Advances are required in strategies, systems, and tools, including hardware/software for intrusion detection, threat mitigation and isolation, and charging system recovery.

Addressing the barriers above can only be done by conducting high risk projects that are beyond the suitable scope and developmental timeframes of industry. Furthermore, the transportation and utility sectors historically have not worked together, which complicates collaboration. A significant level of pre-competitive and vendor-neutral Research and Development (R&D) effort is needed to address the challenges associated with a safe and secure charging ecosystem for EVs at scale.

State of the Art

Electric Vehicle Charging

It is desirable to reduce EV refueling times to be competitive with conventional vehicle refueling times (e.g., 5-10 minutes for 400 miles of LD vehicle driving range). The table below lists the refueling characteristics of several types of installed commercial chargers and a conventional gasoline fueling pump. The technologies employed in the EV charging stations are shown in the figure below. It is important to note that the rate of energy transfer peaks early in the charging cycle and decreases as the battery pack approaches 100% state of charge (SOC). While the energy transfer rate is not constant during charging, given two chargers with different peak power ratings the charger with the higher peak power rating is potentially capable of minimizing EV charging times when compared to the EVSE with a lower maximum power rating. It is notable that the EV must be capable of accepting the higher power provided by the EVSE with the higher maximum power rating. To accomplish this capability some vehicle OEMs are increasing the operating voltage of the on-board battery pack and the maximum C-rate for charging battery cells. Currently Electrify America offers commercial charger solutions with peak power rating of 350 kW DC.[8] However, currently the maximum charge rate that is accepted by a LD vehicle is 300 kW DC (Lucid Air, 900V+ electrical architecture). This LD vehicle can add 20 miles of range per minute when charging at this maximum charge rate using a 350 kW DC Fast Charger (CCS Charging Standard).[9]

Charging Standards

In the U.S. there are two existing open fast charging standards and a third charging standard is "in-development" and listed as a "Work in Progress" by SAE. The two open fast charging standards on the market today CCS and CHAdeMO were both originally designed to work at 400V and have evolved to increase their peak charging power ratings. As of August 2023, The "North American Charging Standard" (NACS) has been widely deployed at Tesla Superstations in North America and is currently being developed by SAE's Hybrid-

---

[8] https://electrify-commercial.com/ 1/25/2021
[9] Source: https://www.lucidmotors.com/media-room/lucid-air-fastest-charging-ev/. August 2020

EV J3400 NACS Electric Vehicle coupler Task Force.[10]. The development of the SAE J3400 NACS has significance and urgency in the context of NACS adoption announcements by nine automakers, four charging networks, four charger manufacturers, and one EV developer during 2023[11]. In 2023, several EV manufacturers announced agreements with Tesla to allow their EV customers to start accessing the Tesla charging network[12] [13]. The EV manufactures will start integrating NACS charging into their future EVs builds[14]. An adapter can be used to enable EVs with CCS connectors to charge using the Tesla charging stations.

The Combined Charging System (CCS) is an open, universal, and international charging system for electric vehicles based on international standards. It provides the solution for all charging requirements. The Combined Charging System is therefore ONE system for ALL. The CCS combines single-phase with fast 3-phase AC charging using alternating current of maximum of 43 kW. It also provides very fast high-power DC charging (up to 450 kW) within a single system. Members are presently also working on a High-Power charging connector for commercial vehicles that can take multiple MW charging power. This extended High-Power charging will be used for specialty EV like busses, truck, etc. The CCS system includes the connector, the managing of control functions and the charging communication between electric vehicle and infrastructure.[15] The standard is backed by major European and U.S. OEMs.

CHAdeMO was an initiative of Japanese car companies and was originally designed to charge at up to 50 kW at 400V.

The mid-term objective of XFC is to reduce LD charging time to approximately 10 minutes via a charge rate of approximately 350 to 400 kW. The long-term objective is to achieve charge rates of greater than 1 MW that will enable fast charging of both LD and Heavy Duty (HD) vehicles. The CHARIN connector standard is dedicated to achieving charge rates of up to 4 MW.

In addition to the conductive charging standards discussed above the wireless power transfer standard J2954 addresses charging of LD vehicles at peak rates of 22 kW and MD/HD vehicle charge rates of approximately 500 kW.

Currently Installed Charging Systems in the U.S

The characteristics of charging stations that are currently installed in the U.S. are provided in Table 4 and are included in Figure 15.

---

[10] https://standardsworks.sae.org/standards-committees/hybrid-ev-j3400-nacs-electric-vehicle-coupler-task-force. Accessed 9/21/2023.
[11] "More automakers plug into Tesla's EV charging network", Reuters,, September 21, 2023. https://www.reuters.com/business/autos-transportation/more-automakers-plug-into-teslas-ev-charging-network-2023-09-21/
[12] https://media.ford.com/content/fordmedia/fna/us/en/news/2023/05/25/ford-ev-customers-to-gain-access-to-12-000-tesla-superchargers--.html. 5/25/2023.
[13] https://www.media.volvocars.com/global/en-gb/media/pressreleases/316416/electric-volvo-car-drivers-will-get-access-to-12000-tesla-superchargers-across
[14] https://www.caranddriver.com/news/a44133661/gm-electric-vehicles-tesla-charging-2024/
[15] https://www.charinev.org/faq/ 1/25/2021.

Table 4 Light Duty Conventional and Electric Vehicle Refueling Characteristics

Type of Refueling	Gasoline	Level 1 110V (~1.4 kW)	Level 2 220V (~7.2 kW)	DC Fast Charger (50 kW, 150 kW, 350 kW)	Tesla V2 & V3 SuperChargers (145 kW,250 kW)
Range per Charge Time	400 miles /5 mins	3–5 miles /60 mins	25 miles /60 mins	50 kW: 150 miles /90 mins	250 kW:~360 miles[16] /60 mins
Time to Charge for 200 miles	<5 mins	37 hours	8 hours	50 kW: 2 hours	250 kW: 24 mins
Number of U.S. stations/connectors circa 2023[17]	153,000	676/3130	54,038/129,184	8,255/34,281	1,911/21,039

The summary of charge connector standards provided in the figure below includes the connector diagram, maximum output power, applications, and development status for each of the connector standards. It is notable that several of these charging standards are evolving as evidenced by the frequency of the "in development" and "updating" status of the charge connector standards in Figure 15.

---

[16] Source: Tesla Model 3 range, battery & charging, June 2021. https://www.drivingelectric.com/tesla/model-3/range
[17] Source: Alternative Fuels Data Center, National Renewable Energy Laboratory, June 2021. https://afdc.energy.gov

Diagram	Main Standard/ System	Maximum Output Power, Volts, Amps	Standard Status as of August 2023	Application Notes
	SAE J1772 / AC Level 1, AC Level 2	19.2 kW AC, 208/240VAC., 80A	Released	Used for Level 1 and Level 2 in North America. Commonly found on home, workplace, and public chargers.
	SAE J1772+ IEC 61851 / CCS1	450 kW DC, 1000VDC, 500A	Updating	Used for DC fast charging most vehicles in North America. Generally installed at public chargers.
	IEC 61851 IEEE 2030.1/ CHAdeMO	400 kW DC, 1000VDC, 400A	Released	Used for DC fast charging select vehicles in North America. Generally installed at public chargers.
	SAE J3400 / NACS	250 kW DC, 410VDC, 610A	In-development	Used for both AC and DC fast charging. Standard is under development and is based on Tesla's design.
	SAE J3068	166 kW AC, 600VAC, 160A / 450 kW DC, 1000VDC, 450A	Updating	Standard for both AC and DC charging using the IEC 61851 'type 2' connector for North America three-phase charging.
	SAE J2954	22 kW AC light duty, 480VAC, 30A / 500 kW AC heavy duty, 480VAC, 670A	Released	Wireless power transfer standard for MD/HD vehicles is J2954/2. In U.S. the maximum power for light-duty is 11KW (WPT3).
	SAE J3105	1.2 MW DC, 1000VDC, 1200A	Released	Automated connection device to charge MD/HD vehicles. Variants include pantograph up or down and pin-and-socket.
	IEC 61851 IEEE 2030.1 / Chaoji	900 kW DC, 1500VDC, 600A	In-development	Sub-MW conductive charging for LD/MD/HD vehicles in Asia
	SAE J3271 IEC 63379 / MCS	3.75 MW DC, 1500VDC, 3000A	In-development	Conductive MW level charging for MD/HD vehicles.

Figure 15 Examples of EV Connector Standards, Sources:ANL[18], SAE[19,20,21], ORNL[22] , CEC [23,24,25,26,27,28,29]

[18] ANL T. Bohn, "Global DC Charging Systems" SAE Committee Presentation Slide (draft) August 2023.
[19] SAE 2022 "Wireless Power Transfer for Heavy-Duty Electric Vehicles J2954/2_202212",
https://www.sae.org/standards/content/j2954/2_202212/.
[20] "SAE PUBLISHES TIR J2954, WIRELESS POWER TRANSFER EV/PHEV",31 May 2016 | Jesse Schneider, David Law,
https://www.standardsuniversity.org/e-magazine/june-2016/sae-publishes-tir-j2954-wireless-power-transfer-evphev/
[21] SAE 2023 "WIP 2023-7-11 SAE J3400: NACS Electric Vehicle Coupler J3400", https://www.sae.org/standards/content/j3400/
[22] ORNL Veda Prakash Galigekere and Omer Onar, Interview by author, September 26, 2023.
[23] U.S. Department of Energy Alternative Fuels Data Center. "Developing Infrastructure to Charge Plug-In Electric Vehicles."
https://afdc.energy.gov/fuels/electricity_infrastructure.html
[24] CharIn. 2020 "Mapping Standards for Low- and Zero-Emission Electric Heavy-Duty Vehicles," presentation. International Transportation Forum February 18-20, 2020 Workshop. https://www.itf-oecd.org/sites/default/files/docs/charging-infrastructure-standardisation-developments-bracklo.pdf.
[25] ChAdeMO. "Technology Overview." https://www.chademo.com/technology/technology-overview/.

Prototype Charging Systems

The research community has developed prototypes that charge at rates greater than 400 kW.

Light Duty Charging Station Prototype

Initiated in July 2016, the "Fast Charge" research project has received €7.8 million in funding from the German Federal Ministry of Transport and Digital Infrastructure. The implementation of the funding guidelines is being coordinated by the German National Organization Hydrogen and Fuel Cell Technology (NOW). The industrial consortium includes automotive manufacturers the BMW Group and Dr. Ing. h. c. F. Porsche AG, as well as operators Allego GmbH, Phoenix Contact E-Mobility GmbH (charging technology) and Siemens AG (electrical engineering)

The research consortium presented a prototype for a charging station with an output of up to 450 kW in Jettingen-Scheppach, located near the A8 motorway between Ulm and Augsburg. The new charging station is suitable for electric models of all brands with the European standard Type 2 variant of the widely used Combined Charging System (CCS) and is now available for use free of charge. A Porsche research vehicle with a net battery capacity of approximately 90 kWh achieved a charging capacity of over 400 kW on the new charging station, allowing for charging times of less than 3 minutes for the first 100 km range

Medium and Heavy-Duty Charging Station Prototype

Portland General Electric and Daimler Trucks North America are co-developing "Electric Island," a large public charging site for medium- and heavy-duty electric commercial vehicles expected to be the first of its kind in the United States. It is designed to support up to nine vehicle charging stations with charging levels of up to greater than one megawatt.[30]

Charging at Scale

The largest EV fast charging station in the U.S. in 2023 boasts 98 Tesla Supercharging spots at Tesla's Harris Ranch station located in Southern California [31]

There are several charging networks that have been initiated in the U.S.

- The Electrify America charging network currently has 843 installed charging stations and 118 charging stations that are 'coming soon'. The network currently has 3702 Fast chargers, and 116 Level 2 chargers.[32]

- The FordPass network will include more than 12,000 charging stations with a total of 35,000 plugs in the United States and some parts of Canada.[33]

- The Tesla charging network has 1911 public charging stations with about 21,039 plugs in the United States, according to the Alternative Fuels Data Center.

- General Motors Co. is working with electric-vehicle charging operator EVgo Services to build a nationwide fast-charging infrastructure as the automaker prepares a major push into battery-powered

---

[26] Tesla Motors. 2015. Form 10-K. Edgar Online. http://large.stanford.edu/courses/2015/ph240/romanowicz2/docs/tesla-annual.pdf

[27] Tesla Motors. 2019. "Introducing V3 Supercharging." https://www.tesla.com/blog/introducing-v3-supercharging.

[28] SAE. 2013. "Wireless Power Transfer of Heavy-Duty Plug-In Electric Vehicles and Positioning Communication J2954/2 Standard". https://www.sae.org/standards/content/j2954/2/.

[29] CharIn. 2020. "Mapping Standards for Low- and Zero-Emission Electric Heavy-Duty Vehicles," presentation. International Transportation Forum February 18-20, 2020 Workshop. https://www.itf-oecd.org/sites/default/files/docs/charging-infrstructure-standardisation-developments-bracklo.pdf.

[30] https://www.greenfleetmagazine.com/10131365/daimler-announces-electric-island-commercial-vehicle-charging-showcase?utm_source=feedburner&utm_medium=feed&utm_campaign=Feed%3A+GreenFleetMagazine-All+%28Green+Fleet+Magazine%29. December 1, 2020.

[31] "Tesla's Mega 98-Supercharger Location Runs In Part On A Diesel Generator: Report", Jalopnik, Sept. 6,2023. https://jalopnik.com/tesla-supercharger-location-diesel-generator-report-1850804146

[32] Source: https://www.electrifyamerica.com/locate-charger/

[33] https://www.cnn.com/2019/10/17/cars/ford-electric-vehicle-charging-network/index.html

models. The two companies will jointly invest in 2,750 fast chargers in cities and suburbs across the U.S. as GM moves to solve a chicken-and-egg problem that comes with selling EVs: A sparse network of chargers has turned off some potential buyers, but utilities and charging companies have been loath to expand the infrastructure until more plug-ins are on the road.[34] As of August 2023, the GM-EVgo network has established nearly 230 public charging locations with a network total of 1000 DC Fast Charging stalls.[35]

Goals and Objectives

Program Goal

The goal of the Grid and Infrastructure Program is to identify system pathways and conduct research to facilitate the development and harmonization of robust, interoperable, and cyber-secure electric vehicle charging and grid infrastructure that supports EVs at scale and incorporates advanced charging technologies, Distributed Energy Resources (DER), and grid services

The G&I Program is focused on EVs, Electric Vehicle Supply Equipment (EVSE or chargers), and integration with the grid. The emphasis is upon foundational systems analyses; exploratory Research, Development, and Deployment (RD&D); and Cyber-Physical Security (CPS); especially in critical areas that other stakeholders

Figure 16 Strategic areas of the Grid and Infrastructure Program.

are not able to address. The three strategic areas addressed by the program are SCM, HPC, and CPS of charging infrastructure, as shown in Figure 16.

Each strategic area informs the others, providing a feedback mechanism to continuously refine and adjust program direction and focus. R&D activities span electrification of the LD, MD, and HD sectors of transportation. Additionally, given the cross-sectoral nature (vehicle, charging infrastructure, and the electric grid) of these activities, the program emphasizes close communication and coordination with other governmental and industry stakeholders, including Federal agencies, charger and vehicle OEMs, utilities, and charging network providers.

The G&I Program has established two targets for each of these strategic areas (SCM, HPC, and CPS) for the years 2023 and 2026. The strategic area targets directly support the long-term 2030 G&I Program targets, which are focused on resolving barriers and operationalizing solutions, in concert with transportation electrification stakeholders. All targets for 2023, 2026, and 2030 are listed below.

Year 2023

- SCM: Develop at least two viable smart charge management strategies and relevant tools to reduce the potential grid impacts of EVs at scale and enhance the value of EV charging systems by enabling grid services.

---

[34] https://www.ttnews.com/articles/gm-build-nationwide-ev-charging-network. July 31, 2020.

[35] "EVgo and General Motors Open 1,000th DC Fast Charging Stall as Part of Metropolitan Charging Collaboration", Aug. 1, 2023. https://www.evgo.com/press-release/evgo-and-general-motors-open-1-000th-dc-fast-charging-stall-as-part-of-metropolitan-charging-collaboration/.

- HPC: Develop strategies and technologies for high power dynamic wireless charging and multi-port 1+ MW charging stations that enable vehicle charging through direct connection to medium voltage ($\geq$ 12.47 kV) distribution.

- CPS: Develop a comprehensive threat model, prioritize high consequence events, and identify appropriate defense, detection, and mitigation strategies and tools for the EV charging ecosystem.

Year 2026

- SCM: Demonstrate and validate smart charge management strategies and relevant tools capable of controlling wide-scale utilization of high-power charging at 400 kW and above, while incorporating robust cyber-physical security methodologies.

- HPC: Demonstrate and validate viable high power dynamic wireless charging, and multi-port 1+ MW charging stations with direct connection to medium voltage distribution.

- CPS: Conduct wide-scale demonstrations to validate viable and robust cyber-physical security for the charging ecosystem in support of EVs at scale.

Year 2030

- Address technical barriers to the development and harmonization of a grid-integrated, robust, interoperable, and cyber-secure electric vehicle charging ecosystem that supports EVs at scale.

- Operationalize two technologies, tools or platforms that will enable interoperable, secure charging solutions that reduce costs for EV owners and fleets.

Program Design and Execution

The G&I Program carries out its mission by focusing its R&D investments on early stage, medium and long-term technology projects that are unlikely to be pursued by industry alone but have significant potential public benefit.

G&I R&D Functions

Smart Charge Management (SCM)

Importance

The focus of SCM is to identify pathways to reduce the potential grid impacts of EVs at scale, while providing enhanced value for EV/charging/grid systems, including reduced costs and increased opportunities for grid services. If unmanaged, EVs at scale connecting to the grid would create numerous challenges for utilities, particularly at the distribution level. SCM techniques can be employed to intelligently control, and shift charging loads to mitigate this problem and facilitate the provision of advanced grid services from EV charging.

Specific challenges and barriers to SCM include determining the impact of controlled charging versus uncontrolled charging, identifying critical strategies, and enabling technologies, developing, and demonstrating

SCM in integrated networks of building systems and DERs including stationary storage, and facilitating bi-directional power flow. Interoperability and scalability of SCM systems are needed to allow EVs from all OEMs to charge at EVSEs from multiple vendors to enable EVs at scale. High speed communication and controls with compatible device protocols and test tools for verification are required. SCM research is also needed to develop strategies and technologies for charging all EVs to enhance station resilience and mitigate potentially negative grid impacts. Finally, costs should be factored into the design of SCM hardware and grid upgrades so that they are minimized, while still providing the necessary charging service.

VTO's current SCM R&D efforts

The G&I Program's SCM activities include systems analyses; research, development, and validation of critical enabling strategies and technologies; and demonstrations. Current projects have created tools and methodologies that form the building blocks for effective SCM. The DOE National Laboratories are focused on quantifying the effects of uncontrolled charging versus controlled charging, developing and evaluating the effectiveness of smart charge control strategies, and

Figure 17 Key elements of Smart Charge Management.

identifying required constraints and mechanisms to implement high-value charge control strategies.

In the fall of 2020, VTO launched utility-managed SCM projects that include research, development, and execution of a wide-scale demonstration that enables grid services from EVs and provides benefits to electricity grid operators, energy services providers, charging network operators, and EV owners. Figure 16 illustrates key elements of SCM including predictive charge decision making, controls, and integration of vehicle charging and distributed energy resources with buildings and the grid.

VTO R&D Outlook for Key Focus Areas

Building on the advances from current R&D efforts, future SCM activities target LD, MD, and HD EVs and fleets at charging stations, fleet depots, and travel centers. R&D is needed for real time detection and implementation of mitigation procedures when an EV charging station is acting out of the norm or has suffered a cyber breach. Likewise, for MD/HD EV fleet charging at depots and travel centers, the focus is to develop and demonstrate SCM strategies, systems, and tools to provide benefit to MD/HD fleets and owners, and to reduce potential grid impacts. To achieve effective SCM, a thorough understanding of HPC charge profiles, both conductive and inductive, is required for optimal integration of charging stations and the utility distribution grid. Another future thrust is to identify viable vehicle-to-everything (V2X) applications and requirements, and to subsequently develop and demonstrate technologies (on and off board) for low cost, interoperable, controllable, and bi-directional power flow. The following identifies specific targets for SCM for the years 2023 and 2026.

YEAR 2023

- Develop at least two viable smart charge management strategies and relevant tools to reduce the potential grid impacts of EVs at scale and enhance the value of EV charging systems by enabling grid services.

YEAR 2026

- Demonstrate and validate smart charge management strategies and relevant tools capable of controlling wide-scale utilization of high-power charging at 400 kW and above, while incorporating robust cyber-physical security methodologies.

High Power Charging

Importance

Successful deployment of HPC for LD (up to 400 kW) and MD/HD (1+ MW) EVs offers numerous benefits, including greater vehicle utilization, extended range, and recharging times comparable to refueling for conventional vehicles. However, HPC systems face multiple technical challenges and must be intelligently designed and integrated with the grid and DERs to mitigate ramp rates and surge power demands, lower system total cost of ownership, maximize the potential for grid services, and enable interoperability of HPC infrastructure with MD and HD EVs.

HPC exploratory R&D and analyses are needed to address issues associated with materials, power electronics, thermal management, and overall costs. Specific barriers exist with thermal loading of equipment and cables that enable service from the medium voltage grid and power transfer to the vehicle. Investigations are also needed into automated EVSE for HPC, especially above 400 kW charging levels. Advances in wireless charging are required, including the development of novel coils, advanced field shaping technologies, and mitigation of stray electric and magnetic fields.

Likewise, assessment and research are needed to understand the impacts of HPC on the grid, and unexpected grid events on HPC-enabled vehicles, and to help determine the appropriate response from EVs and EVSE. Clear understanding of both the impact of large numbers of HPC systems on distribution feeders and of methods to integrate and control stationary storage and other DERs, in support of HPC, are needed. Furthermore, identification and development of control strategies will be required to enable HPC stations to provide grid and building services.

Figure 18 Conceptual configuration of an HPC station.

VTO's current HPC R&D efforts

The G&I Program supports RD&D of HPC in three areas: charging stations with multiple 400 kW EVSE for LD EVs, multi-MW charging stations for MD/HD EVs, and high-power static and dynamic wireless charging. For LD EVs, the focus is on developing and demonstrating charging stations with charging ports rated up to 400 kW and a total combined power rating that exceeds 1 MW. These stations will connect directly to medium voltage distribution networks and utilize stationary storage systems to minimize negative impacts on the grid. For MD/HD EVs, efforts are focused on developing strategies and technologies for 1+ MW multi-port chargers at fast charging travel plazas/truck stops and/or fleet depots. The G&I Program will conduct charging station utilization and load analysis, grid impacts and interconnection analysis, detailed power electronics component design, site and battery charge control, and charging connector design. Figure 18 provides a conceptual configuration of an HPC station for MD/HD EVs. High power

static and dynamic wireless charging activities target establishing feasibility, overcoming technology gaps, and validating high power wireless charging with vehicle-level demonstrations. Efforts will analyze, design, build, and validate integrated high-power static and dynamic wireless charging systems that are viable for real world traffic conditions in the U.S.

VTO R&D Outlook for Key HPC Focus Areas

Future HPC activities target several areas including integration of dynamic wireless power transfer (dWPT) into roadways and development of innovative means to provide service to charging facilities. Deployment of dWPT into the roadway will require researching performance, field emissions, and power and control requirements, and addressing integration of the charging system. DC-as-a-Service (DCaaS) is an approach to provide direct current (DC) to charging stations that seamlessly integrates facility and EVSE loads, and DER. Research is needed to address DC isolation, metering, measurement, and protection. The following identifies specific HPC targets for 2023 and 2026.

YEAR 2023

- Develop strategies and technologies for high power dynamic wireless charging and multi-port 1+ MW charging stations that enable vehicle charging through direct connection to medium voltage ($\geq$ 12.47 kV) distribution.

YEAR 2026

- Demonstrate and validate viable high power dynamic wireless charging, and multi-port 1+ MW charging stations with direct connection to medium voltage distribution.

Cyber-Physical Security

Importance

EVs and their connectivity with external systems have become increasingly complex. Apart from AC Level 1 chargers, EVSE have evolved rapidly to be networked and maintain a wide variety of communication functions. As communication networks for EVs, EVSE, and external systems increase, attack vectors and cyber-physical risks also increase for the charging infrastructure. Since EVSE at workplaces and public charging stations connect with many different EVs to provide charging services, it makes assuring CPS extremely difficult.

A major challenge posed by compromised charging infrastructure is the threat it poses to the electric grid. A localized cyber-physical attack on a set of EVSE/charging stations can lead to a sudden addition or reduction of loads that can cause local disruptions, brownouts, voltage imbalances, and undesirable power quality impacts. Large-scale, coordinated cyber-physical attacks on charging infrastructure supporting EVs at scale can also lead to wider grid disruptions, such as blackouts over large geographical areas. The lack of a comprehensive understanding of threats; disjointed implementation approaches; and limited best practices are major barriers to ensuring overall security of EVs, charging infrastructure, and the grid.

VTO's current CPS R&D efforts

Current CPS activities include research, development, and validation of technologies for real-time threat detection, mitigation, isolation, and restoration of charging infrastructure based on its physical signatures and performance. Activities at the National Laboratories include developing a comprehensive threat model, attack graphs, and technical risk assessment of the EV charging ecosystem, and prioritizing charging infrastructure high consequence events and mitigation strategies. Additional activities include penetration testing of 50 kW DC fast chargers and 400 kW HPC and developing recommendations for secure communications. VTO-funded projects led by industry, academia, and non-profit organizations are developing real-time detection, defense, and mitigation systems to protect EVs, charging infrastructure, and the grid. This includes hardened

controllers, converters, and monitoring systems; a retrofittable and scalable open-source cybersecurity architecture; and game theory-based hardware and software to provide secure charging.

VTO R&D Outlook for Key CPS Focus Areas

Based on the assessments of risk and high consequence events, future activities will implement the best approaches to mitigate vulnerabilities and threats associated with the EV charging ecosystem. This effort will incorporate strategies, systems, and tools for secure charging, including hardware/software for cyber-physical intrusion detection, threat mitigation and isolation, and recovery. The most promising CPS countermeasures will be identified based on risk formulation (e.g., public key infrastructure, blockchain, moving target defense, and redundancy). Identified countermeasures that address the highest consequence events will be demonstrated and validated. The following identifies specific CPS targets for 2023 and 2026.

YEAR 2023

- Develop a comprehensive threat model, prioritize high consequence events, and identify appropriate defense, detection, and mitigation strategies and tools for the EV charging ecosystem.

YEAR 2026

- Conduct wide-scale demonstrations to validate viable and robust cyber-physical security for the charging ecosystem in support of EVs at scale.

EA2020 Vehicle Grid Integration

In FY21, the Energy Act of 2020 (Division Z of the Consolidate Appropriations Act, 2021 Public Law No. 116-260) directed the DOE Secretary to (a) Establish a research development, and demonstration program to advance the integration of electric vehicles, including plug-in hybrid electric vehicles, onto the electric grid, and (b) produce a 'Vehicles-To-Grid Integration Assessment Report' that presents the results of a study that examines the research, development, and demonstration opportunities, challenges, and standards needed for integrating electric vehicles onto the electric grid. The results and knowledge gained from all of the projects in the G&I portfolio were used in preparing the study requested by Congress and the report.

Bipartisan Infrastructure Law

The Bipartisan Infrastructure Law (BIL) was passed in 2021. The legislation will invest $7.5 billion to build out a national network of EV chargers in the United States. This is a critical step in the President's strategy to fight the climate crisis and it will create good U.S. manufacturing jobs. The legislation will provide funding for deployment of EV chargers along highway corridors to facilitate long-distance travel and within communities to provide convenient charging where people live, work, and shop. This investment will support the President's goal of building a nationwide network of 500,000 EV chargers to accelerate the adoption of EVs, reduce emissions, improve air quality, and create good-paying jobs across the country.

A Joint Office of Energy and Transportation has been established to support the implementation of the EV charging objectives of the BIL.

Information from the G&I projects is being fed to the Joint Office of Energy and Transportation and is being used to create requirements for the infrastructure funding established in the BIL.

EVs@Scale Consortium

In FY21 the Grid and Infrastructure program established the EVs@Scale Consortium to accelerate progress of EV Charging Infrastructure RD&D and engage stakeholders. It is an effort to streamline and coordinate Vehicle-Grid Integration activities across the national lab complex and increase the agility of the program to address rapidly evolving challenges and barriers to Vehicle-Grid Integration. The EVs@Scale Consortium includes the following national laboratories:

- Argonne National Laboratory (ANL)

- Idaho National Laboratory (INL)

- National Renewable Energy Laboratory (NREL)

- Oak Ridge National Laboratory (ORNL)

- Pacific Northwest National Laboratory (PNNL)

- Sandia National Laboratories (SNL)

- Lawrence Berkeley National Laboratory (LBNL)[36]

The EVs@Scale organizes its activities within the following pillars:

1. Vehicle-Grid Integration and Smart Charge Management

2. High Power Charging

3. Advanced Charging & Grid Interface Technologies

4. Cyber-Physical Security

5. Codes and Standards

6. Consortium Management.

Specific activities identified in the pillars above will be covered in future Annual Progress Reports.

Grid and Infrastructure Research Highlights

Accomplishments	Organization	Focus Area	Project Title
Made progress on developing and demonstrating a megawatt plus wireless charging system for a HD truck capable of a complete charge in 30 minutes. The team completed vehicle design and procurement. The team made significant progress on designing the charge equipment.	Kenworth Truck Company	Industry Awards	Long-Range, Heavy-Duty Battery-Electric Vehicle with Megawatt Wireless Charging
Developed and began process of demonstrating an electric Innovation Fleet eCascadia 2.0 to improve cost, reliability, and performance over DTNA's completed heavy-duty electric truck. The project team has completed Phase 1a: Research, Design, Building, and Commissioning and Phase 1b: Commercial Scale Production Model including production tests, commercial series production, and has finalized the design elements. The infrastructure installation and evaluations were completed. The team delivered their first vehicle to their demonstration customer.	Daimler Trucks North America LLC	Industry Awards	Development and Commercialization of Heavy-Duty Battery Electric Trucks Under Diverse Climate Conditions

---

[36] LBNL became a member of the EVs@Scale Consortium in September 2023.

Accomplishments	Organization	Focus Area	Project Title
<u>The objective of the project is to use vehicle and operations data to increase the vehicle range and lower the operating cost of battery electric class 8 trucks that operate more than 250 miles per day using physics-aware machine learning algorithms.</u> The second electric truck, NME-8 was prepared for delivery to Minnesota for winter testing. Final testing planning began to validate the developed models and test the eco-routing algorithm and driver-vehicle interface in operation.	Volvo Technology of America, LLC	Industry Awards	Improving the Freight Productivity of a Heavy-Duty, Battery Electric Truck by Intelligent Energy Management
<u>The B-Sample inverters have been built and successfully tested on the bench through the EOL testing and functional testing, as well as mechanical environmental tests.</u> The bench tests with RL load confirmed the inverter power efficiency of 98.5%+ efficiency. The Ricardo team commenced the inverter/motor dyno testing, with inverter closed loop speed and torque controller tuning completed.	Ricardo Inc.	Industry Awards	High Efficiency Powertrain for Heavy Duty Trucks using Silicon Carbide (SiC) Inverter - DE-EE0008806
<u>There is a critical need to develop solutions for intelligent EV charging that supports, rather than strains, grid operations.</u> The eMosaic team demonstrated a preliminary platform to meet these needs, validating it in a lab setting using various hardware-in-the-loop modeling tools. Based on these efforts, several price-based approaches to managing EV load show promise.	ABB Inc.	Industry Awards	eMosaic: Electrification Mosaic Platform for Grid-Informed Smart Charging Management
<u>Exelon's Maryland Utilities and its program partners performed work to prepare for year one launch of the smart charge demonstration in 2023</u> with all three of its target customer groups: residential, commercial fleet and public charging.	Exelon - BGE	Industry Awards-	Demonstration of Utility Managed Smart Charging for Multiple Benefit Streams
The team validated the vision of the EVs-at-RISC program to enable interoperable metering, telemetry, and command-and-control capabilities across diverse, heterogeneous, and highly distributed EV charging/DER infrastructure assets and stakeholders within a zero-trust architecture leveraging free and open-source software technologies and minimal COTS components.	Liberas (formerly Dream Team)	Industry Awards	Development and Demonstration of EVs-at-RISC: A Secure and Resilient Interoperable Smart Charge Management Control System Architecture for EVs-at-ScaleMedium-Heavy Duty PHEV Work Trucks
<u>The WAVE team has completed the procurement of all the parts and systems needed to run the wireless chargers.</u> The validation of these systems was completed in a lab setting. Cummins completed the validation of the two trucks and got the motor and inverter combination certified.	WAVE, Inc	Industry Awards	Wireless Extreme Fast Charging for Electric Trucks
<u>The project completed the test of the hybrid drive strategies and completed the system integration, layout and design to be utilized for the demonstration vehicles</u>	Odyne Systems	Industry Awards-	Development and Demonstration of

Accomplishments	Organization	Focus Area	Project Title
as well as future Odyne production. The drive testing demonstrated that the system is capable of delivering up to 75% fuel economy improvement, depending on duty cycle, although a lessor driving strategy was ultimately be utilized when considering battery cost and size, stationary energy needs, and the real-world duty cycle of the Medium/Heavy Duty work truck.			Medium-Heavy Duty PHEV Work Trucks
A research effort was conducted to capture the DC charging behavior and efficiencies of four modern electric vehicles including a 2020 Tesla Model 3, 2020 Nissan Leaf E-plus, and a 2017 and 2020 Chevrolet Bolt. The experimental study provided data for analysis of over 120 charge sessions, from a wide variety of ambient conditions and public DCFC networks.	ANL	High-Power Charging Enabling Technologies	Assessment and Validation of Next Generation EV High Power Charging Profiles
The project group has successfully executed device characterizations that provide the key data required to deliver an initial industry charging performance report at the end of the next fiscal year. The aim of the analysis is to build a knowledge base and glean industry insights to intelligently integrate HPC systems within the grid and among co-located loads and sources. The characterization and dissemination work in the project is critical for understanding the emerging charge performance industry	ANL, NREL, INL, ORNL	High-Power Charging Enabling Technologies	Assessment and Validation of Next Generation Electric Vehicles High Power Charging Profiles
The first year of the project focused on scoping the work to determine the fundamental components of the system to develop a high-power, DC distribution-based, interoperable, grid-integrated charging hub platform that can scale to MW+ charging hardware development and testing.	EVs@Scale Consortiume – NREL, ANL, ORNL	High Power Charging Enabling Technologies	High-Power Electric Vehicle Charging Hub Integration Platform (eCHIP)
Laboratory characterization of the 200 kW DWPT system was carried out in stationary and dynamic power transfer modes using the DICE. The rated power (200 kW input) tests indicated successful operation in both stationary and dynamic modes, thereby indicating viability of vehicle-integrated dynamic charging tests with couplers embedded in the roadway.	ORNL, INL, and NREL	Wireless Power Transfer Enabling Technologies	High-Power and Dynamic Wireless Charging of Electric Vehicles
Completed project year one to develop a prototype system and reference design for the DC-to-DC power conversion stages for a 50kW WEVC system including ground-side inverter, ground and vehicle electromagnetic couplers and resonant networks, and vehicle side to rectifier. This work featured a comparative study of of LCC-LCC and LCCP resonant networks.	ORNL, Stellantis	Wireless Power Transfer Enabling Technologies	Misalignment Tolerant Three-phase Wireless Fast Charging System for EVs
A concretized coil was designed, and four ground-side units were built and tested. The electrical behavior was characterized before and after the concretization process, and it remained unchanged, suggesting that	EVs@Scale Consortium – ORNL, INL, NREL	Wireless Power Transfer Enabling Technologies	Integrating Dynamic Wireless Power Transfer Systems in Roadways

Accomplishments	Organization	Focus Area	Project Title
the coil is suitable for deployment from the perspective of power transfer capability.			
<u>The benefits of smart charging versus controlled and uncontrolled charging were assessed</u>. From a technical standpoint, optimized smart charging via charge scheduling, although the most technically involved, has the greatest benefit to all actors in the SCM ecosystem.	ANL	Vehicle-Grid Integration and Smart Charge Management	Charging Infrastructure Technologies: Smart Vehicle-Grid Integration
<u>The project made progrees to commercialize a smart charge adapter that enables metering, monitoring and management control of charge sessions in response to local supply/demand levels.</u> The development of the hardware and software under this project helped garner a new industry partner. There still remains additional testing and debugging but the technology is very close to becoming a commercialized product<u>.</u>	ANL	Vehicle-Grid Integration and Smart Charge Management	Electric Vehicle Smart Charge Adapter
The first year of this project has expanded capabilities in transportation analysis, SCM assessments, and EVSE technologies to support EVs@Scale. EV charging loads have been developed across Virginia to represent electrification of 52% of the passenger vehicle stock. These loads represent the vehicle energy needs and charge flexibility, which will be critical in assessing grid impacts and SCM effectiveness throughout the utility partner grid models.	EVs@Scale Consortium – NREL, ANL, INL, SNL	Vehicle-Grid Integration and Smart Charge Management	Flexible charging to Unify the grid and transportation Sectors for EVs at scale (FUSE)
<u>This project helped identify EV charger vulnerabilities and quantify the risk to critical infrastructure when vehicle chargers are maliciously controlled</u>. This risk assessment is only an initial step in a continuous process of hardening charging infrastructure against cyber-attacks.	EVs@Scale Consortium - ORNL, PNNL, INL	Cyber-Physical Security	Electric Vehicle Integrated Safety, Intelligence, Operations (eVision)
<u>This project helped identify EV charger vulnerabilities and quantify the risk to critical infrastructure when vehicle chargers are maliciously controlled.</u>	SNL, PNNL, ANL	Cyber-Physical Security	Securing Vehicle Charging Infrastructure
<u>The multi-lab team within the cybersecurity pillar have initiated a portfolio of work to address key challenges including:</u> <u>• Industry implementation and utilization of latest security methods is not consistent</u> <u>• Lack of methods to identify, protect, detect, respond, and recover from cyber events</u> <u>• Unknown vulnerabilities in new, emerging features and standards</u> <u>• Existing training for the EV charging infrastructure cybersecurity workforce</u>	EVs@Scale Consortium - INL, SNL, NREL, PNNL, ORNL, ANL	Cyber-Physical Security	Cyber-physical Security Pillar for Unified National Lab Collaboration (CyberPUNC)
<u>In this two-year program, two important documents were successfully revised and well-received by the testing community.</u> Testing burden was reduced, and accuracy improved for HEV and PHEV testing. With	ANL	Codes and Standards	Electrified Vehicles Test Procedure Development

Accomplishments	Organization	Focus Area	Project Title
these changes, HEVs, and especially PHEVs can be designed with more control flexibility and opportunities for optimization. The expectation is small but noticeable increases in efficiency for future HEVs and PHEVs.			
INL leveraged previous SAE standards testing and procedure development as well as grid modernization lab consortium (GMLC) work to support the IEEE P2030.13 to review definitions and block diagrams.	EVs@Scale Consortium - INL	Codes and Standards	Wireless Power Transfer, DER Standards Tasks
NREL leveraged previous DOE funded activities under the CharIN MCS work group on previous MCS coupler designs for the latest pre-production prototype couplers. Likewise NREL leveraged grid modernization lab consortium (GMLC) work to support the IEEE P2030.13 to create definitions and block diagrams.	EVs@Scale Consortium - NREL	Codes and Standards	SAE J3271 MCS Coupler Testing, DER Standards Tasks
ORNL staff created industry and academia engagement for direct distribution level medium-voltage (MV) connected charging infrastructures with solid-state transformers or modular multilevel converters (MMC) for high-power charging plazas.	EVs@Scale Consortium - ORNL	Codes and Standards	Wireless Power Transfer, Medium Voltage Power Converter Standards Tasks
PNNL staff have participated in CharIN MCS work group meetings and EV Charging standards. Knowledge of cyber security, smart charging and other standards was utilized to draft wording in the EVSP standards roadmap augmenting the input from industry participants. I.e. perform the actual writing of the roadmap documents as well as SAE J3271 MCS standard first draft	EVs@Scale Consortium - PNNL	Codes and Standards	Wireless Power Transfer, Medium Voltage Power Converter Standards Tasks
To determine DC fast charger technologies compliance and calculation methods that help check the compliance with NIST's HB44-3.40, ANL conducted benchmark research on DC meters and cables. A conclusion from this benchmarking research is that manufacturers of EVSE DC fast charging equipment do not need to have a revenue grade meter in the coupler at the end of the cable to comply with HB44-3.40 specifications for measurement.	ANL	Codes and Standards	DC Meters for Commercial Charging Benchmark Study

In this report the Grid and Infrastructure project reports that follow have been grouped into the chapter categories of Industry Awards (IA), High Power Charging (HPC) Enabling Technologies, Vehicle-Grid Integration (VGI) & Smart Charge Management (SCM), and Cyber-Physical Security (CPS), and Wireless Power Transfer (WPT) Enabling Technologies. Many of the projects address multiple programs objectives. The Industry section describes projects that were awarded to commercial industry performers via DOE's Funding Opportunities Announcement (FOA) solicitation process. The HPC, VGI & SCM, CPS, and WPT projects were awarded to National Laboratories via direct funding agreements.

Questions regarding the Grid and Infrastructure Program can be directed to the Technology Manager, Lee Slezak via email: lee.slezak@ee.doe.gov or telephone: (202) 586-2335

I   Electric Drive Technologies

I.1   Electric Drive Technologies Research

I.1.1   Highly Integrated Power Module (Oak Ridge National Laboratory)

Lincoln Xue, Principal Investigator
Oak Ridge National Laboratory
1 Bethel Valley Road
Oak Ridge, TN 37830
Email: xuel@ornl.gov

Susan Rogers, DOE Technology Development Manager
U.S. Department of Energy
Email: Susan.Rogers@ee.doe.gov

Start Date: October 1, 2021   End Date: September 30, 2022
Project Funding: $750,000   DOE share: $750,000   Non-DOE share: $0

Project Introduction

This project covers the design and development of next-generation wide-bandgap (WBG) power modules and the associated components within the system. Various component challenges were addressed to reduce the footprint of the system and increase the level of integration. Challenges included substrates, integrated heat sinks, and automated design tools for power electronics to advance the power density.

Objectives

The overall objective of the project is to develop technologies for next-generation advanced integrated power electronic systems. These systems enable high power density and reliability to achieve the US Department of Energy (DOE) Electrification Program's 2025 technical targets: 100 kW/L power density, $2.70/kW cost, and 300,000 mile lifetime. Under the overall objective, two main lines of inquiry were identified: (1) power module design and (2) automated design of power electronics.

Approach

The main approach of the project is to increase the power density and reliability of power electronics to meet the DOE Electrification Program's 2025 targets (100 kW/L, $2.70/kW, and 300,000 mi lifetime) by focusing on power module design and the automated design of power electronics.

Under the power module design project line, investigations were conducted on substrates to find power electronic modules that allowed increased power density and high reliability for WBG device–based power modules. The project considered better coefficient of thermal expansion matching between WBG devices and power module materials, improved heat extraction, and enhanced thermal and power cycling capabilities. Additionally, multilayer substrates for enhanced electrical and thermal performance were evaluated. These solutions enabled reduced parasitic inductance in the system for optimum switching performance, reduced power module size, and the direct attachment of high-performance heat sinks.

In Fiscal Year 2022, two main tasks were carried out: (1) design, fabrication, and evaluation of the integrated SiC power module and (2) simulation investigation of direct substrate cooling for both thermal and mechanical performances.

Results

Task 1: Design, Fabrication, and Evaluation of the Integrated SiC Power Module

In previous years, the team designed the TPG-embedded organic, direct bonded copper (ODBC)–based power module, which integrated the gate driver and artificial intelligence (AI)–optimized heat sink. The concept is shown in Figure I.1.1.1. The power module consisted of the ODBC-based substrate, gate driver circuits, and the SiC chips. In the three-layer substrate (shown as the bottom part of the structure in the figure), the top layer was used for placing the dies and terminations, the middle layer was used for common mode shielding, and the bottom layer was used for the integrated heat sink. Additional layers above the top layer could be included for the gate driver and additional termination requirements. The design was optimized by finite element analysis (FEA) simulations for the thermal and electrical performance that meet the requirement.
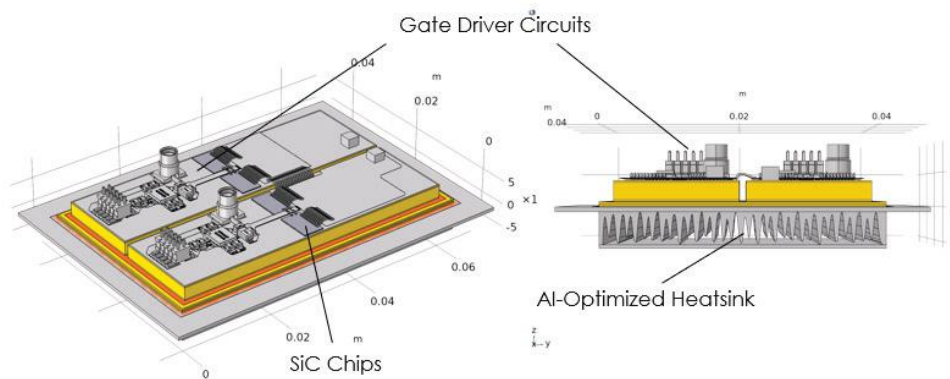
Figure I.1.1.1 ODBC-based power module with integrated gate driver and heatsink

In this fiscal year, the team fabricated the ODBC-based substrates through a partnership with Momentive and DuPont. ODBC substrate samples without embedded TPG were manufactured first, as shown in Figure I.1.1.2. Before the heat sink pattern was machined, the samples were tested for breakdown strength up to 2 kV. Two points were measured to ensure the dielectric strength between layers. The top layer test was used to test the first dielectric layer, which insulated the two TPG-embedded Cu islands. The bottom layer test was used to test the strength of two dielectric layers in series that provided insulation between the Cu islands and heat sink. The results are shown in Figure I.1.1.3. The leakage current was measured as less than 100 nA under all testing conditions.

The substrate's thermal performance was evaluated by the following method. Two resistors were used to emulate the heat source (5 W per resistor). The ODBC substrate was placed in an enclosed environment with minimized air flow. Researchers measured the top and bottom surface temperatures of the ODBC using thermocouples after 2 h of operation. A 4°C difference was observed between the top and bottom surfaces at 10 W, indicating a 0.4 K/W thermal resistance. The testing setup and results are shown in Figure I.1.1.4.

The substrate sample was machined for the designed geometry of the heat sink. A manifold was also designed to pair with the ODBC substrate so that the structure can be connected to a liquid cooling system. Figure I.1.1.5 shows the ODBC substrate with machined heat sink geometry and the assembled view of the substrate with the designed manifold.
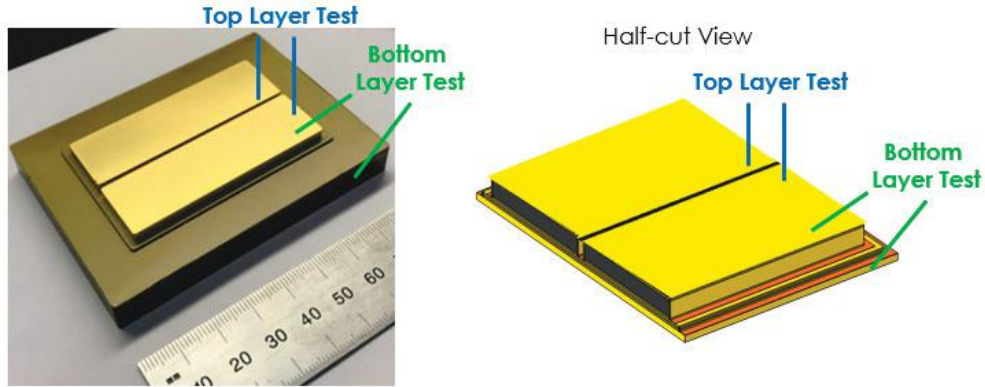
Figure I.1.1.2 Fabricated ODBC-based substrate.
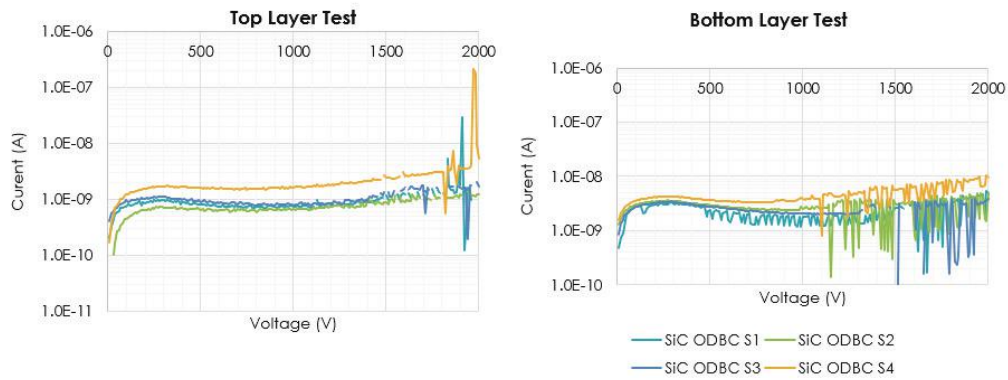
Figure I.1.1.3 Measured leakage current values of the ODBC substrates.
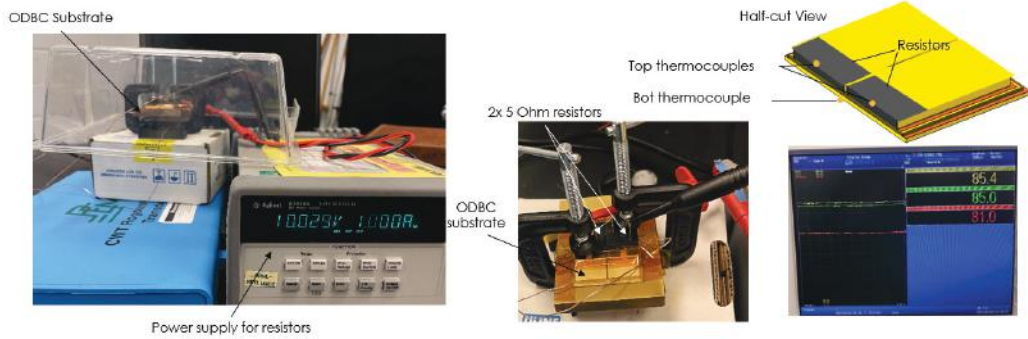
Figure I.1.1.4 Substrate thermal evaluation setup and test results.
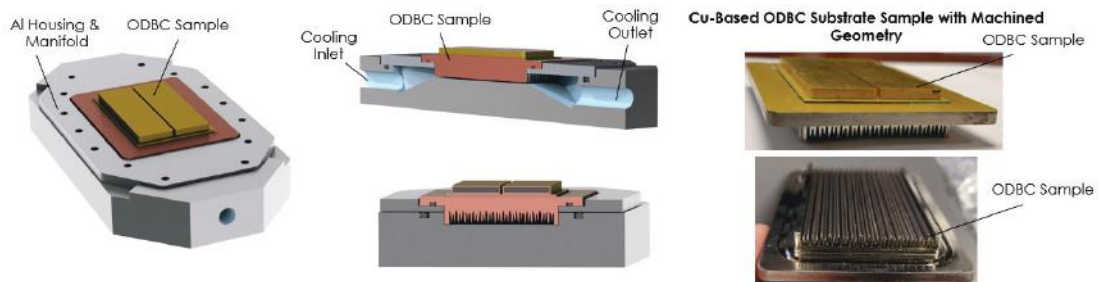
Figure I.1.1.5 Completed ODBC substrate with heat sink and manifold.

Task 2: Simulation Investigation of Direct Substrate Cooling for Thermal and Mechanical Performances

In this fiscal year, the team evaluated and compared indirect and direct substrate cooling schemes. Those two schemes are illustrated in Figure I.1.1.6. Indirect substrate cooling requires a thermal interface between the substrate and heat sink, which increases the thermal resistance. In contrast, a direct substrate cooling scheme eliminates layers in the thermal path (e.g., solder layer, base plate) and enables a very high localized heat transfer coefficient (HTC) for devices with high heat flux. Therefore, direct substrate cooling can potentially enable high power density.
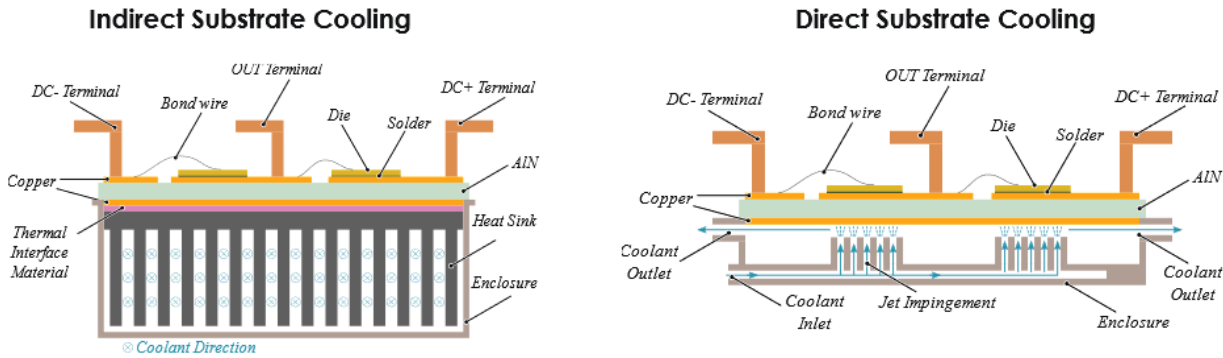
Figure I.1.1.6 Illustration of indirect and direct substrate cooling schemes.

Indirect and direct cooling schemes were compared in the FEA simulation. For the indirect cooling scheme, the genetic algorithm (GA)–optimized design was used. For the direct cooling scheme, the number of nozzles and spreading exit angle of nozzles were optimized [1]. Figure I.1.1.7 shows the FEA results of chip temperature in both cases. As shown in the figure, the direct cooling scheme can achieve a lower chip temperature and smaller heat sink size than the indirect cooling counterpart. Figure I.1.1.8. shows the simulated HTC at the DBC lower copper interface. The direct cooling scheme has nonuniform (oscillated) heat transfer, which can cause a potential issue with reliability. A thermomechanical modeling framework was built for both indirect and direct substrate cooling schemes. The stress and strain (elastic and plastic) for solder and other components of the power module stack were compared. Researchers discovered that because of highly localized heat transfer, direct cooling showed higher plastic strain in solder, which can cause reliability issues. Oak Ridge National Laboratory's (ORNL's) GA-optimized heat sink showed better performance than the pin-fin heat sink design.
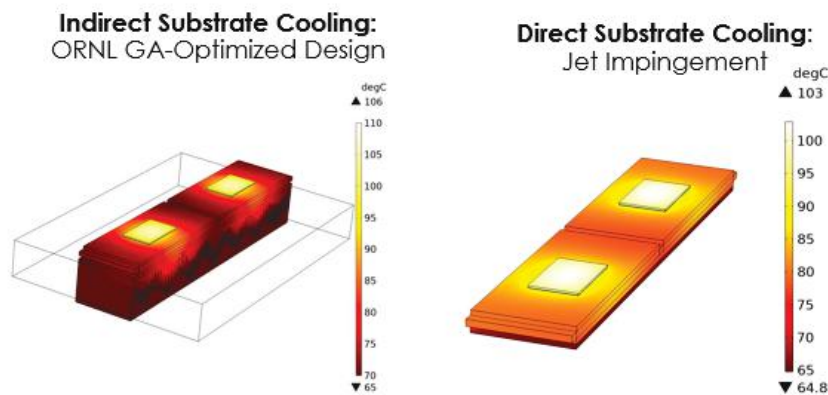
Figure I.1.1.7 Simulated chip temperature.
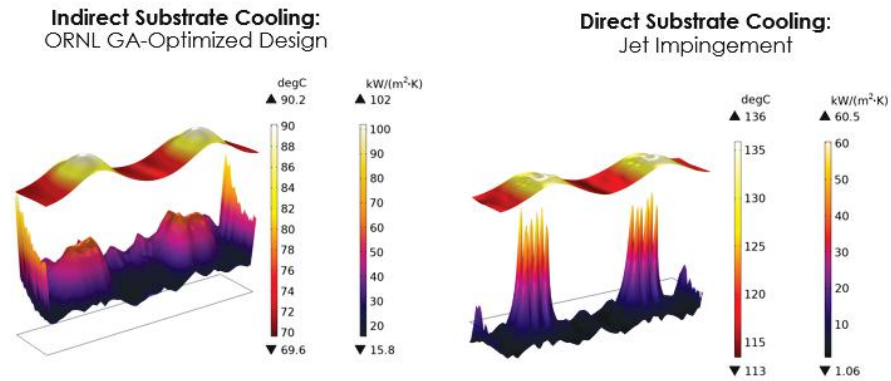
Figure I.1.1.8 Simulated temperature plot and HTC plot at DBC lower copper interface.
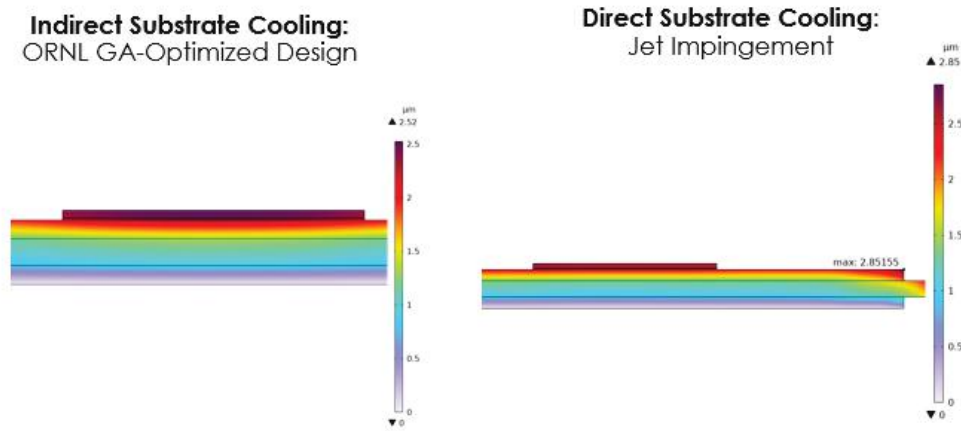
Figure I.1.1.9 Simulated displacement magnitude.

Conclusions

The designed multilayer ODBC substrate was fabricated and evaluated. The thermal evaluation of the substrate indicates 0.4 K/W thermal resistance between the top and bottom surface of the ODBC substrate. To further improve the thermal performance, the direct substrate cooling scheme was evaluated by simulation. This work found that although the direct substrate cooling scheme may achieve a lower chip temperature and higher density than the indirect substrate cooling, the thermomechanical simulation showed a higher displace magnitude for the direct cooling scheme.

Key Publications

1. Himel Barua, Emre Gurpinar, Lingxiao Xue, and Burak Ozpineci, "Comparative Analysis of Direct and Indirect Cooling of Wide-Bandgap Power Modules and Performance Enhancement of Jet Impingement–Based Direct Cooling," *American Society of Mechanical Engineers (ASME) Conference*.

2. R. Sahu, E. Gurpinar, and B. Ozpineci, "Liquid-Cooled Heat Sink Optimization for Thermal Imbalance Mitigation in Wide-Bandgap Power Modules," *ASME Journal of Electronic Packaging* 144, no. 2 (June 2022): 021103. doi: 10.1115/1.4052068.

3. S. Chowdhury, E. Gurpinar, and B. Ozpineci, "Capacitor Technologies: Characterization, Selection, and Packaging for Next-Generation Power Electronics Applications," *IEEE Transactions on Transportation Electrification* 8, no. 2 (June 2022): 2710–2720. doi: 10.1109/TTE.2021.3139806.

4. E. Gurpinar, R. Sahu and B. Ozpineci, "Heat Sink Design for WBG Power Modules Based on Fourier Series and Evolutionary Multi-Objective Multi-Physics Optimization," *IEEE Open Journal of Power Electronics* 2 (2021): 559–569. doi: 10.1109/OJPEL.2021.3119518.

References

1. Himel Barua, Emre Gurpinar, Lingxiao Xue, and Burak Ozpineci, "Comparative Analysis of Direct and Indirect Cooling of Wide-Bandgap Power Modules and Performance Enhancement of Jet Impingement–Based Direct Cooling," *American Society of Mechanical Engineers (ASME) Conference*.

Acknowledgements

I.1.2 High-Voltage, High Power Density Traction Drive Inverter (Oak Ridge National Laboratory)

Gui-Jia Su, Principal Investigator
Oak Ridge National Laboratory
1 Bethel Valley Road
Oak Ridge, TN 37830
Email: sugj@ornl.gov

Susan Rogers, DOE Technology Development Manager
U.S. Department of Energy
Email: Susan.Rogers@ee.doe.gov

Start Date: October 1, 2021   End Date: September 30, 2022
Project Funding: $650,000   DOE share: $650,000   Non-DOE share: $0

Project Introduction

The direct current (DC) bus capacitor in the inverter is one of the barriers to meeting the US Department of Energy (DOE) Electrification (ELT) Program's 2025 power electronics targets [1]. Using pulse width modulation (PWM) schemes in the voltage source inverter in a traction drive to produce a desired set of alternating current voltages generates large ripple components in the DC-link current with root mean square values greater than 60% of the motor root mean square currents. The DC bus filter capacitor must absorb the ripple currents and suppress transient voltage spikes, both of which are detrimental to the battery life and reliability of the semiconductor switches in the inverter. Available capacitors that can meet these requirements are costly and bulky: they make up one-fifth of the volume and cost of the inverter. Therefore, researchers urgently need to minimize this bulky component by significantly reducing the inverter DC ripple current. The goal for this project is to increase the power density of the traction drive power electronics system to meet DOE ELT 2025 targets (100 kW/L, $2.70/kW, and 300,000 mi lifetime) by focusing on power inverter architecture research and bus bar designs to reduce the need for passive components.

Objectives

The overall objective of this project is to develop technologies for next-generation traction drive power electronics systems with an 8× increase in power density. This objective will achieve the DOE ELT 2025 power density target of 100 kW/L using novel traction drive inverter architecture, optimizing the bus bar design, and minimizing passive components. The objectives for fiscal year (FY) 2022 were to (1) test and characterize the 100 kW segmented inverter prototype built in FY2021 and (2) design a 200 kW segmented inverter using technologies developed in the Electric Drive Technologies Consortium.

Approach

Three technical approaches were considered in this project. The first approach selected inverter architectures that can reduce the DC bus capacitor requirements. Multiphase inverters, segmented inverters [2], and open stator winding inverter drive configurations were evaluated. The second approach increased the inverter DC bus voltage to 800 V or higher. This increase took advantage of the inherently higher voltage ratings of SiC switching devices, reduced the size of SiC dies (thus lowering the cost), and reduced phase and DC bus currents. The third approach optimized the designs for the inverter DC bus bars by employing embedded and distributed capacitors and direct cooling of the bus bars.

Results

The segmented inverter topology was selected because of its significantly reduced DC bus capacitance requirement [2]. Figure I.1.2.1 shows a block diagram for the major components of a three-phase segmented inverter, and Table I.1.2.1 lists the specifications of two inverter designs. The inverter design optimized the SiC metal–oxide semiconductor field-effect transistor (MOSFET) power module packaging with double-side

cooled heat sinks, a gate drive, and current sensing. Wolfspeed SiC MOSFET dies (CPM3-1200-0013A) were selected for the power modules. A 100 kW design and a 200 kW design for segmented inverters were completed using the power modules developed by Electric Drive Technologies Consortium members Virginia Tech and the University of Arkansas. A 100 kW inverter prototype based on the first design using the Virginia Tech–designed power modules was fabricated in FY 2021, and it was refined and tested in FY 2022.
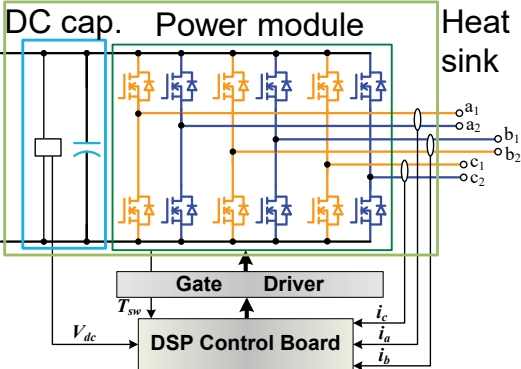
Figure I.1.2.1 Major components of a three-phase segmented inverter.

Table I.1.2.1. Inverter specifications

Design	1	2	Note
Vdc (V)	800	800	
Power (kW)	100	200	1: 143 kVA, 2: 286 kVA at power factor of 0.7
Efficiency (%)	98	98	
Coolant flow rate (L/min)	10	10	Ethylene-glycol water 50/50 mixture,

Test and Characterization of the 100 kW Segmented Inverter Prototype

Functional verification tests were conducted for the 100 kW segmented inverter. Figure I.1.2.2 shows a photo of the test setup, and Figure I.1.2.3 shows operating waveforms for gate signals and output voltage and current in single-phase combinations with a resistor–inductor (RL) load at a DC bus voltage of 48 V. The results verified (1) that the gate signals' propagation delay time and dead band are within the design limits and (2) proper functionality of the power modules and control logics.
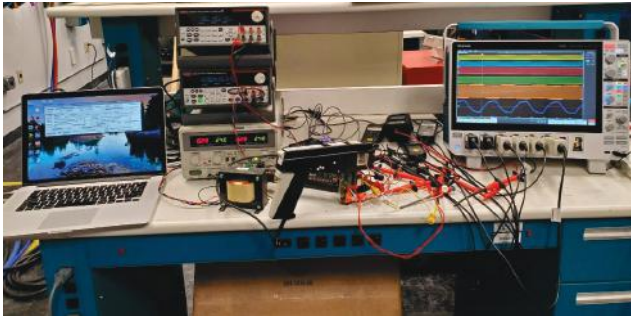
Figure I.1.2.2 Setup for inverter functionality test.
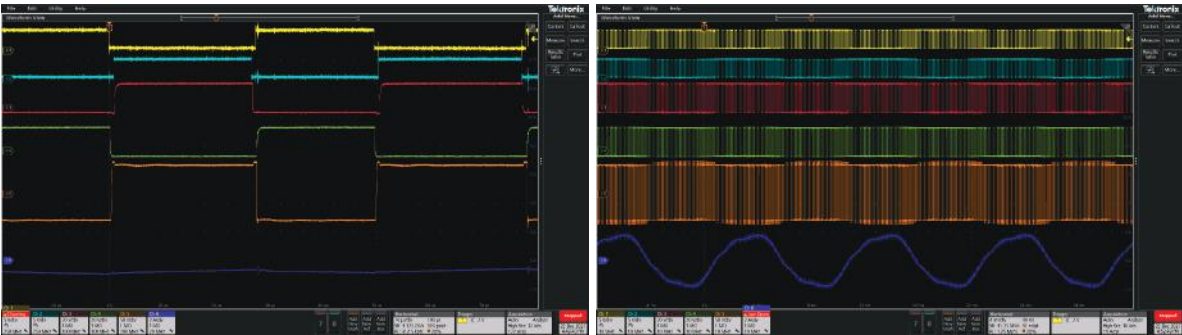
Figure I.1.2.3 Operating waveforms: (*left*) gate signals and (*right*) output voltage and current for a RL load.

The inlet and outlet manifolds were modified for more secure attachment of the cooling hoses. The power modules and heat sinks were then assembled with the new manifolds. Before adding the gate drive and DC bus capacitor boards, the cooling subsystem was tested for leaks, and a pressure drop measurement was taken. Figure I.1.2.4 shows photos of the cooling subsystem test setup. Figure I.1.2.5 plots measured cooling subsystem pressure drops at various flow rates. At the rated flow rate of 10 L/min, the measured pressure drop was 1.5 psi, which is 25% lower than the maximum specification of 2 psi.

Figure I.1.2.4 Photos of cooling subsystem pressure test setup.
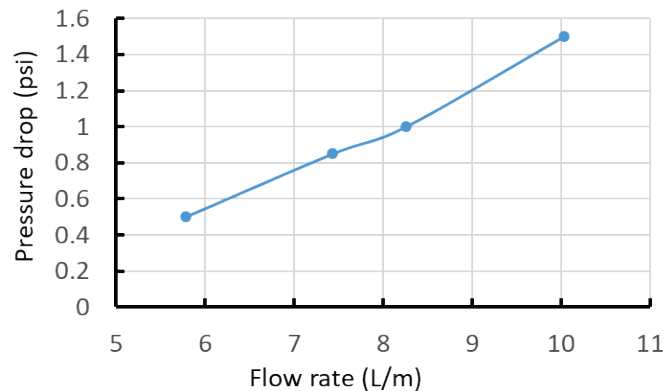
Figure I.1.2.5 Measured cooling system pressure drop vs. flow rate.

After the successful test of the cooling subsystem, the gate drive and DC bus capacitor boards were installed into the power modules to complete the 100 kW inverter assembly. Figure I.1.2.6 shows photos of the reassembled inverter prototype. The inverter was tested with a resistive load bank, and the test setup is shown in Figure I.1.2.7. Figure I.1.2.8 shows typical operating waveforms for (from top to bottom) DC bus voltage, line-to-line voltage, and three-phase currents. Figure I.1.2.9 plots measure inverter efficiency vs. output power; the measured inverter efficiency is more than 99.2% over the tested load conditions.
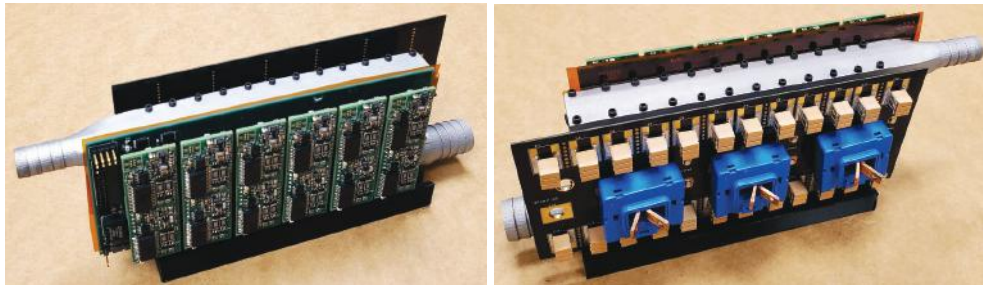
Figure I.1.2.6 Photos of the 100 kW inverter prototype with the refined manifolds.
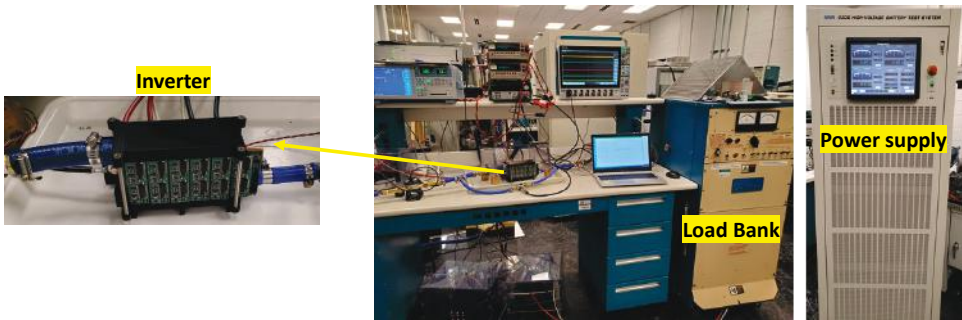
Figure I.1.2.7 Test setup for the 100 kW segmented inverter.

Figure I.1.2.8 Operating waveforms. From top to bottom: DC bus voltage, line-to-line voltage, and three-phase currents.
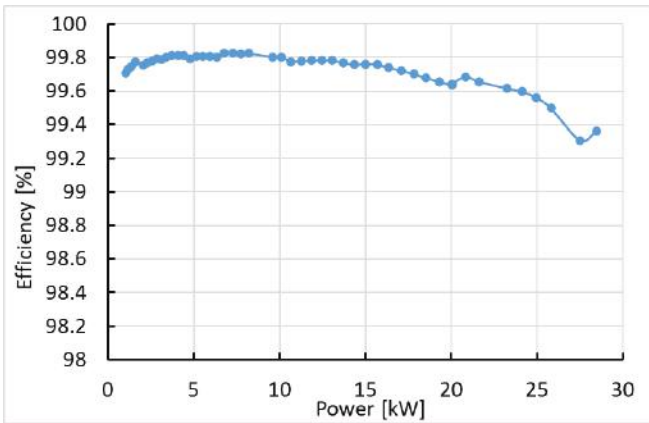
Figure I.1.2.9 Measure inverter efficiency vs. output power.

Design of 200 kW Segmented Inverter

To estimate the MOSFET junction temperature (T_j) variations with inverter switching operations, a lumped thermal impedance model for the 200 kW segmented inverter design was derived from finite element analysis (FEA) results in COMSOL and simulated in PLECS. Figure I.1.2.10 plots the cooling-down response FEA results on the left and shows the third-order Foster thermal network in PLECS on the right.
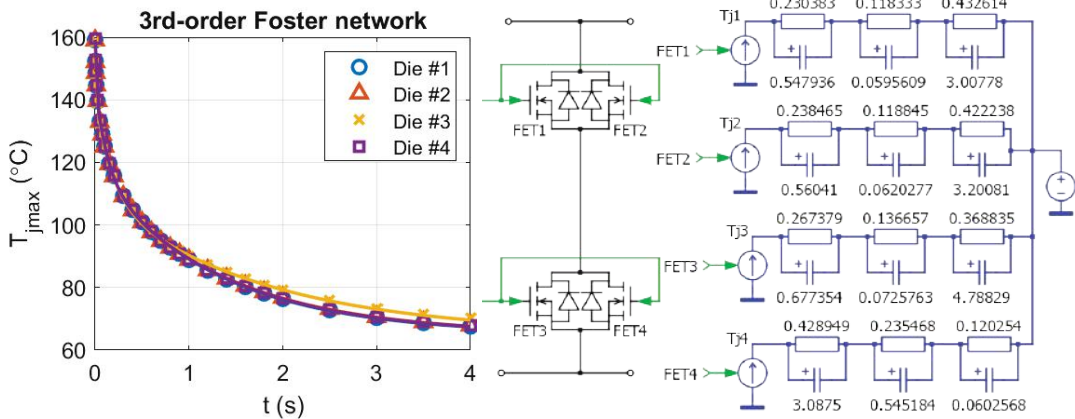
Figure I.1.2.10 (left) Cooling-down resopnse FEA results and (right) third-order Foster thermal network in PLECS for prediction of MOSFET junction temperature fluctuation in inverter operation.

On the left, Figure I.1.2.11 plots simulated PWM signals and inverter current waveforms for the symmetrical space vector (SV) PWM (SVPWM), and the bus-clamp SVPWM are on the right. The figure illustrates a reduced switching loss owing to no switching for 60° over each half-cycle with the bus-clamp SVPWM.

Figure I.1.2.12 shows simulation results at inverter output power P_o = 200 kW, switching frequency f_{sw} = 30 kHz, and power factor pf = 0.7. Table I.1.2.2 summarizes a comparison of the maximum, minimum, and average junction temperatures of the four MOSFETs. Compared with a symmetrical SVPWM, the bus-clamp SVPWM leads to a 20°C reduction in maximum junction temperature T_{jmax} and 34.9% less variation between the maximum and minimum temperatures.
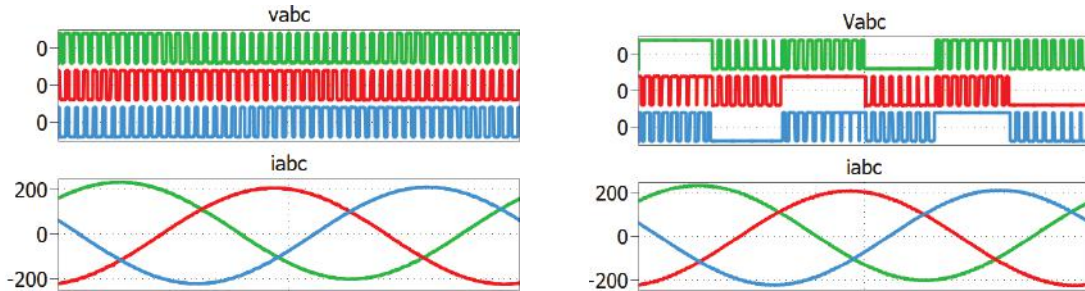
Figure I.1.2.11 Simulated PWM signals and inverter current waveforms for (*left*) symmetrical SVPWM and (*right*) bus-clamp SVPWM.
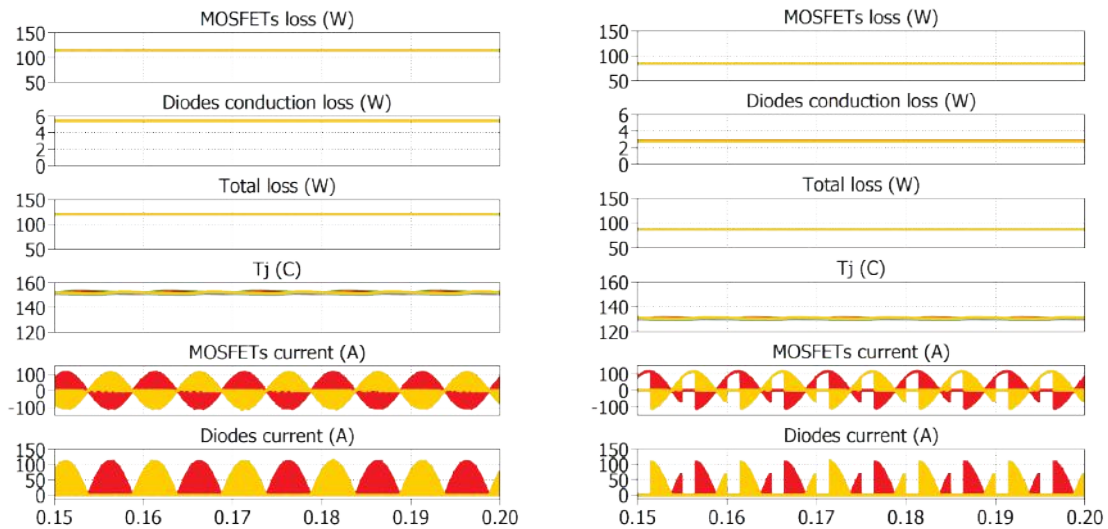
Figure I.1.2.12 Simulation results for symmetrical SVPWM (left) and bus-clamp SVPWM (right).

Table I.1.2.2 Comparison of MOSFET junction temperatures

	T_j (°C)	FET1	FET2	FET3	FET4
Symmetrical SVPWM	Min.	151.9	151.0	150.3	151.2
	Max.	153.5	152.6	151.8	152.9
	Δ(Max.−Min.)	1.6	1.5	1.5	1.7
	Average	152.6	151.8	151.0	152.0
Bus-clamp SVPWM	Min.	130.3	130.1	129.4	130.3
	Max.	131.3	131.1	130.4	131.4
	Δ(Max.−Min.)	1.0	1.0	1.0	1.1
	Average	130.8	130.6	129.9	130.8

Figure I.1.2.13 shows the finalized design for a 200 kW segmented inverter on the left and FEA flow simulation results on the right, indicating an even coolant flow distribution among the 12 heat sinks and a pressure drop of 11,543 Pa (1.67 psi) at a flow rate of 10 L/m. The inverter volume was 2.59 L, of which 10%

is taken by the current sensor and 23% by the interface boards. Integrated current sensors and gate drives planned in second generation designs are expected to reduce the volume below 2 L.
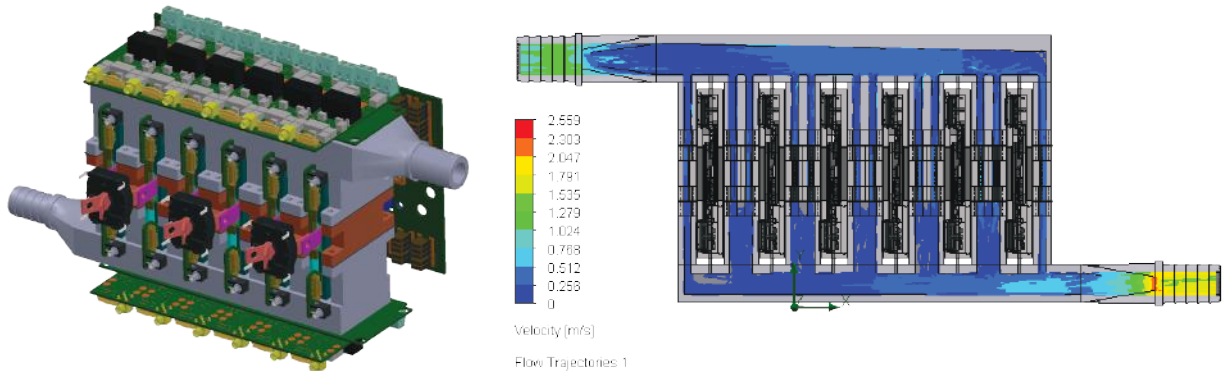
Figure I.1.2.13 Design for (*left*) a 200 kW segmented inverter and (*right*) FEA flow simulation results.

Conclusions

This report summarizes the successful test results for the 100 kW, 143 kVA segmented inverter from the cooling subsystem, gate drive, and control logic functionality to power tests (up to 28.5 kW) with a resistive load bank. Test results show high inverter efficiency above 99.2% over the tested load conditions.

This report also summarizes the design results for a 200 kW inverter using the segmented topology, double side–cooled SiC MOSFET power modules, CeraLink capacitors, and mini-channel heat sinks optimized using genetic algorithm–based tools to achieve high power density and reliability. The design used commercial off-the-shelf current sensors and control interface boards, resulting in an inverter volume larger than the target of 2 L. Future work will pursue further optimizing the power module packaging and integrating gate drive and current sensing capabilities into the power modules.

Key Publications

1. S. Chowdhury, T. Raminosoa, B. Ozpineci, R. H. Wiles, E. Gurpinar, G. J. Su, and J. L. Pries, Electric Drive System, US Patent application 17/733,251 (filed on April 29, 2022).

References

1. US Driving Research and Innovation for Vehicle efficiency and Energy sustainability (DRIVE) Partnership, *Electrical and Electronics Technical Team Roadmap*, U.S. DRIVE, US Department of Energy, October 2017, https://www.energy.gov/sites/prod/files/2017/11/f39/EETT%20Roadmap%2010-27-17.pdf.

2. G. Su and L. Tang, "A Segmented Traction Drive System with a Small DC Bus Capacitor," *Proceedings of the 2012 IEEE Energy Conversion Congress and Exposition (ECCE)*, (Raleigh, NC: IEEE, 2012), 2847–2853. doi: 10.1109/ECCE.2012.6342375.

Acknowledgements

I.1.3   Non-heavy Rare-Earth, High-Speed Motors (Oak Ridge National Laboratory)

Mostak Mohammed, Principal Investigator

Oak Ridge National Laboratory
1 Bethel Valley Road
Oak Ridge, TN 37831
E-mail: mohammadm@ornl.gov

Susan Rogers, DOE Technology Development Manager

U.S. Department of Energy
Email: Susan.Rogers@ee.doe.gov

Start Date: October 1, 2021   End Date: September 30, 2022
Project Funding: $550,000   DOE share: $550,000   Non-DOE share: $0

Project Introduction

Global CO_2 emissions have steadily increased since 1900, with a sharp rise since 1945 [1]. In the United States, the transportation sector is responsible of 28% of greenhouse gas emissions. These observations have led to global environmental consciousness and tighter regulations of CO_2 emissions in several countries, resulting in the expansion of the electrification of passenger and commercial vehicles.

Because of their high torque, power density, and excellent efficiency, most electric traction motors currently in production are permanent magnet (PM) synchronous motors, which use costly heavy rare-earth magnet material such as dysprosium (Dy). However, the price and supply of Dy have historically shown volatilities. To mitigate these risks, substantial progress has been made in PM material technologies to significantly reduce or eliminate Dy from the material's composition. Dy-free PM materials, now commercialized by major suppliers, can help lower the cost of traction motors and accelerate the market penetration of electric vehicles. However, Dy-free PM materials have lower coercivity; thus, they are more prone to demagnetization compared with their conventional heavy rare-earth counterparts. Therefore, special attention should be paid to demagnetization when designing Dy-free PM motors.

This report presents a Dy-free PM motor design for an outer rotor, enabling the integration of the drive and a shared cooling system between the power electronics and the motor.

Objectives

The overall objectives of this project are to enable the adoption of high-speed, high–power density, non-heavy rare-earth traction motors and to analyze the effect of new, advanced materials for non-heavy rare-earth electric motors. More specifically, the objectives for fiscal year (FY) 2022 are to complete:

- mechanical design, material selection, and stress analysis of the integrated motor drive and

- winding trials, design modifications, and updates to enable motor prototyping.

Approach

The overall objective of this project is to develop a 100 kW, high-speed and high–power density, Non-Heavy rare-earth traction motor to target the U.S. Driving Research and Innovation for Vehicle efficiency and Energy sustainability (DRIVE) specifications presented in Figure I.1.3.1. A Dy-free PM motor with an outer rotor configuration was designed to enable the integration of the drive and a shared cooling system between the power electronics and the motor. The electromagnetic, thermal, and mechanical feasibility of the design was verified. Because low-coercivity, Dy-free PMs were used, the robustness of the design against demagnetization was also confirmed. The current rating and direct current (DC)–link voltage were selected in accordance with the power

devices used in the drive. The design used a dual three-phase winding configuration powered by a dual three-phase segmented drive featuring interleaved switching to reduce the current ripple and DC-link capacitor [2].

Peak power (kW)	100
Continuous power (kW)	55
Maximum speed (rpm)	≤20,000
Power factor	> 0.8
Maximum current (A)	600
Maximum efficiency (%)	> 97
Torque ripple (%)	5
Volume (@50 kW/l)	2L
Mass (@5kW/kg)	20kg
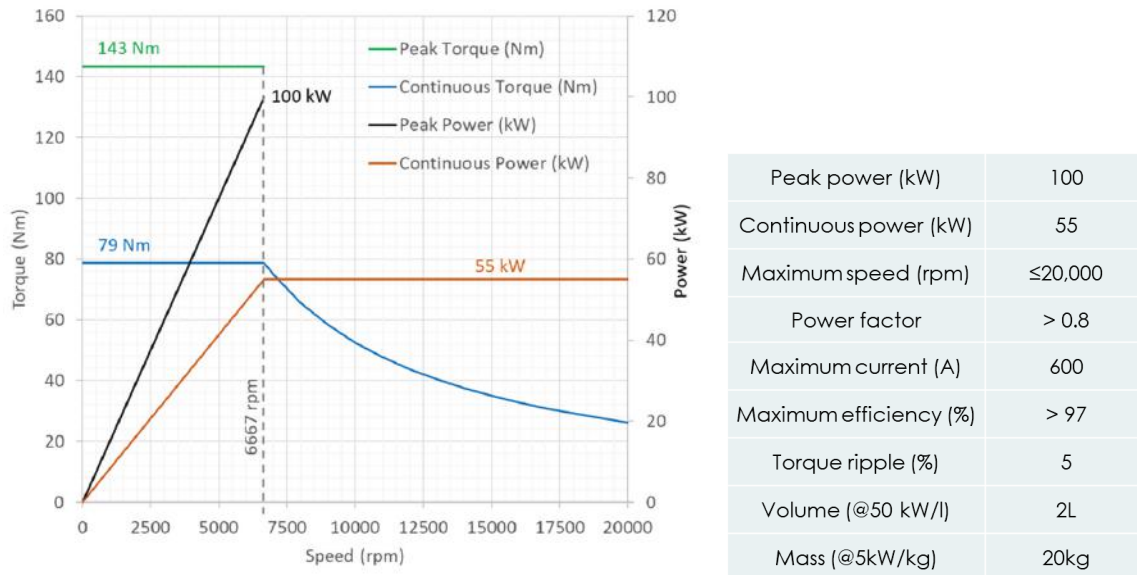
Figure I.1.3.1 Summary of specifications.

Results

An 18 slot/16 pole PM motor was designed in FY 2020–2021. Because the design used low-coercivity, non-heavy rare-earth PMs, a Halbach magnetization arrangement was selected to maximize the air–gap flux density and reinforce the resistance to demagnetization. The operating frequency ranged from 888 Hz at the base speed to approximately 2.67 kHz at the top speed of 20,000 rpm. The slot passing frequency at the maximum speed was 6 kHz. To minimize the PM eddy current loss, the PMs were axially laminated with a segment thickness of 1 mm. Litz wire with 150 strands of 33 AWG (American wire gauge) and 2 wires in hand was used for the coils to minimize alternating current losses [3]. Winding trials were conducted on 3D-printed plastic stator teeth (Figure I.1.3.2). Each coil had eight turns. An overall slot fill factor of 25% was achieved. The reason for this relatively low value is a combination of the litz wire fill (51%) and the slot space taken up for the heat exchanger (21% of the slot area).

The motor was originally designed with TDK NEOREC 45MHF PMs. However, the material was modified to N50 because of the unavailability of the 1 mm magnet segments and the 4-segment Halbach array. The N50 material is Dy-free, but its maximum operating temperature is limited to 80°C [4].

Figure I.1.3.2 Winding trials on a 3D-printed statorette.

The motor performance with N50 PMs was calculated (Table I.1.3.1). Owing to availability issues, COGENT NO-18 was used again as core material for the stator and rotor. The performance was calculated from a

combination of 2D and 3D time-stepped finite element analysis (FEA). 3D FEA was used to calculate the magnet loss as well as the end winding inductance and leakage.

Table I.1.3.1 Motor performance with N50 PMs and the COGENT NO-18 steel

Operating point	Total root mean square current [A]	Torque [Nm]	Peak line voltage [V]	Output power [kW]	Efficiency [%]
Steady state, 58 kW, 6,666 rpm	194	84	263	59	97
112 kW, 6,666 rpm	388	162	285	113	96
58 kW, 20 krpm	64	28	766	59	90

Two issues arose with the replacement of the 150°C-capable TDK magnets with N50: (1) lower coercivity leading to a reduced margin against demagnetization and (2) ensuring that the rotor operating temperature was 80°C or less.

To evaluate the design's resistance to demagnetization, a three-phase fault was simulated (Figure I.1.3.3). The motor operated at the peak power condition, and a 3-phase winding fault was suddenly applied at approximately $t = 1.2$ ms; the fault cleared at $t = 8$ ms. The magnet operating temperature was assumed to be 80°C. A 2D time-stepped FEA showed a 30% reduction in torque owing to the irreversible demagnetization at short circuit—this is the worst-case condition.

The rotor temperature was calculated from a steady-state thermal analysis. The loss distribution in the motor, including winding, core, and PMs, were calculated and used as inputs to the thermal model. The stator windings were cooled using in-slot ceramic heat exchangers [5]. The thermal analysis and the design of the cooling system were carried out by the National Renewable Energy Laboratory (NREL) (refer to project elt214, "Electric Motor Thermal Management" by Emily Cousineau [NREL]). The heat transfer coefficient on the rotor surface was calculated based on a relationship derived for rotating cylinders. The temperature distribution at the steady-state operating condition of 50 kW and 6,666 rpm showed that the magnet temperature was under 80°C (Figure I.1.3.4).
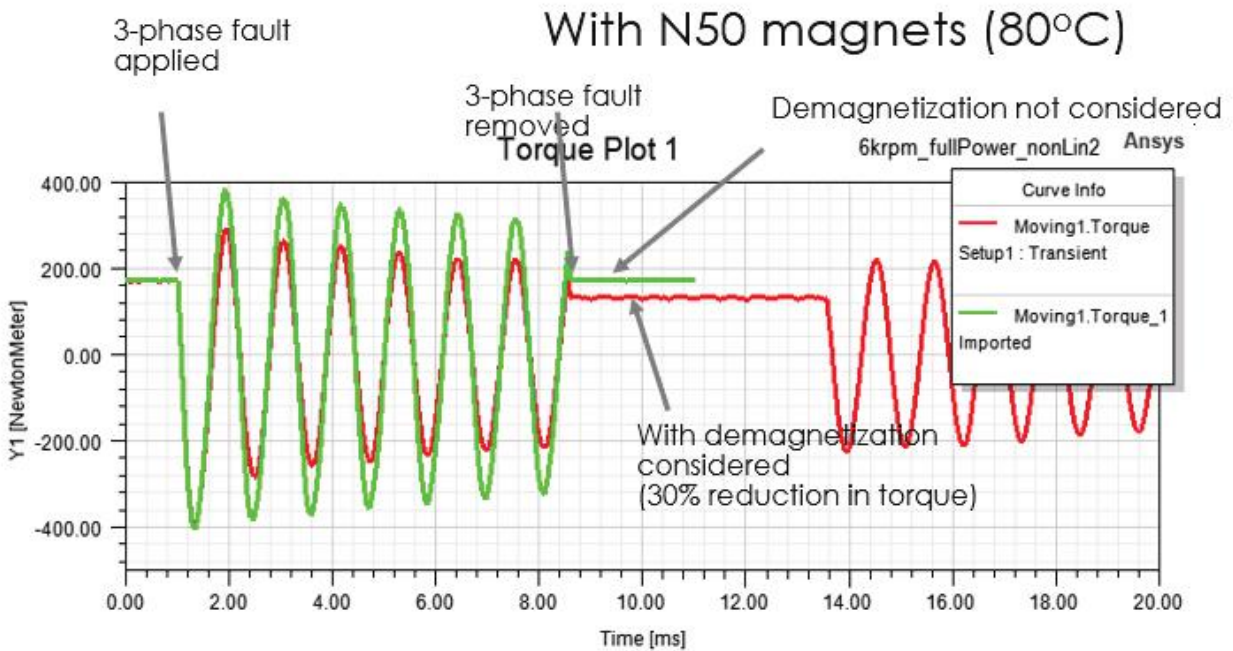
Figure I.1.3.3 Torque before, during, and after a short circuit fault, with and without considering PM demagnetization. A 30% reduction in torque was estimated following a 3-phase short circuit fault owing to irreversible demagnetization.

- Windings: 131°C
- Stator: 124°C
- Magnets: 76.6°C
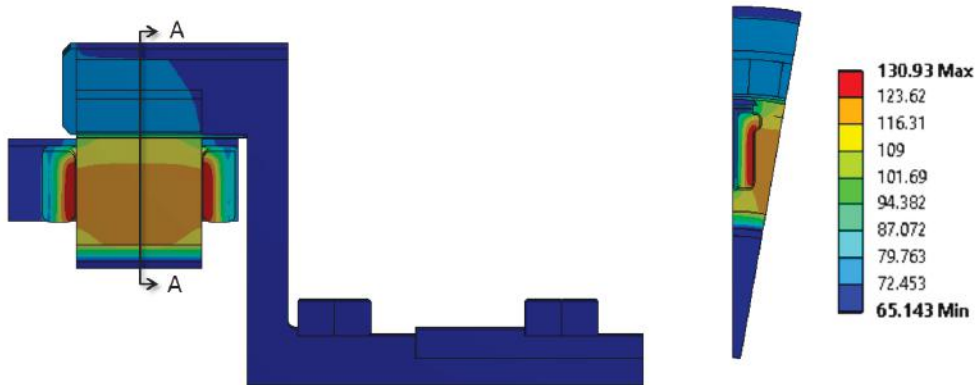
Figure I.1.3.4 Steady-state temperature map at the continuous power (50 kW), 6,666 rpm condition.

Two versions of the mechanical assembly are shown in Figure I.1.3.5 and Figure I.1.3.6. The rotor support structure was made from steel, and the stator support was made from Al. Eddy current loss was calculated in the stator and rotor structures under different operating conditions using 3D FEA and found to be small (Figure I.1.3.7). The assembly was designed at DOE's Oak Ridge National Laboratory (ORNL) to enable the integration of the drive and a cooling system shared between the power electronics and the motor (refer to project elt221, "Integrated Electric Drive System" by Shajjad Chowdhury [ORNL]). Two variations of the design are shown: (1) Design #1 in Figure I.1.3.5, a design supported by bearings on either side, and (2) Design #2 in Figure I.1.3.6, a design supported only on one side. Although Design# 1 would result in a stiffer

mechanical assembly because of being supported on both sides, no possibility to remove the power electronics exists without motor disassembly. Design #2, supported only on one side, uses 75 mm bore diameter bearings capable of rotating at a maximum speed of 24,000 rpm with grease lubrication.
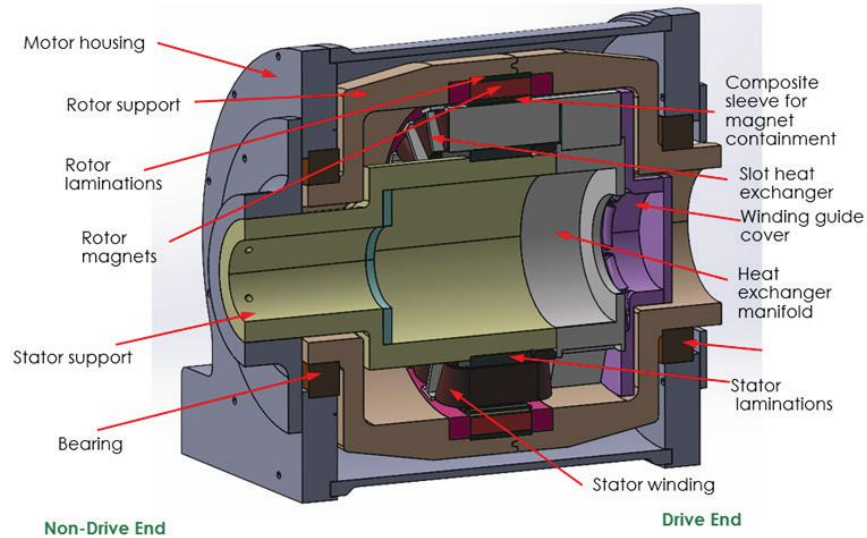
Figure I.1.3.5 Design #1, supported on both sides. The ability to remove the power electronics converter post assembly is lost.
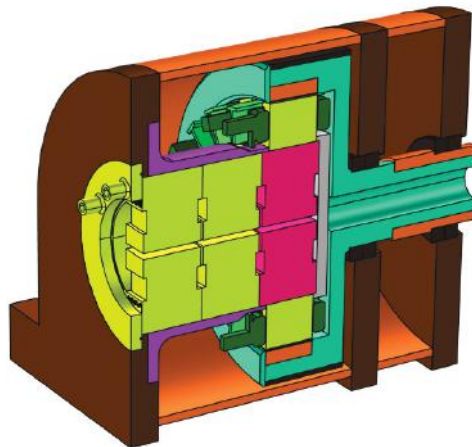
Figure I.1.3.6 Design #2, cantilever design. The power electronics converter can be removed post assembly.
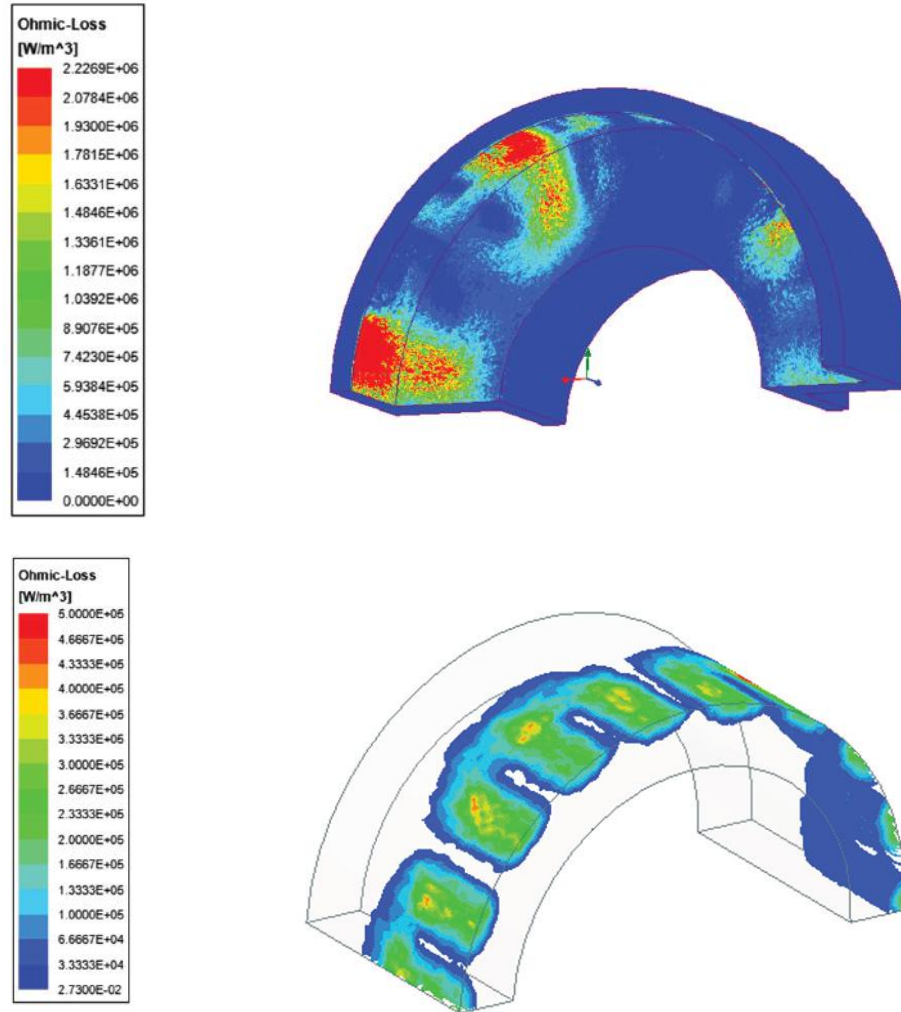
Figure I.1.3.7 Loss distribution in the (*upper*) stator bushing and (*lower*) rotor support structure. The loss densities were small.

The magnets have unequal tensile and compressive strengths, with the tensile strength (80MPa being substantially lower than the compressive strength (1100 MPa). Therefore, maintaining the magnets under compression is desirable. To maintain the magnets under compression, a preload needed to be applied using a carbon fiber wrap. Carbon fiber wraps are commonly used in high-speed PM rotors [6], [7]. The preload was applied by wrapping layers of carbon fiber and adjusting the tension in each layer [8]. Mechanical stress analysis was conducted using COMSOL and ABAQUS, the model is shown in Figure I.1.3.8. With no preload, the magnet and rotor stresses far exceed the material yield strength (Figure I.1.3.9). A preload of 100 MPa was able to maintain the magnet tensile stress under the limits of 80MPa (Figure I.1.3.10).
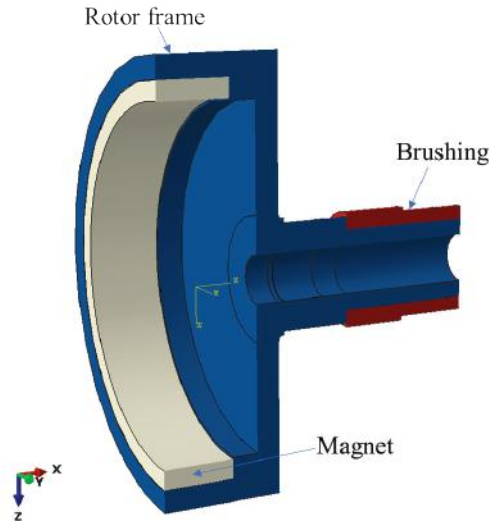
Figure I.1.3.8 Rotor model used for 3D mechanical stress analysis.
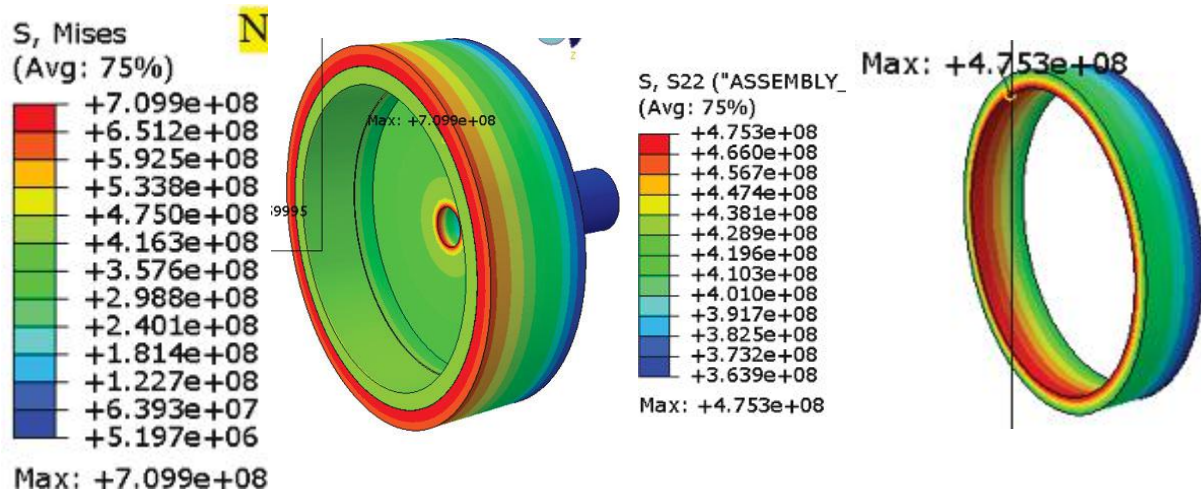
Figure I.1.3.9 Rotor Von Mises stresses (left) and PM hoop stress (right) with no preload applied. The PM hoop stresses greatly exceeded the tensile yield strength of 80MPa.
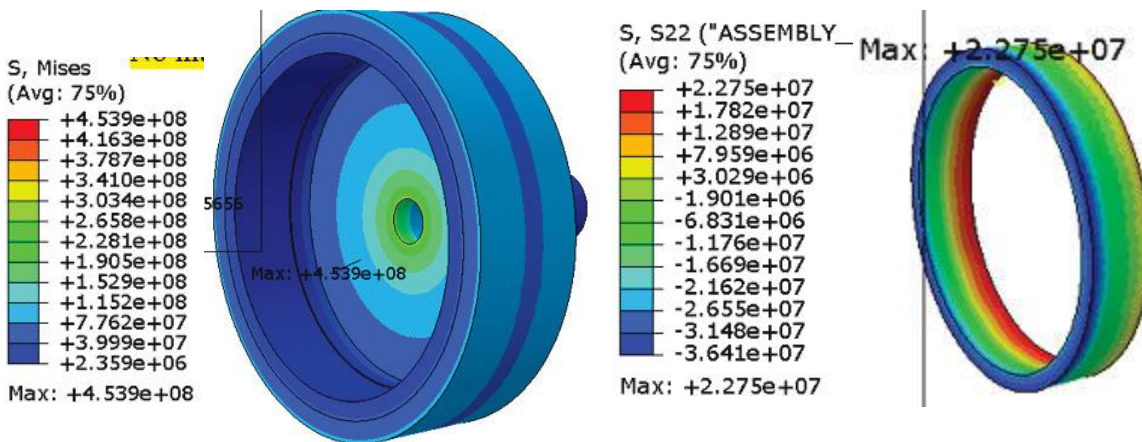
Figure I.1.3.10 Rotor von Mises stresses at 20,000rpm with a preload of 100 MPa (left), and the PM hoop stress with a 100MPa preload (right). The steel and PM stresses are within the material limits (410 stainless steel strength: 575-1000MPa depending on the annealing temperature: PMs tensile strength: 80MPa and compressive strength: 1100 MPa).

Conclusions

A high-speed and high–power density, non-heavy rare-earth PM traction motor was designed to enable the integration of the drive and a shared cooling system between the motor and the power electronics. The electromagnetic design as well as mechanical assembly were modified to accommodate the available bearings, PMs, and laminations. With the available Dy-free N50 PMs, 2D time-stepped FEA showed that the motor experienced a 30% reduction in torque following irreversible demagnetization under the worst-case scenarios. Thermal analysis showed that the magnet temperature was maintained under its maximum operating temperature of 80°C. Mechanical stress analysis showed that the stresses in the magnet and rotor support structure were under the yield strengths when a preload of 100 MPa was applied using a carbon fiber wrapping. Winding trials were conducted, and a fill factor of 25% was achieved. Future research will include analysis of rotor dynamics and initiation of motor prototyping. The motor performance will be compared with other state-of-the-art EV motor technologies.

Key Publications

Abstracts are being prepared for the Energy Conversion Conference and Expo (ECCE) 2023, IEEE Transportation Electrification Conference and Expo (ITEC) 2023, and International Electric Machines and Drives Conference (IEMDC) 2023.

References

1. U.S. DRIVE Partnership, *Electrical and Electronics Technical Team Roadmap*, U.S. DRIVE, U.S. Department of Energy, October 2017, https://www.energy.gov/sites/prod/files/2017/11/f39/EETT%20Roadmap%2010-27-17.pdf.

2. G. Su and L. Tang, "A Segmented Traction Drive System with a Small DC Bus Capacitor," *Proceedings of the 2012 IEEE Energy Conversion Congress and Exposition (ECCE)*, (Raleigh, NC: IEEE, 2012), 2847–2853. doi: 10.1109/ECCE.2012.6342375.

3. New England Wire Technologies, *Litz Wire Technical Information*, 2003

4. Arnold Magnetic Technologies, *The Important Role of Dysprosium in Modern Permanent Magnets*, https://www.arnoldmagnetics.com/wp-content/uploads/2017/10/Important-Role-of-Dysprosium-in-Modern-Permanent-Magnets-150906.pdf.

5. W. Sixel, M. Liu, G. Nellis, and B. Sarlioglu, "Cooling of Windings in Electric Machines via 3D Printed Heat Exchanger," *2018 IEEE Energy Conversion Congress and Exposition (ECCE)*, (Portland, Oregon, USA: 2018), 229–235. doi: 10.1109/ECCE.2018.8557845.

6. J.-H. Ahn, C. Han, C.-W. Kim, and J.-Y. Choi, "Rotor Design of High-Speed Permanent Magnet Synchronous Motors Considering Rotor Magnet and Sleeve Materials," IEEE Transactions on Applied Superconductivity 28, no. 3 (April 2018): 1–4, article no. 5201504.

7. Y. Chen, R. Sanchez, A. Yoon, and K. S. Haran, "Mechanical Design Considerations of an 'Ironless,' High-Specific-Power Electric Machine," *IEEE Transactions on Transportation Electrification* 3, no. 4 (December 2017): 855–863.

8. Lei Zu, Hui Xu, Bing Zhang, Debao Li, Huabi Wang, and Bin Zi, "Filament-wound composite sleeves of permanent magnet motor rotors with ultra-high fiber tension," *Composite Structures* 204, (2018): 525–535.

Acknowledgements

I.1.4 Integrated Electric Drive System (Oak Ridge National Laboratory)

Shajjad Chowdhury, Principal Investigator

Oak Ridge National Laboratory
1 Bethel Valley Road
Oak Ridge, TN, 37932
E-mail: chowdhuryms@ornl.gov

Susan Rogers, DOE Technology Development Manager

U.S. Department of Energy
E-mail: susan.rogers@ee.doe.gov

Start Date: October 1, 2021	End Date: September 30, 2022	
Project Funding: $400,000	DOE share: $400,000	Non-DOE share: $0

Project Introduction

The U.S. Department of Energy (DOE) in 2017 announced technical targets for light-duty electric vehicles. DOE targets a power density of 33 kW/L for a 100 kW traction drive system by 2025 [1]. This target would increase the current state-of-the-art power density by a factor of 8 compared to 2020 target. This project focuses on the tight integration of motor and inverter components to improve power density and thus achieve the target. Furthermore, this project optimizes the bulky direct current (DC)–link capacitor's volume and identifies optimal substrate technology for space-restricted applications to improve performance and lifetime.

Objectives

This project aims to research technologies that enable tight integration of the inverter with the motor and that, as a result, enable a high–power density, integrated traction drive. FY 2022 included the following tasks:

- Identify suitable substrate technologies for space-restricted, integrated drive applications.

- Develop and evaluate an inverter phase leg that integrates bus bars, gate drivers, and capacitors.

Approach

The approaches to achieving the project objectives included the following:

- Compare state-of-the-art substrate technologies to find the best solution for thermal performance.

- Design a single-phase-leg module that integrates gate drivers, capacitors, and bus bars that fits inside the motor.

- Evaluate the designed module's electrical performance.

Results

Form-Factor Identification of Power Modules

In the electric-motor development project (keystone 2), an outer rotor motor was designed to achieve high power density, as shown in Figure I.1.4.1 (a) [2]. The designed outer rotor motor has a rotating part outside the motor and a complex mechanical structure; therefore, not all the traditional integration techniques can be used. Two options are an axial end-plate mount and a radial housing mount, but they may not suit tight integration. Therefore, a novel internal stator mount integration technique has been identified in which the inverter can be integrated inside the stator. A six-phase segmented inverter was selected for this project. The inverter was placed in the cylindrical hollow space inside the stator of the designed motor. Figure I.1.4.1 (a) shows the placement of each phase leg with dimensions. Figure I.1.4.1 (b) shows a cross section of the cylindrical space and shows that the inverter components' (i.e., substrate, gate driver, and capacitor) heights must be less than 30 mm to fit inside the cylindrical space. This report shows the component sizing and selection to fit the inverter within this volume.
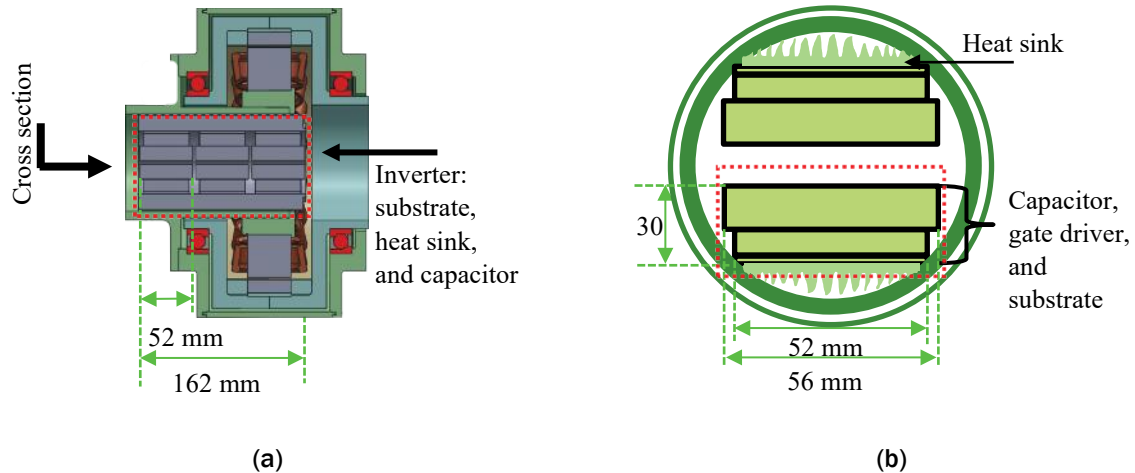
Figure I.1.4.1 (a) Inverter dimensions for integrating an internal stator mount with an outer rotor motor and (b) an inverter cross section that shows the height and width of the inverter.

Substrate Technologies for Space-Restricted Application

There is limited space inside the motor to incorporate the six-phase inverter. Therefore, a study has been conducted to determine suitable substrate technologies for better thermal performance. Three substrate technologies were selected for evaluation (identified in Keystone 1) [3]: direct bonded Cu (DBC), an insulated metal substrate (IMS), and thermally pyrolytic graphite (TPG)–encapsulated IMS (IMSwTPG). Diagrams with substrate structures are shown in Figure I.1.4.2 – Figure I.1.4.4. A 3D model was developed in COMSOL—finite element analysis software—to identify the thermal performance with varying substrate size and device location. In FY 2021, it is determined that, in a six-phase system, each phase-leg module would handle a 200 A current; thus, two devices were paralleled. These modules would generate a 500 W loss for peak-power operation, as estimated by Chowdhury [4], which translates to a 125 W loss in each semiconductor device.
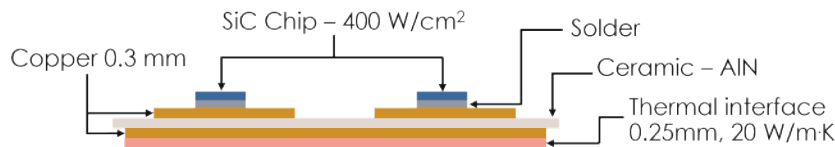
Figure I.1.4.2 Traditional DBC substrate structure.
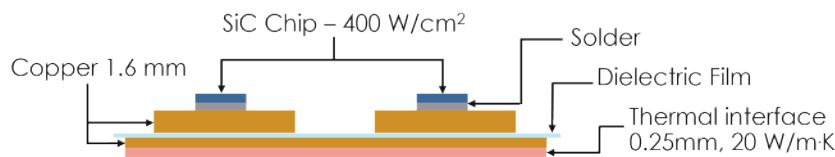
Figure I.1.4.3 Traditional IMS substrate structure.
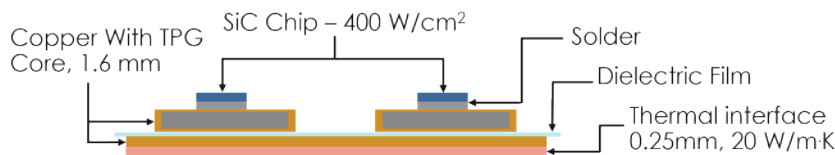
Figure I.1.4.4 IMSwTPG substrate structure shown in Keystone 1.

Losses were evenly distributed on the top surface of the semiconductor devices to evaluate thermal performance. Substrate areas were varied from 1,200 to 2,000 mm^2, and for each substrate area, the four semiconductor device locations were varied to identify optimal placement of the devices within the substrate. The ambient temperature was set to 65°C, and the heat-transfer coefficient was set to 10 kW/mK. The heat-transfer coefficient value was selected based on the FY 2021 analysis, in which it is determined that a heat-transfer coefficient of 10 kW/mK is required to keep the device temperature below 150°C for an area of 2,000 mm^2 if a DBC substrate is used.

Figure I.1.4.5 (a–c) shows the thermal results. For each substrate area, device placement yielded different average temperatures in the semiconductors. The highest temperatures were observed when the semiconductor devices were near each other because this proximity caused thermal loading. High temperatures were also observed when the devices were at the corners of the substrate; therefore, two sides of the devices did not have enough area to dissipate heat. The optimal temperature was observed when the devices were away from the substrate corners and the other semiconductor devices.

The optimal results for each substrate area for DBC, IMS, and IMSwTPG are plotted in Figure I.1.4.5 (d). The IMSwTPG yields a better result when the substrate area is large because IMSwTPG relies on the substrate area to improve thermal resistance. This result is similar for IMS-based substrates with an offset in device temperature. However, the DBC substrate shows a different result: worse performance than TPG and IMSwTPG at large substrate areas but much better performance with reduced substrate dimensions (<1,700 mm^2). Unlike TPG and IMSwTPG, DBC utilizes little substrate area. The heat generally propagates vertically downward at a 45° angle; thus, shrinking the substrate area would not affect the device temperature drastically. Owing to this phenomenon, DBC would perform better for space-restricted applications such as integrated electric drives.
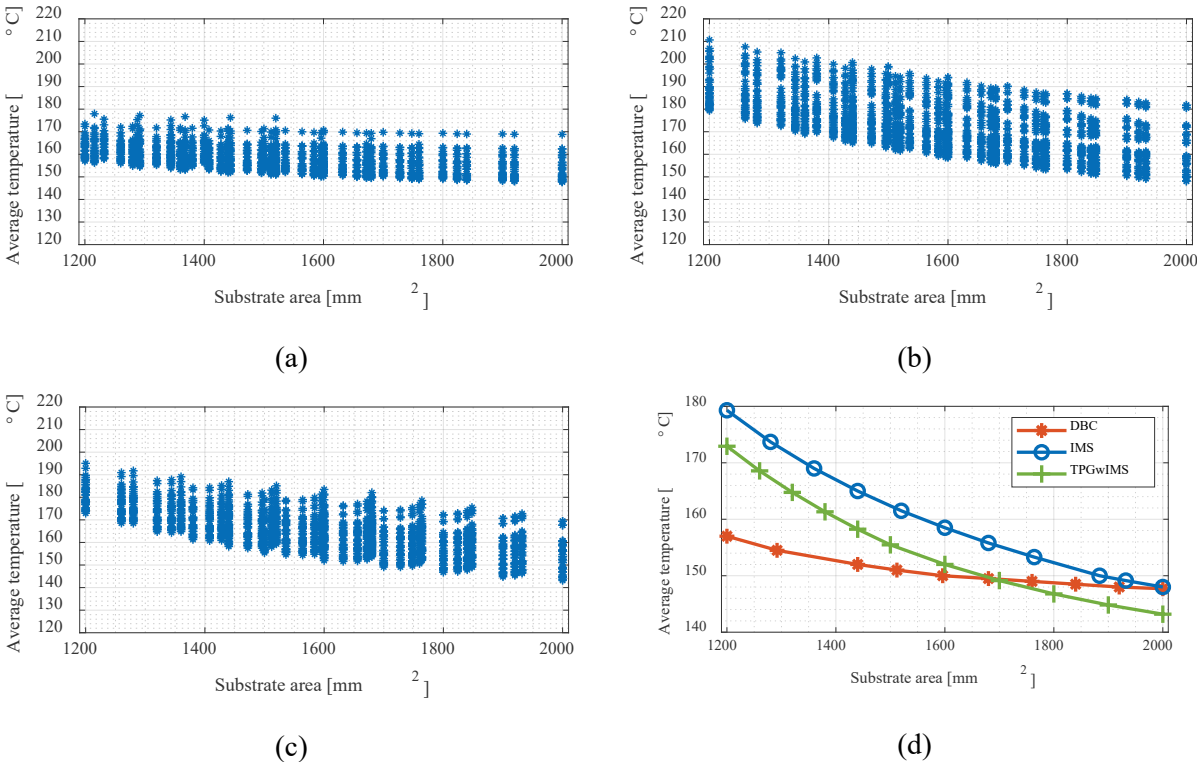
Figure I.1.4.5 Average surface temperature of the SiC semiconductor devices with varying substrate area and device location: (a) DBC showing 5% temperature variation with 40% reduction in substrate area, (b, c) IMS and IMSwTPG showing a more than 20% increase in device temperature, and (d) optimal temperature for each substrate area.

In DBC substrates, the heat propagates vertically at a 45° angle; thus, most of the substrate area is unused. The thermal performance of the DBC substrate can be improved if the area utilization is increased. Similar to IMS and IMSwTPG, if the heat can spread underneath the semiconductor, the thermal performance may improve. To enhance heat spreading, Cu block– or TPG-encapsulated Cu (Cu/TPGwCu) was soldered between the semiconductor chip and the DBC substrate. The reason is that a highly conductive (400 W/mK) Cu/TPGwCu block may spread the heat before reaching the DBC substrate. Figure I.1.4.6 shows a block diagram of the modified DBC substrate, in which an additional Cu block—DBC-encapsulated Cu (DBCwCu)—or a TPG-encapsulated DBC (DBCwTPG) Cu block was sandwiched between the substrate and the semiconductor chip. A 3D model was developed in COMSOL to evaluate the modified DBC's performance, and a 10 × 10 mm Cu block was selected to increase the heat-spread area by 400% compared with traditional DBC. First, the simulation model was set for a parametric study to identify the optimal thickness of the Cu block. Figure I.1.4.7 (a) shows the results: Notably, the semiconductor devices had the lowest temperature with 1.5 mm Cu thickness; thus, this thickness was used throughout the study. Three additional substrate technologies developed by DOWA METALTECH—direct bonded Al (DBA), double-sided cooling with DBC, and a modified DBC with TPGwCu—were selected for evaluation, and parameters are provided in Table I.1.4.1 and elsewhere [3], [5], [6].
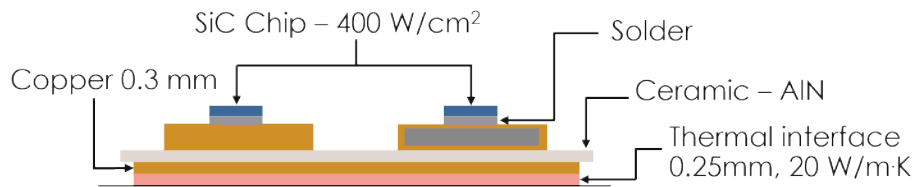
Figure I.1.4.6 Modified DBC substrate to improve thermal performance.

Table I.1.4.1 Evaluated substrate parameters

Substrate technologies	Comments
DBC [5]	• Insulator: AlN (0.63 mm) • Copper thickness: 0.3 mm • Interface material: 0.5 mm and 10 W/mK
IMS [5]	• Insulator: HT-07006 • Copper thickness: 1.6 mm • Interface material: 0.5 mm and 10 W/mK
IMSwTPG [5]	• Insulator: HT-07006 • Copper thickness: 0.25 mm • TPG thickness: 1.1 mm • Interface material: 0.5 mm and 10 W/mK
DOWA DBA [6]	• Insulator: Al_2O_3 (0.63 mm) • Aluminum thickness: 0.3 mm • Interface material: no material, directly bonded
Double-sided cooling	• Insulator: AlN • Copper thickness: 0.3 mm • Post : Cu • Height: 5 mm • Area: 50% smaller than SiC chip • Interface material: 0.5 mm and 10 W/mK
DBCwCu	• Same as DBC • Additional block: Cu, 10 × 10 × 1.5 (L × W × H) mm
DBCwTPG	• Same as DBC • Additional block: Cu insulated TPG core same as IMSwTPG

(a)   (b)
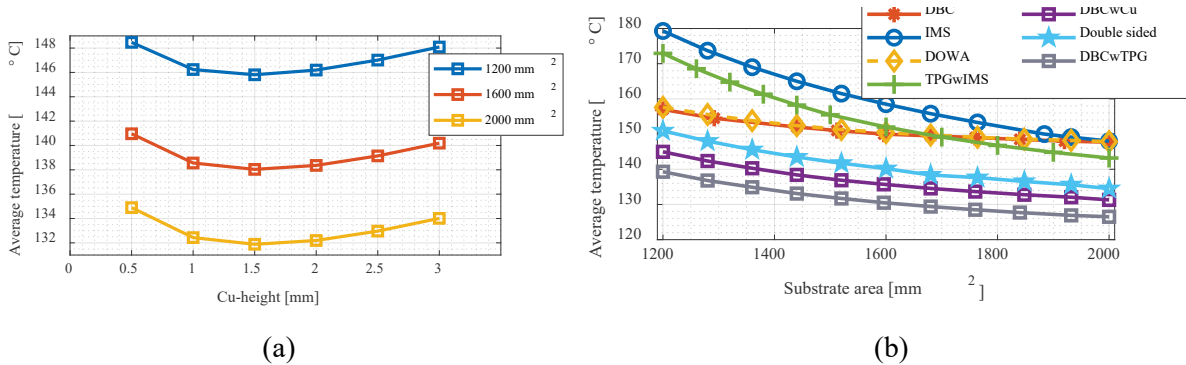
Figure I.1.4.7 Modified DBC performance: (a) the modified DBC, which performed better with 1.5 mm Cu thickness, and (b) a performance comparison of DBCwCu with well-known substrate technologies.

All the substrates were simulated by using finite element (FE) software with the varying area and device locations, and the optimal temperature results for each area are plotted in Figure I.1.4.7 (b) for comparison. DBCwTPG performed 30% better than TPG and IMSwTPG and performed 15% better than traditional DBC and DOWA substrates. It also performed 7% better than the popular DBC-based, double-sided, cooled package despite having minimal manufacturing complexity. The modified DBC could be a high-performance solution for space-restricted applications.

Power Block for an Integrated Electric Drive

A power electronic system requires a power module, gate driver, capacitors, bus bars, and heat sink. Traditionally, these subcomponents are designed separately and integrated to form an inverter/converter system. This approach sometimes leads to high-voltage overshoot due to large power-loop inductance and gate-voltage oscillation, especially at high-voltage and high-current operation. Thus, power electronic components must be co-optimized and codesigned to achieve better performance. A building block for power electronics—the power block—was designed that contains a power module, gate driver, capacitor, and bus bars (Figure I.1.4.8). The core idea was to use multiple power blocks to develop an inverter/converter with little or no compromise on performance. Figure I.1.4.9 shows the power-block components. The module was designed with two parallel SiC devices to handle 800 V and 150 A currents. A gate-driver board with decoupling capacitors was added on top of the module to reduce the gate-loop and power-loop inductance. A secondary capacitor board was placed on the gate-driver board to handle higher currents and suppress voltage oscillation. The entire capacitor board was designed to handle a more than 80 A ripple current. The capacitors were also placed symmetrically from the termination to achieve low-layout inductance and equal current-sharing among the parallel capacitor branches [7].
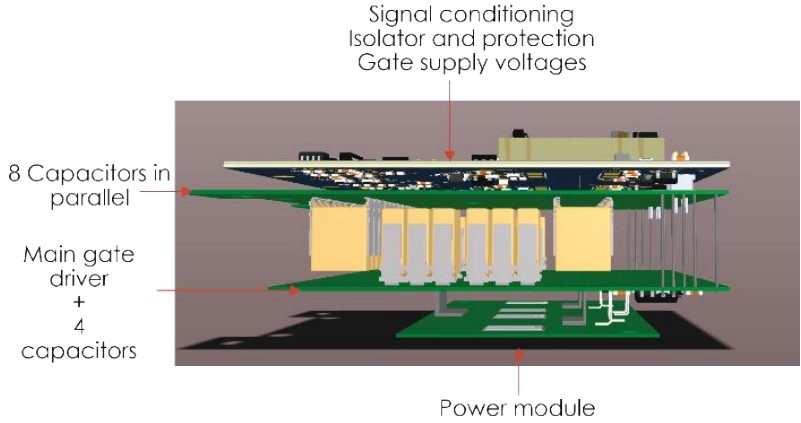
Figure I.1.4.8 Assembled power block containing a SiC module, capacitor, gate driver, and protection circuitry.

Power module

Gate driver + capacitor

Capacitor board

Gate driver power supply and protection circuitry
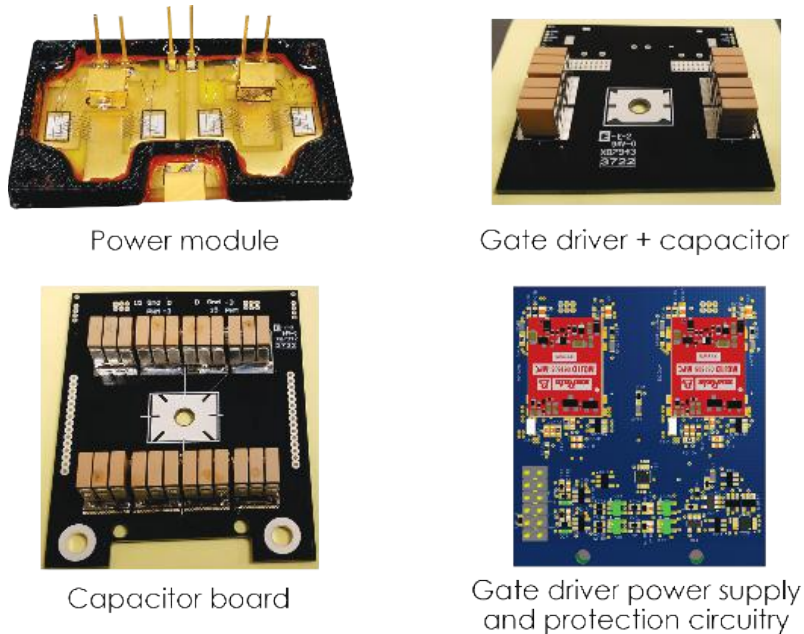
Figure I.1.4.9 Designed power block's components.
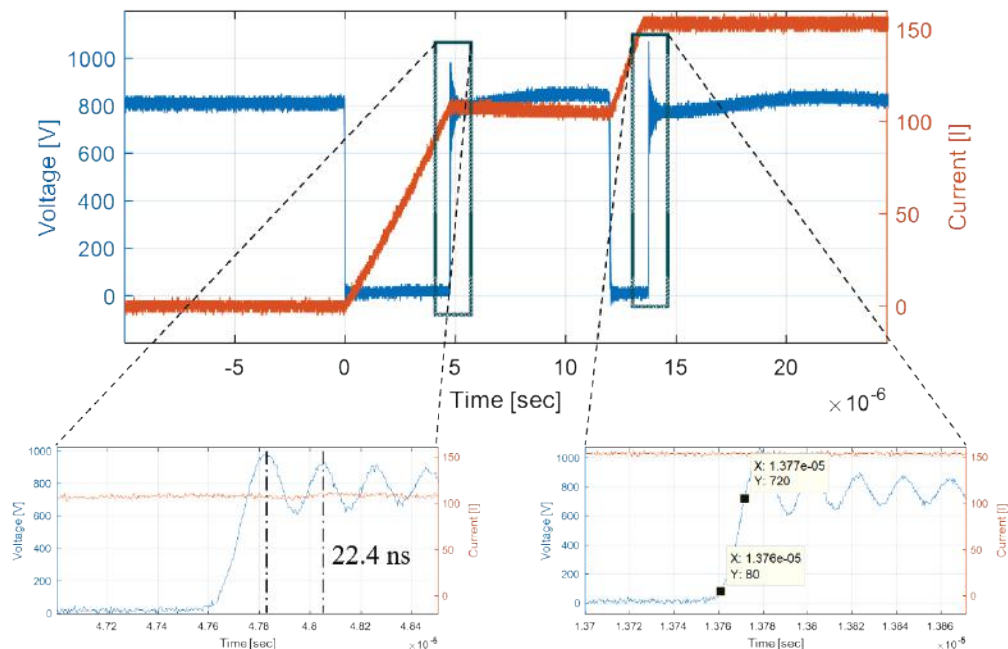
Figure I.1.4.10 Double-pulse test results of the module's switching performance at high-voltage (800 V) and high-current (150 A) operation.

Finally, a gate-driver power-supply board was installed. The power-supply board contains protection circuitry, including dead-time and shoot-through protection. The power board was then evaluated by using a double-pulse test setup in which the DC bus was 800 V and the current was 150 A (Figure I.1.4.10). In the figure, the blue curve represents the device turn-on and turn-off voltages, and the red curve represents the output current. The designed power board was tightly integrated; thus, there was no space to measure the device current. The turn-off transient of the device was enlarged to evaluate the dV/dt and the power-loop inductance (Figure I.1.4.10). The loop inductance of the power board was calculated from the device-output capacitance (Coss)

and the voltage-oscillation frequency. The oscillation period identified from the double-pulse test was 22.4 ns, and the device capacitance was 235 pF (470 pF total because two devices were paralleled), as specified in the datasheet [8].

Using these values, the inductance was estimated approximately 27 nH and that the overshoot was approximately 250 V for 800 V and 150 A operation, which is well within the manufacturer's specified voltage margin of 1,200 V. The inductance of the power module was characterized by using an impedance analyzer, which showed the module had approximately 20 nH inductance, which is similar to off the shelf high current modules. The layout inductance of the capacitor board and bus bars were estimated by subtracting the module inductance from the total power-loop inductance, which was 7 nH. The module inductance dominated the power-loop inductance and can be further optimized by redesigning the power-module layout, which the Keystone 1 project leads will further explore.

Conclusions

This report identified the modified dimensions inside the outer rotor motor to evaluate the size and shape restriction for the inverter components. The challenge was to miniaturize inverter components to fit inside the available space. In FY 2021, the capacitor board was designed to fit inside the available space. In FY 2022, various substrates were analyzed to identify the best solution. The DBC substrate showed much better thermal performance than the IMS and IMSwTPG substrate for space-restricted applications; thus, the DBC substrate was selected for this project. Additionally, a modified DBC substrate was proposed to improve thermal performance and to compare it with various available substrates. The FE simulation suggests that the modified DBC, which has minimal manufacturing complexity, performs better than the popular double-sided cooling strategy.

In FY 2022, a single-phase-leg power module was also designed that complied with the available form factor inside the motor. The power board—integrates the substrate, capacitor board, bus bars, and gate-driver circuitry. The board was designed to operate at 800 V and 150 A currents, and the performance was experimentally evaluated. The results demonstrate that the module can fit inside the available space and can operate at 800 V and 150 A.

Key Publications

1. S. Chowdhury, E. Gurpinar, and B. Ozpineci, "Capacitor Technologies: Characterization, Selection, and Packaging for Next-Generation Power Electronics Applications," *IEEE Transactions on Transportation Electrification* 8, no. 2 (June 2022): 2710–20, https://doi.org/10.1109/TTE.2021.3139806.

References

1. *Electrical and Electronics Technical Team Roadmap*, U.S. DRIVE, October 2017, https://www.energy.gov/sites/prod/files/2017/11/f39/EETT%20Roadmap%2010-27-17.pdf.

2. T. Raminosoa, "Non-Heavy Rare-Earth High-Speed Motors," Oak Ridge National Laboratory, DOE Vehicle Technologies Office Annual Merit Review, June 22, 2021, https://www.energy.gov/sites/default/files/2021-06/elt212_raminosoa_2021_o_5-14_202pm_KS_TM.pdf.

3. E. Gurpinar, "Highly Integrated Power Module," Oak Ridge National Laboratory, DOE Vehicle Technologies Office Annual Merit Review, June 2, 2020, https://www.energy.gov/sites/default/files/2020/06/f75/elt208_gurpinar_2020_o_4.27.20_254PM_LR.pdf.

4. S. Chowdhury, "Integrated Electric Drive System," Oak Ridge National Laboratory, DOE Vehicle Technologies Office Annual Merit Review, June 22, 2021,

https://www.energy.gov/sites/default/files/2021-06/elt221_chowdhury_2021_o_5-14_438pm_KF_TM.pdf.

5. E. Gurpinar, S. Chowdhury, B. Ozpineci, and W. Fan, "Graphite-Embedded High-Performance Insulated Metal Substrate for Wide-Bandgap Power Modules," *IEEE Transactions on Power Electronics* 36, no. 1 (January 2021): 114–28, https://doi.org/10.1109/TPEL.2020.3001528.

6. "Metal Substrate Technology Trends," DOWA METALTECH, accessed December 1, 2022, https://www.dowa.co.jp/metaltech/en/products_m_substrates.html.

7. S. Chowdhury, E. Gurpinar, and B. Ozpineci, "Capacitor Technologies: Characterization, Selection, and Packaging for Next-Generation Power Electronics Applications," *IEEE Transactions on Transportation Electrification* 8, no. 2 (June 2022): 2710–20, https://doi.org/10.1109/TTE.2021.3139806.

8. "Silicon Carbide Power MOSFET C2MTM MOSFET Technology," Cree, CCPM2-1200-0025A, last revised January 2021, https://assets.wolfspeed.com/uploads/2021/05/CPM2-1200-0025A.pdf.

Acknowledgements

I.1.5 Magnetics for Ultra-High Speed Transformative Electric Motor (Ames National Laboratory)

Iver Anderson, Principal Investigator

Ames National Laboratory (USDOE), Iowa State University
222 Metals Development, Iowa State University
Ames, IA 50011
E-mail: andersoni@ameslab.gov

Matthew Kramer, Principal Investigator

Ames National Laboratory (USDOE), Iowa State University
125 Metals Development, Iowa State University
Ames, IA 50011
E-mail: mjkramer@ameslab.gov

Jun Cui, Principal Investigator

Ames National Laboratory (USDOE), Iowa State University
106 Wilhelm, Iowa State University
Ames, IA 50011
E-mail: cuijun@ameslab.gov

Susan Rogers, DOE Technology Development Manager

U.S. Department of Energy
Email: Susan.Rogers@ee.doe.gov

Project Introduction

This project is part of the multi-lab Electric Drive Systems Consortium that will leverage U.S. research expertise and facilities at the national labs and universities to improve the power density of electric drives by 10x compared with the 2015 numbers while reducing the cost by 50% and doubling the lifetime miles within the next 5 years. The project is organized around three Keystones: (1) Power Electronics; (2) Electric Motors; and (3) Traction Drive System. The research activities at Ames support the Electric Motors Keystone 2 project.

The DOE 2025 target on electric motor power density is 50 kW/L. Such an aggressive target limits the choices for permanent magnets (PM) to the most powerful Nd-Fe-B based magnets, whose magnetic properties are strongly temperature dependent. Better thermal stability is achieved currently by adding significant amounts of Co and Dy/Tb (i.e., Heavy rare-earth elements (HREE)) [1], both with increased cost and supply chain vulnerability. Unfortunately, HREE are extremely scarce and regionally limited in supply. The U.S. Department of Energy (DOE) highlighted Dy as the single most critical strategic metal not only in the U.S., but world-wide. According to the USGS Minerals Commodities Summaries, the average price of Dy_2O_3 jumped from $295/kg in 2010 to $1410/kg in 2011, then retreated to $179/kg in 2018. Since then, Dy_2O_3 price has been steadily increasing, $239 in 2019, $258 in 2021, and fluctuating around $600/kg in 2022 [2]. With foreseeable large increase in the number of electrical vehicles and their dependence on permanent magnet traction motors, the supply risk for Nd, Pr and Dy is expected to remain high with their projected demand to more than double by 2030 [3]. Strategies to mitigate the RE materials criticality issues include increasing and diversifying the supply, and reducing demand. While several mines outside of China-- in Australia, Vietnam and the US-- have opened and have begun production of RE elements, the most desired "heavy" RE (HRE) elements, in particular, Dy and Tb, remain low in supply because none of these newly opened mines are rich in heavy RE reserves. To reduce the demand for heavy RE elements, alternative magnet technologies that eliminate or use significantly less Dy have to be developed, where Dy is used now for maintaining Nd-Fe-B's

coercivity at high temperature [4]. In 2020, Ames Lab researchers have demonstrated that significantly reducing the grain size of a Nd-Fe-B magnet will improve its coercivity, making it possible to use a microstructure engineering grain-refinement approach to replace the chemistry approach, i.e., a Dy addition. However, fine-grain magnet requires ultra-fine feedstock powders (<2 µm), which are much more sensitive to degradation when exposed to oxygen. To manufacture fine grain magnet from ultra-fine powders, the manufacturing process must be modified with additional controls of oxygen. Alternatively, one can passivate the powder and reduce its oxygen sensitivity to that of normal powders (3-5 µm). We plan to focus on developing a novel passivation technology that can enable the mass production of fine-grain magnet using ultra-fine Nd-Fe-B powders.

One viable approach to drastically increase motor power density is to increase motor speed. Although not specified by the DOE 2025 target, 90% efficiency is a key operational limit for electric motors because less efficient motors consume more power (including power for extra motor cooling), reduce vehicle range by imposing extra load on the vehicle battery, and diminish the impact of increasing motor power density. To maintain such high efficiency at high speed, the magnetic materials, especially soft magnetic cores, need to exhibit exceptionally high electrical resistivity in order to minimize otherwise substantially higher energy loss caused by increased eddy current heating. These tight constraints on materials are further tightened by the 2025 cost target of $3.3/kW, which disqualifies most of the existing advanced soft magnetic materials (e.g. amorphous and nanocrystalline) from meeting these requirements. It appears that one of the barriers for meeting the DOE 2025 targets of 50 kW/L power density is the lack of cost-effective soft magnetic materials that can run at high frequency without excessive eddy current heating. 6.5% Si steel has been demonstrated as a cost effective (from raw materials perspective) advanced soft magnetic materials suitable for high-speed motor application. Previously, Ames researchers have successfully addressed the brittleness problem associated with the high silicon content. However, the developed solution is based on planar flow casting process that requires heavy capital investment. We plan to lower the requirement on the processing equipment by enabling direct use of melt-spun wires, which are much simpler and cost-effective to manufacture than wide thin sheets.

Objectives

This project will develop the PM and SM materials and their processes for high-speed traction drive motors. For PM materials, the objective is to enable fine grain RE permanent magnet free of heavy rare earth elements by developing grain boundary engineering necessary to mass produce sintered magnet with ultrafine grains. For SM materials, the objective is to lower the application cost of the 6.5% Si steel by developing the novel wire-bundle near-net-shape stator concept that can use cost-effective melt-spun wires.

Approach

Grain size reduction is a viable approach for eliminating or reducing critical heavy RE (HRE) elements usage in the magnets for PM motors while maintaining their high temperature performance. It is possible to push the coercivity to beyond 20 kOe with ultrafine grains. With such high coercivity at room temperature, even with the typical rate of coercivity decay with increasing temperature (-0.6%/K) [1], there will still be enough coercivity at the 450 K, where the high-speed motor may operate. The challenge for the ultrafine grain approach is to develop feedstock powders with particle size near 1 µm; and more importantly, to keep the grain size less than 2 µm during sintering to full density. This also requires development of synthetic particle surface passivation methods and extreme care in handing powders to restrict oxidation. In FY20, Ames Lab successfully demonstrated the fine-grain magnet concept. In FY21, Ames Lab carried out investigations of industrially viable processing methods to passivate feedstock powders with particle size (< 3 µm) and demonstrated the effectiveness of NF_3 gas on passivating Nd-Fe-B at elevated temperature. In FY22, Ames Lab optimized the passivation process and the bulk magnet fabrication process using PrCu as a low temperature sintering aid to produce high density sintered PM without significantly growing the grains.

Melt-spinning is a viable approach for enabling 6.5% Si steel for high power density motor applications, in spite of its higher cost than traditional methods for producing common 3.2% Si steel. It has been established that the electromagnetic properties of 6.5% Si steel are superior to that of commonly-used 3.2% Si steel [6], except that the 6.5% Si steel is brittle and cannot be readily mass-produced using the cost-effective slab-casting and cold-rolling method. Ames Lab has showed that 6.5% Si steel becomes ductile after rapid quenching from high temperature [7]. Melt-spinning is traditionally used for manufacturing amorphous and nanocrystalline materials where rapid cooling rate is essential for preventing grain growth. One of the shortcomings of current industrial planar flow casting is the limited throughput due to the difficulty in making a wide ribbon with smooth surfaces, which requires thin and steady feeding of molten steel over a wide wheel width. The full width ribbon should be manufactured about 220 mm wide for current motors. In comparison, narrow ribbon (or a thin wire) doesn't need smooth surface control. In theory, one can place many small nozzles in parallel and simultaneously melt-spun steel wires, thereby dramatically increasing the productivity. In FY22, Ames lab has refined the motor stator geometry with ORNL and assembled U-shaped wire bundles made of 6.5%Si steel. To consolidate the wire bundles, Ames lab has investigated thermal oxidation conditions for increased electrically insulating SiO_2 surface growth. Laminated structures have been achieved through hot pressing of the coated 6.5%Si. To improve the magnetic properties and electrical resistivity, Ames lab has started investigation of alloying the 6.5%Si with third elements such as B, P, Co, Ni, and will pursue these and other alloying elements in FY22.

Permanent magnet traction motors are the most compact and efficient electric drive motors. Their optimization is a fine balance between the properties and topology of SM and PM components and the demagnetization fields. Clearly, a new motor topology with complex flux patterns that can take full advantage of new PM and SM materials is needed. The Ames team will continue to work with ORNL, NREL, and SNL to demonstrate the newly developed magnetics in an electric motor.

Results

Task 1: Develop fine grain RE permanent magnet with high coercivity at high temperature

While continuing to implement the fine grain magnet approach by developing the passivation technologies for the feedstock powder that is 20% smaller than the current state of the art, the team started working on a new approach to further improve the magnet's coercivity without including any critical HREs. The new approach is based on the understanding of Nd-Fe-B's coercive mechanism, i.e., the reversal of magnetic domains is through nucleation and growth. The hypothesis is if we can separate magnet's grains with a layer of non-magnetic material, we may impede the propagation of the magnetic domain reversal, such that the early reversal in the grains with defects will not trigger any reversal in the "good" grains. Experimentally, this concept can be achieved by two steps: 1) identify the material suitable for forming the non-magnetic grain boundary phase, 2) mix the identified materials with the magnet's regular feedstock powder, then proceed with the normal magnet sintering process.

After examined a number of metals and oxides, Ames researchers found PrCu alloy was the most suitable material for the grain boundary phase. It is non-magnetic, has a significantly lower melting point and wets the Nd-Fe-B grains relatively well. A series of magnets with different amount of PrCu powders blended with the regular Nd-Fe-B feedstock powders were prepared. Figure I.1.5.1a shows the magnetic properties of these magnets. It shows adding PrCu significantly increases the coercivity as expected, but it decreases the remanent magnetization because PrCu is non-magnetic. There is an optimal amount of PrCu, 7.5 wt.%, that can be added to the magnet to increase coercivity without significantly reducing the maximum energy product. Figure 1b shows the temperature dependence of properties for these magnets. It shows that the energy products of the PrCu-added magnets are inferior at room temperature, but once the temperature exceeds 100 °C, their coercivity decrease (green and blue curves) is much slower than the conventional Nd-Fe-B magnet (black curve). These results directly proved Ames researchers' approach is effective in eliminating HRE in Nd-Fe-B magnets while maintaining its advantage for high temperature performance.
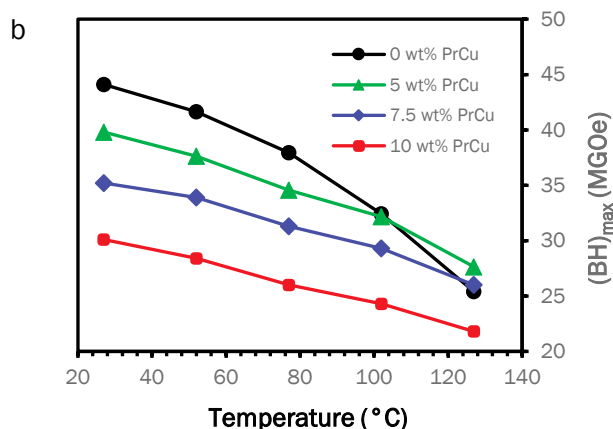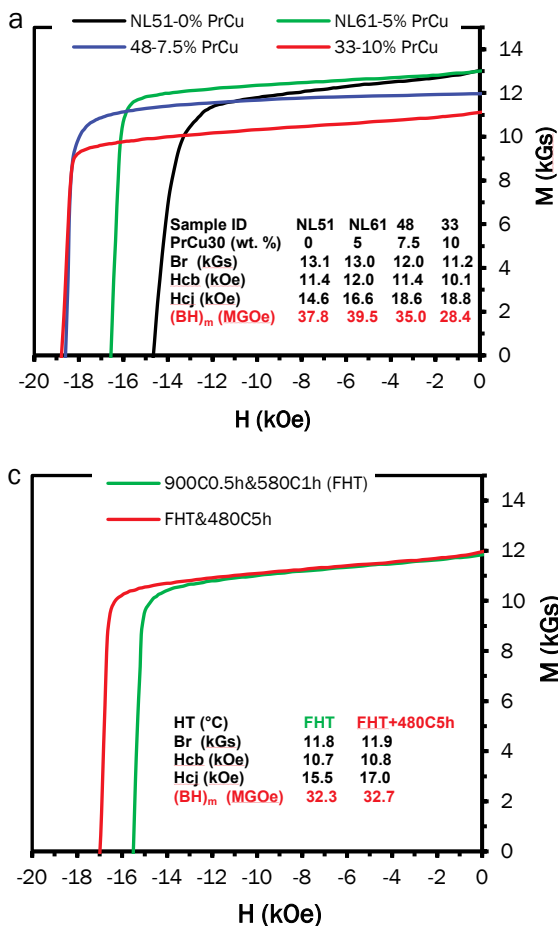
Figure I.1.5.1 Magnetic properties of the magnet with PrCu as grain boundary phase material. 1a) MH curves of the magnets with different amount of PrCu powders blended with the normal magnet feedstock powders. The black curve is the control, i.e., the one without any PrCu; 1b) the temperature dependence of the maximum energy products of the magnets with difference amount of PrCu. The magnet with 5% PrCu shows clear advantage over the one without; 1c) MH curves of the magnet with two different heat treatment schedules. Post sintering annealing helps the magnet to gain about 2 kOe coercivity.

Task 2: Development of cost-effective manufacturing process for high performance soft magnetic materials in thin sheet form

Previous research showed that the planar flow casting method is a suitable manufacturing method for mass production of ductile thin sheets of 6.5% Si steel for motor applications. Such method has been used for producing amorphous and nanocrystalline materials that are ideal for stationary transformer and power electronic applications due their brittleness as the result of nano scale grain size. Most nanocrystalline materials are brittle because grain boundaries' effect in pinning dislocation movement. The melting point of 6.5% Si steel is 1475 °C, about 400-600 °C higher than those of the amorphous or nanocrystalline metals. Such high processing temperature impose excessive thermal load on the melt spinning system, making it difficult to control nozzle to wheel distance, which in turn, making it difficult to produce wide and smooth ribbons. In FY20, after successfully produced 20 mm wide 6.5% Si steel ribbon, Ames researchers concluded that the capital cost of the wide ribbon approach might be too high for the industry to adopt. An innovative approach is needed to cost-effectively produce rapidly solidified 6.5% Si steel. In FY21, Ames researchers creatively solved problem with the wire-bundle approach, which reduces the ribbon width to as narrow as 1 mm.

In FY22, Ames researchers has worked with the ORNL and developed a new motor stator design that can take full advantage of the 6.5%Si wire bundle. The revised motor design and the demonstration of the U-shaped 6.5%Si steel bundle is shown in Figure I.1.5.2. The 18-pole stator is designed with 18 U-shaped wire bundles. The 18 U-shaped bundles are bonded side by side forming a circle. The stems of the U bundle form the inside diameter of the stator providing structural support and its integrity. The necks of the U bundles guide the magnetic flux generated by the copper windings to the surface mount magnets on the outer rotor assembly. The two necks of each U shape wire bundle are forming one half of the adjacent poles. To realize this design, we

have built the U bundles using 6.5%Si wires and epoxy. The wires are wound onto two glass bottles to form a toroid first and then sliced into halves to form two identical U-shaped bundles. The first set of bundles we made having a thickness of ~5 mm (defines the pole width) and the height of ~20 mm (defines the laminate thickness). The process can be repeated for building the rest of the U bundles to assemble the full motor stator.
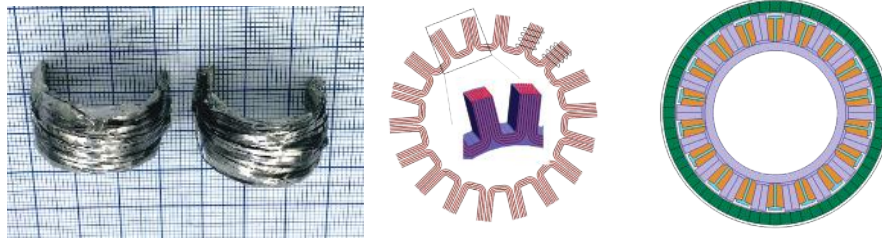
Figure I.1.5.2 Demonstration of AMES wire bundle concept (left); wire bundle stator (mid); ORNL stator/rotor assembly (right)
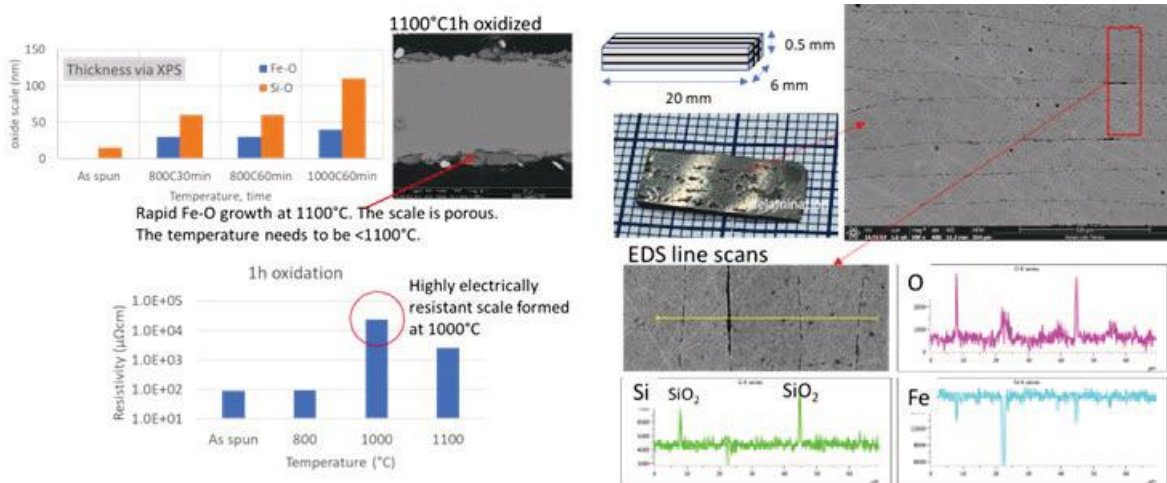
Figure I.1.5.3 oxide scale thickness and electrical resitivity for as spun and thermal treated ribbon, and micrograph for 1100 °C treated ribbon.

Figure I.1.5.4 Hot pressed sample showing the lamination by a inter ribbon SiO2 layer.

In the U-shaped bundle shown above, the 6.5%Si steel wires are insulated by epoxy resin which prohibited further stress relief heat treatment. In order to allow for further heat treatment to optimize the magnetic properties of the stator, an inorganic and insulating coating would be ideal. Since SiO_2 is electrically insulating, we had investigated the formation of surface SiO_2 on 6.5%Si steel ribbon after thermal exposure. Using X-ray photo-electron spectroscopy (XPS) depth profiling with controlled ion-milling, we had studied the oxide formation on 6.5%Si steel at various temperatures. The as-spun ribbon was found to have a naturally occurring SiO_2 scale of 15 nm. Thermal treatment at 800 °C for 30 minutes or 1 hour result in a four-fold growth in SiO_2 scale thickness (60 nm). The growth of SiO_2 is more prominent at 1000 °C, where it grows into a thickness of 110 nm after 1h exposure. However, at 1100°C, rapid formation of Fe-O dominates and results in a porous scale (Figure I.1.5.3). The resistivity of the ribbon was also evaluated. It was found that the resistivity has increased by more than two orders of magnitude in the 1000 °Cx1h thermal exposed ribbon. The resistivity of the 1000 °C oxidized ribbon is 23,700 μΩ-cm while that of the as-spun ribbon was 90 μΩ-cm, as measured by 4 probe method. Our thermal oxidation study has determined that the 1000 °C thermal exposure can be optimum for high resistivity SiO_2 scale formation on 6.5%Si steel ribbons.

In order to consolidate the insulated ribbon to a bulk sample at near-net shape with highest densification, we had also studied the hot pressing process for the insulated ribbons. 1000 °C x 1 h oxidized ribbons were sized,

aligned in an Inconel mold and hot pressed at 880 °C at 50 MPa into a plate shape sample 20 mm x 6 mm x 0.5 mm. The densification of the hot pressed sample is 97.3%, significantly higher than any epoxy bonded samples. The cross-sectional images and the EDS maps (Figure I.1.5.4) show the presence of a thin SiO_2 layer at the ribbon boundaries. Though inter-ribbon lamination is clearly visible, the sample is not fully insulated electrically. It is possible that there is lateral flow of SiO_2 which reduces the SiO_2 thickness between the ribbons. The hot pressing condition is being optimized for a thicker SiO_2 layer without compromising overall densification.

Conclusions

In FY22, the Ames team has been working on development of permanent and soft magnetic materials for the next generation of high power density drive motors. These two efforts were aimed at improving the coercivity of PMs without HRE elements for motor rotors through grain size refinement and at reducing eddy current losses in motor cores by enabling highly resistive 6. 5% Si steel to be cost effectively produced. Both magnetic materials were developed with methods that can be scaled for manufacturing. A passivation technique also was developed and demonstrated to handle the ultrafine Nd-Fe-B powders for PMs with highly refined grain size. A novel wire-bundle concept was demonstrated for making near-net-shape stators from narrow Fe-6.5Si melt spun ribbons. U shape wire bundles have been demonstrated. A thermal oxidation treatment was defined for the growth of electrically insulating native oxide for 6.5%Si steel.

Key Publications

1. Tang, W., Ouyang, G., Cui, B., Wang, J., Dennis, K.W., Kramer, M.J., Anderson, I.E. and Cui, J., 2021. Magnetic and mechanical properties of grain-refined Dy-free Nd-Fe-B sintered magnets. Journal of Magnetism and Magnetic Materials, 521, p.167533.

2. Ouyang, G., Macziewski, C.R., Jensen, B., Ma, T., Choudhary, R., Dennis, K., Zhou, L., Paudyal, D., Anderson, I., Kramer, M.J. and Cui, J., 2020. Effects of Solidification Cooling Rates on Microstructures and Physical Properties of Fe-6.5% Si Alloys. Acta Materialia, p.116575.

3. Ouyang, G., Jensen, B., Tang, W., Schlagel, J., Hilliard, B., Pan, C., Cui, B., Dennis, K., Jiles, D., Monson, T. and Anderson, I., 2020. Near Net Shape Fabrication of Anisotropic Fe-6.5% Si Soft Magnetic Materials. Acta Materialia. 201, p.209-216.

4. Ouyang, G., Jensen, B., Macziewski, C.R., Ma, T., Meng, F., Lin, Q., Zhou, L., Kramer, M. and Cui, J., 2019. Characterization of ordering in Fe-6.5% Si alloy using X-ray, TEM, and magnetic TGA methods. Materials Characterization, 158, p.109973.

Conference presentations
1. G. Ouyang, Recent development in processing and application of Fe-6.5%Si soft magnetic material. 25th Soft Magnetic Materials Conference, Grenoble, France, May 2022. (Invited conference plenary, presented remotely)

2. G. Ouyang, R. Claude, A. Kovar, M. Kramer, I. Anderson, J. Cui, The processability and physical properties of boron alloyed melt-spun Fe-6.5%Si ribbons. The 67th Annual Conference on Magnetism and Magnetic Materials, Minneapolis, MN, USA, 2022.

3. Wei Tang, Gaoyuan Ouyang, Jing Wang, Matthew Kramer, Jun Cui, and Iver E. Anderson, Coercivity enhancement of PrCu diffused Dy-free NdFeB sintered magnets, presented in MMM 2022 conference, Minneapolis, MN, Oct31-Nov 4, 2022.

References

1. Liu, S., and G. E. Kuhl. Development of New High Temperature and High Performance Permanent Magnet Materials. No. UDR-TR-2000-00092. DAYTON UNIV OH RESEARCH INST, 2000.

2. M. Garside, Global price forecast of rare earth oxides 2019-2025, Statista, 2020.

3. J. Ormerod, "Rare earth magnets: yesterday, today and tomorrow." Magnetics 2019, 23 January, Orlando. https://www.linkedin.com/pulse/rare-earth-magnets-yesterday-today-tomorrow-john-ormerod/ Castilloux, R., Rare Earth Magnet Market Outlook to 2030, Adamas Intelligence. U.S. Geological Survey, 2022, Mineral commodity summaries 2022: U.S. Geological Survey, 202 p., https://doi.org/10.3133/mcs2022

4. Nothnagel, P., K-H. Müller, D. Eckert, and A. Handstein. "The influence of particle size on the coercivity of sintered NdFeB magnets." Journal of magnetism and magnetic materials 101, no. 1-3 (1991): 379-381.

5. Bance, Simon, et al. "Grain-size dependent demagnetizing factors in permanent magnets." Journal of Applied Physics 116.23 (2014): 233903.

6. K. Hono and H. Sepehri-Amin, "Strategy for high-coercivity Nd-Fe-B magnets," Scripta Materialia, vol. 67, no. 6, pp. 530–535, Sep. 2012, doi: 10.1016/j.scriptamat.2012.06.038.

7. W. Tang, G. Ouyang, B. Cui, J. Wang, K.W. Dennis, M.J. Kramer, I.E. Anderson, J. Cui, "Magnetic and mechanical properties of grain-refined Dy-free Nd-Fe-B sintered magnets," Journal of Magnetism and Magnetic Materials 521 (2021) 167533.

8. Ouyang, Gaoyuan, et al. "Review of Fe-6.5 wt% Si high silicon steel—A promising soft magnetic material for sub-kHz application." Journal of Magnetism and Magnetic Materials 481 (2019): 234-250.

9. Ouyang, Gaoyuan, et al. "Characterization of ordering in Fe-6.5% Si alloy using X-ray, TEM, and magnetic TGA methods." Materials Characterization 158 (2019): 109973.

I.1.6 Advanced Packaging Designs – Reliability and Prognostics (National Renewable Energy Laboratory)

Douglas DeVoto, Principal Investigator
National Renewable Energy Laboratory (NREL)
15013 Denver West Parkway
Golden, CO 80401
E-mail: douglas.devoto@nrel.gov

Susan Rogers, DOE Technology Development Manager
U.S. Department of Energy
Email: Susan.Rogers@ee.doe.gov

Start Date: October 1, 2018　　　　End Date: September 30, 2024
Project Funding: $175,000　　　　DOE share: $175,000　　　　Non-DOE share: $0

Project Introduction

The U.S. Department of Energy's Office of Energy Efficiency and Renewable Energy Vehicle Technologies Office and the Electrical and Electronics Technical Team have proposed aggressive research and development targets [1] aimed at improving power electronics technology to enable the mass-market penetration of electric-drive vehicles. Achieving these aggressive power electronics targets will require a decrease in cost (year 2025 cost target: $2.70/kW) and an increase in power density (year 2025 power density target: 100 kW/L) as compared with current, on-road technology. Replacing traditional silicon device-based components with more efficient and higher-temperature wide-bandgap semiconductor device-based components will enable increasing the power density. However, meeting the power density target will also require innovative packaging and thermal management solutions to increase the heat fluxes dissipated and allow for compact electronics packaging.

Decreasing the thermal resistance pathway in power electronics packages is a primary objective for maximizing the performance of wide-bandgap devices. This can be accomplished by either replacing package layers with new materials that enable greater thermal, electrical, and reliability performance, or eliminating layers and components through new packaging designs. Safe and robust operation of the power electronics requires electrical isolation of the high-voltage circuitry within the power electronics module. For example, typical power electronics modules use a ceramic material within the package for electrical isolation.

Objectives

The primary deliverable for this project will be to construct a power electronics package utilizing an organic, electrically insulating substrate material and demonstrate superior thermal performance and greater reliability under thermal cycling, thermal aging, vibration, power cycling, and electrical high-potential evaluation over traditional packages. This will be accomplished through the following tasks:

- Design optimization of a power electronics package. A multiphysics optimization process will incorporate the electrically insulating substrate alternative into a novel power electronics package. Electrical, thermal, and mechanical constraints will be balanced through this optimization.

- Prototype construction and evaluation. Example power electronics packages based on an electrically insulating substrate alternative will be developed. A multiphysics modeling evaluation of the sample geometries will determine thermal and thermomechanical performance, while a reliability assessment will measure performance during accelerated tests.

Approach

The project aim is to develop a power-dense, reliable, and cost-effective 3D power electronics package enabled by an alternative electrical isolation material: an organic direct bond Cu (ODBC) substrate. This material

provides equivalent electrical isolation to current technologies while providing high thermomechanical reliability at high device junction temperatures, as well as enabling higher power densities. In addition, eliminating design constraints associated with traditional ceramic substrates reduces device-to-coolant thermal resistance, simplifies package design, and offers more design flexibility. This package design will eliminate component layers in a new, low-cost, simplified manufacturing process for a packaging design that will allow for higher power densities and reliability. Additionally, the new circuit board structure will transport heat out of encapsulated component areas within a 3D structure. This work is being performed in collaboration with Oak Ridge National Laboratory (ORNL) and DuPont.

Traditional ceramic substrates perform three functions in a power module assembly: a thermal management path from the switching devices to the heatsink or cold plate, electrical connections between the devices and external busbars, and electrical isolation of the thermal management components. Direct bond Cu (DBC) substrates with an aluminum oxide (Al_2O_3) ceramic were conventionally selected for power modules due to their adequate performance in electrical isolation, thermal management, and reliability. A thin Cu oxide layer on the Cu foils is used to bond the metallization layers to the ceramic in an oxygen-rich environment at a eutectic point of 1,066°C. The process temperature must be carefully controlled, as the melting point of Cu is 1,085°C. Foils are symmetrically bonded to both sides of the ceramic to prevent cracking or warping during cooling to room temperature [2]. Alternative ceramic materials have aimed to improve performance over Al_2O_3 substrates by increasing bending strength, fracture toughness, thermal conductivity, dielectric strength, or more closely matching their coefficient of thermal expansion (CTE) to Si or wide-bandgap devices. Zirconia-toughened alumina (ZTA) substrates add a percentage of zirconium oxide (ZrO_2) to Al_2O_3 prior to sintering to improve the ceramic's bending strength. ZTA substrates typically have a lower thermal conductivity than Al_2O_3 substrates but can compensate for this by using a thinner ceramic layer due to their enhanced mechanical properties [3]. Aluminum nitride (AlN) ceramics have been selected for their higher thermal conductivity and low CTE that is closely aligned with semiconductor devices. AlN is bonded to Al metallization layers through a direct bond aluminum (DBA) brazing process using an Al-Si alloy film that exhibits a eutectic phase at 577°C [4]. Further package CTE alignment with DBA substrates can be obtained by selecting aluminum silicon carbide (AlSiC) baseplates. AlN substrates can also be bonded with Cu metallization layers through the DBC process or by active metal brazing (AMB). AMB commonly bonds AlN or silicon nitride (Si_3N_4) to Cu with a brazing material under an inert gas or vacuum environment. The higher fracture toughness of Si_3N_4 and ZTA ceramics has allowed for thicker Cu metallization layers and higher device operating temperatures, but metallization layers have typically not exceeded thicknesses of 1.0 mm. Substrate reliability studies have shown that the lifetime of substrates significantly decreases as metallization layer thickness increases from modeling [5] and experimental [6] results.

Results

Organic Insulating Substrate Fabrication

Previous work has outlined the thermal performance and reliability of the ODBC substrate [7], [8] and shown that the thermal resistance of an ODBC substrate is comparable to ceramic-based substrates. Reliability experiments have shown no concerns with thicker (>1.0 mm) Cu metallization layers under thermal cycling conditions. Initial efforts to synthesize ODBC substrates were the primary focus of work in the previous year [9]. Instead of chemical etching or thick-film processes, a mechanical etching process was used to fabricate ODBC substrates. A computer numerical control (CNC) router first partially machines the bottom face of the topside metallization layer, as shown in Figure I.1.6.1, Step 1. This step is required, as later attempts to machine electrical features would damage the polyimide electrical insulating layer. The Cu and polyimide layers are stacked and then bonded under pressure and temperature in an oven (Steps 2 and 3). A mirrored pattern of the CNC machining process in Step 1 is completed to remove the remaining Cu material (Step 4) to create the final electrical pattern.
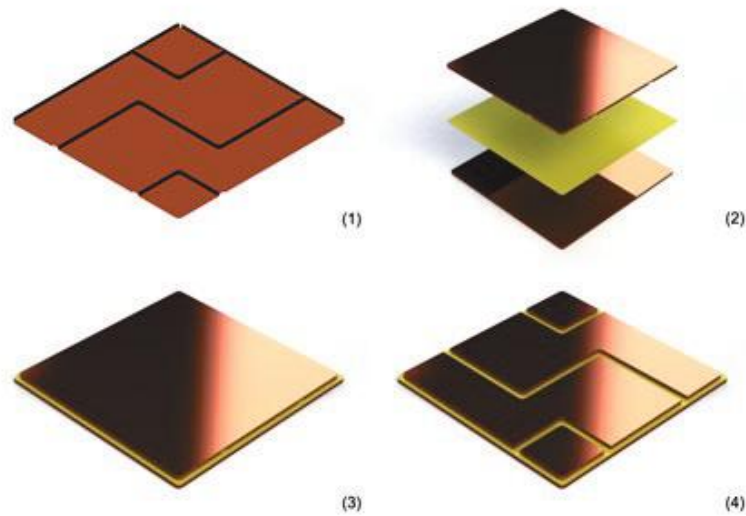
Figure I.1.6.1 ODBC assembly process via mechanical etching

One downside to this process is the requirement of two machining processes and care with fixturing the substrate to ensure that alignment is preserved. An alternative approach was developed that can be considered a hybrid of chemical and mechanical etching processes, shown in Figure I.1.6.2 below. The Cu and polyimide layers can be stacked and bonded under pressure and temperature without the initial mechanical etch process (Steps 1 and 2). Then, a photoresist coating is applied to the Cu surface (Step 3). Masking with UV exposure and photoresist development steps are skipped for this hybrid process and instead the photoresist and most of the Cu metallization layer are removed through mechanical etching (Step 4). Approximately 25 μm of Cu remains after the mechanical etching step. A chemical etchant, such as ferric chloride, is then applied to the remaining Cu to complete the removal of desired material (Step 5). The substrate can then be cleaned to remove the photoresist (Step 6) and prepared for next power module fabrication steps.
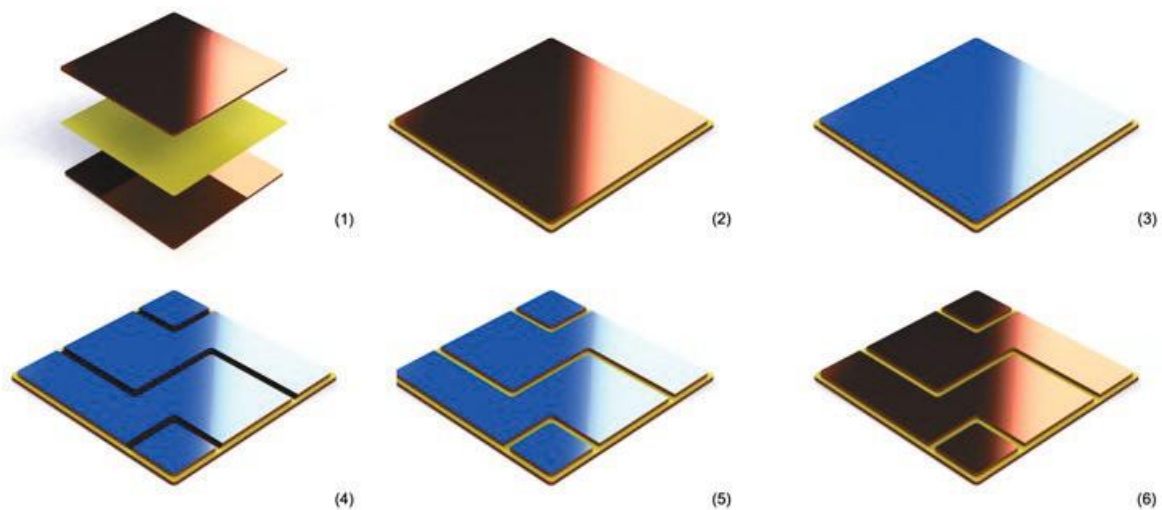
Figure I.1.6.2 Hybrid etching process

An example substrate etched using this hybrid process is shown in Figure I.1.6.3 below.
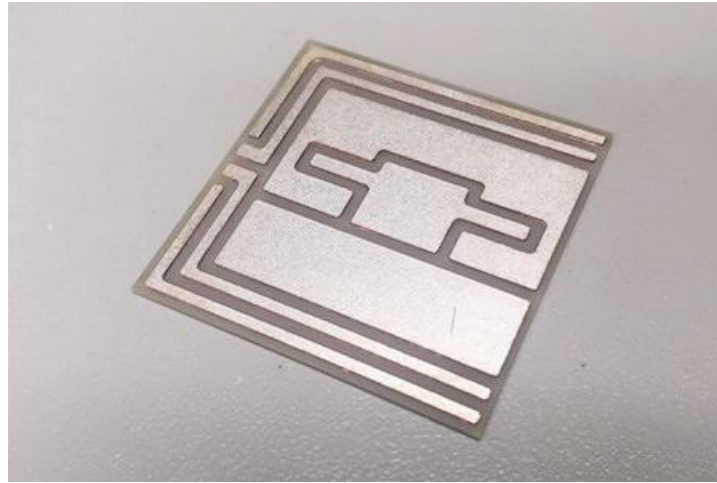
Figure I.1.6.3 Example substrate via hybrid etching process

While thermomechanical reliability of the polyimide-Cu interface was previously evaluated, no direct shear measurements had been made. It was also desired to further optimize bonding parameters of temperature and pressure to maximize shear strength. To explore these research objectives, a high-temperature press was constructed to have similar functionality as a universal testing machine, but in a more compact formfactor with improved ability to align top and bottom platens. Two NEMA 23 motors interfaced parallel linear rails through 77:1 planetary gearboxes for high-torque displacement control. A Phidgets load cell was integrated into the bottom platen for optional pressure control. Mica sheets were used to isolate high temperatures generated in a heater cartridge plate from the mechanical components of the press. All sensors and controls were integrated through Phidgets controllers to a laptop, but the setup is also capable of being operated from a Raspberry Pi in the future. The user interface was developed in python to monitor temperature and pressure during the bonding process. Pressure-sensitive paper was used to align the platens for uniform application of force and the system was tested up to 12 kN.
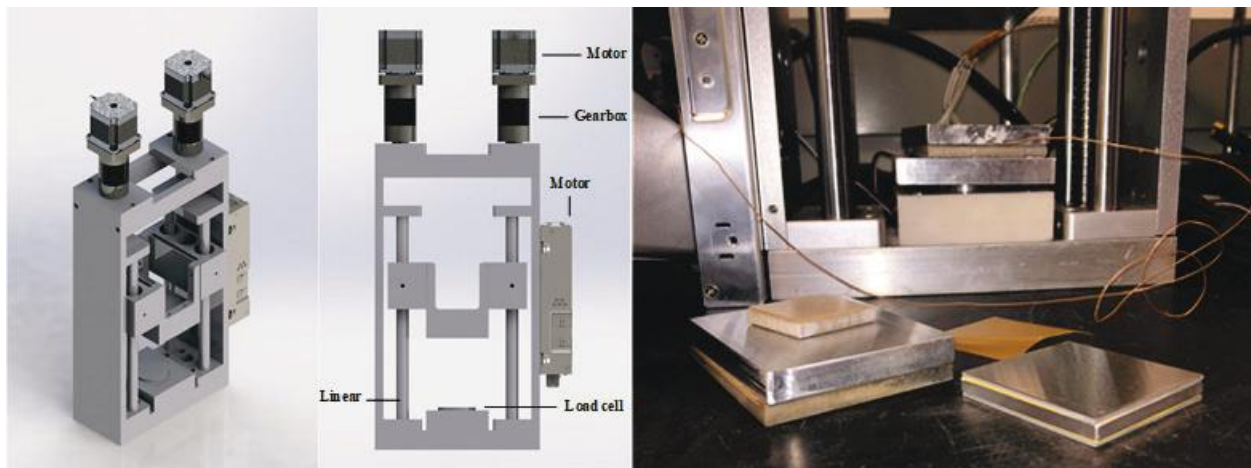
Figure I.1.6.4 High-temperature mechanical press

Two layers of polyimide material were bonded to three metallization layers to form double-lap shear samples. The same sample geometry was developed for the evaluation of sintered silver bonded interfaces [10]. The middle metallization layer is approximately 5 mm thick, and the two outer metallization layers are 1.8 mm thick. An example of a 50×50-mm sample is shown in Figure I.1.6.5.
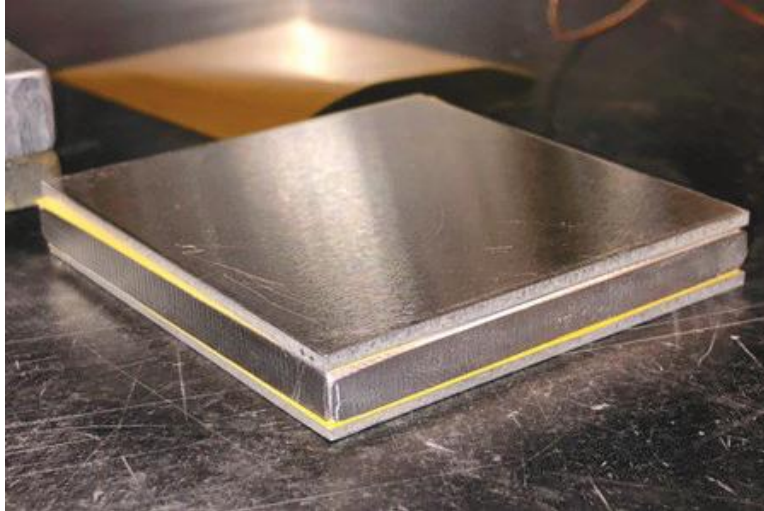
Figure I.1.6.5 Double-lap shear sample

Both Al and Cu samples were bonded at temperatures ranging from 250°C to 300°C at approximately 2.4 MPa. Samples were then sectioned into twenty-five 10×10-mm coupons for shear strength evaluation. These coupons fit into a custom shear fixture shown in Figure I.1.6.6, where the fixture supports the outer metallization layers while applying a load to the middle metallization layer. The coupon's symmetry allows for the two bonded interfaces to be loaded in a pure shear direction. The shear fixture and coupon are placed in an Instron 5966 dual column testing system that was configured with a 10-kN load cell. An environmental chamber has a temperature range from -100°C to 350°C for capturing temperature-dependent material properties, but preliminary tests were conducted at room temperature. A noncontact video extensometer can also be used for strain measurements.
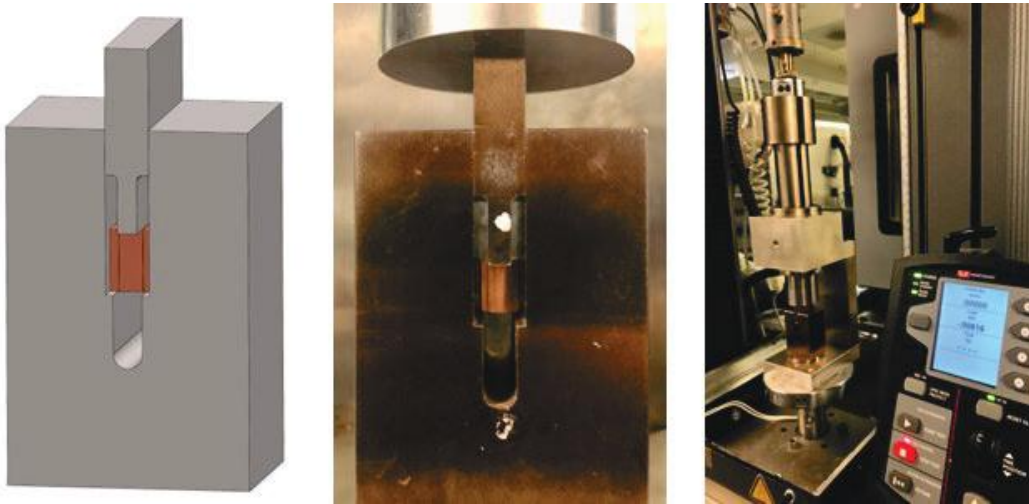
Figure I.1.6.6 Shear fixture setup

The original location of each 10×10-mm coupon within the 50×50-mm sample was recorded to observe any trends in bond strength across a sample. The shear strength results of an ODBC sample bonded at 300°C is shown in Figure I.1.6.7.
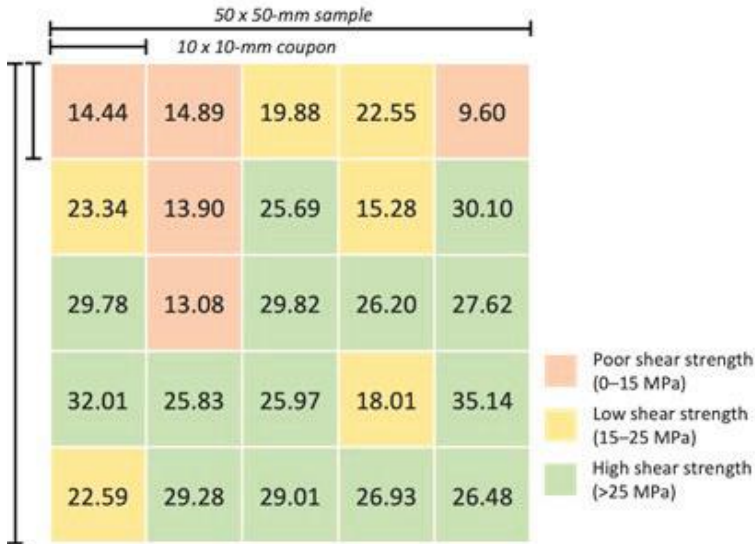
Figure I.1.6.7 Shear strength (MPa) for ODBC sample bonded at 300°C

It can be observed that one edge of the sample shows lower shear strength than the remainder of the sample. Additional planarity refinement between upper and lower platens can be completed and future samples will also be rotated 90 degrees and pressed a second time to eliminate undesirable variations in pressure application. Samples bonded at temperatures lower than 300°C did not achieve adequate adhesion with metal surfaces. All organic direct-bond aluminum (ODBA) samples failed at very low shear values, and it was determined that additional surface preparation to remove oxidation will be required. The high-temperature press will be installed in a vacuum chamber to create an inert environment during bonding for samples in FY 2023.

Power Electronics Module Design With Organic Insulating Substrate

As most manufacturing concerns have been addressed for etching thick metallization layers and bonding large-area substrates, a simplified manufacturing process has been envisioned to incorporate ODBC substrates into a double-side-cooled half-bridge power module. The individual steps are outlined in Figure I.1.6.8 and require three layers of Temprion and four bonding steps. The conservative use of additional bonding steps to bond the Temprion one side at a time arises from the inability to apply uniform pressure to a lower metallization layer when the upper metallization layer has large sections etched away. Machined hard platens or conformal soft platens are also being explored to further reduce the number of fabrication steps.

1. Bond lower Temprion layer to lower cold plate.

2. Etch bottom face of drain busbar and traces.

3. Bond drain busbar and traces to lower Temprion layer.

4. Etch top face of drain busbar and traces.

5. Bond middle Temprion layer and output 2 busbar.

6. Sinter and wire bond devices.

7. Bond output 1 and source busbars to upper Temprion and upper cold plate.

8. Sinter previous assembly to devices.

9. Fill cavity with encapsulant.

Figure I.1.6.8 ODBC half-bridge power module fabrication steps

Additional views of the concept power module are provided in Figure I.1.6.9.
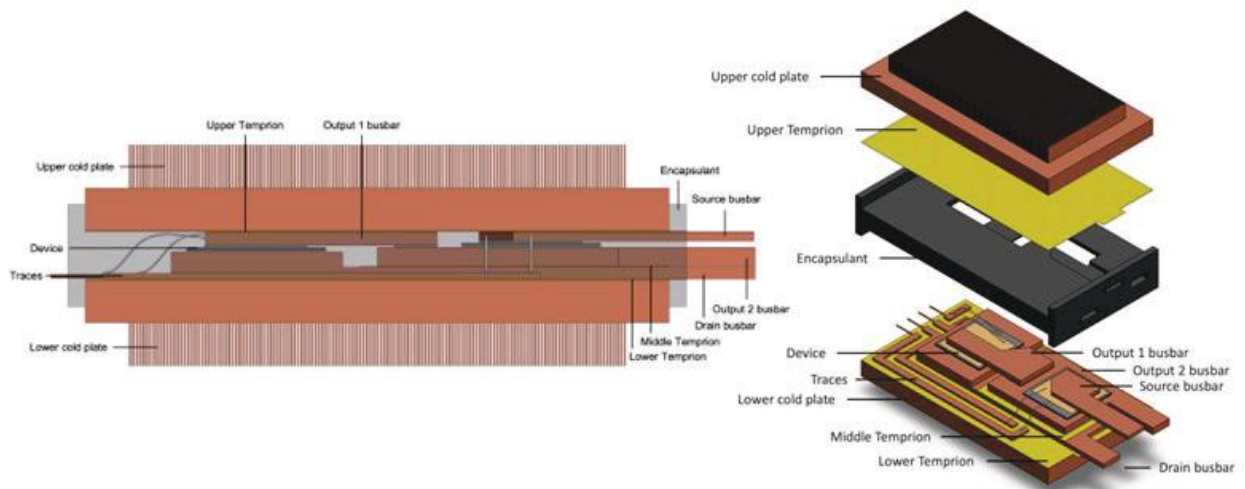
Figure I.1.6.9 ODBC half-bridge power module components

After additional experimental and modeling milestones are met, the goal of an assembled half-bridge module in collaboration with ORNL and DuPont will be endeavored in FY 2023.

Conclusions

The project aim is to develop a power-dense, reliable, and cost-effective 3D power electronics package enabled by an alternative electrical isolation material. The project accomplishments for FY 2022 are summarized below.

- Prototype substrates utilizing organic electrically insulating materials were fabricated and evaluated for shear strength. An additional alternative etching process was developed.

- A simplified packaging process was envisioned with ODBC substrates in a double-side-cooled module. ODBC substrates will be integrated into power module prototypes following this process in FY 2023.

Key Publications

1. DeVoto, D. 2022. "Advanced Packaging Designs – Reliability and Prognostics (NREL)." In *Electrification: 2021 Annual Progress Report*, Washington, D.C.: U.S. DOE EERE VTO, 70–77.

2. Gurpinar, E., Sahu, R., Ozpineci, B., and DeVoto, D. 2020. "Analysis and Optimization of a Multi-Layer Integrated Organic Substrate for High Current GaN HEMT-Based Power Module." *2020 IEEE Workshop on Wide Bandgap Power Devices and Applications in Asia (WiPDA Asia)*, Japan, September 2020.

References

1. U.S. DRIVE. 2017. *Electrical and Electronics Technical Team Roadmap*. Washington, D.C.: U.S.DRIVE. https://www.energy.gov/eere/vehicles/downloads/us-drive-electrical-and-electronics-technical-team-roadmap.

2. Miric, A., and Dietrich, P. 2015. "Inorganic Substrates for Power Electronics Applications." *Heraeus Deutschland.*

3. Park, J., Kim, M., and Roth, A. "Improved thermal cycling reliability of ZTA (Zirconia Toughened Alumina) DBC substrates by manipulating metallization properties." *CIPS 2014; 8th International Conference on Integrated Power Electronics Systems*, 2014, pp. 1–9.

4. Lin, H. T., Wereszczak, A. A., and Waters, S. 2013. "Low-Cost Direct Bonded Aluminum (DBA) Substrates." *2013 DOE VTO Annual Merit Review*, Washington, D.C., May 2013.

5. Xu, L., Zhou, Y., and Liu, S. 2013. "DBC substrate in Si- and SiC-based power electronics modules: Design, fabrication and failure analysis." *2013 IEEE 63rd Electronic Components and Technology Conference*, 2013, pp. 1341–1345, doi: 10.1109/ECTC.2013.6575747.

6. Dupont, L., Khatir, Z., Lefebvre, S., and Bontemps, S. 2006. "Effects of metallization thickness of ceramic substrates on the reliability of power assemblies under high temperature cycling." *Microelectronics Reliability*, 46 (9–11), pp. 1766–1771, https://doi.org/10.1016/J.MICROREL.2006.07.057.

7. DeVoto, D. 2020. "Advanced Packaging Designs – Reliability and Prognostics (NREL)." In *Electrification: 2019 Annual Progress Report*, Washington, D.C.: U.S. DOE EERE VTO, 95–101, doi:10.2172/1637435.

8. DeVoto, D. 2021. "Advanced Packaging Designs – Reliability and Prognostics (NREL)." In *Electrification: 2020 Annual Progress Report*, Washington, D.C.: U.S. DOE EERE VTO, 57–64.

9. DeVoto, D. 2022. "Advanced Packaging Designs – Reliability and Prognostics (NREL)." In *Electrification: 2021 Annual Progress Report*, Washington, D.C.: U.S. DOE EERE VTO, 70–77.

10. P. Paret, J. Major, D. DeVoto, S. Narumanchi, Y. Tan, and G.-Q. Lu. 2018. "Mechanical Characterization Study of Sintered Silver Pastes Bonded in a Double-Lap Configuration." *ASME 2018 International Technical Conference and Exhibition on Packaging and Integration of Electronic and Photonic Microsystems*, August 2018, doi: 10.1115/IPACK2018-8276.

Acknowledgments

I.1.7 Integrated Traction Drive Thermal Management (National Renewable Energy Laboratory)

Bidzina Kekelia, Principal Investigator
National Renewable Energy Laboratory
15013 Denver West Parkway
Golden, CO 80401
E-mail: bidzina.kekelia@nrel.gov

Susan A. Rogers, DOE Technology Development Manager
U.S. Department of Energy
E-mail: susan.rogers@ee.doe.gov

Start Date: October 1, 2018   End Date: September 30, 2024
Project Funding: $250,000   DOE share: $250,000   Non-DOE share: $0

Project Introduction

To enable the mass-market penetration of electric-drive vehicles and meet consumer electric vehicle performance expectations, the U.S. DRIVE 2017 Electrical and Electronics Technical Team Roadmap [1] proposes aggressive research and development targets aimed at reducing costs and increasing electric traction-drive system power density to 33 kW/L by 2025. This target includes high-voltage power electronics and a single traction-drive electric motor. Achieving this level of system power density requires integration of the inverter and the electric motor into a single traction module. However, this approach also requires innovative thermal management solutions to provide adequate cooling to more densely pack electrical components and keep their operating temperatures within optimal range.

Objectives

The main objectives of this project are to:

- Research and evaluate motor-integrated power electronics topologies and thermal management solutions for electric traction drives.

- Identify candidate driveline fluids suitable for direct cooling of traction-drive components and high-voltage power electronics.

- Characterize selected driveline fluids by measuring convective cooling and, if appropriate and feasible, electrical properties.

- Provide support to other collaborating researcher teams in the Electric Drive Technologies (EDT) Consortium in thermal management aspects for their integrated drive concepts.

Approach

We will consider previous research into the most efficient heat removal techniques from power electronics and electric machine components, as well as best integration practices, when evaluating the thermal management approaches of EDT Consortium teams' integrated drive concepts.

We are continuing to collaborate with Oak Ridge National Laboratory (ORNL) on thermal management component design and thermal simulations for their integrated traction drive. Support activities for the University of Wisconsin's integrated drive team are also ongoing.

Results

The focus of our FY22 research was designing thermal management system components for ORNL's outer-rotor integrated drive and providing thermal management assistance to the University of Wisconsin's

integrated drive design team. As the electromagnetic and mechanical design of ORNL's drive evolves, there's a constant need for thermal management component adjustments to accommodate the design modifications.

Supporting ORNL's Outer-Rotor Integrated Motor Design

One of the most recent designs of ORNL's integrated drive is presented in Figure I.1.7.1. The design illustrates the increased diameter of the internal cavity due to the substitution of the large bearings with a set of smaller, radially distributed bearings. This change allowed for an increase in the inverter cylindrical housing diameter, consequently allowing more internal space for six-phase inverter modules and larger coolant passage channels in the cylindrical housing walls (Figure I.1.7.2).
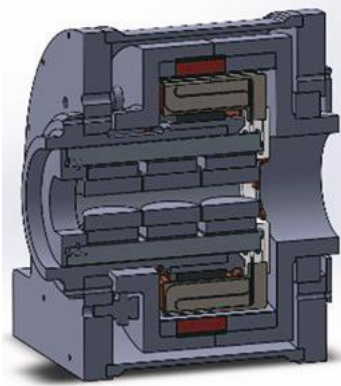
Figure I.1.7.1 ORNL's outer-rotor motor with integrated inverter and cooling system components. *Illustration by Bidzina Kekelia, NREL*
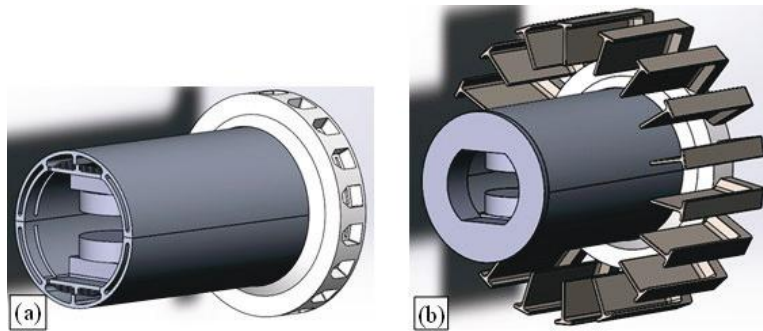
Figure I.1.7.2. Cooling system assembly (a) with exposed internal channels in the inverter housing walls and (b) with in-slot T-shape heat exchangers attached to the distribution manifold-disk. *Illustration by Bidzina Kekelia, NREL*

Ongoing mechanical design changes in the drive call for adjustments in the thermal management system layout and components. The following figures illustrate the slightly lengthened in-slot T-shape heat exchanger (Figure I.1.7.3) and its insertion between windings (Figure I.1.7.4). The material selection and manufacturing process for the heat exchanger has not been finalized yet. We are evaluating 3D printing from ceramic materials (aluminum oxide, silicon nitride, boron nitride) or thermally enhanced polymers/resins. We are also considering alternative low-pressure injection molding with highly thermally conductive resin.
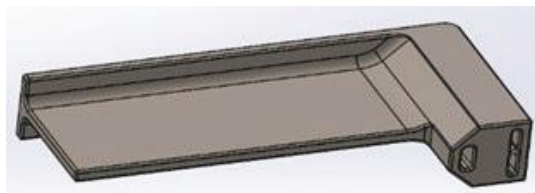
Figure I.1.7.3. T-shape in-slot heat exchanger, version 6. *Illustration by Bidzina Kekelia, NREL*

Figure I.1.7.4. T-shape heat exchangers embedded between stator windings. *Illustration by Bidzina Kekelia, NREL*

Below, in Figure I.1.7.5, the current evolution of the coolant distribution manifold is presented. Due to its size and complex geometry (internal channels), we are planning for additive manufacturing using polymer material.
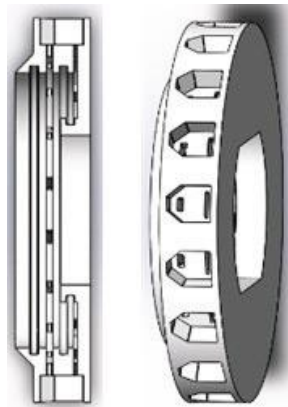
Figure I.1.7.5. Coolant distribution manifold-disk, version 8. *Illustration by Bidzina Kekelia, NREL*

At the end of FY22, further changes to ORNL's outer-rotor motor were conceived. Due to a lack of high-speed bearings (higher than 20,000 rpm is expected in the set of small, radially distributed bearings in the current design), the ORNL team is planning a cantilever mounting of the outer rotor using two moderately sized bearings that do not require constant oil lubrication for rotational speeds up to 20,000 rpm. This change would require major revisions to the thermal system components and their layout, although this should yield more efficient cooling. This approach would result in parallel fluid paths to the inverter and to the motor winding heat exchangers, thus reducing the fluid pressure drop and coolant temperatures. These modifications are planned in FY23.

Supporting the University of Wisconsin's Integrated Motor Design Team

The NREL team continues regular biweekly and as-needed meetings (with an emphasis on general design and thermal management, respectively) with the University of Wisconsin (UW) team. NREL's expertise in thermal modeling and material/interface testing helps the UW team with design and material selection for their integrated drive (Figure I.1.7.6). Currently, the UW team is finalizing thermal modeling tasks and is on track to manufacture the hardware for their demonstration unit. Some of UW's thermal simulations are illustrated in Figure I.1.7.7.
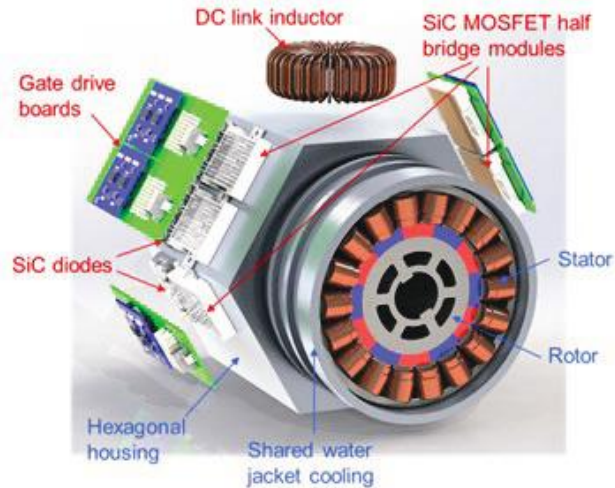
Figure I.1.7.6. General exploded view of the University of Wisconsin's integrated traction drive. *Image from University of Wisconsin*
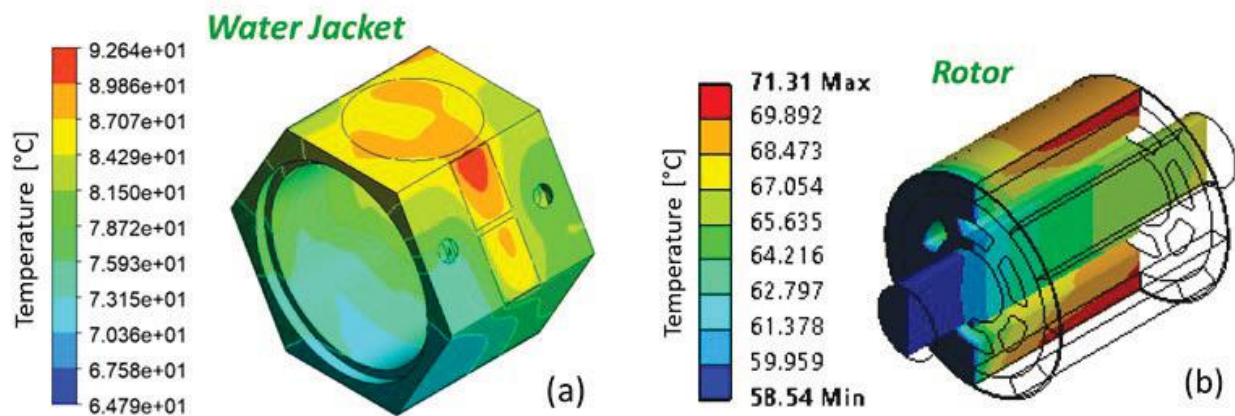
Figure I.1.7.7. Illustrative figures for thermal simulations of the University of Wisconsin's integrated traction drive: (a) water jacket cooling of the case and (b) air cooling of the rotor. *Image from University of Wisconsin*

Conclusions

The project accomplishments and conclusions for FY22 are summarized as follows:

- Collaboration with the integrated drive teams at ORNL and the University of Wisconsin is continuing successfully.

- We have completed several design revisions of thermal management system components (T-shape in-slot heat exchangers, coolant distribution manifold-disk, and cylindrical inverter housing) for ORNL's outer-rotor integrated drive due to changes in the drive's evolving mechanical design.

- Manufacturing options (3D printing, extrusion, low-pressure injection molding) and potential novel materials (ceramics, thermally enhanced polymers) are still being explored.

- Further design changes to the thermal system components and their layout to accommodate cantilever mounting of the outer rotor in ORNL's drive are expected.

- In FY23, the NREL team is planning thermal modeling and experimental evaluation of key thermal management system components for ORNL's integrated drive.

- With NREL's advisory assistance, the University of Wisconsin team is close to finalizing thermal modeling tasks and is on track to manufacture key parts of their integrated traction-drive prototype.

Key Publications

1. Kekelia, B., and Narumanchi, S. "Thermal Management of Integrated Traction Drives in Electric Vehicles." In *Electronics Cooling: The 2022 Annual Guide*. https://learn.electronics-cooling.com/electronics-cooling-2022-annual-edition/.

References

1. U.S. DRIVE. 2017. *Electrical and Electronics Technical Team Roadmap.* Washington, D.C.: U.S. Department of Energy Office of Energy Efficiency and Renewable Energy Vehicle Technologies Office. https://www.energy.gov/sites/prod/files/2017/11/f39/EETT%20Roadmap%2010-27-17.pdf.

Acknowledgements

I.1.8 Power Electronics Thermal Management (National Renewable Energy Laboratory)

Gilbert Moreno, Principal Investigator

National Renewable Energy Laboratory
15013 Denver W. Pkwy.
Golden, CO 80401
Email: gilbert.moreno@nrel.gov

Susan Rogers, DOE Technology Development Manager

U.S. Department of Energy
Email: susan.rogers@ee.doe.gov

Project Introduction

The 2017 *Electrical and Electronics Technical Team Roadmap* [1] proposes aggressive research and development targets aimed at improving power electronics technology to enable the mass-market penetration of electric-drive vehicles. Achieving these aggressive targets will require a decrease in cost (year 2025 cost target: $2.70/kW) and an increase in power density (year 2025 power density target: 100 kW/L) as compared with current on-road technology. Replacing traditional silicon device-based components with more efficient and higher-temperature wide-bandgap (WBG) semiconductor device-based components will enable increased power density. However, meeting the power density target will also require innovative thermal management solutions to increase the heat fluxes dissipated and allow for compact electronics packaging.

This project conducts research to develop new power electronics thermal management technologies to increase power density, enable high WBG device temperature operation, and decrease cost. The performance (e.g., thermal resistance, pumping power) of the power electronics cooling technologies developed in this project are compared to the performance of current, on-road technology. One of the main challenges to achieving high power densities is associated with packaging high-temperature (up to 250°C) WBG devices near lower-temperature-rated components (e.g., electrical boards and capacitors).

Objectives

The primary project objective is to develop novel thermal management technologies to enable achieving the 100-kW/L power density target. Additional project objectives are to:

- Develop cooling solutions that enable high-heat-flux, high-temperature WBG operation and low-temperature, low-cost capacitors

- Decrease cost by proposing low-cost cooling technologies that enable decreasing the number of semiconductor devices and use automotive-qualified fluids (e.g., water-ethylene glycol [WEG], automatic transmission fluid [ATF]).

Approach

This project designs and evaluates dielectric fluid, single-phase heat-transfer cooling systems for automotive power electronics modules. Dielectric fluids have poor thermal properties compared with WEG, but they enable a redesign of the power module to eliminate thermal bottlenecks (i.e., dielectric ceramic) within the package. Jet impingement configurations are used to augment the fluid's convective cooling and offset the fluid's poor properties. The single-phase dielectric fluids proposed are synthetic hydrocarbons (oils), have properties similar to ATFs, are relatively inexpensive, and are environmentally friendly (e.g., global warming potential <1). This proposed cooling concept may enable the use of new driveline fluids (ATF-like fluids) that are tailored for these power electronics cooling applications. Single- and double-side-cooled dielectric fluid

concepts were designed via modeling, and their performance was predicted and compared to current, on-road technology. Experiments were conducted and used to validate model predictions under different operating conditions (e.g., different fluid flow rates, types, and temperatures). NREL is also collaborating with Georgia Tech to evaluate two-phase-based, dielectric fluid cooling strategies for power modules.

Results

The work conducted in Fiscal Year (FY) 2022 was focused on three research efforts. Co-optimization of the dielectric fluid, double-side cooled power module concept was an effort to optimize the module geometry to maximize thermal and thermomechanical performance. The second effort focused on designing of a silicon carbide (SiC) module for fabrication and experimental characterization. The third effort focused on designing a fluid loop to evaluate the long-term reliability of the dielectric fluid and heat exchanger. The results from each topic are discussed below.

Co-Optimization of the Dielectric Fluid, Double-Side-Cooled Module Concept

A dielectric fluid, double-side cooled power module concept was described in the FY21 Power Electronics Thermal Management Report [2]. The concept eliminates the ceramic substrates and bonds SiC devices on copper substrates. A lightweight fluid manifold was designed to impinge dielectric fluid jets on both sides of 12 devices, cool three half-bridge modules, and remove heat through single-phase heat transfer. Series and parallel flow manifolds were designed for the double-side-cooled power module concept that are described in [3]. The designs required relatively low flow rates (≤6 L/min), yield low pressure drop (< 0.6 psi at 4 L/min), and prevent direct fluid contact with the devices (i.e., the fluid contacts the copper heat spreaders but not the devices) [4]. Various single-phase heat transfer dielectric fluids, including AmpCool-100 [5] and Alpha 6 [6] and one ATF (Ford Mercon LV [7]), have been evaluated (modeling and experiments) as potential coolants for this application.

Figure I.1.8.1 shows a schematic and computer-aided design (CAD) renderings of the series flow concept. The series flow design impinges fluid jets on one side of all 12 devices. The fluid is then routed around the modules and impinged on the opposite side of all devices. Figure I.1.8.2 shows the model-predicted temperature contours for the double-side cooled concept. Maximum junction temperatures of about 155°C and maximum temperature variations between devices of 5°C are predicted for a per-device heat flux of 716 W/cm^2.
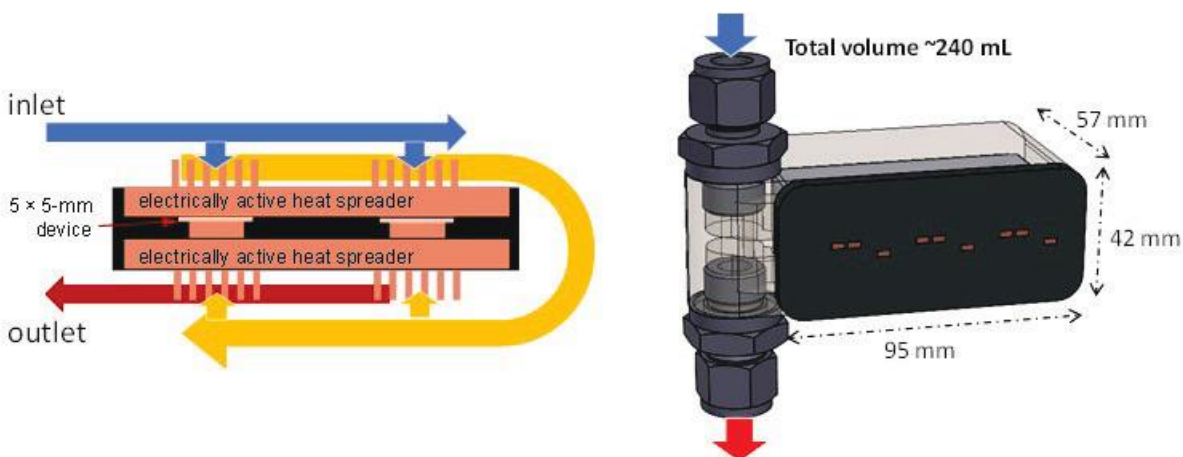
Figure I.1.8.1 Dielectric fluid, double-side-cooled concept. Schematic on the left shows the series flow configuration and the CAD on the right shows the manifold.
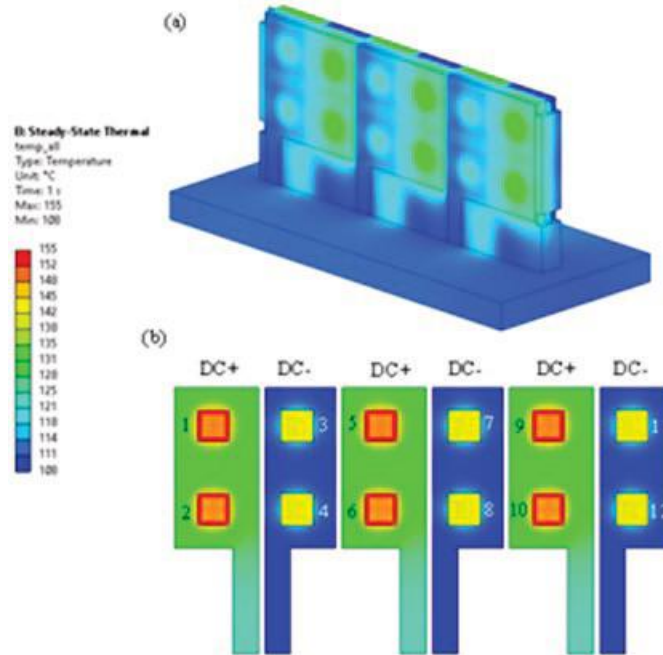
Figure I.1.8.2 (a) Temperature contours in the entire power module. (b) Temperature contours in 12 devices.

A design process was conducted to co-optimize the thermal and thermomechanical performance of the double-side concept. The process optimized the module geometry to minimize device temperatures, device temperature variations, and minimize module stresses. ANSYS Response Surface Optimization was used for the co-optimization process. The optimization process begins with a finite element analysis (FEA) model of the module with appropriate boundary conditions to replicate the jet impingement, dielectric fluid convective cooling strategy, and the structural support methods. The FEA model imposed a total of 2.5 kW of heat evenly distributed between the 12 devices, resulting in a 716 W/cm^2 device heat flux.

The Optimal Space Filling design method was used for the design of experiments (DOE). A response surface was then created from the DOE data to correlate the input parameters to the output metrics. Finally, the Multi-Objective Genetic Algorithm (MOGA) method was used to find the input parameters to meet the optimization objectives of minimizing junction temperatures, minimizing device temperature variation, and minimizing stresses. The co-optimization process is outlined in Figure I.1.8.3. The thickness and width of the copper heat spreaders and thickness of the spacers located on the source side of the devices were the only parameters optimized. The overall sizes (e.g., total module width, total module thickness, and device location) were unaltered to enable using the previously designed fluid manifold shown in Figure I.1.8.1.
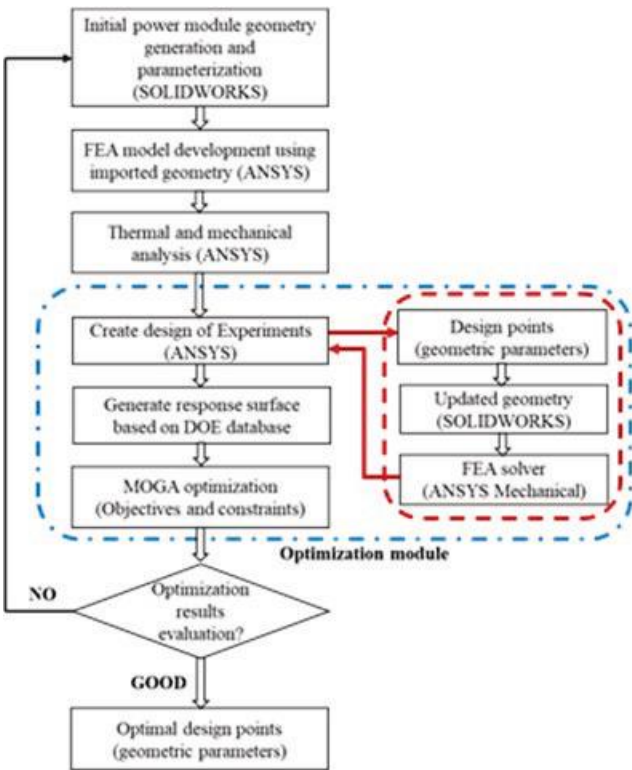
Figure I.1.8.3 Flowchart showing the optimization process

Figure I.1.8.4 shows temperature contours for the optimized power module geometry. The maximum junction temperatures for the optimized design decreased to 153°C and the device temperature variation was 4.7°C—an improvement over the initial baseline design. The temperature improvements compared to the initial design were relatively minor but were associated with minor changes to the package geometry. The optimization also reduced the module stresses 14% compared to the baseline design. Additional details and results of the co-optimization process can be found in [8].
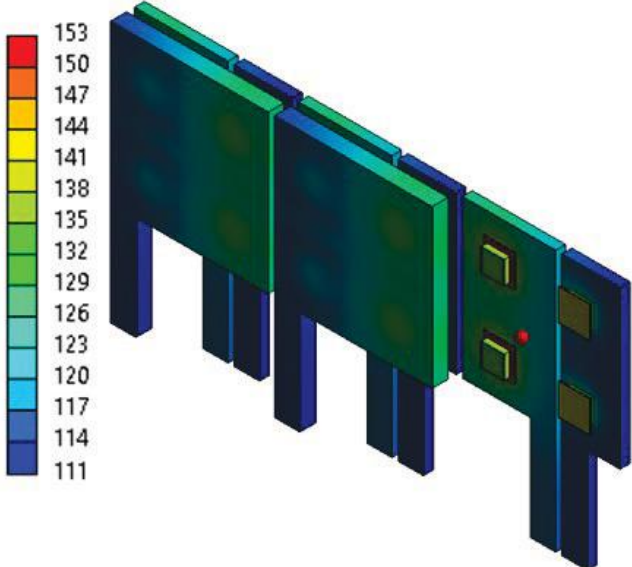
Figure I.1.8.4 Temperature contours for the optimized design that is predicted to achieve a junction-to-fluid thermal resistance of 11 mm²-K/W and reduce mechanical stress by ~14%

Experimental Demonstration Using a SiC Power Module

A module was designed to enable a demonstration of the dielectric fluid, single-side-cooled concept using SiC devices. The module uses two SiC metal–oxide–semiconductor field-effect transistors (MOSFET) connected in parallel and soldered to a finned copper heat spreader (Figure I.1.8.5). Electrical connections were included to enable providing approximately 145 A of current through the devices, switching the devices on/off via gate connections, and measurement of the junction-to-fluid thermal resistance using NREL's PowerTester. The demonstration module was similar to the dielectric fluid, single-side-cooled module described in [9]. Prior experiments using resistance heaters and described in [9] have confirmed model predictions for the heat exchanger/cold plate thermal resistance. The proposed experiments using SiC-based modules will provide the thermal resistance from the junction-to-fluid and thus an improvement over past experimental work. The SiC-based module design that will be used for the experimental demonstration is shown in Figure I.1.8.5. The module will be cooled on one side with dielectric fluids using the previously designed heat exchanger described in [9].
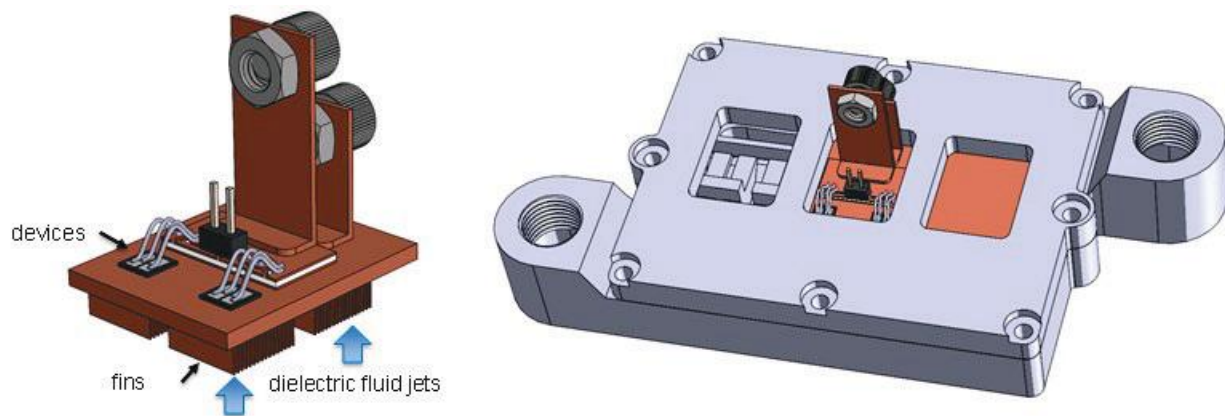
Figure I.1.8.5 CAD drawings of the SiC module that will be used to measure the junction-to-fluid thermal resistance of the dielectric fluid, single-side cooled concept. The module within the heat exchanger is shown in the image to the right.

A thermo-electric FEA model was created to simulate the test conditions of powering the two devices with a DC current to predict the operating temperatures. The model included all the electrical connections including the top-side wire bonds and 1-micrometer-thick device metallization (source-side) and computed the joule heating through all electrical connections in the module including the devices. The device's electrical resistively was imposed on a 10-micrometer-thick section on the source-side of the SiC devices and was adjusted to match the ON-resistance of the device. A low electrical resistivity was used for the majority, lower side of the device to allow for current flow but minimize heating. This modeling approach allowed most of the device heat to be generated at the source-side of the device in an attempt to mimic actual conditions. The model was used to design the module to minimize the joule heating effects (minimize temperatures) on the electrical connections.

The thermal-electrical FEA computed temperature contours are shown in Figure I.1.8.6. The results for two cases are shown—175°C maximum junction temperature at 515 W/cm^2 heat flux and 131 Amps, and 200°C maximum junction temperature at 631 W/cm^2 heat flux and 145 Amps. The model confirms that the maximum temperatures are predicted to occur on the devices and not the electrical connections. The model also computes a 20 mm^2-K/W junction-to-fluid thermal resistance, which is consistent with past model predictions reported in [9]. The next steps include module fabrication and thermal characterization with dielectric fluids.
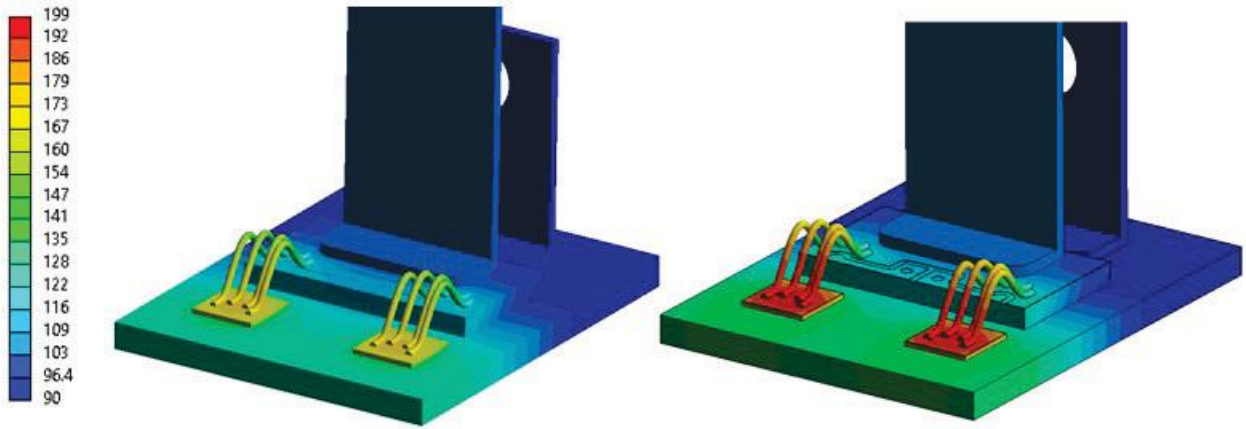
Figure I.1.8.6 Predicted temperature contours from the Thermal-Electric FEA model. Maximum junction temperature of 175°C (left) and 200°C (right) are predicted for 515 W/cm² and 631 W/cm² heat flux conditions, respectively.

Long-Term Reliability Evaluation

A fluid loop was designed to evaluate the long-term reliability of the dielectric fluid and heat exchanger. This reliability study is meant to address reliability concerns associated with a power electronics dielectric fluid cooling system. Figure I.1.8.7 shows a schematic of the dielectric fluid loop that will be used for the reliability evaluation. The loop will expose the dielectric fluid to elevated temperatures (70°C bulk fluid temperature and 100°C surface contact temperatures), expose the fluid to a 650-V voltage potential, and will expose the fluid to various materials to evaluate for material compatibility.
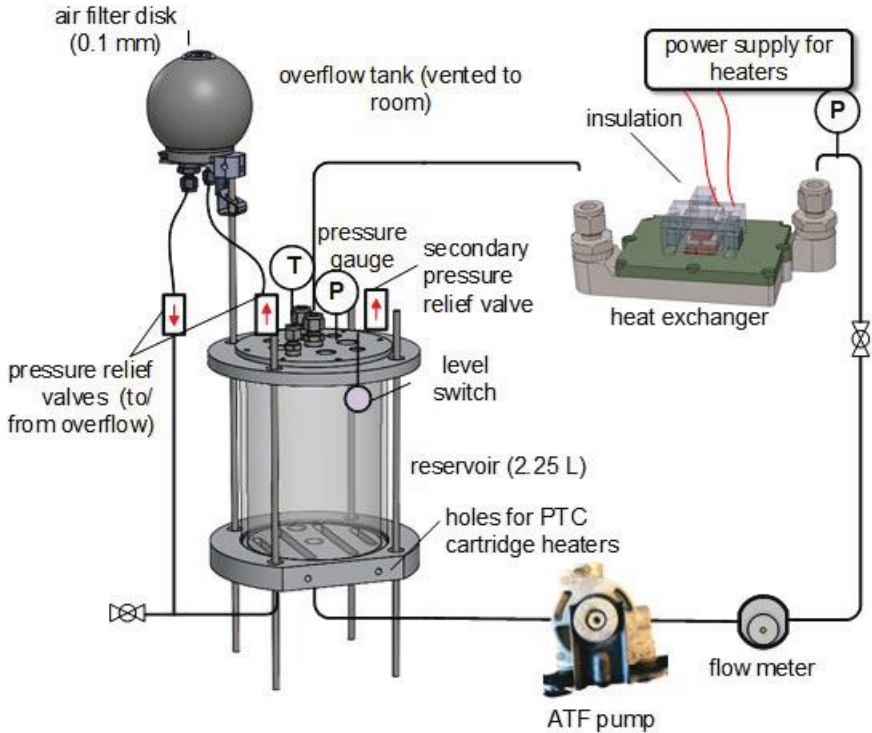
Figure I.1.8.7 Schematic of the flow loop that will be used to evaluate the long-term reliability of the dielectric fluid and heat exchanger

A heat exchanger identical to the one described in [9] will be installed in the loop to enable thermal resistance measurements. The experiments will be conducted for one year to quantify any degradation in fluid properties or a reduction in the heat exchanger thermal resistance. Fluid thermal conductivity, specific heat, viscosity, dielectric constant, and breakdown voltage will be measured at various stages during the yearlong evaluation period.

Collaboration With Georgia Tech to Evaluate Two-Phase Cooling of Power Modules

NREL is collaborating with Georgia Institute of Technology (Georgia Tech) to experimentally demonstrate Georgia Tech's two-phase-based cooling strategies. A new fluid loop is currently being fabricated at NREL and will be used to circulate a dielectric fluid (HFE-7200) through a custom-designed cold plate to cool SiC devices. NREL's PowerTester will be used to power the SiC devices and measure junction-to-fluid thermal resistance values.

Conclusions

The project's major conclusions are summarized below.

- A process was conducted to co-optimize the thermal and thermomechanical performance of a dielectric fluid, double-side-cooled power module. The FEA-based process optimized some module dimensions to minimize thermal resistance, minimize device temperature variation, and minimize stresses. The process yielded maximum junction temperature of 153°C and the device temperature variation was 4.7°C at a device heat flux of 716 W/cm^2 and reduced module stresses by 14%—an improvement over the initial baseline design.

- A SiC-based power module was designed and will be fabricated for an experimental demonstration of the dielectric fluid concept. A thermo-electrical FEA model was used to estimate the test conditions, compute joule heating, and predict module temperatures. The FEA model results were consistent with prior results reported in [9] and used to design the electrical connections. Future work will be conducted to fabricate the SiC module to enable junction-to-fluid thermal measurements using NREL's PowerTester.

- A new fluid loop has been designed and will be used to evaluate the long-term reliability of the dielectric fluid and heat exchanger. The loop will expose the fluid to elevated temperatures, a voltage potential, and various materials (to evaluate for compatibility) for a one-year duration. Work is currently underway to fabricate the loop to begin the experimental evaluation.

Key Publications

1. Xuhui, F., Moreno, G., Paret, P., and Narumanchi, S., 2022, "Multiphysics Co-Optimization Design and Analysis of a Double-Side-Cooled Silicon Carbide-Based Power Module, Published in the proceedings of the 2022 ASME InterPACK Conference, October 2022.

2. Moreno, G., Narumanchi, S., Tomerlin, J., and Major, J., 2022, "Single-Phase Dielectric Fluid Thermal Management for Power-Dense Automotive Power Electronics," IEEE Transactions on Power Electronics, 37(10), pp. 12474–12485.

3. Moreno, G., Narumanchi, S., Feng, X., Anschel, P., Myers, S., and Keller, P., 2022, "Electric-Drive Vehicle Power Electronics Thermal Management: Current Status, Challenges, and Future Directions," ASME Journal of Electronic Packaging, 144(1), pp. 011004

4. Cousineau, E., Moreno, G., Bennion, K. S., Roan, T. J., and Singh, B. N., 2022, "Condensers and Electronic Assemblies." Patent US 11,388,840 B2, Issued on July 12, 2022.

5. Moreno, G., Narumanchi, S. V. J., Bennion, K. S., Kotecha, R. M., Paret, P. P., and Xuhui, F., "Jet Impingement Manifolds for Cooling Power Electronics Modules." Non-Provisional Patent Application 17/084,236, Filed on October 29, 2020.

References

1. U.S. DRIVE. 2017. *Electrical and Electronics Technical Team Roadmap: October 2017*. U.S. Department of Energy Office of Energy Efficiency and Renewable Energy Vehicle Technologies Office, Washington, D.C.

2. Moreno, G. 2021. "Power Electronics Thermal Management." In *Electrification: 2021 Annual Progress Report*, U.S. Department of Energy Office of Energy Efficiency and Renewable Energy Vehicle Technologies Office, Washington, D.C.

3. Moreno, G., Narumanchi, S. V. J., Bennion, K. S., Kotecha, R. M., Paret, P. P., and Xuhui, F., "Jet Impingement Manifolds for Cooling Power Electronics Modules." Non-Provisional Patent Application 17/084,236, Filed on October 29, 2020.

4. Moreno, G. 2021. "Power Electronics Thermal Management." Annual Merit Review Presentation.

5. "AmpCool dielectric coolants," Engineered Fluids, Tyler, TX, 2020. [Online]. Available: https://www.engineeredfluids.com/get-documents.

6. DSI Ventures, Inc., "Alpha-6 fluid." DSI ventures," DSI Ventures, Inc.,Tyler, TX, USA, Accessed: May 2022. [Online]. Available: https://dsiventures.com/wp-content/uploads/2013/02/PDS-Alpha-6.pdf.

7. Motorcraft MERCON LV automatic transmission fluid," Motorcraft, Accessed: May 2022 [Online] Available: https://www.fcsdchemicalsandlubricants.com/additionalinfo/Product%20Data%20Sheet%20MERCON%20LV.pdf.

8. Xuhui, F., Moreno, G., Paret, P., and Narumanchi, S., 2022, "Multiphysics Co-Optimization Design and Analysis of a Double-Side-Cooled Silicon Carbide-Based Power Module, Published in the proceedings of the 2022 ASME InterPACK Conference, October 2022.

9. Moreno, G., Narumanchi, S., Tomerlin, J., and Major, J., 2022, "Single-Phase Dielectric Fluid Thermal Management for Power-Dense Automotive Power Electronics," IEEE Transactions on Power Electronics, 37(10), pp. 12474–12485.

Acknowledgements

I.1.9 Power Electronics Materials and Bonded Interfaces – Reliability and Lifetime (National Renewable Energy Laboratory)

Paul Paret, Principal Investigator
National Renewable Energy Laboratory
15013 Denver West Parkway
Golden, CO 80401
E-mail: paul.paret@nrel.gov

Susan Rogers, DOE Technology Development Manager
U.S. Department of Energy
E-mail: susan.rogers@ee.doe.gov

Start Date: October 1, 2018   End Date: September 30, 2024
Project Funding: $175,000   DOE Share: $175,000   Non-DOE Share: $0

Project Introduction

Increased electrification of various technologies across renewable energy and energy efficiency sectors has brought a great deal of attention to power electronics components and systems which can achieve cleaner and efficient modes of energy storage, conversion, and transmission. The efficiency of power conversion processes depends heavily on the semiconductor die material, device topology, and related properties. Equally important as the device structure is the power electronics package, which can be defined as the integrated system of components surrounding the device that enables the transfer of electrical signals to and from external connections in addition to providing thermal pathways and mechanical support.

Robust and reliable power electronics packaging technologies are critical for the safe operation of wide-bandgap devices such as silicon carbide and gallium nitride, particularly at high temperatures. The cost and power-density targets for these packages or modules only increase the challenges associated with their design and development. A careful and meticulous design of the package, including material selection, geometric layout, and integration of components—from an electrical, thermal, and mechanical standpoint—is critical to bridge the gap between theoretical and measured performance and efficiency of the devices.

From a thermomechanical perspective, the high-temperature operation of wide-bandgap devices presents a strong materials challenge for other component layers within the package. Materials typically used in packages with Si devices such as solders cannot withstand the operating temperature range (200°C and beyond) with wide-bandgap devices, and as a result, new material formulations need to be considered. It is widely documented that the failure mechanisms within conventional power electronics packages involve crack formations at the bonded interfaces (die-attach, substrate-attach), along with electrical interconnect (wire bonds, ribbon bonds) failures. As most of these failures are temperature-dependent, the high-temperature environment only serves to exacerbate the thermomechanical performance of these components, and it thus deserves a great deal of attention in the context of wide-bandgap devices.

This report describes research at the National Renewable Energy Laboratory (NREL) on the thermomechanical performance and reliability of bonded interfaces: copper-aluminum (Cu-Al) transient liquid-phase (TLP) alloy, near-vertical carbon fibers embedded in polymers, and sintered copper. Here, we describe the collaborative efforts between NREL and the Georgia Institute of Technology (Georgia Tech) on the fabrication and thermal cycling of Cu-Al bonded interface samples. We purchased two types of polymeric materials (one with a thermoplastic and the other with a thermoset polymer) and fabricated samples at NREL for reliability evaluation. We also established a plan to collaborate with the Institute of Innovative Mobility in Germany to study the degradation mechanics of sintered copper—a promising alternative to sintered silver—under thermal cycling accelerated experiments. In addition to evaluating the reliability of different materials, we worked on creating novel frameworks to develop lifetime prediction models. To this end, we employed statistical models

in a time series forecasting exercise to predict the crack growth behavior of solders using scanning acoustic microscope (SAM) images.

Objectives

The major objectives of this project are to:

- Evaluate the reliability of high-temperature bonded interfaces by subjecting coefficient of thermal expansion (CTE)-mismatched coupons to accelerated thermal cycling. Crack propagation and any other failure mechanisms that originate and evolve under thermal cycling will be periodically monitored through SAM imaging.

- Develop thermomechanical models to obtain theoretical parameters such as strain-energy density and formulate a lifetime prediction model based on these modeling outputs and experimental data.

- Investigate the performance of statistical and machine learning models in predicting the crack growth of bonded interfaces under thermal cycling.

Approach

Cu–Al Transient Liquid-Phase Bond

A TLP bond was developed at Georgia Tech using a Cu-Al eutectic, which can be used as a bonded material in high-temperature power electronics applications. To create this bond, Cu and Al foils are joined in a specific bulk ratio and heated above their eutectic point but below the melting temperature of the constituent metals. Although this material has demonstrated potential for high reliability under certain configurations in other projects, its reliability—when used for bonding in CTE-mismatched samples under a thermal cycle of −40°C to 200°C— needs to be evaluated. To this end, in previous years, researchers at Georgia Tech attempted to improve the bond quality of Cu-Al samples in which the alloy was bonded between AlN (0.63-mm-thick) and AlSiC (3-mm-thick) coupons. The size of these coupons was 25.4 mm × 25.4 mm (1 inch × 1 inch). Initial characterization of these samples was conducted at NREL through SAM imaging and thermal resistance measurements using an ASTM thermal interface material (TIM) stand. Figure I.1.9.1 shows the bonded samples. After the initial characterization, thermal cycling from −40°C to 200°C was conducted on these samples.
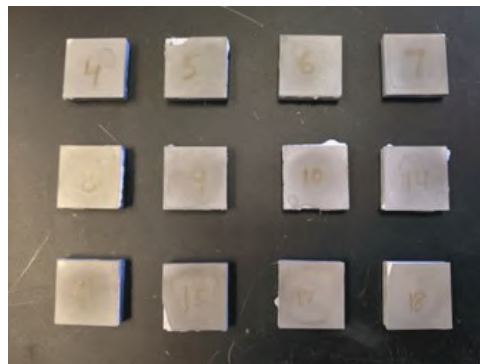
Figure I.1.9.1 Samples with Cu-Al as the bond material for thermal cycling.

Polymeric Materials

In the past, experiments were conducted at NREL on a material named HM-2 (manufactured by *btech*corp). HM-2 is a composite structure consisting of 8- to 10-μm-diameter near-vertical carbon fibers embedded in a polyamide adhesive at approximately 40% fill factor by volume. HM-2 exhibited excellent reliability under a thermal cycling profile of −40°C to 150°C; however, the maximum operating temperature of ~165°C prevented its application in wide-bandgap device-based packages (maximum operating temperature of 175°C and above). Newer versions of HM-2, known as HM-3 and HM-4 (manufactured by ADA Technologies), are high-temperature-compatible and have a thermoplastic and thermoset polymer, respectively.

To study the thermomechanical behavior of HM-3 and HM-4 under thermal cycling, we fabricated samples in which the material was bonded between AlN (0.63-mm-thick) and Cu (3-mm-thick) coupons. The size of these samples was the same as for Cu-Al TLP bonds. Table I.1.9.1 shows the thermal cycling plan for the HM-3 and HM-4 samples.

Table I.1.9.1 Thermal Cycling Plan for the Polymeric Materials

Material	Thermal Cycling Profile		
	Temperature	Ramp Rate	Dwell Time
HM-3	Case 1: -40°C–150°C Case 2: -40°C–150°C Case 3: -40°C–150°C	5°C/min >10°C/min 5°C/min	10 mins 10 mins 30 mins
HM-4	Case 1: -40°C–150°C Case 2: -40°C–175°C Case 3: -40°C–200°C	5°C/min 5°C/min 5°C/min	10 mins 10 mins 10 mins

Sintered Copper

Sintered copper is considered to be a promising alternative to sintered silver for high-temperature power electronics packaging due to its low cost and reliable performance under low-temperature thermal cycling profiles [1]. The performance of this material under high-temperature accelerated conditions has not yet been reported in the literature; hence, we included it in our research study. The sample configuration consists of Cu baseplates bonded to active-metal-bonded substrates with silicon nitride as the ceramic layer. These substrates were supplied by Rogers Corporation, and the Cu baseplates were fabricated at NREL. The bonding of the samples will be conducted at the Institute of Innovative Mobility using their formulation of sintered copper. As the tasks related to sintered copper will be conducted in FY23, we will report the corresponding results in next year's report.

Image-Based Lifetime Prediction

In this task, we computed the void fraction from a time series of SAM images of eutectic solder under accelerated thermal cycling and used it to compare the prediction capability of different statistical models. These models included Holt linear, simple exponential smoothing, and autoregressive models.

Results

Cu–Al Transient Liquid-Phase Bond

One of the main challenges with the fabrication of Cu-Al samples is the amount of initial defect fraction. SAM images of these samples revealed a significant presence of white regions, indicating poor bond quality. In FY21, different variations were attempted in the fabrication process; however, the defect fraction was still not within the acceptable range of less than 5% of the entire bonding area. Thermal cycling was initiated on these samples in FY21 and continued in FY22. Figure I.1.9.2 shows the initial C-SAM images of a couple of Cu-Al joints (top row) and the same samples after 850 thermal cycles (bottom row). Large patches of white regions, which denote the presence of cracks or voids, can be observed in the initial images. A total of 15 samples were subjected to high-temperature thermal cycling from −40°C to 200°C. On an average, the defect fraction increased from 20% at the initial stage to 29% at 850 cycles. Among these samples, two were selected for cross-sectional analysis after 50 cycles. Figure I.1.9.3 shows the scanning electron microscope (SEM) images of one of these samples along with the SAM image. It is clear from the SEM images that there is poor adhesion between the AlN layer and the bond at certain locations; however, these cracks did not propagate at a high rate under thermal cycling, mainly due to the low CTE mismatch within the sample.
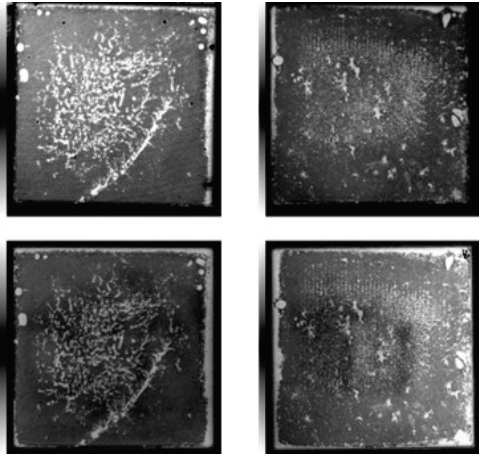
Figure I.1.9.2 SAM images of Cu-Al bond samples before cycling (top row) and after 850 cycles (bottom row).
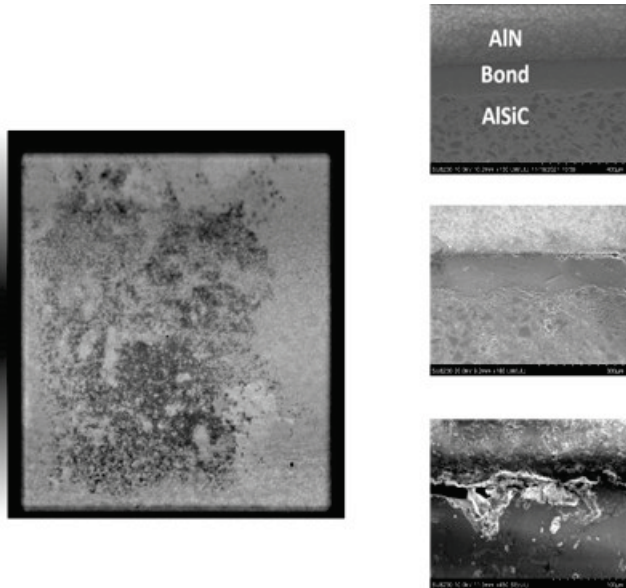
Figure I.1.9.3 SAM image of a Cu-Al bond sample with significant defects (left), and the SEM images at various locations of the bond (right). The image at the bottom has a higher resolution and shows the interface between the bond and the AlN.
SEM images by Chidinma Imediegwu, Georgia Tech

Polymeric Materials

Figure I.1.9.4 shows the SAM images of the HM-3 samples. It is evident that there is good bonding throughout the joint region. These results indicate that the applied bonding temperature and pressure are sufficient for these samples. Next steps include fabricating samples with HM-4 and conducting thermal cycling of both HM-3 and HM-4 samples under different cycling conditions.
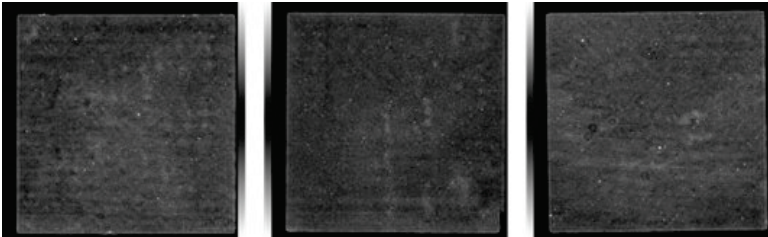
Figure I.1.9.4 SAM images of HM-3 samples.

Image-Based Lifetime Prediction

Previously, we conducted thermal cycling experiments on eutectic lead solder and developed a lifetime prediction model. SAM images were obtained at regular periodic intervals during thermal cycling and serve as spatial data that reveals the amount of degradation within the solder layer. Three cycling profiles—thermal cycle (−40°C–150°C, 5°C/min, 10-min dwell), thermal shock (−40°C–150°C, ~25°C/min, 10-min dwell), and extended dwell (−40°C–150°C, 5°C/min, 30-min dwell)—were included in the accelerated experiment plan. Among all the SAM images that were generated as part of these experiments, we selected 143 to develop a lifetime prediction model. After the SAM images were cropped and edited to filter out the noise, we computed the void fraction of each image using the *OpenCV* library in Python and categorized the data based on the cycling profiles. Figure I.1.9.5 shows the crack growth curve obtained from the lead solder SAM images.
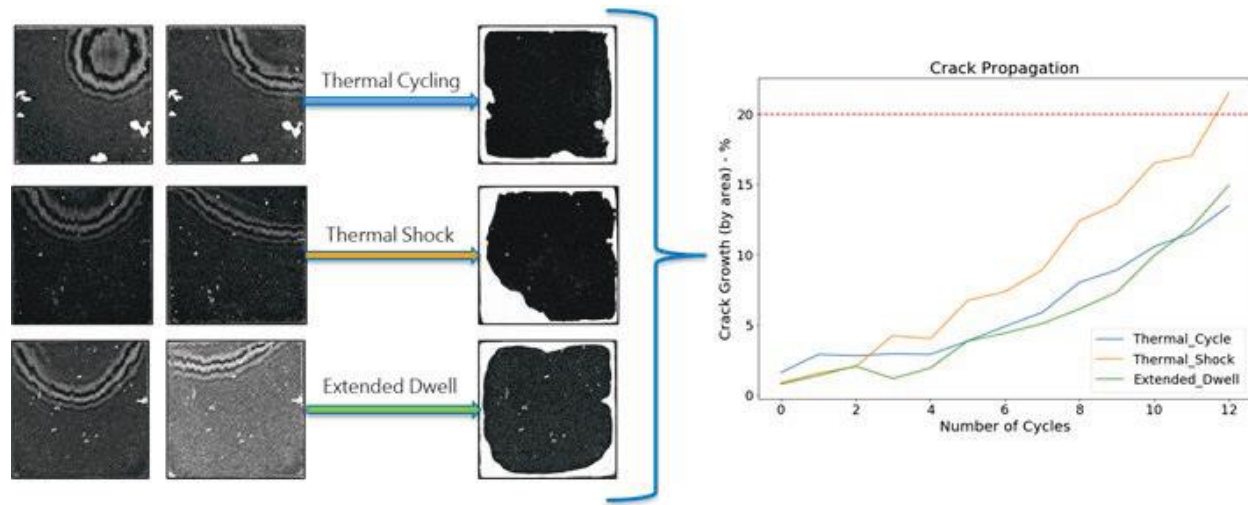
Figure I.1.9.5 SAM images of lead solder under different thermal cycling profiles (left) and crack growth curves obtained from the SAM images (right).

For any time-series data, investigating the autocorrelation function (ACF) and partial autocorrelation function (PACF) are important, especially for forecasting. These functions provide a measure of association between past and current values in a time series and seek to identify the most relevant past information in predicting the future behavior of the data. The PACF differs from ACF in that it represents the unique relationship between two data points in the time series that excludes the effect of the data points between them. Also, if time-series data has a strong autocorrelation, it indicates the presence of certain patterns or periodicity within the data. Figure I.1.9.6 shows the ACF and PACF plots of the data obtained from the different thermal cycling profiles. In these graphs, the x-axis represents the lag order and the y-axis represents the correlation coefficient. Here, a lag order of zero refers to the correlation between a data point and itself, and will always be 1. Similarly, a lag order of 1 corresponds to the correlation between a data point and the subsequent point and so on. A positive autocorrelation for a certain lag order points to a direct relationship between the corresponding values in the time series, and a negative autocorrelation denotes an inverse relationship. The shaded regions within these plots represent the uncertainty intervals, and it can be seen that only a lag order of 1 is statistically significant. Also, the uncertainly intervals are high due to the limited number of data samples for each cycling profile.
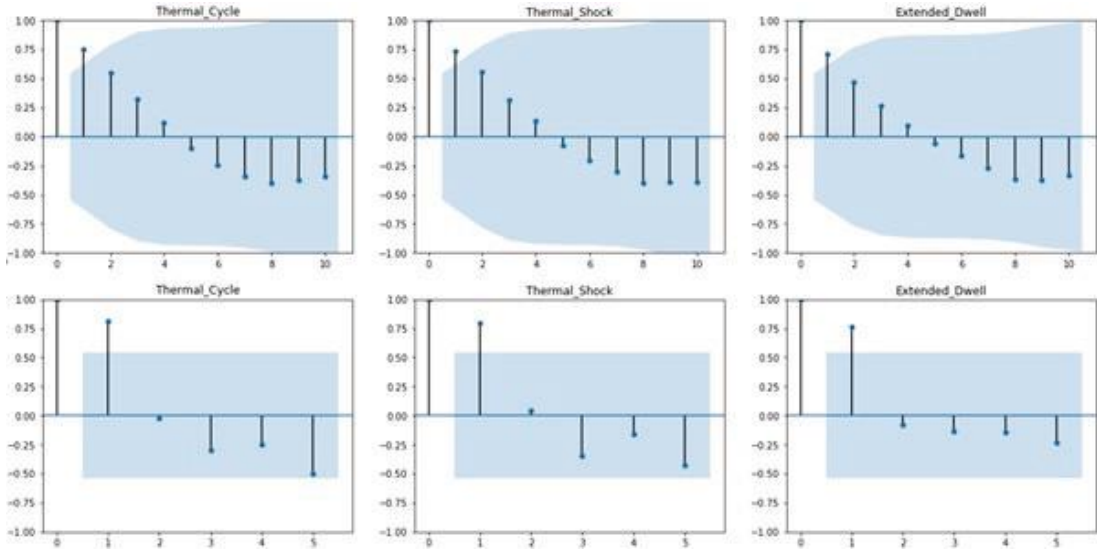
Figure I.1.9.6 Autocorrelation plots (top) and partial autocorrelation plots (bottom).

In addition to autocorrelation and partial autocorrelation, another important aspect to consider when dealing with time series data is the concept of stationarity. A weak definition of stationarity is that certain features of the data, such as mean, variance, and autocorrelation, are independent of time. In other words, if data is not stationary, then it becomes challenging to model, due to the constantly changing feature set. To check for stationarity, we employed the Augmented Dickey-Fuller (ADF) test [2], and the test results indicated that the raw data is nonstationary, which can mainly be attributed to the upward trend in the crack growth behavior within the solder layer. Hence, we transformed the data by taking the first-order difference between the log of the values. As a result, the thermal shock data passed the ADF test (the null hypothesis was rejected), whereas additional transformations are required for the thermal cycle and extended dwell data sets.

The thermal shock data was split into training (0–900 cycles) and validation (900–1200 cycles) sets, and different statistical models were exercised on the training data, as shown in Figure I.1.9.7. Among the models we selected from the statsmodels package in Python, Holt Linear proved to be the most accurate in predicting the crack growth behavior in the later stages of the thermal shock experiments. Next steps in this task involve investigating ways to increase the size of data set through techniques such as interpolation, exploring the performance of advanced machine learning models such as long short-term regression, and applying these models to the SAM images of other bonded materials.
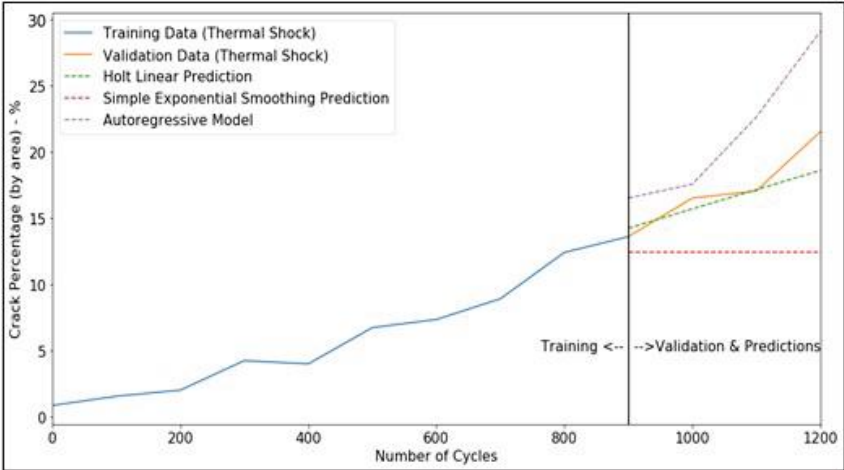
Figure I.1.9.7 Predictive performance comparison of different statistical models.

Conclusions

Power electronics packaging for the safe and reliable operation of wide-bandgap devices at high temperatures is a challenging research goal. This project focuses on reliability evaluation and lifetime prediction of bonded materials to determine their applicability in high-temperature packaging. The bonded materials of interest are transient liquid-phase Cu-Al bond, polymeric materials, and sintered copper.

Cu-Al bonds show promise of excellent reliability when bonded in a low-CTE-mismatch configuration; however, challenges remain in addressing the initial bond quality of the material. Initial SAM images of polymeric materials indicate good bonding quality, and thermal cycling experiments will be conducted on these materials and on sintered copper in FY23.

A lifetime prediction framework based on SAM images of eutectic lead solder was developed, and different statistical models were compared based on their accuracy for time-series forecasting. Building on this framework, additional models and material degradation data will be incorporated to expand the scope of this lifetime or crack growth prediction tool.

Key Publications

1. P. Paret, J. Major, D. DeVoto, S. Narumanchi, C. Ding and G. -Q. Lu. 2022. "Reliability and Lifetime Prediction Model of Sintered Silver Under High-Temperature Cycling." *IEEE Journal of Emerging and Selected Topics in Power Electronics* vol. 10 (no. 5): 5181-5191. doi: 10.1109/JESTPE.2021.3121195.

2. C. Imediegwu, S. Graham, D. G. Pahinkar, S. Narumanchi, P. Paret, and J. Major. 2022. "Interdiffusion and formation of intermetallic compounds in high-temperature power electronics substrate joints fabricated by transient liquid phase bonding." *Microelectron. Reliab.* vol. 137: 114788. doi: 10.1016/j.microrel.2022.114788.

References

1. M. Wang, Y. Shan, Y. Mei, X. Li, and G. Lu. 2020. "Sintered-copper Die-attach: Processing, Properties, and Reliability." In CIPS 2020; 11th International Conference on Integrated Power Electronics Systems, pp. 1–6.

2. D. Dickey and W. Fuller. 1979. "Distribution of the Estimators for Autoregressive Time Series With a Unit Root." JASA J. Am. Stat. Assoc. vol. 74. doi: 10.2307/2286348.

Acknowledgements

I.1.10 Electric Motor Thermal Management (National Renewable Energy Laboratory)

Emily Cousineau, Principal Investigator

National Renewable Energy Laboratory
15013 Denver West Parkway
Golden, CO 80401
E-mail: emily.cousineau@nrel.gov

Susan Rogers, DOE Technology Development Manager

U.S. Department of Energy
E-mail: susan.rogers@ee.doe.gov

Start Date: October 1, 2018	End Date: September 30, 2024	
Project Funding: $250,000	DOE Share: $250,000	Non-DOE Share: $0

Project Introduction

This project is part of a multi-lab consortium that includes multiple universities, the National Renewable Energy Laboratory (NREL), Oak Ridge National Laboratory (ORNL), Sandia National Laboratories (SNL), and Ames National Laboratory. The project and consortium leverage research expertise and facilities at national labs, universities, and industry to significantly increase electric drive power density and reliability while reducing cost. The consortium is organized around three keystone projects: (1) Power Electronics, (2) Electric Motors, and (3) Traction Drive System. The Electric Motors keystone project at NREL focuses primarily on improvements (reductions) in the passive thermal resistance of components and interfaces in electric motors and improved active fluid-based cooling technologies to increase power density, in line with the most recent research priorities outlined in the U.S. DRIVE *Electrical and Electronics Technical Team (EETT) Roadmap* [1].

In the area of electric-drive motors, the EETT Roadmap highlights the importance of reducing the thermal resistance of the motor packaging stack-up to increase power density. The Roadmap also mentions that the thermal conductivities of the materials within the motor influence the amount of material necessary to generate the required mechanical power. The Roadmap emphasizes research areas with a focus on material physics-based models, improved materials, and thermally conductive epoxy and fillers.

Heat transfer and thermal management are critical to electric motors because—as mentioned in the EETT Roadmap —thermal constraints place limitations on how electric motors ultimately perform. The thermal management of electric motors for vehicles is complex because of the multiple heat transfer paths within the motor, the variations in heat arising from motor operating conditions, and the multiple material interfaces through which heat must pass to be removed. For these reasons, "heat transfer is as important as electromagnetic and mechanical design" [2] for improving the power density, cost, and reliability of electric motors, as outlined by the EETT Roadmap.

Objectives

Research under this project will be performed within the framework of a research consortium consisting of a multidisciplinary team that will plan, establish, conduct, and manage a portfolio of multi-lab and multi-university research efforts to advance the state of the art in electric drive technologies. The objective of the consortium is to develop a 100-kW traction drive system that achieves a power density of 33 kW/L, has an operational life of 300,000 miles, and costs $6/kW. The system will be composed of a 100-kW/L inverter and a >20,000-rpm, 50-kW/L electric motor. Building on the research experience and capabilities within each laboratory, the multi-lab consortium will focus on achieving research objectives within three keystone projects: (1) Power Electronics, (2) Electric Motors, and (3) Traction Drive System.

For the Electric Motors keystone project, the consortium will focus on investigating motor technology gaps to enable increased power density and reliability, supporting research pathways in power electronics

technologies. As power electronics technologies develop to enable higher operating temperatures, higher system voltages, and higher switching frequencies, motor technologies will also be necessary to realize the electric-drive system benefits. Key consortium motor research pathways include motor material improvements (electrical, magnetic, and thermal), higher motor operating speeds, and higher system voltages. NREL research will provide motor researchers—within and outside the consortium—with the data and models necessary to enable motor innovations and the use of novel materials and designs. This work supports the broad demand for data, analytical methods, and experimental techniques to improve and better understand motor thermal management. It also incorporates unique capabilities, facilities, and expertise in addition to the data, analysis methods, and experimental techniques to improve and better understand heat transfer within electric motors to meet the demands of electric-drive vehicles. NREL's focus in fiscal year (FY) 2022 included:

- Developing models, simulation tools, and experimental prototypes in support of consortium team members to quantify thermal performance and heat transfer technologies and support motor development efforts.

- Utilizing NREL's mechanical characterization setup to measure mechanical properties of soft magnetic materials for consortium team members.

Approach

The ability to remove heat from an electric motor depends on the passive-stack heat transfer within the motor and the convective cooling heat transfer of the selected cooling technology. In addition, as new materials are developed, it is important to characterize temperature-dependent material properties and thermal interface properties. Characterization of new materials enables motor designers to evaluate their potential performance trade-offs for motor applications. For this reason, the approach for the research project is split between two primary areas. The first focus area for NREL during FY 2022 utilized experimental facilities at NREL to measure new motor materials in collaboration with consortium members. The second focus area involved providing motor system thermal analysis for electric motor research efforts performed within the consortium.

Material and Interface Thermal and Mechanical Characterization

NREL measured mechanical properties of soft magnetic materials in collaboration with SNL. The experimental setup is shown in Figure I.1.10.1. The image shows the dogbone test sample provided by SNL loaded into the tensile testing setup. The work during FY 2022 focused on mechanical characterization of the epoxy material at various loadings of iron nitride.

Figure I.1.10.1 Mechanical tensile test setup with sample loaded prior to testing. *Photo by Emily Cousineau, NREL*

Motor System Thermal Analysis

The research performed in the motor system thermal analysis area focused on working with consortium collaborators University of Wisconsin–Madison, Georgia Institute of Technology (Georgia Tech), and ORNL.

The collaboration with the University of Wisconsin focused on NREL providing technical support, thermal data, and material information to support the University of Wisconsin-led integrated cooling for motor and power electronics effort. The collaboration with Georgia Tech focused on NREL providing technical support and facilities to support the Georgia Tech-led experimental work. The collaboration with ORNL is described in more detail below.

The collaboration with ORNL supported motor thermal analysis and thermal design of advanced machine designs led by ORNL. This collaboration is summarized in Figure I.1.10.2. ORNL led the overall iterative electric machine design process with an emphasis on the electromagnetic and mechanical assembly design. NREL, in collaboration with ORNL, performed the thermal analysis and cooling design. A summary of the initial work is provided in an ORNL-led paper presented at the 2020 IEEE Energy Conversion Congress and Exposition (ECCE). In FY 2022, NREL focused on refining the motor slot heat exchanger shown in Figure I.1.10.3.
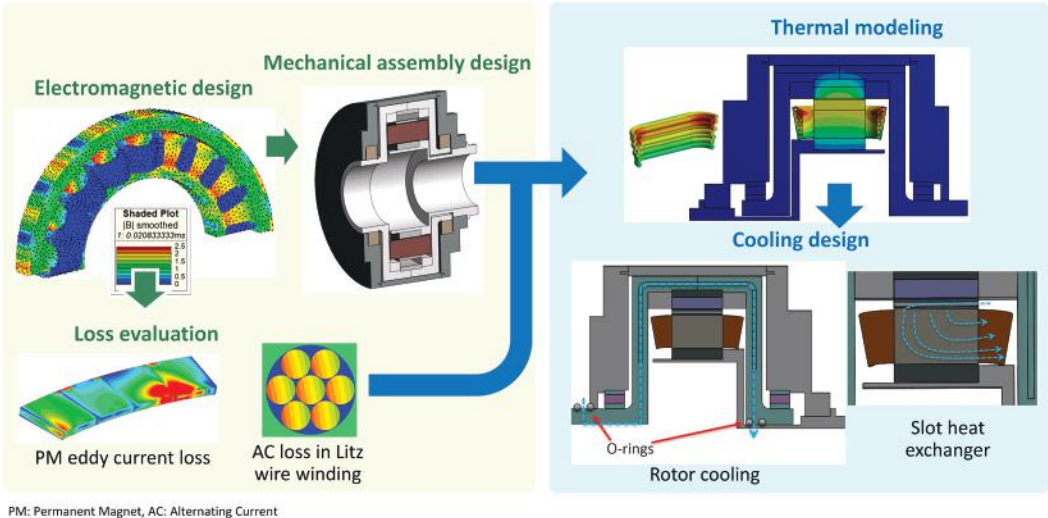
Figure I.1.10.2 ORNL and NREL motor analysis approach.
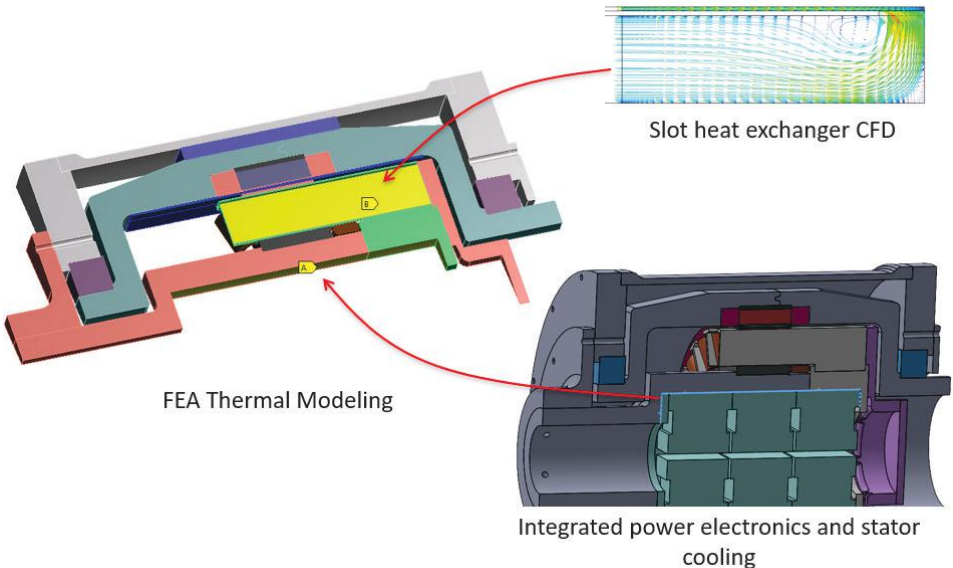
Figure I.1.10.3 Illustration of refined motor model including slot heat exchanger heat transfer coefficient obtained from computational fluid dynamics simulations, and combined power electronics and stator cooling. *Illustration by Emily Cousineau, NREL*

Results

The following sections summarize the results of both the mechanical experimental work for material characterization and the motor system thermal analysis collaborations.

Material and Interface Thermal and Mechanical Characterization

NREL utilized experimental methods to measure soft magnetic materials in collaboration with SNL. In FY 2022, NREL characterized the tensile strength and stiffness versus volume fraction loading of iron-nitride-filled epoxy samples as compared to base epoxy samples, as shown in Table I.1.10.1. The measurements demonstrated that the iron nitride fill increases the brittleness of the material. Specifically, the material's tensile modulus (stiffness) increases with increasing loading combined with reduced elongation at the yield point. The ultimate tensile strength decreases by 35% with the iron nitride fill, but is not proportional to the loading fraction for the tested materials.

Table I.1.10.1 Experimental Results Performed at NREL with SNL-Developed Materials
The results show the average value of three tests

Vol% loading Iron Nitride	Elongation at Yield	Tensile Strength (MPa)	Tensile Modulus (GPa)
0%	9.7%	51.7	3.8
30%	6.2%	35.7	10.3
40%	5.4%	32.7	15.4
65%	3.5%	33.0	33.0

Motor System Thermal Analysis

The work supporting the ORNL-led motor research efforts focused on an outer-rotor motor configuration, as shown in Figure I.1.10.2. The motor went through multiple design iterations in FY 2022. This iterative design approach investigated design configurations to facilitate integration with the inverter that was designed in parallel. NREL led the thermal analysis aspects of the motor design to reduce steady-state rotor magnet temperatures to 80°C to meet ORNL temperature requirements. Figure I.1.10.4 highlights the FY 2022 accomplishments. The analysis includes several refinements in the thermal design, including the windage losses, heat flow paths through air gaps, and airflow cooling the rotor surface. The finite element analysis work performed during FY 2022 shows that a modest airflow achieving a heat transfer coefficient of 10 W/m²-K meets the 80°C temperature requirement of the rotor magnets.
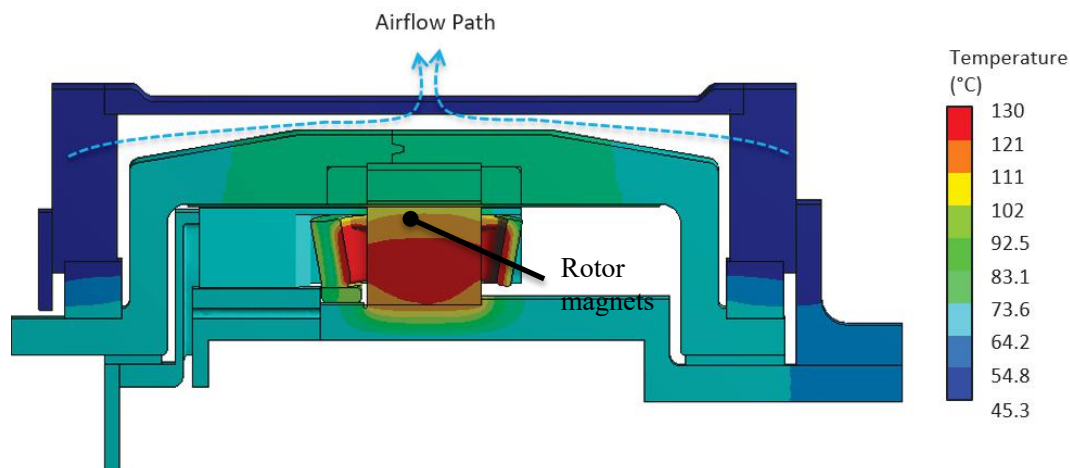
Figure I.1.10.4 Steady-state motor temperature showing the airflow needed over the rotor to ensure that magnet temperatures do not exceed 80°C.

Conclusions

During FY 2022, NREL efforts focused on supporting collaborations with external research partners within the Electric Drive Technologies research consortium. The primary collaborations described in this report included ORNL and SNL. The collaboration with SNL utilized NREL's experimental capabilities to mechanically characterize SNL-provided material samples for motor applications. The collaboration with ORNL supported efforts to refine the design of a high-speed, non-heavy-rare-earth outer-rotor motor. NREL supported the effort by leading the thermal analysis and design of advanced machines. A manuscript was also published in an international collaboration with IFP Energies Nouvelles and is highlighted in the key publications section.

Key Publications

1. Bennion, K. 2022. "Electric Motor Thermal Management." 2022 DOE VTO Annual Merit Review, Washington D.C., June 2022.

2. Poubeau, Adele, Vinay, Guillaume, Kekelia, Bidzina, and Bennion, Kevin. "Conjugate Heat Transfer Simulations of High Prandtl Number Liquid Jets Impinging on a Flat Plate." https://ssrn.com/abstract=4059091.

References

1. U.S. DRIVE. 2017. *Electrical and Electronics Technical Team Roadmap: October 2017*. Washington, D.C.: U.S. Department of Energy Office of Energy Efficiency and Renewable Energy Vehicle Technologies Office. https://www.energy.gov/sites/prod/files/2017/11/f39/EETT%20Roadmap%2010-27-17.pdf.

2. J.R. Hendershot and T.J.E. Miller. 1994. *Design of Brushless Permanent-Magnet Motors*. Oxford, UK: Magna Physics Publishing.

Acknowledgments

I.1.11 High-Reliability Ceramic Capacitors to Enable Extreme Power Density Improvements (Sandia National Labs)

Jack Flicker, Principal Investigator
Power Electronics and Energy Conversion Systems
Sandia National Labs
1515 Eubank Blvd
Albuquerque, NM, 87123
E-mail: jdflick@sandia.gov

Susan Rogers, DOE Technology Development Manager
U.S. Department of Energy
E-mail: susan.rogers@ee.doe.gov

Start Date: October 1, 2018   End Date: September 30, 2024
Project Funding: $70,000   DOE share: $70,000   Non-DOE share: $0

Project Introduction

A detailed Genetic Algorithm (GA) topology optimization [1] for the vehicle Electric Traction Drive (EDT) synchronous boost converter and inverter is being carried out. Candidate designs from pareto frontiers have been identified for SiC and GaN based semiconductor switches that achieve large power densities. However, these optimal designs are enabled only through the use of high energy density of multilayer ceramic capacitors (MLCCs) in a distributed architecture of many (~250) small value MLCCs. Use of these distributed small MLCC capacitors on a DC bus enables significant gains in system power density, but, due to the increased component count, has a detrimental effect on system-level mean time to failure (MTTF). To achieve system-level power density and cost requirements while still meeting reliability targets, it will be necessary to significantly increase MTTF of base-metal electrode MLCCs. For these devices, the primary failure mechanism at high voltage and high temperature is low insulation resistance and shorting caused by electromigration of defects in the dielectric layer. Oxygen vacancies, a natural defect which occurs during firing of the capacitors in reducing atmospheres to enable base-metal electrodes (Ni), migrate under the applied electric field and gather at the cathode. This decreases the Schottky barrier at the metal-dielectric interface causing leakage and, eventually, shorting. Minimization of this failure mechanism is paramount for increasing MTTF.

Objectives

The objective of this research is to investigate ways to extend MTTF through system level control instead of from a material science approach. Decades of R&D have gone into minimizing oxygen vacancies, preventing their diffusion via the addition of migration barriers (*i.e.* grain boundaries), binding dopants to pin them in place, etc. This vast amount of research and development has resulted in the current state of base-metal electrode MLCC's with significantly increased lifetimes. However, further increases in lifetime are difficult to achieve compositionally/microstructurally, and other solutions may be necessary on a device level. This work investigates that approach.

Approach

Instead of addressing performance/reliability through material composition and microstructure, we take an innovative approach to prevent oxygen vacancies from reaching the cathode by applying a reverse bias periodically (*i.e.* an AC waveform) to push the oxygen vacancies back to their original positions. This approach may be difficult to implement on a circuit level, but, if successful, may allow for unique circuit designs based on much longer lifetime, high density MLCC capacitors.

A system to simultaneously evaluate 40 capacitors under AC conditions with temperature control was fabricated using a custom heating stage, multiple relays, and a H-bridge. This scale-up allows for much quicker measurements than previously, as well as for Weibull statistics to be performed. This is important due to the

propensity for X7R MLCC capacitors to contain infant mortality (Weibull β<1) and early-wear-out (Weibull β ~1.5) failures in conjunction with wear-out (Weibull β~5-10). The unit contains a power/voltage bus that delivers the high voltage for accelerated degradation, and a low-voltage measurement bus to which capacitors can be switched to allow for any 2-terminal device measurement - most importantly insulation resistance. The capacitor can then be returned to the high voltage bus to continue degradation.

Initial test results in FY21 using the 40-capacitor test setup showed a distinctly different trend than the initial test results. Namely, the increased frequency of voltage application resulted in *lower* lifetimes instead of *longer* lifetimes. Work during FY22 focused on expanding the capacitor study to multiple other acceleration conditions on similar parts and understanding the lifetime dependence and failure mechanism under AC conditions in different regimes.

Results

Since the latest results using the 40-capacitor accelerated testing setup was contrary to the seed data that was used to start this project (taken using an older, lower sample count setup), the original testing conditions were applied to re-take data using the original conditions. The capacitors were tested at an applied bias of 45V at 255ºC. This voltage level was chosen to give an equivalent electric field across the capacitor as for the original test conditions. Under these conditions, the expected behavior of increasing lifetime with increasing frequency was verified (Figure I.1.11.1). This behavior was also verified for other low voltage, high temperature test conditions.
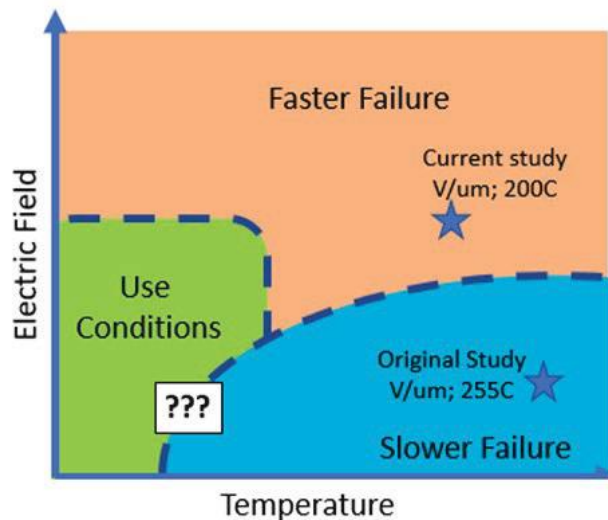
Figure I.1.11.1 Schematic representation of current results showing change in frequency-dependent time to failure as a function of acceleration conditions. The differentiation between these two and the behavior at use conditions is unknown.

Capacitor MTTF is plotted vs log frequency in Figure I.1.11.1. There is a clear trend of increasing lifetime with frequency that saturates at higher frequencies (> 0.1 Hz). This saturation is in some way expected, as capacitors would not be expected to achieve 'infinite life' at infinite frequency and there must be some limiting mechanism. It is unclear if this saturation is caused by a transition to a different failure mechanism or some other limiting mechanism. During this condition, the maximum achievable MTTF increase is ~10x (12 hours at DC to ~100-110Hr at >0.1 Hz).

During testing, it was noticed that capacitors exhibited two distinct failure mechanisms (Figure I.1.11.2). One failure mechanism was a gradual, degradation failure exemplified by increasing leakage current over time. The other failure mechanism was dominated by catastrophic failure ('go pop') via breakdown and shorting. The

catastrophic failure mechanism was more prevalent at DC and near-DC conditions while the degradation failure was more prevalent at higher frequencies.
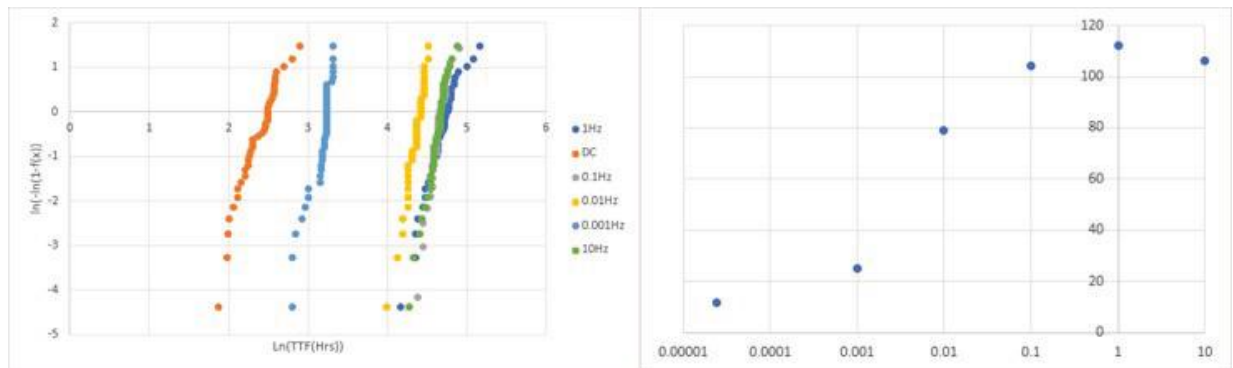
Figure I.1.11.2 (Left) Weibull curves of MLCC devices at 45V, 255ºC at frequencies ranging from DC to 10Hz. (Right) Measured MTTF in hours vs. applied frequency. The capacitors show an increasing MTTF as frequency increases that saturates at higher frequencies.

To further elucidate these different failure mechanisms, a series of tests were carried out on capacitors at 100V/ 200ºC, 60V/ 225ºC, and 45V/ 255ºC (Figure I.1.11.3). While the low voltage, high temperature condition (blue curve) shows increased MTTF with frequency, the higher voltage, lower temperature condition shows decreasing MTTF with frequencies.
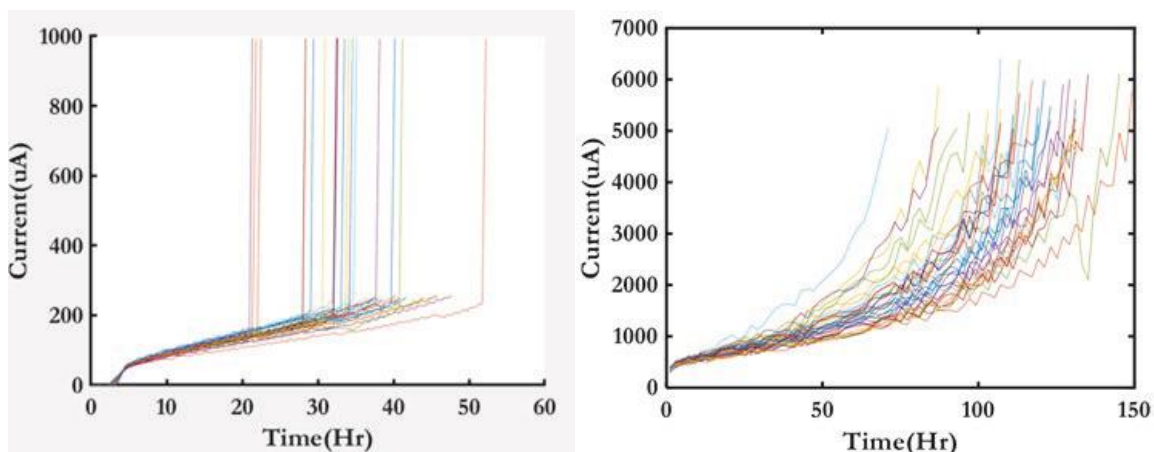
Figure I.1.11.3 (Left) At DC bias, capacitors show a catastrophic failure mechanism where the devices are shorted. This is compared to higher frequencies (right) where the capacitors exhibit a slow, degradation failure mode.

The different frequency and temperature conditions show significantly different onset of catastrophic vs. degradation failure mechanisms (Figure I.1.11.4). In all samples tested, applied DC voltage resulted in catastrophic breakdown of the samples. This failure mechanism transitioned to a degradation breakdown at higher frequencies, although the point of this transition varied greatly between runs. For example, the samples at 60V, 200ºC exhibited catastrophic breakdown up to 1Hz, while the samples at 45V, 255ºC transitioned at 0.01 Hz. The relationship between frequency, voltage, and temperature is being actively evaluated to elucidate this transition.
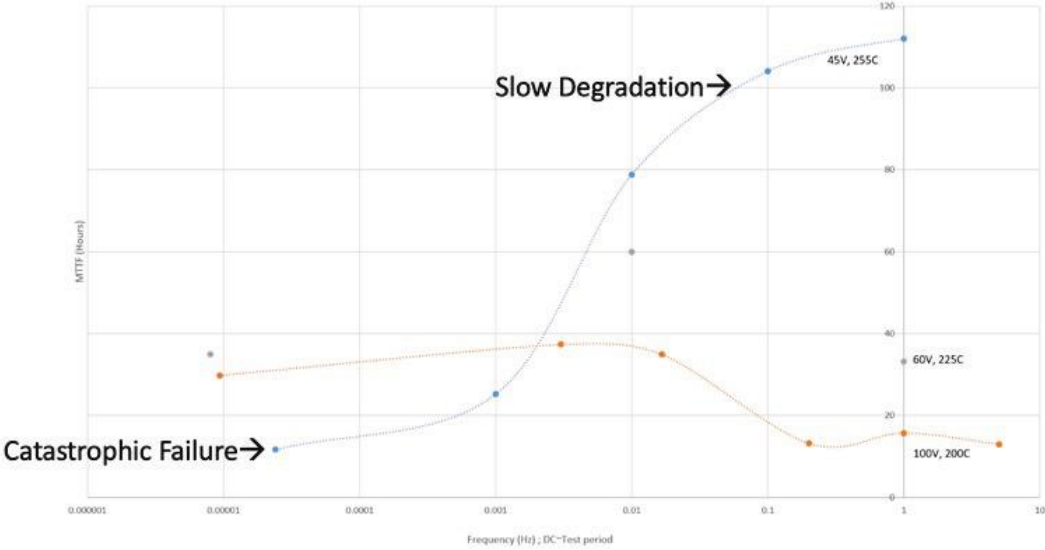
Figure I.1.11.4 MTTF vs. frequency for MLCCs measured at different voltage and temperature points. Some testing conditions show increasing MTTF vs. frequency while other conditions show small or negative changes in MTTF with frequency. These samples also have different frequencies where the change between catastrophic and degradation failure modes occurs (although catastrophic failure is more typical of DC and low frequency while degradation is more prevalent at higher frequencies).

Testing is currently ongoing to re-evaluate DC data at a higher failure criterion to see if the same failure trends exist. This testing will be followed by evaluation of capacitor MTTF using a less aggressive acceleration condition. The goal is to evaluate a stress on the capacitor that results in a degradative failure mode at DC and evaluate the MTTF vs. failure behavior when no catastrophic failure is present.
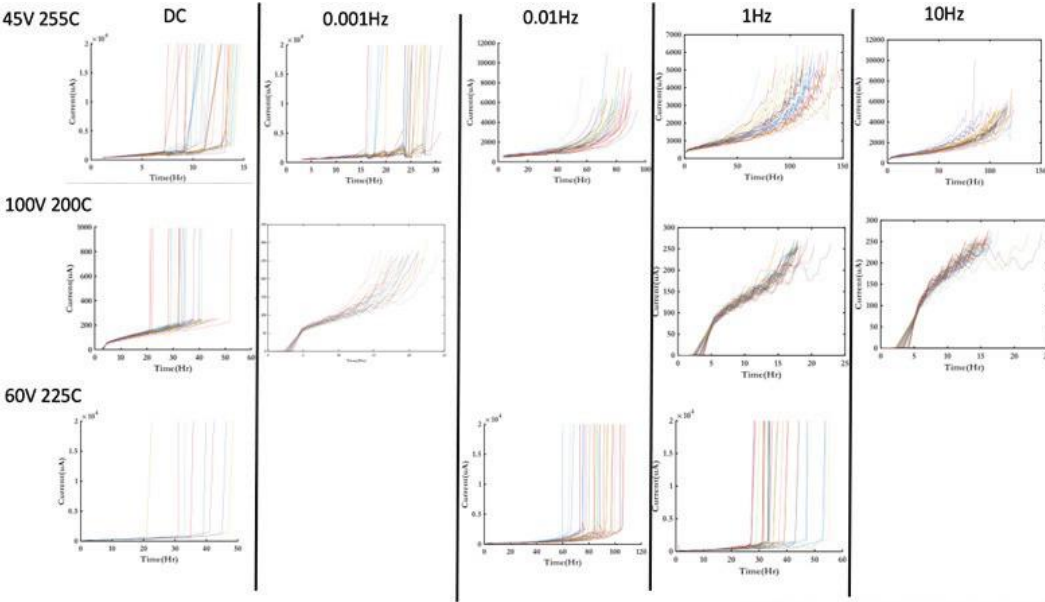
Figure I.1.11.5 Failure modes for capacitor tests at three testing conditions and different frequencies. Depending on the specific voltage and temperature conditions (e.g., 1Hz) the capacitors may exhibit either catastrophic or degradation failure modes. The regime change between these failure modes depends on the specific temperature and voltage conditions.

Degraded (not catastrophically failed) samples will be undergoing testing and are being evaluated using typical capacitor characterization techniques to clarify the mechanisms leading to failure under both AC and DC bias. These evaluation techniques include impedance spectroscopy to evaluate the equivalent circuit of the

capacitors, bipolar IV curves to evaluate if AC degrades evenly in both directions compared to the unipolar degradation of DC, and Thermally Stimulated Depolarization Current (TSDC)[1] to compare the results of an applied DC bias compared to an AC signal (AC application should be smaller as the oxygen vacancy relaxing in both directions should cancel out).

Future work will include expanding the current study to multiple other acceleration conditions on similar parts and understanding the lifetime dependence and failure mechanism under AC conditions in different regimes. These tests include:

1. Re-evaluating the 100V, 200°C stress condition at a higher failure criterion (10Hz, 1Hz, 0.1Hz, etc. down to 0.001Hz)

2. Completing the 60V, 225°C stress condition measurements (0.1Hz, 0.001Hz, 10Hz)

3. Evaluate capacitor MTTF under low acceleration conditions (e.g., 200V, 150°C, which represent more 'typical' usage values) with the goal to eliminate catastrophic failure entirely and determine MTTF vs. frequency.

4. Perform TSDC, bipolar IV, and impedance spectroscopy on degraded (not shorted) samples as a function of frequency to explore the as-degraded state

Once the above tests are completed, a publication will be prepared comparing catastrophic vs degradation failure, how that is impacted by the frequency of bias, and what that reveals regarding the kinetics of oxygen vacancies in MLCCs.

Conclusions

AC square wave application during accelerated testing has been found to both increase and decrease lifetime in different testing conditions. The root cause for these different behaviors is currently unknown but could be due to oxygen vacancy migration under AC conditions and electrostrictive strain-based microcracking, respectively. Testing at different conditions has shown two competing failure modes in the capacitors: one resulting in a degradation failure and one resulting in a catastrophic failure. These failure modes are dependent on the frequency and temperature of the test. More testing and evaluation of the capacitors is needed to fully evaluate these different failure modes and explore the MTTF vs. frequency behavior in the purely degradation failure regime.

References

1. "Co-Optimization of Boost Converter Reliability and Volumetric Power Density Using Genetic Algorithm,". 2020 IEEE Energy Conversion Congress and Exposition (ECCE). Detroit, MI, October 2020.

Acknowledgements

---

[1] A technique where a capacitor is charged, cooled, and the discharge current is evaluated as it is warmed to determine the kinetics of defect relaxation (in this case, oxygen vacancies) in the capacitor dieletric.

I.1.12 Power Electronics: Vertical GaN Device Development (Sandia National Laboratories)

Andrew Binder, Principal Investigator

Sandia National Laboratories
P.O. Box 5800, MS 1086
Albuquerque, NM 87185
E-mail: abinder@sandia.gov

Susan Rogers, DOE Technology Development Manager

U.S. Department of Energy
E-mail: susan.rogers@ee.doe.gov

Project Introduction

This project is part of a multi-lab consortium that leverages U.S. research expertise and facilities at national labs and universities to significantly advance electric drive power density and reliability, while simultaneously reducing cost. The final objective of the consortium is to develop a 100 kW traction drive system that achieves 33 kW/L, has an operational life of 300,000 miles, and a cost of less than $6/kW. One element of the system is a 100 kW inverter with a power density of 100 kW/L and a cost of $2.7/kW. New materials such as wide-bandgap semiconductors, soft magnetic materials, and ceramic dielectrics, integrated using multi-objective co-optimization design techniques, will be utilized to achieve these program goals. This project focuses on a subset of the power electronics work within the consortium, specifically the design, fabrication, and evaluation of vertical GaN power devices suitable for automotive applications.

Objectives

Gallium Nitride (GaN) is a promising wide-bandgap (WBG) semiconductor material that could enable higher-performance power electronic devices than traditional Silicon (Si) or even its WBG counterpart, Silicon Carbide (SiC). This is based on the increased critical electric field of GaN, which would enable lower-resistance devices with the same hold-off voltage as devices fabricated from the other materials. This is a key performance metric for power devices. Laterally-oriented, High Electron Mobility Transistors (HEMTs) based on AlGaN and GaN materials are common in high-frequency applications and are being established in lower-voltage power switching applications (approximately 600 V and below). However, with the emerging commercial maturation of GaN substrates, traditional vertically-oriented device structures (such as are common in Si and SiC) can now be realized in GaN, with several promising demonstrations of high-voltage pn diodes and vertical transistors appearing in the literature [1], [2], [3]. While GaN pn diodes may be of interest, the ~3 V turn-on voltage, determined mainly by the bandgap of the material, discourages their use in some power-switching circuits due to the loss of power conversion efficiency resulting from this high turn-on voltage. Instead, more promising candidates for these power conversion systems, including automotive inverters, are GaN Schottky barrier diodes (SBDs) and Junction Barrier Schottky (JBS) diodes, shown in Figure I.1.12.1 (a), which have turn on voltages of ~1 V as determined by the Schottky barrier height of the metal to the semiconductor material, rather than the semiconductor bandgap.

Similarly, vertically-oriented GaN transistors promise high-performance as power electronic devices if several key growth and fabrication challenges are overcome for the GaN material system. Interestingly, several different types of vertical GaN transistors have been demonstrated including Metal Oxide Semiconductor Field-Effect Transistors (MOSFETs) in the trench configuration (T-MOSFET, shown in Figure I.1.12.1 b), the double-well (D-MOSFET) configuration (shown in Figure I.1.12.1 c), and the Current Aperture Vertical Electron Transistor (CAVET) configuration [4], [5], [6]. Each of these device topologies has benefits and challenges associated with fabrication and performance, but the MOSFET designs show the most promise for power switching applications and are being investigated during this effort. With the MOSFET device designs,

challenges exist in making the semiconductor/insulator (or oxide) interface due to the lack of a good native oxide for GaN (Si and SiC both have native oxides). In addition, selective-area doping control, which is needed to form lateral pn junctions, cannot be easily achieved in GaN. Current state-of-the-art GaN devices use techniques such as ion implantation with special anneal processes (high-pressure and high-temperature) [7] or epitaxial regrowth [8] to realize selective-area doping control. Both techniques are relatively immature in GaN, and their behavior needs to be studied and techniques need to be developed to control these processes for eventual use in power systems for electric vehicles.
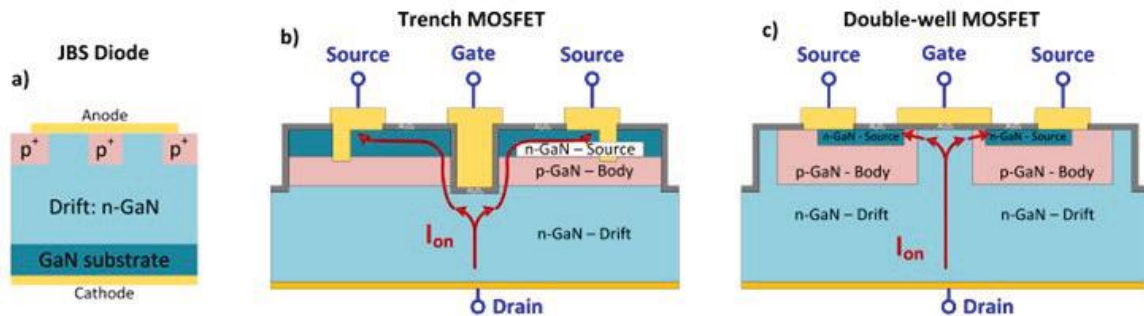
Figure I.1.12.1 (a) Schematic drawing of JBS diode, (b) schematic drawing of Trench MOSFET, and (c) schematic drawing of a Double-well MOSFET.

The first year of this effort focused on the development of simulation and modeling capabilities to help drive the designs of future GaN diodes and transistors. In parallel, epitaxial growth and fabrication processes were initiated toward realizing and demonstrating these devices. The second year of this effort has focused on fabrication and a first-generation demonstration of these devices. With demonstrators for both the JBS and trench MOSFET complete, the third year of the program focused on improving the baseline performance by improving passivation quality, tackling challenges related to etch-and-regrowth, and improving off-state characteristics for both the JBS and MOSFET devices. This year's effort is focused again on improving baseline performance. These efforts resulted in doubling the MOSFET blocking voltage, further improvements in etch-and-regrowth processes, and an optimization for the edge termination process. In the future, once devices of sufficient performance are achieved these will be further characterized in a performance and reliability test-bed (created under a different project within the consortium) to evaluate their suitability for electric drive applications, especially regarding their ability to meet the DOE consortium targets. Also, with increasing maturity, the devices can be shared with the consortium partners, who will evaluate them in electric drive systems and provide feedback to us for further improvement in their performance for power electronics.

Approach

The focus of this past year has been on improving baseline performance for both the JBS and MOSFET device. In many cases, challenges faced by both devices can more easily be addressed through cycles of learning on a simpler device. For instance, the pn diode platform can be used to benchmark passivation quality and to evaluate edge termination effectiveness, a simple Schottky Barrier diode can be used to understand the influence of etch damage and etch-damage recovery procedures on n-type GaN, and the MOSCAP can be used to evaluate gate dielectric performance on m-plane GaN. Experiments on these three devices were heavily leveraged in the past year to improve device performance for the JBS and MOSFET platforms. Examples of the three devices are shown in Figure I.1.12.2.
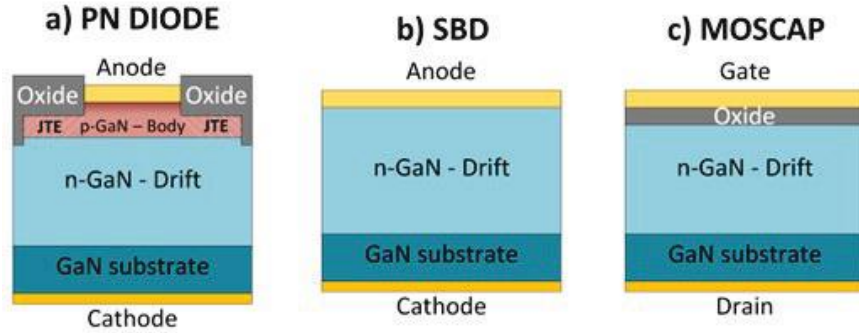
Figure I.1.12.2 Studies on these three devices, the pn diode, the Schottky Barrier diode, and the MOSCAP lends insight into improving performance for the JBS and MOSFET devices.

Results

Vertical GaN PN Diodes

Last year (FY21) we established a new passivation process for GaN pn diodes using a bilayer film consisting of 100 nm of atomic layer deposited (ALD) alumina (Al_2O_3) and 2 µm of silicon nitride (SiN) by plasma enhanced chemical vapor deposition (PECVD). Compared to early attempts to establish a passivation process, this new film resulted in low leakage diodes and the ALD-Al_2O_3 film appears robust to the addition of PECVD-SiN as a subsequent layer. This bilayer passivation has been robust across multiple device lots and has even been successfully deployed to other diode projects at Sandia. With a new and robust passivation process established, it is critical to consider how the passivation can affect the edge termination and breakdown performance of the device. When examining reverse IV curves from a select few devices, it is apparent at first glance that the addition of a passivation film causes a reduction in breakdown voltage as seen in Figure I.1.12.3a. Further statistical analysis demonstrates a similar trend, where three varieties of passivation all established a nominal reduction in breakdown voltage of 300V compared to the unpassivated sample (Figure I.1.12.3b). According to theory, a 200-300 V drop in breakdown voltage corresponds with a reduction of charge of 4×10^{12} cm^{-2} in the step-etched JTE (junction termination extension) which is a reasonable amount of charge to expect at the interface between the passivation and semiconductor and is consistent with some preliminary models and data from the GaN MOSFET and MOSCAP work.

Theory: 200-300V drop every 4e12 cm^{-2} charge
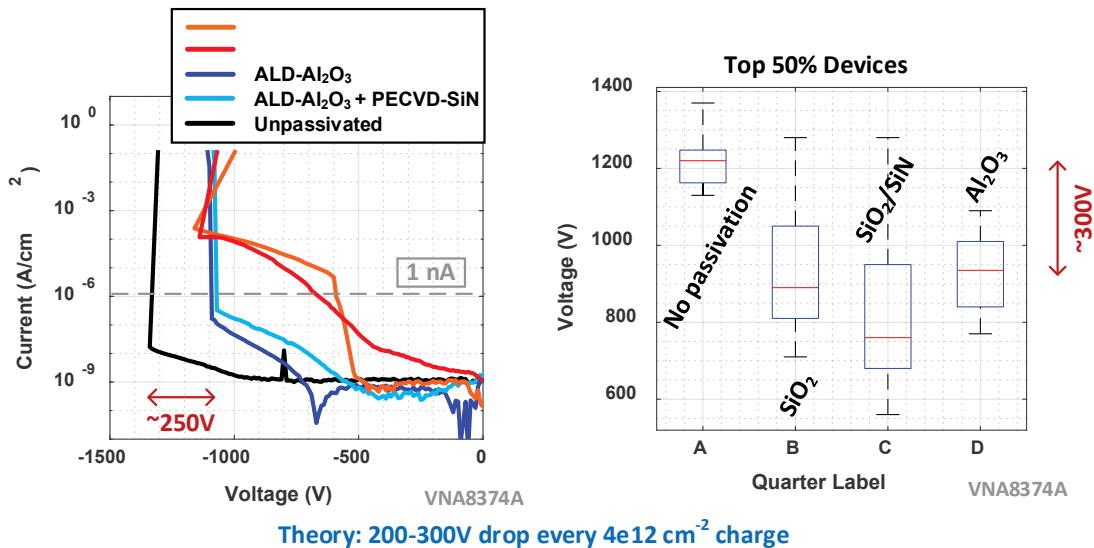
Figure I.1.12.3 Sandia's recent progress for GaN passivation and the impact passivation has on breakdown voltage: showing (a) the reverse IV performance for diodes with various passivations, and (b) the statistical breakdown for the top 50% of yielding devices. Note, all devices are tested under flourinert during high voltage testing.

The results from the passivation work highlights a need to optimize the design of the edge termination to account for non-idealities such as the charge from the passivation, epitaxy and doping variations, and other factors that impact the effectiveness of the edge termination. An edge termination is designed to minimize and distribute the peak electric field at the edge of the device where the junction has been terminated. In the case of a step-etched JTE, proper management of the surface electric field requires precise control of the charge in the JTE. This charge is set primarily by the product of doping and thickness for the JTE but many factors can alter the charge in the JTE including charge from the passivation layer as seen in Figure I.1.12.3. According to theoretical calculations the breakdown voltage can be quite sensitive to the dose in the JTE, and when considering the unknowns, it is near impossible to know the optimal etch depth to achieve the required dose. Therefore, we ran a multivariable JTE experiment to pinpoint the optimal JTE thickness target. These results presented are the first multipoint step-etched JTE study reported in GaN. The diode and single-zone step-etched JTE are presented in Figure I.1.12.4a. Three experiments were carried out on separate quarters of the same wafer, each with a different JTE etch depth target. The statistical data shown in Figure I.1.12.4b represents the results after screening for yield of the top 50% of devices with the highest breakdown. This data demonstrates a clear trend of increasing breakdown voltage with increasing JTE thickness. Compared to the simulation data (Figure I.1.12.4c), the shape of the data matches well to a theoretical prediction with some offset in terms of total charge (shift in the x-axis). This data serves to guide future designs and indicates a shift in total dose of approximately 1×10^{13} cm^{-2} to reach the optimal JTE target compared to an ideal simulation scenario. This shift is consistent with several non-ideal conditions such as: (1) plasma damage on the surface from ICP etching, (2) non-idealities in the doping profile near the junction, (3) surface charge, and others. The results of this study clearly highlight the need to account for these non-idealities when designing the edge termination, and the impact on breakdown voltage as a direct result of the quality of the termination strategy.
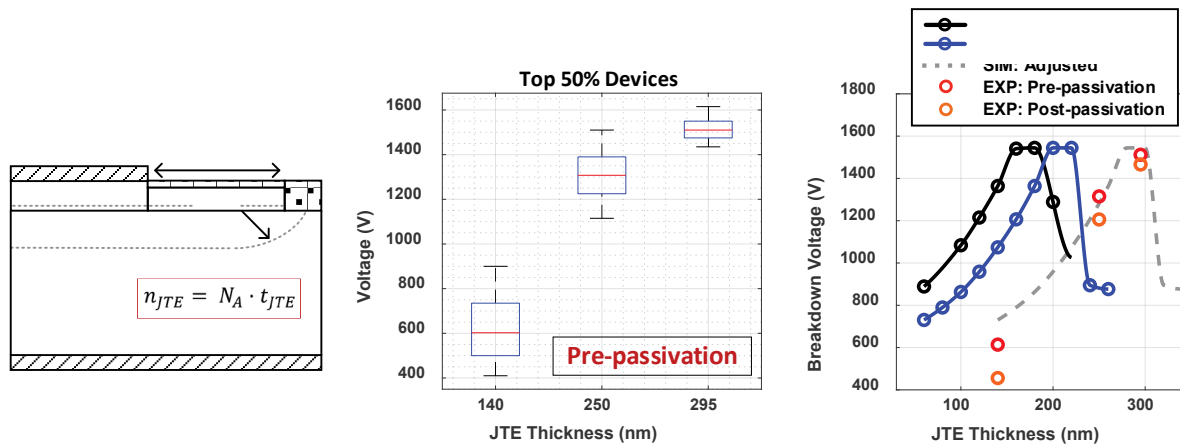
Figure I.1.12.4 A diagram of the single-zone step-etched JTE is shown in (a) and is the baseline device for the etch depth experiment. After screening for yield, a statistical representation of the top 50% highest breakdown devices is shown in (b). This data is then superimposed with simulation data in (c) demonstrating an excellent match to the theoretical data with an offset in the x-axis representing a difference in total charge.

Vertical GaN Schottky Barrier Diodes

The vertical GaN Junction Barrier Schottky (JBS) process that we are developing utilizes an etch-and-regrowth process to form the selective-area doped regions. Similarly, advanced trench-MOSFET and double-well MOSFETs require one or more selective-area doped regions. This selective-area doping process by etch-and-regrowth generally results in a junction with considerably more leakage than a continuously grown sample. To tackle this challenge, we have been developing a process that can reduce the etch damage that contributes to leakage. Last year we showed considerable success in removing residual ICP etch damage for Schottky Barrier diodes. This year we have worked towards finding a solution that results in etched-and-regrown PN diodes with low reverse leakage current. Although our understanding of the etch-and-regrowth process has improved,

we are still working to identify a process that can improve on the leakage characteristic compared to what was shown for our JBS devices in Ref. [9]. This effort is expected to continue into the next year.

Vertical GaN MOSFETs

In the previous years we demonstrated a 1st generation process for the vertical GaN trench MOSFET, then identified several key challenges [10] to address based on that result. Last year we demonstrated a 2nd generation gate dielectric process that improved on the leakage and breakdown strength for ALD-SiO$_2$ gate dielectrics. This year we incorporated all those revisions into the 2nd generation MOSFET process resulting in doubling the MOSFET blocking voltage. The first generation MOSFETs suffered from surface and channel leakage that dominated the off-state characteristics and resulted in a 250V breakdown with high leakage current. Revisions to the design and incorporation of new processes developed in the last year resulted in a 500V breakdown with nearly six orders of magnitude reduction in leakage current (Figure I.1.12.5 a). Failure at 500V is attributed to rupture of the gate dielectric at the bottom of the trench due to high electric-fields during the blocking state as depicted in Figure I.1.12.5 b. This is in agreement with TCAD modeling which predicts that for a device with an avalanche voltage of 1400V, an early failure will occur in the 450-550V range due to high fields in the gate dielectric at the trench bottom (Figure I.1.12.5 c). The agreement between TCAD and experimental results is a positive outcome which highlights that many early failure points for the MOSFET have been solved and the device behavior is as expected. From this point the blocking voltage can be further improved by applying conventional rules of scaling.
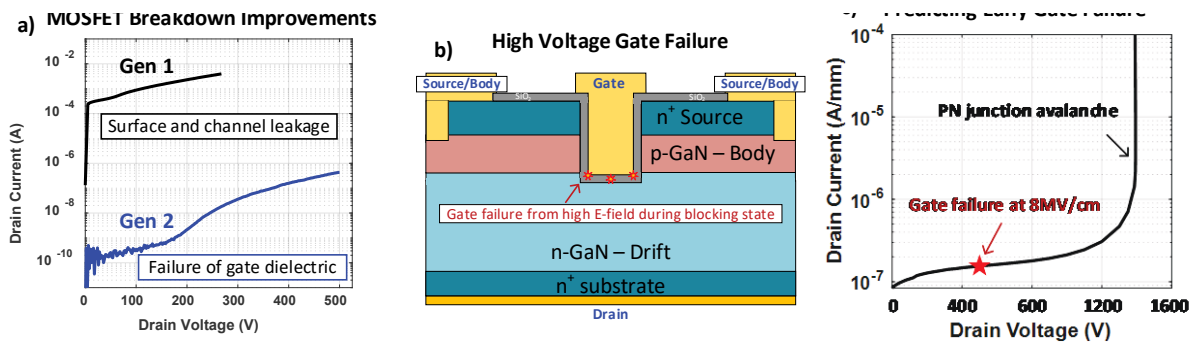
Figure I.1.12.5 Generational improvements for the MOSFET continue, showing (a) a doubling of breakdown voltage from generation 1 to generation 2 and several orders of magnitude reduction in leakage current. The failure point of the new generation of MOSFETs is due to failure of the gate dielectric at the bottom of the trench (b). TCAD simulations (c) show good agreement with failure mechanism and give insight into improving breakdown voltage further.

Several techniques can be employed to improve breakdown voltage for future MOSFET generations. First, the magnitude of electric-field strength in the gate dielectric below the trench is proportional to the depth that the trench protrudes below the body/drift pn junction. To ensure the trench etch fully penetrates through the junction we use a margin of 10% over-etch into the drift. For our 1st generation epitaxy design with a source and body total thickness of 1.7 μm the over-etch into the drift is on average 170 nm. If the combination of the source and body thickness is reduced, then the over-etch can be reduced and the field-strength in the gate dielectric will be less for the same applied blocking voltage. Additionally, reducing the thickness of the p-GaN body layer reduces the channel length, which is a significant portion of the total device resistance. For these reasons we have designed a 2nd generation epitaxy design (Figure I.1.12.6) with a total source and body thickness of 700 nm, half the body thickness of the 1st generation epi, and 40% of the total source and body thickness. This brings the trench over-etch depth target from 170 nm in gen-1 epi to 70 nm in gen-2 epi which will serve to reduce high electric-fields in the gate dielectric.
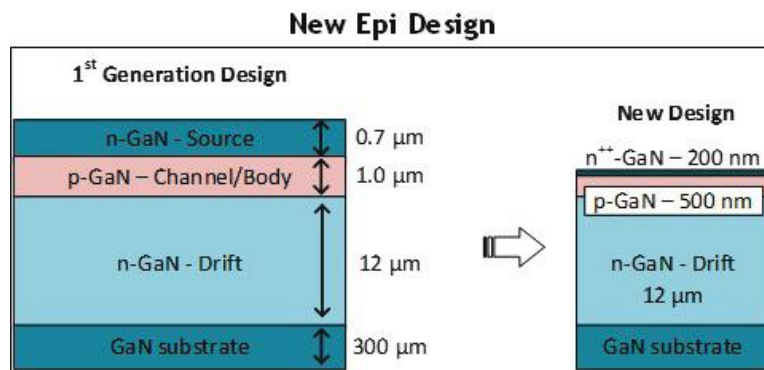
Figure I.1.12.6 MOSFET epitaxy has been redesigned to accommodate a thinner channel region, and a more highly doped and thinner n-GaN source region. This will not only improve on-state performance metrics but allows for better tolerance on the trench etch which will improve breakdown voltage when the etch depth past the channel is minimized.

Although the breakdown voltage can be improved by reducing trench etch depth below the junction, or by over designing the drift region by lowering doping and increasing thickness, the better method is to design a structure that will protect the gate dielectric from high electric-fields during blocking. Due to difficulty of selective-area doping in GaN, conventional techniques for forming a structure to protect the gate dielectric are not viable. We developed a new method to form a buried field shield by an etch-and-regrowth process. This field shield serves to protect the gate dielectric during the blocking state from high electric fields. The method devised is outlined in the provisional patent [11] and an example of one possible topology of the field shield is shown in Figure I.1.12.7. This structure relies heavily on our developed etch-and-regrowth processes, and as such it will be difficult to demonstrate until the etch-and-regrowth process matures. However, this method is in theory one of the best ways to protect the gate and to achieve the theoretical maximum performance from GaN.
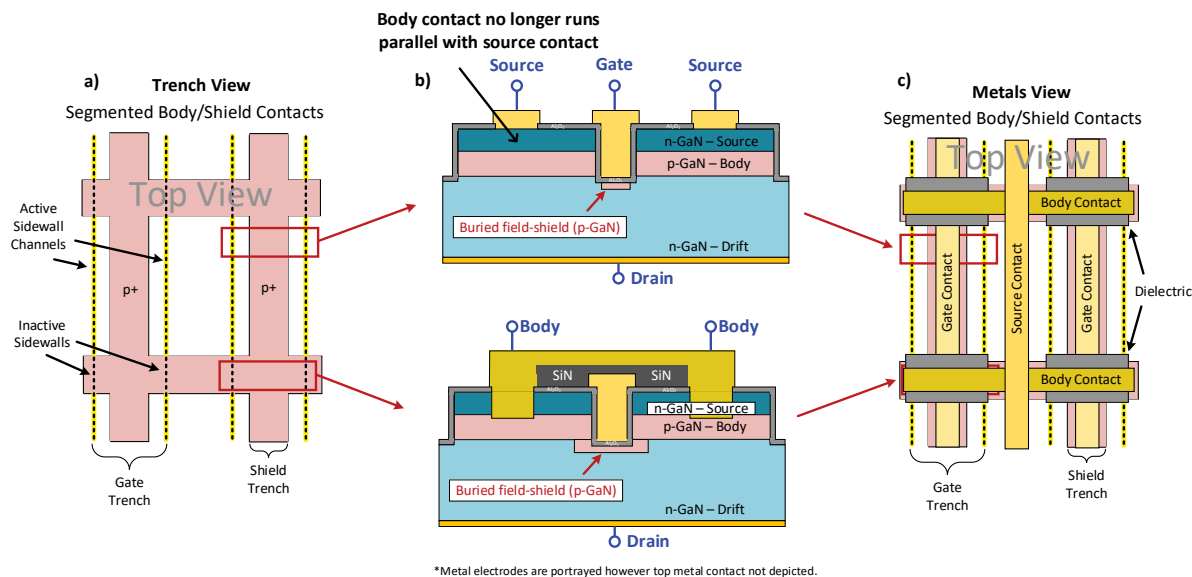
Figure I.1.12.7 Method for forming a buried field shield via etch and regrowth showing a) the trench view, b) the cross-section view, and c) the metals view of a segmented body contact approach. More details are available in Ref. [11].

Conclusions

GaN offers the promise of power electronic devices with performance that exceeds conventional Si and even SiC-based devices. This is due to its advantageous material properties, chiefly its higher breakdown electric field. Due to the increased maturity of GaN substrates, vertical GaN devices showing promising performance are being demonstrated and are being considered for insertion into power conversion applications. This project

has focused on the design, simulation, and fabrication processes needed to build vertical GaN diodes and transistors for use in electric drive traction systems. This year we developed a process for edge termination in vertical GaN power devices and our group is the first to report a multipoint fit from theory to experiment, which serves to mark a milestone of maturity for these devices. For the GaN MOSFET the second-generation device demonstrated double the blocking voltage (500 V) compared to the previous generation and a reduction of leakage current by six orders of magnitude. The groundwork has been set to increase blocking voltage further for next device generations, including a new method for protecting the gate dielectric by way of an etched-and-regrown buried field shield. With substantial improvements in device maturity, especially for GaN diodes, we anticipate an increased effort for device packaging and evaluation of packaged parts performance next year.

Key Publications

1. A. Binder and J.A. Cooper, "Buried Field Shield in GaN Trench MOSFETs via Etch and Regrowth," US Provisional Patent 63/208,119.

2. A. T. Binder *et al*., "Etched and Regrown Vertical GaN Junction Barrier Schottky Diodes," in *The 8th Workshop on Wide Bandgap Power Devices and Applications (WiPDA 2021),* 2021.

3. C. E. Glaser, A. T. Binder, L. Yates, A. A. Allerman, D. F. Feezell, and R. J. Kaplar, "Analysis of ALD Dielectric Leakage in Bulk GaN MOS Devices," in *The 8th Workshop on Wide Bandgap Power Devices and Applications (WiPDA 2021),* 2021.

4. L. Yates, A. Binder, J. Dickerson, G. Pickrell, and R. Kaplar, "Electro-thermal Simulation and Performance Comparison of 1.2 kV, 10 A Vertical GaN MOSFETs," Rio Grande Symposium on Advanced Materials, Albuquerque, NM (September 2019).

References

1. I. C. Kizilyalli, A. P. Edwards, O. Aktas, T. Prunty, and D. Bour, "Vertical power p-n diodes based on bulk GaN," IEEE Trans. Electron Devices, vol. 62, no. 2, pp. 414–422, Feb. 2015.

2. A. Armstrong et al., "High voltage and high current density vertical GaN power diodes," 2016.

3. H. Ohta, K. Hayashi, F. Horikiri, M. Yoshino, T. Nakamura, and T. Mishima, "5.0kV breakdown-voltage vertical GaN p-n junction diodes," Jpn. J. Appl. Phys., vol. 57, no. 4, pp. 4–09, 2018.

4. T. Oka, Y. Ueno, T. Ina, and K. Hasegawa, "Vertical GaN-based trench metal oxide semiconductor field-effect transistors on a free-standing GaN substrate with blocking voltage of 1.6 kV," Appl. Phys. Express, vol. 7, no. 2, p. 021002, Feb. 2014.

5. H. Otake, S. Egami, H. Ohta, Y. Nanishi, and H. Takasu, "GaN-based trench gate metal oxide semiconductor field effect transistors with over 100cm2/(Vs) channel mobility," Japanese J. Appl. Physics, Part 2 Lett., vol. 46, no. 25–28, p. L599, Jul. 2007.

6. S. Chowdhury, M. H. Wong, B. L. Swenson, and U. K. Mishra, "CAVET on bulk GaN substrates achieved with MBE-regrown AlGaN/GaN layers to suppress dispersion," IEEE Electron Device Lett., vol. 33, no. 1, pp. 41–43, Jan. 2012.

7. T. J. Anderson et al., "Activation of Mg implanted in GaN by multicycle rapid thermal annealing," Electron. Lett., vol. 50, no. 3, pp. 197–198, Jan. 2014.

8. G. W. Pickrell et al., "Regrown Vertical GaN p–n Diodes with Low Reverse Leakage Current," J. Electron. Mater. 2019 485, vol. 48, no. 5, pp. 3311–3316, Mar. 2019.

9. A. T. Binder et al., "Etched and Regrown Vertical GaN Junction Barrier Schottky Diodes," in 2021 IEEE 8th Workshop on Wide Bandgap Power Devices and Applications (WiPDA), 2021, pp. 288–292.

10. C. E. Glaser, A. T. Binder, L. Yates, A. A. Allerman, D. F. Feezell, and R. J. Kaplar, "Analysis of ALD Dielectric Leakage in Bulk GaN MOS Devices," in 2021 IEEE 8th Workshop on Wide Bandgap Power Devices and Applications (WiPDA), 2021, pp. 268–272.

11. A. Binder and J.A. Cooper, "Buried Field Shield in GaN Trench MOSFETs via Etch and Regrowth," US Provisional Patent 63/208,119.

Acknowledgements

I.1.13 Component Modeling, Co-Optimization, and Trade-Space Evaluation (Sandia National Laboratories)

Jason Neely, Principal Investigator
Sandia National Laboratories
P.O. Box 5800, MS 1152
Albuquerque, NM 87185
E-mail: jneely@sandia.gov

Susan Rogers, DOE Technology Development Manager
U.S. Department of Energy
E-mail: susan.rogers@ee.doe.gov

Start Date October 1, 2018	End Date: September 30, 2024	
Project Funding: $350,000	DOE share: $350,000	Non-DOE share: 0

Project Introduction

This project is intended to support the development of new traction drive systems that meet the targets of 100 kW/L for power electronics and 50 kW/L for electric machines with reliable operation to 300,000 miles. To meet these goals, new designs must be identified that make use of state-of-the-art and next-generation electronic materials and design methods. Designs must exploit synergies between components, for example converters designed for high-frequency switching using wide band gap (WBG) devices and ceramic capacitors. This project includes: (1) a survey of available technologies; (2) the development of design tools that consider the converter volume, reliability, and electrical performance; (3) exercising the design software to evaluate performance gaps and predict the impact of certain technologies and design approaches, i.e. GaN semiconductors, ceramic capacitors, ceramic thermal management components, and select topologies; and (4) building and testing hardware prototypes to validate models and concepts. Early instantiations of the design tools enable co-optimization of the power module and passive elements and provide some design guidance; later instantiations will enable the co-optimization of inverter and machine. Prototype testing began with evaluation of simpler conversion topologies (i.e. the half-bridge boost converter) and progressed with fabrication of prototype inverter drives.

Objectives

For FY22, objectives included

- Investigate the use of 3D printed ceramics to improve thermal management

- Continue to generate high-fidelity dimensional and electrical models for principal power electronic components within a novel inverter design

- Develop and implement a high-fidelity optimization ⇔ simulation platform that includes a model of vehicle operation

- Co-Optimize inverter design with machine model for power density, reliability/lifetime, and efficiency.

Approach

The R&D approach employed by the team includes four strategies for generating design guidance and optimal designs, listed in order of increased fidelity and resources:

5. ***Empirical and First-Principles Analysis***: This uses first-principles knowledge, such as physical models, as well as comparative designs to inform the design.

6. ***High-Fidelity Modeling and Analysis***: This uses higher-order models that consider the component equivalent circuits, dimensions, reliability calculations, etc.

7. ***Global Co-Optimization***: With the definition of one or more performance metrics, components are simulated together and their performance is measured and compared.

8. ***Hardware Iteration***: Using optimal designs identified in software, hardware exemplars are built and evaluated; 3 and 4 are iterated to create the best results.

In FY22, the project included elements of all four strategies, applied with different weight to the four objectives. Empirical analysis and modeling (strategies 1 and 2) were applied to evaluate the potential performance improvement of using 3D printed ceramic surround cooling components (i.e. for heat spreading) to cool bare-die or passivated die power devices. The team also worked to create a new simulation + optimization platform with greater capability and flexibility than the highly customized Matlab-based code developed through FY21 (strategies 2 and 3). This has allowed the team to start conducting optimizations that consider the vehicle operation and vehicle lifetime in miles (strategy 3). Hardware experimentation was limited in FY22, but this is expected in FY23 to validate designs identified with new tools.

Based on previous optimization results attained for an inverter drive, the principal contributors to inverter volume remained to be the thermal management components (i.e. the cold plate) and the AC EMI filter that connected the inverter drive to the motor. To address the filter size, the feasibility of using nano-composite materials to realize a distributed EMI filter was investigated. Unfortunately, the achievable permeabilities of the nano-composite was not sufficient to make this practicable. To address the thermal management component size, the team investigated the use of 3D printed ceramic components that could be used to realize a "surround cooling" capability. Fortunately, this approach was shown in COMSOL Multi-physics simulations to have a lot promise, and in FY22, the team began preparing hardware experiments to validate simulation results.

For the optimization work, the team had previously used the Genetic Optimization System Engineering Tool (GOSET) developed by Purdue University [1] in concert with a highly customized simulation of the power electronics. In FY22, the team developed a new platform with optimization and parameter evaluation workflow process between power electronics simulation platform, PLECS [2] and Python [3]. A detailed multi-domain model (electrical, thermal, and mechanical) of an electric drivetrain with electro-mechanical subsystems, was developed in PLECS. Previously, to evaluate system reliability, component mean time between failure (MTBF) quantities were also computed for SiC MOSFETS and capacitors using MIL-HDBK-217F calculations [4]. On the new platform, the optimization (implemented in Python) includes a metaheuristic approach to optimizing the system reliability and efficiency based on the semiconductor material properties, thermal management, and mechanical dynamics of the vehicle via multi-objective genetic algorithm [5]. The optimization also considers realistic drive profiles [6].

Results

Investigation of 3D printed ceramics to improve thermal management

To improve thermal management, either to reduce the volume of thermal management components, or to reduce junction temperatures for a given volume, a new approach was investigated for the removing heat from the semiconductor devices. Specifically, 3D printed Al_2O_3 ceramic components can be used to surround and even encase electronic components with significant thermal loads. With this approach, a cold plate would still be used, but the ceramic components would route heat away from the top of devices down to the cold plate. This accomplishes double-sided cooling but avoids the complexity of contemporary assemblies. These components can have high resolution features ~100 μm and thus tightly fit around components and potentially include additional features, such as fins.

In FY21, samples were acquired from Lithoz and tested using flash diffusivity measurements, and COMSOL thermal models were developed to investigate and compare three convectively cooled options, Cases 1,2,3. In FY22, the models were expanded using ANSYS Fluent to consider the addition of fluid channels with ethylene-glycol as the coolant flowing through a 1 mm high duct at 6 mm^3/s, 60 mm^3/sec, and 600 mm^3/sec. Figure I.1.13.1 illustrates these three cases, Case 4a, 4b, and 4c. These three cases are compared with the three convectively cooled designs considered in FY21; see Figure I.1.13.2. Therein, it is seen that the Case 4a option is 56ºC cooler (44ºC versus 100ºC) than the best convectively cooled option, Case 3. Case 4b is 80ºC cooler, and Case 4c is 85ºC cooler. Case 4b flow rate would be achievable with a commercial pump.
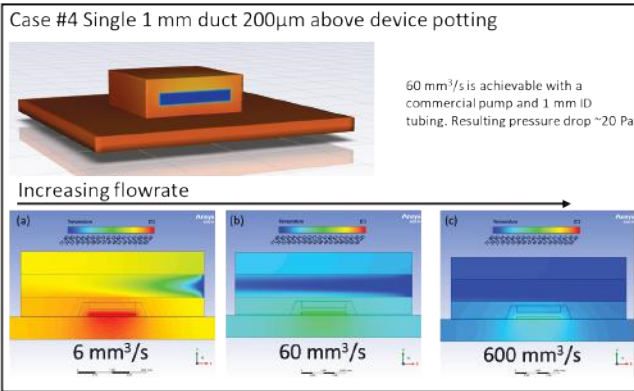
Figure I.1.13.1 Illustrates three design cases that consider ceramic surround cooling components with liquid cooling channels
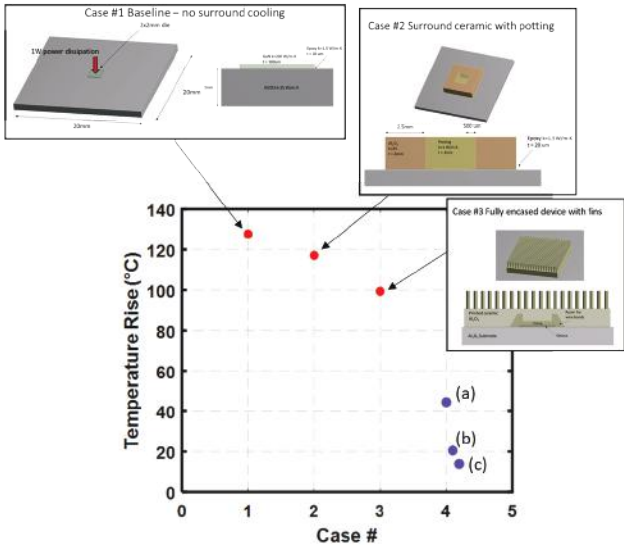
Figure I.1.13.2 Illustrates six design cases and the simulated temperature rise of the device junction for each

Test boards were built to enable precise heating of passivated die power devices with enough board real estate to try different ceramic surround cooling designs. DC testing will be used to determine a steady state temperature as a baseline to compare 3D printed ceramic heatsinks. Baseline temperatures were determined using a high-resolution thermal camera. See Figure I.1.13.3
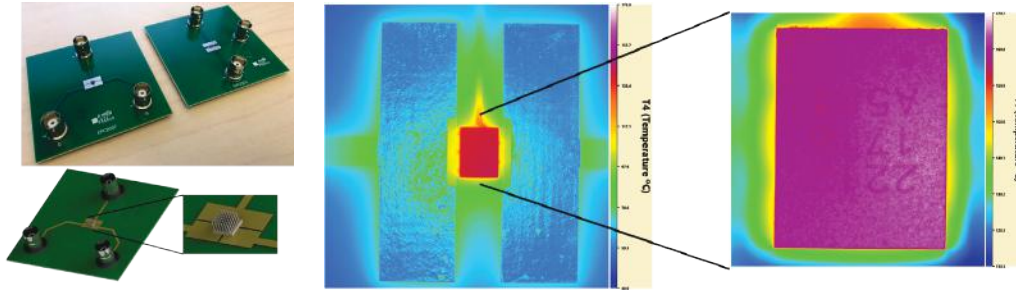
Figure I.1.13.3 (Left) Test boards built to evaluate thermal performance (right) high-resolution thermal imaging is used to establish baseline thermal performance

Optimization of Inverter Drive Volumetric Power Density, Efficiency, and Reliability

In FY22, the team developed a new approach to optimization that built upon the previous work [7], [8] but uses a new performance evaluation process developed between PLECS [2], a simulation platform for power electronic systems and the optimization computation of genetic algorithm based on NSGA-II in Python 3 to achieve a reliable repetition of varied operating modes of the inverter to seek optimized parameters and non-dominant solutions.

The EV powertrain system, shown in Figure I.1.13.4 is made up of several different moving parts, including the battery, power electronic system, electric motor, transmission drive shafts, and vehicle wheels. In this EV model, a three-phase wye-connected permanent magnet synchronous machine (PMSM) is used. The motor parameters, including stator inductance, stator resistance, flux induced by magnets, number of pole pairs, inertia, friction coefficient, etc have been modeled based on approximated physical parameters of the Nissan Leaf electric vehicle motor [9]. The power electronic and control system, also represented in Figure I.1.13.4, illustrates an inverter model with a motor controller. The battery is connected to a two-level voltage source inverter through a DC-link capacitor. The inverter model allows a selection of power modules of different material properties, such as Si-IGBT or SiC with user-specified or manufacturer provided loss characteristics. The simulation was then done over a short 60 second period with acceleration, deceleration, and cruising periods.
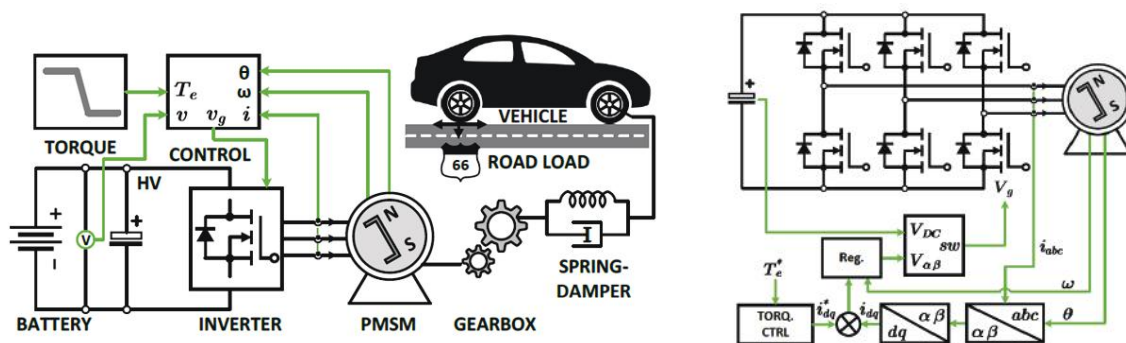
Figure I.1.13.4 (Left) Electric Vehicle Powertrain System Model and (Right) EV Drivetrain Power Electronics and Control System Model

The Non-dominated Sorting Genetic Algorithm (NSGA) was used to perform the optimization studies and parameter analysis. In particular, the NSGA-II [10] was used to implement the sorting of non-dominated and feasible solution space while maintaining a diverse spread of solutions with better convergence. To make the optimizations more relevant to normal driving cycle of vehicles, the EPA provided driving profile US06/Supplemental FTP [6] was selected to represent a mix of highway and city driving over 600 seconds. The derivative of speed was used to identify regions of acceleration, deceleration, and cruising to enable

scaling of the 60 second simulation results. The optimization ⇔ simulation platform and an illustration of the US06 driving profile are shown in Figure I.1.13.5.
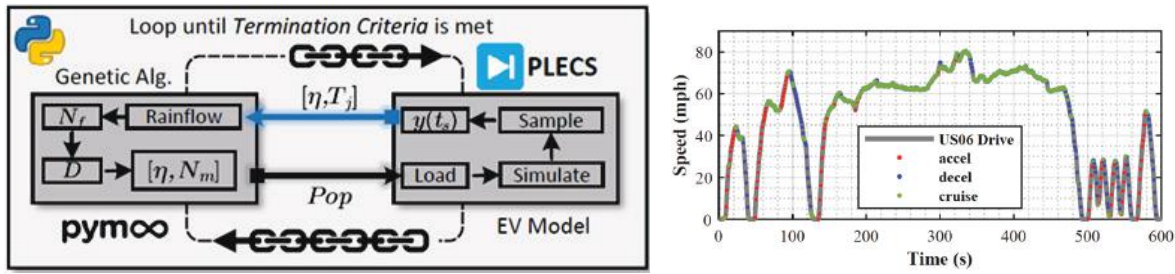
Figure I.1.13.5 (Left) PLECS-Python multi-objective optimization process to integrate the EV model developed in PLECS and NSGA computation analysis through pymoo (Right) US06 driving profile with periods of acceleration, deceleration, and cruising denoted as accel, decel, and cruise, respectively [6].

Initial Pareto-optimization results considered the trade-off between efficiency and vehicle lifetime in miles. Figure I.1.13.6 provide some initial results showing the GA iteration as well as comparative results between converters built with SiC FETs from Wolfspeed and Si IGBTs. A complete description of this work is provided in [11].
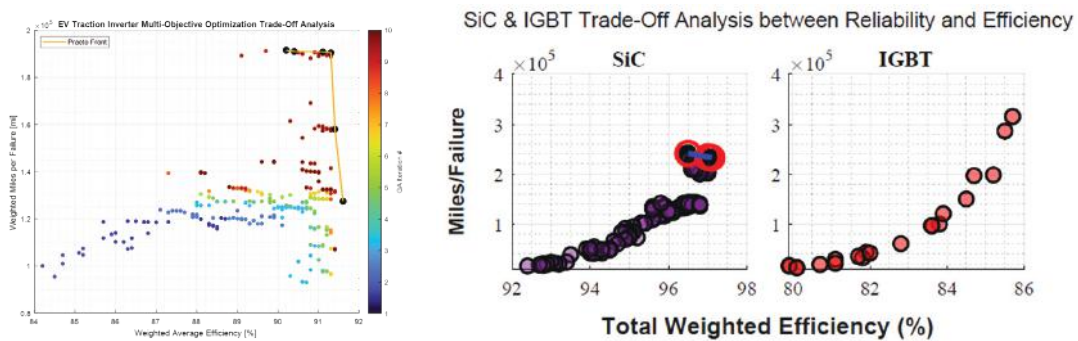
Figure I.1.13.6 (Left) GA iteration and Pareto-Optimal front showing trade-off between weighted efficiency and lifetime (Right) Comparison of SiC and IGBT-based inverter performance between reliability in weighted miles per failure and weighted average efficiency for the given driving cycle and physical vehicle parameters [11].

Conclusions

This project is focused on developing improved designs for future traction drive systems through the combined use of WBG devices, ceramic capacitors, high-frequency switching, advanced component development (i.e. for thermal management) and multi-phase designs that enable considerable improvements in power density. Designs are developed with the help of tools developed to perform multi-objective optimizations on electric drive designs. Unlike previous work, these include optimizations that consider component reliability. In FY22, the project team developed a new optimization⇔simulation platform using PLECS for simulation and the NSGA-II genetic optimization tool using Python. The simulations were expanded to be more comprehensive representations of the vehicle, including drive profiles, but still capable of predicting both thermal and electrical stresses at the power electronic assembly level. Preliminary results considering the trade-off between efficiency and reliability\lifetime (in miles) look promising. The team also continued to investigate the use of 3D printed Al_2O_3 ceramic components to aid in thermal management with a focus on ceramic components with liquid cooling channels. Simulation results suggest that even modest fluid flows in channels adjacent to bare-die power devices could reduce temperatures by > 80ºC, when compared to the convective cooling approach.

Key Publications / Presentations

1. J. Neely, G. Pickrell, J. Flicker, L. Rashkin, R. Kaplar; "The Case for Vertical Gallium Nitride Devices in Electric Vehicle Drives," *2020 IEEE Applied Power Electronics Conference* (APEC2020), Industry Session: Vehicle Electrification II.

2. L. Gill, J. C. Neely, L. J. Rashkin, J. D. Flicker and R. J. Kaplar; "Co-Optimization of Boost Converter Reliability and Volumetric Power Density Using Genetic Algorithm," *2020 IEEE Energy Conversion Congress and Exposition (ECCE)*, Detroit, MI, USA, 2020, pp. 5302-5309, doi: 10.1109/ECCE44975.2020.9235716.

3. L. Rashkin, J. Neely, L. Gill, J. Flicker and R. Darbali-Zamora; "Optimal Power Module Design for High Power Density Traction Drive System," *2020 IEEE Transportation Electrification Conference & Expo (ITEC)*, Chicago, IL, USA, 2020, pp. 134-138, doi: 10.1109/ITEC48692.2020.9161703.

4. L. Gill, L. Rashkin, L. Yates, J. Neely, R. Kaplar; "Multi-Objective Parametric Analysis of EV Traction Inverter between Reliability and Efficiency," 2023 IEEE Applied Power Electronics Conference (APEC2023), Orlando, FL, March 19-23, 2023

References

1. S. D. Sudhoff, GOSET: Genetic Optimization System Engineering Tool: For Use with MATLAB®, version 2.6, January 1, 2014.

2. J. Allmeling and W. Hammer, "PLECS-piece-wise linear electrical circuit simulation for Simulink," in Proceedings of the IEEE 1999 International Conference on Power Electronics and Drive Systems. PEDS'99 (Cat. No.99TH8475), vol. 1, 1999, pp. 355–360 vol.1.

3. J. Blank and K. Deb, "pymoo: Multi-objective optimization in python," IEEE Access, vol. 8, pp. 89 497–89 509, 2020.

4. *Military Handbook: Reliability prediction of electronic equipment*, 1991. Available: https://snebulos.mit.edu/projects/reference/MIL-STD/MIL-HDBK-217F-Notice2.pdf

5. F. Blaabjerg, H. Wang, I. Vernica, B. Liu, and P. Davari, "Reliability of Power Electronic Systems for EV/HEV Applications," Proceedings of the IEEE, vol. 109, no. 6, pp. 1060–1076, 2021.

6. US Environmental Protection Agency (EPA). Dynamometer Drive Schedules. [Online]. Available: https://www.epa.gov/vehicle-and-fuelemissions-testing/dynamometer-drive-schedules

7. L. Gill, J. C. Neely, L. J. Rashkin, J. D. Flicker and R. J. Kaplar, "Co-Optimization of Boost Converter Reliability and Volumetric Power Density Using Genetic Algorithm," *2020 IEEE Energy Conversion Congress and Exposition (ECCE)*, Detroit, MI, USA, 2020, pp. 5302-5309, doi: 10.1109/ECCE44975.2020.9235716.

8. L. Rashkin, J. Neely, L. Gill, J. Flicker and R. Darbali-Zamora, "Optimal Power Module Design for High Power Density Traction Drive System," *2020 IEEE Transportation Electrification Conference & Expo (ITEC)*, Chicago, IL, USA, 2020, pp. 134-138, doi: 10.1109/ITEC48692.2020.9161703.

9. S. Oki, S. Ishikawa, and T. Ikemi, "Development of High-Power and High-Efficiency Motor for a Newly Developed Electric Vehicle," SAE International Journal of Alternative Powertrains, vol. 1, no. 1, pp. 104–111, 2012.

10. K. Deb, A. Pratap, S. Agarwal, and T. Meyarivan, "A fast and elitist multiobjective genetic algorithm: NSGA-II," IEEE Transactions on Evolutionary Computation, vol. 6, no. 2, pp. 182–197, 2002.

11. L. Gill, L. Rashkin, L. Yates, J. Neely, R. Kaplar; "Multi-Objective Parametric Analysis of EV Traction Inverter between Reliability and Efficiency," 2023 IEEE Applied Power Electronics Conference (APEC2023), Orlando, FL, March 19-23, 2023

I.1.14 Bottom-Up Soft Magnetic Composites (Sandia National Laboratories)

Todd Monson, Principal Investigator

Sandia National Laboratories
P.O. Box 5800, MS 1415
Albuquerque, NM 87185
E-mail: tmonson@sandia.gov

Susan Rogers, DOE Technology Development Manager

U.S. Department of Energy
E-mail: susan.rogers@ee.doe.gov

Start Date: October 1, 2018	End Date: September 30, 2024	
Project Funding: $125,000	DOE share: $125,000	Non-DOE share: $0

Project Introduction

In order to meet 2025 goals for enhanced peak power (100 kW), specific power (50 kW/L), and reduced cost (3.3 $/kW) in a motor that can operate at $\geq$ 20,000 rpm, improved soft magnetic materials must be developed. Better performing soft magnetic materials will also enable rare earth free electric motors. In fact, replacement of permanent magnets with soft magnetic materials was highlighted in the Electrical and Electronics Technical Team (EETT) Roadmap [1] as a R&D pathway for meeting 2025 targets. Eddy current losses in conventional soft magnetic materials, such as silicon steel, begin to significantly impact motor efficiency as rotational speed increases. Soft magnetic composites (SMCs), which combine magnetic particles with an insulating matrix to boost electrical resistivity (ρ) and decrease eddy current losses, even at higher operating frequencies (or rotational speeds), are an attractive solution. Today, SMCs are being fabricated with values of ρ ranging between 10^{-3} to 10^{-1} μohm·m [2], which is significantly higher than 3% silicon steel (~0.05 μohm·m) [3]. The isotropic nature of SMCs is ideally suited for motors with 3D flux paths, such as axial flux motors. Additionally, the manufacturing cost of SMCs is low and they are highly amenable to advanced manufacturing and net-shaping into complex geometries, which further reduces manufacturing costs. There is still significant room for advancement in SMCs, and therefore additional improvements in electrical machine performance. For example, despite the inclusion of a non-magnetic insulating material, the electrical resistivities of SMCs are still far below that of soft ferrites ($10 - 10^8$ μohm·m).

We are developing SMCs from the bottom up, with a final objective of creating composites with high magnetic material loading (and therefore high magnetization) while increasing the value of ρ several orders of magnitude over current state-of-the-art SMCs. To accomplish our goals, we are starting with particles of γ'-Fe$_4$N, which have a saturation magnetic polarization (J_s) of 1.89 T, or slightly greater than Si steel [4] and a ρ of ~ 2 μohm·m [5]. In our bottom-up approach we begin by coating the magnetic particles with a diamine, which chemically reacts directly with epoxide terminated monomers to form a cross-linked epoxy composite. This "matrix-free" approach to composite formation will not suffer from the same nanoparticle aggregation and phase separation effects commonly observed in most nanocomposites [6]. Furthermore, it should ensure better separation between magnetic particles and significantly reduce or eliminate inter-particle eddy currents. A precedent already exists for the use of epoxies in electrical machine construction [7], [8]. Additionally, it is possible to design epoxy systems with glass transition temperatures (T_g) well in excess of the target maximum motor operating temperature of 150 °C [9], as was documented in 2020's annual progress report. Furthermore, composites have been successfully demonstrated in high-speed motors [10] and even flywheels rotating at speeds up to 60,000 rpm [11].

Objectives

The project objective is to develop high-magnetization, low-loss iron-nitride-based soft magnetic composites for electrical machines. These new SMCs will enable low eddy current losses and therefore highly efficient

motor operation at rotational speeds up to 20,000 rpm. Additionally, iron nitride and epoxy composites will be capable of operating at temperatures of 150 °C or greater over a lifetime of 300,000 miles or 15 years.

Approach

A high-level overview of our approach is:

1. Convert commercially available mixed-phase iron nitride powder to nearly phase-pure γ'-Fe_4N

2. Coat iron nitride particles with diamine molecules (part A of epoxy chemistry)

3. Combine surface functionalized particles with epoxide terminated monomers (part B of epoxy chemistry)

4. Fabricate SMC parts by adding mixture from #3 into a hot-pressing die

5. Evaluate and test fabricated SMC parts

6. Optimize SMC magnetic volume loading, magnetic properties, and physical properties.

Results

1. Mechanical Characterization of iron nitride/epoxy SMCs

To ensure our magnetic composites are well designed for electric motor operation, it is important to characterize, and in some cases tune, their mechanical strength. Additionally, understanding the mechanical properties of our composites will be important for the consortium members attempting to integrate our bottom-up SMCs into their motor designs. Sandia once again partnered with EDTC consortium member NREL to complete mechanical measurements of our epoxy-based composites.

A significant amount of this fiscal year's effort was devoted to fabrication of dog bone structures for mechanical evaluation at NREL. ASTM standard D638 was a guide for choosing the size and shape of our dog bone test structures. Three test structures each of the following compositions were fabricated: neat epoxy, 30 vol.% Fe_4N, 40 vol.% Fe_4N and 65 vol.% Fe_4N. The first step in the fabrication process was to create a CAD drawing of an anti-mold for the dog bone structure and then 3D print that anti-mold. Next, the anti-mold is used to fabricate a silicone mold for the dog bone structure. An image of a silicone mold used for dog bone fabrication is displayed in Figure I.1.14.1. Once the silicone mold was completed, an appropriate amount of iron nitride powder was SPEX milled with our diamine, 4-aminophenyl sulfone (4-AS). After the surface of the iron nitride particles were coated with the 4-AS, they could be mixed with the second part of our epoxy, a triepoxide molecule: N,N-diglycidyl-4-glycidyloxyaniline (NND). This uncured mixture is then transferred into the silicone mold where it undergoes an initial cure at 180 °C for 4 hrs. After this initial curing step the test piece is transferred to a jig to prevent bowing during the final high temperature cure (see Figure I.1.14.2). The final high temperature cure occurs at 255 °C for 12 hrs. in tube furnace under flowing Ar with 3% H_2. X-ray diffraction (XRD) confirmed no oxidation of the Fe_4N occurred during this final high temperature curing step. After cooling, the dog bone structures are polished to remove most remaining surface defects and to minimize or eliminate camber. An example of a final polished dog bone structure prior to mechanical measurement can be seen in Figure I.1.14.3.

Figure I.1.14.1 Silicone mold for the fabrication of dog bone test structures.

Figure I.1.14.2 Jig to prevent bowing of dog bone structures during final cure with a completed test structure resting on top.

Figure I.1.14.3 Dog bone structure ready for measurement at NREL.

The dog bone structures next underwent tensile testing at NREL. See Figure I.1.14.4 for a picture of a Fe_4N/epoxy composite undergoing tensile testing. The values obtained from tensile testing (elongation at yield, tensile strength, and tensile modulus) for our neat 4-AS/NND are comparable to other epoxies. The stiffness (tensile modulus) of the composite samples increases proportionally with the volume loading of iron nitride powder. Additionally, as iron nitride vol.% increased from 0 to 65 vol.% the tensile strength of the composite test structures decreased by approximately 18 MPa. For a full summary of the tensile testing results please see Table I.1.14.1.
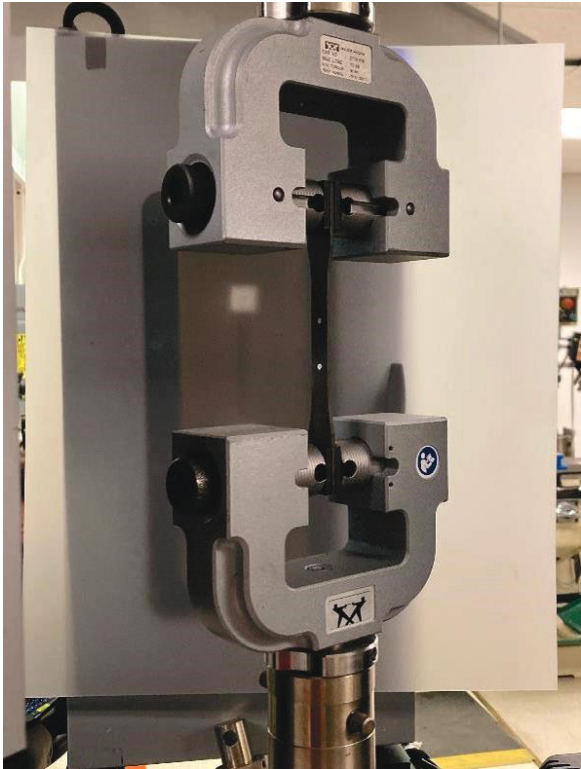
Figure I.1.14.4 Picture of a Fe_4N/epoxy composite undergoing tensile testing at NREL.

Table I.1.14.1 Summary of Fe_4N/epoxy composite tensile testing results.

Fe_4N vol.% loading	Elongation at yield (%)	Tensile strength (MPa)	Tensile modulus (GPa)
0	9.7	51.7	3.8
30	6.2	35.7	10.3
40	5.4	32.7	15.4
65	3.5	33.0	33.0

2. Iron nitride/epoxy composite fabrication via hot pressing

Once again this fiscal year, additional iron nitride based SMCs were constructed using our in house hot pressing setup. The processing parameters were optimized such that Fe_4N loadings $\geq$ 75 vol.% could be achieved. A SMC with 75.3 vol.% Fe_4N was achieved using a pressure of 500 MPa and a temperature of 180 °C. The sample was pressed for 18 hours (overnight) and allowed to cool for 2 hours before removing from the die. The sample can be seen in Figure I.1.14.5.

Figure I.1.14.5 75.3 vol.% Fe4N in epoxy SMC. The shorter cylinder was cut using a diamond saw for VSM analysis.

The sample's magnetic properties were characterized using a vibrating sample magnetometer (VSM) from Quantum Design. The magnetic hysteresis curve is plotted in Figure I.1.14.6. This sample achieved a saturation magnetic polarization (J_s) of 1.19 T. This is more than double that of soft ferrites ($J_s \sim 0.5$ T), and nearly two-thirds the value of Si steel ($J_s = 1.87$ T). This puts iron nitride/epoxy SMCs in good standing amongst other state-of-the-art insulating soft magnetic materials. Further increases in J_s can be expected as the volume loading of iron nitride is increased further through additional process and material improvements.
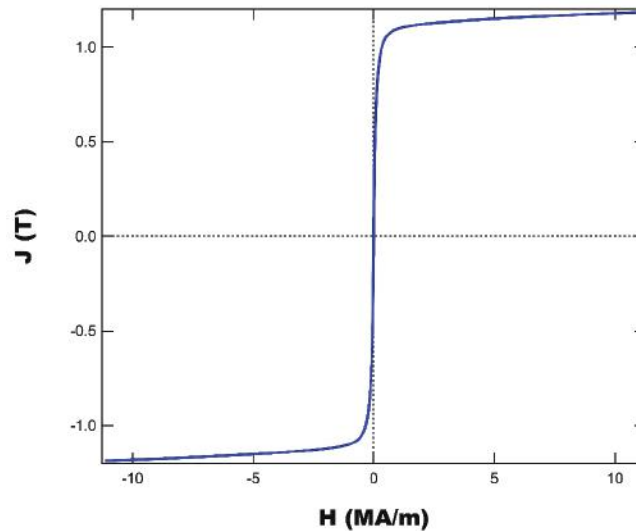
Figure I.1.14.6 Magnetic hysteresis curve (plotted as J vs. H) for an iron nitride based SMC containing 75.3 vol.% Fe4N.

3. Fabrication of Larger SMCs

As our capability to produce Fe4N/epoxy samples improves we are progressing to the fabrication of larger samples. This is a key step towards producing inductor cores for motor drives and soft magnetic parts for electric motors. We have acquired die that enable us to hot press toroids with an outer diameter (O.D.) of 35 mm and squares of 2 cm x 2 cm. During the upcoming fiscal year we will transition to fabricating specialized stator soft magnetic components. A photograph of newly acquired die for fabricating larger toroids and cubes is displayed in Figure I.1.14.7.

Figure I.1.14.7 New die for pressing larger toroids and cubes.

Conclusions

During FY22, important progress was made in the fabrication and characterization of iron nitride (γ'-Fe$_4$N) based soft magnetic composites for electric motors. Please keep in mind that these materials also show substantial promise as inductor cores for motor drives. A lab based hot pressing setup was used to produce Fe$_4$N based SMCs with an iron nitride vol.% loading > 75 %. The J$_s$ of these samples was nearly 1.2 T, which is more than double that of a leading state-of-the-art insulating soft magnetic material (ferrite). Additionally, further increases in J$_s$ for Fe$_4$N based SMCs are still possible. Samples were fabricated for mechanical testing by consortium member NREL. The mechanical strength of our neat custom epoxy formulation is equivalent to other commercially available epoxies. Although the tensile strength of the composite test structures decreased by approximately 18 MPa as iron nitride vol.% increased from 0 to 65 vol.% this will have no impact on the use of iron nitride based SMCs in stator designs. In order to adopt Fe$_4$N based SMCs in rotor construction it may be necessary to utilize carbon fiber sleeves for added mechanical strength. However, there is considerable precedence already for the use of carbon fiber sleeves in electric motor construction [12]. Future work will focus on continuing to increase magnetic material volume loading and enhancing magnetic performance in both electric motor and motor drive applications. We will also increase the size of our fabricated SMC parts and begin constructing soft magnetic stator parts for prototype motor designs in collaboration with EDTC university and lab partners. Finally, during FY 2023 we will continue to collaborate with EDTC consortium member NREL and complete additional measurements on the thermal conductivity of Fe$_4$N/epoxy composites at elevated temperatures.

Key Publications

1. A.B. Kustas, D.F. Susan, T.C. Monson, "Emerging Opportunities in Manufacturing Bulk Soft-Magnetic Alloys for Energy Applications: A Review," *Journal of Materials*, **74**, 1306-1328 (2022). DOI: 10.1007/s11837-021-05019-9.

2. T.C. Monson, B. Zheng, R. Delaney, C. Pearce, Y. Zhou, S. Atcitty, E. Lavernia, "Synthesis and Behavior of Bulk Iron Nitride Soft Magnets via High Pressure Spark Plasma Sintering," *Journal of Materials Research*, **37**, 380-389 (2022). DOI: 10.1557/s43578-021-00379-z.

References

1. U.S. Drive, "Electrical and Electronics Technical Team Roadmap," Partnership Plan, Roadmaps, and Other Documents 2017.

2. H. Shokrollahi and K. Janghorban, "Soft magnetic composite materials (SMCs)," Journal of Materials Processing Technology, vol. 189, no. 1-3, pp. 1-12, 2007, doi: 10.1016/j.jmatprotec.2007.02.034.

3. J. S. Corporation. Super CoreTM Electrical steel sheets for high-frequency application. (2017). JFE Steel Corporation. [Online]. Available: http://www.jfe-steel.co.jp/en/products/electrical/catalog/f1e-002.pdf

4. J. M. D. Coey, Magnetism and Magnetic Materials. New York: Cambridge University Press, 2010.

5. T. C. Monson et al., "Soft Magnetic Multilayered FeSiCrB–Fe4N Metallic Glass Composites Fabricated by Spark Plasma Sintering," IEEE Magnetics Letters, vol. 10, pp. 1-5, 2019, doi: 10.1109/LMAG.2019.2906832.

6. M. Qu et al., "Magneto-photo-acoustic imaging," Biomed. Opt. Express, vol. 2, no. 2, pp. 385-396, 2011/02/01 2011, doi: 10.1364/BOE.2.000385.

7. M. Magazine. https://magneticsmag.com/new-structural-adhesive-from-delo-for-magnet-bonding-has-high-temperature-stability/ (accessed).

8. Crosslinktech. http://www.crosslinktech.com/products-by-application/featured-electric-motor-products.html (accessed).

9. M. Bond. https://www.masterbond.com/techtips/how-optimizing-glass-transition-temperature-tg (accessed).

10. A. Schoppa and P. Delarbre, "Soft Magnetic Powder Composites and Potential Applications in Modern Electric Machines and Devices," IEEE Transactions on Magnetics, vol. 50, no. 4, pp. 1-4, 2014, doi: 10.1109/TMAG.2013.2290135.

11. P. Mason, K. Atallah, and D. Howe, Hard and soft magnetic composites in high speed flywheels. 1999.

12. V. C. d. Nascimento and S. D. Sudhoff, "Non-Axisymmetric Structural Analysis of High Speed Rotor Orthotropic Retention Sleeve," in 2019 IEEE International Electric Machines & Drives Conference (IEMDC), 12-15 May 2019 2019, pp. 797-804, doi: 10.1109/IEMDC.2019.8785324.

Acknowledgements

I.1.15 Device- and System-Level Thermal Packaging for Electric-Drive Technologies (Georgia Institute of Technology)

Yogendra Joshi, Principal Investigator
Georgia Institute of Technology
771 Ferst Drive,
Atlanta, GA 30332
E-mail : yogendra.joshi@me.gatech.edu

Samuel Graham, Co-PI
Georgia Institute of Technology
801 Ferst Drive,
Atlanta, GA 30332
E-mail: sgraham@gatech.edu

Satish Kumar, Co-PI
Georgia Institute of Technology
771 Ferst Drive,
Atlanta, GA 30332
E-mail: satish.kumar@me.gatech.edu

Susan Rogers, DOE Technology Development Manager
U.S. Department of Energy
Email: Susan.Rogers@ee.doe.gov

Project Introduction

This project aims to research, develop, and test Electric Traction Drive System Technology for use in vehicle applications capable of meeting the targets set by the Department of Energy Vehicle Technologies Office. The project is categorized into three major thrusts: Bonding interfaces for packaging, Thermal management of electric vehicles (EVs) power inverters, and electric motor thermal management.

A transient liquid phase bonding technique has been developed to directly bond dielectric substrates with AlSiC heatsinks for use in power electronic packages. The formation of intermetallic compounds between bonded component layers is driven by interdiffusion between the mixing materials based on their atomic concentration gradients. This process is governed by Fick's second law, which describes the migration of atoms in isotropic materials and may be used to understand diffusion in crystalline structures. To evaluate diffusion within the system, a computational model was developed and analyzed using the transport of diluted species module within the commercial COMSOL Multiphysics software. By parameterizing geometry, temperature inputs, processing time, and volume concentrations, a computational model could lead to extensive improvements in power electronics substrate-attach designs, allowing for evaluation of material interdiffusion at bond interfaces and process modifications before expensive experimentation.

For thermal management of electric vehicles, the performance of a novel package, that uses a dielectric fluid as the coolant for wide-bandgap (WBG) devices, is investigated. These devices have higher breakdown voltages, higher efficiencies, thermal conductivities, operating temperatures, and switching speeds than silicon devices. However, using them as a drop-in solution for silicon-based power modules, rather than designing specifically for WBG devices does not fully utilize their potential, particularly in regard to system-miniaturization and high-temperature operation. Thermal management occupies a large volume within conventional power

conversion units in electric vehicles (EVs), so improvements in cooling size and efficiency will improve inverter performance, as well as system-level metrics such as volumetric power density and specific power.

High torque- and volumetric power density motor performance for electric vehicle applications faces a bottleneck due to the thermal degradation of the motor windings. There is therefore a need to develop enhanced cooling solutions to take heat away from the hotspots (end windings) in the motors, and in doing so, raise the effective heat transfer coefficient. In-slot liquid cooling heat exchangers with integrated microchannels, that reduce the thermal resistance between the windings and the ambient, are being explored and optimized as a thermal management solution. Specifically, enhancements are being made to integrate end-winding cooling with in-slot cooling for these heat exchangers. Additionally, an optimized thermal modeling framework for analyzing the impact of proposed motor cooling solutions at a multiscale level is being explored. Such improvements in cooling efficiency and insights will improve performance, efficiency and longevity of EV motors.

Objectives

- Develop an approach to model the interdiffusion of Cu and Al atoms in the transient liquid phase bonding system between AlN and AlSiC.

- Demonstrate the effects of material, geometric, and time constraints on bond composition under isothermal heating conditions.

- Investigate thermal management solutions of WBG devices in electric vehicles. Specifically, this work involves developing and testing a novel power electronics package for dielectric liquid thermal management.

- Investigate the two-phase cooling performance with copper metal foams, with and without vapor channels

- Investigate a direct liquid-cooling in-slot heat exchanger integrating in-slot winding and end-winding cooling for electric vehicle applications

- Develop a multiscale thermal modeling framework in order to rapidly and accurately predict the motor-level impact of proposed cooling solutions, such as the novel heat exchanger design.

Approach

Diffusion Modeling Bonded Packaging Interface

To model the Cu-Al transient liquid phase system, a two-dimensional geometry representing a cross-sectional view of the bond interlayer was developed, which adopts the assumption of isotropic and uniform diffusion in one direction. The Transport of Diluted Species module computes the concentration gradients of the solute materials based on the following mass balance equation:

$$\frac{\partial c\,(r,t)}{\partial t} + \nabla j = 0 \tag{1}$$

According to Fick's law:

$$j = -D\nabla c \tag{2}$$

Combining both equations, the expression that governs transport phenomena is given by:

$$\frac{\partial c}{\partial t} - D\nabla^2 c(r,t) = 0 \tag{3}$$

In the equations, c represents the atomic concentration, r is the position vector, j is diffusion flux, D is diffusivity, and t represents time.

For isotropic diffusions, such as in crystalline structures, the diffusion coefficient D can be expressed in terms of a pre-exponential coefficient D_0 (m²/s), ideal gas constant R (J/mol·K), temperature (K), and activation energy EA (KJ/mol) as follows:

$$D = D_o \, exp\left(-\frac{E_A}{RT}\right) \tag{4}$$

The Cu and Al elements of the bond are modeled as components. Since the sintered AlN dielectric substrate has been shown to have no influence on the formation of the bond, the AlN material was neglected in this analysis. For simplicity, the bond material is modeled as a binary material consisting of pure Cu and Al, as shown in Figure I.1.15.1.
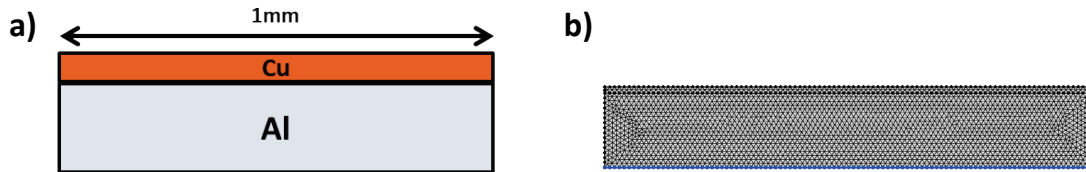
Figure I.1.15.1 (a) Schematic illustrating Cu-Al bond geometry. (b) Meshed geometry.

One 25 µm thick Cu foil and three 50 µm thick Al foils were used in TLP bonding of the substrates to AlSiC (Figure I.1.15.2). A representative uniform width of 1 mm was used for all samples in the model, while the thickness of the Cu layer was varied to examine the impact of Cu concentration on the final bond composition and intermetallic compound formation. Three sample combinations were studied: AlN bonded to AlSiC, as well as 2mm thick Al- and Cu- coupons bonded to AlSiC.

At the onset of the simulation ($t = 0$), Cu was assigned a concentration of 100% in the top domain and 0% in the lower segment, and Al a concentration of 0% and 100% in the top and bottom components, respectively. A boundary condition of zero flux was applied along all edges except the interface to allow for interlayer mixing. The material properties, diffusion and gas constants, and activation energy in the Cu-Al system are reported in Figure I.1.15.2(c). The temperature profile in Figure I.1.15.2 is resolved into a time-dependent function and imported as a global input. As the diffusion coefficient of Cu in Al changes with temperature, this value was parameterized using Eq. (4) over the temperature range 500–570ºC.

Name	Value	Unit	Description
D_Cu	6.50E-05	m²/s	Pre-exponential factor
E_Cu	60	kJ/mol	Activation energy
R	8.314	J/(mol·K)	Gas constant
flux	1.00E-06	m³/mol/s	Flux
roh_Al	2.7	g/cm³	Al density
roh_Cu	8.92	g/cm³	Cu density
molar_mass_Al	26.98	g/mol	Al molar mass
molar_mass_Cu	63.546	g/mol	Cu molar mass
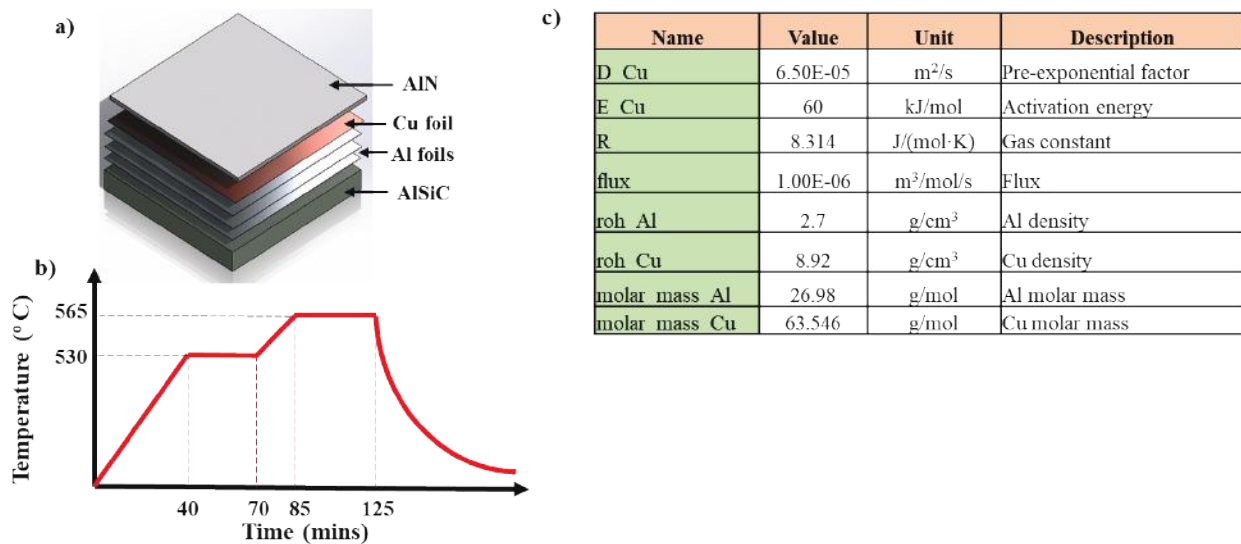
Figure I.1.15.2 a) Assembly stack showing the sequence of the bonded sample layers b) TLP process temperature profile c) Material properties of the bond materials applied as parameters in the COMSOL model.

Thermal management of electric vehicles (EVs) power inverters

The package was designed specifically for use with a dielectric fluid. Using a dielectric allows elimination of the need for an expensive ceramic layer, with poorer thermal conductivity than metals. This allows the fluid to come much closer to the junction allowing for "near-junction" cooling. The project consists of the complete development of a package that can be incorporated both for single and double-sided cooling of power electronics. Figure I.1.15.3 depicts the single- and double-sided cooling packages. The system proposed is modular, with the option of having multiple half-bridge modules (which are four devices each). Depending on the power requirement of the vehicle, the cold plate can be chosen accordingly and applied.
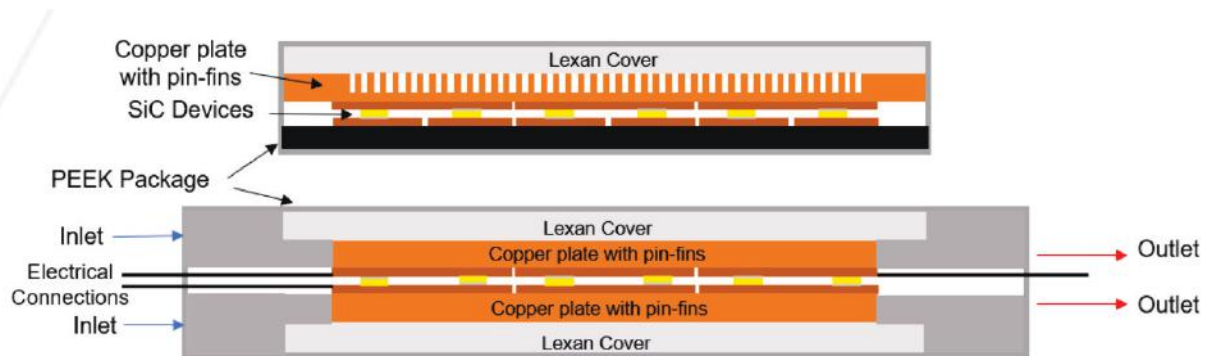
Figure I.1.15.3 Single and double-sided cooling techniques

Figure I.1.15.4 shows the designed cold plate with the manifold designed for in-house testing. The cold plate is 56 mm × 38.1 mm, and has a staggered arrangement of pin-fins to promote heat transfer. A Lexan cover is used to enable visualization of the flow boiling and understand the bubble formation and patterns. The heater block is designed with four legs (each of cross-section 3.1 mm × 3.1 mm) to replicate four devices half-bridge module arrangement. Each leg has two holes with thermocouples in them to measure the heat flux at every leg. The project is broken down into 2 parts, i.e., Phase 1 which includes testing the package with resistance heaters and the heater block that supply the power, and Phase 2 which tests the package with actual SiC devices. These devices will be characterized and tested with the T3STER (Siemens Transient Thermal Tester).
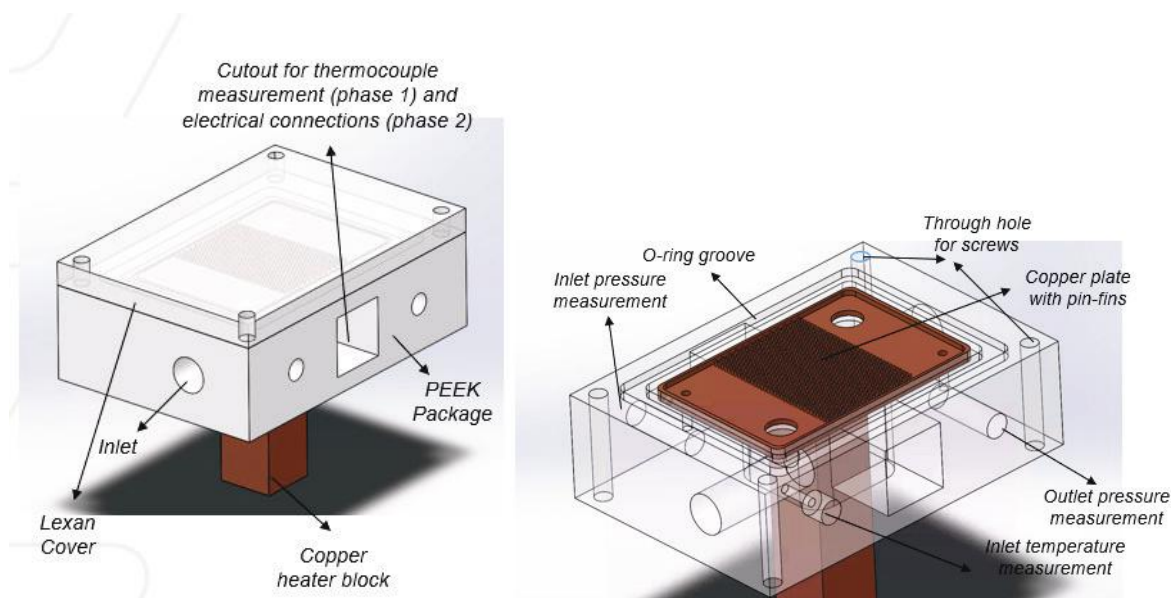
Figure I.1.15.4 Cooling manifold with cold plate designed for testing

This package would initially be tested with resistance heaters as the power source, and then with actual SiC MOSFET's obtained from SUNY Polytechnic Institute. Heat transfer measurements and visualization will be conducted. Figure I.1.15.5 shows the completed flow loop built for testing in both Phase 1 and 2.

Figure I.1.15.5 Completed flow loop

For testing the copper metal foam performance under two-phase flow with a dielectric fluid, two test samples were fabricated using direct metal laser sintering based on the rhombic dodecahedron unit cell. The first was uniformly populated and consequently named "uniform sample", whereas the second, termed "vapor pathway sample", was non-uniformly populated by removing each alternate row from the halfway point downstream. Figure I.1.15.6 displays and compares both the CAD files and the manufactured pieces prior to finishing machining operations but post heat treatment. The samples were experimentally tested, and numerical flow boiling simulations were performed afterwards
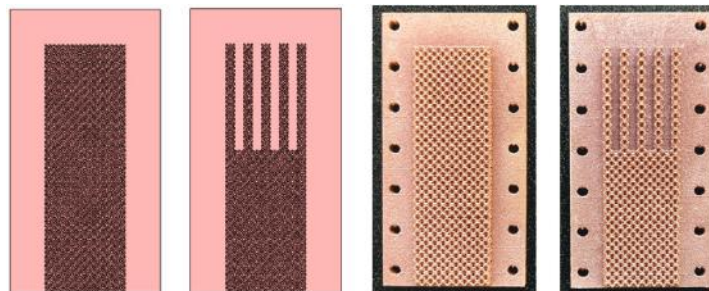
Figure I.1.15.6 CAD files of the printed AM cold plates for the uniform and vapor pathway structures (left), and corresponding printed structures (right)

Electric Motor Thermal Management

Direct in-slot liquid-cooling heat exchangers will be investigated as the thermal management solution, with the focus of the work being the quantification of a novel heat exchanger design that integrates end winding cooling with in-slot cooling. A combination of experimentation and multiscale computational methodology will be used to evaluate and compare the performance of the baseline and novel heat exchanger designs. First, the designs are computationally evaluated at component-level in Ansys Fluent, then at sub-motor level FEA model (half-slot) for steady-state thermal performance insights at a system level, and subsequently in a reduced-order full motor-level model in Ansys MotorCAD for rapid insights at full scale level. This multi-scale modelling approach provides useful insights regarding the enhancement in cooling with the novel heat exchanger design.

Subsequently, the computational results are validated via proof-of-concept experimental testing, where the cooling impact on windings of the two heat exchanger designs is experimentally determined in a thermal motorette test, performed using a single-phase liquid cooling test bench. The prior work done on end-winding cooling channels designed for an existing industrial motor is expanded and optimized for the concept motor design being explored by NREL, ORNL and Georgia Tech under the EDT objectives.

Results

Bonded interfaces

The simulation produces a three-dimensional matrix that showcases the concentration gradient of Cu in terms of mol/m^3 for all positions r over time t. The report is then analyzed using a MATLAB script to discretize the data based on the concentration of Cu-Al phases obtained from the binary phase diagram in Figure I.1.15.7. Figure I.1.15.8 shows the progression of Cu diffusion through the modeled geometry. Comparing the simulated model to microstructural analysis conducted in [1], it may be observed that EDS spectral results for the AlN-AlSiC and Al-SiC assemblies showed less than 1% atomic concentration of Cu, while XRD patterns revealed an abundance of the α-Al solid compound. This is validated by simulation results exhibiting that over a hold time of 40 min at 565°C, the 12.5-μm Cu foil used in initiating the bond between AlN-AlSiC and Al-AlSiC completely diffused through the system, leaving behind a mostly Al bond.

Conversely, when 2-mm-thick Cu was bonded to AlSiC at 565°C, the diffusion rate of copper, coupled with the high initial volume, dwell time, and favorable solubility limit on the Cu side, resulted in the nucleation of multiple phases. This is corroborated by the diffusion modeling results shown in Figure I.1.15.8(c), which correctly predicts formation of intermetallic phases Cu$_9$Al$_4$, CuAl, and CuAl$_2$ given the starting concentration of Cu and dwell time at isothermal heating temperature. It should be noted that although the diffusion model is likely to aid in the determination of intermetallic compounds formed between two materials given initial concentrations, thermal conditions, and time inputs, various other factors may influence the order of IMC formation such as the heat of formation, thermodynamic stability of phases, bonding conditions, and cooling rate.
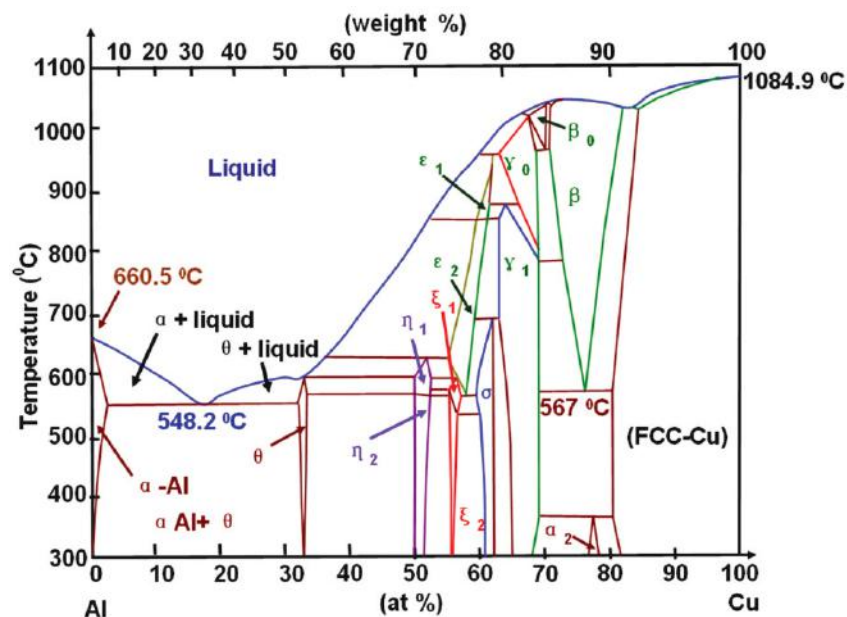
Figure I.1.15.7 Phase diagram of the Cu-Al binary system showing the intermetallic phases and aluminum and copper solid solutions [2], [3], [4].
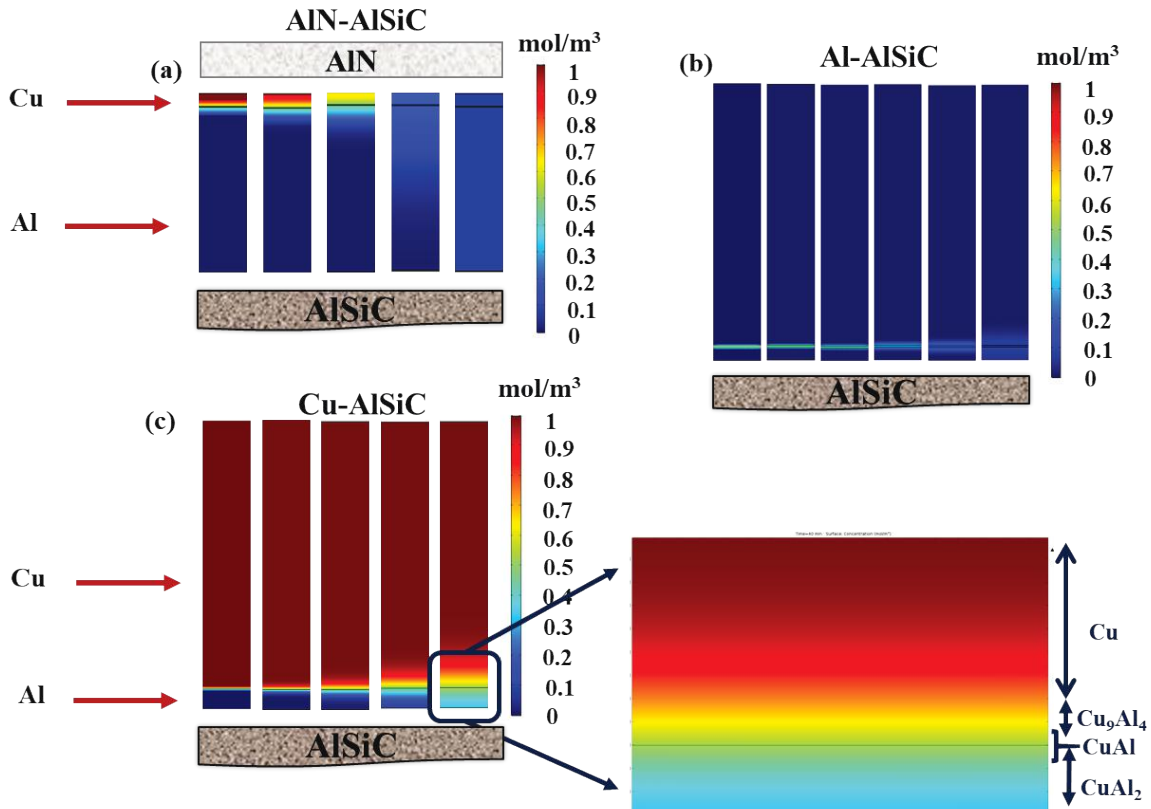
Figure I.1.15.8 Modeling results: isothermal diffusion of Cu at 565°C over 40 minutes in a pure Cu-Al binary system as in TLP-bonded (a) AlN-AlSiC, (b) Al-AlSiC, and (c) Cu-AlSiC.

Thermal Management of Electric Vehicle (EV) power inverters

Steady state computational fluid dynamics and heat transfer (CFD/HT) simulations on this cold plate were conducted to understand their performance. Figure I.1.15.9 depicts the boundary conditions supplied to the system for the simulation. Mass flow inlet of 1 LPM with heat flux maximum of 1 kW/cm^2 was applied to the system. CFD/HT results are seen in Figure I.1.15.10(a) and Figure I.1.15.10(b).
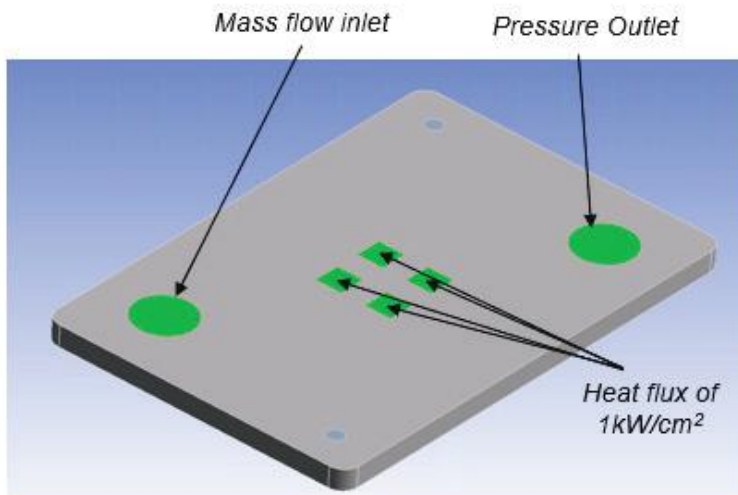
Figure I.1.15.9 Boundary conditions for single phase CFD/HT simulation
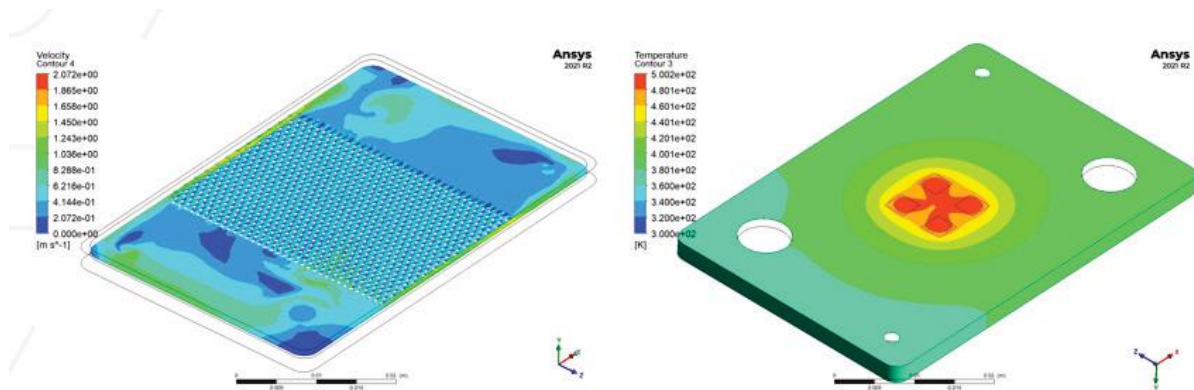
Figure I.1.15.10 (a) Velocity contours across plane of flow and (b) temperature contours on the back of cold-plate

With just single-phase results, we can see that even at that heat flux of 1 kW/cm^2, the maximum junction temperature is <230ºC. However, our goal is to maintain junction temperature below 200ºC, which should be achievable with boiling flows. A steady state thermal analysis was conducted, sweeping heat transfer coefficient (HTC) values across the cooled surfaces to understand what HTC we would need to maintain maximum junction temperature below 200ºC. Figure I.1.15.11 depicts those results, and from that we can conclude that a value higher than 17,500 W/m^{2}K would be sufficient.
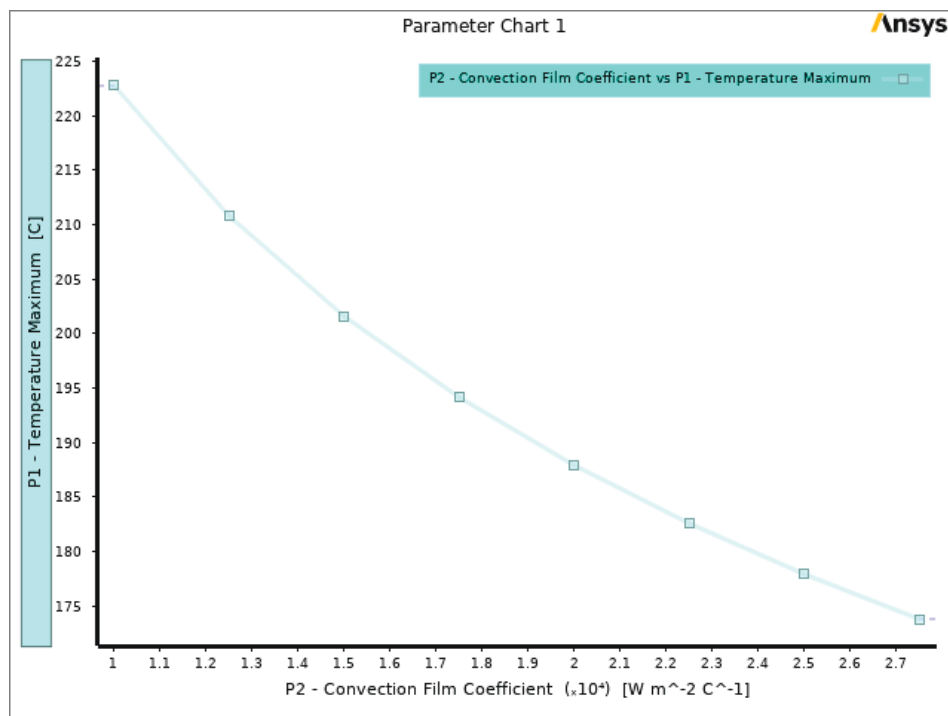
Figure I.1.15.11 Sweep of convection coefficient across cooled surfaces vs. maximum junction temperature

Referencing work from G. Moreno et al. [5] and A. Reeser et al. [6], the calculated heat transfer coefficients were > 20,000 W/m^{2}K and > 35,000W/m^{2}K at certain conditions. This would be verified with experimental trials in Phase 1 and 2 of the present study.

For the copper metal foam testing, integrating vapor pathways into the foam structure considerably lowers the pressure drop, as seen in Figure I.1.15.12. The maximum pressure drop reached 6.5 kPa for the uniform structure. The addition of vapor pathways decreased the pressure drop to 1.3 kPa (at the same q'' values) for

the second tested thermal management solution. A corresponding drop in pumping power occurs as well. However, the two-phase heat transfer coefficient h_{tp} shows less significant differences between the two structures.

Volume renderings (Figure I.1.15.13) showing the vapor volume fractions for both structures illustrated how the multiphase flow regimes changed by integrating vapor pathways. The uniform structure showed primarily churn-like flows due to the foam struts interrupting the fluid path, but the vapor pathway sample showed annular-like flow inside the removal channel. Additional effects of the vapor pathway were shown in the foam adjacent to the channel, where stagnant bubbles were shown to grow and eject vapor into the lower resistance channels.
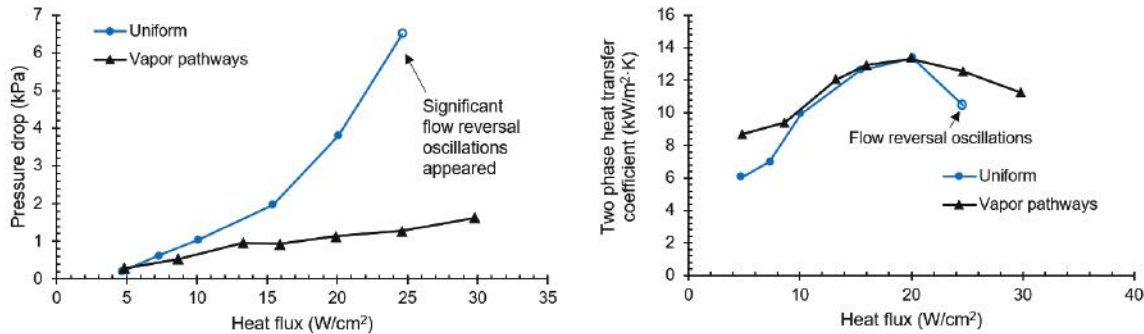
Figure I.1.15.12 Pressure drop (left) and two-phase heat transfer coefficient (right) versus heat flux comparison plots for both structures at G = 160 kg/m²s
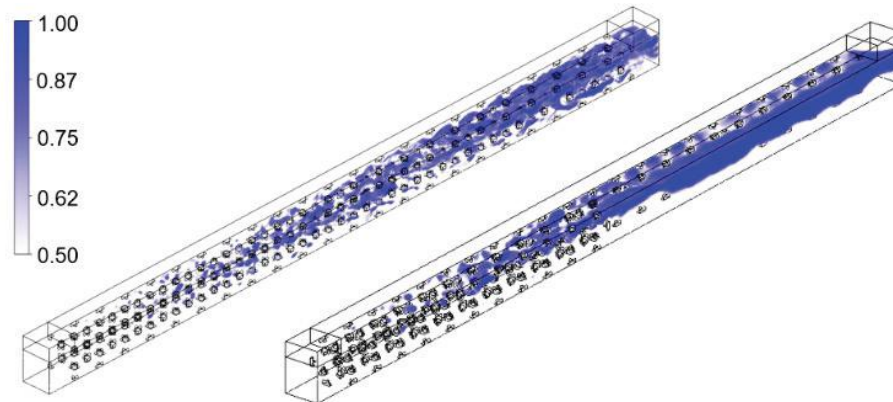
Figure I.1.15.13 Isometric views showing vapor volume fraction renderings for both structures (left: uniform, right: vapor pathway)

Electric Motor Thermal Management

The recent work involved the further optimization of in-slot heat exchangers identified as direct liquid-cooling solutions for the 100kW high-power density outer rotor motor being developed under the EDT program objectives. The baseline design for these heat exchangers does not specifically address the cooling of end windings which extend out of the stator lamination stack. Hence, a novel design is developed that addresses end winding cooling with two major advantages – (1) minimal alterations in motor critical design parameters, and (2) no additional provision required for coolant delivery to end windings (see Figure I.1.15.14).
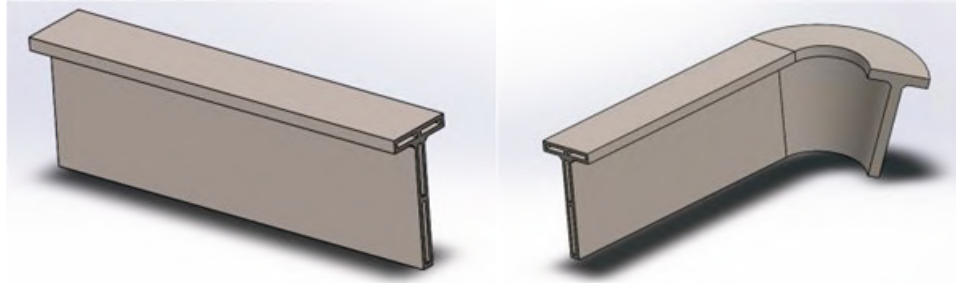
Figure I.1.15.14 (L) Baseline heat exchanger design, (R) Novel heat exchanger design optimized for integrated end winding cooing

The two heat exchanger designs were evaluated at component-level via computational fluid dynamics simulations of WEG 50/50 coolant flow through the geometries. A mass flux condition was applied to the inlet at 65°C, and a pressure outlet condition was applied at the outlet. Heat flux conditions were applied at various walls of the heat exchanger to simulate heat transfer from the windings to the heat exchangers. The mesh-independent results were post-processed to calculate an effective heat transfer coefficient (h_{eff}) for the designs, and revealed that the novel heat exchanger design (4080 W/m^{2}K) exhibits a 28% increase in h_{eff} relative to the baseline design (3144 W/m^{2}K) (see Figure I.1.15.15). The temperature contours for both designs also show the greater thermal balance and reduction of hotspots and dead zones achieved with the novel design.
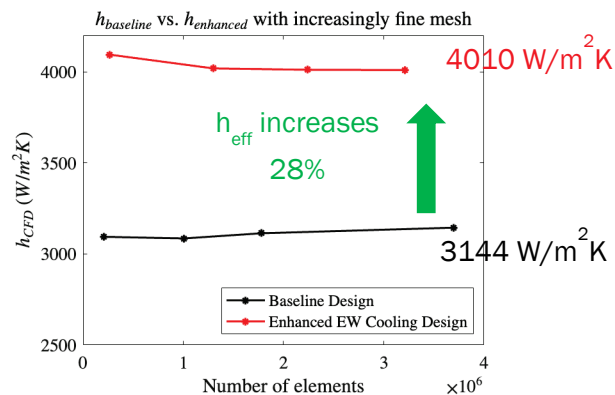
Figure I.1.15.15 Novel design for heat exchanger shows 28% enhancement in effective heat transfer coefficient

The component-level comparison of the heat exchanger designs is then extended to a steady-state thermal analysis of the two designs in an Ansys Mechanical FEA model of a half-slot radial slice through the motor design. The heat loads in the system are parametrized as volumetric generation rates in various heat generating components for specific operating points. The heat exchangers are configured with the walls having convection coefficients equivalent to the h_{eff} values computed using the Fluent simulations. The resulting temperature contours in the windings show a ~7°C temperature reduction with the novel design. Following this, reduced order models of the motor and its proposed cooling solutions are developed using motor simulation tool Ansys MotorCAD. The motor geometry and drive parameters generate electromagnetic model results, including system loss distribution data, that in turn drive the thermal model. The thermal model details the cooling solution and solves an inbuilt customizable lumped parameter thermal network (LPTN) to generate rapid thermal distributions in motor components for the chosen operating point. The accuracy of the reduced-order model is further refined by customizing the default LPTN to include all existing heat flow paths (and the accompanying flow resistances, estimated analytically) in the motor system, leading to increased accuracy and sensitivity in reduced-order results (see Figure I.1.15.16). This combination of modeling approaches creates a holistic framework for analyzing and predicting the impact of a proposed cooling solution at the full motor level.
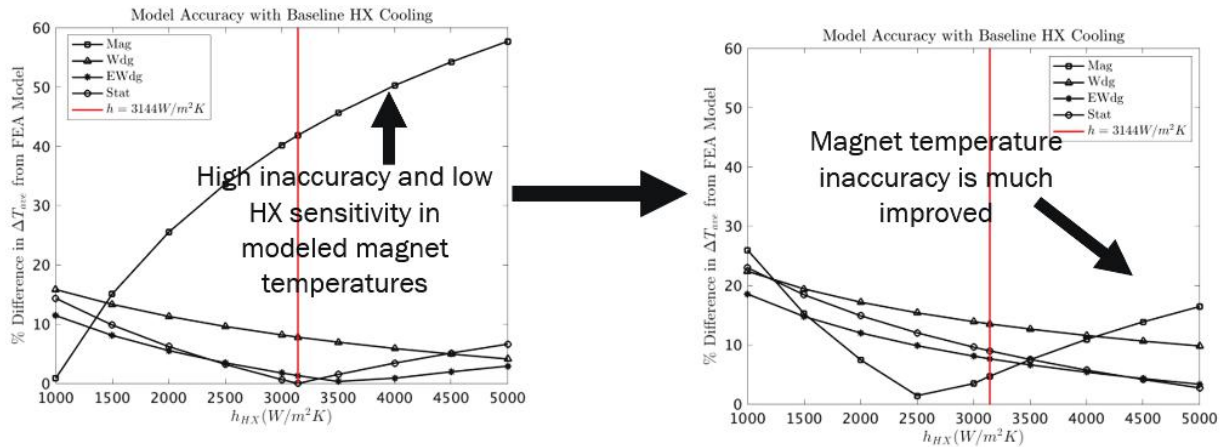
Figure I.1.15.16 MotorCAD model refinement leads to greater result accuracy (graph on right)

The predicted computational results evaluating the heat exchanger designs will be validated experimentally. This ongoing work involves the use of a single-phase liquid cooling test bench with WEG coolant flow, that will test the heat exchanger effectiveness (h_{eff}) using patch heaters simulating heat loads on the walls, as well as the impact of the heat exchangers at a system level in 2-slot thermal motorettes.

Conclusions

- A diffusion model, developed using the Transport of Diluted Species module in COMSOL, was shown to correctly predict the intermetallic compounds formed during TLP bonding. The model demonstrates the dependence of the nucleated bond on the original concentrations of diffusing elements, and the results indicated that dwell time had a strong effect on the formation of compounds in the bond interface.

- X-ray diffraction results of cross-sectioned AlN-, Cu- and Al-AlSiC samples compared with C-SAM, EDS and SEM images revealed that samples with higher intermetallic compound content exhibited greater rates of defects upon cooling. Maintaining initial Cu-Al volume ratio of 1:5 as in the AlN-AlSiC sample facilitated development of high-quality bonds with low void concentration. By parameterizing geometry, temperature inputs, processing time, and volume concentrations, the computational model could lead to extensive improvements in substrate-attach designs.

- For SiC device level thermal management, single and double-sided cooling techniques were outlined. The package was designed and implemented into a flow loop for testing. Phase 1 tests, with test heaters, have begun, and both phase 1 and phase 2 tests (with actual SiC devices) will be completed before the end of the year. Performance of the cold plate was evaluated through simulations, and future work includes summarizing the experimental results, and characterizing thermal resistances.

- Integrating vapor pathways into the foam structure considerably lowers the pressure drop.

- For motor end windings cooling, the work outlines component-level and system-level thermal simulations for liquid-cooled in-slot heat exchanger designs, to be incorporated into a proposed outer rotor motor for EV applications. The component-level, sub-motor level as well as reduced-order motor-level models show reasonable agreement to indicate that the novel design has superior thermal balance and leads to enhanced cooling of windings and end windings. The work done here lays the foundation for experimental testing of these various heat exchanger geometries, to validate a design that is enhanced for thermal management of the motor end windings.

Key Publications

1. Imediegwu, Chidinma, Samuel Graham, Darshan G. Pahinkar, Sreekant Narumanchi, Paul Paret, and Joshua Major. "Interdiffusion and formation of intermetallic compounds in high-temperature power

electronics substrate joints fabricated by transient liquid phase bonding." *Microelectronics Reliability* 137 (2022): 114788.

References

1. Imediegwu, Chidinma, Samuel Graham, Darshan G. Pahinkar, Sreekant Narumanchi, Paul Paret, and Joshua Major. "Interdiffusion and formation of intermetallic compounds in high-temperature power electronics substrate joints fabricated by transient liquid phase bonding." *Microelectronics Reliability* 137 (2022): 114788.

2. Kouters, M. H. M., G. H. M. Gubbels, and C. A. Yuan. *Characterization of intermetallic compounds in Cu-Al ball bonds: mechanical properties, delamination strength and thermal conductivity*. IEEE, 2012.

3. Massalski, Thaddeus B., Hiroaki Okamoto, PRnbsp Subramanian, Linda Kacprzak, and William W. Scott, eds. *Binary alloy phase diagrams*. Vol. 1, no. 2. Metals Park, OH: American society for metals, 1986.

4. Database, P.E.M.a. *Al-Cu Alloy Phase Diagram*. [cited 2022; Available from: https://www.globalsino.com/EM/page2000.html.

5. Moreno, Gilberto, Sreekant Narumanchi, Jeff Tomerlin, and Joshua Major. "Single-Phase Dielectric Fluid Thermal Management for Power-Dense Automotive Power Electronics." *IEEE Transactions on Power Electronics* (2022).

6. Reeser, A., A. Bar-Cohen, and G. Hetsroni. "High quality flow boiling heat transfer and pressure drop in microgap pin fin arrays." *International Journal of Heat and Mass Transfer* 78 (2014): 974-985.

Acknowledgements

I.1.16 Advanced Electric Machines for High Power Density Automotive Electric Drives (NC State University)

Victor Veliadis, Principal Investigator
North Carolina State University
930 Campus Shore Dr., suite 200
Raleigh, NC 27606
jvveliad@ncsu.edu

Iqbal Husein, Principal Investigator
North Carolina State University
930 Campus Shore Dr., suite 200
Raleigh, NC 27606
ihusain2@ncsu.edu

Susan Rogers, DOE Technology Development Manager
U.S. Department of Energy
Email: Susan.Rogers@ee.doe.gov

Project Introduction

DOE EDT 2025 has set an ambitious target for traction electric motors. The targets are to increase power density (kW/L), and to reduce cost ($/kW) using Heavy Rare Earth (HRE) free permanent magnets. The targets for power density, efficiency, and cost are 50 kW/L, 97%, and 3.3 $/kW, respectively. The research approach adopted by North Carolina State University is to meet or exceed these targets by 2025 through design innovations, new manufacturing processes, and innovations in materials and thermal management. So far, two motor designs namely- Space-shifted dual three-phase (SS-DTP) IPMSM with novel segmented V-shaped magnets (Design II) and Slotless Halbach outer rotor PMSM with winding embedded liquid cooling (WELC) (Design III), have been down selected from several designs and also shown to be most promising in achieving the specified targets. The SS-DTP IPMSM was chosen for its high power density, high efficiency, fault-tolerant capabilities, and the established industry acceptance of its rotor structure amongst electric traction motors in commercial electric vehicles. Meanwhile, the choice of the Slotless-Halbach design is due to its lightweight structure and high efficiency; these machines are extremely compact, completely HRE-free, and can be operated at very high speeds. However, the low thermal mass and high electrical loading result in thermal management issues. To tackle this challenge, innovations in liquid cooling design and materials need to be further explored.

Objectives

The overall objective of this project portion is to design, evaluate and verify the performance of a high-speed electric machine optimized for high power density (kW/L) and ultra-high efficiency with HRE-free magnets.

In the past year, the electric machines research team's objective are as follows

- To explore using Samarium Cobalt SmCo magnets as an alternative to the HRE-free NdFeB magnets, and HF-10 steel as an alternative to the Hiperco 50 steel, in Design II. This decision was due to unavailability of the NEORECMHF45 HRE-free magnets and the high cost of the Hiperco 50 lamination.

- To conduct further analysis and experiments to validate the WELC concept for Design III.

Approach

Design II

Recently, there has been research into performance and energy density improvements of SmCo magnets. The EEC 2:17-34 magnet from Electron Energy Corporation, showed very promising results and was readily available. In addition, the cost of Hiperco 50 lamination stack was almost 7 times the cost of HF-10 steel. As a result, Design II was optimized with different combinations of the two core materials and the two magnet types, as shown in Table I.1.16.1, keeping the original SS DTP winding arrangement and single-V segmented magnets. The objective of the optimization was to establish the least costly solution to meet the DOE's target.

Table I.1.16.1 Cost-Performance comparison of laminate materials and magnets

	Case I	Case II	Case III	Case IV	Case V	Case VI
Material						
Stator	Hiperco 50	Hiperco 50	Hiperco 50	Hiperco 50	HF-10	HF-10
Rotor	Hiperco 50	HF-10	Hiperco 50	HF-10	Hiperco 50	HF-10
Magnets	NEO45MHF	NEO45MHF	EEC 2:17-34	EEC 2:17-34	EEC 2:17-34	EEC 2:17-34
Electromagnetic Performance						
Peak Torque (Nm)	144.5	144.87	143.5	142.9	142.4	142.6
Power Density (kW/L)	50.69	50.82	50.30	50.13	49.95	50.02
Current Density (A/mm2)	34.21	34.21	34.21	34.21	46.39	46.01
Regions wt. Eff ≥ 97%	39.50	31.03	42.90	34.95	0.00	1.33
Cost ($ per-unit)						
Stator ($ per-unit)	1.00	1.00	1.00	1.00	0.20	0.20
Rotor ($ per-unit)	0.75	0.22	0.75	0.22	0.75	0.22
Magnet Vol. (x10-3cm3)	5.35	5.35	3.81	3.81	4.70	4.70

Design III

- A novel Winding Embedded Liquid Cooling (WELC) strategy has been proposed to achieve a slot current density of up to 33 A/mm^2.

- Cobalt-free HF-10 lamination used in stator to achieve a low cost without sacrificing performance as iron losses are inherently low.

- HRE-free NEOREC45MHF magnets arranged in Halbach Array configuration.

Results

Design II

Table I.1.16.1 summarizes the results of the performance and production cost of the SS DTP IPMSM Design optimized with different material combinations. The results show that the optimized designs meet the power density requirements. The main differences are in the current density and efficiency regions above 97%. The design cases with Hiperco 50 stator material (Cases I, II, III, and IV) outperformed the others in terms of efficiency. This is mainly due to their low current density requirement, resulting in lesser copper loss, and their relatively lower iron loss and magnet loss compared to the design option with HF-10 stator lamination. The high current density and iron loss of Design cases V and VI result in a relatively higher thermal operation. However, this is no issue for the SmCo magnets as they tend to have a high-temperature coefficient and low Curie temperature compared to NdFeB magnets. Regarding cost, cases V and VI are the two least costly

options due to their use of HF-10 lamination. Another cost implication is related to magnet volume. The HRE-free NEO45MHF magnets in Cases I and II are optimized to have thicker heights to prevent demagnetization, which translates to a higher volume and magnet cost. As a result, Design Case VI was chosen for further analysis and experimental verification because it satisfies the design specification for the least expensive option. Figure I.1.16.1 and Figure I.1.16.2 show the performance capability curves and efficiency maps of Design Case VI. Furthermore, design case VI is being fabricated to validate the proposed SS DTP winding concepts. Figure I.1.16.3 and Figure I.1.16.4 show the fabricated stator and rotor lamination stack using the HF-10 laminate material.
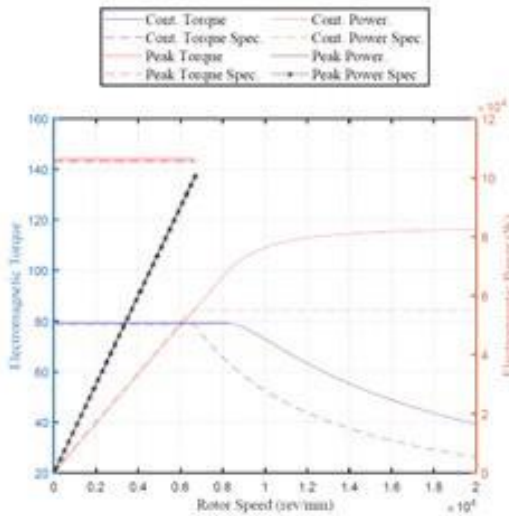
Figure I.1.16.1 Performance capabilty curve of the IPMSM design with HF-10 lamination and SmCo magnets
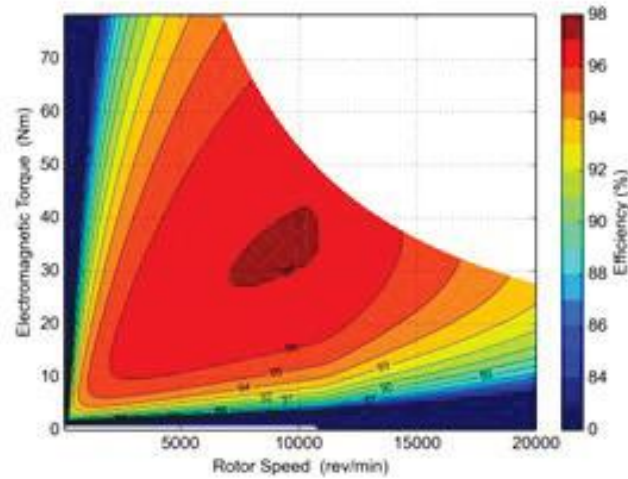
Figure I.1.16.2 Efficiency map of design case VI for 55 kW of continuous power operation

Figure I.1.16.3 Fabricated HF-10 stator lamination

Figure I.1.16.4 Fabricated HF-10 rotor lamination

Design III

A scaled-down prototype stator of the Slotless-Halbach outer rotor PMSM with winding embedded liquid cooling has been designed, fabricated, and experimentally verified to demonstrate the effectiveness of the WELC concept. The design was carried out using Altair Flux 2D electromagnetic FEA tool and the output parameters obtained from the FEA simulation are listed in Table I.1.16.2. The scaled-down prototype has a rated power of 10.8 kW at 6670 rpm, which corresponds to a rated torque of 15.5 Nm.

Table I.1.16.2 Parameters of scaled-down, 10.8 kW version of Design III

Parameters	Value
Output Torque (Nm)	15.5
Base Speed (rpm)	6670
RMS Phase Current (A)	28
Current Density (A/mm^2)	33
Output Power (kW)	10.8
Core Loss (W)	15
DC Copper Loss (W)	274
Magnet Loss (W)	59
Efficiency (%)	96
Power Density (kW/L)	28.2

The winding supports with embedded cooling channels were injection molded from thermally conducting Coolpoly D5506 plastic which has a thermal conductivity of 9.6 W/mK. The stator windings were encapsulated in Resbond 906 ceramic epoxy to enhance the thermal contact between the windings and coolant channels in the winding support. The lamination was fabricated from HF-10 non-grain oriented steel as the slotless machine does not have highly saturated laminated teeth, where most of the iron losses occur in a slotted machine. Therefore, the use of a high saturation flux density steel, such as Hiperco 50, is not justified in this design due to the high cost associated with this material. The injection molded winding supports are designed with lateral fins which fit into grooves cut into the lamination for a stable mechanical and thermal contact. PVC tubing is interfaced to the coolant channel in the winding supports using thermally stable nylon tube to provide a path for coolant to flow between winding supports. The coolant used is a 50/50 mixture of ethylene glycol and water. The windings are composed of 65 turns of AWG 20 wire per coil and two coils per slot.
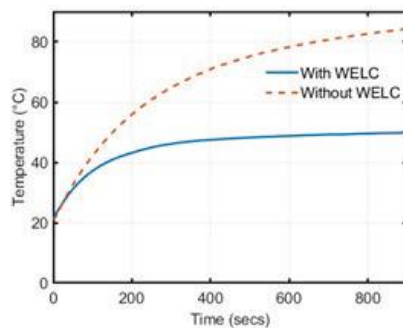
Figure I.1.16.5 Temperature rise with time with and without WELC at 12 A/mm^2
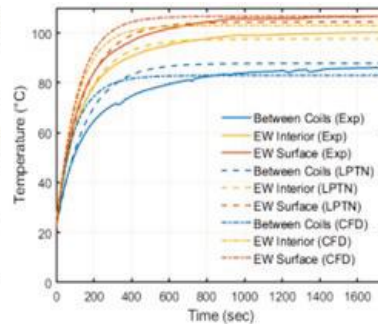
Figure I.1.16.6 Torque Profile of the Design III scaled-down prototype
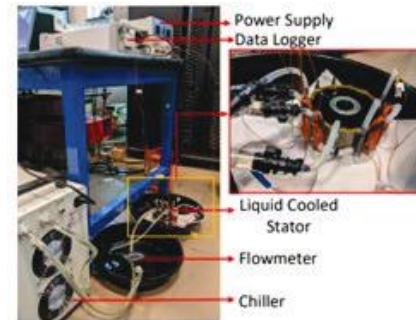
Figure I.1.16.7 Magnetic Flux Density in Design III at peak operating point.

In the previous annual report, partial results of the thermal testing of the WELC concept were presented. Since then, the complete thermal testing for the fabricated prototype has been completed. The temperature rise starting from ambient was observed for both with and without WELC at 12 $/mm^2$, and it was observed that employing WELC, the temperature rise is 46% of the case without WELC. The temperature at various locations in the machine was observed, and the experimental results were compared against the developed CFD and lumped parameter models to verify them.

For a temperature rise of 80 °C, the maximum continuous current density was found to be 19.0 A/mm^2, which is a 35% improvement over conventional axial water jacket cooling. The maximum peak current density for a duration of 18 seconds was found to be 39.8 A/mm^2, while for longer durations of 30 and 60 seconds it was found to be 34.1 A/mm^2 and 30.0 A/mm^2, respectively. All the results are for a low rate of 0.9 liter/min.

Conclusions

In the past year, we explored using low-cost laminate materials and SmCo magnets for the proposed SS DTP IPMSM in Design II. Several material combinations were optimized for performance and cost. The design option with HF-10 steel lamination and SmCo magnet was shown to be the best in terms of performance and production cost. However, this comes at a cost of low overall efficiency and high thermal operation. For Design III, further detailed analysis, design, and prototyping of the down-selected HRE-free designs have been carried out to meet the DOE EDT targets. A scaled-down prototype of Design III has been fabricated to evaluate the novel WELC concept and detailed thermal testing shows promising results consistent with CFD simulations. This cooling strategy enables higher electrical loading and allows Design III to be operated at current densities as high as 39.8 A/mm^2, peak, and 19.0 A/mm^2 continuous, allowing it to meet the 50 kW/l target power density.

Key Publications

1. Md Sariful Islam, Iqbal Husain, Ritvik Chattopadhyay, and Gregory D. Buckner, "Three-Dimensional Air-gap Electric Machines Employing Winding Embedded Liquid Cooling", US 17/482,645.

2. M.S. Islam, S. Agoro, R. Chattopadhyay, and I. Husain, "Heavy Rare Earth Free High Power Density Traction Machine for Electric Vehicles", 2021 *IEEE International Electric Machines & Drives Conference (IEMDC)* (pp. 1-8).

3. R. Chattopadhyay, M.S. Islam, R. Mikail, and I. Husain, " Partial Discharge Analysis and Insulation Design of High-Speed Slotless Machine for Aerospace Applications", 2021 *IEEE Energy Conversion Congress & Expo,* Vancouver, BC.

I.1.17 Rugged WBG Devices for High Power Density Automotive Electric Drives (NC State University)

Victor Veliadis, Principal Investigator
North Carolina State University
930 Campus Shore Dr., suite 200
Raleigh, NC 27606
jvveliad@ncsu.edu

Subhashish Bhattacharya, Principal Investigator
North Carolina State University
930 Campus Shore Dr., suite 200
Raleigh, NC 27606
sbhatta4@ncsu.edu

Susan Rogers, DOE Technology Development Manager
U.S. Department of Energy
Email: Susan.Rogers@ee.doe.gov

Start Date: April 2019   End Date: March 2024
Project Funding (FY20): $300,000   DOE share: $300,000   Non-DOE share: $0

Project Introduction

Towards meeting the DOE ELT 2025 targets, GaN devices are investigated in this work for traction inverter applications. The commercially available enhancement-mode GaN HEMT (GaN E-HEMT) have an excellent figure of merit but are limited in their voltage rating to 650V. Hence for the 800V DC bus application considered in this work, a three-level active neutral point clamped converter (3L-ANPC) inverter topology is considered. The 3L-ANPC topology provides the benefits of lower motor insulation stress, lower EMI, higher efficiency, and better fault-tolerant operation. The design and operation of a high-power GaN-based 3L-ANPC inverter have been the focus of this year's work. Insulated metal substrate (IMS) PCBs are used in the power layout design for their excellent thermal performance. The design guidelines had been discussed in detail in the previous reports. This report presents a suitable switching strategy that reduces the critical switching transient overvoltage and reduces zero-state conduction losses. Double pulse test results are presented for the proposed switching strategy to confirm the safe switching operation at 800V DC bus voltage and 40A device current. The thermal performance of the designed inverter phase leg is verified with a DC-AC-DC regenerative test setup delivering 3.24kW output power from a phase leg at 98.9% efficiency and $R_{th(case-ambient)} = 1.65°C/W$. The three-phase inverter operation's preliminary results are presented with a resistive-inductive load.

Objectives

1. Identification of a suitable switching strategy for GaN-based 3L-ANPC inverter.

2. Experimental thermal evaluation of the designed 3L-ANPC power block in a DC-AC-DC regenerative test setup.

3. Testing three-phase inverter prototype with RL load.

Approach

1. Identification of a suitable switching strategy for GaN-based 3L-ANPC inverter.

A switching pole of a 3L-ANPC is shown in Figure I.1.17.1. The 3L-ANPC topology offers several possible ways of switching operations for the realization of P, 0, and N states. The redundant switching operations are fundamentally associated with two key decisions:

a) Switching state of voltage balancing switch (S6 during P state and S5 during N state).

b) Selection of 0 state from 0+, 0- and 0F

Commercial discrete GaN devices have a high-temperature co-efficient of $R_{ds,on}$, leading to high conduction loss. Hence use of full zero (0^F) for zero states as shown in Figure I.1.17.2(d) will parallel the devices and thereby reduce the conduction loss. However, parallel operation of short and long loop paths can lead to damaging overvoltage stress across the inner switches S2 and S3. The different switching transient nomenclature is shown in Figure I.1.17.3. T1.2 and T2.2 transients are identified as the most severe transients because of long-loop coupling. T1.2 is the most severe turn-on transient, and T2.2 is the most severe turn-off transient. For the T1.2 transient, full SM operation has a coupled L_{st} and L_{lg} operation that can result in high device

Figure I.1.17.1 Schematic diagram with the 3L-ANPC pole and its different devices.

overvoltage. Figure I.1.17.3(d) shows the proposed innovative switching transient, which operates the clamping switches S5 and S6 for active coupling and decoupling of the long and short loops to reduce the transient voltage overshoot during T1.2 and T2.2 transient. The severity of the turn-off transient is mainly dependent on the di/dt. Therefore, during T2.2 turn-off transient, the proposed switching mode ensures the di/dt is reduced to half by the simultaneous operation of S2 and S6. The transients are evaluated in Double Pulse Test (DPT).

Figure I.1.17.2 Key switching modes of operation for zero state realization in 3L-ANPC
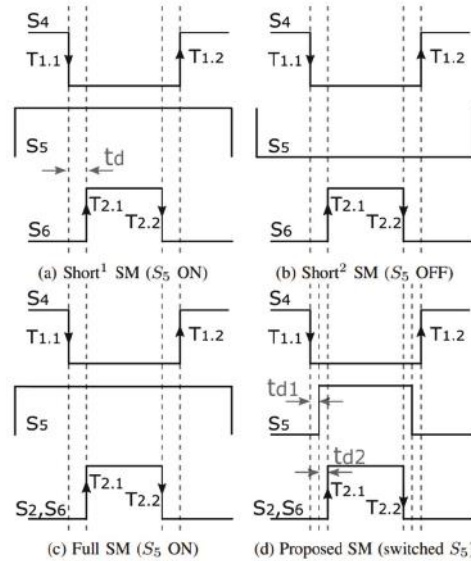
Figure I.1.17.3 Switching sequence for operation of N to 0 in short, full and proposed switching mode (SM).

2. Experimental thermal evaluation of the designed 3L-ANPC power block in a DC-AC-DC regenerative test setup.

For thermal evaluation of 3L-ANPC switching poles two poles are designed and connected as shown in Figure I.1.17.4. The poles are designated as A and B. A and B are connected through a high-frequency inductor as shown in Figure I.1.17.4. A Luna fiber optic temperature sensors for measurement of case temperature rise of individual devices is connected to pole A. Pole A is set at desired operating modulation index $m_A=m$. The operating conditions of pole B, i.e m_B and phase shift between A and B are selected to operate pole A at the desired test conditions. The case temperature rise of the different switches – outer, clamping and inner are

monitored for continuous operation of the inverter till the case temperature rise settles. The temperature rise results are presented in this report. The loss and efficiency results are determined using a Power Analyzer.
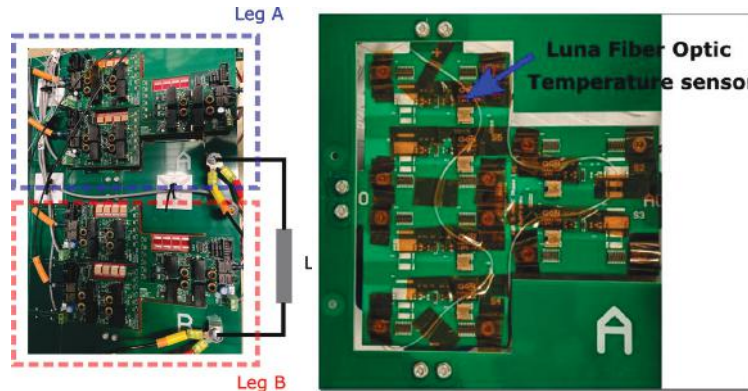
Figure I.1.17.4 Experiment test set-up for DC-AC-DC regenerative test between phase leg A and B (left) and Tcase measurement (right).

3. Testing three-phase inverter prototype with RL load.

A three-phase 3L-ANPC inverter is designed using above mentioned three 3L-APNC poles. A picture of the three-phase inverter is shown in Figure I.1.17.5. The inverter is tested using RL load at a switching frequency of 70kHz, and the results are presented in the next section.

Figure I.1.17.5 Three-phase 3L-APNC inverter

Results

1. 3L-DPT Results for Proposed Switching Mode
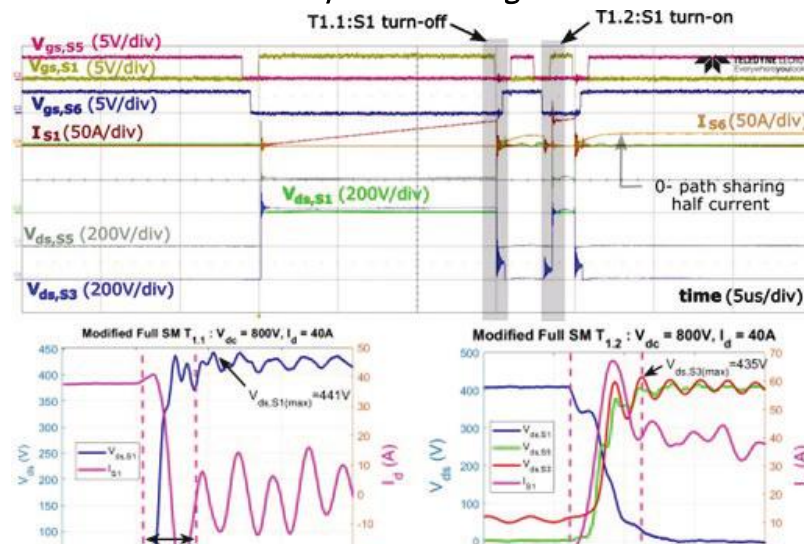
Figure I.1.17.6 Experimental result of T1.1 and T1.2 transient for proposed switching mode operation at V_{dc} = 800V and Io = 40A.
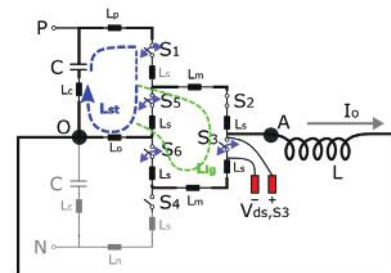
Figure I.1.17.7 DPT circuit for P↔0 switching transient evaluation. The short loop and long loop commutation paths are highlighted along with the most severely stressed inner switch S3.

Test condition: P↔0 event is tested with dead-time =500ns, $R_{gs,on}$ =12Ω, $R_{gs,off}$=4Ω, V_{dc} = 800V, and I_o=40A. Measured Eon = 290μJ and Eoff = 39 μJ.

2. *Thermal evaluation of 3L-ANPC using a DC-AC-DC Regenerative test set-up:*
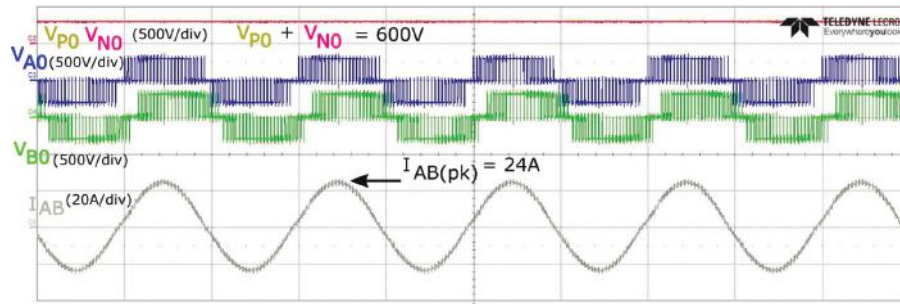
Total Loss = 35W, ŋ = 98.9%
T_{amb} = 25°C
ΔT_{outer} = 10.4°C
ΔT_{inner} = 10°C
$\Delta T_{clamping}$ = 8.8°C
$R_{th(case-amb)}$ = 1.65 °C/W

Figure I.1.17.8 Experimental test results of 3L-ANPC inverter continuous operation in a DC-AC-DC regenerative test set up. (Time scale: 500μs/div)

Figure I.1.17.9 Case temperature (T_{case}) rise of outer, inner and clamping switch and other experimentally determined parameters.

Test condition: P_o = 3.24kW, V_{dc}=600V, I_{pk}=24A through a single GaN switch at m=0.91, unity pf, f_e=1000Hz and f_{sw}=50kHz.

The test results determine the power loss of the inverter phase leg operation from power analyzer. A high efficiency of 98.9% is observed with a low worst case device case temperature rise of 10.4°C at T_{amb}=25°C. This confirms the low $R_{th(case-ambient)}$=1.65°C/W of the realized GaN-based 3L-ANPC phase leg design.

3. *Three-phase 3L-ANPC Inverter Operation with Designed Control Card:*
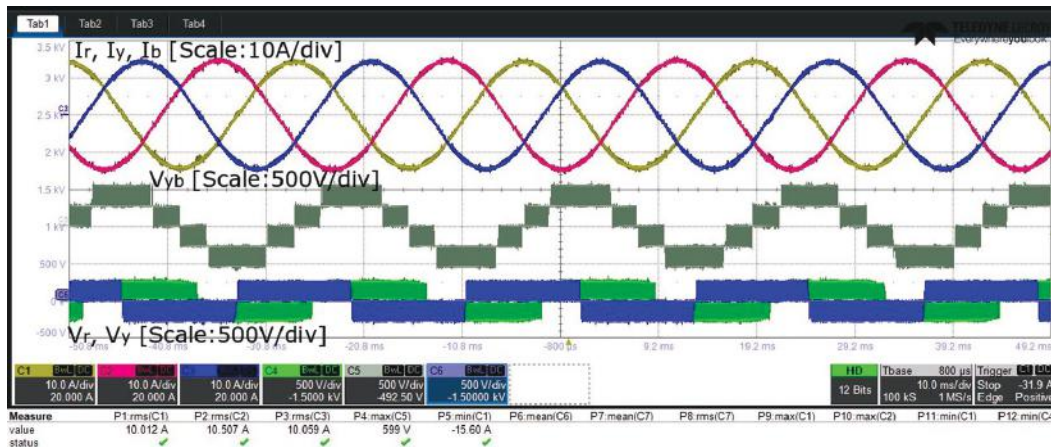
Figure I.1.17.10 Continuous testing of three-phase 3L ANPC at 5.1kW with RL load (Time scale 10ms/div)

Test condition: Hardware test result of 3ph 3L-ANPC converter with R-L load (Test conditions: R = 16.4Ω, L= 1mH, Vdc = 550V, Po = 5.1kW, fundamental freq. = 60Hz and f_{sw} = 70kHz).

Conclusion

In conclusion, a prototype GaN-based three phase 3L-ANPC traction inverter has been designed. An innovative switching strategy is proposed to mitigate the effect of long loop inductance on switching transient overvoltage. Three-level DPT results are presented for switching transients at 800V DC bus voltage and 40A device current to show safe turn-on and turn-off operation at desired rated conditions. The designed hardware has a modular structure with IMS PCBs for power layout enabling a low $R_{th(case-ambient)}$ = 1.65°C /W. A DC-AC-DC regenerative test set up is used to experimentally determine the phase leg loss under continuous

operation. The test results present an efficiency of 98.9% at 3.24kW output power from a 3L-ANPC phase leg. Further, a three-phase inverter operation with R-L load is presented at 5.1kW output power.

Key Publications

1. S. Satpathy, P. P. Das, S. Bhattacharya and V. Veliadis, "A New Switching Strategy for a GaN-based Three-Level Active Neutral Point Clamped Converter," *2022 IEEE Energy Conversion Congress and Exposition (ECCE)*, 2022, pp. 1-8, doi: 10.1109/ECCE50734.2022.9947699.

2. S. Satpathy, P. P. Das, S. Bhattacharya and V. Veliadis, "Design Considerations of a GaN-based Three-Level Traction Inverter for Electric Vehicles," *2022 IEEE 9th Workshop on Wide Bandgap Power Devices & Applications (WiPDA)*, 2022, pp. 192-197, doi: 10.1109/WiPDA56483.2022.9955248.

3. P. P. Das, S. Satpathy, S. Bhattacharya and V. Veliadis, "Generalized Control Technique for Three-Level Inverter Fed Six-Phase Permanent Magnet Synchronous Machines Under Fault Conditions," *2022 IEEE Energy Conversion Congress and Exposition (ECCE)*, 2022, pp. 1-8, doi: 10.1109/ECCE50734.2022.9947672.

I.1.18 Integrated Motor and Drive for Traction Application (University of Wisconsin Madison) Year 4 – Final IMD Design and Prototype IMD Component Construction

Bulent Sarlioglu

University of Wisconsin – Madison
1415 Engineering Dr
Madison, WI 53706
E-mail: sarlioglu@wisc.edu

Susan Rogers, DOE Technology Development Manager

U.S. Department of Energy
E-mail: susan.rogers@ee.doe.gov

Start Date: April 1, 2019   End Date: April 1, 2024
Project Funding: $300,000   DOE share: $300,000   Non-DOE share: $0

Project Introduction

The objective of the project is to research, design, develop, and test a high-performance traction motor and a high-efficiency traction inverter and then to combine them into a state-of-the-art integrated motor drive (IMD) that requires only a single housing for use in vehicle applications.

The new IMD system will significantly increase the motor and inverter power density values to meet the aggressive DOE targets while simultaneously taking steps to minimize their cost. The high-power-density, reduced-cost prototype IMD will become a valuable source of technical data that can be used by automakers and their suppliers to improve the performance of future EV traction drive systems.

Objectives

This project has two separate sets of performance targets for the power electronics and motor presented together in Table I.1.18.1.

Table I.1.18.1 Power Electronics and Motor Requirements

Power Electronics Requirement	
Parameter	**Measure**
Cost ($/kW)	≤ 2.7
Peak Power Density (kW/L)	≥ 100
System Peak Power Rating (kW)	100
Electric Motor Requirement	
Parameter	**Measure**
Cost ($/kW)	≤ 3.3
Peak Power Density (kW/L)	≥ 50
System Peak Power Rating (kW)	100

Approach

This project began with an evaluation of several types of electric motors and inverters that are candidates for future land-based vehicle traction applications. The evaluation results led to the selection of the most desirable machine plus inverter topology that is in the process of being developed into a working state-of-the-art prototype integrated motor drive (IMD).

During Budget Period #1, a literature review was carried out that set the stage for trade-off studies to evaluate several alternative motors and inverters that are candidates for adoption in the target integrated motor drive system. The motor configurations, as well as the power inverter topologies, were compared, leading to the selection of the surface permanent magnet (SPM) machine and the current source inverter (CSI) as the best candidates for further development.

During Budget Period #2, a preliminary motor electromagnetic design and power electronics electrical design has been carried out for the SPM machine and CSI power converter. A bench-top inverter was designed, fabricated, and tested to verify key IMD concepts and reduce technical risks. In addition, we carried out thermal and mechanical designs of the motor and inverter, including their physical integration into an IMD.

During Budget Period #3, the IMD design was finalized in preparation for prototype IMD construction. Construction of the prototype SPM machine and current source inverter was initiated. A dynamometer test stand was designed and assembled, including instrumentation for testing the motor and power inverter.

During Budget Period #4, the fabrication of the prototype SPM machine and current source inverter is being completed. These major system components are being integrated into the same IMD enclosure and made operational during the last quarter of this budget period. Initial tests will then be carried out to demonstrate the functionality of the prototype IMD.

During Budget Period #5, the combined prototype IMD system will be tested. The IMD performance will be measured to verify the ability of the prototype IMD to meet its performance targets.

Results

Bench-top prototype inverter

The CSI-based motor drive including the front-end dc/dc converter is shown in Figure I.1.18.1. This dc/dc converter is responsible for converting the battery voltage source into a regulated current that is delivered to the dc link of the CSI.
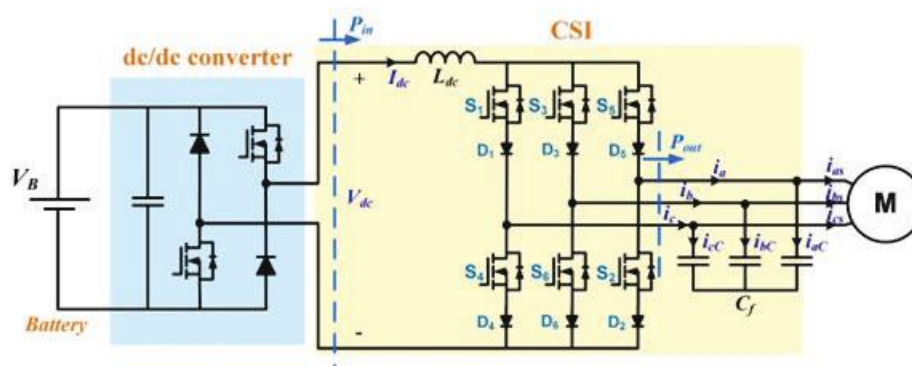
Figure I.1.18.1 Baseline CSI-based motor drive system for traction application

The design of the bench-top prototype CSI with discrete devices was presented in the last annual progress report. To reduce the switching oscillation and improve the power density of the prototype inverter, compact SiC MOSFET module [1] and SiC Schottky diode modules [2] were selected and the layout of the prototype inverter was optimized. Figure I.1.18.2 provides views of the fabricated benchtop prototype dc/dc converter, dc link inductors, and CSI. The fabricated module-based CSI designed for the IMD was tested with a three-phase *RL* passive load to evaluate the performance of the power electronics system. The DC power supply was initially operated in its current-limit mode to serve as a current source to supply the adjustable dc link current to the CSI.

| (a) dc/dc converter + dc-link inductors | (b) CSI |

Figure I.1.18.2 Fabricated benchtop prototype CSI + dc/dc converter system.

Measured experimental results showing the line-to-line voltage and phase current waveforms at the *RL* load terminals for an operating point with 400 $V_{LL,\text{peak}}$ line-to-line voltage and 70 $A_{phase,peak}$ are provided in Figure I.1.18.3. These conditions correspond to 22.8 kW delivered to the 3-phase *RL* load, which is approximately 50% of the required 55 kW continuous rated load in the IMD configuration. It can be observed that the CSI delivers sinusoidal output voltage and current waveforms to the machine that have higher waveform quality compared to the baseline VSI.
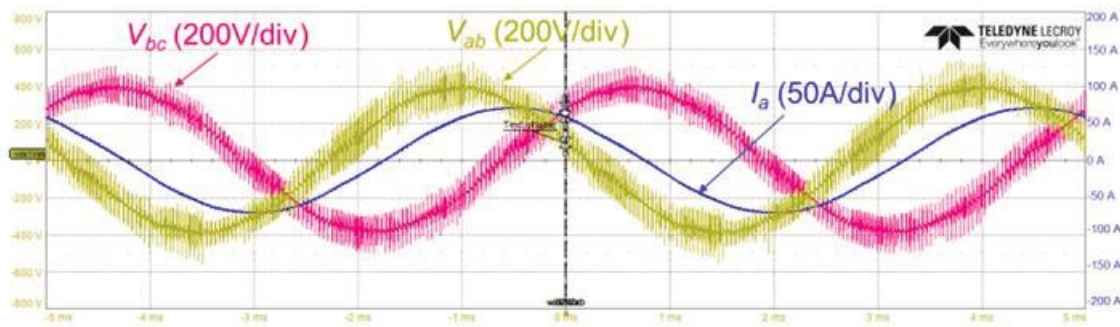
Figure I.1.18.3 Experimental measured waveforms of line-to-line voltage and phase current at RL load terminals for CSI operation at 400 $V_{LL,\text{peak}}$ line-to-line voltage and 70 $A_{phase,peak}$

These experimental results using the 3-phase benchtop CSI connected to an *RL* load demonstrate that changing the power switches from discrete devices to modules has significantly reduced the volume of the power electronics system and suppressed the peak voltage overshoot by 40%.

DC-link inductor design

The toroidal dc-link inductor was designed and fabricated using a toroidal powder core, as shown in Figure I.1.18.2 (a). The core material is High-Flux™ which has superior performance under the high dc current bias operating conditions, combined with low core losses and soft saturation characteristics. The inductance of each inductor is approximately 47 µH at the peak dc link current (210.1 A). If two inductors are used (one inductor in the positive dc-link and the other inductor in the negative dc-link), the total dc-link inductance is 93.92 µH. Efforts are being made to reduce the number of dc-link inductors to one using special PWM coordination of the dc/dc converter and CSI stages. The measured height of one inductor is 30.4 mm, the outer diameter is 95 mm, and the active volume is approximately 0.2 L. The CSI and dc-dc converter switching frequencies are 80 kHz to reduce the required inductance in the dc-link and achieve a compact inductor design. In addition, the 8 AWG equivalent Litz wire minimizes winding losses caused by ac proximity and skin effects. The estimated

total inductor winding and core losses at rated (55 kW) and peak (100 kW) conditions are shown in Table I.1.18.2.

Table I.1.18.2 Estimated Inductor Losses

System output power (kW)	55	100
I_{dc} (A)	141.5	210.1
Winding loss/inductor @ 120 ℃ (W)	371.9	825.5
Core loss/inductor (W)	36.4	22.6
Total loss/inductor (W) @ 120 ℃	408.4	848.1

Control development summary

The closed-loop control algorithm for the IMD is under development. The structure of the controller algorithm is shown in Figure I.1.18.4. The CSI's output voltages v_{as}, v_{bs}, v_{cs} and the current flowing in the traction motor (denoted as permanent magnet machine or PMSM in Figure I.1.18.4.) i_{as}, i_{bs}, i_{cs} are measured using voltage and current sensors, respectively. The rotor position θ_e is measured using the position sensor attached to the rotor shaft. The closed-loop control algorithm for the three-phase CSI is designed in the *dq* synchronous reference frame.
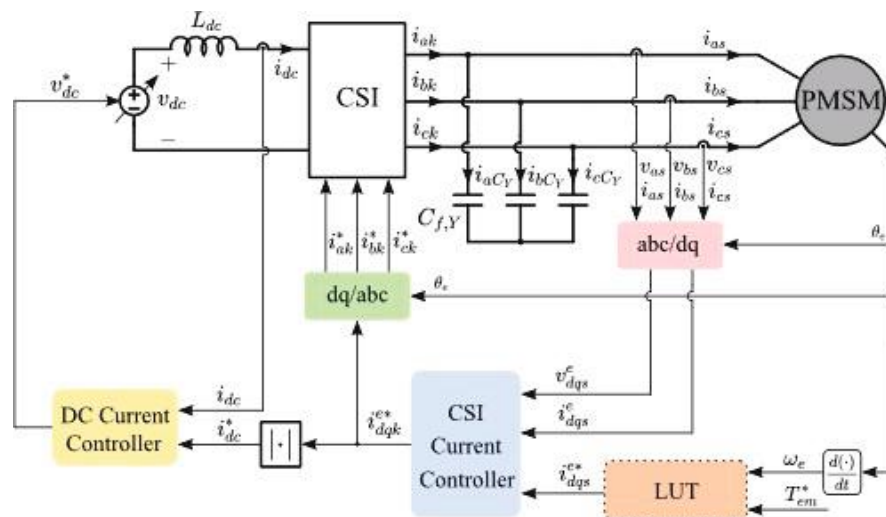
Figure I.1.18.4 Closed-loop control algorithm architecture for IMD

The dc-current controller is also designed for the dc-dc converter represented as the variable voltage source v_{dc} in Figure I.1.18.4. The dc-link current i_{dc} is regulated by the dc-dc converter by varying the output voltage. The dc-link current command is generated from the CSI current controller, as shown in Figure I.1.18.4.

Prototype machine design and fabrication

Based on the design requirements, the peak power is set at 100 kW and the continuous power is 55 kW. The maximum speed of the machine is 20,000 rpm, and the corner speed is 6,667 rpm, resulting in a constant power speed ratio (CPSR) of 3. As a result of these requirements, the rated torque of the machine for 55 kW operation is 78.8 Nm and the peak torque for 100 kW operation is 143.2 Nm. The active power density of the machine is 50 kW/L, and no heavy rare earth magnet material is used in the machine design.

The SPM machine design was presented in the last annual report. A decision was made during this past year to build a second rotor using a surface inset permanent magnet (SIPM) geometry. The major difference between the two rotors is that the SPM rotor uses a carbon fiber sleeve to contain the magnets, while the SIPM rotor

uses a thin strip of lamination steel around the outer surface of the magnets to perform this containment function. Both rotors are designed for use in the same stator. Figure I.1.18.5 provides a cross-section view of the SIPM machine including the identification of concentrated stator winding, stator and rotor cores, and rotor magnets. Figure I.1.18.6 shows the predicted flux density distribution in the SIPM rotor and stator for rated 55 kW, 6,667 rpm operation. The designed SIPM machine can operate at a maximum speed of 20,000 rpm and peak power at 100 kW to meet the same performance requirements as the machine using the SPM rotor.
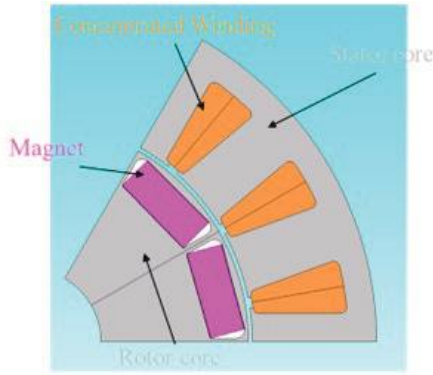
Figure I.1.18.5 cross-section view of SIPM machine
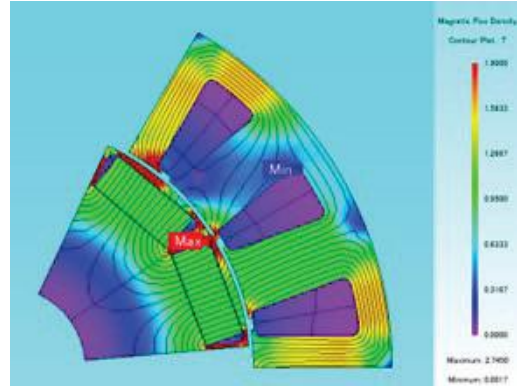
Figure I.1.18.6 Predicted flux density distribution for rated 55 kW, 6,667 rpm operation

This year, the team worked to finalize the remaining details of the electric machine design in preparation for the prototype machine fabrication. Frequent communications were held with the engineers at Arnold Magnetic Technologies (AMT), the vendor responsible for fabricating the final prototype machine, to complete the fabrication plans. The UW project team members and the AMT engineers worked together to generate and share 3D models of the machine assembly, as well as engineering drawings for individual components, in order to clearly define all of the machine design features. An exploded view of the most recent 3D model of the prototype machine assembly is provided in Figure I.1.18.7. The AMT team used the shared 3D model to review the design features and evaluate the manufacturability of the prototype integrated machine drive. This led to detailed discussions about the purpose of specific features, suggested design changes to make the fabrication process less costly, and the impact of the changes on the machine's operating characteristics and performance.
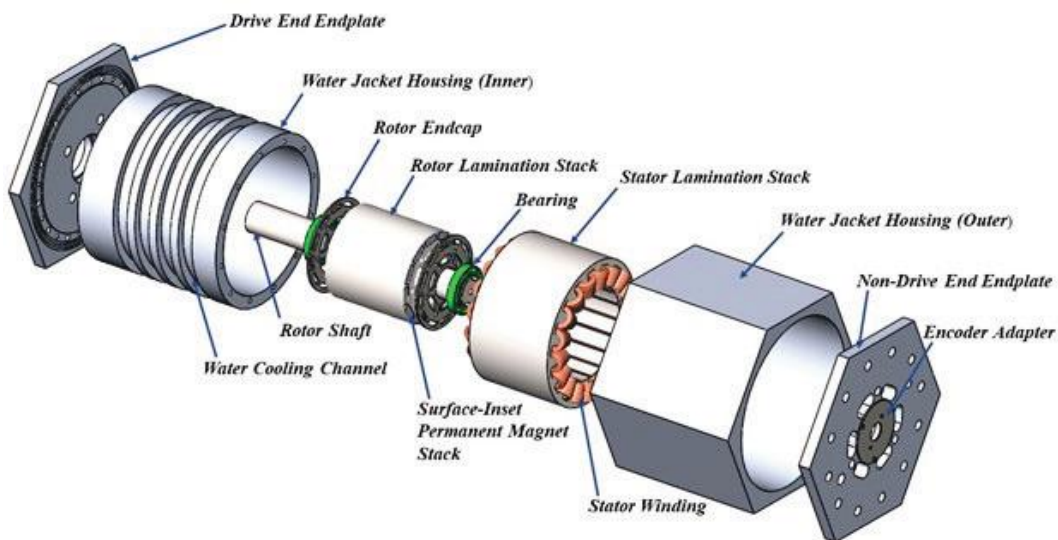
Figure I.1.18.7 Exploded view of the prototype integrated machine drive 3D assembly model

First-tier components with longer lead times and more influence on the fundamental assembly parameters were finalized first, while components with shorter lead times and design features that depended on those of the first-tier components followed afterward. Manufacturing drawings were generated for each individual machine component via a collaborative effort with the AMT engineers.

Overall IMD layout including 3D mockup and fabricated IMD components

A mock-up version of the machine housing has been 3D printed, and the dc-link inductor cooling cup has been fabricated. Figure I.1.18.8 (a) shows a conceptual rendered drawing of the IMD. The fabricated printed circuit boards for the benchtop 100 kW (pk) CSI and dc/dc converter have been designed, built, and mounted on a 3D-printed hexagonal housing, as shown in Figure I.1.18.8 (b). This mock-up exercise was carried out to move beyond the conceptual IMD drawings to a physical 3D structure in order to retire technical risks associated with the integration of the machine and the power electronics components. It should be noted that larger film capacitors were used in the benchtop CSI during the preliminary tests of the CSI operation, and they appear in the mock-up version of the IMD shown in Figure I.1.18.8 (b). In the final version of the IMD, much smaller ceramic capacitors will replace the film capacitors to significantly reduce the volume of the prototype IMD unit, as shown in Figure I.1.18.8 (a).

(a) (b)
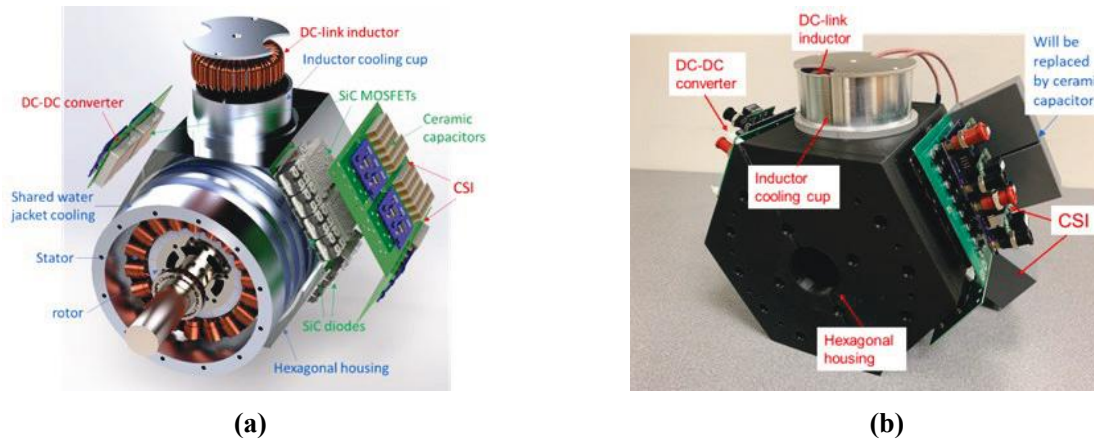
Figure I.1.18.8 Radially mounted integrated motor drive. (a) 3D rendered drawing of the conceptual integration of the machine and power electronics. (b) IMD mock-up unit including power electronics mounted on the 3D printed hexagonal housing with dc-link inductor cooling cup

Three views of fabricated components of the prototype IMD unit are provided in Figure I.1.18.9.

(a) (b) (c)
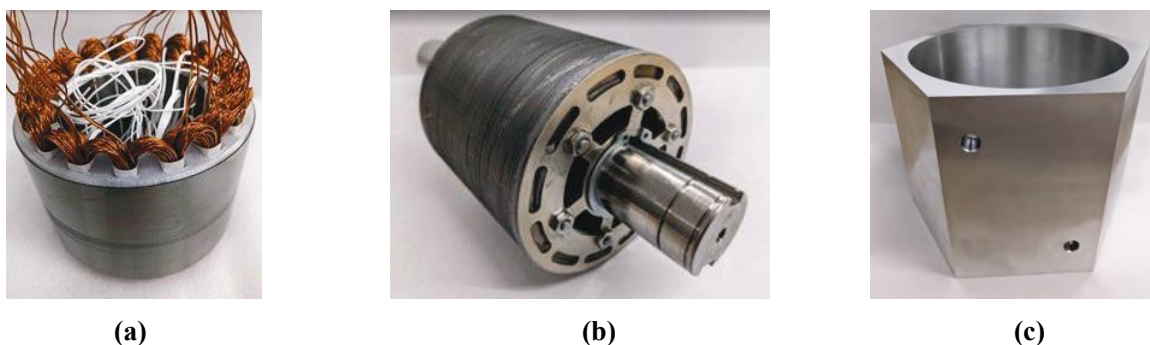
Figure I.1.18.9 Views of fabricated components of prototype IMD unit. (a) Assembled machine stator.
(b) Assembled SIPM rotor. (c) Aluminum IMD housing showing hexagonal outer mounting surfaces for current source power converter and water coolant inlet/outlet ports

Thermal system design

Thermal management is a critical feature of the integrated motor drive. Heat losses generated by both the power electronics and the motor must be dissipated via a well-designed cooling system to maintain all component temperatures within their maximum limits. An integrated cooling system shown in Figure I.1.18.10, including two different cooling techniques, is designed to minimize the total volume of the IMD. The water jacket dissipates heat from the stator assembly and the power electronics. Forced air that enters through the machine's drive-end endplate and exits through the non-drive-end endplate flows through the airgap and rotor ducts to remove heat from the rotor, stator inner bore, and end windings. In addition to dissipating the maximum steady-state heat losses when delivering rated 55 kW power at both rated and maximum speeds, the cooling system must safely dissipate significantly higher losses for 30 sec periods when operating at peak 100 kW power at rated speed.
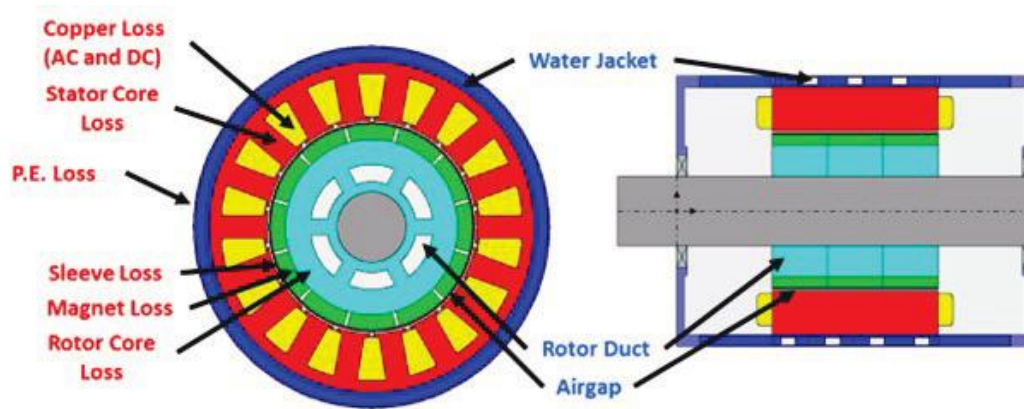
Figure I.1.18.10 Radial and axial view of the machine with the SPM rotor highlighting the machine loss sources and the water and air cooling system features

Power losses calculated from electromagnetic FEA results are the heat sources positioned in different parts of the IMD. Convection coefficients and related reference coolant temperatures calculated from CFD results shown in Figure I.1.18.11 provide the cooling boundary conditions of the cooling system. These inputs are then fed to the corresponding thermal FEA models to evaluate the thermal performance of each part of the IMD system.

(a)   (b)
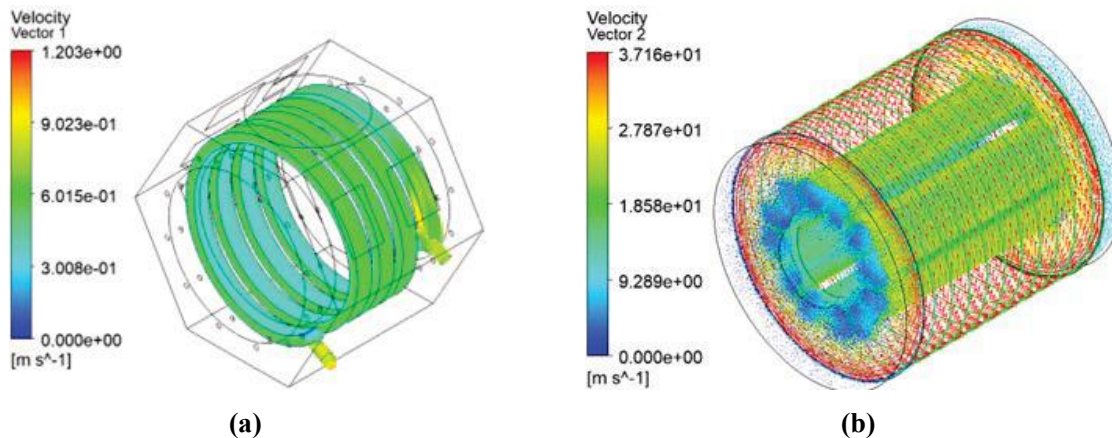
Figure I.1.18.11 CFD calculated speeds of fluid coolants. (a) Water jacket (b) Rotor forced air cooling

The predicted temperatures of each critical IMD component at the end of the 30 sec period during 100 kW operation are shown in Figure I.1.18.12. The predicted peak temperatures of the machine winding, magnets, and dc-link inductor are 192.0 °C, 65.5 °C, and 153.8 °C, respectively, which all fall safely within their thermal limits. This analysis shows that the designed cooling system can safely limit IMD temperatures at all operating points.

(a)   **(b)**
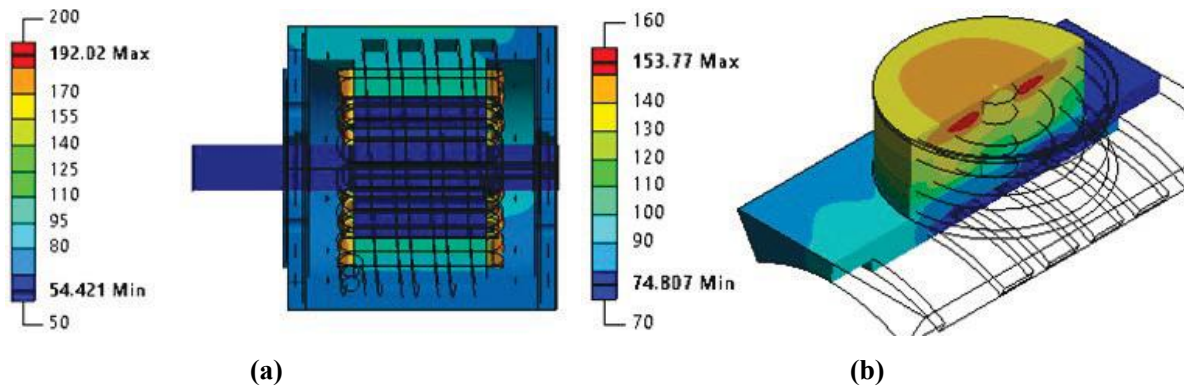
Figure I.1.18.12 Predicted IMD temperature distribution at the end of 30 s period during 100 kW peak power operation. (a) Machine (b) DC-link inductor

Conclusions

Major progress has been accomplished during the past year toward the objective of building and testing the prototype integrated motor drive unit designed to meet aggressive DOE performance targets and power density metrics. More specifically, the designs of the prototype SPM machine and the current source power converter have been completed, and fabrication efforts are well underway. A second rotor using a surface inset permanent magnet (SIPM) geometry is also being fabricated for testing in the same stator, providing a welcome opportunity to explore a promising approach for lowering the rotor cost by eliminating the carbon fiber sleeve required for the baseline SPM rotor.

Delivery of the prototype machine with the SIPM rotor is scheduled to occur before the end of the calendar year 2022, setting the stage for machine characterization and testing during the last quarter of Budget Year #4. Fabrication and testing of the current source power converter are proceeding in parallel. Plans call for the tested machine and power converter subsystems to be combined together into the final prototype IMD configuration before the end of BY#4, consistent with the SOPO project plans. This will set the stage for dynamometer testing of the complete prototype IMD unit during BY#5, the final year of this project. Based on all analytical and preliminary test results gathered to date, the prospects for meeting the key project objectives are very promising.

Key Publications

1. S. Lee, W. Feng, F. Chen, K. Chen, T. M. Jahns, and B. Sarlioglu, "Modeling of RMS current in CS filter capacitor and minimum conduction loss operation of CSI-fed PMSM drives for traction applications," in *Proc. IEEE Transportation Electrification Conference & Expo (ITEC)*, 2022, pp. 720-726.

2. S. Lee, R. A. Torres, F. Chen, T. M. Jahns, and B. Sarlioglu, "Thermal Stress Reduction in Power Devices using Distributed Loss PWM for CSIs," in Proc. *IEEE Energy Conversion Congress & Expo. (ECCE),* Detroit, MI, 2022.

3. F. Chen, S. Lee, T. M. Jahns, and B. Sarlioglu, "A High-Accuracy Power Loss Model of SiC MOSFETs in Current Source Inverter Considering Current Commutation and Parasitic Parameters," in Proc. *IEEE Energy Conversion Congress & Expo. (ECCE),* Detroit, MI, 2022.

4. F. Chen, S. Lee, T. M. Jahns and B. Sarlioglu, "Comparative Investigation of Current-Source Inverters using SiC Discrete Devices and Power Modules," in Proc. *IEEE 9th Workshop on Wide Bandgap Power Devices & Applications (WIPDA),* 2022, pp. 215-220.

References

1. "Datasheet FF6MR12W2M1_B70," Infineon, accessed December 1, 2022,
   https://www.infineon.com/dgdl/Infineon-FF6MR12W2M1_B70-DataSheet-v02_00-
   EN.pdf?fileId=5546d46277fc7439017839e7ffac498c

2. "GHXS100B120S-D3_Summary," SemiQ, accessed December 1, 2022,
   https://semiq.com/pdf/GHXS100B120S-D3.pdf

I.1.19 Multi-Objective Design Optimization of 100 kW Non-Rare-Earth or Reduced-Rare Earth Machines (Purdue University)

Scott Sudhoff, Principal Investigator
Purdue University
1285 Northwestern Avenue
West Lafayette, IN 47906
E-mail: sudhoff@purdue.edu

Steve Pekarek, Co-Principal Investigator
Purdue University
1285 Northwestern Avenue
West Lafayette, IN 47906
E-mail: spekarek@purdue.edu

Susan Rogers, DOE Technology Development Manager
U.S. Department of Energy
Email: Susan.Rogers@ee.doe.gov

Start Date: May 15, 2022   End Date: May 14, 2023
Project Funding: $300,000   DOE share: $300,000   Non-DOE share: $0

Project Introduction

The goal of this project is to reduce the size, weight, cost, and losses associated with rotating electric machinery and its associated power electronics for electric and hybrid vehicle applications. In particular, the goal of this effort is to facilitate electric machinery that will meet the requirements set forth in the U.S.DRIVE Electrical and Electronics Technical Team Roadmap of October 2017. This document calls for an electric machine with a peak power of 100 kW, a continuous rated power of 55 kW, a peak speed of less than 20,000 rpm, a volume of no more than 2 liters, a mass of less than 20 kg, and a useful life of 15 years or 300,000 miles of vehicle service. This will be achieved through a combination of (i) new materials, (ii) new electric machine topologies, (iii) advances in power electronics, and (iv) superior design through the use of formal and rigorous multi-objective optimization-based design built on advanced analysis techniques. This effort is being conducted by a large consortium comprised of national laboratories (Sandia National Laboratories, Oak Ridge National Laboratories, Ames National Laboratory, and the National Renewable Energy Laboratory) and universities (Virginia Tech, Georgia Tech, SUNY, Arkansas, Ohio State, IIT, Purdue, University of Wisconsin – Madison, University of California Berkeley, and North Carolina State). Purdue's role focuses on (ii) and (iv).

Objectives

The objective of this effort is to explore the use of new materials and develop new design paradigms to enable unprecedented propulsion motor power densities at a reduced cost. In order to achieve this objective, Purdue's goals will be to investigate new machine topologies, such as the homopolar ac machine, and to develop new improved design codes which (*i*) incorporate high switching frequency performance analysis, (*ii*) thermal performance, (*iii*) high-speed rotor structural analysis, and (*iv*) advanced magnetic analysis techniques into its existing design paradigm based on rigorous multi-objective optimization in order to take best advantage of new materials and machine topologies developed by Purdue and other team members. An additional objective will be to build and test a prototype machine whose design is based on the enhanced design paradigm developed under this effort.

Approach

To achieve the objectives described in the previous section, Task 4.1 is the focus of the fourth year of the program. The SOPO for the fourth year of this effort and Task 4.1 are summarized below.

Milestone	Type	Description	Status	Completion Date
DHAM design code revision	Technical	The design code for the winning topology will be revised in accordance with any opportunities of improvement and a final design will be selected by the end of BP4: Q1	Complete	June 31, 2022
DHAM final design validation	Go/No Go	The design will be validated using 3rd party FEA tools while also demonstrating reasonable agreement between the design code magnetic analysis and FEA analysis. This will be complete by BP4: Q2	Complete	September 30, 2022
Inverter completion	Technical	The inverter and support electronics will be complete by BP4: Q3	In Progress	N/A
DHAM prototype completion	Technical	At the end of BP4: Q4, the prototype machine will be completed (including integration with the inverter)	In Progress	N/A

Results

Before discussing the results, is appropriate to review the performance requirements. These are shown in Figure I.1.19.1 and have not been changed since the previous budget period. Recall that the requirements were based on the ORNL-led machine group within the VTO consortium. The key requirements include a maximum operating speed at 20,000 rpm, a 55-kW continuous power, and a 100-kW peak power. The 3:1 constant power speed range ensures good driving characteristics for passenger vehicles. Note that to characterize these requirements, six operating points are considered. The weighting of these operating points in determining aggregate loss is also indicated in the figure.

In the remainder of this section, results will be presented for the Dual Rotor Homopolar AC Machine (DHAM), Inert Core Permanent Magnet Machine (ICPM), and Asymmetrical Reluctance Machine (ARM).

α_{CPSR}	3
$P_{mx,pk}$ (kW)	100
$P_{mx,ct}$ (kW)	55
$P_{nom,ct}$ (kW)	27.5
$\omega_{rm,mx}$ (rpm)	20,000
$\omega_{rm,crn}$ (rpm)	$\omega_{rm,mx}/\alpha_{CPSR}$
$\omega_{rm,nom}$ (rpm)	$\sqrt{\omega_{rm,crn}\omega_{rm,mx}}$

	Op1	Op2	Op3	Op4	Op5	Op6
Speed	$\omega_{rm,crn}$	$\omega_{rm,crn}$	$\omega_{rm,mx}$	$\omega_{rm,crn}/2$	$\omega_{rm,nom}$	$\omega_{rm,crn}/4$
Power	$P_{mx,pk}$	$P_{mx,ct}$	$P_{mx,ct}$	$P_{mx,ct}/3$	$P_{mx,ct}/3$	$P_{mx,pk}/4$
Weight	5%	15%	5%	20%	40%	15%
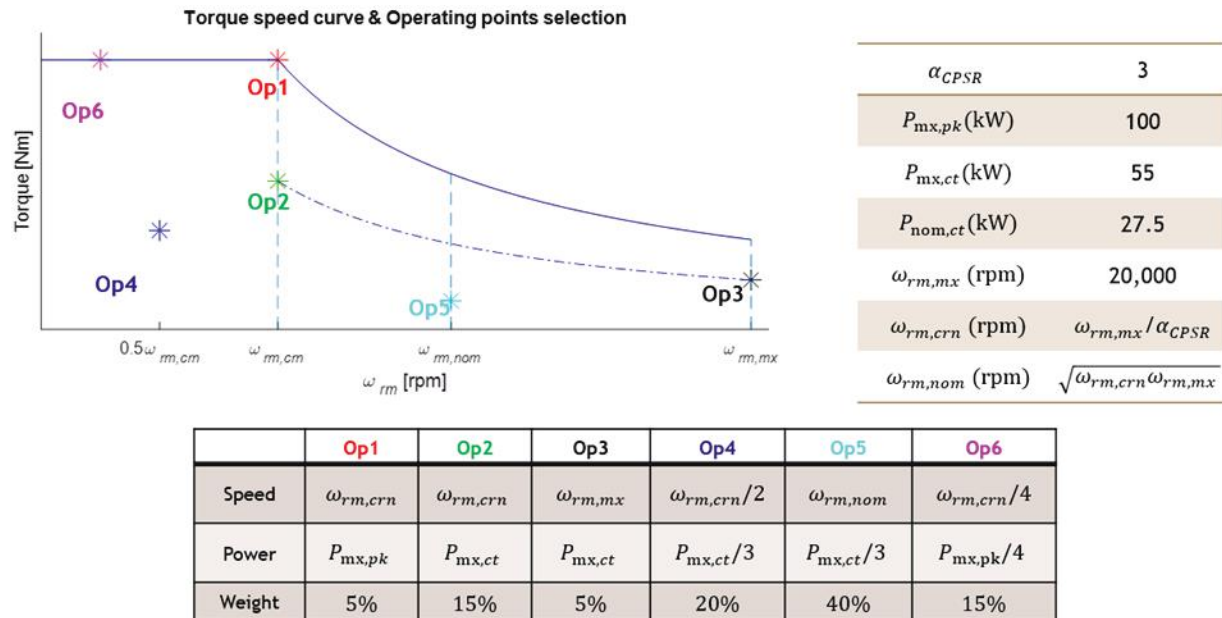
Figure I.1.19.1 Performance requirements.

Dual Rotor Homopolar AC Machine

The Dual Rotor Homopolar AC Machine (DHAM) is a novel rotating electric machine which can operate either as a motor or as a generator. The advantages of the machine include that it is conductive to low mechanical stresses even in high-speed designs, it is conducive to using rare-earth free magnets, it is easy to cool, and, in the permanent magnet version, it is the only permanent magnet machine with an infinite constant power speed range. The design code was revised during BP4:Q1 and key parameters within the rotor shaping algorithm were improved. The corresponding airgap reluctance is validated by commercial FEA software. Another major area of the revision was implemented in the thermal analysis. A thermal equivalent circuit (TEC) network model has been added to the design code to predict the machine operating point temperature and losses. Like the magnetic analysis, the TEC temperature results were validated by a thermal FEA using commercial software.

During BP3, the DHAM was compared to a standard surface mounted permanent magnet ac machine (PMAC), but without a thermal model. In order make a better comparison, a thermal analysis was added to both design codes. The revised machine optimizations were conducted with 2 sets of metrics: minimize size vs aggregate loss and minimize cost vs aggregate loss. Herein, the results for size vs loss are shown in Figure I.1.19.2. The plots include 3 different optimization runs. The blue curves represent performance obtained with the DHAM using Dysprosium-free magnets, the performance obtained using a DHAM with a ferrite magnet is depicted by the red curves, and the yellow curves captures the PMAC using any (including rare-earth) PM material. As can be seen, the inexpensive ferrite DHAM has a Pareto-Optimal front that exceeds that of the rare-earth PMAC. Since the DHAM has an inherent cooling advantage, it can use the Dy-free PMs. Figure I.1.19.2 shows that the Dy-free neodymium-iron-boron PM DHAM dominates the rare-earth based PMAC. The maximum torque density of the DHAM more than doubles that of the PMAC, reaching close to 50 kW/L.
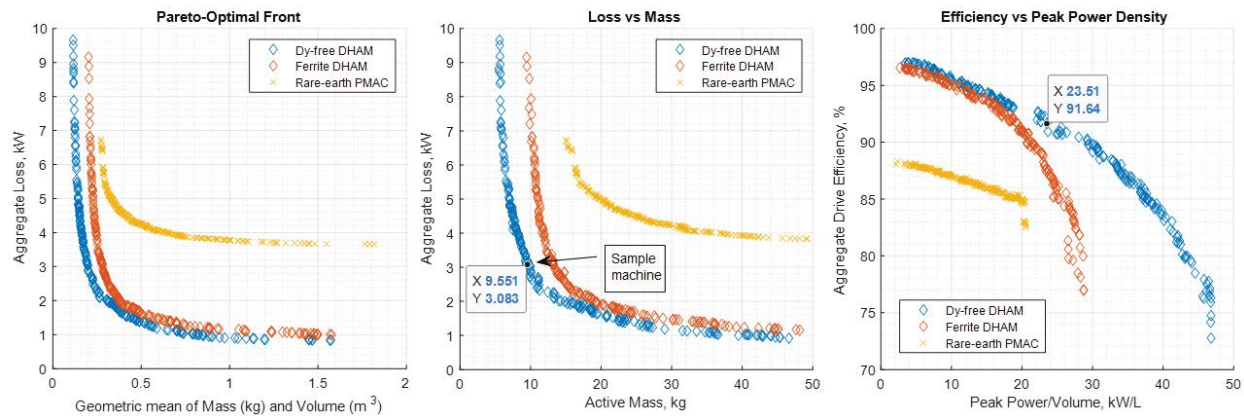
Figure I.1.19.2 DHAM and PMAC comparisons.

Cross sectional diagrams and 3D CAD rendering of a 23.5 kW/L Dy-free DHAM are shown in Figure I.1.19.3. The performance of this sample machine is also denoted within Figure I.1.19.2. The revised design model now yields DHAM with more attainable rotor geometry. This sample has 10 poles and a large inert region inside the rotor steel. A 3D CAD rendering of 100-kW DHAM at 23.5 kW/L machine is included in Figure I.1.19.3. The support structures in the form of 2 slotted end bells are to be seen therein.
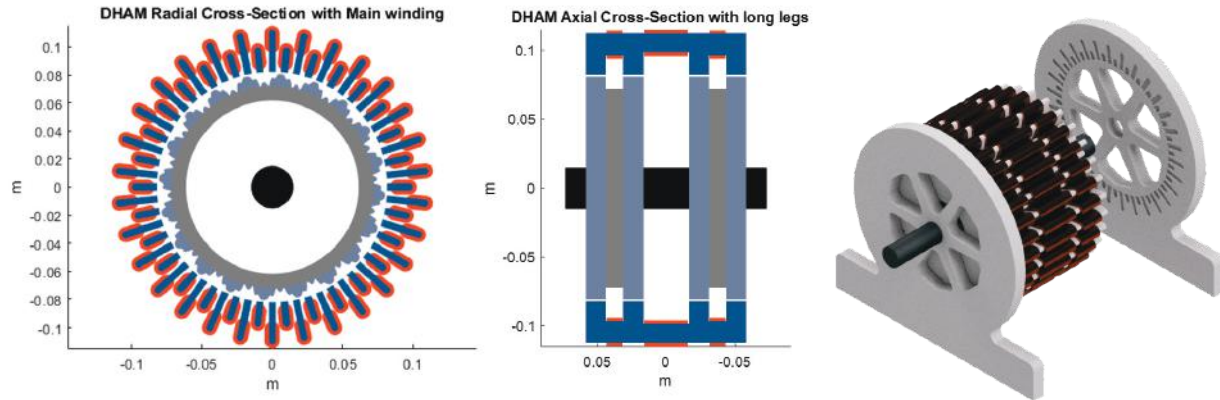
Figure I.1.19.3 23.5 kW/L Dy-free DHAM.

A proof-of-concept DHAM prototype has been designed. This prototype machine has a 10-kW continuous power rating, a peak power of 18-kW, and a maximum speed of 20,000 rpm. The prototype was validated using FEA to test its EM and thermal capabilities. Figure I.1.19.4 depicts 18-kW DHAM in FEA environments and plots the airgap reluctances. The figure on the left shows the field distribution of the 6-pole, 18-stator-leg prototype design. The blacklines outside the steel region sketches the windings and the overall 3D FEA solution domain. The plots on the right side of Figure I.1.19.4 illustrate the airgap reluctances in alpha and beta rotor ends respectively. The curves are calculated via FEA flux and field intensity results. As can be seen, The FEA reluctances match the desired sinusoidal waveforms well. This indicates that the revised rotor shaping algorithm is working as intended. Since the torque is produced within the airgap of the machine, the matching reluctance results lays solid foundation for obtaining the anticipated torque production.
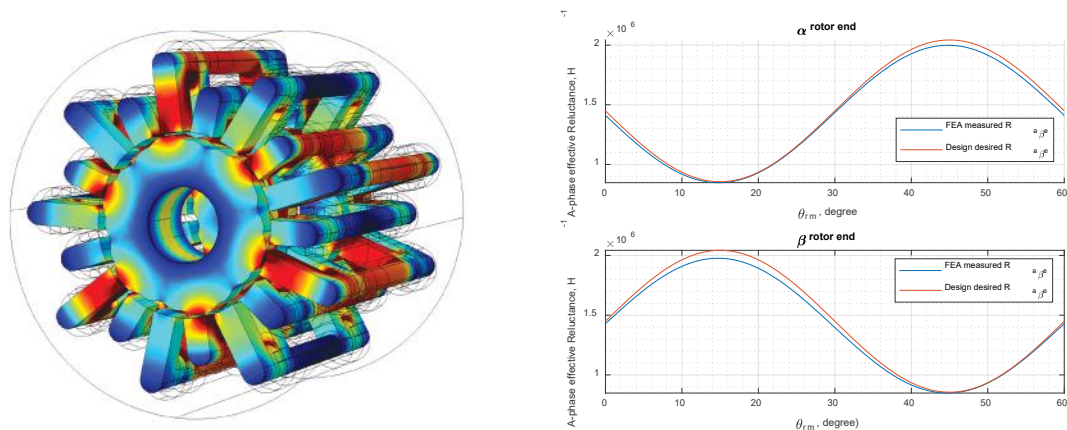
Figure I.1.19.4 Prototype DHAM FEA results.

Torque is produced individually in all 4 air-gap regions of the DHAM. The FEA torque results are plotted in Figure I.1.19.5. Therein, the torque production of each air-gap region is illustrated separately to the total torque. Individual air-gap regions have large torque ripple, as expected. The total torque is ideally constant because the torque ripple of the four airgaps will ideally cancel. However, the upper and lower rotor end air gaps don't produce the exact amount of desired torque. The ideal DHAM model ignores the steel reluctances while FEA accounts for all. Nonetheless, the torque FEA predicted torque is within 1 Nm of the desired torque.
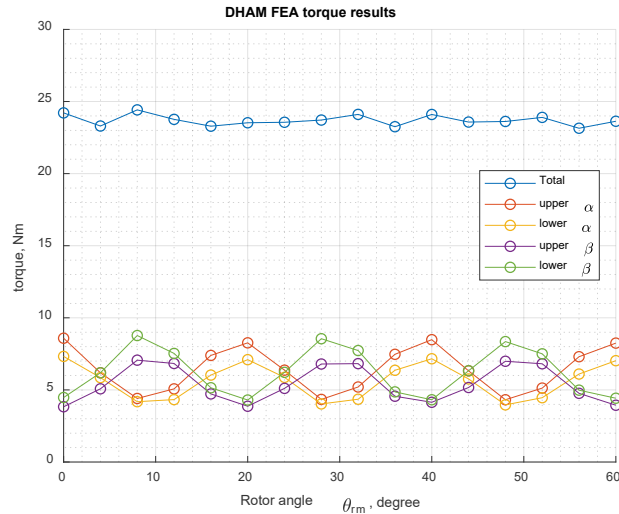
Figure I.1.19.5 Prototype DHAM torque results.

Figure I.1.19.6 depicts cut-off views of the complete prototype DHAM. The rotor ends are secured to the shaft by collar clamps and shaft keyways. Notches on the inner radius of the rotor ends are added to properly align the alpha and beta rotor ends. The stator legs extend into the end bells for alignment and fastening purposes.
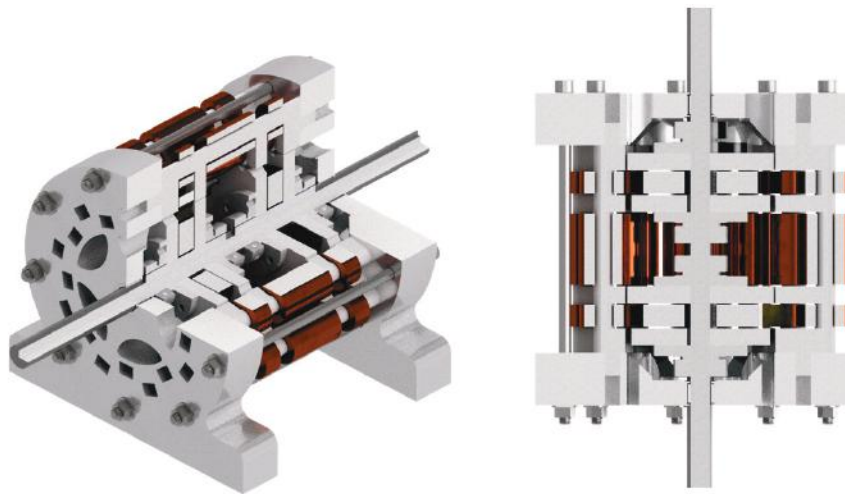
Figure I.1.19.6 Prototype DHAM CAD cut-off views.

The prototype construction is currently in progress. The housing part of the design includes machining the rotor shaft, laser cutting the end bells, and 3D printing encoder holder. All other parts are off-the-shelf. The majority of the parts has been made and assembled as shown in Figure I.1.19.7. The stator and rotor laminations are currently being made by Carpenter Technology. Laminations have been cut, and are now being bonded. It is also worth noting that the inverter module to drive the DHAM prototype is near completion, and it is shown in Figure I.1.19.7. The inverter uses SiC switches with TI microcontrollers which can clock over 200 MHz. The inverters is more than capable of driving the 6-pole DHAM prototype at 20,000 rpm.
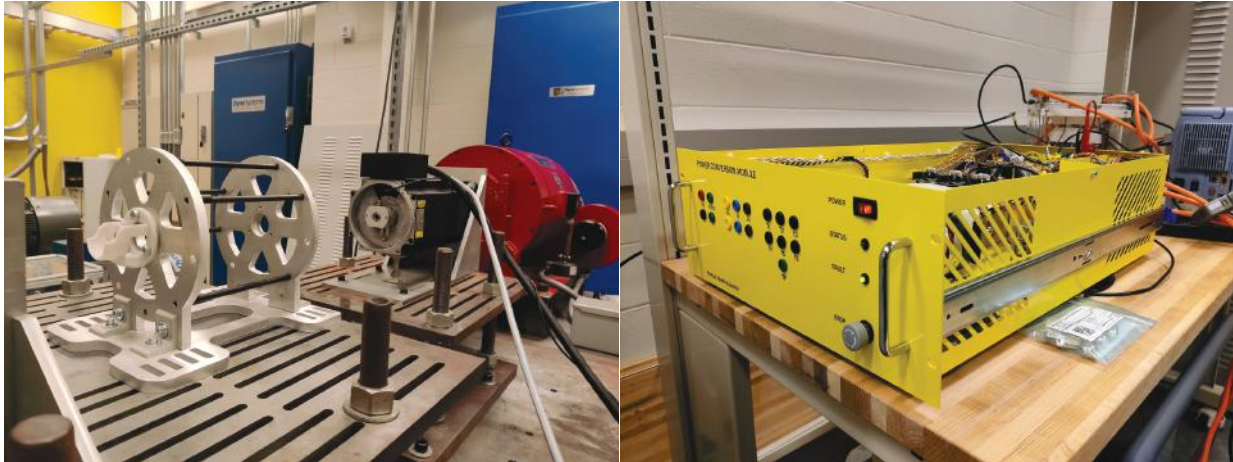
Figure I.1.19.7 Prototype DHAM frame (left) and inverter (right).

We have also been further developing the inert-core machine and the asymmetric reluctance machines and the design codes based upon our method-of-moments modeling technique. A size-competitive ICM topology from BP3 is shown in Figure I.1.19.8. The ICM shown has embedded slot cooling and reached power densities on the order of 30 kW/L for the specified driving cycle. It is recognized that this is a bit shy of the target, and lower than the power density of the DHAM. It also requires a dual Halbach array (one on an inner rotor and one on an outer rotor). This is certainly a disadvantage of the geometry. However, we are modifying the ICM to potentially improve its performance by first creating a new in-slot cooling approach wherein a cooling pipe made of a thermally conductive plastic, such as CoolPoly is notched to increase the contact surface between the pipe and the stator conductor. This is shown in Figure I.1.19.8. We are also eliminating the outer rotor and its corresponding Halbach array and replacing it with a stationary steel cylinder that will serve as a flux path as well as a means to prevent flux outside of the machine. The design code for this new ICM is presently being finalized and in BP4 Q3 Pareto fronts of the new ICM will be developed and compared to the alternatives, including the DHAM.
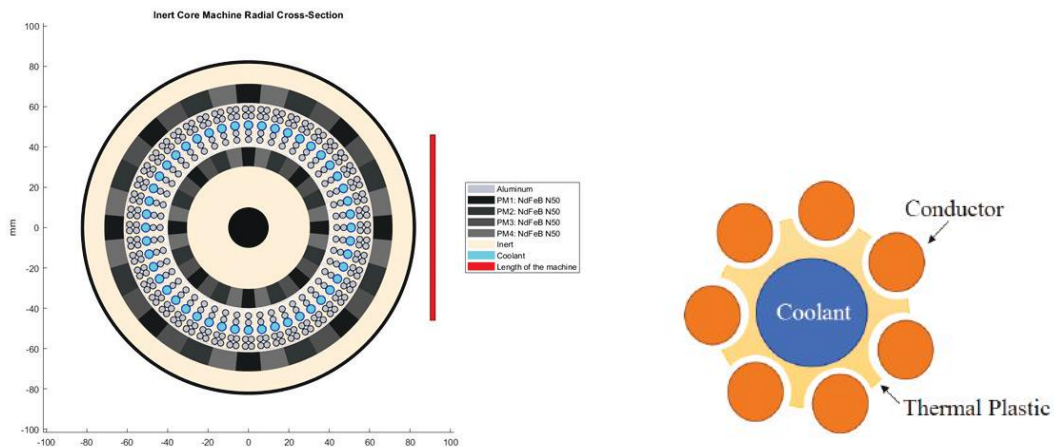
Figure I.1.19.8 Inert-core machine (left) and new notched-pipe cooling topology (right).

For the ARM topology, we recognize that it is not competitive from a power-density perspective. Specifically, the best we could achieve was on the order of 2 kW/L. The attractiveness of the ARM, however is really in its simplicity, that no magnets are used in the design, and the relative ease of construction. As a result, we have focused on designing ARMS that minimize material cost. We have been able to achieve designs that have electromagnetic material cost on the order of $150 for the given drive cycle, which may still make it attractive

when considering overall manufacturing cost. The cross-section of the $150 ARM design (at weighted drive cycle loss of 3 kW) is shown in Figure I.1.19.9.
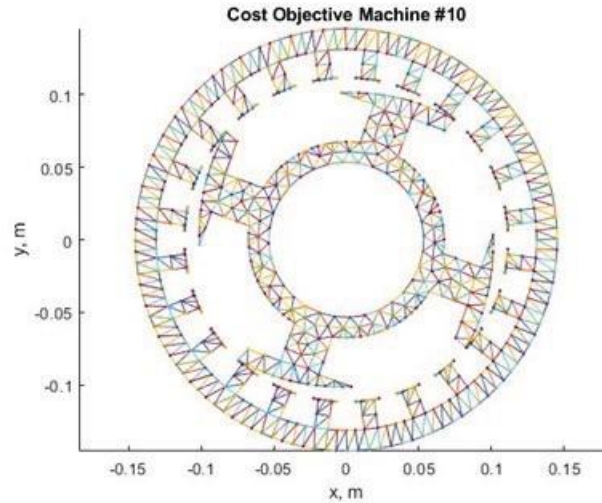
Figure I.1.19.9 Low-cost version of ARM.

Finally, a focus of has been on several updates related to the method-of-moment (MoM) toolbox that we developed the foundation for in BP1 and BP2. For one, we are updating our codes to perform calculation of winding flux linkage and winding inductance using closed-form expressions, rather than numerical approximations. Specifically, in traditional approaches for machine analysis that rely on the finite element method, the unknown is the magnetic vector potential. Knowledge of the magnetic vector potential enables direct calculation of the winding flux linkage using:

$$\lambda = \int_C \mathbf{A} \cdot dl$$

where C is the path of the winding, $\mathbf{A}$ the magnetic vector potential, and λ the winding flux linkage. Within MoM, the unknown is the tangent component of magnetization. To compute flux linkage within the MoM, we have developed a technique in which the magnetization is first used to establish the bound current on the material surface. Knowledge of the bound current enables one to replace the magnetic material with the bound currents and treat the system as a set of free and bound currents in free space. Subsequently, we have shown that analytical expressions for the vector magnetic potential from filaments in free space can be leveraged to obtain closed-form expressions for the contributions of the winding flux linkage that result from all free and bound currents. These expressions have been validated by comparing calculations with a converged FEA. A representative comparison for self- and mutual-inductance between windings of a machine are shown in Table I.1.19.1. The MoM-based toolboxes have been updated to include the calculation technique.

Table I.1.19.1 MoM versus FEA for validation of inductance/flux linkage calculation technique.

Method	No. Elements	Inductance (µH/m)							
		L_m	Err (ppm)	L_{nm}	Err (ppm)	L_n	Err (ppm)	L_{mn}	Err (ppm)
MoM	104	89.3042	−2085.66	−352.5085	−2385.86	1431.6777	−2216.80	−352.4547	−2232.53
MoM	416	89.1310	−141.85	−351.7168	−134.64	1428.6726	−113.09	−351.7193	−141.19
MoM	1664	89.1199	−17.39	−351.6712	−4.92	1428.5331	−15.46	−351.6713	−4.97
MoM	6656	89.1190	−7.28	−351.6675	5.64	1428.5210	−6.97	−351.6675	5.90
MoM	26 624	89.1189	−6.29	−351.6672	6.65	1428.5197	−6.08	−351.6672	6.93
FEA	9 169 966	89.1183	0	−351.6695	0				
FEA	13 576 186					1428.5110	0	−351.6696	0

Conclusions

The main conclusion is that the DHAM seems to be a very promising technology for the vehicle market. This year's work should be critical in bringing this technology to fruition. The ICP also has promise; however, there is more work that needs to be done on this machine.

Key Publications

1. Scott Sudhoff, Jiazhou Zhong, Steve Pekarek, "Dual Rotor Homopolar AC Machine," nonprovisional patent application submitted to U.S. patent office in November 2021. Attorney docket number PRF-69245-02.

2. D. Horvath, R. Howard, S. Pekarek, "Calculating Inductance in 2D Method of Moments," IEEE Transactions on Magnetics, in review.

Acknowledgements

I.1.20 Cost competitive, high-Performance, highly Reliable (CPR) Power Devices on SiC and GaN

Woongje Sung, Principal Investigator
Research Foundation for SUNY Polytechnic Institute
257 Fuller Rd
Albany, NY 12203
E-mail: wsung@sunypoly.edu

Susan Rogers, DOE Technology Development Manager
U.S. Department of Energy
Email: Susan.Rogers@ee.doe.gov

Start Date: April 16, 2019   End Date: April 15, 2024
Project Funding: $333,000   DOE share: $300,000   Non-DOE share: $33,000

Project Introduction

The primary objective of this project is to ensure that the next-generation of wide-bandgap devices have sufficient performance, reliability, and price to achieve the system-level DOE goals. In this project, we will develop 1200V SiC MOSFETs that are superior to Silicon counterpart (IGBT) in all aspects, such as cost, performance, and reliability. To accomplish the goal, many different variations in device/process design will be pursued and the proposed device will be fabricated at a production-grade cleanroom facility.

Objectives (BP3)

- Cost competitive

- High-performance (BV=1700 V, $R_{on,sp}$=4 mΩ-cm^2, V_{th}=2 V)

- High reliability (Short Circuit SOA of >4μs, TDDB> 10 C/cm^2, PBTI < 0.5V, HTRB 1000hrs at 1460V).

Approach

Over the 5 years of the entire project span, this project aims to develop cost competitive, high performance, and highly reliable SiC MOSFETs to assist the team to achieve system level DOE goal.

Cost

A dramatic reduction in chip price can be achieved by conducting ion implantations at room temperature (RT). The process flow will be significantly simplified by RT implants. Appropriate analyses due to RT implants will be conducted. An innovative approach for the gate oxide formation will further reduce the chip size, and thus, chip price. Unipolar diode integration within the MOSFET structure will be demonstrated.

Performance

Cell optimization will be carried out using 2-D simulation, such as reducing cell pitch and optimization of the JFET region. Various edge termination structures, such as FFRs, RA-JTE, and Hybrid-JTE will be designed. Process split, such as gate oxide using ALD, self-alignment channel, and channeling implant to form deep junction will be conducted.

Reliability

Short-circuit and avalanche characteristics will be evaluated by mixed-mode device simulations. Process splits such as p-well implant and thin gate oxide will be carried out.

Results

1. Characterization for MOSFETs with short channel length and deep P-well [1]

Despite many efforts to increase channel mobility, the channel resistance still accounts for a large portion of the total on-resistance for 1.2 kV SiC MOSFETs. To further reduce the channel resistance, short channel lengths are preferable. However, short channel lengths cause a high leakage current from the channel during the blocking-mode of operation, resulting in a reduction in the breakdown voltage (BV). Additionally, short channel lengths result in poor short-circuit withstand time (SCWT) due to the larger saturation currents. In order to break the conventional trade-off relationship between $R_{on,sp}$ and BV or the SCWT, SiC MOSFETs with short channel (0.3 μm) and deep P-wells (1.8 μm) are proposed by SUNY Polytechnic Institute.

Figure I.1.20.1 (a) and (b) show the cross-sectional view of the conventional and proposed MOSFETs, respectively. The channel length (L_{ch}) was varied to investigate the trade-off between $R_{on,sp}$ and BV or the SCWT. L_{ch} of 0.3, 0.4, and 0.5 μm were designed keeping other design rules the same for both the conventional and proposed MOSFETs as shown in Table I.1.20.1. Figure I.1.20.1 (c) shows the SEM cross-sectional view of the proposed 1.2 kV MOSFETs. The net doping profiles for the conventional and proposed MOSFETs are shown in Figure I.1.20.1 (d) and (e), respectively. To form the deep junction in the proposed MOSFETs, the channeling implantation was conducted. There are no additional photo mask processes to fabricate the proposed MOSFETs with deep P-well. For the fabrication of the deep JFET and P-well, a channeling implant was added during the same implantation step as the conventional random implantation. By adopting the channeling implant, the 1.8 μm deep P-well structure was formed using low energy implantation.

(a)　　　　　　　(b)　　　　　　　(c)

(d)　　　　　　　　　　　　(e)
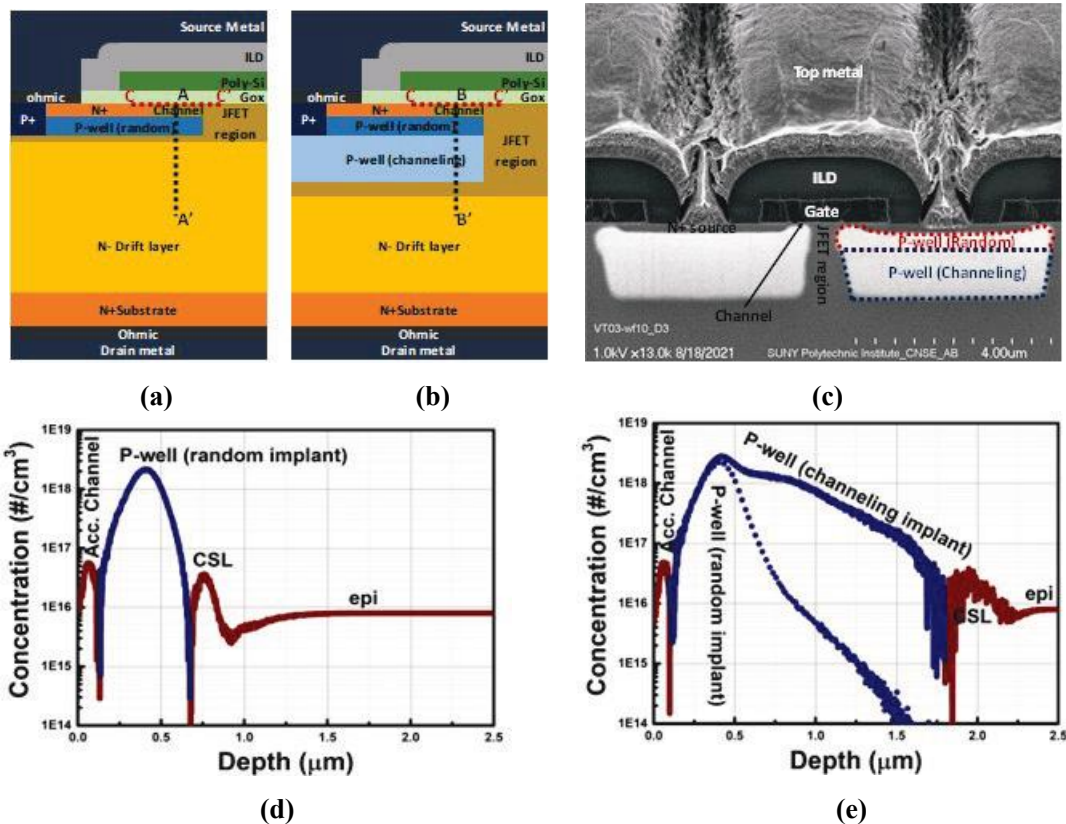
Figure I.1.20.1 Cross-sectional view of (a) conventional 1.2kV 4H-SiC MOSFETs and (b) proposed 1.2kV 4H-SiC MOSFETs. (c) The SEM cross-sectional view of the proposed 1.2 kV MOSFETs. (d) Net doping profile (A-A' shown in Fig. 1 (a)) for the conventional MOSFETs using SPROCESS. (e) Net doping profile (B-B' shown in Fig. 1 (b)) for the proposed MOSFETs using SPROCESS.

The measured forward blocking characteristics of the conventional and proposed MOSFETs are shown in Figure I.1.20.2 (a). High breakdown voltages with low leakage currents were achieved regardless of channel length in the proposed MOSFETs, whereas in the conventional MOSFETs very high leakage is present with short channel lengths (0.3 µm (D1) and 0.4 µm (D2). The deeper P-well increases the channel potential due to the better shielding effect, contributing to suppressing the leakage current from the channel.

Table I.1.20.1 Summary of the fabricated 1.2 kV MOSFETs

	P-well depth	Channel length	Ron,sp	P-well depth	Channel length
D1	~0.7 µm	0.3 µm	3.25	263	-
D2	~0.7 µm	0.4 µm	3.47	992	-
D3	~0.7 µm	0.5 µm	3.74	1669	-
D4	~1.8 µm	0.3 µm	3.35	1609	~5
D5	~1.8 µm	0.4 µm	3.76	1608	~6
D6	~1.8 µm	0.5 µm	4.12	1615	~7

*Ron,sp was extracted at Vgs of 20V and Vds of 0.1V. BV was extracted at Ids of 1 mA.

Figure I.1.20.2 (b) shows output characteristics at V_{gs} of 20 V for the fabricated MOSFETs with different channel lengths. The conventional MOSFETs offer better conduction behaviors for the same channel length because the proposed MOSFETs have a higher JFET resistance component due to the deeper P-well. However, the reduced channel lengths in the proposed MOSFETs substantially improve $R_{on,sp}$ due to the lower channel resistance, while maintaining high BV. Although the shorter channel lengths provide the better conduction behaviors, D1 and D2 have low BV because of high leakage currents. However, D4 allows high BV with low leakage current. In consequence, $R_{on,sp}$ was improved by approximately 10 % using D4 when compared to D3.

(a)

(b)

Figure I.1.20.2 Measured forward blocking characteristics and (b) output characteristics at V_{gs} of 20 V of the fabricated 1.2 kV MOSFETs with different channel lengths.

(a)

(b)

(c)
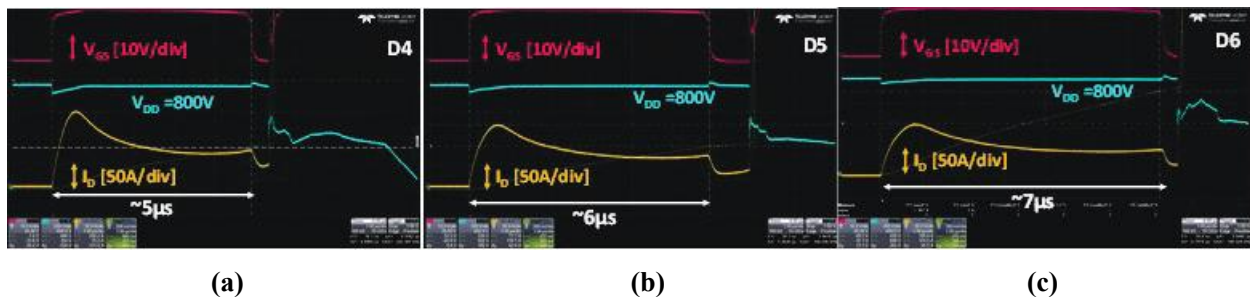
Figure I.1.20.3 Short-circuit waveforms of the proposed MOSFETs; channel length of (a) 0.3 µm (b) 0.4 µm, and (c) 0.5 µm.

Short-circuit (SC) waveforms of the proposed MOSFETs; channel length of (a) 0.3 µm, (b) 0.4 µm, and (c) 0.5 µm are shown in Figure I.1.20.3. SC characteristics were measured at R_g of 20 Ω, V_{gs} of 20 V, and V_{ds} of 800 V. Regardless of the channel length, significantly improved short-circuit withstand time (SCWT) was achieved in the proposed MOSFETs due to the deeper P-well. Shorter channel lengths have a larger maximum drain

current during the SC condition due to the lower $R_{on,sp}$. As a result, SCWT decreases with the reduction in L_{ch} due to this large drain current, resulting in high junction temperatures. Although the proposed MOSFETs with shorter channel length still show a trade-off relationship between $R_{on,sp}$ and SCWT, thanks to the deep P-well structure, the trade-off relationship was significantly improved in the proposed MOSFETs.

(a)

(b)
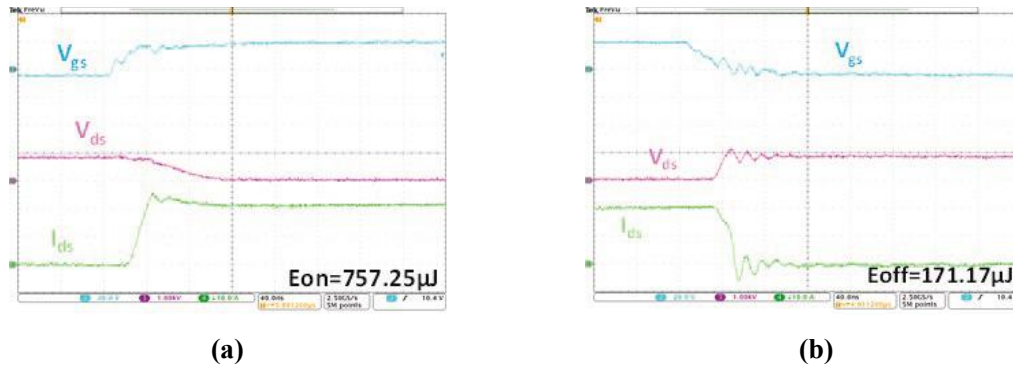
Figure I.1.20.4 (a) Measured switching turn-on waveforms and (b) switching turn-off waveforms of the fabricated 1.2 kV 4H-SiC MOSFETs with deep P-well.

(a)

(b)

(c)
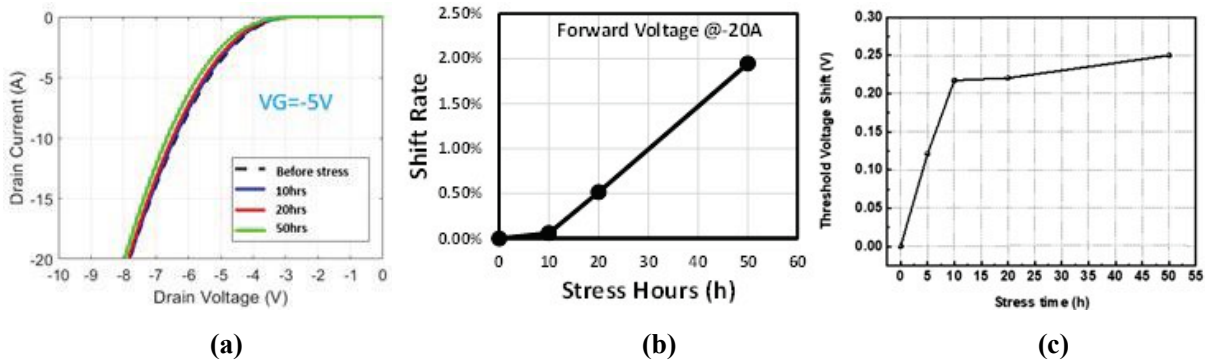
Figure I.1.20.5 (a) Degradation of third quadrant characteristics before and after stress at current of -10 A. (b) The change rate of forward voltage drop under third quadrant characteristics after stress. (c) Time-dependent threshold voltage shifts for positive bias stress of +20 V of the fabricated 1.2 kV SiC MOSFETs with deep P-well.

2. *Dynamic characteristics, Reliability, and ruggedness for MOSFETs with deep P-well*

Figure I.1.20.4 (a) and (b) show the measured switching waveforms of the fabricated 1.2 kV 4H-SiC MOSFETs. The typical switching turn-on and turn-off waveforms at V_{dc} of 800 V are shown in Figure I.1.20.4 (a) and (b), respectively. The double test with R_g of 20 Ω was conducted to measure switching characteristics. Normal switching behaviors were achieved. Degradation of third quadrant characteristics before and after stress at current of -10 A is shown in Figure I.1.20.5 (a). The change rate of forward voltage drop under third quadrant characteristics after stress is shown in Figure I.1.20.5 (b). Small body diode degradation was observed. Although it is negligible degradation level, the P+ body implantation will be further optimized to reduce the body diode degradation in the future lot. Figure I.1.20.5 (c) shows time-dependent threshold voltage shifts for positive bias stress of +20 V of the fabricated 1.2 kV SiC MOSFETs with deep P-well. The relatively small V_{th} shift was achieved due to the utilization of thermal gate oxide. In order to further minimize V_{th} shift
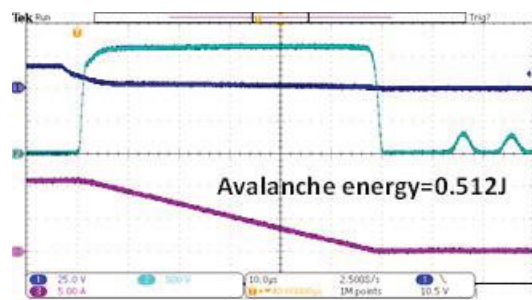
Figure I.1.20.6 Measured avalanche waveforms of the fabricated 1.2 kV SiC MOSFETs with deep P-well.

during BTI measurement, different gate oxide processes will be applied. Figure I.1.20.6 shows the measured avalanche waveforms of the fabricated 1.2 kV SiC MOSFETs with deep P-well. The test was conducted at V_{dc} of 100 V and L of 11 mH. Avalanche energy of 512 mJ, which is reasonable value in the ~25 A 1.2kV MOSFETs, is achieved.

3. Static characteristics of JBSFETs [2]

Figure I.1.20.7 shows the layout approach and cross-sectional views of the MOSFETs and Ti JBSFETs with deep P-well (~1.8 μm) implemented by channeling implantation. The removal of the P+ body implant in the horizontal direction in JBSFETs allows the same cell pitch as the MOSFETs. The tight cell pitch of 5.0 μm for both MOSFET and JBSFET was accomplished through enhanced doping concentrations in the JFET region.

(a)   (b)   (c)
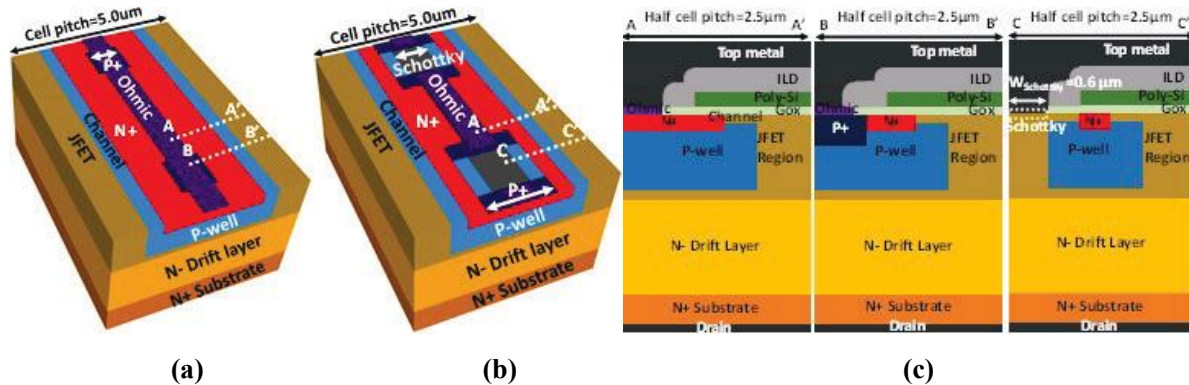
Figure I.1.20.7 (a) The layout approach of the MOSFET and (b) JBSFET, and (c) The cross-sectional views of A-A', B-B' from MOSFET (see (a)), and A-A', C-C' from JBSFET (see (b)).

(a)   (b)   (c)
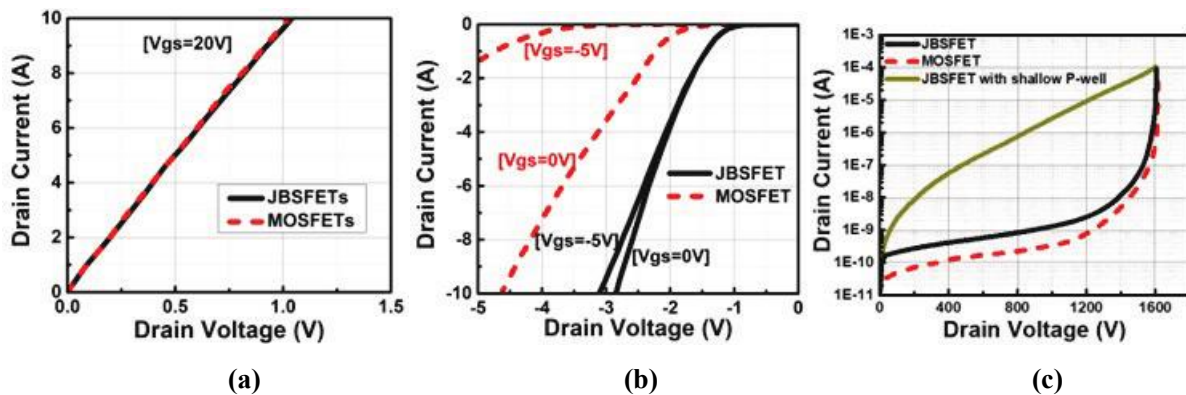
Figure I.1.20.8 (a) The measured output characteristics, (b) measured third quadrant characteristics, and (c) blocking characteristics of the fabricated 1.2 kV 4H-SiC MOSFETs and JBSFETs.

Figure I.1.20.8 (a) shows the typical output characteristics of the fabricated 1.2 kV 4H-SiC MOSFETs and JBSFETs. Due to the same cell pitch, identical conduction behaviors were achieved; the specific on-resistance ($R_{on,sp}$) of the MOSFETs and JBSFETs are 4.23 and 4.24 mΩ-cm², respectively (On-wafer measurement; substrate resistance is included). $R_{on,sp}$ was extracted at V_{gs} of 20 V and V_{ds} of 0.1 V. The measured third quadrant characteristics of the fabricated MOSFETs and JBSFETs are shown in Figure I.1.20.8 (b). Low knee voltage was achieved in the JBSFETs thanks to the operation of Ti Schottky contact before the body diode turned on. As a result, low forward voltage drop under third quadrant condition was achieved in the JBSFETs. Figure I.1.20.8 (c) shows the typical forward blocking characteristics of the fabricated devices. All devices have identical breakdown voltages. However, the JBSFET with shallow P-well has a high leakage current originated from the Schottky barrier lowering. Although the Schottky width was reduced, the enhanced JFET doping concentration increases the electric field at the Schottky interface, increasing the leakage current. The

(a) **(b)**
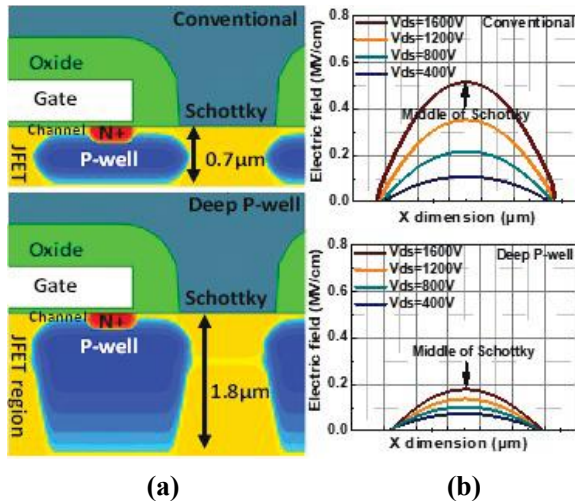
Figure I.1.20.9 (a) The cross-sectional view of simulated 1.2 kV JBSFETs with conventional (shallow) P-well and deep P-well. (b) The electric field on the Schottky contact of the simulated 1.2 kV JBSFETs with conventional (shallow) P-well and deep P-well.

proposed deep channeling implanted P-well minimizes the electric field at the Schottky contact and suppress the leakage current. Figure I.1.20.9 (a) shows the cross-sectional views of simulated 1.2 kV JBSFETs with conventional (shallow) P-well and deep P-well. Figure I.1.20.9 (b) compares the electric fields at the Schottky contacts; it was discovered that the maximum electric field at the middle of Schottky contact drastically decreases when using the deep P-well structure. Due to the reduction in the electric field, very low leakage current from the proposed JBSFET with the deep P-well was achieved as shown in Figure I.1.20.8 (c).

4. Device design and fabrication of Lot 7

For further improvement in the trade-off relationship between $R_{on,sp}$ and the SCWT, the optimization of the JFET region was conducted. In order to reduce the cost of fabrication, the number of series implantation steps were reduced and optimized for each implantation process. The mask for Lot 7 includes 47 different devices, including a PiN diode, MOSFETs, SQUAFETs, and HEXFETs. MOSFETs with different channel lengths and JFET widths were included as well. There are 11 photolithography process steps, including 5 implant processes. Fabrication for Lot 7 will be completed by the end of January, 2023.

Conclusions

This year, SUNY Poly has focused on improving the conduction behaviors with superior ruggedness and reliability. MOSFETs and JBSFETs with a deep P-well structure have been successfully fabricated and demonstrated. Promising static performances, short-circuit characteristics, and reliability were achieved. Many different variations in both device designs and process conditions were examined through previous Lots. Lessons learned from previous Lots have been reflected in the design of Lot 7 (1st lots for BP4). The fabrication for Lot 7 will be completed by the end of January, 2023.

Key Publications

1. D. Kim, S. Y. Jang, A. J. Morgan, and W. Sung, "Implementation of a short channel (0.3 μm) for 4H-SiC MOSFETs with deep P-well using 'channeling' implantation," in *2022 IEEE 34th International Symposium on Power Semiconductor Devices and ICs (ISPSD)*, May 2022, pp. 217–220.

2. D. Kim, S. Y. Jang, S. DeBoer, A. J. Morgan, and W. Sung, "An Optimal Design for 1.2kV 4H-SiC JBSFET (Junction Barrier Schottky Diode Integrated MOSFET) With Deep P-Well," *IEEE Electron Device Letters*, vol. 43, no. 5, pp. 785–788, May 2022.

3. D. Kim, N. Yun, S. Y. Jang, A. J. Morgan, and W. Sung, "Channel Design Optimization for 1.2-kV 4H-SiC MOSFET Achieving Inherent Unipolar Diode 3rd Quadrant Operation," *IEEE Journal of the Electron Devices Society*, vol. 10, pp. 495–503, 2022.

4. D. Kim, S. DeBoer, S. Y. Jang, A. J. Morgan, and W. Sung, "A Comparison of Short-Circuit Failure Mechanisms of 1.2 kV 4H-SiC MOSFETs and JBSFETs," *in 2022 IEEE 9th Workshop on Wide Bandgap Power Devices and Applications (WiPDA),* Nov. 2022.

5. D. Kim, N. Yun, A. J. Morgan, and W. Sung, "The Effect of Deep JFET and P-Well Implant of 1.2kV 4H-SiC MOSFETs," IEEE Journal of the Electron Devices Society, vol. 10, pp. 989–995, 2022.

References

1. D. Kim et al, "Implementation of a short channel (0.3 μm) for 4H-SiC MOSFETs with deep P-well using 'channeling' implantation," in *2022 IEEE 34th International Symposium on Power Semiconductor Devices and ICs (ISPSD)*, May 2022, pp. 217–220.

2. D. Kim et al, "An Optimal Design for 1.2kV 4H-SiC JBSFET (Junction Barrier Schottky Diode Integrated MOSFET) With Deep P-Well," *IEEE Electron Device Letters*, vol. 43, no. 5, pp. 785–788, May 2022.

Acknowledgements

I.1.21 Cost competitive, high-Performance, highly Reliable (CPR) Power Devices on GaN

Shadi Shahedipour-Sandvik, Principal Investigator
SUNY Polytechnic Institute
257 Fuller Rd
Albany, NY 12203
E-mail: sshahedipour-sandvik@sunypoly.edu

Susan Rogers, DOE Technology Development Manager
U.S. Department of Energy
Email: Susan.Rogers@ee.doe.gov

Start Date: April 16, 2019   End Date: April 15, 2024
Project Funding (FY22): $300,000   DOE share: $300,000   Non-DOE share: $0

Project Introduction

The primary objective of this project is to demonstrate highly reliable wide bandgap AlGaN/GaN HEMT power devices in comparison to HEMT on foreign substrate. In this project, we will demonstrate AlGaN/GaN HEMT power devices with greater performance and reliability. To accomplish this goal, growth conditions and processing are optimized for HEMT devices on foreign substrates as well as on resistive bulk GaN to reduce the effect of structural defects in the bulk and at interfaces.

Objectives

* AlGaN/GaN HEMT growth optimization

* HEMT device fabrication and characterization.

Approach

Improvement of Off-State Leakage in AlGaN/GaN HEMTs

The main objective of our project is to offer deeper understanding of the impact of dislocation defects/substrate on AlGaN/GaN HEMT performance. However, to do so, having a high quality HEMT structure itself is important so that the contributing factors to performance can be distinguished. A poor quality AlGaN/GaN HEMT will mask the impact of substrate.

Over the last year, several sets of HEMT devices were grown and fabricated. However, all devices fabricated on material grown in-house resulted in little-to-no gate control. To pinpoint the issue, all aspects of fabrication process were examined, with no noticeable improvement. Next was to assess potential issues with in-house grown material. To do this, we fabricated AlGaN/GaN HEMT devices on bulk GaN and on sapphire purchased from a third party vendor, along with in-house grown wafers. Devices made on in-house grown wafers showed sub-par performance indicating that the issue is with material. We are currently working to improve in-house grown material. Results shown in Figure I.1.21.1 and Figure I.1.21.2 are on third party obtained HEMT wafers.
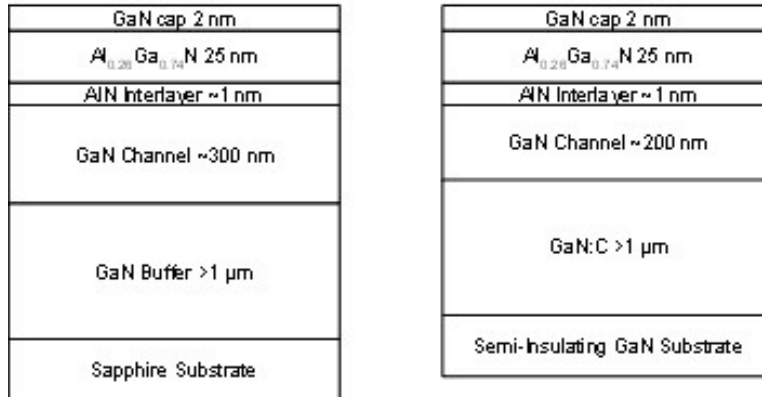
Figure I.1.21.1 Cross-section schematics of (left) HEMT on sapphire and (right) HEMT on bulk GaN purchased from vendor.

Results

Characterization of HEMTs Fabricated on Material from Vendor

Devices were fabricated on each of the samples described in Figure I.1.21.1. DC IV measurements were completed to assess the performance of the devices. DC output and transfer characteristics for representative devices with gate length 4 µm and gate width 150 µm are shown in Figure I.1.21.2 and Figure I.1.21.3.
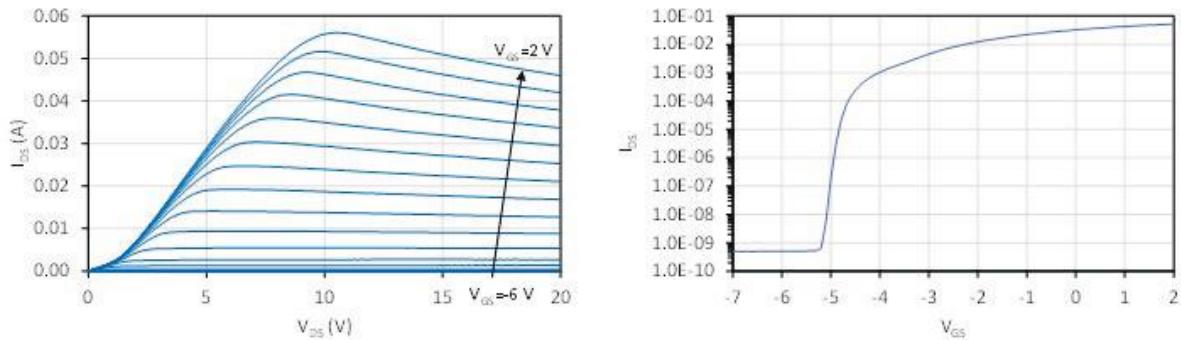
Figure I.1.21.2 (Left) output and (right) transfer (V_{DS}=11 V) characteristics of HEMT on sapphire. Maximum output at V_{GS}=2 V is 373 mA/mm and V_{th}=-5.2 V.
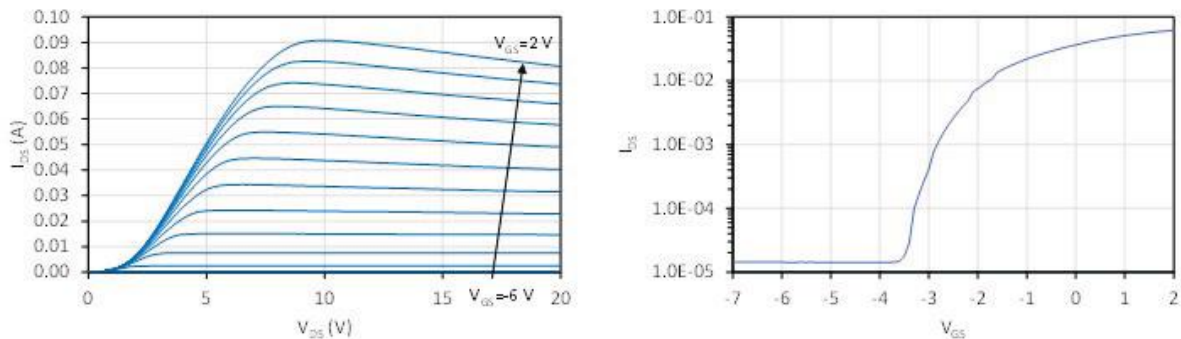
Figure I.1.21.3 (Left) output and (right) transfer (VDS=11 V) characteristics of HEMT on bulk GaN. Maximum output at VGS=2 V is 606 mA/mm and Vth=-3.5 V.

Despite nominally having the same GaN cap, AlGaN barrier, and AlN interlayer, the devices fabricated on different substrates differ in several key ways. Most noticeable from the output curves is that the HEMT on GaN has a significantly higher maximum output than the HEMT on sapphire: 606 mA/mm, compared to

373 mA/mm. Furthermore, due to the superior thermal conductivity of GaN, the negative differential output resistance in the saturation region is less pronounced in devices fabricated on GaN compared to devices fabricated on sapphire. Due to poor heat dissipation, the saturation current of devices fabricated on sapphire decreases by 18% from the maximum to the saturation at 20 V drain bias. In contrast, saturation of devices on GaN decreases by 11%.

However, while devices fabricated on GaN showed higher output and lower self-heating, they also showed significantly higher off current leakage than devices fabricated on sapphire. HEMTs on sapphire demonstrated I_{ON}/I_{OFF} ratios of 8 orders of magnitude, but the I_{ON}/I_{OFF} ratio of HEMTs on GaN was less than 4 orders of magnitude. The reason for this discrepancy is unknown, as off-state leakage is expected to be lower in devices fabricated on bulk GaN due to the lower defect density in the buffer layer. Furthermore, as shown in Figure I.1.21.4, devices fabricated on sapphire demonstrated ~2 orders of magnitude lower reverse bias gate leakage than devices fabricated on GaN. The reasons for higher off-state and gate leakage in devices on GaN is under investigation.
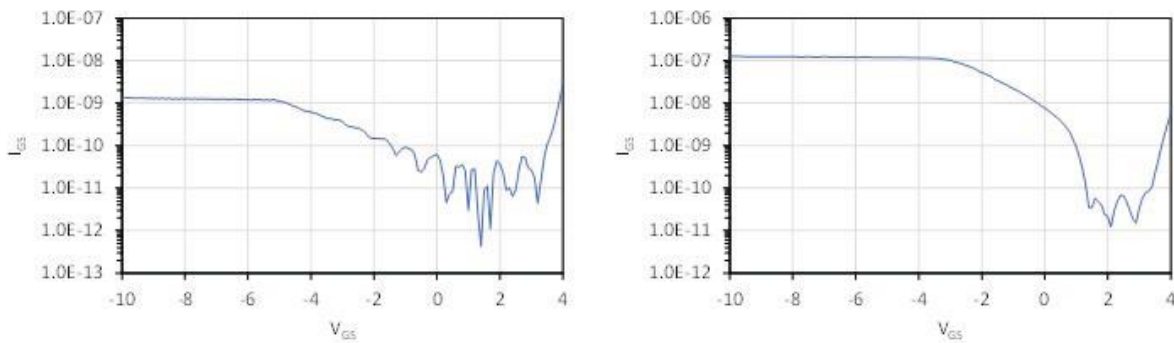
Figure I.1.21.4 gate leakage characteristics with V_{DS}=11 V for (left) HEMT on sapphire and (right) HEMT on GaN.

Although the HEMTs on GaN demonstrated higher leakage than the HEMTs on sapphire in the DC IV measurements, they already show promise in their reliability, with noticeably lower negative differential saturation resistance due to superior heat dissipation. Further reliability measurements will be performed to determine on-resistance degradation after drain voltage stress biasing, as well as maximum output drop under constant on-state biasing.

Acknowledgements

I.1.22 Design, Optimization, and Control of a 100 kW Electric Traction Motor Meeting or Exceeding DOE 2025 Targets (Illinois Institute of Technology)

Ian P. Brown, Principal Investigator
Illinois Institute of Technology
3301 S. Dearborn St.
Chicago, IL 60616
E-mail: ibrown1@iit.edu

Susan Rogers, DOE Technology Development Manager
U.S. Department of Energy
Email: Susan.Rogers@ee.doe.gov

Project Introduction

The Illinois Institute of Technology (IIT) is a member of the Department of Energy Electric Drives Technologies (EDT) Consortium. IIT's role in the consortium focuses on developing electric traction motors for electric vehicles with 8x the power density and half the cost of state-of-the art traction motors.

Objectives

The overall objective of the electric motor portion of the Electric Drives Technology consortium is to research, develop, and test electric motors for use in electric vehicles capable of the specifications in Table I.1.22.1. Reduced scale physical prototypes and full-scale design studies are planned at regular intervals to ensure progress towards the targets.

Table I.1.22.1 EDT Consortium Motor Targets

Parameter	Target Value
Peak Power Rating (kW)	100
Power Density (kW/l)	≥ 50
Cost ($/kW)	≤ 3.3

Approach

To meet the electric traction motor power density and cost targets of Table I.1.22.1, a number of approaches are being pursued simultaneously throughout the course of this project which address all of the major volumetric power density influences. Many of the approaches are synergistic and complementary with the approaches being taken by partner Electric Drive Technology Consortium member national laboratories and universities. Specific areas of focus during this past budget period include the following.

- The development of a spaced orthocyclic winding pattern for high slot fill die compressed windings which minimizes the risk of insulation damage.

- Design of a 100 kW interior permanent magnet synchronous machine (IPMSM) with die compressed concentrated windings which targets a power density of 50 kW/l.

- Initial development of a continuous wave winding forming and insertion process.

- Design of a 100 kW dual three phase IPMSM with a shaped conductor continuous wave winding which targets a power density of 50 kW/l.

- Initial development of techniques to estimate the thermal time constants of electric machines in situ.

- Prototyping and initial dynamometer testing of an IPMSM with high slot fill shaped conductor lap windings and a 2-layer V magnet configuration to validate the metamodeling drive cycle efficiency optimization approach developed in previous budget periods.

Results

Spaced Orthocyclic Windings for Die Compressed Windings to Minimize Insulation Damage Risk

Die compressed coils represent a promising means of increasing the slot fill, coil fill, or packing factor in electric motors. The slot fill of an electric machine is highly correlated with its power density and efficiency. Die compressed windings were first proposed for increasing the slot fill of a fractional slot concentrated winding permanent magnet synchronous machine constructed with segmented soft magnetic composite magnetic cores [1]. Die compressed windings for other concentrated winding machines including switched reluctance machines or the field coils of wound field synchronous machines have also been explored [2], [3].

Typically die compressed windings are made by winding magnet wire on a bobbin in an orthocyclic pattern, Figure I.1.22.1(a). The wound bobbin is then inserted into a die and compressed by a moving punch which deforms the round magnet wires into hexagons and squeezes out all the space between the wires. An orthocyclic winding pattern nests as closely as possible, the turns of one layer of the winding into the gaps provided by another layer of turns, Figure I.1.22.1(b). The orthocyclic winding pattern is the densest possible without compression and results in an orderly layout of the turns with three close packed directions. When the orthocyclic winding is compressed, however, the wires which are right next to one another become unstable, and some pop up into higher layers causing dislocations in the cross-section of the winding pattern and over deformation of the turn itself. The dislocations and deformations often result in damage to the insulative coating on the magnet wire.

| (a) | (b) | (c) | (d) |
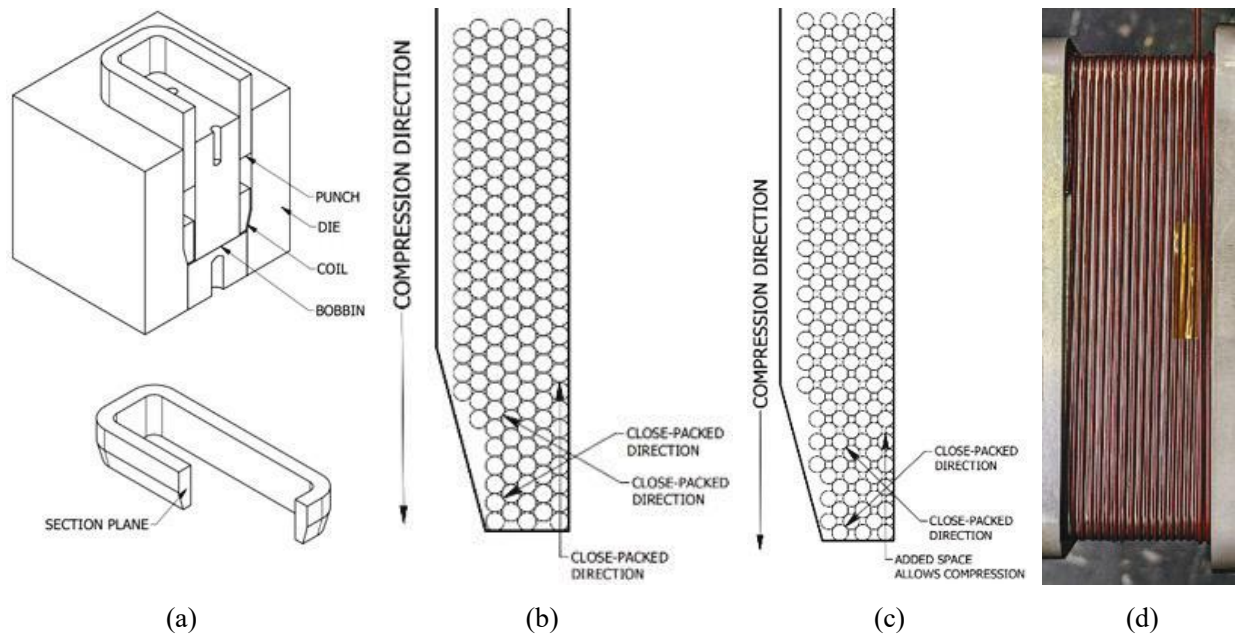
Figure I.1.22.1 For die compressed coils, a (a) die set where the coil wound on a bobbin is compressed by the movement of a punch is used, (b) with a typical orthocyclic winding pattern of the coil before compression on the bobbin, (c) alternatively a spaced orthocyclic winding pattern before compression with spacers in first layer, (d) which can be implemented as a co-wound nylon mono filament to space first layer of the turns.

To minimize the magnet wire insulation damage, an alternative spaced orthocyclic winding pattern was proposed. In this winding pattern, the turns of the first layer are spaced out, such that the when the second layer is wound on top of the first layer it is able to settle deeper between the turns of the first layer and so on. The amount by which the first layer is spaced out is relative to the size of the wire. In the spaced orthocyclic

winding, the turns are only close packed in two axes, Figure I.1.22.1(c). This introduces space for the turn to deform without displacing or jumping to the next layer and causing a dislocation.

One way to establish the spacing of the turns on the first layer is to co-wind an additional deformable filament, e.g. nylon monofilament, alongside the magnet wire turn on the first winding layer, Figure I.1.22.1(d). The co-wound filament is only needed on the first layer and can be removed easily after compression. Spacers could alternatively be deposited, printed or cast on the bobbin.

A design of experiments was carried out to access the advantages of the spaced orthocyclic winding on coil quality and slot fill based on wire gauge, co-wound filament diameter, and compression pressure. A number of quantitative and qualitative coil quality metrics were established. Cross-sections of representative samples of the 18 AWG coils from the design of experiments study are shown in Figure I.1.22.2. Die compressed coils wound with an orthocyclic pattern are shown in Figure I.1.22.2(a) and Figure I.1.22.2(b) for two different pressure levels. Dislocations in the winding pattern and over deformation of turns are clearly evident in these two coils. Figure I.1.22.2(c) through Figure I.1.22.2(d) were coils wound using a spaced orthocylic pattern but different co-wound filament diameters. In these cross-sections the spaced orthocyclic coils were all compressed to the same pressure. Coordination of the co-wound filament diameter with the wire gauge is critical. Figure I.1.22.2(c) with the correct co-wind diameter has minimum dislocations or over deformations. If the co-wound filament diameter is not properly selected dislocations and over deformations result, Figure I.1.22.2(d) and Figure I.1.22.2(e). The compression pressure is also critical for coil quality and slot fill.

(a)   (b)   (c)   (d)   (e)
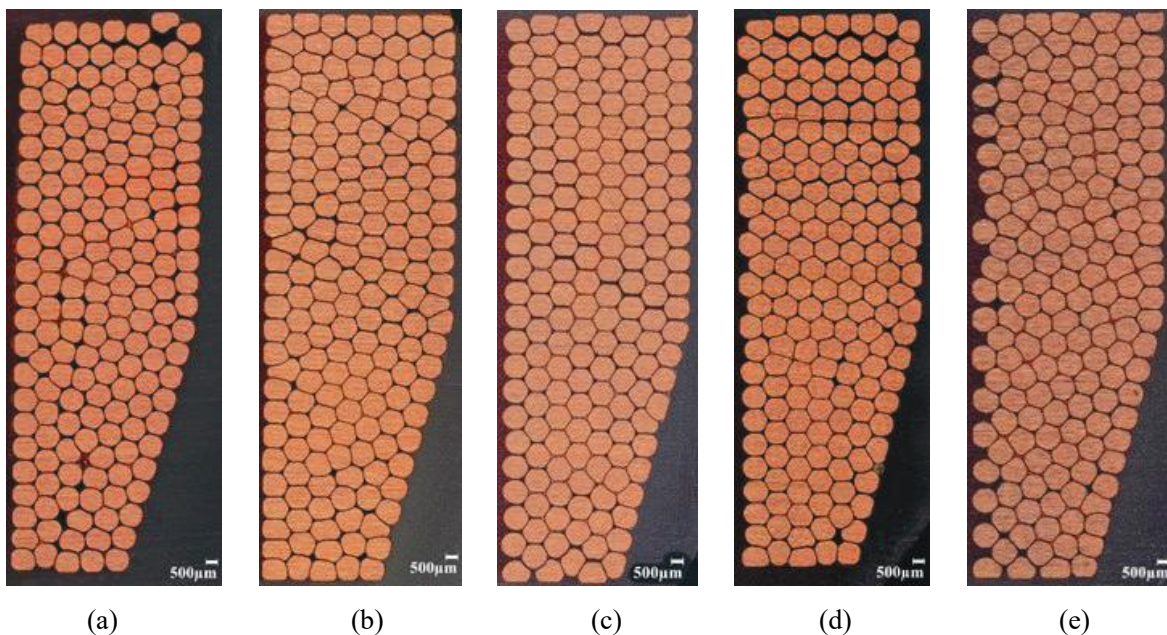
Figure I.1.22.2 Die compressed 18 AWG coil cross sections for (a) orthocyclic winding, 56.2 MPa, dislocations visible, (b) orthocyclic winding, 112.3 MPa, dislocations visible, (c) spaced orthocyclic winding, 0.56 mm monofilament cowind, 84.2 MPa, minimal dislocations, (d) spaced orthocyclic winding, 0.43 mm monofilament cowind, 84.2 MPa (e) spaced orthocyclic winding, 0.71 mm monofilament cowind, 84.2 MPa.

The proper use of a spaced orthocyclic winding pattern results in high slot fill coils with minimized insulation damage, Figure I.1.22.3.

Figure I.1.22.3 Representative example of a die compressed coil using a spaced orthocyclic winding without dislocations or over deformed wires.

Design of a Traction Motor with Die Compressed Stator Windings

To demonstrate the advantage of the spaced orthocyclic winding pattern for die compressed windings a 100 kW, three-phase 12-slot 10-pole traction motor using die compressed concentrated coils and double-layer V-shape interior permanent magnet (IPM) rotor was optimized. A drive cycle metamodeling approach developed in previous budget periods was utilized which considered both electromagnetic and structural aspects. The motor was designed for a maximum speed of 20,000 RPM and to withstand a 20% overspeed condition, i.e. 24,000 RPM. A representative design from the optimization is shown in Figure I.1.22.4.

(a)   (b)
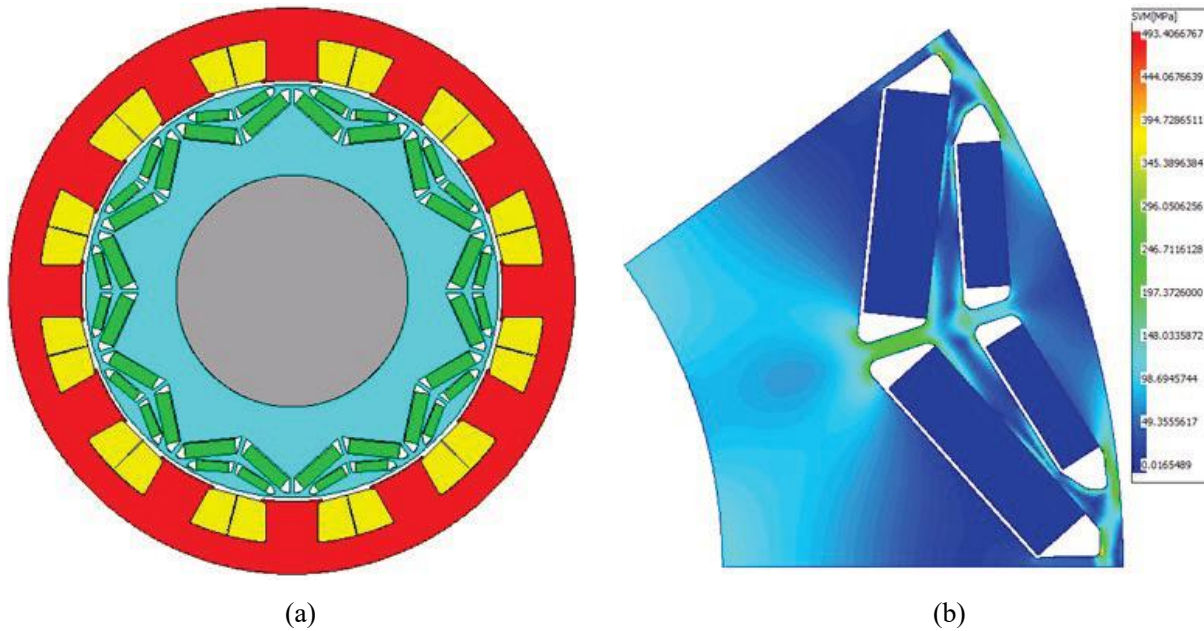
Figure I.1.22.4 100 kW, three phase, 12-slot 10-pole, 2-layer v-style IPMSM design with die compressed windings: (a) motor cross-section, (b) Von Mises stress during an over-speed condition of 24,000 RPM.

Shaped Conductor Continuous Wave Winding Forming and Insertion Process

Initial work on a continuous wave winding technique with shaped conductors was also carried out. A continuous wave winding offers a high slot fill similar to a hairpin winding but minimizes the number of welds. The welds in a hairpin winding can be a manufacturing quality issue and may also increase the winding head length on the weld side of the machine. The downside of a continuous wave winding is that open slots are

needed to insert all the turns which may increase core and magnet losses. A continuous former for the shaped conductor coil and an initial simultaneous inserter were developed. Trials of the forming and insertion process are ongoing. A portion of a formed coil of a continuous wave winding is trial fitted into a mockup stator in Figure I.1.22.5. This coil would be interwoven with other coils for simultaneous insertion into the stator.

Figure I.1.22.5 Partial continuous shaped conductor continuous wave winding inserted into a mockup 3D printed stator.

Design of a Traction Motor with Shaped Conductor Continuous Wave Winding

A metamodeling-based drive cycle efficiency optimization was carried out to design a 100 kW dual three phase 60 slot 10 pole IPMSM with 2 layer V magnet configuration. The cross-section of representative high-performance design predicted to have a power density of 50 kW/l is shown in Figure I.1.22.6(a) and the stress analysis of the rotor for the overspeed condition of 24,000 RPM is shown in Figure I.1.22.6(b).

(a)   (b)
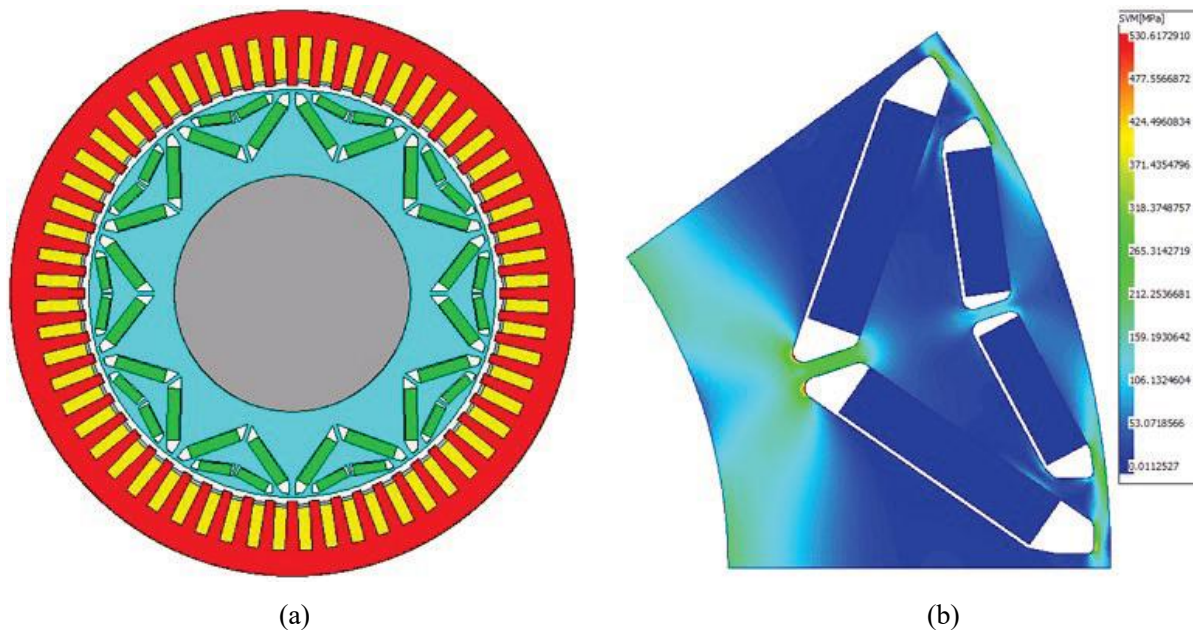
Figure I.1.22.6 100 kW, dual three phase, 60 slot, 10 pole, 2 layer v-style IPMSM design for a shaped conductor continuous wave winding: (a) motor cross-section, (b) Von Mises stress during an over-speed condition of 24,000 RPM.

Electric Machine Thermal Network Parameter Identification

The thermal time constants of electric machines are subject to considerable manufacturing variation. Examples of manufacturing variations that affect the thermal time constants are the surface finish and compression pressure of the housing onto the stator lamination stack or the average amount of impregnation varnish in the slots. Accurate estimation of the thermal time constants of individual components or interfaces in the electric machine is useful for a number of reasons. It can diagnosis manufacturing variations or issues and help prevent thermal performance from being under the minimum specification. Additionally, the thermal time constants can be used in real time observers for estimating the time and spatially varying temperatures in the machine. The temperature estimates can then be used for electro-thermal control to fully exploit the capabilities of the machine safely up to its thermal limits while ensuring reliability.

In this budget period, black box and white box systems identification approaches were initially developed for estimation of the thermal equivalent circuit parameters of electric machines. A Motor-CAD model of a physical electric machine instrumented with thermal couples was used to develop a thermal state space model with 66 state variables. Model order reduction techniques were used to reduce the thermal system models with 10 or less states that could still closely track temperatures of interest compared to the full 66 state model.

To estimate the thermal time constants of the physical electric machine and use them in a reduced order model pseudo random noise plus bias currents are injected into the stator at different frequencies to attempt to excite all the thermal dynamics in the electric machine. Data from the thermocouples embedded in the electric machine are sampled and fed into system identification algorithms to separate and identify the individual thermal time constants.

Prototyping and Initial Testing of High-Power Density Interior Permanent Magnet Synchronous Machine

The high-power density interior permanent magnet synchronous machine (IPMSM) prototype designed in the previous budget year using a drive cycle metamodeling optimization technique was prototyped successfully and initial dynamometer testing carried out. This design targeted a peak power output of 100 kW with a power density of 50 kW/l. The prototype was created to validate the drive cycle metamodeling optimization approach created in earlier budget periods. The stator design emulated a hairpin winding with a high slot fill lap winding using a shaped conductor, Figure I.1.22.7(a). The rotor used a 2-layer V magnet configuration with a magnet grade equivalent to a reduced dysprosium content magnet, Figure I.1.22.7(b). Thermal management of the machine is provided by a WEG stator jacket and ATF spray cooling of both the stator end turns and rotor endcaps. The waste heat is removed from the liquid coolants to the room air using liquid to air heat exchangers.

(a)   (b)
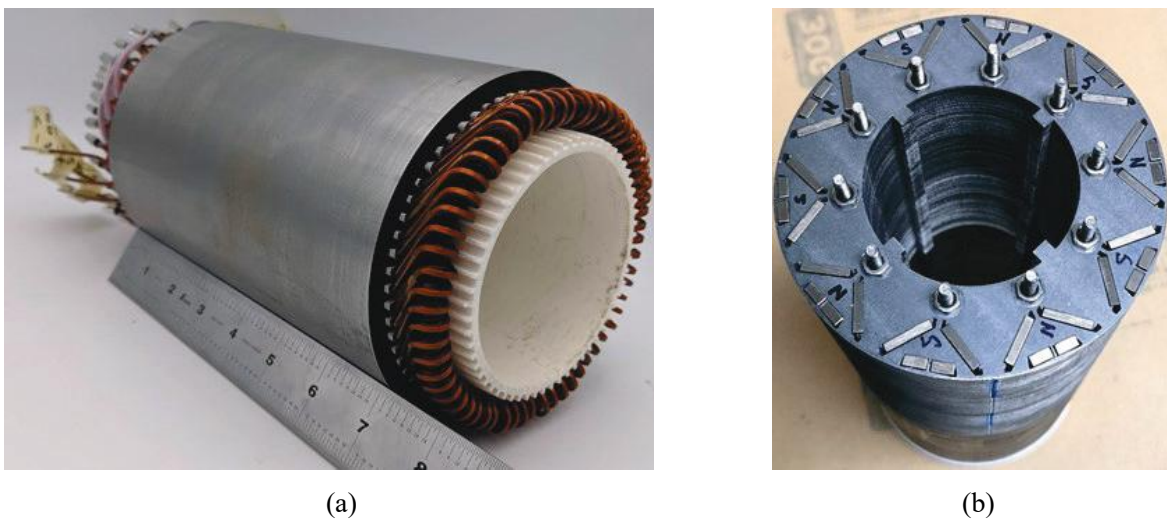
Figure I.1.22.7 100 kW, three phase, 60 slot, 10 pole, IPMSM prototype to validate metamodeling drive cycle efficiency optimization approach, (a) high slot fill shaped conductor lap wound stator, (b) 2 layer v-style magnet configuration.

The prototype machine was tested to the capabilities of the dynamometer at IIT, Figure I.1.22.8. The open-circuit back-emf and electromagnetic torque agreed very close to the predicted performance from the drive cycle metamodeling. The open circuit back-emf is shown in Figure I.1.22.9.
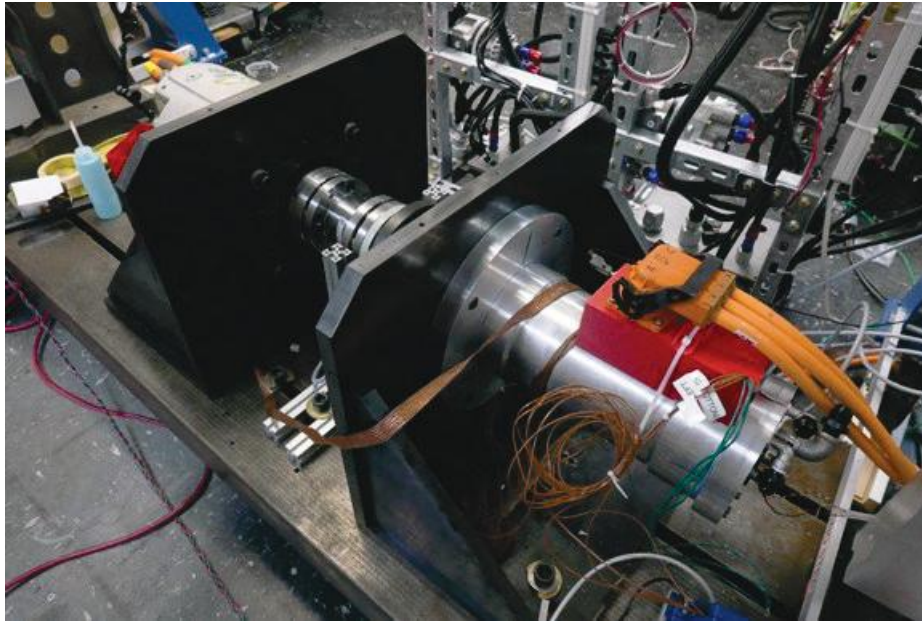
Figure I.1.22.8 Prototype IPMSM (right) mounted on the dynamometer at IIT for partial power testing.
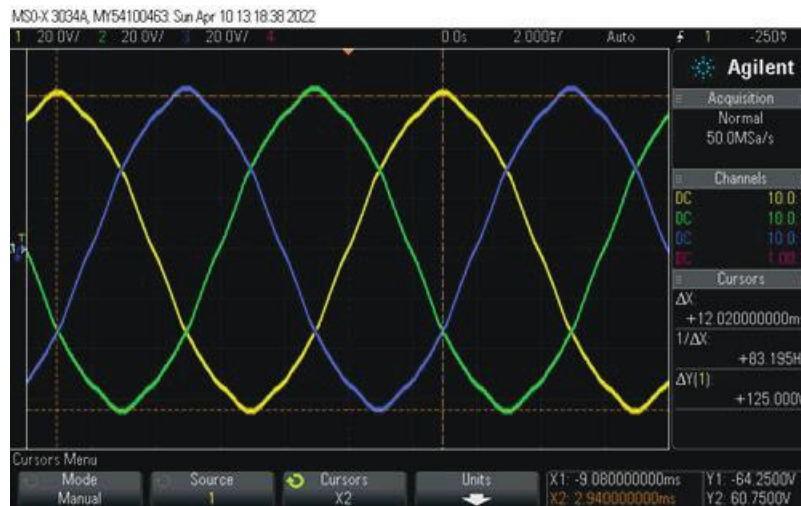
Figure I.1.22.9 Open circuit back-emf waveforms at 1000 RPM of high-power density IPMSM prototype.

Conclusions

In this budget period, develop work on two high slot fill winding technologies was carried out, spaced orthocyclic windings for die compressed windings and shaped conductor continuous wave windings. Metamodeling based drive cycle efficiency optimization was used to design machines featuring these winding technologies. Both of these winding technologies are promising for increasing the power density of electric traction motors. Initial work was also carried out to estimate the thermal time constants in electric machines using system identification approaches. A high-power density 100 kW IPMSM designed in the last budget period was prototyped and initial dynamometer tested to validate the metamodeling-based drive cycle-based optimization methodology.

Key Publications

1. D. Sossong, I.P. Brown, "Spaced Orthocyclic Winding Pattern for Improved Die Compressed Coils", Proceedings of the 2022 Energy Conversion Congress and Exposition, Detroit, MI, 2022.

2. N. Tang, I.P. Brown, "Low Space Harmonic Content Windings (LSHWs) Applied to Improve the Pareto Front in Design Optimization of Electric Machines, Proceedings of the 2022 Energy Conversion Congress and Exposition, Detroit, MI, 2022.

3. F. Guo, I.P. Brown, "Magneto-Structural Combined Dimensional and Topology Optimization of Interior Permanent Magnet Synchronous Machine Rotors", IEEE Transactions on Industry Applications, vol. 58, no. 6, 2022.

References

1. A.G. Jack, et Al., "Permanent magnet machines with powdered iron cores and pre-pressed windings," in the conference record of the 1999 IEEE Industry Applications Conference, 1999, vol. 1, pp. 97-103.

2. J.D. Widmer, R. Martin, and B.C. Mecrow, "Precompressed and stranded aluminum motor windings for traction motors," IEEE Transactions on Industry Applications, vol. 52, no. 3, pp. 2215-2223, May 2016.

3. M. Salameh, T. Spillman, M. Krishnamurthy, I.P. Brown, and D.C. Ludois, "Wound field synchronous machine with segmented rotor laminations and die compressed field winding," in proceedings of the 2019 IEEE Energy Conversion Congress and Exposition (ECCE), Baltimore, MD, 2019.

I.1.23 Integration Methods for High-Density Integrated Electric Drives (University of Arkansas)

H. Alan Mantooth, Principal Investigator
Department of Electrical Engineering
University of Arkansas
1475 W. Cato Springs Road, Rm. 211
Fayetteville, AR 72701
E-mail: mantooth@uark.edu

Fang Luo, Principal Investigator
Department of Electrical and Computer Engineering,
Stony Brook University (SUNY at Stony Brook),
259 Light Engineering Building, Stony Brook, NY 11794-2350
E-mail: fang.luo@stonybrook.edu

Susan Rogers, DOE Technology Development Manager
U.S. Department of Energy
Email: Susan.Rogers@ee.doe.gov

Start Date: October 1, 2021   End Date: September 30, 2022
Project Funding: $300,000   DOE share: $300,000   Non-DOE share: $0

Project Introduction

This project focuses on two key aspects of advancing electric drive technologies: integrated circuits and power electronic packaging. As part of the team's electronics portion, this project seeks to provide technologies that enable new power density advances. The first technology effort is integrating gate driving, sensing, and protection functions into the various packaging platforms that will be pursued by the team. Several technologies are possible, but the most advanced is high-temperature SiC / SOI based integrated circuitry that can be co-packaged with the SiC power devices. The team will pursue designs that serve the target electric drive train's specifications, but can survive at the junction temperatures expected to enhance power density while maintaining robustness and resiliency. The second technology effort is in advancing electronic packaging for electric drive train applications. Getting the most out of the advances in wide bandgap power semiconductor devices requires attention to careful packaging to minimize parasitic electrical influences on circuit performance and generated electromagnetic interference. Thermal management of the power devices and the surrounding circuit components must also be carefully managed. This leads to tradeoffs in the layout, arrangement, and interconnection of electronic components to balance these items. This effort will be performed in collaboration with several other organizations to achieve power density improvements for electric drives.

Objectives

The objective of the project is to research, develop, and test a heterogeneously integrated power module platform that will insert into a traction inverter system for power electronics modules capable of the following:

Table I.1.23.1 Power Electronics Requirements

Power Electronics Requirements	
Parameter	**Measure**
Cost ($/kW)	≤2.7
Power Density (kW/L)	≥100
System Peak Power Rating (kW)	100
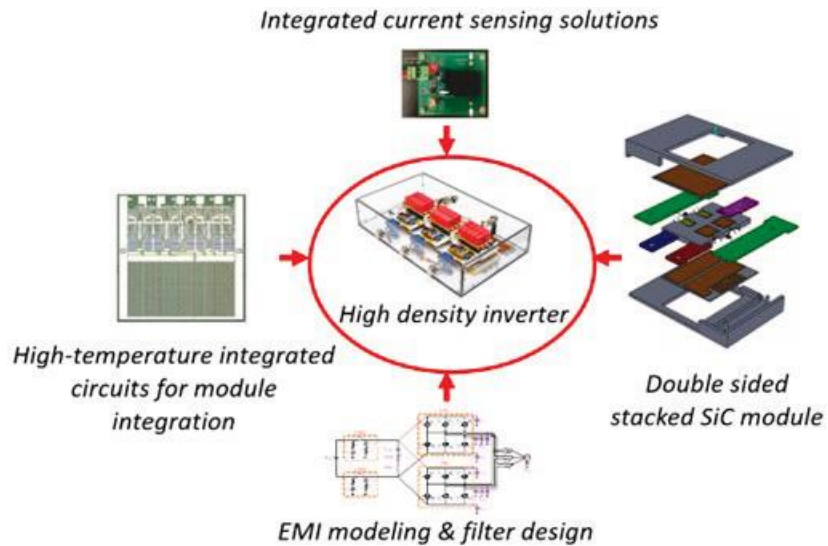
Figure I.1.23.1 Integration methods for high-density inverter.

Approach

The combined Arkansas and Stony Brook team broke down its activities across three major areas. The packaging research approach is to develop a detailed power module fabrication procedure and fabricate the necessary parts of the power module, such as interposers, housing, and direct bond copper (DBC) substrates. Later parts come as assembly and testing of the integrated components, such as gate driver and signal conditioning circuits for the sensors. The IC design group focuses on designing and testing the high-temperature integrated circuits for module integration. For the power electronics group, the focus is to develop current measurement methods having features such as small size, high accuracy, lightweight, low cost, and easy integration. In the following section, some key results from FY22 are described.

Results

On the packaging side of the project, a stacked half-bridge power module was designed with integrated gate driver boards. The power module was validated through ANSYS^{TM} and SolidWorks simulations. The proposed power modules' fabrication procedure was developed in detail, and necessary modifications were applied to the substrates, fixtures, and housings. Different fabrication approaches were developed and tested for comparison. Then, the most preferred approaches were selected for fabricating each part of the power module. The integrated gate driver boards and the differential boards were assembled and tested to switch discrete devices in a half-bridge configuration in a double pulse test (DPT) setup at 800 V, 115 A. This verified the gate driver board's functionality. The fabrication process flow was finalized, and functional power modules (known as Gen 1(b)) were fabricated, as shown in Figure I.1.23.2.

A DPT printed circuit board (PCB) to test the fabricated power module was designed in Cadence's Allegro tool. The LTspice simulation circuit for this DPT setup indicated that the external gate resistors must be removed to meet power loss requirements. The external gate resistors could be eliminated because the CPM3-1200-0013A power device has ~6.7 Ω gate resistance integrated within the bare die. Also, the effective pull-up and pull-down output resistances of the gate driver IC used are 4.62 Ω and 1.81 Ω, respectively. The necessary voltage and current measurements were made using differential probes and Rogowski coils, as shown in Figure I.1.23.3.
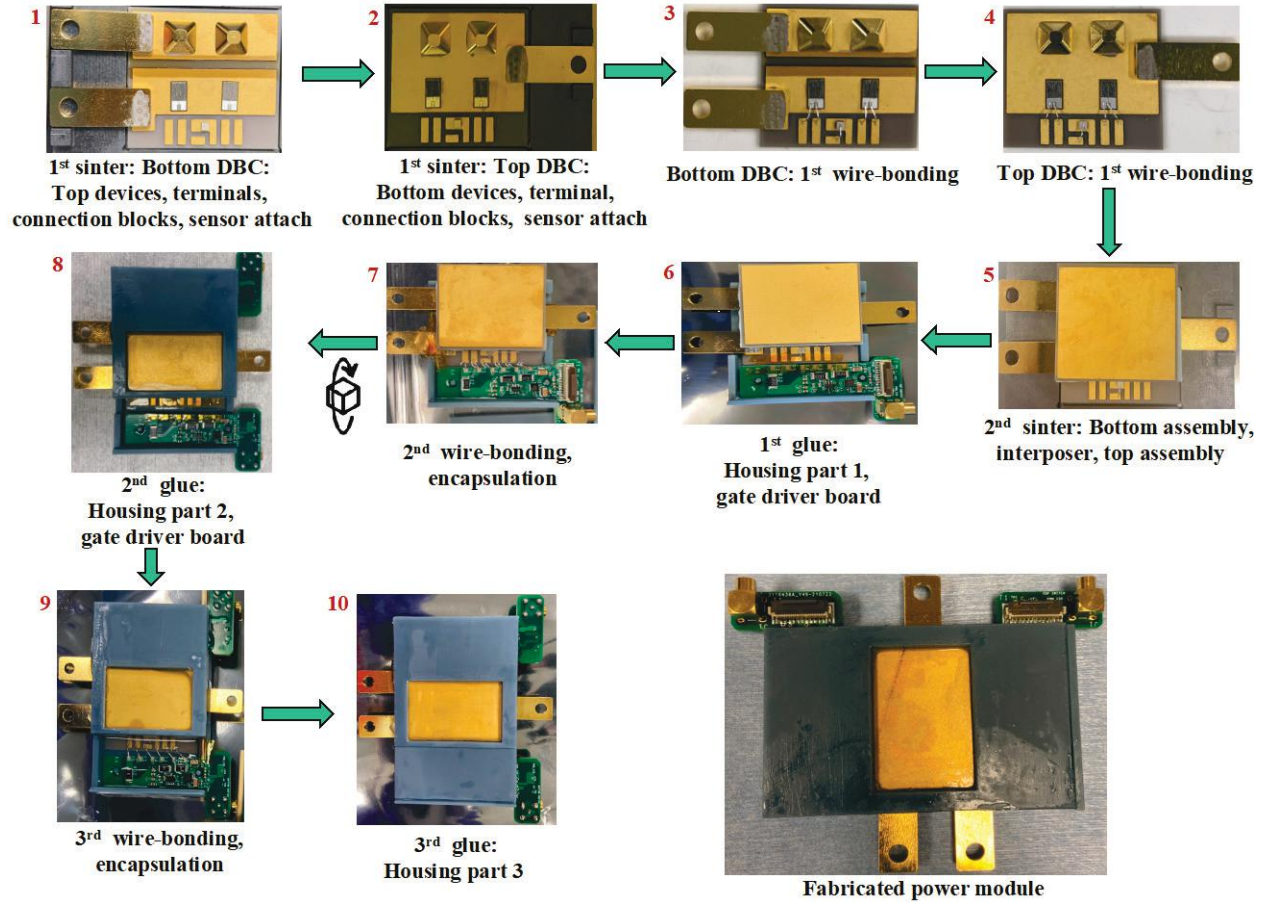
Figure I.1.23.2 Fabrication flow and fabricated power module.
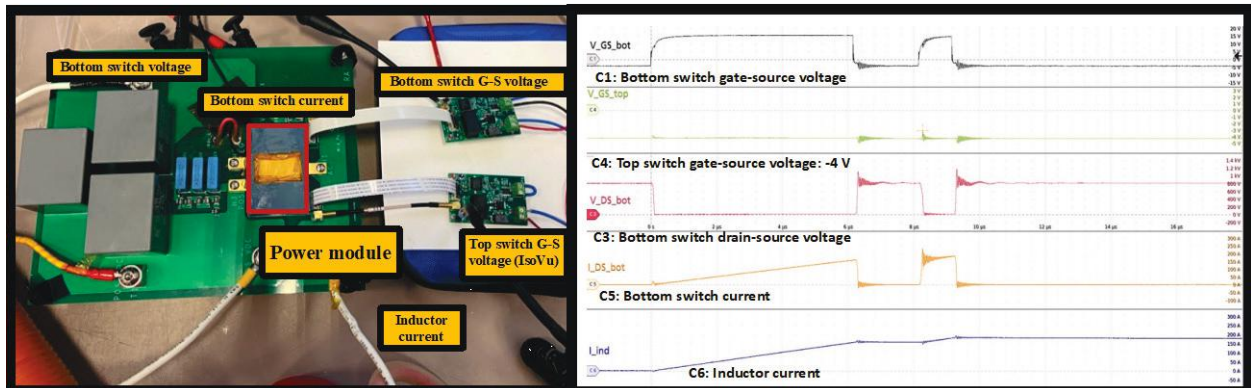
Figure I.1.23.3 DPT setup and resulting waveforms at 800 V, 164 A.

The DPT result at 800 V is shown in Figure I.1.23.3. Channel C1 shows the output of the gate driver IC to switch on and off the bottom switch. Channel C4 shows the -4V output of the top switch gate driver IC, to always keep the top switch off during the DPT. Channel C3 shows the drain-source voltage for the bottom switch. Channel C5 shows the current for the bottom switch. Channel C6 shows the inductor current. Table I.1.23.2 gives the simulated power loss capability per device and the experimentally calculated power loss per device, which matches the simulation results sufficiently given that the simulations are pessimistic estimates. Six of the fabricated power modules (Figure I.1.23.4) were ready to be inserted into the segmented, two-level, three-phase inverter system by May 2022.

Table I.1.23.2 Power Loss per Device from Simulation and Experiment

Module design	Convection co-efficient (W/m²K)	Power dissipation capability per die (W) (Simulation)	Power dissipation per die (W) (Experiment)
Two paralleled CPM312000013A	10,000	120	103.3
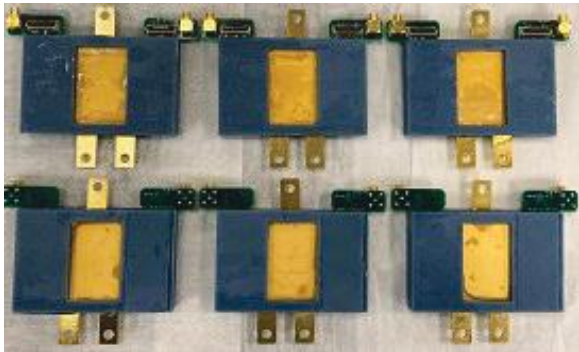
Figure I.1.23.4 Six of the fabricated and tested power modules.

As a subsequent step, the next-generation power module design (Gen 2), including more heterogeneously integrated features, was finalized. It includes decoupling capacitors to reduce the power loop inductance and integrated current sensors to measure current in addition to the SOI-based gate drivers and temperature sensors. The integration of all these parts into the power module housing makes this a high-density inverter system (~106 kW/L volumetric system power density). The details and implementation of this Gen 2 power module will be included in the next report.

The IC design team received the first version of Gen 2 silicon-on-insulator (SOI) integrated circuits in February 2022. Figure I.1.23.5(a) shows the die micrograph of this fabricated SOI gate driver chip along with the protection circuitry. Two separate analog control voltage pins, 'control_N' and 'control_P,' effectively control the gate driver's pull-up and pull-down drive strengths. The pull-up and pull-down outputs have been separated to facilitate the flexibility of different gate resistors. Table I.1.23.3 and Table I.1.23.4 summarize the test conditions and performance figures of the gate driver, which meets the specifications derived from the acceptable switching loss for the targeted inverter efficiency rating.

(a)   (b)   (c)
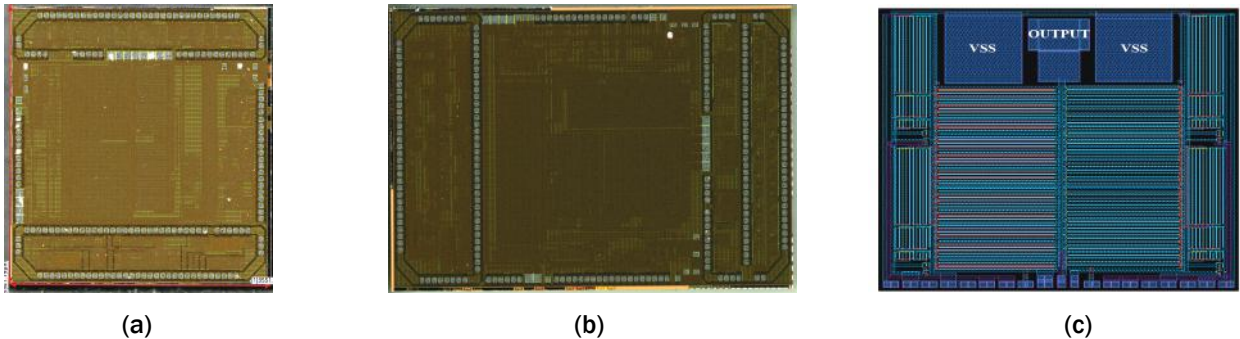
Figure I.1.23.5 (a) Die micrograph of the fabricated 1st version SOI Gen 2 IC (b) 2nd version SOI Gen 2 IC (c) Layout of the flip-chip capable SiC gate driver.

Table I.1.23.3 Gate Driver Test Conditions

Parameter	Value
VDD	15 V
REF	0 V
VSS	-3 V
Input	- 3 V / 0 V
Load (out_low and out_high shorted)	16 nF (representation of two CREE CPM3-1200-0013A SiC power die placed in parallel in a switching position)
control_P	0 V (max. pull-up strength)
control_N	0 V (max. pull-down strength)
output	~ -3 V / 15 V

Table I.1.23.4 Performance Figures of the Gate Driver

Parameters	25°C		175°C	
	Simulated	Measured	Simulated	Measured
Rise time	255 ns	401 ns	288 ns	442 ns
Fall time	196 ns	350 ns	218 ns	382 ns
Average propagation delay	185 ns	287 ns	210 ns	318 ns

The auxiliary protection circuitry (active Miller clamping, under-voltage lockout, desaturaton detection) has also been tested and validated. Based on these test results, the IC team modified and designed additional circuit blocks and successfully taped out the second version of Gen 2 IC on the same process in May 2022. The team received the fabricated second version of the Gen 2 IC in December 2022. Figure I.1.23.5(b) shows the die micrograph of this SOI gate driver. The chips are currently under evaluation. In addition to building complex gate drives in the SOI process, the IC design team designed flip-chip capable gate drivers having basic functionalities in low voltage SiC process for heterogeneous integration inside the module in an effort to push the parasitic gate loop inductance even lower. The layout is customized in such a way that its output and source pads overlap the Cree CPM3-1200-0013A power die's gate and source, respectively. Connections can be made between the two die using solder bumps and other techniques. The driver design is realized on Fraunhofer IISB's 1 μm SiC CMOS process and successfully taped out in July 2022. Figure I.1.23.5(c) shows the complete gate driver chip layout.

The other major design block of the IC is the sensor readout interface circuitry. One of the principle components to be integrated into the Gen 2 power module is the current sensing. A GMR sensor is chosen for its various capabilities, and its interface circuit is designed accordingly. Details of the sensing technique is described in the later sections. The sensor interface circuit consists of three instrumentation amplifiers to read the signal from the sensor and cancel out noise. A final stage is used for gain variability as well as load drivability, as shown in Figure I.1.23.6. The circuits have been tested, and the results are shown in Table I.1.23.5. It is operated using a 3-bit gain controllability. The measured bandwidth of the readout interface is approximately 5-10 MHz (changing slightly with a change in gain).
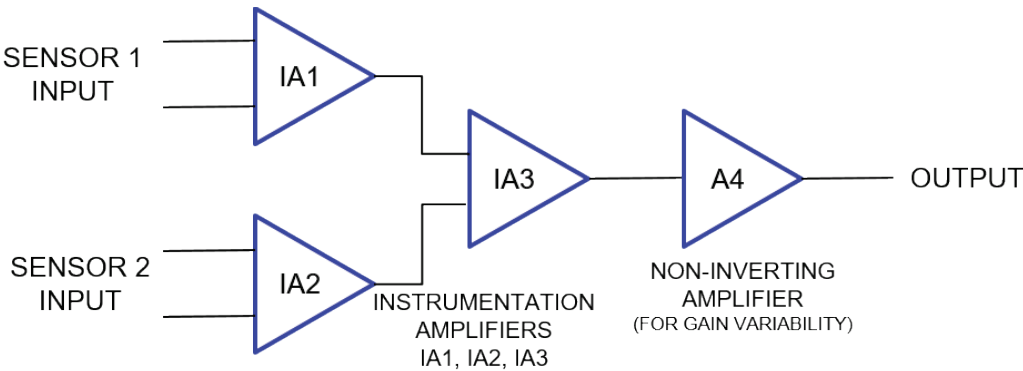
Figure I.1.23.6 Block diagram of the sensor interface circuit

Table I.1.23.5 Measured Results of the Sensor Interface Circuit Block

INPUT		GAIN BITS			OUTPUT			GAIN		
INP_IA1	INP_IA2	G0	G1	G2	VOUT_IA1	VOUT_IA2	VOUT	Simulated VOUT/ INP_IA1	Measured VOUT/ INP_IA1	Measured VOUT/ (INP_IA1+ INP_IA2)
50 mV	50 mV	1	0	0	200 mV	200 mV	1 V	24	20	10
50 mV	50 mV	0	1	0	195 mV	200 mV	1.24 V	28	24.8	12.4
50 mV	50 mV	0	0	1	200 mV	200 mV	1.56 V	32	31.2	15.6

The current measurement method selected for integration into the power module should be small, have high bandwidth, and be capable of measuring both AC and DC currents. A potential solution is using the Two GMR Sensors (TGS) method [1]. Figure I.1.23.7 shows a different configuration for implementing the TGS method where two sensors are placed on two sides of the current trace, which is a copper terminal. Selection of the most accurate current sensors and proper placement of them, along with creatively designed signal conditioning circuitry, can help to cancel the effect of external magnetic fields and temperature fluctuations. The proposed design for applying the TGS method is a simple, small, and feasible solution for power modules.
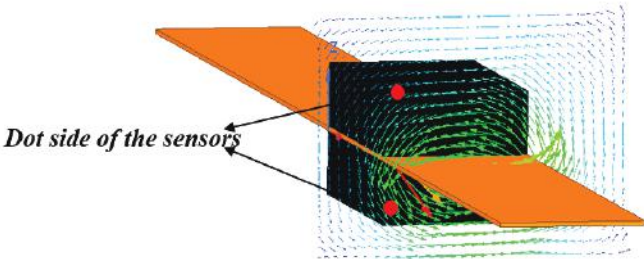
Figure I.1.23.7 TGS solution with the proposed configuration.

Placement of the sensors, similar to Figure I.1.23.7, requires two boards sandwiching the sensors with the copper terminal to supply the sensors and route out the sensor output voltage. Figure I.1.23.8 presents the front and side views of the proposed configuration.
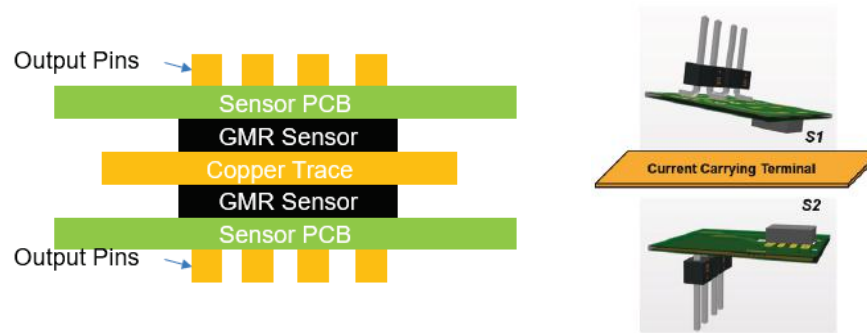
Figure I.1.23.8 Front and side view of the TGS solution with the proposed configuration.

Based on finite element analysis (FEA) simulations, the magnetic field around the terminal generated with 200 A and 1 MHz current passing through the terminal is approximately 5 mT. Therefore, using both bidirectional current sensors, AB001-02E from NVE and CT100 from Crocus can help measure the 200 A current passing through the AC terminal of the designed power module. For the implementation of the configuration shown in Figure I.1.23.8, boards for both NVE and Crocus current sensors were designed. Figure I.1.23.9 shows both sides of the developed board for the NVE sensor and the final assembly of the sensor on the copper terminal prepared for tests.

(a)   (b)

Figure I.1.23.9 (a) Designed PCB for the GMR current sensors, (b) TGS method implementation on AC copper terminal.

For validating the effectiveness of the TGS method, a current probe waveform was compared with a single GMR sensor (VS2) and then with the system output (VS1-VS2). Figure I.1.23.10 shows the results of this comparison. The system output follows the current probe better than a single sensor output. Also, it should be noted that the error of the single sensor output is small because the maximum current passing through the terminal is not high, just 6 A, and by increasing the current to higher values, this difference will be more considerable.

(a)   (b)
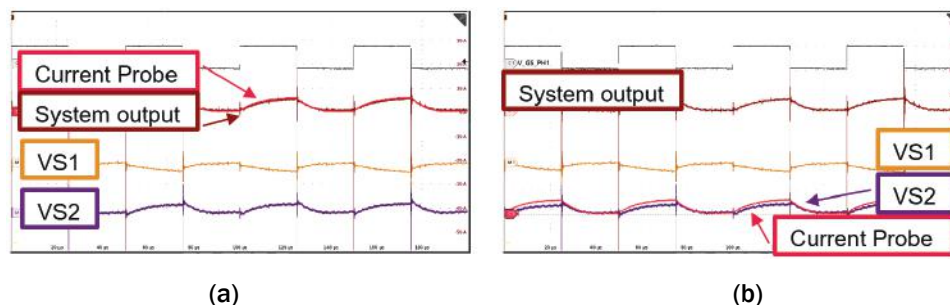
Figure I.1.23.10 Effectiveness assessment of the TGS solution, (a) current probe and system outputs, (b) current probe and single sensor outputs are overlapped.

As can be observed from Figure I.1.23.10, comparing the measurement results with GMR sensors with the current probe output, the accuracy of the measurement when using two sensors is higher than the measurement with a single current sensor, which validates the performance of the TGS method. In the next step, a similar

test is performed using a Crocus current sensor for approximately 40 A and 70 kHz current. The test result is shown in Figure I.1.23.11. As it is presented, the output voltage of the system, which is equal to the difference of the output voltages of both sensors, follows the current probe precisely, while single outputs have considerable spikes and noise on them.

Figure I.1.23.11 TGS method on terminal with CROCUS sensors.

Conclusions

UA and Stony Brook are making great progress. Weekly project meetings continue. The UA team experienced delays in getting modules built and delivered to ORNL for their intended 200 kW inverter build. These delays were both technical and supply-chain oriented. At present, all six (6) power modules (Gen 1b) have been successfully built and experimentally validated and are waiting to be inserted into the inverter. The Gen 2 design is complete, the fabrication flow is being finalized, new chips are ready for insertion, and a second inverter can be built in CY23. The project is on track technically and financially. More publications are expected in the coming months as results are obtained from the IC and module developments.

Key Publications

1. R. Paul, R. Alizadeh, A. Rahouma and H. A. Mantooth, "Fabrication of a Double-Sided Cooled Half-Bridge Silicon Carbide Power Module for Electric Vehicles," PCIM Europe 2022; International Exhibition and Conference for Power Electronics, Intelligent Motion, Renewable Energy and Energy Management, 2022, pp. 1-7, doi: 10.30420/565822062.

2. R. Paul et al., "A Heterogeneously Integrated Double-Sided Cooling Silicon Carbide Power Module," 2022 20th IEEE Interregional NEWCAS Conference (NEWCAS), 2022, pp. 475-479, doi: 10.1109/NEWCAS52662.2022.9842249.

3. Affan Abbasi, Asif Faruque, Sajib Roy, Robert Murphree, Tobias Erlbacher, Alan Mantooth; Gate Driver Design in a 1 μm SiC CMOS Process for Heterogeneous Integration Inside SiC Power Module. International Symposium on Microelectronics 1 September 2020; 2020 (1): 000281–000285. doi: https://doi.org/10.4071/2380-4505-2020.1.000281.

4. Rana Alizadeh, Kaoru Uema Porter, Tom Cannon, H. Alan Mantooth; Fabrication of Ceramic Interposers for Module Packaging. Journal of Microelectronics and Electronic Packaging 1 April 2020; 17 (2): 67–72. doi: https://doi.org/10.4071/imaps.1114553.

References

1. C. Mușuroi et al, "High Sensitivity Differential Giant Magnetoresistance (GMR) Based Sensor for Non-Contacting DC/AC Current Measurement," *Sensors (Basel, Switzerland),* vol. 20, *(1),* pp. 323, 2020.

I.1.24 Heterogeneous Integration Technologies for High-temperature, High-density, Low-profile Power Modules of Wide Bandgap Devices in Electric Drive Applications

Guo-Quan Lu, Principal Investigator
Virginia Tech
Department of MSE and ECE – 0111
Blacksburg, VA 24060
E-mail: gqlu@vt.edu

Rolando Burgos, Co-Principal Investigator
Virginia Tech
Department of ECE, CPES – 0179
Blacksburg, VA 24060
E-mail: rolando@vt.edu

Khai D.T. Ngo, Co-Principal Investigator
Virginia Tech
Department of ECE, CPES – 0179
Blacksburg, VA 24060
E-mail: kdtn@vt.edu

Susan Rogers, DOE Technology Development Manager
U.S. Department of Energy
Email: Susan.Rogers@ee.doe.gov

Project Introduction

The goal of this project is to develop packaging technologies for making high-temperature, high-density, and low-profile wide-bandgap (WBG) power electronics modules. These modules are aimed at enabling the DOE VTO Electrification Technologies' University Consortium to reach its 2025 targets (listed below) for the cost, power density, and system peak power rating of automotive electric drive systems.

Table I.1.24.1 Power Electronics Requirements

Parameters	Measure
Cost ($/Kw)	≤ 2.7
Power Density (kW/L)	≥ 100
System Peak Power Rating (kW)	100

The objectives of this project are to:

- develop a low-cost sintered-silver interconnect technology for packaging power modules and gate drivers

- develop designs and fabrication processes of double-side cooled power modules with parasitic inductances < 5 nH, heat flux density > 400 W/cm^2, and working junction temperature > 200°C

- design and prototype intelligent gate drivers with integrated current sensors and protection for the 200°C module.

A schematic of the hardware to be developed in this project is shown below in Figure I.1.24.1. Planar, double-side cooled phase-leg modules capable of working at 200°C junction temperature will be designed and fabricated. Multiple phase-leg modules will be assembled on cooling plates (with or without double-side cooling) and interfaced to a bus bar and gate-driver boards. The gate driver boards will have integrated current sensors, power supplies, and other components that are capable of working at 65°C ambient.
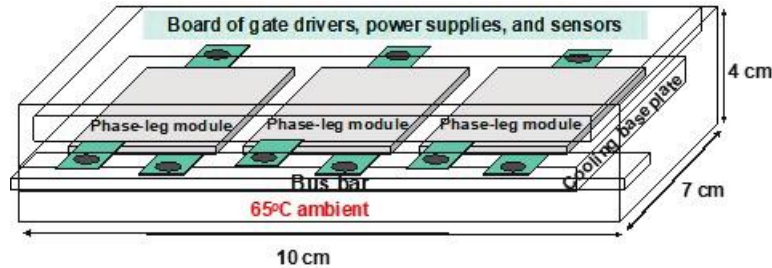
Figure I.1.24.1 Schematic of the hardware to be developed in this project.

For this reporting period, we focused on achieving the following specific objectives:

- Layout modification and fabrication of high-temperature SiC phase-leg module;

- Study of thermo-mechanical effects of different encapsulation materials on double-side cooled power module by FEA simulations;

- Design, analysis, and test of a current sensor with two compensation schemes to mitigate the impact of the temperature on the output of the current sensor.

- Characterization of the efficiency of a single-output class-e power supply and analysis of the loss breakdown.

- Design and test of air-core transformer winding structures for a gate power supply with six secondary windings.

Approach

In the third year of this project, we selected one of the two previously designed layouts of a double-side cooled SiC phase-leg module with better thermal performance and lower parasitic inductances and developed fabrication process of the power module. A total of fourteen SiC phase-leg modules were fabricated, and six of them were assembled with the gate-driver board for delivery to ORNL for inverter assembly. In this year, we modified layout of the phase-leg module and developed tools to improve the yield of module fabrication. To achieve the M2.5 milestone which is to demonstrate high-temperature module packaging technology, a new commercial high-temperature encapsulation was identified and used to encapsulate fabricated backup modules. Simulations were also run to study thermo-mechanical effects of different encapsulation materials on the double-side cooled power module.

As for the gate driver part, the gate driver integrated with the short-circuit protection based on the parasitic inductance were designed and tested in the six-phase inverter. The current sensor based on the parasitic inductance of the power module was designed and verified in experiments. To eliminate the influence of the temperature on the parasitic resistor between the kelvin terminal and the power source terminal, two methods were proposed and verified in the test.

In the continued effort for the gate power supply development, a six-output power supply with an air-core transformer was manufactured and tested. PCB windings are utilized to minimize the converter profile. The design of the air-core inductor and transformer was reported in the last annual report. The inductances were

measured to verify the design. The designed power supply was then tested with resistive load to verify the output voltage and efficiency. The ambient temperature for the power supply is estimated as 65°C when the junction temperature of the power module is 200°C. The power supply was then characterized in the environment chamber to 72°C. Finally, the power supply was tested with the gate driver and power module to justify its performance as a gate power supply.

Results

1. Layout Modification and Fabrication of High-Temperature SiC Phase-Leg Module

Last year we reported a layout design (Layout 2.0) for the double-side cooled SiC MOSFET phase-leg module. The layout has ten signal pins. There are two pins connecting to the top device's Kelvin source and two pins connecting to the bottom device's Kelvin source. The signal pins were redesigned to accommodate the current sensing in layout 3.0 as shown in Figure I.1.24.2. The new layout has a power source pin for each device. All ten pins are connected to the same DBC, and the pin-to-pin pitches are the same at 2.0 mm. To control the pitch of pins and provide stronger soldering bonds, we designed an aluminum fixture shown in Figure I.1.24.3. The fixture helped level the pins with the DBC substrate and defined the 2.0-mm pitch spacing during the solder-reflow process.
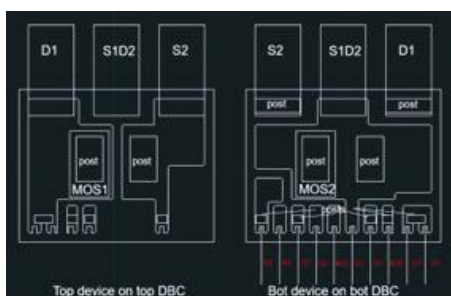
Figure I.1.24.2 Layout 3.0 for the double-side cooled SiC MOSFET phase-leg module.
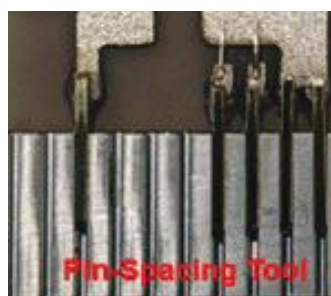
Figure I.1.24.3 An aluminum fixture was made to increase the yield during the soldering of the gate-driver pins on a DBC substrate of the module.

Figure I.1.24.4 A fabricated double-side cooled SiC phase-leg power module encapsulated by EP-2000 for 200°C-T_j operation.

To achieve the M2.5 milestone which is to demonstrate planar packaging technology of SiC phase-leg module working at a junction temperature of 200°C, a module shown in Figure I.1.24.4 with Layout 3.0 was made and encapsulated with a high-temperature material, EP-2000 from LORD LCC. Table I.1.24.2 is a list of the measured static characteristics of the packaged switches in the module. More modules of this kind are being made as backups to the six modules previously delivered to ORNL for inverter assembly. Some will be tested for high-temperature and reliability study.

Table I.1.24.2 Electrical Test Results Fabricated Power Module

	Top Device	Bottom Device
On-Resistance @ VGS = 15 V, ID = 40 A	16.9 mΩ	16.1 mΩ
Blocking Capability @ VGS = -3.3 V, VDS = 1.2 kV	254 nA	

2. Simulation of the Thermo-Mechanical Effects of Different Encapsulation Materials on the Double-Side Cooled Power Module

This year we also examined the effects of rigid encapsulant materials on the thermo-mechanical reliability of the sintered-silver bonds inside the double-side cooled power module. Figure I.1.24.5 shows a cross-sectional schematic of the module that was utilized for the analysis done via ANSYS finite element analysis (FEA) simulations. The two encapsulation materials used to package the module were studied. The simulated material

properties are listed in Table I.1.24.3. The thermo-mechanical reliability was evaluated by measuring the plastic deformation located at the three bonded interfaces inside the module, i.e., interposer–substrate attach, interposer–chip attach, and chip attach, during a standard JESD22-A104-B temperature cycling test.
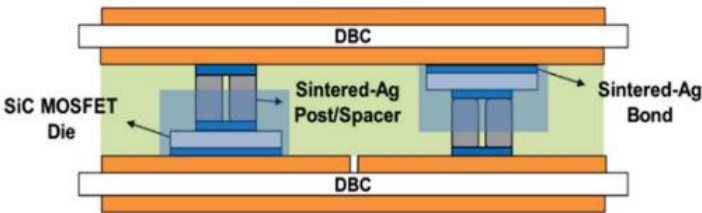
Figure I.1.24.5 Cross-sectional view of the simulated module.

Table I.1.24.3 Material Properties of the Two Encapsulants Used in the Analysis

Encapsulation Material Name	Encapsulation Type	Elastic Modulus (GPa)	Coefficient of Thermal Expansion, CTE (ppm/°C)
LORD ME-531 underfill	Rigid	6.0	21.0
LORD EP-2000 underfill	Rigid	17.1	14.9

Figure I.1.24.6 is a summary of the results from the FEA simulations showing the plastic deformation at each of the three bonded interfaces for the two different encapsulants. A configuration without encapsulant was also studied and included in the plot for comparison. The results suggest that encapsulating the module with either of the two rigid encapsulants, ME-531 and EP-2000, can reduce the deformation inside the bonds, thus improving the joint reliability over the use of no encapsulants at all. Future FEA simulations will be refined and run by subjecting the module to compressive stresses like the ones we expect to see when the module is integrated into the cooling manifold of the traction inverter. Further analysis will also need to be done to determine the physical mechanism through which these rigid encapsulants help improve the bond reliability of the module.
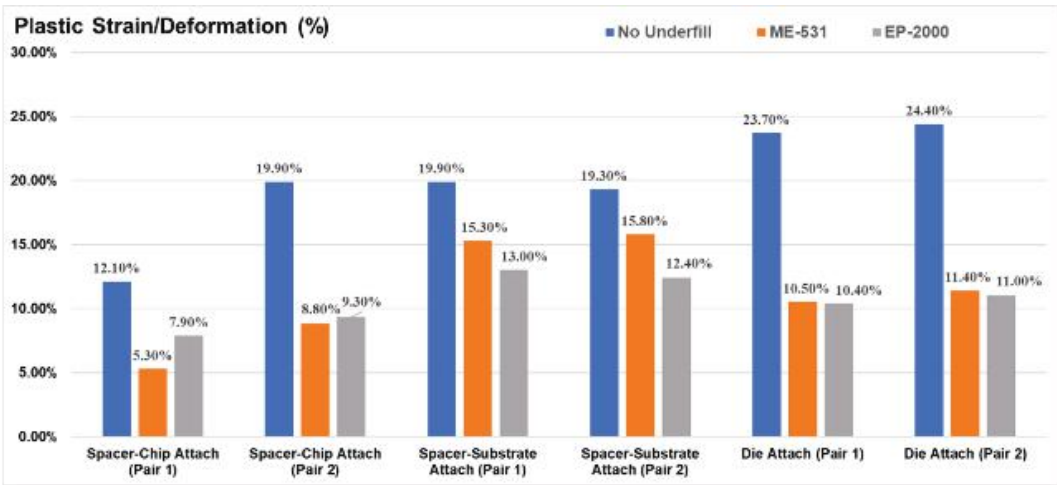
Figure I.1.24.6 Plots of the simulated deformation at the three bonded interfaces of the double-side power module.

3. *Current Sensor Based on Parasitic Inductance of the Power Device*

In the last annual report, a proposed current sensor with dynamic feedback compensation was presented. The designed sensor was validated on a CREE power module under the DPT test. In the past experiment, the temperature of the power module is room temperature, and the initial correction factor β is assigned with

different values so that the adjustment of β to the optimal one corresponding to the room temperature is observed. Experimental results show that β converges quickly to its optimal value, which results in a good current sensor's output. In this report, the test is extended to the condition, where the operating temperature of the power module is changed by a heat plate. The experimental sensing current is compared with that obtained by a commercial Rogowski coil. Two methods are proposed to eliminate the influence of the temperature on the parasitic resistor between the kelvin and power source terminal. Figure I.1.24.7 shows the proposed current sensor scheme with compensation of the temperature effect and the algorithm implemented in MCU to calculate the updated correction factor.
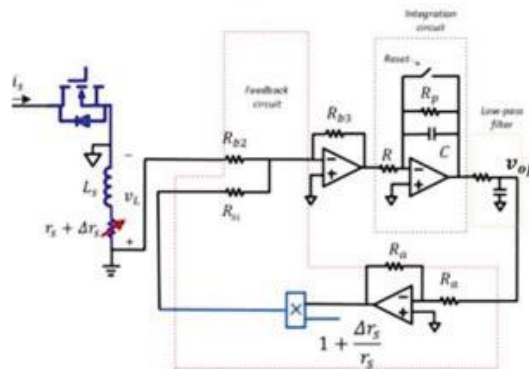
(a) Current sensor scheme
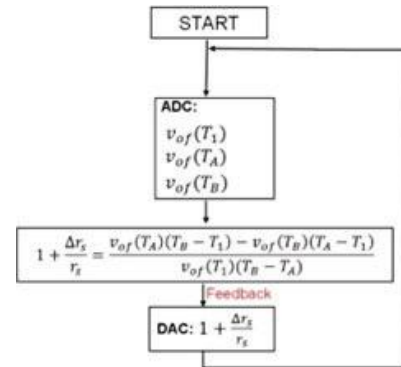
(b) Algorithm to calculate β (v_of (T_1),v_of (T_A),v_of (T_B) are samplings of the current sensor's output at T_1,T_A,T_B, respectively)

Figure I.1.24.7 Proposed current sensor scheme and algorithm to calculate the correction factor.

The parameters of the current sensor scheme in Figure I.1.24.7 are designed at the maximum operating temperature of $150^{\circ}C$. It is observed from Figure I.1.24.8 that, at $150^{\circ}C$, the sensing current agrees well with the one measured with the Rogowski coil probe.
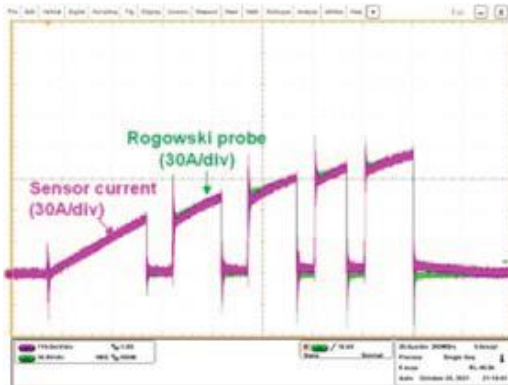
(a) Sensing current compared to the current measured by the Rogowski probe

(b) Magnified area of the fifth pulse

Figure I.1.24.8 Sensing current with the proposed sensor with dynamic feedback versus the one measured by the Rogowski coil at $150^{\circ}C$.

A simplified current sensor is proposed with the following improved features:

- Independence of temperature

- Having fewer components compared to the current sensor with feedback.

- Providing possibility for extension to high-temperature operation. High-temperature components are available for this proposed scheme.

- Algorithm for reconstruction of the switching current is less complicated.

The proposed simplified sensor scheme is presented in Figure I.1.24.9. The processing circuit is similar to the Rogowski-coil-based method. The following modified features have been applied.

- Added active reset switch with modified switching pattern

- Method to reconstruct the switching current based on two samplings of the current sensor's output
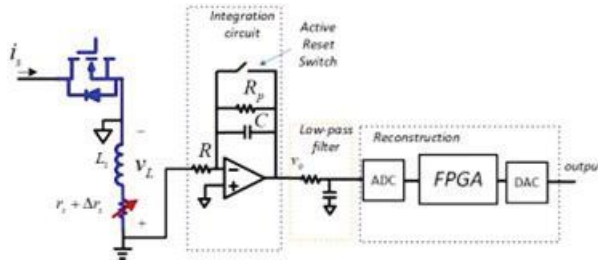
Figure I.1.24.9 Proposed simplified current sensor scheme.

For simplification in testing, the current sensor board is designed separately from the gate driver board, as shown in Figure I.1.24.10. The designed sensor board includes two proposed current sensor schemes: the one with feedback compensation in Figure I.1.24.7, and the simplified one with temperature independence in Figure I.1.24.9.
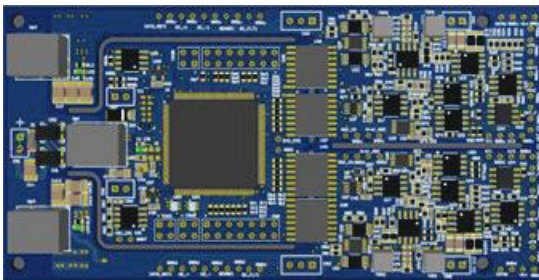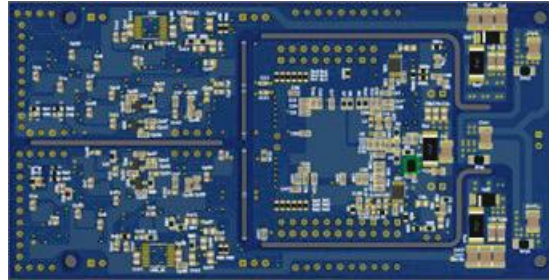
(a) Top   (b) Bottom

Figure I.1.24.10 Designed current sensor (122mm x 61.5mm).

4. Design and test of the Six-Output Power Supply with An Air-Core Transformer

4.1. Manufactured Power Supply

A six-output Class-E dc-dc converter was fabricated. Figure I.1.24.11 shows the schematics and the hardware. Both the input inductor and 6-output transformer are designed with PCB winding and without any magnetic core. Power resistors are used as the load.

(a) (b)
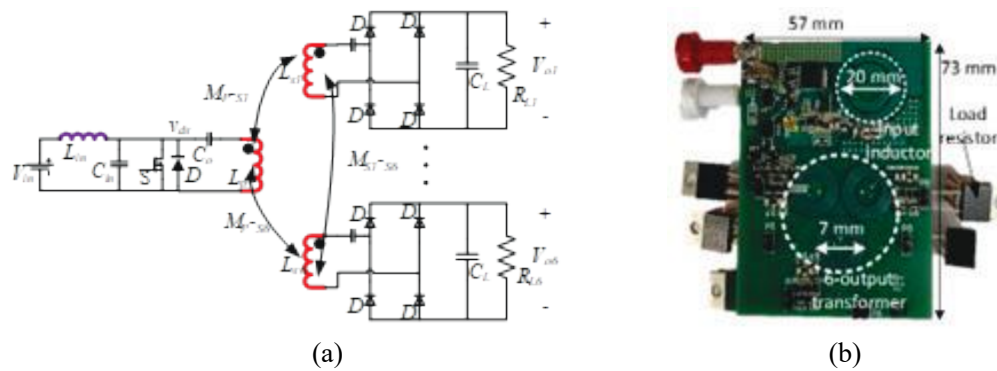
Figure I.1.24.11 The schematics and hardware of the six-output Class-E gate power supply.

Table I.1.24.4 summarizes the measurement results of the inductances compared with the Q3D simulation. It can be seen that the measured inductances match very well with the simulation.

Table I.1.24.4 Inductance measurement results

Parameters	Description	Simulated	Measured	Error
L_{in}	Input inductance	162 nH	163 nH	0.6%
L_P	Primary self-inductance	488 nH	532 nH	9%
L_{S1}	Secondary self-inductance	1.2 μH	1.286 μH	7.2%
M_{P-S1}	Primary-Secondary mutual inductance	273 nH	303 nH	11%
M_{S1-S6}	Secondary-Secondary mutual inductance	550 nH	601 nH	11%

4.2. Performance of the Power Supply with Load Resistor

The power supply was tested with the load resistor shown in Figure I.1.24.11(b). Figure I.1.24.12 shows the waveforms with output voltage regulation at 12 W. The output voltage is 20 V. The load resistance is 200 Ω for each output. On-off control is used with an upper limit of 19.6 V and a lower limit of 19 V. The average output voltages of the six outputs are shown in Table I.1.24.5. From the transient waveforms in Figure I.1.24.12(b), the transient time for each on period is about 8 switching cycles.   ZVS is observed from the steady-state waveforms. The ac component of V_o shows the ripple is as expected.

(a) (b) (c)
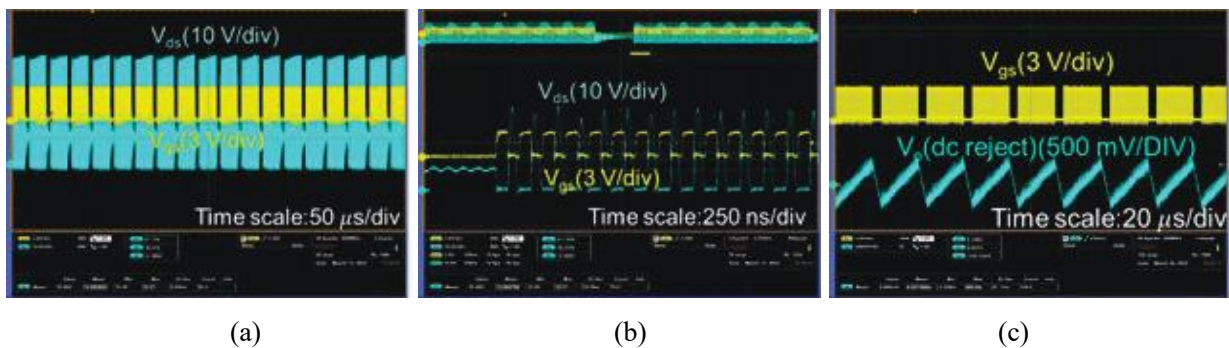
Figure I.1.24.12 Testing waveforms at 12 W output power. (a) Waveforms of V_{ds} and V_{gs}. (b) V_{ds} waveforms during on transient. (c) AC component of the output voltage.

Table I.1.24.5 Summary of the output voltages and efficiency

Vo1	Vo2	Vo3	Vo4	Vo5	Vo6	Pin	Efficiency
19.3 V	19.6 V	19.3 V	19.6 V	19.6 V	19.6 V	13.6 W	84%

4.3. Performance at Different Ambient Temperatures

The high-temperature testing was conducted by placing the PCB in the environment chamber by Tenney. Figure I.1.24.13 shows the testing setup in the environment chamber. The temperature in the chamber varied from 25°C to 72°C. Figure I.1.24.14 shows the efficiency at different temperatures. Figure I.1.24.15 shows the waveforms at 72°C. ZVS was maintained.

Figure I.1.24.13 Test setup in the environment chamber.
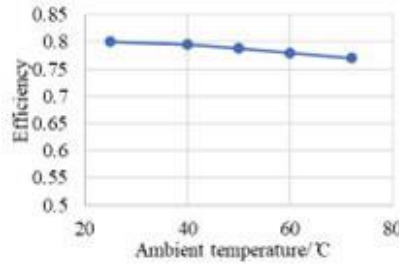
Figure I.1.24.14 Efficiency at different ambient temperatures.
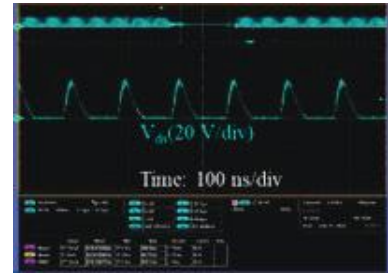
Figure I.1.24.15 Zoomed in waveforms of V_{ds} during steady state.

4.4. Performance of the Power Supply with Gate Driver and Power Module

The testing is to justify that the power supply provides the right voltage and enough power to drive the power module. Figure I.1.24.16 shows the test setup. The six outputs are paralleled as a single output and connected with the power input of the gate drivers on the daughter board. The power module is plugged under the motherboard The PWM signals come from the function generator. The gate output is measured with the oscilloscope. Figure I.1.24.17 shows the measured two gate waveforms at 40 kHz switching frequency. The gate output voltage satisfies the requirement of the power module as +15V/-4V. The output power for the two gates is 1.6 W. Therefore, the rated 12 W output of the power supply is enough for six gate drivers.
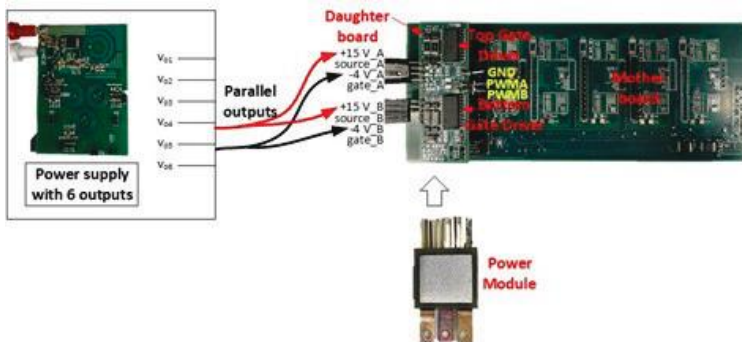
Figure I.1.24.16 Hardware setup for the testing with gate driver and power module.

Figure I.1.24.17 Gate waveforms of one power module at 40 kHz.

Summary

Yield of module fabrication was improved with modified layout and refined fabrication process. A high-temperature encapsulation material was identified and used to encapsulate fabricated phase-leg modules. Thermo-mechanical effects of different encapsulation materials on the double-side cooled power module were studied by running simulations.

A gate driver integrated with the short-circuit protection based on the parasitic inductance was designed and tested in the six-phase inverter. A current sensor based on the parasitic inductance of the power module was designed and integrated with the gate driver. To eliminate the temperature influence on the parasitic resistor between the kelvin terminal and the power source terminal, two methods were proposed and verified in the test. The performance of the current sensor was verified in a double pulse test (DPT).

Air-core inductor and transformer with six secondary windings were designed for a single power supply with six outputs. The measured inductances agree well with the design. The power supply provides identical voltages for all six outputs at the rated power. The efficiency is 84% at room temperature, while it gradually drops to 77% at 72℃ ambient temperature. Since the ambient temperature is estimated to be 65℃ when the junction temperature of the power module is 200℃, the design of the power supply meets the temperature requirement. The testing with the gate driver and power module proved the function of the gate power supply.

Key Publications

1. Guo-Quan Lu and Chao Ding, "Double-Side Cooled Power Modules With Sintered-Silver Interposers," Patent Application: PCT/US2022/071087.

2. S. Lu, T. Zhao, Z. Zhang, K. D. Ngo, R. Burgos, and G.-Q. Lu, "Low Parasitic-Inductance Packaging of a 650 V/150 A Half-Bridge Module Using Enhancement-Mode Gallium-Nitride High Electron Mobility Transistors," *IEEE Transactions on Industrial Electronics,* vol. 70, no. 1, pp. 344-351, 2022.

3. S. Lu, Z. Zhang, C. Buttay, K. D. Ngo, and G.-Q. Lu, "Improved Measurement Accuracy for Junction-to-Case Thermal Resistance of GaN HEMT Packages by Gate-to-Gate Electrical Resistance and Stacking Thermal Interface Materials," *IEEE Transactions on Power Electronics,* vol. 37, no. 6, pp. 6285-6289, 2022.

Acknowledgments

I.1.25 Implementation of WBG devices in circuits, circuit topology, system integration as well as SiC devices (The Ohio State University)

Dr. Anant Agarwal, Principal Investigator
The Ohio State University
2015 Neil Avenue
Columbus, OH 43210
E-mail: agarwal.334@osu.edu

Dr. Jin Wang, CO-Principal Investigator
The Ohio State University
2015 Neil Avenue
Columbus, OH 43210
E-mail: wang.1248@osu.edu

Susan Rogers, DOE Technology Development Manager
U.S. Department of Energy
Email: Susan.Rogers@ee.doe.gov

Start Date April 1, 2022   End Date: March 31, 2023
Project Funding: $300,000   DOE share: $300,000   Non-DOE share: $0

Project Introduction

All device vendors have compromised reliability/ruggedness of SiC MOSFETs to reduce cost. Short channel length is a good example that reduces device size and cost at the expense of reduced short-circuit time of 2 - 3 µs. Another example is the gate oxide thickness which has been thinned to 30 - 40 nm without reducing the gate voltage in order to reduce device size and cost. This leads to gate oxide leakage issues and susceptibility to rupture during extreme events such as short-circuit and exposure to static electricity. Hence, commercial devices, available to-date, are not suitable for insertion into a vehicle powertrain for long operational life. A comprehensive reliability study is warranted for commercially available devices both as discrete devices and in an inverter to uncover failures such as threshold voltage instability, inadequate short circuit time, gate oxide failures due to gate voltage overshoot and high junction temperature, as well as body diode instability (Figure I.1.25.1). OSU is working collaboratively with Sandia National Lab and Suny Poly on this project (Figure I.1.25.2).
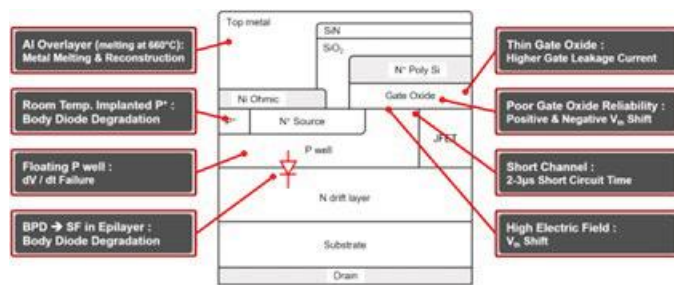
Figure I.1.25.1 SiC MOSFET Reliability Issues.
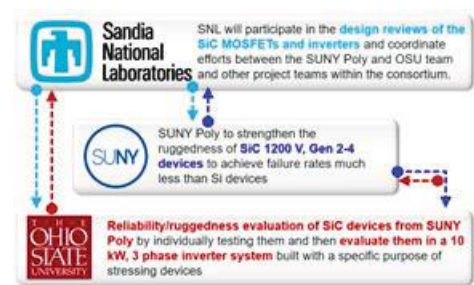
Figure I.1.25.2 Key Partnerships.

Objectives

The overall objective of the project is to ensure that SiC devices are reliable and rugged as required in automotive applications for the operational life of 300,000 hrs and create new device designs to address various weaknesses in currently available commercial devices. OSU work will focus on reliability/ruggedness evaluation of SiC devices by individually testing them and then evaluating them in a 10 kW, 3-phase inverter system built with a specific purpose of stressing devices using realistic drive cycles such as a 10-minute hill climb. It should be noted that the primary purpose of the 10 kW inverter is to provide a platform for stressing

the SiC devices under accelerated but realistic drive conditions and NOT to meet the 100 kW power and power density goals. The 100 kW inverter will be built by other team members. OSU will share the findings with SUNY Poly and collaborate with them to strengthen the existing device designs to overcome the specific weaknesses in the device. These devices will be fabricated in a state-of-the-art commercial SiC Foundry. The new designs will be improved every year through extensive testing by OSU, re-design (in collaboration between OSU and SUNY Poly) and subsequent fabrication.

Objectives (FY2022)

- Reliability/ruggedness evaluation of Gen-2 MOSFETs from SUNY Polytechnic.

- An improved three-phase Inverter (Inverter-4) is built using Gen-2 MOSFETs to test the devices under realistic drive cycles.

Approach

Collaboration with National Laboratory

OSU will coordinate and collaboratively conduct work with the Sandia National Laboratory (SNL) on selected tasks integral to the completion of the project. The results of this collaborative effort with the national laboratory will be included in all project reporting. SNL will participate in the design reviews of the SiC MOSFETs and inverters and coordinate efforts between the SUNY Poly and OSU team and other project teams within the consortium.

Results [Task 1 - Reliability evaluation of Gen-2 MOSFETs]

The Gen-2 1.2 kV 4H-SiC planar power MOSFETs from SUNY Poly are tested in this report. To investigate the Gen-2 device performance, the reliability measurements including double pulse test, short circuit test, body diode degradation test and bias-induced threshold voltage instability test are performed.

A. Double Pulse Test

A double Pulse Test (DPT) is used to determine the switching performance of the Gen-2 MOSFETs. The DPT setup is a load inductor connected with a freewheeling diode that measures the switching performance of the device under test (DUT). For this work, as an alternative to a freewheeling diode, a sample device from SUNY Poly having the same rating as the upper device is used as shown in Figure I.1.25.3 (a). The 1.2 kV Gen-2 MOSFETs are biased at a constant drain voltage of 800 V. The gate terminal of the DUT is subjected to a gate pulse of [-4 V,18 V] (Figure I.1.25.3 (b)) using an appropriate gate driver. The gate terminal resistor is set up to be 20 Ω. The first pulse is used to charge the inductor and the end of the first pulse gives the turn-off transient, whereas the beginning of the second pulse results in a turn-on transient. A 375 µH inductor is used to establish a steady state current of 20 A.

(a)   (b)
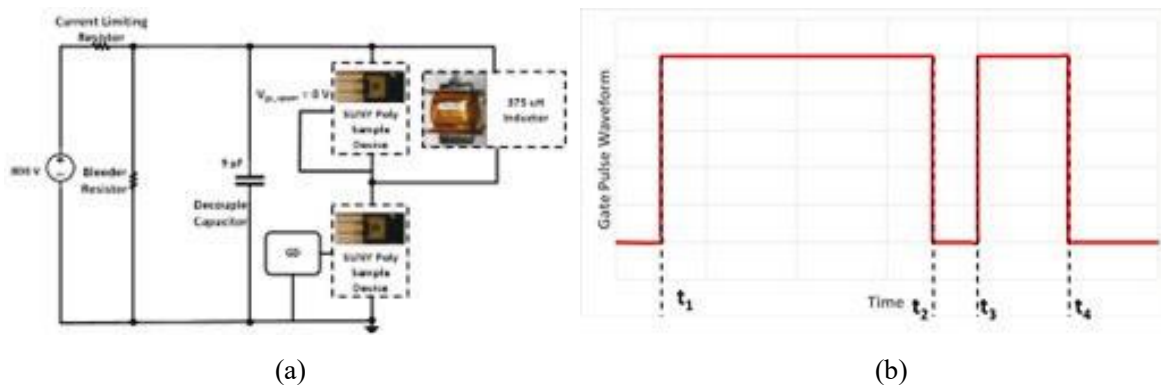
Figure I.1.25.3 (a) DPT Test Setup and (b) Gate Pulse Waveform

Figure I.1.25.4 shows the typical switching characteristics of a fabricated device. Switching speed is defined by switching on and off times. Switching on time can be defined as the time between 10% of gate-source voltage and 10% of drain-source voltage in the turn-on transient. The switching dV/dt can be defined as the changing rate of drain-source voltage while switching is happening. Numerical integration of Drain current (IDS) and drain-source voltage for both on and off transient over the switching period gives the net switching loss. The Gate resistor in the test is 20 Ω for both turn-on and turn-off, which maintains a relatively high switching speed and reduces the ringing on gate-source voltage. Test results are extracted in the following Table I.1.25.1.

| (a) | (b) |
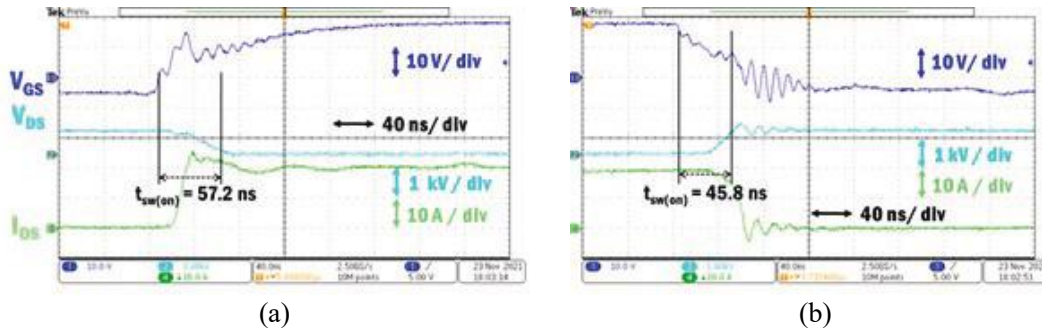
Figure I.1.25.4 (a) Device switch on (b) Device switch off

Table I.1.25.1 Switching Results

Device	On-Time (ns)	Off Time (ns)	Switch on dV/dt (kV/μs)	Switch off dV/dt (kV/μs)	Switch on Loss (μJ)	Switch off Loss (μJ)
1-A3	76.4	48.4	9.89	32.58	516.56	163.55
1-B3	73	69.8	3.97	22.96	487.08	262.11
1-C1	68.8	62	11.27	26.49	469.37	217.47
1-E1	99.6	50.2	7.74	36.54	705.13	153.73
1-F1	96.4	47.8	5.19	38.41	645.60	142.19
1-G1	77.8	48.8	10.58	34.54	529.68	155.41
1-H3	75.4	52.6	10.61	37.68	538.99	137.56
1-I1	74	50	10.39	39.76	514.85	143.50
1-J1	58	61.6	3.77	34.39	377.45	163.61
1-K1	49	70.2	16.90	28.47	320.40	196.52

B. Short Circuit Test

The Short circuit withstand times (SCWTs) for 1.2 kV Gen-2 devices are measured at a drain voltage of 800V. The devices are tested with a gate turn-on voltage of 20 V and a gate turn-off voltage of 0 V. A 1 μs turn-on pulse is used as the initial test pulse, then increased in 0.1 μs increments until the device fails. The short circuit withstand time (SCWT) is defined from the start of the gate turn-on to the start of the gate turn-off. In this study, the effects of different design considerations are examined with regard to the SCWT.

Test results are summarized in Table I.1.25.2. The SCWTs with respect to the peak current for Gen-2 devices are shown in Figure I.1.25.5 below. As the peak current decreases, the SCWT increases. In terms of design considerations for 1.2 kV Gen-2 devices, the P-well structure depth is 1.8 μm, with variations in the width of the JFET region (1/2 W_{JFET}) and the length of the channel (L_{ch}). Figure I.1.25.6 shows the effects of varying the half

JFET width with a channel length of 0.5 µm, with a sharp decrease in SCWT as the 1/2 W_{JFET} increase from 0.4 µm to 0.5 µm. Figure I.1.25.6 also shows the effects of varying the length of the channel at 1/2 W_{JFET} of 0.4 µm and 0.8 µm. For 1/2 W_{JFET} = 0.8 µm, there is a steady improvement in SCWT from L_{ch}= 0.3 µm to L_{ch}= 0.5 µm. For 1/2 W_{JFET}= 0.4 µm, there is no improvement from L_{ch}= 0.3 µm to L_{ch}= 0.5 µm. **In conclusion, the Gen-2 MOSFETs with a deep p-well junction and narrow JFET can achieve SCWT of 7 µs.**

Table I.1.25.2 Short Circuit Test Results

Device		1/2WJFET (um)	Lch (um)	Peak Current (A)	SCWT (us)
A	2-A2	0.8	0.5	196	2.41
	2-A3			190	2.48
B	2-B3	0.6	0.5	198	2.56
	2-B4			198	2.55
C	2-C2	0.4	0.5	118	7.05
D	2-D1	0.8	0.4	252	2.0496
	2-D3			262	2.0488
E	2-E1	0.4	0.4	132	6.5836
	2-E2			136	6.5936
F	2-F1	0.8	0.3	320	1.6284
G	2-G1	0.4	0.3	140	7.0984
H	2-H1	Aggressive Design		128	5.6068
	2-H2			152	4.0748
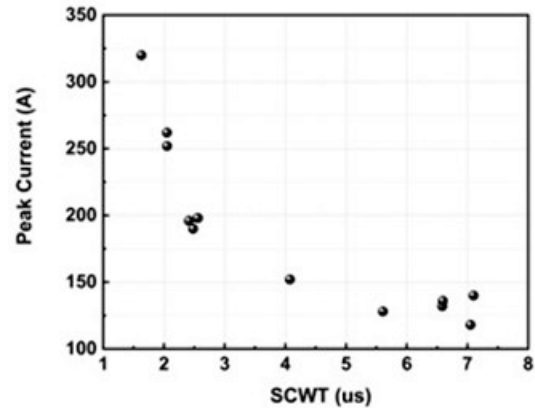
Figure I.1.25.5 Peak current as a function of SCWT.
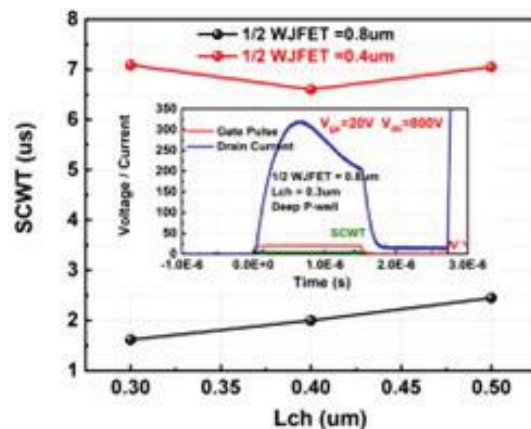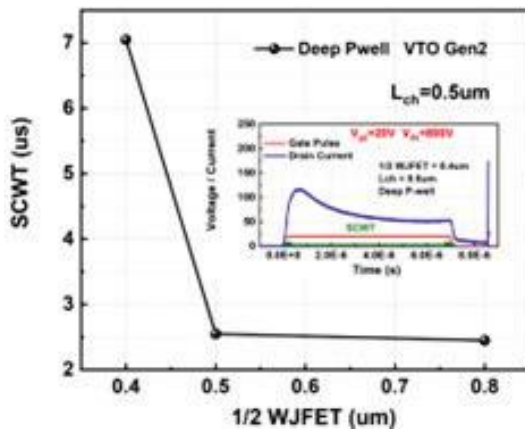
Figure I.1.25.6 SCWT of Gen-2 Devices.

C. Body Diode Stability

In previous reports, the effects of the body diode degradation on the device performance of the 4H-SiC power MOSFETs can be concluded as the increase in the forward voltage drop of the built-in body diode, the increase in the on-state resistance, and the increase in the forward leakage current in the blocking mode. These effects can be attributed to several reasons that may be responsible for the body diode degradation. Firstly, the device may use epi-layers with many basal plane dislocations (BPDs). Furthermore, the device may use room temperature ion implantation to form the P^+ contact resulting in BPDs.

A Gen-2 device with a JFET width of 0.4 µm is forward-bias stressed with 10 A for 50 hours. The electrical tests are performed before the stress and repeated after stress at several time points. The after-stress tests are all performed after cooling down the device to room temperature. The evolution of the electrical performance as a function of the stress time is presented in Figure I.1.25.7. As shown in Figure I.1.25.7, no degradation of the on-state resistance can be observed. A slight increase in the forward voltage drop of the built-in body diode and a decrease in the forward leakage current in the blocking mode is shown in Figure I.1.25.7. During the

long-term body diode stress with a negative gate bias, the threshold voltage shows an increasing trend. The increased threshold voltage makes the 3rd quadrant I-V of the body diode shift to the left and reduces the forward leakage current in the blocking mode. It can be concluded that no significant body diode degradation can be observed in 1.2 kV Gen-2 MOSFETs.
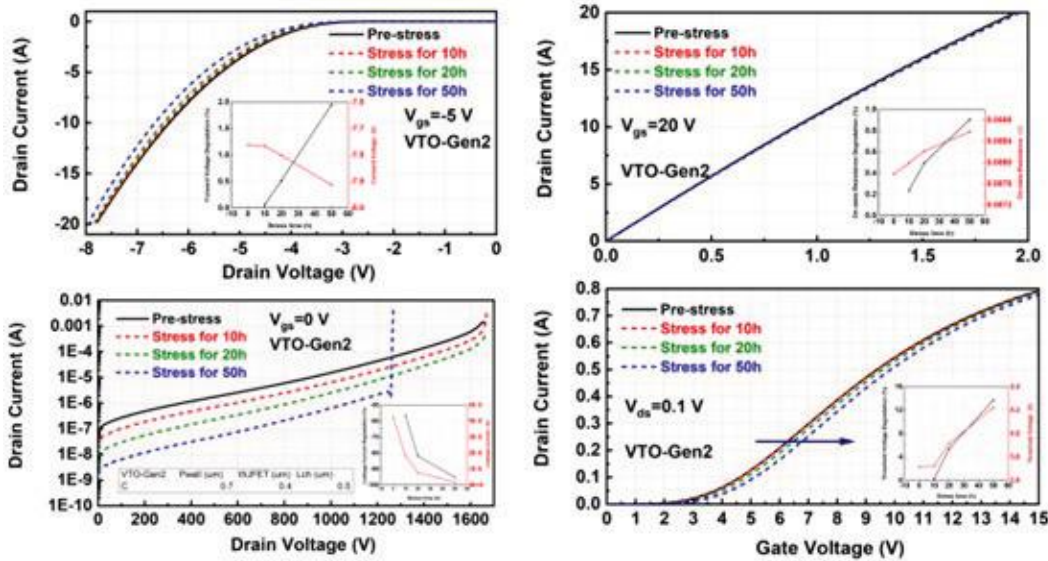
Figure I.1.25.7 The evolution of the 3rd quadrant body diode Id-Vd curve at V_{gs} = -5 V (top left), 1st quadrant output Id-Vd curve at V_{gs} = 20 V (top right), 1st quadrant forward I_d-V_d curve in the blocking mode at V_{gs} = 0 V (bottom left), and 1st quadrant transfer I_d-V_g curve V_{ds} = 0.1 V (bottom right) as a function of the body diode stress time.

D. Bias-induced threshold voltage instability measurement

The threshold voltage shift of Gen-2 MOSFETs as a function of stress time is shown in Figure I.1.25.8. When a positive DC bias of +20 V is applied to the gate for 50 hours, the threshold value shift in the positive direction is about 0.2 V for Gen-2 devices. Conversely, when a negative bias of -10 V is applied to the gate for 50 hours, the threshold voltage shifts in the negative direction. Threshold voltage shifts are caused by the capture of electrons and holes by traps in the oxide layer near the SiC/SiO2 interface for positive and negative gate stresses respectively. When positive bias stress is applied to the gate, electrons are injected into the near interface traps from the inversion layer in the conduction band via band-to-trap tunneling. This injection efficiency is determined by the tunneling probability and the barrier height as a function of time and electric field. Under negative bias stress, the holes are trapped into oxide traps while previously trapped electrons back-tunnel into the conduction band, thus resulting in a negative shift of threshold voltage.
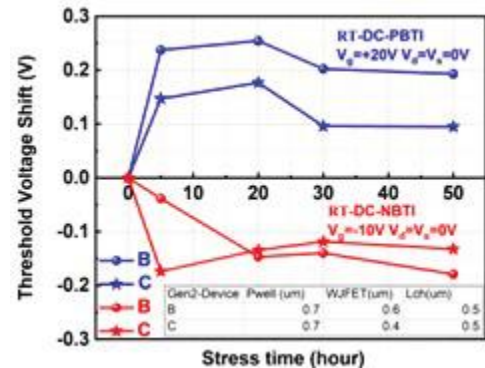
Figure I.1.25.8 Time-dependent threshold voltage shifts for positive bias stress of +20 V and negative bias stress of -10 V for 50 hours.

Results [Task 2 - Inverter-4 build with Gen-2 MOSFETs]

A. Inverter-4 with separate capacitor bank design

The capacitor bank is optimized to reduce the switching interference between inverter phase legs during high-power operation. During high power operation, the WBG power devices inevitably generate high-frequency noises due to high dv/dt and di/dt switching events. During the test in previous generations, the device gate waveform displayed noise caused by other phase leg switching events, which can potentially lead to shoot-

through or exceed the allowable gate voltage range. To solve this issue, additional stray inductance is introduced between phase legs by using a separate capacitor bank design. Figure I.1.25.9 shows the new capacitor bank design. The value of the additional stray inductance is properly designed to provide a sufficient impedance to attenuate the interference while avoiding increasing the current stress on dc link capacitors.
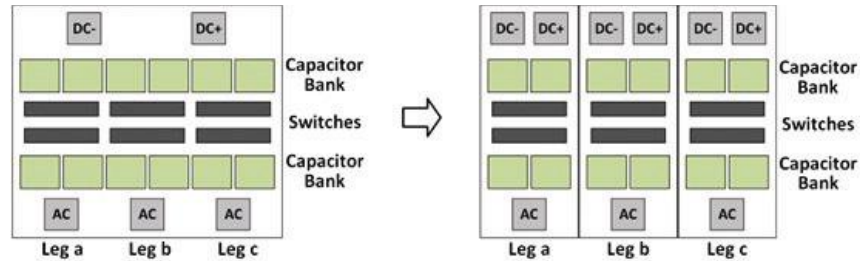
Figure I.1.25.9 Separate capacitor bank design in Gen-4 inverter

Simulations are conducted to verify the dc-link capacitor current stress with additional stray inductance between phase legs. The equivalent inverter circuit diagram and simulation results are shown in Figure I.1.25.10. The current stress on the dc link capacitor increases from 3.15 Arms to 5.46 Arms when implementing the separate capacitor bank design. Considering the high current capability of the ceramic capacitor used, the penalty is acceptable. As shown in Figure I.1.25.11, the proposed inverter prototype has been built and tested. Connected with RL load, the inverter prototype reaches a power density of more than 120 kVA/liter and efficiency of more than 98% at 800 V input and 480 V output voltage. Preliminary comparisons in Figure I.1.25.12 have shown improved interference mitigation for the separate capacitor bank design.
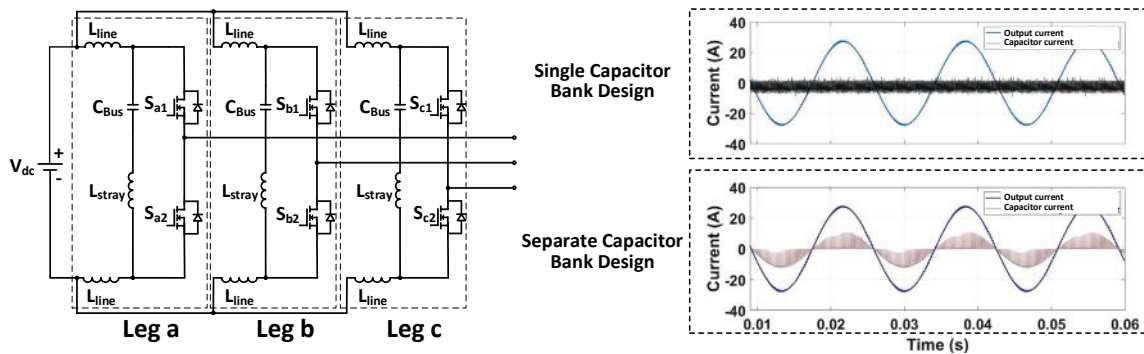
Figure I.1.25.10 Separate capacitor bank design in Gen-4 inverter
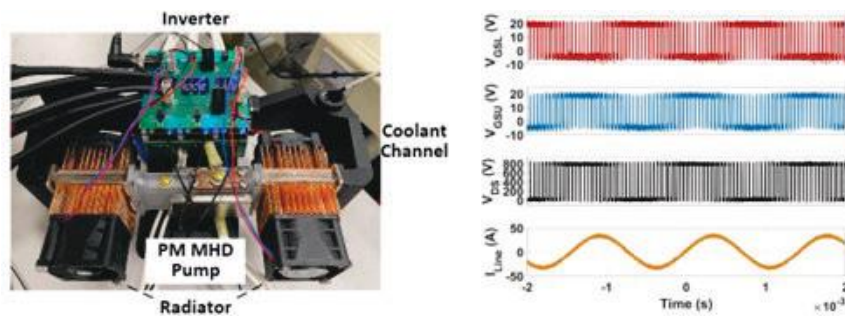
Figure I.1.25.11 Gen-4 inverter prototype operation under 20 kVA output
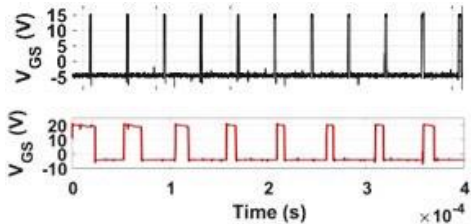
Figure I.1.25.12 Inverter gate signal waveform comparison

B. Thermal and mechanical design of the Inverter-4

Compared with previous generations, the Gen-4 inverter implements a liquid metal cooling system driven by an integrated permanent magnet (PM) magnetohydrodynamic (MHD) pump. By replacing water coolant with liquid metal, a significant reduction of the cold plate's thermal resistance can be realized. To push the power density of the inverter design to the next level without sacrificing system efficiency, the coolant pump is integrated into the dc bus. Instead of using an external auxiliary power source to inject current into the channel, the dc bus current will directly go into the liquid metal coolant channel. Thus, the higher the output power, the higher the input dc current and the larger the flow rate.
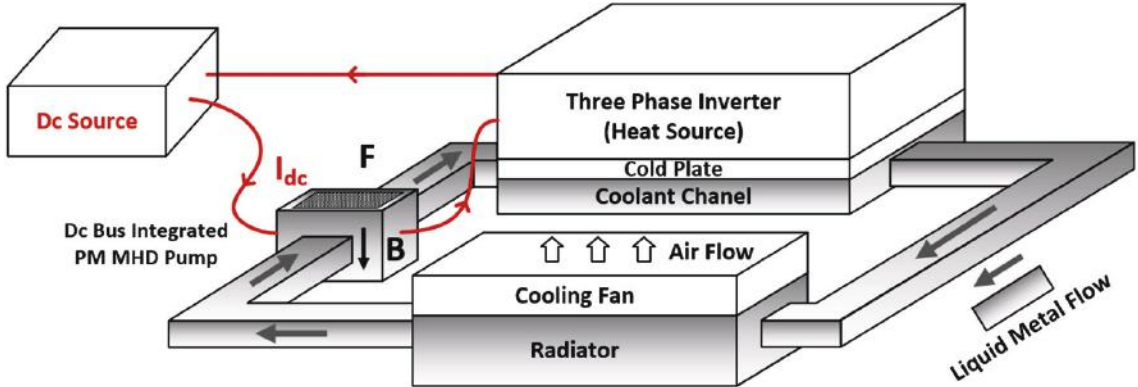
Figure I.1.25.13 Schematic of liquid metal cooled Gen-4 inverter with PM MHD Pump

Based on the derived flow rate equation and the aid of FEA simulation tools, the flow resistance in the cooling loop is optimized by using 3D-printed conduits with smoothly varying cross-sections. The overall cooling loop design is shown in Figure I.1.25.14. Cold plate and radiator channels are made of stainless steel for its compatibility with the liquid Gallium alloy. Thanks to the great thermal conductivity of liquid metal material, internal pin fins on metal cold plates and radiators can be eliminated without sacrificing heat exchange efficiency.
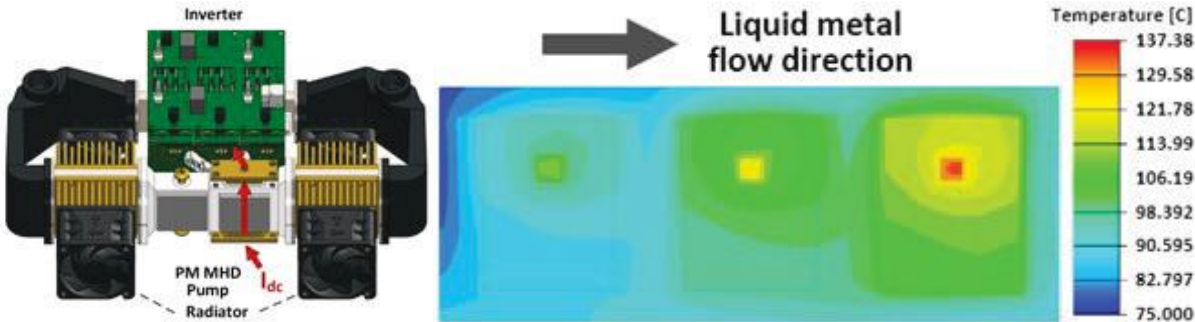
Figure I.1.25.14 Overall inverter cooling loop design and thermal simulation results

The thermal simulation is conducted to verify the cooling system capability. In FEA simulation, the highest junction temperature is lower than 150°C with 41 W power loss on each device at 25°C ambient, the coolant temperature is around 65°C. The critical measurements and estimations in the experimental test are summarized in Table I.1.25.3. The measurement of the case temperature is obtained from two sets of optical temperature sensors. And a difference of about 15°C between the hottest and coldest devices can be seen, which matches well with the Icepak thermal simulation. The coolant temperature is measured by the thermal couple immersed in the cooling channel.

Table I.1.25.3 critical measurements and estimations

Measurements & Estimations	Value
T_{Case}	103.4 °C
$T_{Coolant}$	62.4 °C
Estimated P_{Loss}	41 W (per device)
Q	0.55 L/min
P_{Pump}	< 0.1 W
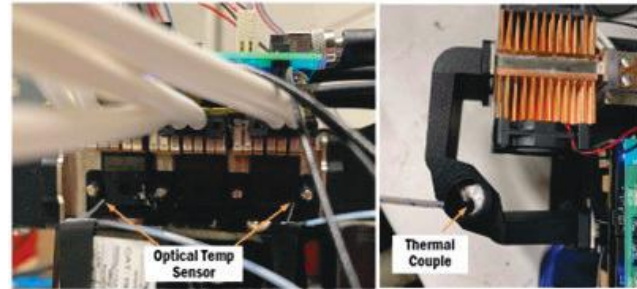
Figure I.1.25.15 Device case temperature and coolant temperature measurements

Conclusions

The reliability characteristics of the Gen-2 devices are evaluated in this report. During short circuit conditions, a much narrower JFET region and a deeper P-well region in the Gen-2 MOSFETs, achieve long SCWT. Body-diode stability in Gen-2 devices with room temperature implants has been demonstrated which indicates that ion implantation at room temperature for p$^+$ contact does not cause process-induced BPDs in 1.2 kV Gen-2 MOSFETs fabricated by SUNY POLY. Threshold voltage shift value below 0.3 V under positive and negative gate bias demonstrates that Gen-2 MOSFETs have smaller Near Interface Oxide Trapss in the gate oxide. Inverter-4 reaches a power density of more than 120 kVA/liter and an efficiency of more than 98% at 800 V input and 480 V output voltage. This inverter is being used to test Gen-2 devices under realistic drive conditions and will be used to test Gen-3 devices as well.

Key Publications

1. Jiashu Qian, Tianshi Liu, Jake Soto, Mowafak Al-Jassim, Robert Stahlbush, Naeemulah Mahadik, Limeng Shi, Michael Jin, Marvin H White and Anant K Agarwal, "A Comparison of Ion Implantation at Room Temperature and Heated Ion Implantation on the Body Diode Degradation of Commercial 3.3 kV 4H-SiC Power MOSFETs," 2022 IEEE 9th WiPDA.

2. Suvendu Nayak, Susanna Yu, Hema Lata Rao Maddi, Michael Jin, Limeng Shi, Swaroop Ganguly, and Anant K. Agarwal, " Non-isothermal simulation of SiC DMOSFET short circuit capability," 2022 Japanese Journal of Applied Physics.

3. Maddi, Hema L.R., Susanna Yu, Shengnan Zhu, Tianshi Liu, Limeng Shi, Minseok Kang, Diang Xing, Suvendu Nayak, Marvin H. White, and Anant K. Agarwal. "The Road to a Robust and Affordable SiC Power MOSFET Technology" Energies. 2021; 14(24): 8283.

4. Junchong Fan, Yue Zhang, Jin Wang, Madhu S. Chinthavali and Radha K. Moorthy, "Liquid Metal based Cooling for Power Electronics Systems with Inductor Integrated Magnetohydrodynamic Pump (MHD Pump)," 2021 IEEE 8th WiPDA.

References

1. D. Kim and W. Sung, "Improved Short-Circuit Ruggedness for 1.2kV 4H-SiC MOSFET Using a Deep P-Well Implemented by Channeling Implantation," in IEEE Electron Device Letters, vol. 42, no. 12, pp. 1822-1825, Dec. 2021.

2. Y. Abdullah, X. Li, K. Wang, J. Wang, L. Liu, and S. Bala, "High temperature design of a gan based modular integrated drive with natural cooling using metal clad pcbs," in 2019 IEEE Energy Conversion Congress and Exposition (ECCE), 2019, pp. 4012–4017.

3. K. Konishi, R. Fujita, Y. Mori and A. Shima, "Inducing defects in 3.3kV SiC MOSFETs by annealing after ion implantation and evaluating their effect on bipolar degradation of the MOSFETs" Semicond. Sci. Technol. vol. 33, issue 12, 2018.

4. R. E. Stahlbush, K. N. A. Mahakik, A. J. Lelis, R. Green, "Effects of Basal Plane Dislocations on SiC Power Device Reliability", in Proc. 2018 IEEE International Electron Devices Meeting (IEDM), pp. 448-449, 2018.

I.2   Electric Drive Technologies Development

I.2.1   Cummins High Power Density Inverter (Cummins Inc.)

Santhosh Krishnamoorthi, Principal Investigator
Power Electronics Technical Specialist
Cummins Inc.
1900 McKinley Ave.,
Columbus, IN 47201
E-mail: santhosh.krishnamoorthi@cummins.com

Susan Rogers, DOE Technology Development Manager
U.S. Department of Energy
E-mail: susan.rogers@ee.doe.gov

Project Introduction

In medium- and heavy-duty (MD/HD) electric commercial vehicles (ECVs), gross vehicle weight (GVW), lifetime, and total cost of ownership (TCO) are more critical compared to light-duty (LD) vehicles. Increasing the inverter power density enables a smaller electric drive and better management of GVW. Using high-power dense (HPD) and low-cost inverter, the ECV fleet owners can optimize vehicle use by extending the battery range or having more payload reducing the TCO.

ECV inverters must meet higher gradeability, start-ability, and lifetime requirements compared to LD vehicles. Hence, they must be designed for higher current and handle severe and frequent thermal stresses. Additionally, moving to higher DC voltage rating adversely affects inverter volume, thus, increasing the power density of MD/HD inverters has greater challenges compared to LD inverters. Cummins has developed an inverter rated up to 600 kW, 900 V DC and 750,000 miles for MD/HD ECVs. The power density of the Cummins-designed 300 kW MD inverter is 49 kW/L using discrete components. This project proposes the research, development, testing, and integration of wide band gap (WBG) semiconductors, heat sink, high-energy density capacitors, gate drivers, current sensors, and control board innovatively. The main objective of this project is to develop and demonstrate a 300 kW, 3-liter HPD traction inverter for MD ECVs scalable to HD ECVs meeting the 100 kW/L target. Innovations to increase the power density of the proposed inverter include: 1) use of metal post interconnects in 1.7 kV WBG devices and double-sided cooling, 2) optimization of integrated heat sink designs using genetic algorithm, 3) selection of high-energy dense capacitors and novel packaging to reduce DC link volume, 4) optimized planar- or coil-based filter to mitigate EMI, and 5) component reliability and lifetime studies under various ECV mission profiles. The proposed inverter will be rated for 235 kW continuous, 300 kW peak, 1000 V, and 750,000+ miles meeting or exceeding the Department of Energy (DOE) targets. Cost models for the HPD inverter components will be developed and pathways to achieve 2.7 $/kW target will be proposed. The HPD inverter will be characterized with an application-target motor in a dyno setup. Novelties of increased DC voltage, current density, lifetime, and modular design targeted towards MD/HD applications can enable compact and reliable class of 1 kV WBG traction inverter technology which can also be beneficial to LD inverters.

Objectives

The objective of the project is to develop a 3 L, 1000 V inverter for MD to HD ECVs with a continuous power rating of 235 kW, peak rating of 300 kW and lifetime of > 750,000 miles. The goal of 100 kW/L power density will be achieved by applying the emerging and novel technologies to the inverter. **Error! Reference source not found.** shows the achievable inverter volume reduction through optimal design, careful identification, and selection of components. The current state-of-the-art ECV inverters are enabled by Silicon (Si) power modules

with film capacitors and standalone sensors. In addition, to lower costs and enable manufacturability, conventional topologies viz., 2-level or H-bridge are preferred.

The project will target to improve the Cummins inverter bounding box power density from the current 49 kW/L by 104% to the target of 100 kW/L

Approach

The project will address the following technologies for different stages inside the bounding box:

- Optimal integration of the power module with heat sink, gate driver and sensors to reduce parasitic inductance and losses while enabling higher switching frequencies

- Novel topologies that enable operation at higher DC bus voltages and reduce electromagnetic interference

- Capacitor technologies and packaging concepts that enable a tighter integration of the components to further reduce stray inductance and increase the density of the bounding box volume

- Optimization of heat sink/cold plate design through analytical and experimental approaches including thorough validation of the inverter at component and system level.

- Component reliability and lifetime modeling and assessment under ECV mission profile for longer life.

The critical success factors to achieve the high-power density goal include:

- A two-level Auxiliary Resonant Circuit Pole (ARCP) topology which enables zero voltage switching (ZVS) reducing losses and improving the EMI performance. Alternatively, a T-type three level topology that will help reduce the noise emission for higher DC bus voltages (1kV+) at higher switching frequencies

- Customized 1.7 kV Silicon Carbide (SiC) metal oxide field effect transistor (MOSFET) integrated module with gate-driver, Rogowski current sensors and double-sided cooling with metal post interconnects which reduces the inductance and the footprint

- Heat sink/cold plate that is optimized for the application through genetic algorithm

- Exploration of printed circuit board (PCB)-mounted film/ceramic capacitors with novel packaging, evaluation of different concepts, and finalization of the selected packaging through experimental analysis

Finally, cost models for the HPD inverter components will be developed and pathways to achieve 2.7 $/kW target will be proposed.

Results

Inverter Technical Profile:

The goal is to collect requirements and drive cycles from MD/HD applications to develop the inverter components and the inverter. The team used the expertise in Cummins to collect relevant MD and HD application drive cycles both harsh and steady state to identify all the transient and extreme conditions to design the inverter for. The data from the applications has been used to create a technical profile for the development of the inverter. The technical profile contains details about the required DC bus voltage, phase current (torque), etc., to help select the appropriate design and components for the inverter. The requirements for the inverter will be updated if needed as the project evolves and needs changes.

Inverter Topology Selection:

The goal is to evaluate different options for inverter topology and identify a suitable candidate for the project that will help the team achieve all the goals. The project team at Virginia Tech led the efforts to evaluate different topologies through simulations with the candidate motor model provided by Cummins. The candidates included two-level, quasi-2-level, 3-level and soft-switching topologies. The last option was ruled out early on due to its mismatch for high power, high current application which doesn't use very high switching frequency. The 3-level option was ruled out since it requires higher capacitance on the DC bus compared to the 2-level topology.

In comparison between 2-level and quasi-2-level topologies, the quasi-2-level topology requires higher capacitance similar to the 3-level topology even though it derives advantages from both 2-level and 3-level topologies. Higher capacitance implies bigger size and lower power density which works against the primary goal of the project. Table I.2.1.1 shows the comparison of capacitance required between 2-level and 3-level topologies for both 3 phase and 6 phase options and Table I.2.1.2 shows the comparison of the module volumes for different topologies both pointing towards a lower volume for 2-level inverter topology. Both 3 phase and 6 phase architectures will continue to be evaluated for the 2-level topology. The 6-phase architecture overall is expected to produce a smaller size inverter, but the 3-phase inverter might be more cost-effective for HD solutions where 2 of the MD drive solution might be required.

Table I.2.1.1 Comparison of capacitance requirement for different topology options

Topology	Maximum required capacitance (µF)
Two level (2L) 3 phase	80
Two level 6 phase	45
Segmented 6 phase	52
Three level 3 phase	1000
Three level 6 phase	700
Quasi 2 level (Q2L)	1000

Table I.2.1.2. Comparison of capacitance requirement for different topology options

Topology	Module volume (cm³)
Two level	227.7
Quasi 2 level	683.0
Three level (ANPC)	1024.5
Three level (TT)	683.0
Three level (FC)	683.0

Power Module, gate drive design and current sensor selection:

The goal is to develop a compact power module with integrated current sensing and gate driver circuitry, and double-sided cooling for improved inverter performance and power density. The project team at Virginia Tech is designing the power module using SiC dies based on the results from the simulations and analysis done for evaluation of inverter topologies. The team has completed a few iterations of the design and each design was analyzed using a constant temperature profile to determine the rise in temperature due to the calculated losses across the module and identify any hotspots. The power module design has been modified to reduce any identified hotspots and to reduce the size by lowering the number of dies per module to remove any warpage issues and increase reliability. The team is currently working on module terminal design and practicing wirebonding to build the modules in upcoming months. Few commercial power modules from suppliers are being evaluated as backup/secondary options to the customized module that is being designed. This will give us a path to compare the customized module against the commercial options and act as a backup or an initial

prototype to demonstrate the design. Figure I.2.1.1 below shows design of the power module being designed by Virginia Tech.
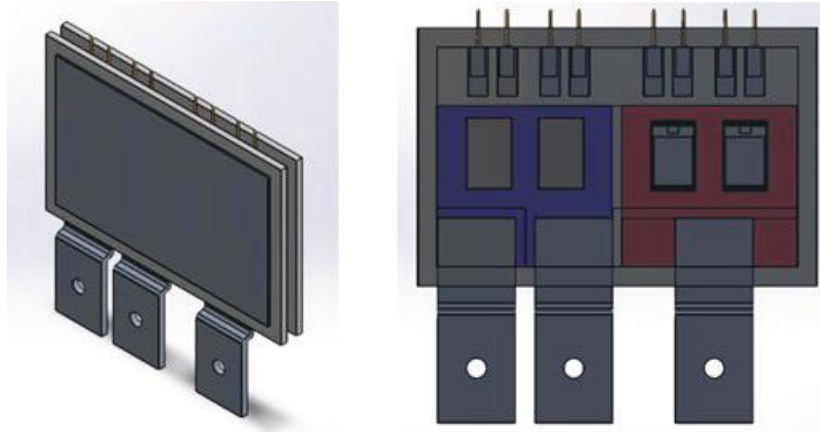
Figure I.2.1.1 Customized SiC power module design for high power density inverter

The gate drive power supply is currently being designed by the team based on the calculations from the topology simulations and power module design. A single-turn transformer is currently being evaluated as part of the design and is being optimized based on a figure of merit which is a product of volume and coupling capacitance. A commercial hall effect current sensor has currently been selected out of the multiple options that were evaluated. The hall effect sensor will be placed on top of the bus bars which are being designed to optimize and reduce the loop inductance between the DC bus capacitors and the power modules. The design itself factors in the design of the power module and selected capacitors.

DC Link Capacitor Optimization:

The goal is to review and compare emerging capacitor technologies and design and optimize the DC capacitor board to minimize inverter volume. The project team at ORNL has been evaluating the required capacitance for different topology options including 2-level, 3-level and quasi-2-level inverters. The conditions used to evaluate the capacitance were derived from the technical profile and the simulations were completed in PLECS simulation tool under steady state conditions. The different technologies considered for capacitors include film, ceramic and PLZT ceramic capacitors as shown in Figure I.2.1.2. The ceramic and PLZT ceramic capacitors offer the best energy density but also are more expensive compared to the film capacitor options.

Based on the calculation of capacitance, 2-level inverters require the least of all three options with quasi-2-level and 3-level inverters requiring same capacitance. Both these topologies have similar split DC bus and produce enough current ripple to be compensated by higher capacitance.
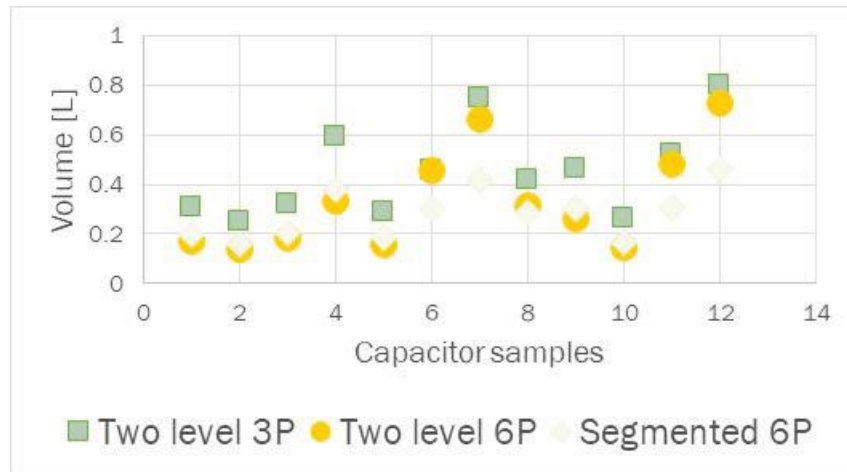
Figure I.2.1.2. Volume of different types of capacitor technologies for the selected two level inverter topologies

Heat sink design optimization:

The goal is to review and compare heat sink technologies and design and optimize the heat sink to integrate with the selected power module to minimize inverter volume The project team at ORNL is designing a heatsink for the inverter and the design is based on the thermal properties of the customized power module and the determined heat losses during the operation. The team started the design with a FFT function of the surface of the heat sink. The FFT function is then modified using a genetic algorithm. The function produces a heat sink surface that will design the fins to concentrate more towards the higher sources of heat losses in the power module. This will help to increase the heat transfer coefficient of the heat sink and produce a smaller size hence increasing the power density. Figure I.2.1.3 shows a design made by ORNL for the latest power module design.
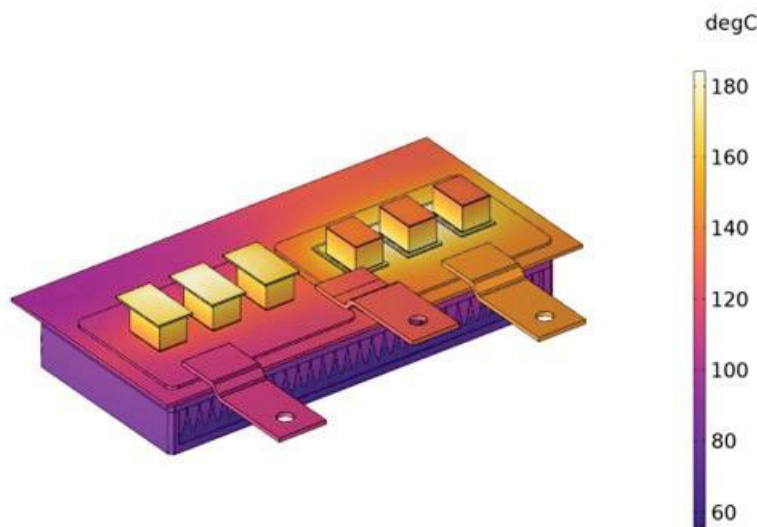
Figure I.2.1.3. Analysis of a heat sink design for the customized SiC power module

The team completed an initial design of heat sink based on the power module design provided by Virginia Tech. This design is now being modified based on the updated design of power module. The heat transfer coefficient required for the power module based on losses was estimated to be ~10000 W/m^{2}K control the junction temperatures to 150ºC and below.

A simple heat sink design for the commercial modules is also being evaluated based on the obtained parameters from the manufacturer. This will serve as the solution for the backup/secondary inverter option.

EMI Mitigation and Filter Design:

The goal is to explore EMI mitigation measures, simulate, design and fabricate EMI filter for WBG system to minimize inverter volume. The project team at ORNL has been evaluating different methods to determine the sources of EMI and is currently looking into methods to reduce the EMI and noise in the inverter system. One of the methods is to implement a segmented 6-phase inverter with interleaved modulation which injects switching vectors to oppose the produced noise in the system. The EMI filter design will be started once the parasitics in the system are determined including the values relevant to the power module, DC link and the motor load that will be used to test the inverter.

Inverter Control Board:

The goal is to design the control board to drive a WBG-based traction inverter. Components will be selected, printed circuit board (PCB) will be laid out, PCB will be developed, and components will be assembled on PCB. The project team at Cummins is responsible for designing the control board for the inverter and started out with evaluating different options for the processor to implement the controls. Among the options were a processor from Infineon, TI DSP, Renesas DSP and TI ARM processor. The options were evaluated on different parameters in a scoring Pugh matrix and the two processor options from TI were finalized.

Based on the selected topology and architecture, the ARM processor was selected to meet all the needs of the inverter. With ARM processor starting to emerge in the Currently, the component selection and schematics for the control board have been started and the low voltage power supply design is almost completed based on the requirements for the gate driver, current sensors and the control board itself.

High-Fidelity Model Development and Agile Lifetime Modeling:

The goal is to develop thermal and thermo-mechanical models of power module packaging, analyze system cooling and reliability, and experimentally evaluate new packaging materials. The project team at NREL has evaluated the material properties of the candidate power module from Virginia Tech and the material properties were used to determine the thermal impedance of the selected device. The impedance was confirmed through two methods viz., Foster and Cauer thermal networks for single-sided and double-sided cooling options.

These material properties and the thermal networks were hence used with the drive cycles provided by Cummins to evaluate the temperature cycles of the junction in the power modules. The amplitude of these temperature cycles and the frequency of the cycles will hence help us determine the lifetime of the power module. Currently, models in Simulink MATLAB and Siemens Aemsim are being developed and evaluated to determine the temperature cycles based on averaged and detailed models of the power module in the drive system. The next steps include evaluation of the power module experimentally to improve the built models and determine the lifetime using rainflow counting.

Conclusions

In conclusion, in year 2022, the Cummins High Power Density project evaluated different topology options for the inverter and selected the 2-level topology with both the 3ph and 6ph architectures being considered. The team has also made significant progress in design of the customized SiC power module and has selected a commercial power module option as a backup option and to provide a point of comparison for the design of the customized module. A gate drive power supply design has been started with single turn transformer and will be coupled with a gate driver to be started along with the control board using the ARM processor. A hall effect current sensor from off-the-shelf has been selected as current option and will be coupled with the bus bar that is being designed using the parameters from the power module and capacitor parts. Two heat sink designs are being pursued by the team; one for the customized module and one for the commercial module. The team is also evaluating methods to reduce EMI noise in the system are being investigated along with measurements

of system parasitics to design the EMI filter. Finally, models to evaluate lifetime of the power modules have been developed and will be used to calculate the temperature cycles to measure the reliability of the high power density inverter.

I.2.2 Cost Effective Rare-Earth-Free Flux Doubling, Torque Doubling, 8X Power Density Traction Motor with Near-Zero Open-Circuit Back- Electromotive Force (EMF) and No Cogging Torque (University of North Carolina at Charlotte)

James Gafford, Principal Investigator

University of North Carolina at Charlotte
9201 University City Blvd
Charlotte, NC 28223
E-mail: jgafford@uncc.edu

Susan Rogers, DOE Technology Development Manager

U.S. Department of Energy
E-mail: Susan.rogers@ee.doe.gov

Start Date: October 1, 2019	End Date: June 30, 2023	
Project Funding: $270,638	DOE share: $210,638	Non-DOE share: $60,000

Project Introduction

This project proposes to develop a high-power density, high speed traction motor architecture called QMag, driven by a high-power density motor drive inverter using silicon carbide semiconductor devices. This new architecture will achieve the efficiency and power density targets by means of innovative winding and rotor structures, high bandwidth controls, and advanced thermal management solutions. The project team will pursue the goals of the project systematically, through Finite Element Analysis for machine design, through simulation and co-simulation techniques for power electronics and controls evaluation, and finally system design, fabrication, testing and evaluation. If this project successfully achieves and demonstrates the DOE targets for power density, cost, and reliability, the technology has the potential to become a core enabler of the flagship higher power product portfolio in commercial traction businesses, which has so far been confined to DC, induction, Brush Less DC (BLDC), Permanent Magnet AC (PMAC), and reluctance machines.

Objectives

The U.S. DRIVE Electrical & Electronics Technical Team Roadmap (2017) [1] identified key challenges and R&D targets for Electric Traction Drive Systems in the year 2025 including: (1) cost reduction – achieving cost parity with ICE drivetrains at $6/kW for 100 kW peak power rating; (2) power density improvement - addressing packaging challenges and achieving a motor power density of 50 kW/litre and power electronics density of 100 kW/litre, and an overall system figure of 33 kW/litre; (3) reliability improvement up to 300,000 miles (distance) or 15 years (lifetime); (4) reduction of reliance on rare-earths, with NdFeB –free/reduced, Dy-free/reduced designs. To achieve these targets, this project proposes to develop and demonstrate a novel 125kW motor architecture and SiC converter based electric traction drive system that can achieve 8X power density at half cost and 2X useful life, while applying the QMag principle to power conversion and motor design and advanced cooling. The project activities will focus on:

1. Feasibility evaluation, practical implementation and scaling of QMag principle

2. Design and implementation of power converter and motor drive system

3. Design and implementation of advanced cooling system

4. Overall system (motor + power converter) optimization for traction applications and testing

Approach

Traction motor

This project proposes to use the QMag topology to design the traction motor, which is based on the QMag technology, alternatively termed as the Parallel Path Magnetic Technology [2]:

- The QMag topology features permanent magnets placed in magnetically attracting manner (circumferentially vs radially) and inter-dispersed with control winding coils, enabling greater flexibility in flux path shaping, as shown in Figure I.2.2.1

- The castellated rotor has no interior or surface magnets, offering high-speed operation, reliability, and high-power density to achieve DOE targets

- Direct winding cooling techniques boost current density capability, hence the torque performance

(a)	(b)
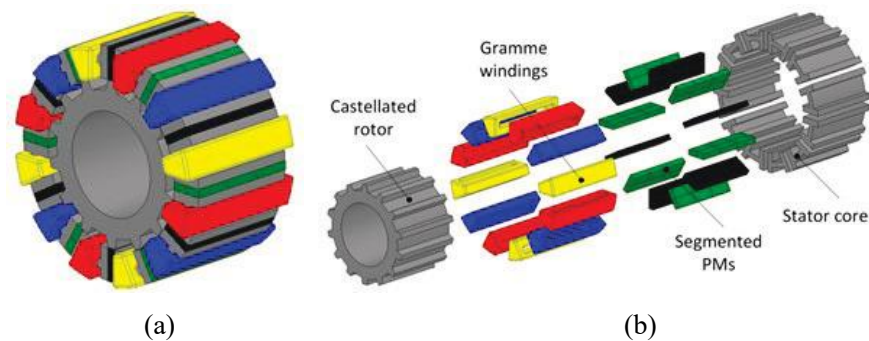
Figure I.2.2.1 Concept Visualization of the QMag Technology, (a) assembled view, (b) exploded view.

Motor drive inverter

This project will develop a motor drive inverter using half-bridge silicon carbide (SiC) modules. The inverter will operate at high switching frequencies, thereby low distortion output current and reduced torque ripple. SiC power modules optimized for reduced conduction losses will be utilized to handle high current drive requirements by the QMag motor. The switching frequency of the inverter will be optimized for all operating power ranges, high power quality, power density, and efficiency. Thermal management of the semiconductor devices will be achieved through liquid cooling, with a water – ethylene glycol mix being the coolant.

Integration of traction motor and drive inverter

The traction motor and drive inverter are being designed concurrently, with frequent coordination of operating conditions and performance specifications. Finite Element Analysis platforms (Ansys) are used to design, optimize and validate the traction motor; power electronic simulation platforms (Powersim, Matlab) are used to design the drive inverter – the integrated traction system will be validated using co-simulation methods. The prototypes of traction motor and inverter drive are integrated and tested on a dynamometer testbed.

Results

A survey of state-of-the-art designs for existing products and reported research studies was conducted to establish a basis of comparison for the electric machine performance and characteristics. The results provide the research team with a benchmark for evaluation of the QMag motor design under development and for substantiating relative merits and capabilities in terms of high-power density, high speed operation, simplified modular manufacturability, improved cooling, etc. Parametric models for several motor topologies were developed following the principle of operation of QMag motors. Based on a parametric electromagnetic finite element analysis (FEA) model for the QMag topology with Gramme-type windings illustrated in Figure I.2.2.1 with 10 independent geometric and control variables, a large-scale design optimization was performed. The objective was to maximize the power density with a 50kW/L target, efficiency and power factor, assuming an

equivalent electric loading, i.e., the product of current density and slot fill factor, equal to 9.75A/mm^2 can be achieved by the cooling design and advanced winding technology.

Multiple design generations of the adopted heuristic optimization yielded a satisfactory Pareto front. Several candidate designs were identified, with estimated power density capable of meeting DOE targets, as shown in Figure I.2.2.2. The torque-speed and efficiency maps have also been calculated based on 2D electromagnetic FEA, showing that the optimally designed motor can operate with constant power 125kW at up to 3X the base speed 12,500r/min.

(a)   (b)
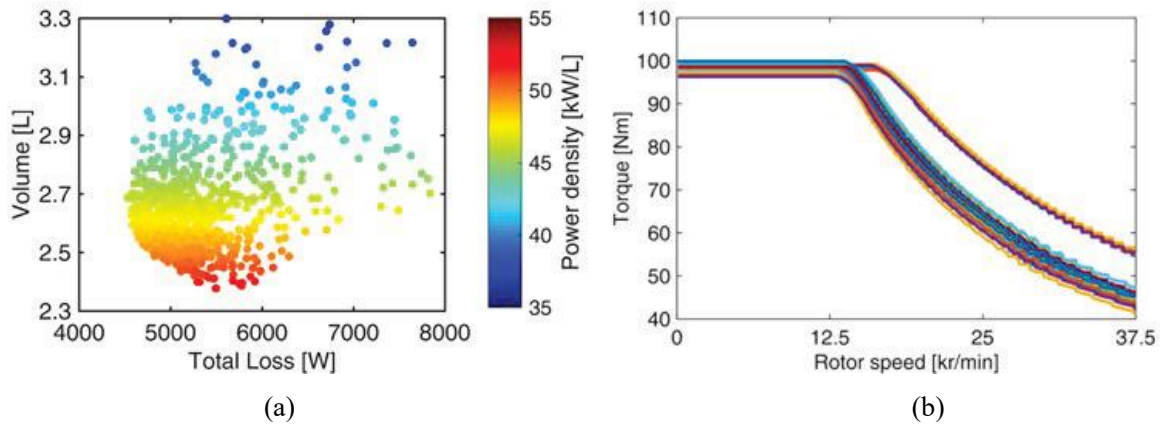
Figure I.2.2.2 Large-scale design optimization of one implementation of the QMag technology. (a) Designs evaluated by FEA, (b) Torque-speed envelops of all the Pareto front designs in (a).

To validate the high-power density motor and the adopted design optimization approaches, as well as to identify the potential challenges in manufacturing and testing to achieve the final goal of 50kW/L, a 28hp open frame lab prototype (OFLP) motor rated at 40Nm and 5,000r/min was fabricated, as shown in Figure I.2.2.3. Experimental testing was conducted to measure the OC back-electromotive force (EMF) for a single phase with 4 coils connected in series, as plotted in Figure I.2.2.4 (a), showing good agreement between the experimental measurements and 2D FEA calculations. A back emf test was performed up to 3,500 rpm (limited by prime mover ratings). Observed stator line-line voltage at 3,500 rpm shown, with highly sinusoidal waveform of fundamental frequency 583 Hz, has been shown in the Figure I.2.2.4 (b).
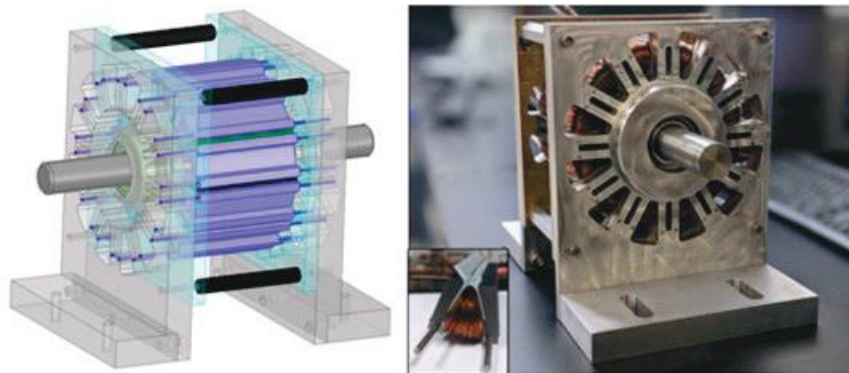
Figure I.2.2.3 The CAD drawing and photo of the full assembly for the open frame lab prototype motor.

A locked rotor test setup was designed and fabricated consisting of an indexing head and a locking block. The rotor position was moved in 1° (mechanical) increments, over a total span of 36°. Motor stator phases B & C were connected to a common terminal and in series with phase A. DC current was injected up to 500 A.

Torque performance up to 90 Nm measured, compared to 96 Nm in simulation results, with the difference explained by material tolerances, deviation in physical properties between simulation components and real-world materials, and lack of liquid cooling.

(a)   (b)
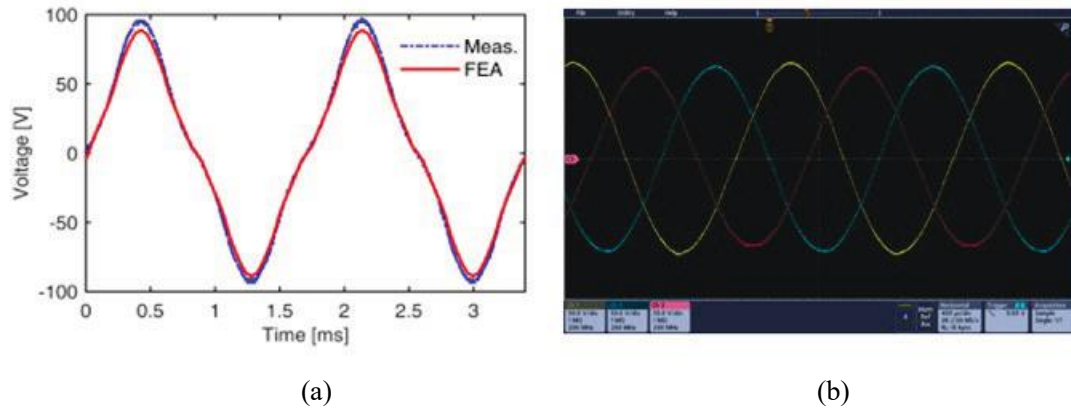
Figure I.2.2.4 a) Simulated and experimental open-circuit back EMF for phase-A open ended winding. (b) Experimental open-circuit back EMF for phase-A, B, and C in star connection topology.

Unity power factor tests were performed to identify the parameters of open frame lab prototype Q-Mag motor. The Q-Mag motor proof-of-concept prototype was operated in an "uncontrolled generator" mode where a prime mover provides motive force to spin the OLFP and the stator windings are loaded by a 3-phase resistive load bank. The empirical data gathered was analyzed to establish motor parameter estimation, and loss analysis. 2-D and 3-D finite element analyses were conducted to accurately estimate losses such as proximity effects and eddy current losses. These losses are summarized in Table I.2.2.1

Table I.2.2.1 Experimental Results Components Calculated by 2D and 3D FEA

Operating Points		Experimental Results			FEA 3D/2D Simulation Results			
Speed [RPM]	I [A]	T_m [Nm]	P_{Joule} [W]	P_{Loss} [W]	T_e [Nm]	P_{Core} [W]	P_{PM} [W]	$P_{Winding\text{-}Eddy}$ [W]
3500	65	26.7	8075	191	30.5	282	50	171

A workflow consisting of four modules, as shown in Figure I.2.2.5 (a) was developed to implement motor drive inverter control algorithms to test the open frame laboratory prototype Q-Mag motor in constant torque and constant power regimes. The four modules may be described as:

1. Demonstration of closed-loop control algorithm for control of Q-Mag motor proof-of-concept prototype using JMAG and PSIM has been completed.

2. The evaluation of controller performance has been completed for all load levels at a base speed (5000 rpm) employing controller hardware in loop (C-HIL). A field-weakening control evaluation (for speeds above base speed) is currently being developed. PSIM, Typhoon, and TI DSP F28379D are used to implement C-HIL [6].

3. The development of sensing, feedback, and signal conditioning circuits for inverter control was completed.

4. Performance of an FEA Model of the motor prototype in Ansys + Simplorer is validated against empirical data. The model is calibrated to the empirical results.

The system in the loop simulation model of the OFLP motor drive has been reconfigured into a discrete domain to replicate a precise model of the hardware setup of the traction motor drive system employing a high-performance TI microcontroller F28379D. The discrete PSIM simulation model of the Q-MAG motor prototype consists of an analog to digital (ADC) port, Texas Instruments digital motor control (TI-DMC) blocks, PWM ports, and an encoder. sampled at appropriate employing zero-order hold operation.

(a)   (b)
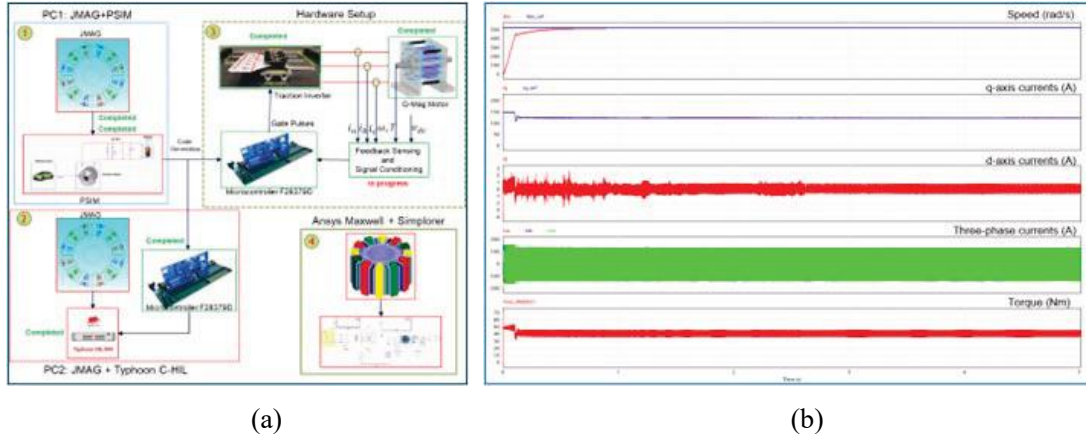
Figure I.2.2.5 (a) Workflow of implementation of the control algorithms considering a high-fidelity model of prototype of the Q-MAG motor drive system. (b) Discrete domain simulation results of the prototype of the Q-MAG motor drive system consists of speed (rad/s), synchronous frame reference currents (A), three phase currents (A) and load torque (Nm).

The feedback signals have been digitalized and transformed into synchronous reference frames using TI DMC blocks. The speed controller has been configured to generate a reference current proportional to the load torque of the motor. The reference currents have been compared with the feedback currents to implement current controller algorithms to generate respective d-axis and q-axis voltages. The voltages have been normalized and sinusoidal pulse width modulation has been performed to generate switching pulses with an appropriate deadtime. Average torque of 41Nm, 135A peak at a rated speed of 523.5 rad/s or 5000 RPM have been observed in the discrete domain simulations as shown in the Figure I.2.2.5 (b). The results are a close match to the specifications of the OFLP of the Q-Mag motor. Validation of the code employing Typhoon controller hardware in the loop (C-HIL) system and hardware implementation of the OFLP motor drive system have been completed.

A hardware prototype of the SiC power electronic drive inverter was constructed. The prototype is air-cooled and rated to operate at up to 20 kW. Control of inverter using the Texas Instruments C2000 microcontroller has been achieved and the inverter was operated with a passive load up to 15 kW. Demonstration of closed-loop control algorithms for control of Q-Mag motor using controller hardware in the loop (cHIL) was completed. The evaluation of controller performance was completed for all load levels at base speed (12500 rpm). Field-weakening control evaluation (for speeds above base speed) is currently being developed.

The development of sensing and signal conditioning of three-phase currents has been completed. Performance of the signal conditioning board has been characterized at different frequencies of input currents. The embedded code generation platform has been configured using PSIM to sense encoder signals. Software has been verified by performing three-phase to synchronous transformation with position (electrical angle) as an input. Mechanical integration of the encoder with the motor shaft was completed as well as installation of encoder sensing hardware. This encoder is capable of sensing signals at 1024 pulses per revolution up to a maximum speed of 10,000 rpm. Integration of the encoder and sensor head are shown in Figure I.2.2.6.
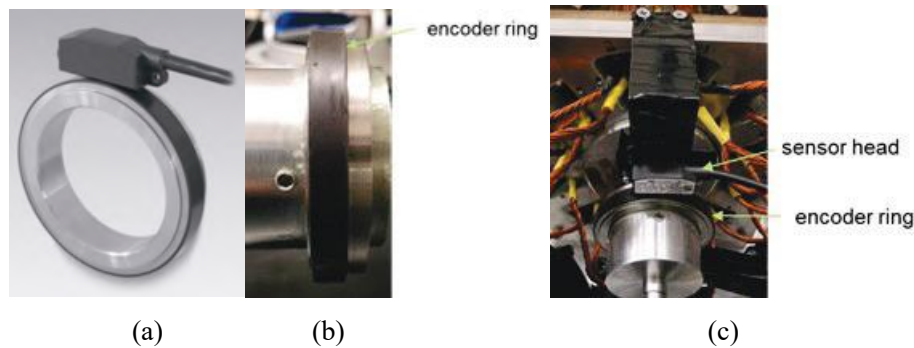
Figure I.2.2.6 Incremental Bearingless Encoder Installation (a) Baumer ITD69H00, (b) Encoder Ring Installed on motor shaft, (c) Shaft mounted encoder ring with sensor head mounted to motor frame.

Conclusions

The proposed Q-Mag electric drivetrain system shows promise to meet DOE EETT targets power density improvement, cost reduction, and magnetics utilization. Motors based on Q-Mag technology have been analyzed through large-scale design optimization studies and shown to be feasible candidates for traction applications with a maximized power density of over 50kW/litre. Additional merits of high-speed operation capability, a wide speed range of 3X base speed, simplified modular manufacturability increase the viability of this approach. Performance tradeoffs mainly lie between the power density and efficiency. Large-scale design optimizations are required to achieve the optimal designs with multiple objectives. Advanced winding technologies that can substantially increase the copper slot fill and cooling techniques that can effectively dissipate the heat generated by losses in the stator are two enabling technologies to achieve the 50kW/L target for the proposed topology. The design and simulation of high-fidelity nonlinear model of motor and drive system consisting of a SiC inverter and control algorithm show power densities at 100 – 150 kW/litre for the inverter, also meeting DOE targets. The project team is in the final stages of preliminary prototype performance evaluation. The completed prototype machine, motor drive, and embedded control algorithm will be operated and analyzed for comparative analysis with previously developed and validated system and component models.

Key Publications

1. C. S. Goli, S. Essakiappan, J. Gafford, D. Ionel, M. Manjrekar and N. Shah, " Modeling and Speed Control for a Doubly-Salient Special Machine Employing a High-Fidelity Plant Model," 2022 IEEE Vehicle Power and Propulsion Conference, Merced, CA, Nov 2022.

References

1. U.S. DRIVE Electrical and Electronics Technical Team Roadmap, October 2017

2. Charles J. Flynn, "Parallel Magnetic Circuit Motor", US Patent US 2011/0089775A1

3. N. Simpson, C. Tighe, and P. Mellor, "Design of high-performance shaped profile windings for additive manufacture," in IEEE Energy Convers. Congr. Expo. (ECCE), 2019, pp. 761–768.

4. S. A. Semidey and J. R. Mayor, "Experimentation of an electric machine technology demonstrator incorporating direct winding heat exchangers," IEEE Trans. Ind. Electron., vol. 61, no. 10, pp. 5771–5778, 2014.

5. "Motor Control Development Tools Work with JMAG," JMAG Users Conference Proceedings, Feb 2021.

6. "Ultra-High-Fidelity Hardware in the Loop (HIL) Simulation for EV Motor Drives with Seamless integration with JMAG-RT," JMAG Users Conference Proceedings, Feb 2021.

Acknowledgements

I.2.3 Amorphous Metal Ribbon and Metal Amorphous Nanocomposite Materials Enabled High Power Density Vehicle Motor Applications (Carnegie Mellon University)

Professor Michael E. McHenry, Principal Investigator
Carnegie Mellon University
243 Roberts Hall, 5000 Forbes Avenue
Pittsburgh, PA 15213
E-mail: mm7g@andrew.cmu.edu

Susan Rogers, DOE Technology Development Manager
U.S. Department of Energy
Email: Susan.Rogers@ee.doe.gov

Start Date: March 1, 2019   End Date: September 30, 2023
Project Funding: $300,000   DOE share: $300,000   Non-DOE share: $0

Project Introduction

A collaborative team from Carnegie Mellon Univ. (CMU), North Carolina State Univ. (NCSU) and Metglas, South Carolina have studied new high-speed motors (HSMs) with high-power density for traction motor applications. These are enabled by hybrid designs, including Flux Switching with Permanent Magnets (FSWPM) motors, exploiting permanent magnets without heavy rare earths (RE-lean) and high induction/high resistivity soft magnetic materials that allow for high switching frequencies needed to increase power densities.

Team members include Michael E. McHenry, Prof. Materials Science & Eng., CMU, with more than 30 years of experience in magnetic materials development; Subashish Bhattacharya, Prof. Electrical Eng. and Freedom Center Director at NCSU with more than 30 years of experience in development of power electronic components and systems and Eric Theisen, Director of Research at Metglas, the only US located supplier of AMR and MANC materials. The team offers novel axial motor architectures exploiting soft magnetic materials (SMMs) that switch with low loss at high frequencies and heavy rare earth free permanent magnets that address materials criticality issues, supply chain risks, and high costs for traction motors.

Axial-flux permanent magnet motors (APFM), offer efficiency improvements reducing rotor losses and also significantly higher power density. Axial-flux construction requires less core material, high torque-to-weight ratio. Since AFPM machines have thin magnets, they are smaller than radial flux motors making them attractive in space-limited applications. Noise and vibration are less and planar air gaps are easily adjusted. Flexibility in air-gap direction allows many topologies.

Objectives

The project objective is to achieve 8-fold increase in power density for an axial motor designed to showcase Amorphous Metal Ribbon (AMR) and Metal Amorphous Nanocomposites (MANCs). Motors are enabled by hybrid designs exploiting rare earth lean permanent magnets and high induction/high resistivity soft MANC allowing high switching frequencies needed to increase power densities.

Approach

Technical components, completed in budget periods, BP1 and BP2, are summarized:

Budget Period 1: Benchmark AMRs and MANC Alloys for HSM Design

AMR materials will be benchmarked, in a Finite Element Analysis (FEA) model. Alloys will be cast at commercial scale and properties relevant to 5 kHz magnetic core losses and audible magnetostrictive losses will be measured and compiled. Sample ribbons will be provided to the DOE. A FEA model of a Traction High Speed Motor (HSM) will be designed and performance evaluated.

Budget Period 2: Properties Optimization, Component Fabrication and Alloy Studies

Properties of AMR materials will be optimized and benchmarked. Rotors and dual stators will be produced for testing and loss validation in the Flux Switching with Permanent Magnet (FSWPM) motor. Magnetic switching frequencies and mechanical properties will be evaluated. The measured properties will be incorporated into a FEA model of a Traction HSM and used to finalize the design. This design will be used to benchmark new materials.

Results

In BP1, we modeled a Flux Switching with Permanent magnet (FSWPM) motor desigh meeting power metrics for the program goals.1,2 The paper: S. Simizu, K. Byerly, K. Schneider, H. Kim, M. Nations, S. Narasimhan, R. Beddingfield, S. Bhattacharya, and M. E. McHenry, "Flux Switching Permanent Magnet Motor with Metal Amorphous Nanocomposite Soft Magnetic Material and Rare Earth Free Permanent Magnets," presented IEEE Energy Conversion Congress and Exposition 2021, Vancouver. Canada, Oct. 10-14, 2021 was awarded the Best Paper Award at the ECCE 2022 Conference, Detroit, MI. Figure I.2.3.1 illustrates the motor topology as compared with the previous 2.5 kW design pursued with AMO funding. [1]
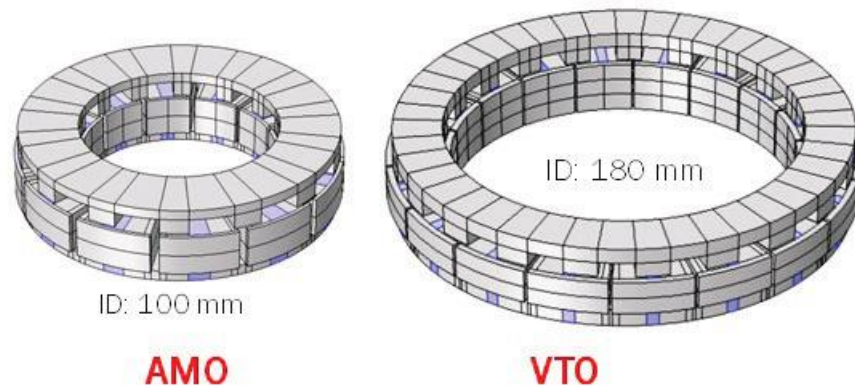
Figure I.2.3.1 FSWPM multi-pole designs for 2.5 kW AMO RE-free [1] and 34 kW VTO RE-lean [2] topologies

This motor exploits amorphous magnetic ribbon or metal amorphous nanocomposite [3], [4] tape wound cores (TWCs) in their construction. Fe-Ni-based MANCs [5] with magnetostrictive losses reduced by 2-5 x with appropriate stress relief anneals [6] developed in this project and reported in K. Byerly, Y. Krimer, C. Phatak, E. Theisen, and M. E. McHenry, Magnetostrictive Loss Reduction through Stress Relief Annealing in an FeNi-based Metal Amorphous Nanocomposite. J. Mat. Res. 36, 2843-55, (2021). https://doi.org/10.1557/s43578-021-00268-5

Table I.2.3.1 Budget Period 2 Milestone Schedule

Budget Period 2			
Fabricate FeCo-based Dual Stators and Rotors.	Demonstrate Manufacturability of FeCo-based AMR motor.	12/15/21	09/15/22
Evaluate Mechanical Properties of AMRs and MANCs Suitable for HSM	Use mechanical properties in FEA to verify that HSM is mechanically able to rotate at >20 krpm.	03/15/22	03/15/22
Report Oxide properties for AMR and MANCs	Demonstrate resistance > coated laminates. Demonstrate Bulk resistivity > 150 $\mu\Omega$-cm, surface resistivity > 500 $\mu\Omega$-cm	6/15/22	6/15/22
Fabricate FeCo-based Dual Stators and Rotors.	Demonstrate Manufacturability of FeCo-based AMR motor.	12/15/21	09/15/22

BP2 Milestone Schedule: We have completed manufacturability studies on FeNi-based MANCs preceding the 12/15/21 milestone. We demonstrated manufacturability of FeCo-based components in 2022. Mechanical properties evaluation was completed 03/15/22, while added analysis of its implications for the motor operation has continued past that date. Oxide properties of AMRs and MANCs were reported at the DOE VTO June 2022 Review and in publications noted in the text of this document. AMR and MANC testing is in progress with our commercial partner.

BP2 Milestone 1 was addressed for FeNi-based MANCS first due to their convenient availability and completed in 2021. The fabricability of FeCo-based AMR's was subsequently demonstrated by our commercial partner in 09/2022. Manufacturing steps were first developed in our AMO funded project and subsequently demonstrated for RE-lean high power motor components.

In BP1 we postulated the importance of epoxy impregnation on TWC fabrication anticipating its importance in a mechanical properties, BP2 2nd Milestone. Tape Wound Core (TWC) mechanical properties reflect epoxy/oxide interfacial bonding probed by sessile drop experiments that guide impregnation. Epoxy mechanical properties were incorporated in models developed in support of Milestone 2. This also required additional TEM in the BP2 3rd Milestone. Based on BP1 work, we used residual funds to perform work: (a) To understand epoxy resin wetting to MANC native oxides using sessile droplet wetting experiments; (b) To perform additional microscopy of MANC/Oxide/epoxy interfaces; (c) To record epoxy properties for FEA models to support BP2 Milestones.

Figure I.2.3.2(a) illustrates an apparatus to measure the contact angle of a liquid droplet on sample to study surface energy; Camera with upgraded lens mounted on a linear stage. Sample (deposited by syringe) sits on a tilting stage mounted in front of the light source. Contact angles are determined using ImageJ software. Fig. 3(b) shows contact angle of a water droplet (right) and epoxy droplet (left) on an FeNi MANC surface. In the course of this work we have made several important observations that has been reported at conferences and will be detailed in a future publication and the Ph.d thesis of James Egbu. Important to the project is the determination that the epoxy contact angle is a strong function of the pre-applied strain in strain annealed (and re-annealed) FeNi based MANCs and that the epoxy wetting is anisotropic in strain annealed samples.

| (a) | (b) | (c) |
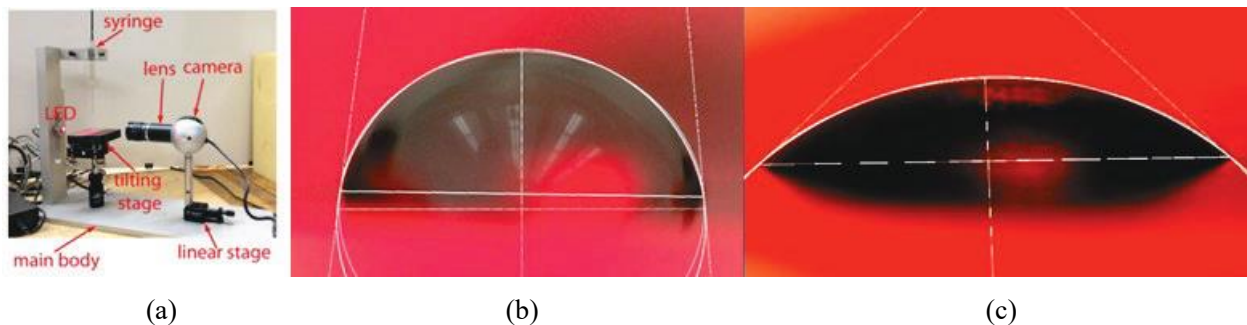
Figure I.2.3.2 (a) Apparatus built to measure the contact angle of a liquid droplet on MANC samples to study surface energy; contact angle of a water droplet (b) and epoxy droplet (c) on an FeNi MANC surface.

CMU Ph.d candidate, Kyle Schneider, completed analysis of mechanical properties of FeNi-based MANCs with the following components: (a) Mechanical Stress Modeling; (b) Model for stress induced by epoxy impregnation and curing; (c) Model for stress induced by rotation of TWC in motor application; (d) Conclusion and recommendations for future work. Work has been submitted for publication (M. P. de Boer, K. Schneider & M. E. McHenry, Strength Distributions of Laminated FeNi-based Metal Amorphous Nanocomposite. Composite Structures. Submitted Sept. 29, 2022.)

Mechanical testing of CMU's FeNi80 base alloy was used to determine stress-strain response, including Young's Modulus (E) and Ultimate Tensile Strength (UTS). The material has high modulus but brittle failure. According to an analysis detailed in our Apr. 30, 2022 Quarterly report the current FSWPM rotor design

would incur high mechanical stresses at a speed of 15 kRPM, leading us to not recommend it for use at 20 kRPM . This high stress results from the high speed, the composite nature of the TWC rotor, and stress concentration zones at the base of each rotor pole due to sharp internal corners. However, these high speeds are not required to achieve the power metric of 34 kW (8x power density increase over 2.5 kW reference design). Such a power density increase can be achieved with designs at lower rotational speeds. A design requiring a speed of 15 kRPM can achieve the power density requirement at the low B limit of 1.03. Since the FeNi80 alloy is now known to achieve saturation flux densities exceeding 1.3 T [7], a reduction of the required speed to 9.4 kRPM is possible, achieving the power metric.

A new method has been developed to prepare tensile specimens of laminated MANC and epoxy layers, to simulate stacking of an epoxy-impregnated tape-wound core (TWC). Tensile tests have been conducted for single layer ribbon and for 5- and 10- multilayer stacks of material laminated with thin layers of thermosetting epoxy. Failure distributions are quantified by Weibull statistics, (Figure I.2.3.3) and shown to have increasing Weibull modulus with increasing layer count. Using a k-failure model, we have demonstrated that single ribbon strength distribution data provides a good prediction of the failure distribution of 5- and 10-layer MANC ribbon laminated stacks with much improved effective ultimate tensile strength and flaw tolerance. Upon further analysis, it should be possible to assess a quantitative measure of the Figure of Safety (FOS) of the component tape wound cores (TWCs).
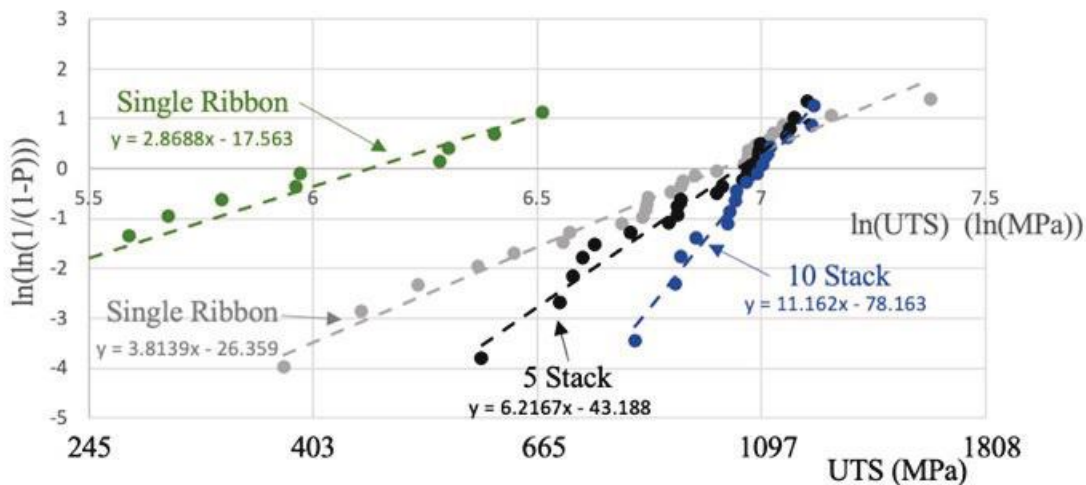
Figure I.2.3.3 Weibull distribution single layer ribbons from two batches (green) and (gray), 5-layer laminated stack (black), and10-layer laminated stack (blue).

As cast single ribbon tensile testing identified ribbon batch variations due to poorer edge quality (roughness) and more variable cast thickness with best properties related to better melt pool control. It should be noted that this work was performed in industrial batch cast ribbons. Single ribbon tensile tests exhibit 3 failure modes in high speed photography:

Type I: Fan-like branching of cracks emanating from edge flaws.

Type II: Less branching but main cracks emanate from edge flaws.

Type III: Cracks emanating from internal flaws (much less prevalent).

Mechanical properties were benchmarked against bend tests and nanoindentation. Continuously cast high throughput production of ribbons results in much improved process control for edge quality but require further scale-up to commercial scale production.

Because rotational stress increases with the square of the rotational speed, this speed reduction has a significant effect on the maximum stress experienced by the rotor. Nevertheless, guided by initial Figure of Safety (FOS) considerations we have limited motor rotational speeds to 5 krpm in the lab and comparative high frequency loss measurements are being pursued on a smaller diameter axial motor for the purposes of materials loss comparisons.

Ribbon flaws can also result from surface structural variations, therefore it is important to understand the MANC ribbon surface roughness. This roughness reflects the passivating surfaces oxides shown in Figure I.2.3.4. For this reason, analysis of MANC oxidation and surface roughness [8] are reported in: J. Egbu, P. R. Ohodnicki, J. P. Baltrus, A. Talaat, R.F. Wright and M. E. McHenry; Analysis of Surface Roughness and Oxidation of FeNi-Based Metal Amorphous Nanocomposite Alloys. J. Alloys & Compounds 912, 165155, (2022).
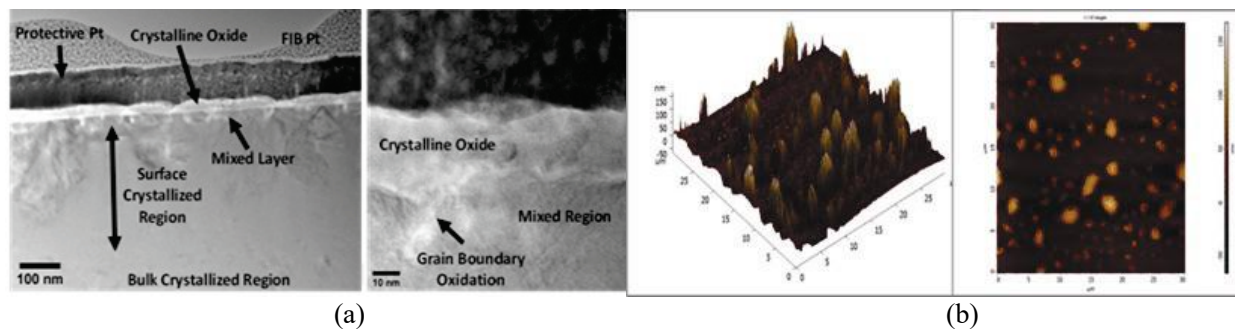
Figure I.2.3.4 (a) Cross-sectional TEM Images of surface crystalline oxides on an FeNi-based MANC and (b) AFM determined surface roughness of the same.

This thin passivation oxide, and its anisotropy derived from strain annealing is also postulated to influence the epoxy wetting in the vacuum impregnation bonding of tape wound cores. Epoxy wetting of the MANCs has been measured with results presented at the 2022 MMM/Intermag (Anaheim) and MMM (Minneapolis) conferences. We view detailed studies as important to future work in the field.

After evaluating mechanical properties of FeNi-based MANCs, and concluding that standards for figures of safety (FOS) for larger diameter motors were necessary before attempting these rotational speeds. In lieu of such tests, to evaluate loss partitioning, our project partner investigated an alternative HSM design to allow MANC and AMR materials comparison with potentially less complicated manufacturing steps for cutting/insulation than for waterjet cut FSWPM topologies. A completed fabrication of the stator topology (Figure I.2.3.5) has been accomplished and loss testing is in progress.
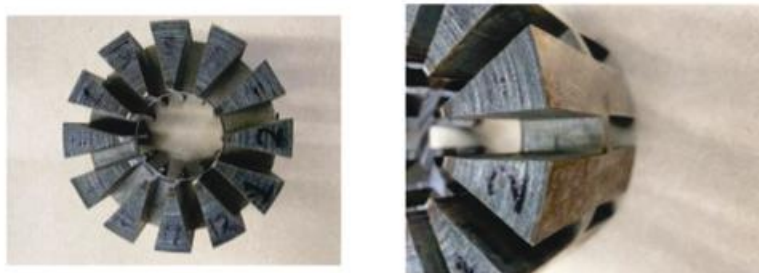
Figure I.2.3.5 Prototype FeCo-based AMR Stator produced by Metglas

Metglas worked with a partner to construct the FeCo-based AMR rotors and stators for comparison with Fe-Ni-based MANCs in a common topology which will allow direct comparison of the loss partitioning for the two materials. Results of final materials comparisons (due December 13, 2022) in this topology will be included in our final report.

Conclusions

The CMU-lead team and its partners have demonstrated pathways to 8x power density increase for RE-lean HSMs designed to showcase Amorphous Metal Ribbon (AMR) and Metal Amorphous Nanocomposite (MANC) materials. CMU presented 4 designs of a 34 kW with active mass 1.7x a 2.5 kW AMO RE-free HSM reference design. The power density is 8x compared on an active mass basis. A rotational speed < 10 krpm is predicted to achieve 34 kW. CMU work has addressed (i) Materials, (ii) Manufacturing, (iii) Properties and Performance issues in new motor designs. Notable accomplishments include:

- Adaptation of materials and manufacturing protocols for higher power HSMs.

- Analysis of magnetostrictive coupling to residual (winding and curvature) stresses in FeNi-based MANCs and stress relief annealing protocols to further reduce losses at scale.

- Evaluation of epoxies for impregnation bonding/electrical resistance in tape wound cores in terms of wetting, adhesion and mechanical strength.

- FEA Modeling of Motor Mechanical Properties with identification of failure modes and methods forincreasing figures of safety.

- Evaluation of limitations on rotor mechanical properties at high rotational speeds.

Key Publications

1. S. Simizu, K. Byerly, K. Schneider, H. Kim, M. Nations, S. Narasimhan, R. Beddingfield, S. Bhattacharya, & M. E. McHenry, "Flux Switching Permanent Magnet Motor with Metal Amorphous Nanocomposite Soft Magnetic Material and Rare Earth Free Permanent Magnets," presented IEEE Energy Conversion Congress and Exposition 2021, Vancouver. Canada, Oct. 10-14, 2021. This paper was awarded the Best Paper Award at the ECCE 2022 Conference in Detroit, MI.

2. K. Byerly, Y. Krimer, Charudatta Phatak, E. Theisen, and M. E. McHenry, Magnetostrictive Loss Reduction through Stress Relief Annealing in an FeNi-based Metal Amorphous Nanocomposite. J. Mat. Res. 36, 2843-55, (2021). https://doi.org/10.1557/s43578-021-00268-5.

3. M. P. de Boer, K. Schneider and M. E. McHenry, Strength Distributions of Laminated FeNi-Based Metal Amorphous Nanocomposite Ribbons. Composite Structures. Submitted Sept. 29, 2022.

4. Y. Krimer, N. Aronhime, P. R. Ohodnicki and M. E. McHenry, Prediction of Good Glass Forming Ability in Amorphous Soft Magnetic Alloys by Thermocalc Simulation and Experimental Validation. J. Alloys and Compounds 814,152294, (2020). https://doi.org/10.1016/j.jallcom.2019.152294

5. J. Egbu, P. R. Ohodnicki, J. P. Baltrus, A. Talaat, R.F. Wright and M. E. McHenry; Analysis of Surface Roughness and Oxidation of FeNi-Based Metal Amorphous Nanocomposite Alloys. J. Alloys & Compounds 912, 165155, (2022).

References

1. M. E. McHenry, "Amorphous and Nanocomposite Magnets for High Efficiency, High Speed Motor Designs". USDOE Technical Report. (2021). https://doi.org/10.2172/1828188. https://www.osti.gov/servlets/purl/1828188.

2. S. Simizu, K. Byerly, K. Schneider, H. Kim, M. Nations, S. Narasimhan, R. Beddingfield, S. Bhattacharya, and M. E. McHenry, "Flux Switching Permanent Magnet Motor with Metal Amorphous Nanocomposite Soft Magnetic Material and Rare Earth Free Permanent Magnets," presented IEEE Energy Conversion Congress and Exposition 2021, Vancouver. Canada, Oct. 10-14, 2021. This paper was awarded the Best Paper Award at the ECCE 2022 Conference in Detroit, Michigan.

3. M. E. McHenry, M.A. Willard, and D.E. Laughlin, Amorphous and Nanocrystalline Materials for Applications as Soft Magnets. Prog. Mat. Sci. **44**, 291-433, (1999). (http://dx.doi.org/10.1016/S0079-6425(99)00002-X).

4. M. E. McHenry and D. E. Laughlin; Chapter 19 - Magnetic Properties of Metals and Alloys. **Physical Metallurgy** - 5th Ed., Elsevier B.V. 1881–2008, (2015). http://dx.doi.org/10.1016/B978-0-444-53770-6.00019-8

5. N. Aronhime, V. DeGeorge, V. Keylin, P. Ohodnicki, and M. E. McHenry, "The Effects of Strain-Annealing on Tuning Permeability and Lowering Losses in Fe-Ni-based Metal Amorphous Nanocomposites. " J. Materials **69(11)**, 2164-70, (2017). 10.1007/s11837-017-2480-x

6. K. Byerly, Y. Krimer, Charudatta Phatak, E. Theisen, and M. E. McHenry, Magnetostrictive Loss Reduction through Stress Relief Annealing in an FeNi-based Metal Amorphous Nanocomposite. J. Mat. Res. 36, 2843-55, (2021). https://doi.org/10.1557/s43578-021-00268-5**.**

7. Y. Krimer, N. Aronhime, P. R. Ohodnicki and M. E. McHenry, Prediction of Good Glass Forming Ability in Amorphous Soft Magnetic Alloys by Thermocalc Simulation and Experimental Validation. J. Alloys and Compounds **814**,152294, (2020). https://doi.org/10.1016/j.jallcom.2019.152294

8. J. Egbu, P. R. Ohodnicki, J. P. Baltrus, A. Talaat, R.F. Wright and M. E. McHenry; Analysis of Surface Roughness and Oxidation of FeNi-Based Metal Amorphous Nanocomposite Alloys. J. Alloys & Compounds **912**, 165155, (2022).

Acknowledgements

I.2.4   Scalable Ultra Power-Dense Extended Range Super Inverter (BorgWarner, Inc.)

David Bauer, Principal Investigator

BorgWarner Inc.
PowerDrive Systems
3800 Automation Ave
Auburn Hills, MI 48326
E-mail: DaBauer@BorgWarner.com

Susan Rogers, DOE Technology Development Manager

U.S. Department of Energy
E-mail: Susan.Rogers@ee.doe.gov

Start Date: October 1, 2021	End Date: December 31, 2024	
Project Funding: $6,240,000	DOE share: $5,000.000	Non-DOE share: $1,240.000

Project Introduction

2025 U.S. Department of Energy (DOE) Vehicle Technologies Office (VTO) goals follow the market trend in setting targets for cost of $6/kW and power density of 33kW/L for electric traction drive system (ETDS). The system targets include high-voltage power electronics such as one inverter and a single traction-drive electric motor. Compared with 2015, the allocation of the 2025 targets for the inverter requires 54% of cost and an 8x increase in power density. The target also addresses the higher bus/battery voltage ($\geq$650 Vdc) and long lifetime expectations ($\geq$300,000 miles) of many new electric vehicle applications. This requires significant improvement in inverter components and manufacturing technologies. By working together with the DOE, the associated technologies can be commercialized up to 5 years faster than by taking an industry only approach.

Objectives

BorgWarner engineering staff, along with resources and technical support from project partners and vendors, aims to develop and build traction inverter with a new power module design in conjunction with a novel thermal solution and high temperature capacitor technology as well as new control architecture to meet DOE 2025 VTO targets of 100kW/L power density at or below $2.7/kW cost.

Approach

Technology development within the project will drive innovations and improvements in each of the four major inverter elements to achieve a higher level of performance, integration and reliability at minimum cost. The project specific innovation areas are:

- Highly integrated and epoxy overmolded power module with double sided cooling, permitting operational junction temperature at or just below 200°C. Subsequently, enabling a higher current carrying capability with similar or less WBG (i.e., SiC) active material area, while maintaining low system losses.

- Next generation cooling module with novel fin structure enabling a scalable and cost-effective solution. Permitting high temperature and performance values based on the new power module requirements.

- Next generation capacitor technology with high temperature (> 160°C) capability and self-healing properties as well as 300% higher energy density. Enabling significant volume reduction in power stack (i.e., power modules, capacitor and busbar) sub-assembly for inverter packaging.

- New electrical control architecture based on next generation μC and ASICs providing faster feedback loop for sensing, control, and actuation. To achieve performance and efficiency targets as well as realizing future functional safety requirements (i.e., ASIL-D).

The project has three (3) phases, i.e., budget periods:

Research, Technology Down Selection and Component Design from Q4-2021 to Q4-2022 for Budget Period (BP) 1:

1) Definition of the component design as well as the supporting technology to achieve 2025 VTO targets in the final prototype hardware.

2) Research materials and processes in the power module, cooling module and capacitor.

3) Definition of the design through the analysis and simulation using newly developed/selected wide bandgap devices, i.e., SiC.

4) Development of the prototype inverter concept design and estimated performance.

Component and Subassembly Verification and System Design from Q1-2023 to Q4-2023 for Budget Period (BP) 2:

1) Manufacture and check out of the components while creating the detailed design of the prototype inverter.

2) Validation of component level performance checked against the BP1 design parameter target.

3) Completion of system-level design with the analysis and simulation for the optimization.

4) Implementing component risk mitigation plans.

Prototype Manufacturing and Verification/Validation from Q1-2024 to Q4-2024 for Budget Period (BP) 3:

1) Manufacture and test of the final inverter prototype hardware.

2) Validation of the components in life and environmental tests.

3) Demonstration of the final inverter performance and efficiency under the dynamometer condition.

4) Documentation of the component and system development as well as the future work to address any issues identified in the component and system validation.

Results

The focus in FY 2022 has been on the research and the component technology down-selection as well as system requirements and design strategy. Basic material and process technologies were investigated, and engineering reviews were held establishing decisions and/or approvals for the component design within the four (4) major inverter elements fulfilling system concept design and performance. In addition, the team completed the milestone for the design concept review on September 30th, 2022. In the beginning, the team faced significant engineering resource constraints related to the COVID-19 pandemic and the tight labor market. Overall, the team made good progress over the last two quarters and the effort continues to hire additional resources as well as to engage resources from other engineering centers of the organization.

Requirement Development

Developed system requirements document (worksheet), that satisfies most of the customer needs and meets or exceeds the 2025 VTO target of 100kW/L power density. Basic system level requirements, including key parameters for typ. operating voltage of 800Vdc, phase currents of peak 650Arms and continues 400Arms, and power ratings up to 400kVA. Mechanical packaging to be constrained to a volume ≤ 4 liters. Environment

parameters include an enclosure protection level of IP67, operational altitude of up to 5000m, and temperature conditions between -40 to 85°C. The parameters outlined above represent future inverter targets for high power passenger vehicles (PV) as well as medium power commercial vehicles (CV) applications. Therefore, power scalability will be achieved by part/component count reduction (i.e., top-down approach) without negatively impacting performance and efficiency.

Established high level components requirements and higher performance specification were derived supporting the top-down approach for system level scalability by part/component reduction. Subsequently appropriate technical solutions within the four (4) major innovation categories were investigated that meet or exceed requirements to date from incoming customers requisition that meet or not exceed 650Arms phase current and 800V DC input for 3-phase high-voltage inverter applications.

Power Module/Strategy Development

Based on the high-level systems requirements various configurations of power module have been considered for the project. The team has reviewed single switch and half-bridge module design with various cooling configurations. The task was complete with design, material, and manufacturing process selection of a double-sided cooled (DSC) silicon-carbide (SiC) single switch, using high- temperature and reliable as well as cost balanced formic acid soldering die attach process in conjunction with a newly established epoxy molding compound (EMC) for the packaged power device. Basic single switch design is shown below in Figure I.2.4.1.
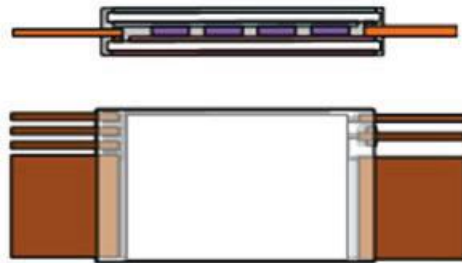
Figure I.2.4.1 Single Switch Design

The basis for this design is a scalable solution. Single switch topology is utilized as it compliant with project timing as well as material and machinery availability. A half-bridge topology will be evaluated analytically and may be reported upon as project timing permits. The primary interconnection has been defined to also include screw mount for power and soldered for auxiliary connections. Work is in progress for finalizing package layout, bill of material and design simulations to accommodate two standard sizes bare dies form different SiC suppliers on the same pad layout with up to 8 dies in parallel per single switch.

Cooling Module/Strategy Development

Material and process selection has been mostly completed including with the best performance material selection using copper (Cu) and cost balanced metal-joining process of brazing for manufacturing of the assembly. Figure I.2.4.2 shows the planar arrangement of a lower (single) heatsink assembly with the core elements such as base, fins and housing are made from stamped high thermal conductivity Cu alloy, which is then brazed together. To improve thermal management, a combination of different type thermal interface material (TIM) has been under investigation including compliant TIM such as print/dispense paste, Carbon-filled pads, hybrid Carbon-based polymer pads, and transient metal-polymer pads/dispense for the top joint area. For the bottom joint area, the team is also pursuing hard TIM types by use of preform with bond line thickness (BLT) control to easily implement with existing power and cooling module manufacturing process. Figure I.2.4.3 shows the top and bottom joint area of the double-sided cooled SiC single switch.
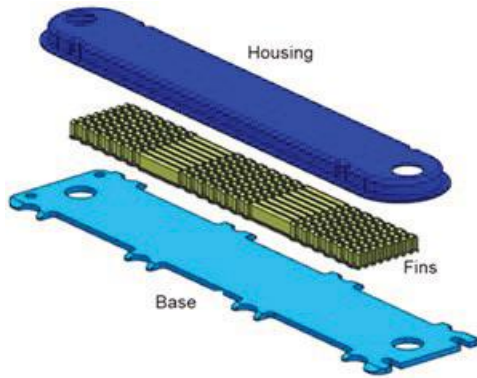
Figure I.2.4.2 Heatsink Assembly
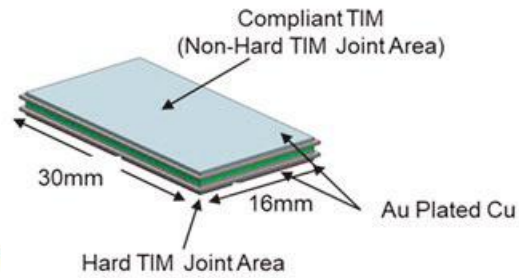
Figure I.2.4.3 Thermal Interface Area

The cooling channel design of the fin structure within the cooling module has been mostly completed establishing a 3D model including thermal, pressure drop and flow analyses. Multiple design simulations for higher efficiency heat sinks to enhance thermal performance and improve pressure drop have been performed. Figure I.2.4.4 displays simulation results for thermal distribution within the heatsink and cooling channel structure including the six power devices heat sources.

Figure I.2.4.4 Thermal Simulation of Heatsink and Cooling Channel Design

The team has planned more optimization iterations and verifications on the designated channel design achieving lowest possible pressure drop within the structural area (fins) and increasing heat transfer area and mixing, while also maintaining a minimum channel gap of greater or equal to 1mm for automotive cleanliness requirements. Compression force analyses for manufacturing underway with resources from National Renewable Energy Laboratory (NREL).

Controller Design/Strategy Development

The team has studied and executed an evaluation of next generation automotive microprocessor from Infineon Technologies in connection with application specific ASICs for the safety critical control, i.e., traction inverter. The task also includes the investigation of new gate driver and current sensing ICs for the high potential to minimize part count, cost, and packaging volume. Additionally, building traction inverter systems that are compliant to ASIL D safety ratings, can add extra system components and design cycle time, increasing cost, size, and power consumption. Therefore, BorgWarner has developed an architecture and integration strategy with the INSSA ASIC (Inverter System Safety ASIC) to drive down cost, size, and power consumption all while decreasing the un-safe failure rate. This innovation allows a smaller footprint of the board layout and most important enables to combine controller and gate driver circuitries within one single main board. Figure I.2.4.5 shows the electrical architecture identified for the project including INSSA and single control / gate driver PCB.
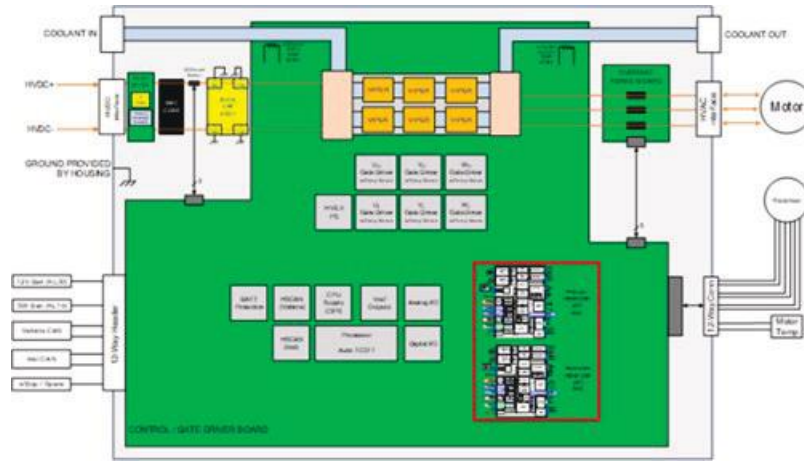
Figure I.2.4.5 Next Generation Architecture with INSSA

Gate driver was selected after technical studies (features/functions need for system and functional safety (i.e., ISO26262 compliance enabling ASIL-D level) and cost evaluation. However, additional studies are still ongoing to determine how to integrate this device with the final microprocessor and INSSA to manage fault detection, response, and diagnostic feedback. The coreless current sensing IC was selected based on data sheet and reference design studies, with subsequent HVAC busbar and HVDC assembly design and electrical performance simulation iterations. There are three (3) AC phase current sensing elements and one (1) DC current sensing element to be integrated within the busbar sub-assemblies of the inverter.

Component Integration and System Design Concept

Capacitor technology evaluation as well as assembly strategy using individual 900V NanoLam™ building blocks was completed by achieving unpackaged capacitance density of 1,717µF/L. Figure I.2.4.6 shows segmentation of capacitors into blocks of approx. 105µF, allows for highly scalable and modular bulk capacitor construction of six (6) blocks at total of 630µF for prototype hardware. Additionally, the parallelization of multiple smaller NanoLam™ blocks provides benefits within the electrical domain such as lowering equivalent series resistance (ESR) also improving thermal management.
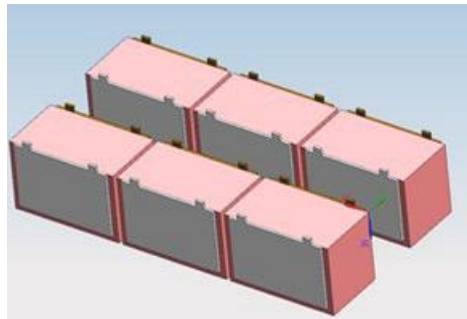
Figure I.2.4.6 Segmented Capacitors and Modular Bulk Construction

The individual NanoLam™ blocks will be interconnected directly by laser welding (metal-to-metal) to a fully laminated DC busbar sub-assembly providing lowest equivalent series inductance (ESL) and therefore highest performance. In addition, Y-capacitors placement within the bulk assembly is also considered.

Figure I.2.4.7 below shows the initial inverter design concept of the product package and specifying the interconnection system. The initial package characteristics are a volume of approx. 4 liters at a dry weight of 7kg. The team is targeting a most simplified (bottom up) assembly process for the core elements starting with

the main housing (step 1), then the bulk capacitor (step 2), the HVAC busbars and HVDC assembly (step 3 & 4), the power module and main circuit board (step 5 & 6), finishing with the cover mounting (step 7).
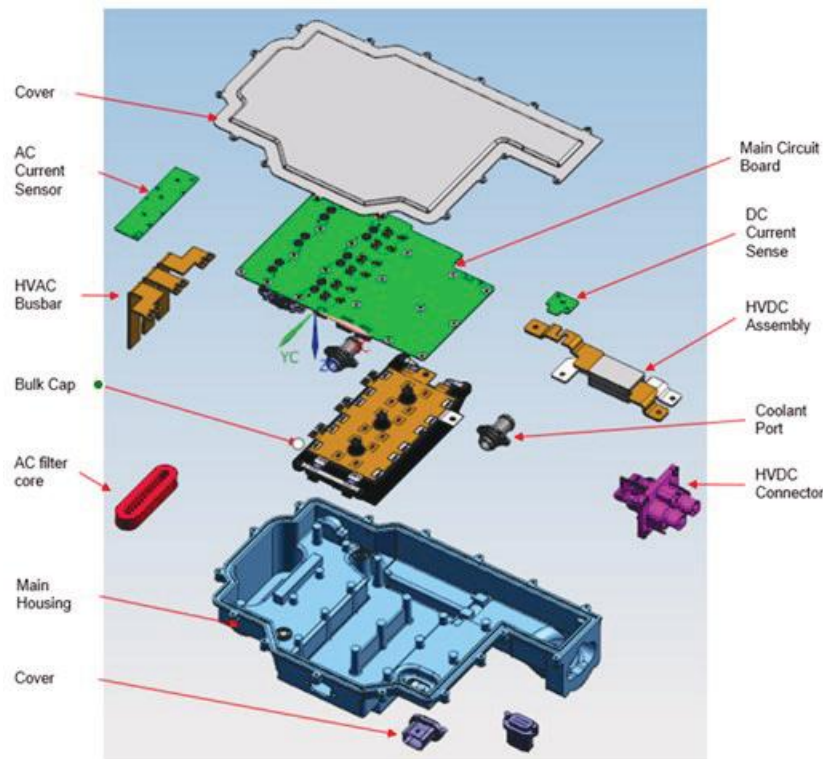
Figure I.2.4.7 Inverter Design Concept - Assembly Exploded View

Remaining inverter design concept activities include finalizing detailed parts and sub-assemblies, settle on power flow interconnection methods such as for busbars, power module and bulk capacitor. As well as confirm materials and manufacturing processes.

Conclusions

During FY 2022, the project team efforts focused on research and collaborations with external partners and suppliers on the component technologies down-selection as well as requirements development and design strategy. The primary tasks described in this report include findings and conclusions the engineering team either reviewed and approved for selections and design strategies. Systems requirements were established for achieving up to 400kVA power rating, with a SiC power module driving up to peak phase current of 650Arms. A double-sided cooled single switch topology provides scalable solution. The power device design resulted in identifying a cooling module design strategy to meet performance objectives. Newly developed controller electrical architecture, including INSSA ASIC, gate diver, and coreless current sensing, being implemented and complying with safety requirements, while reducing cost and volume. With NanoLam™ bulk capacitor showing the largest gains for power density within the product packaging. The next step is to complete concept performance and efficiency estimations confirming the confidence in the design to meet power density target.

I.2.5 Motor with Advanced Concepts for High power density and Integrated cooling for Efficiency (Raytheon Technologies Research Center)

Dr. Jagadeesh Tangudu, Principal Investigator
Raytheon Technologies Research Center
411 Silver Lane
East Hartford, CT, 06108
E-mail: jagadeesh.tangudu@rtx.com

Susan A. Rogers, DOE Technology Development Manager
U.S. Department of Energy
E-mail: susan.rogers@ee.doe.gov

Start Date: October 1, 2019   End Date: June 30, 2022
Project Funding (FY20): $599,611   DOE share: $479,689   Non-DOE share: $119,922

Project Introduction

Raytheon Technologies Research Center (RTRC) is the central research and development (R&D) organization for Raytheon Technologies Corporation (RTX), and has extensive expertise in the design, modeling and analysis of high-performance electrical machines and thermal management for all its business units. The proposing team consists of researchers from RTRC and John Deere (JD), will be referred as "Team". Each organization a has long track record of successful R&D of materials, manufacturing, components, and systems for energy efficiency applications. Motor power density and efficiency are limited by fundamental physical trade-offs between electromagnetics, thermal management, and structural design considerations. The team is proposing to utilize novel technologies and multi-physics design methods to develop a Motor with Advanced Concepts for High power density and INtegrated cooling for Efficiency (MACHINE), demonstrating an 8X improvement in power density.

Objectives

The objective of the project is to demonstrate a high speed (>20,000 RPM) electrical machine using non-heavy rare earth hard magnets, high Silicon soft magnetic steel, and embedded in-slot cooling. To achieve this goal, as part of this seedling effort, the proposed plan to address three key aspects with specific objectives towards meeting the target requirements, a) *Motor design:* Preliminary electromagnetic design meeting target performance metrics. This includes motor design studies to identify key machine parameters such as machine topology, operating speeds, material selection, number of poles, and current density. These parameters are optimized based on optimal magnetic loading, electric loading, airgap shear stress, and heat removal capacity of the select cooling mechanism; b) *Thermal Management:* The thermal management task includes identifying the appropriate materials, manufacturing methods and quantifies effective heat removal capacity for a select flow rate and pressure drop. This shall provide inputs to the motor design tasks in terms of maximum heat loads and achievable current density, and thereby contribute to the target power density; and c) *Build a sectional prototype:* Since this is a seedling effort, the team proposes to build a sectional prototype (3-4 slots) with concentrated winding and in-slot cooling. Heat load is generated by exciting the coils with current at a given current density and quantify the heat removal capacity of the thermal management solution by measuring the inlet and outlet temperatures.

Approach

Permanent magnet machines are proven to have high power density and efficiency. There are mainly two types of permanent magnet machines: concentrated windings and distributed, which will both be explored. State-of-the-art motor drives impose a frequency limit, which sets the allowable maximum speed the motor can possibly achieve. Thus, the maximum frequency limit of the drive is proposed to use here. The main difference between the two topologies is that the windings are wound around a tooth for concentrated windings while the

other spans a certain number of teeth to make a return. The cooling channels are placed in the slot with the windings to effectively cool the copper in a slot. The two design approaches will be optimized so that their best achievable performance can be compared, and a final design will be down selected from the optimization results.

Direct liquid cooling of the stator windings provides temperature and power density benefits over conventional cooling with an outer jacket. To accomplish direct winding cooling, ceramic channels are inserted into slim rectangular openings between adjacent windings. These channels have multiple small openings for flowing cooling fluid. A conformal header distributes flow to the cooling channels and collects the flow at the opposite end of the stack. The header is designed to be low loss and achieve uniform distribution of the flow to each channel in a compact space.

Results

The team has performed detailed modeling and analyses to verify the volumetric power density and efficiency of the final selected design. The simulated flux density, flux linkage, and the resulting torque production of the machine is shown in Figure I.2.5.1. The cost was estimated to be $6.3/kW if a mass production can be considered. The operating temperature is not so high, and it can improve the reliability/life of the machine. In summary, the final design meets all the design metrics.

Specifications	SOA	Target Metrics	Current Design
Power Density (kW/L)	5.7	≥ 50	50.3
Cost ($/kW)	4.7	≤ 6	~6.3*
Life (-)	1X	≥ 2X	TBD
Peak Power (kW)	55	125	125
Max Speed (RPM)	2,800	≥ 20,000	20,000
DC Bus Voltage (V)	325	700	700
Volume (L)	25-35	≤ 2.5	2.485

Figure I.2.5.1 Summary of design metrics achieved in the final design against SOA

Stator and rotor cooling designs

Direct winding cooling in the stator can provide temperature and power density benefits over jacket cooling. The in-slot cooling concept has been refined to provide further benefit. An enhancement on the slot cooling is the "t" channel shown for section of the stator in Figure I.2.5.2. The cooling channels are feasible to be printed in aluminum nitride, which provides electrical insulation to the coolant while having high thermal conductivity for heat dissipation.

(a)　　　　　　　　(b)　　　　　　　　(c)
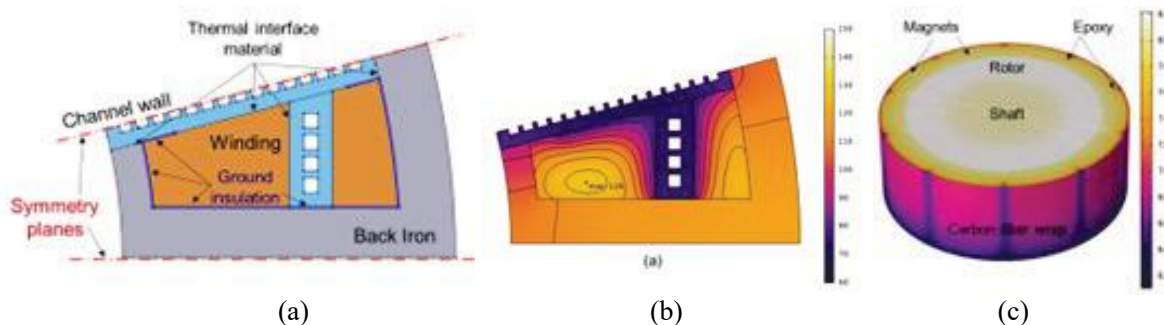
Figure I.2.5.2 (a) Domain used for the thermal model with t-shaped channel section. (b) Temperatures (°C) in the stator. (c) Temperatures (°C) in the rotor.

Assembly and header design

As strategies to route the flow, the team explored two approaches: (1) a topology optimized conformal flow header and (2) individual connector inlets to each channel. While both options are viable, the team down-selected to move forward with path (2) to take advantage of the available space between the windings created by the t-shaped cooling channels. The team considered a flow configuration with tubing and individual connectors between the tubing and flow channels, such as that shown in Figure I.2.5.3. The purpose was to balance the factors of power density and ease of manufacturability compared with the more advanced customized header concept. The configuration with two parallel flow paths emerged as the ideal configuration for this motor thermal management strategy.

	All parallel tube paths	Two parallel tube paths	All series tube paths
Pressure drop	0.09 psi	3.23 psi	24.6 psi
Pumping power	0.09 W	1.80 W	14.2 W
Total power density	51.6 kW/L	53.2 kW/L	53.3 kW/L
Note	--	Selected	--
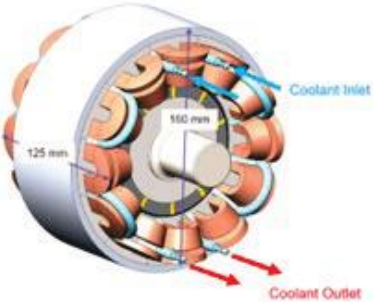
Figure I.2.5.3 Various configurations of flow supply to the cooling channels.

Sectional prototype

A sectional test prototype was designed for testing, as shown in Figure I.2.5.4, which includes two winding slots and three cooling channels. Four heaters will be embedded into the stator to mimic the heating occurring in the stator and the windings. During testing, the middle channel will be the primary area to gather data. The two outer channels serve the purpose of applying the proper boundary conditions around the windings. Water/glycol coolant will be pumped in a fluid loop evenly to the three channels. In the fluid, both temperature and pressure will be measured at the inlet and outlet of the middle channels. In the sectional prototype, temperatures will be measured at various locations within the windings and on the outside of the middle cooling channel. A fixture holds the test piece was designed, along with the main steps in the assembly process. The assembly process includes the following steps: (1) Insert 2 coil assemblies and stator laminations into the frame, (2) insert the cooling channels, and (3) clamp the plenum/headers to the end of the cores. The flow headers will be connected to fluid ports, leading a chiller and a flow meter, as well as temperature and pressure measurement instrumentation for the coolant.
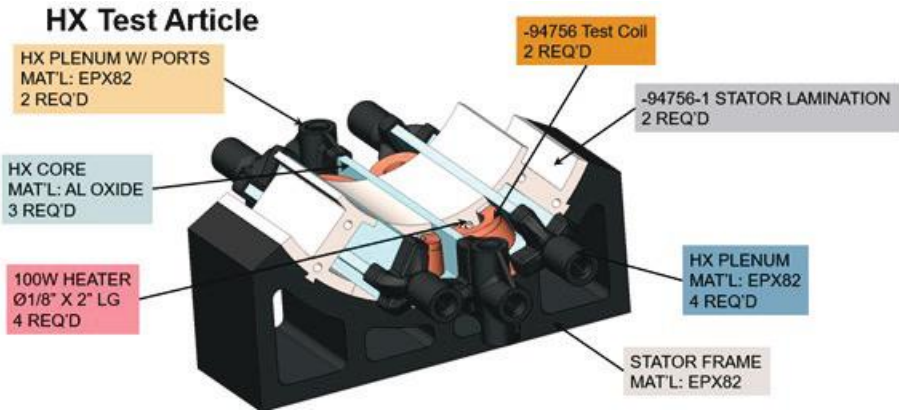
Figure I.2.5.4 Sectional prototype test assembly with integrated fixture.

Channel fabrication

Much of 2022 was spent waiting for the vendor to complete the assembly. The team is pleased to report that this fabrication has recently been completed. Firstly, the cooling channels, which were additively manufactured in alumina, were fabricated by a specialty ceramics 3D printing vendor. These channels are very novel, as ceramics additive manufacturing is very much in research and development phases. In the future, the team envisions aluminum nitride channels, which have high thermal conductivity, and are electrically insulating. These alumina channels represented a step in that direction. The alumina channels are of high quality, as shown in Figure I.2.5.5 and Figure I.2.5.6. Upon checking that the cooling channels are in good condition and that the channels pass fully through the part, the channels were passed on to McCleer power for assembly into the test section.
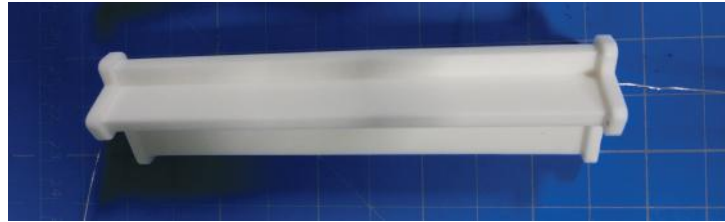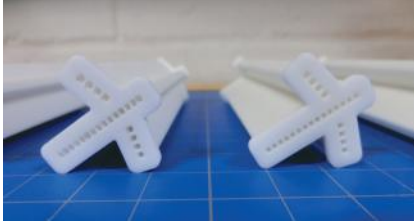
Figure I.2.5.5 Cooling channels, 3D printed in alumina. A wire passes through the internal channels, showing that no channels are blocked.
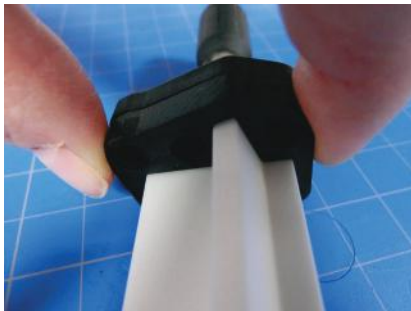
Figure I.2.5.6 3D printed manifold connections fit with the cooling channel flange.

Sectional prototype fabrication

The prototype during assembly is shown in Figure I.2.5.7. Aside from schedule delays, the assembly process went smoothly. Additional experiences from the assembly process are as follows. The glued laminated stacks, 3D printed holder, and the ceramic channels are holding together well. The pieces are a comfortably tight fit. The ceramic pieces are very well made and for the most part are smooth. Unfortunately, the channel surfaces are just rough enough to rub off insulation on the magnet wire. A temporary shim has been installed in between the wire and the ceramic to protect the wire. After the wire is successfully installed, the shim will slide out. A similar process will be done for the RTD. The ceramic tip on the RTDs are a bit sharp and also scrape the magnet wire. The RTDs will be covered with a thin piece of Nomex, then the Nomex was removed.
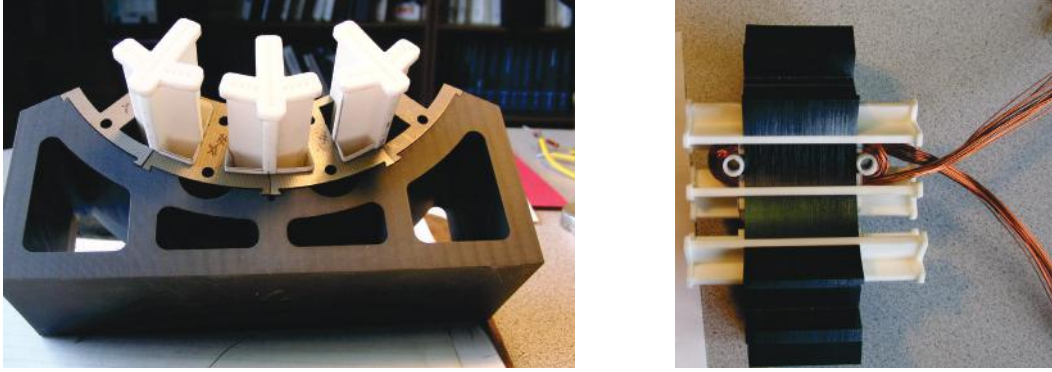
Figure I.2.5.7 Motor test section during the assembly process.

The final assembled prototype is shown in Figure I.2.5.8. The next steps in this project are to begin testing the prototype. During the test, the coils will be excited, which will generate heat. Additional heaters are inserted in the laminations to simulate lower-level heat losses in those locations. Water glycol coolant will be pumped through the cooling channels. Measurements will be temperatures and pressure drops.
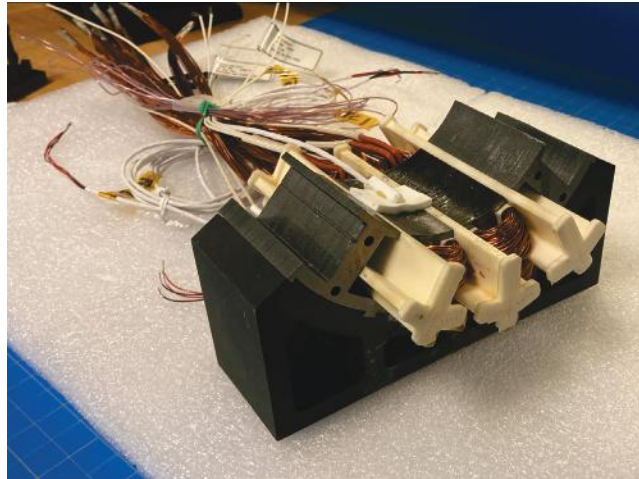
Figure I.2.5.8 Fully assembled motor test section.

Conclusions

Fabrication of cooling channels and the test section build process has been completed successfully. Team is planning to perform testing at various operating conditions to assess and validate the proposed concepts performance.

Key Publications

1. Z. S. Du and J. Tangudu, "High Speed Permanent Magnet Machine Design for Optimum Volumetric Power Density," 2021 IEEE Energy Conversion Congress and Exposition (ECCE), 2021, pp. 4546-4553, doi: 10.1109/ECCE47101.2021.9595044.

References

1. T. A. Lipo, Introduction to AC Machine Design, Wisconsin Power Electronics Research Center, Wisconsin, 2004

Acknowledgements

I.2.6 Low-Cost Rare-Earth Free Electric Drivetrain Enabled by Novel Permanent Magnets, Inverter, Integrated Design and Advanced Thermal Management (Marquette University)

Ayman EL-Refaie, Principal Investigator

Marquette University
1637 W. Wisconsin Ave
Milwaukee, WI 53233
E-mail: ayman.el-refaie@marquette.edu

Susan Rogers, DOE Technology Development Manager

U.S. Department of Energy
Email: Susan.Rogers@ee.doe.gov

Start Date: October 1, 2020   End Date: June 30, 2025
Project Funding: $6,250,000   DOE share: $5,000,000   Non-DOE share: $1,250,000

Project Introduction

This project presents a comprehensive approach to develop low-cost state-of-the art electric drivetrain system enabled by a comprehensive list of novel technologies which will lead to a rare-earth-free system at high DC bus voltage (700-800V) while meeting or exceeding the DOE targets of $7/kW and 12 kW/L and leapfrogging the state-of-the art. At the end of the project a full system will be designed, built, integrated and fully tested.

Objectives

The project brings together a group of organizations and experts with proven track record of technology developed and continuous research in the area of transportation electrification with special focus on electric and hybrid drivetrains for light-duty vehicle. The project team includes Marquette University (MU), Niron Magnetics Inc., Virginia Tech (VT), National Renewable Energy Lab (NREL), and General Motors (GM). MU will lead the overall effort as well as the development of the rare-earth free traction motor. Niron Magnetics will lead the development of the rare-earth free Iron Nitride (FeN) permanent magnets. VT will lead the development of the low-cost inverter. NREL will lead the development of the thermal management system (TMS) including system integration concepts. GM will lead the system integration and testing as well as oversee the overall effort to ensure that the developed technologies can feed into their future electric drivetrains. The baseline system that will be used in the project is the Chevy Bolt

Approach

- Budget Period (BP) 1: [Concepts development and tradeoff studies]:

    o Develop concepts, performing tradeoff studies of the various concepts and down-selecting concepts.

- Budget Period 2: [Detailed design, sub-component/component testing and risk retirement]:

    o Develop a detailed design, conduct design optimization, and conduct sub-component/component testing.

- Budget Period 3: [System integration and verification testing]:

    Procure components, conduct system integration, and perform verification testing.

Results

Traction Motor Development:

Even though there is a broad range of designs that combine different types of magnets have been developed, this section is dedicated to summarize the progress made towards the rare-earth free designs, namely, FeN+Ferrite Design and FeN Design. These two designs are double layer Interior Permanent Magnet motors. The first design blends Ferrite with the newly developed Iron Nitride (FeN) as shown in the 2D-FEA model in Figure I.2.6.1 2D FEA Models for (a) FeN+Ferrite Design, and (b) FeN Design (a). The second design is an assisted PM synchronous reluctance design that uses only FeN as presented in Figure I.2.6.1 2D FEA Models for (a) FeN+Ferrite Design, and (b) FeN Design (b). The FeN PM is shown in red color, while the Ferrite PM is shown in Light Blue color. The Ferrite PM is supplied by Hitachi and the grade of the PM is NMF-15J.

(a)   (b)
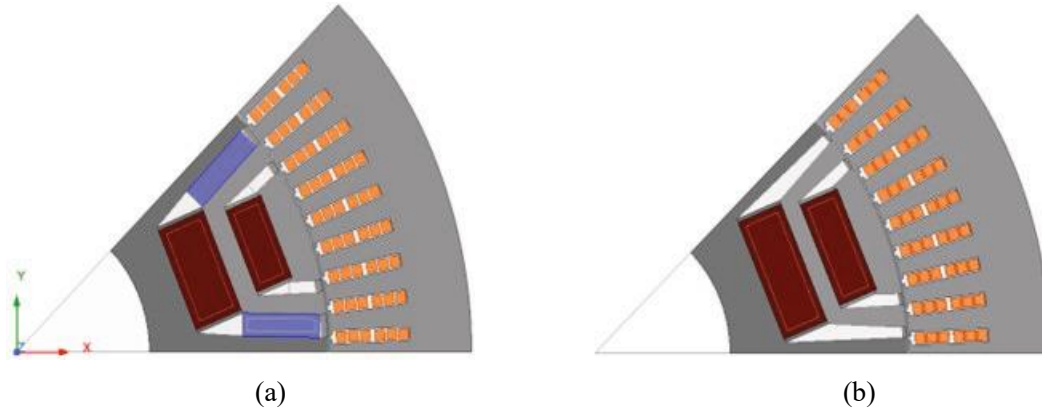
Figure I.2.6.1 2D FEA Models for (a) FeN+Ferrite Design, and (b) FeN Design

Two parametric models have been developed to integrate the above designs with an optimization tool (ANSYS-OptiSLang) to optimize the motor performance. The used parametric models are shown in Figure I.2.6.2 2D FEA Parametric Models for (a) FeN+Ferrite Design, and (b) FeN Design. The optimization results are shown in Figure I.2.6.3 Optimization results for (a) FeN+Ferrite Design, and (b) FeN Design. It can be seen that there are a lot of design that survive demagnetization with a demag ratio of 100 % along the pareto front line for both designs. In addition, FeN+Ferrite design can show higher torque output that hovers around 368 to 372 N.m for non-demagnetized designs. However, the FeN design shows non-demagnetized designs with torque production around 350 N.m.

(a)   (b)

Figure I.2.6.2 2D FEA Parametric Models for (a) FeN+Ferrite Design, and (b) FeN Design

(a)   (b)
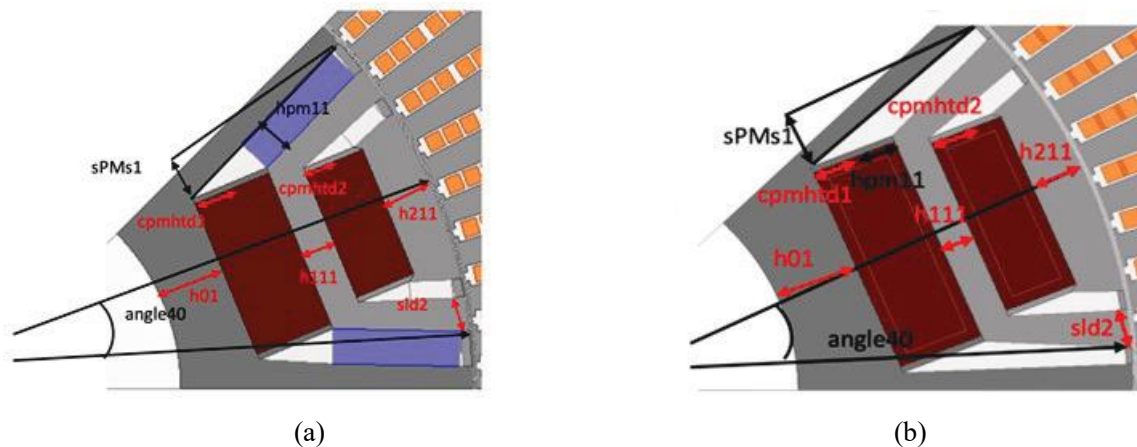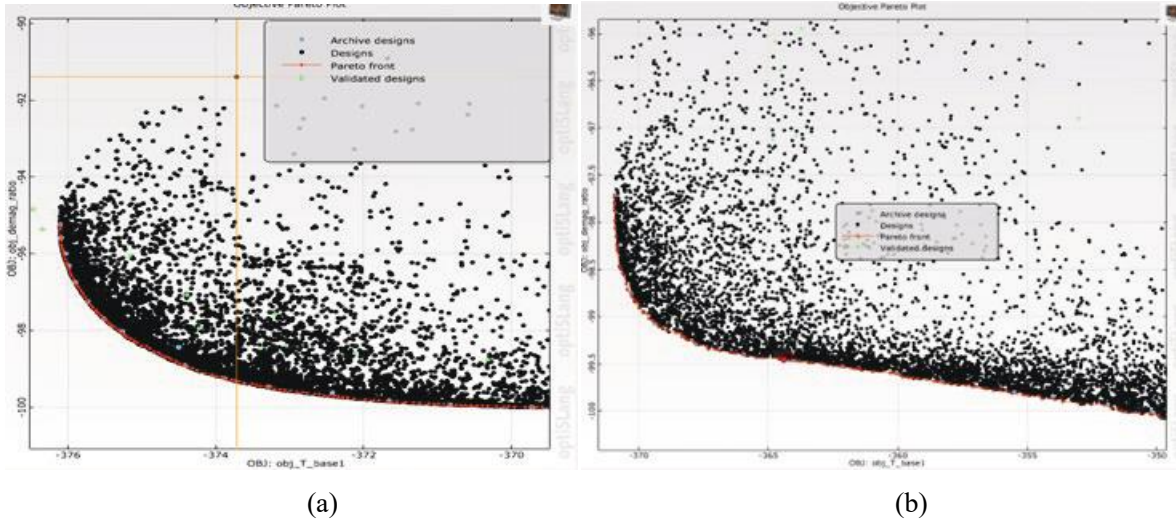
Figure I.2.6.3 Optimization results for (a) FeN+Ferrite Design, and (b) FeN Design
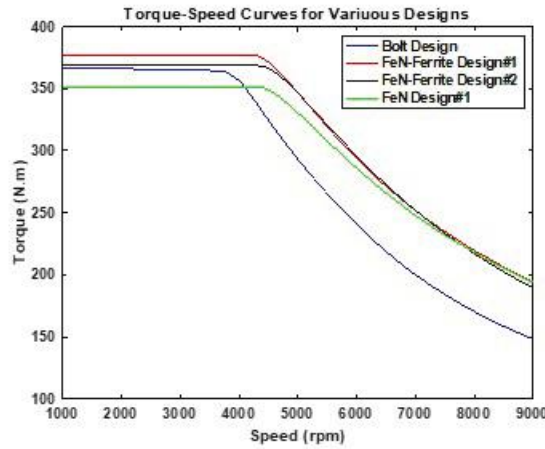
Figure I.2.6.4 Torque-speed curves for various designs

Table I.2.6.1 Torque production at peak and 9000 rpm for various designs

Design	Peak Torque (N.m)	Torque at 9000 rpm (N.m)
Chevy Bolt	368	148
FeN-Ferrite Design#1	376.8	194.1
FeN-Ferrite Design#2	368	189
FeN Design	351.5	194

Two designs have been picked for post-processing analysis to check demagnetization state for two current angles 45 deg (rated current angle at maximum torque) and 90 deg (negative d-axis current), torque production, and generation of torque speed curve. The FeN+Ferrite design shows some demagnetized regions at current angle of 90 deg. For this case, the Ferrite PM thickness has been manually adjusted to minimize the demagnetization.

The three designs have been presented above for the demagnetization analysis are compared in terms of torque production relative to the baseline design Chevy Bolt. The torque-speed curves for the three designs plus the testing's results for the Chevy Bolt are plotted in Figure I.2.6.4 Torque-speed curves for various designs and

given in Table I.2.6.1. It can be seen that the FeN+Ferrite Design#1 and FeN+Ferrite Design#2 produce higher or equal torque relative to the Chevy Bolt design in the constant torque region, while the FeN Design#1 operates at lower torque around 350 N.m with a reduction around 5%.

Regarding the higher speed operation, the presented designs show higher torque production relative to the Chevy Bot designs by above 40 N.m. This is attributed to the fact that the Chevy Bolt motor enters the maximum torque per volt at ~ 6000 rpm and the motor current of 400 Arms cannot be sustained which requires some continuous reduction as speed increases to maintain the motor terminal voltage. In contrast, the FeN+Ferrite Designs and FeN Design can operate 400 Arms continuously with optimal flux weakening capability.

In the upcoming months, the optimization tool will consider higher speed regions, expansion of ranges in the optimization to avoid any major and manual tunning for the output design, and maximization of torque for FeN design.

Iron Nitride Magnet Development:

Technical work started on January 11th, 2021. The first technical achievement was the selection of a candidate material for the ductile coating needed to enable high shear consolidation of iron nitride nanoparticles. After a literature review, appropriate precursor chemicals were identified for the desired coating. Processing parameters were developed for deposition of the coating on the iron nitride nanoparticles. The iron nitride samples were made by reducing, nitriding, and coating iron oxide nanoparticle starting materials. Four successful batches of material have been made to use for further consolidation and alignment trials. TEM images for the latest batch of material are shown in Figure I.2.6.5.
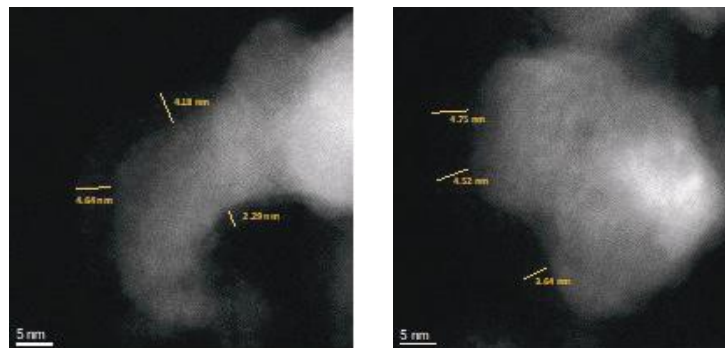
Figure I.2.6.5 TEM of coated nanoparticles.
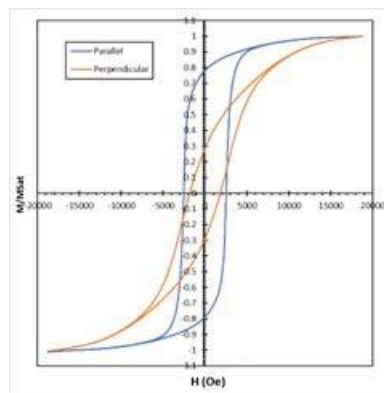
Figure I.2.6.6 Hysteresis loops of deagglomerated sample measured in parallel and perpendicular directions

A series of nanoparticle-epoxy composites were produced to test the ability of surfactant-assisted milling to deagglomerate the coated nanoparticles. Deagglomeration is necessary to enable the nanoparticles to be magnetically aligned prior to consolidation. After milling, the nanoparticles were washed to remove excess surfactant and then dried before mixing into an epoxy resin. Figure I.2.6.6 shows parallel and perpendicular hysteresis loops of the sonicated samples with a nanoparticle volume fraction of 21%. The alignment is indicated by the difference in squareness between the two measurement directions, with a S(90) = 0.71.

The first goal for this project is to achieve a packing density of 95%, a significant step above the theoretical packing density of randomly packed rigid, spherical nanoparticles (63%). Three different forms of powder compaction were used to compact the material to higher density.

The first method produced a sample with a packing density of 5.1 g/cc, or 83%. The tooling is currently being redesigned to yield a high packing density based on the data gathered with the current design. The newly designed tooling is expected to be ready for use in January 2023.

A pressure vs density curve was made using the second powder compaction method. This curve was used to extrapolate the pressure needed to compact the material to 95% density, as shown in Figure I.2.6.7**Error! Reference source not found.**. The highest density that was observed using this method was 4.9 g/cc (79%) at a pressure of 3087 MPa, however the logarithmic curve fit for the data indicates that we will not be able to reach 95% using this method without adjusting additional parameters.
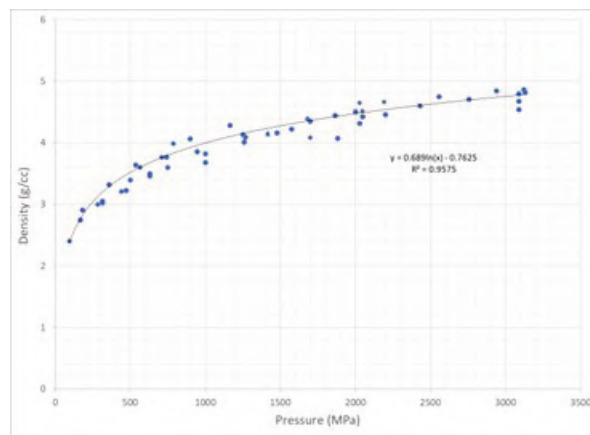
Figure I.2.6.7 Pressure vs density plot of coated nanoparticles.

The third method of consolidation achieved a density of 4.0 g/cc (65%). Additional compaction trials are being attempted with this method to find a process recipe that can yield high packing densities.

Low-Cost Inverter Development:

During FY 2022, Virginia Teach performed a survey of state-of-art electric drive technologies and their power devices, including the platforms from GM Chevy Bolt, GM Chevy Volt, Tesla Model S, Telsa Model 3, Toyota Prius, Nissan LEAF. The main conclusion from the survey is that 1.2 kV SiC discrete MOSFET and 800 V battery system should be adopted for next-generation low-cost elective drive platform.

The team performed the electric drive topology evaluation and comparison by using the three-phase PWM hard-switching topology as the benchmark, two soft-switching topologies as shown in Figure I.2.6.8 and Figure I.2.6.9 are used for comparison purposes.
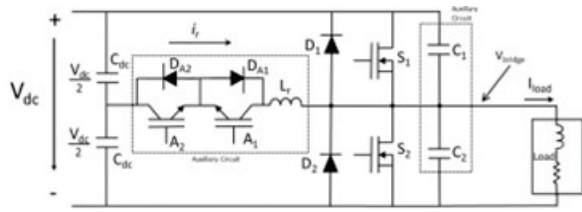
Figure I.2.6.8 AC-side method ARCP inverter.
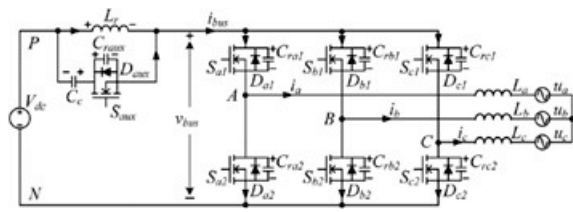
Figure I.2.6.9 DC-side method soft-switching inverter.

In conclusion, when considering low-power or low-current applications, soft-switching techniques can definitely bring benefit for high switching frequency operation. Also, in grid-connected applications, operating at high switching frequency can reduce the passive component at both DC and AC side. However, when considering high-power, low-voltage high-current applications such as motor drives, it may not worth spending much efforts to design soft-switching inverter for tiny improvement of efficiency. Especially of high rated output current, no matter auxiliary circuit or current control techniques, the additional loss caused by high peak current stress just compensates the switching loss that have been eliminated. Furthermore, the high instant peak current may cause stability issue of the system, and resonant inductor design becomes more challenging due to the core saturation issue. Eventually, the overall efficiency using soft-switching only slightly increase when compared with other SiC devices with great performance using hard-switching.

The team also focuses on the survey and evaluation of all possible 1.2 kV SiC MOSFETs devices to identify the best fitting devices for the project. A total of 42 discrete SiC. MOSFETs were selected as potential candidates as the converter's main power switch. After extensive comparison, the following four devices candidates are down selected as the final possible candidate for construction of the electric-drive prototype.

The static and dynamic performance of all four devices are tested. Based on the switching energy and conduction loss, the final device loss evaluation under different conditions are performed. The results will be used for further thermal analysis to finalize the final device selection and number of devices in parallel.

The team also designed two possible electric-drive system based on two different technologies: 1) discrete 1.2 kV SiC MOSFET with heavy-copper-PCB bus integration, 2) PCB-embedded double-side cooling integration. Both technologies are built and evaluated. Figure I.2.6.11 and Figure I.2.6.12 show the three-phase inverter design based on heavy-copper PCB-based and the prototype under test. The TO-247-4L SiC MOSFETs are soldered on the bottom-side of the heavy copper power board, with CeraLink capacitors soldered on both top and bottom-side. The contactless hall sensor is located at the top of the power board with its U shield as shown on the right-hand side of the figure.

		C3M0016120K	IMZA120R007M1H	MSC017SMA120B4	NTH4L020N120SC1
Single	$(dv/dt)_{on, off}$ (at 100 °C, same R_g)	Largest	Smallest	Medium	Medium
	Switching Energy (at 100 °C)	Smallest	Largest	Smallest	Medium
	$R_{ds, on}$	12-13 mΩ	6-7 mΩ	17-24 mΩ	20-22 mΩ
	On Response Time (V_{gs} to I_{ds})	20 ns	45 ns	40 ns	35 ns
	Off Response Time (V_{gs} to V_{ds})	70 ns	72 ns	72 ns	50 ns
Parallel	On I_{pk} (at 100 °C)	122 A	144 A	151 A	X
	Off I_{pk} (at 100 °C)	78 A	79 A	79 A	X
	Ringing	Small	Small	Large	X
Efficiency	$N=4$	2nd	Highest	3rd	Lowest
	$N=6$	Highest	Highest	Lowest	Medium

Figure I.2.6.10 Final 1.2 kV SiC MOSFET candidates
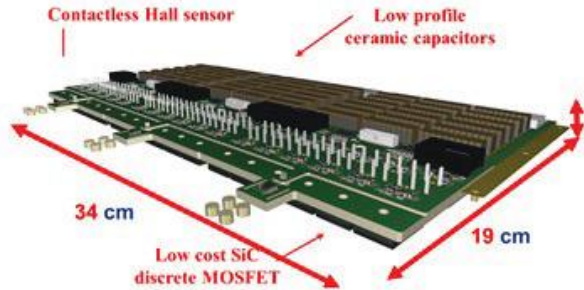
Figure I.2.6.11 Three-phase inverter design based on Heavy Copper PCB bus integration using discrete 1.2 kV SiC MOSFETs and surface-mount sensor
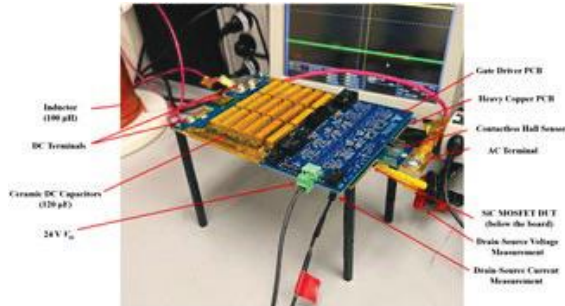
Figure I.2.6.12 Heavy-copper PCB prototype

Another integration that the team evluated is the PCB-embedding technology. The PCB can be used to directly integrate and house the SiC MOSFET die for switching loop minimization the power density improvement. Figure I.2.6.13 shows the PCB-embedding stack-up that the die is sitting inside the PCB laminates. Figure I.2.6.14 shows the single-phase single-die embedded PCB prototype with double-sided cooling design. Preliminary switching test results show superior switching speed.
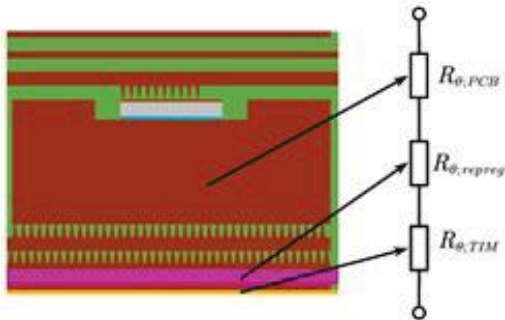
Figure I.2.6.13 PCB-embedding with 1.2 kV SiC MOSFET die for extreme loop inductance minimization and high-density integration.
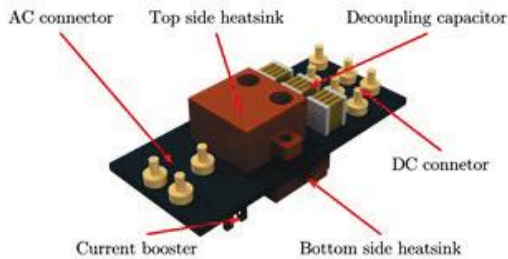
Figure I.2.6.14 Single-phase single-die PCB embedded prototype.

Thermal Management Development:

During FY 2022, NREL performed a review of electric drive thermal management technologies for the power electronics and electric motors to review integration approaches. Figure I.2.6.15 provides a summary of the thermal management integration approaches of the inverter relative to the motor, the potential locations for the integrated inverter, and sample systems from the literature review.
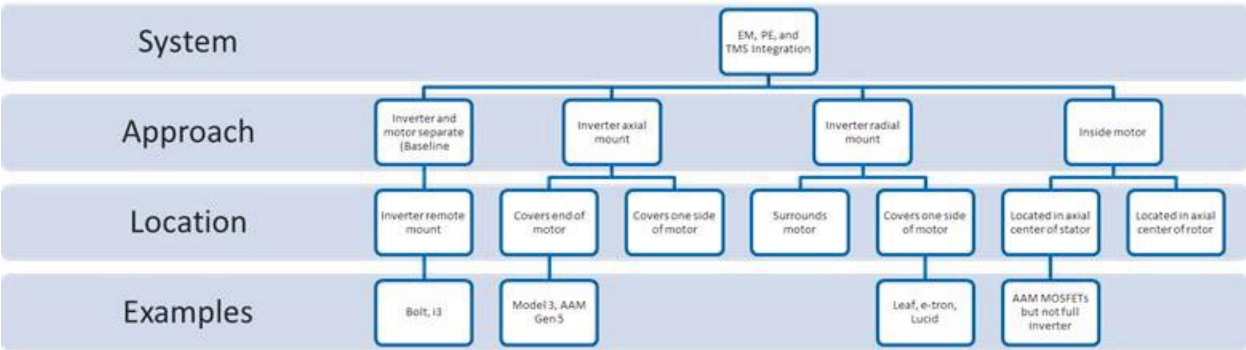
Figure I.2.6.15 Electric drive thermal management system integration approaches with examples highlighted.

In addition to reviewing of existing on the EV market or under development integration approaches, NREL performed a parameter sweeps on GM Bolt motor thermal model for evaluation of optimal cooling strategies. Figure I.2.6.16 provides an overview of cooling methods and their respective heat transfer coefficient ranges.
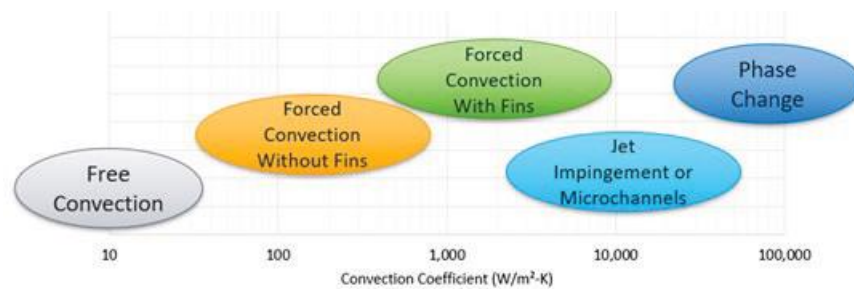
Figure I.2.6.16 Cooling methods and their respective heat transfer coefficient ranges

Following heat transfer coefficients (for standard cooling techniques such as channels and fins) were used:

- Air: 35°C h: 4-100 W/m-K

- WEG: 65°C   h: 100-4000 W/m-K

- Oil: 85°C h: 70-2800 W/m-K

Based on analyzed modeling results following conclusions were made:

- Rotor temperature tends to follow case temperature (The rotor is indirectly heated by the stator)

- Air cooling is generally insufficient to cool case, liquid cooling is needed

- It may be possible to cool windings with air with increased case cooling (possible next step)

- Rotor does not appear to require special cooling so long as the stator is sufficiently cooled.

Conclusions

Technical achievements by Marquette University (MU) include the following:

- Made further modifications to the optimization code to ensure conversing onto the global optimum designs.

- Updated the calculation of the permanent demagnetization risk index

- Developed preliminary hybrid designs including NdFeB and ferrite permanent magnets. Optimum designs were developed based on multiple operating points.

- Developed preliminary hybrid designs including Dy-free NdFeB and ferrite permanent magnets. Optimum designs were developed based on multiple operating points.

- Developed preliminary hybrid designs including NdFeB and FeN permanent magnets. Optimum designs were developed based on multiple operating points.

- Developed preliminary hybrid designs including FeN and ferrite permanent magnets. Optimum designs were developed based on multiple operating points.

- Preliminary exploring of the impact of different number of poles and slot/pole combinations on the performance of various designs with various magnet combinations

Technical achievements by Niron Magnetics include the following:

- Niron Magnetics, Inc. is developing Iron Nitride, a high performance, completely rare earth free permanent magnet technology. The Goals & Objectives of Niron Magnetics are to develop iron nitride permanent magnets with an energy product of 36 MGOe and produce 2 kg of these magnets for integration into a prototype motor. In the first budget period, a process for producing iron nitride nanoparticles with a nanometer scale ductile coating has been demonstrated. The composition, thickness, and uniformity of the coating have been verified experimentally. Alignment of the coated nanoparticles was achieved at lower volume fractions and further consolidation of the material has led to densities of 5.1 g/cc, or ~83% density. Further compaction methods are being investigated to increase the density to 95%.

Technical achievements by Virginia Tech (VT) include the following:

- Virginia Tech has performed the major device evaluation and critical sub-component and circuit integration technology prototyping. The main conclusion is that discrete 1.2 kV SIC MOSFET devices, PCB bus integration, surface-mount-sensor are critical components to enable low-cost high-density high-efficient electric drive system.

Technical achievements by NREL include the following:

- Performed a review of electric drive thermal management technologies for the power electronics and electric motors to review integration approaches.

- performed a parameter sweeps on GM Bolt motor thermal model for evaluation of optimal cooling strategies.

Acknowledgements

I.2.7 Low Cost High-Performance HRE-Free 3-in-1 Electric Drive Unit (American Axle & Manufacturing)

David Crecelius, Principal Investigator
American Axle & Manufacturing
One Dauch Drive
Detroit, MI 48211
E-mail: David.Crecelius@aam.com

Susan Rogers, DOE Technology Development Manager
U.S. Department of Energy
E-mail: susan.rogers@ee.doe.gov

Start Date: October 1, 2020	End Date: March 31, 2024	
Project Funding: $6,250,000	DOE share: $5,000,000	Non-DOE share: $1,250,000

Project Introduction

The project team will expand upon American Axle & Manufacturing's (AAM) baseline technology and develop a high-speed, AC induction electric drive unit (EDU) with total direct-oil-cooling and integrated power electronics. The project will accelerate advancements in EDU technology by allowing AAM to build upon the progress made in developing the underlying baseline technologies. The following seven improvements to AAM's baseline technology are being implemented in this research and development program: 1) Increased speed (30k RPM) AC induction motor, 2) Silver-sintering of discrete silicon carbide (SiC) metal–oxide–semiconductor field-effect transistors (MOSFET) to heat sinks, 3) Electrically insulated rotor bars, 4) Optimized lamination steel, 5) EDU-integrated 650VDC inverter package, 6) Over-molded stator with molded liners, and 7) 650VDC power-dense stator design.

Successful development of the technology will result in a substantial cost reduction for EDU systems in the market. Coupled with falling battery system costs, this will accelerate the market acceptance and related production scaling of battery electric vehicles.

Objectives

The objective of this project is to research, develop, and test a Heavy Rare Earth (HRE)-free 3-In-1 electric drive unit that has class leading power density and cost. The key technologies to be developed will meet or exceed the Department of Energy (DOE) targets of a cost ≤ $7/kilowatt, power density ≥ 12 kW/liter, and operating voltage ≥ 600 VDC.

Approach

Technology development within the project will build upon and reference against the AAM baseline Gen 5.0 EDU.

The project is being conducted in three (3) phases:

Design Development and Technology Research (Budget Period 1)

- Design, investigate, and develop core technologies

- Investigate stator lamination and over molding development, high speed motor development, and silicon carbide MOSFET packaging development

- Investigate, analyze, and assess costs of the developed technologies

- Select an optimized configuration for prototype build in budget period 2

Prototype Component Fabrication and Unit Build (Budget Period 2)

- Fabricate over molded stators, high speed motors, and MOSFET silver sintered attachments

- Assemble motor-only units and full EDUs for subsequent dyno testing

- Test the motor-only units on the dyno with the test results being compared to the baseline

Prototype Testing and Commercialization Planning (Budget Period 3)

- Test the full EDU on the dyno, with the results being compared to the baseline technology

- Document the EDU Bill of Materials (BOM) for comparison to benchmarked EDUs and cost targets

- Prepare a manufacturing and commercialization plan to produce the developed technology in high volume

Results

Task 1.1 – High Efficiency Stator Development

Optimized Lamination Material

Electromagnetic (EM) simulations, using different selected lamination materials, were completed to further evaluate efficiency. The additional EM simulations evaluated lamination materials from JFE, Thyssen, Vacuumschmeltze, and Carpenter, which were then compared against the baseline M15 materials. The results of these simulations were fed into the vehicle drive cycle simulation using the Tesla Model 3 donor platform to determine overall efficiency performance. Table I.2.7.1 shows a summary of the drive cycle efficiency results.

Table I.2.7.1 Summary of Drive Cycle Efficiency with Different Lamination Materials

Drivecycle Average Motor Efficiency
TESLA Model 3 RWD 2021 MY with 22.93:1 reduction ratio and 25 C motor temperature

Supplier	Material	Thickness [mm]	WLTP	EPA CITY	EPA HWY	AVG
Baseline Lamination	M15	0.35	94.21%	93.60%	96.29%	94.70%
Carpenter	Hyperco 50	0.15	95.26%	94.70%	96.98%	95.65%
Vacuumschmeltze	Vacoflux 49	0.2	95.30%	94.77%	96.85%	95.64%
Vacuumschmeltze	Vacoflux 49	0.35	93.25%	92.99%	95.15%	93.80%
JFE	10X	0.1	94.86%	93.85%	96.91%	95.21%
Thyssen	N10	0.1	94.87%	93.99%	96.85%	95.24%
Thyssen	N20	0.2	94.77%	94.00%	96.85%	95.21%
Thyssen	M800-50A	0.5	89.74%	90.47%	91.82%	90.68%

Stator Over Molding Development

Due to the flow barriers within the thin over molded wall and the inability to flow the length of the stator stack, the team decided that the stator slot liner over molding concept would not be feasible for prototyping. Therefore, as a secondary plan in lieu of slot over molding, alternate slot liner materials were investigated and analyzed. Two additional materials were selected to investigate: APTIV 1000, a PEEK material from Victrex, and an e-coat material, Scotchcast 5230 N, from 3M. A finite element analysis (FEA) was completed analyzing the Nomex, PEEK, and Scotchcast materials. An example of the PEEK analysis is shown in Figure I.2.7.1.
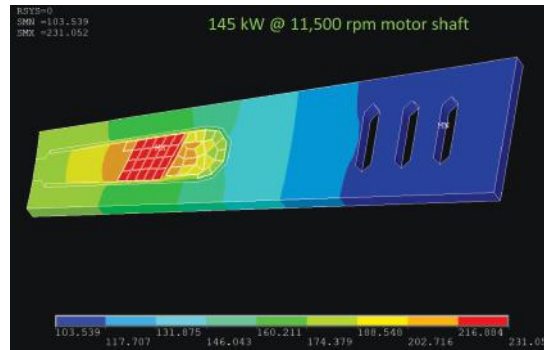
Figure I.2.7.1 FEA simulation showing PEEK slot liner material

Both the Victrex PEEK and 3M Scotchcast materials showed similar thermal capability of 140kW in the FEA analysis. Given their similar thermal performance it was decided to select the Victrex PEEK material to use as the slot liner material for the build due to its known method of assembly in the stator compared to the Scotchcast, which would require additional process development.

The full stator and winding over molding design was completed, resulting in a manufacturable design that will provide improved thermal transfer capability. The 3D model of the final stator winding over mold design is shown in Figure I.2.7.2.
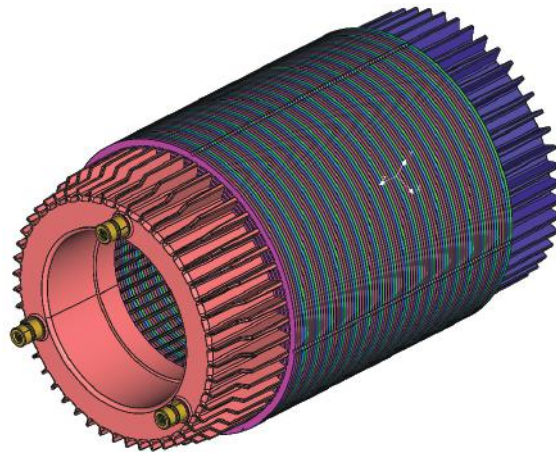
Figure I.2.7.2 Stator winding over mold design

An initial high level "should cost" analysis of the over molded stator was completed. This analysis was completed on the selected motor for prototyping. The cost analysis was conducted in conjunction with a 3rd party estimator and was based on 2022 Q1 material pricing and assumed US based manufacturing. The stator assembly costing included the individual stator components, assembly, and overhead estimates. For this estimate the lamination material used was a standard M15 type. The total estimated cost of the stator assembly with the over molded windings was $133.81. This result would be a 10% cost improvement compared to the baseline stator cost estimate.

Task 1.2 - High Speed Induction Motor Development

High Speed Rotor Design

The high speed rotor mechanical and electromagnetic design was completed, enabling accomplishment of Milestone 1.1, Mechanical Design of Stator and Rotor Complete, on December 1, 2021. A 3D model of this design is shown in Figure I.2.7.3.
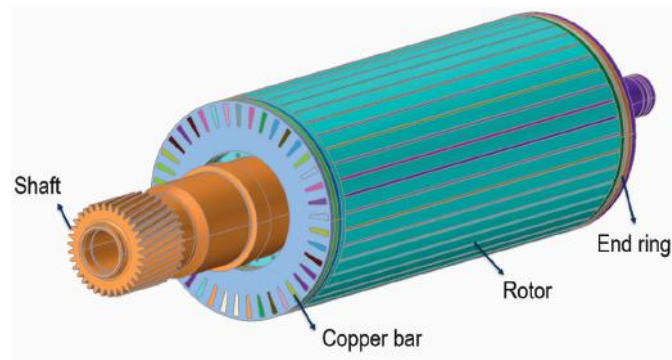
Figure I.2.7.3 Rotor with copper bars and end rings

The rotor design features small holes in the inside diameter of the lamination stack that are used to add pins which provide mass to facilitate balancing of the rotor. With this method, copper material does not need to be removed from the end rings of the rotor and potentially affect motor performance. The rotor shaft features an integrated pinion gear and a hollow core to facilitate cooling of the rotor with oil. Insulated rotor bars have been integrated, with the support of a rotor bar supplier.

To ensure mechanical integrity of the rotor spinning at 30k RPM a FEA stress analysis of the rotor was performed. Figure I.2.7.4 shows the stress at 30k RPM with maximum press fit of the shaft into the rotor.
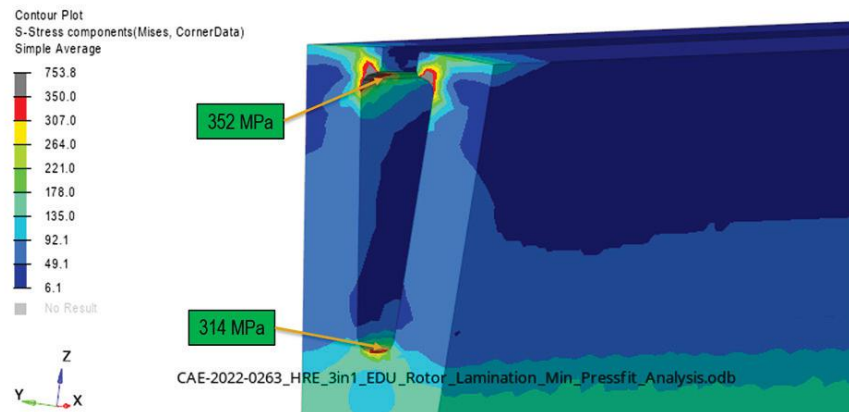
Figure I.2.7.4 Stress of rotor at 30k RPM

The design results in acceptable stress levels except for a small area at the base of the slot, where the analysis shows the stress to exceed the 330 MPa yield strength of the lamination steel. This is likely an artifact of the way the FEA model was constrained by not allowing for a small gap around the copper bar.

In addition to the FEA stress analysis of the rotor, the thermal performance of the selected motor was performed to determine the continuous operating point as well as the peak performance thermal point. Details of the selected motor can be referenced in the FY 2021 Annual Progress Report. A thermal analysis was completed to create a map of peak power capability over the speed range that indicates zones of operation for 20 sec, 30 sec, 90 sec, and continuous time.

Motor Only and Full EDU Mechanical Design

The motor only design includes the motor housing used in the full EDU but will use a modified end plate to allow for the 3 phase motor terminal connections. The gearbox is replaced with an empty housing and output shaft. Figure I.2.7.5 (left) shows the cross section of the motor only design. This design incorporates the 30k RPM motor with a copper induction rotor and insulated rotor bars. Rotor cooling is accomplished by using an

oil cooling media that flows through the shaft and integrated shaft heat sink. The stator assembly includes the PEEK slot liners and over molded windings and end turns.

The full EDU cross section with the integrated gearbox and ring inverter is shown in Figure I.2.7.5 (right).

Figure I.2.7.5 Motor only (left) and full EDU cross sections (right)

The full EDU design includes a dual layshaft gearbox design that splits the torque from the motor output into 2 paths to the output gear. The integrated ring inverter using discrete TO-247 MOSFETs and oil cooling is shown integrated into the inner diameter of the motor end windings. The DC link capacitor is integrated onto the top side of the motor housing.

Task 1.3 - Advanced Packaging & Attachment Development of Discrete SiC MOSFETs

Silver Sintering Discrete Power Devices

Additional silver sintering was completed by using a sample heat sink instead of a copper plate in the sintering process. Figure I.2.7.6 shows the copper heat sink that was sintered onto the TO-247 MOSFET.
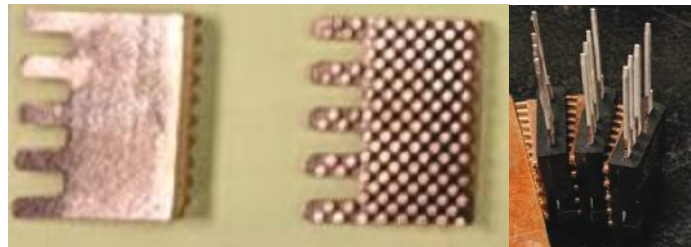
Figure I.2.7.6 Copper heat sink for TO-247 silver sintering attachment

Five sample parts using the copper heat sinks were silver sintered to the TO-247 MOSFET backplate. Several different sintering methods were performed during the process development. These methods are designated "old" and "new" in this report.

To inspect the integrity of the silver sintered bond line the parts were cut apart and the cross section was inspected. Under 200x magnification the silver sintered bond line between the package and the heatsink looked good. There was no evidence of delamination or voiding within the sintered bond line.

Additionally, AAM investigated a new copper sintering paste as an alternative to the silver sintering material, to determine if a copper sintering process could provide improved benefits when compared to silver sintering. Working with the supplier of the copper paste material, MOSFET/heat sink assemblies were fabricated using the copper paste in a new copper sintering process.

To better evaluate the silver sintered and copper sintered bond thermal interface performance, a test procedure was developed to measure the thermal resistance from the MOSFET junction to the oil cooling media. The sintered parts were tested in a custom designed thermal fixture to evaluate the bond thermal performance. The thermal resistance of the copper sintered parts proved to be quite good and very similar to the new silver

sintering process. There are added benefits of the copper sintering, which include a less complicated sintering process and less capital expense. Thermal performance results of the copper sintering, silver sintering (old and new methods), and the baseline soldered process are shown in Figure I.2.7.7.
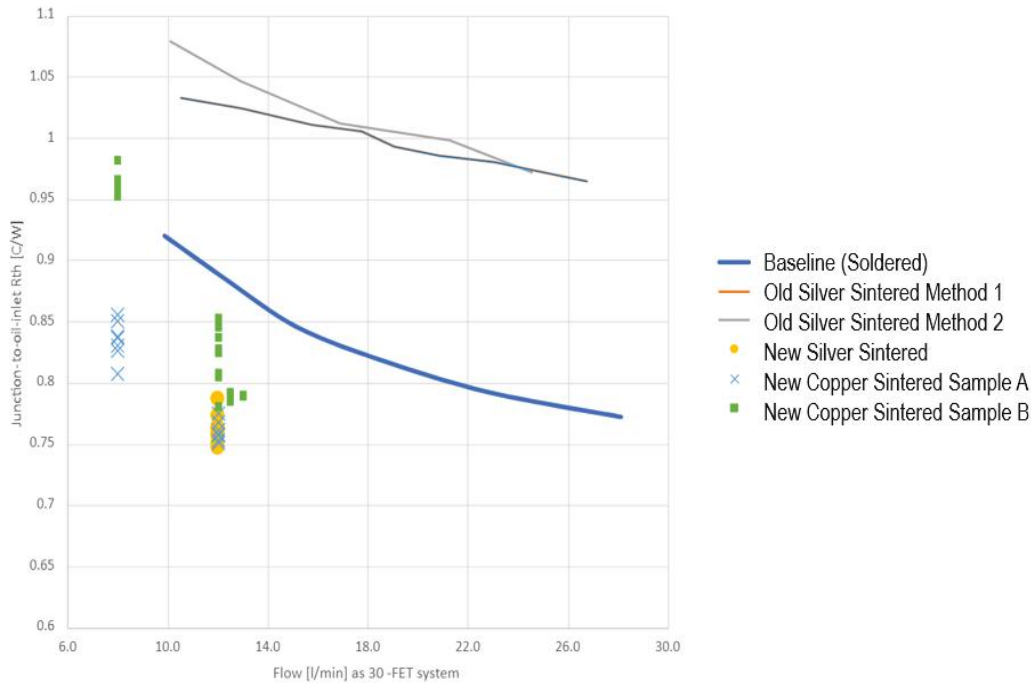
Figure I.2.7.7 Thermal resistance results sintered vs. baseline soldered bond

Optimized TO-247 Electrical Lead Attachment and Packaging Design

Within the design of the stator end turn leads, it was determined that better thermal performance and heat transfer could be accomplished by forming the end turn geometry to be longer and thinner. Due to this design package change and the wound stator insert molding process, the phase lead attachment terminal that connects to the TO-247 MOSFETs was optimized to a crimp and weld method. With this crimp and weld method the phase leads coming from the stator assembly are captured by the injection over molded stator material and provide a threaded attachment point for the inverter bus bar. The phase lead terminal utilizes a crimp and weld process to make the electrical and mechanical connection to the phase lead magnet wires.

Task 1.4 – Configuration Selection

Input into the configuration selection decision has been ongoing throughout the project in the form of EM simulations, FEA analysis, thermal analysis, and observational analysis for the rotor and stator designs. These activities have been conducted within tasks 1.1, 1.2, and 1.3 and have been summarized in this report and the FY 2021 and FY2022 quarterly reports. Task 1.4 was completed on December 17, 2021, after conducting a review of all available data generated within the project and making a determination for the optimal design to build into hardware.

Based on EM design analysis of many high speed motor options and results from thermal and mechanical FEA, AAM determined that the optimal design configuration to move forward with into Budget Period 2 and subsequent hardware build is with selected motor #12, for which information is provided in the FY 2021 Annual Progress Report. The motor performance was shown in simulation to meet the specification requirements and the thermal performance requirements. Additionally, it was decided the MOSFETs within the inverter would utilize the successfully developed copper sintered heat sink attachment method.

Based on AAM's analysis, selection of the configuration as indicated is projected to achieve the DOE program objectives of power density > 12kW/L and a bus voltage > 600VDC.

Task 2.1 – Fabricate Prototype Components

MOSFET Heat Sinks

Due to a change required in the ring inverter, the heat sink design was modified. Figure I.2.7.8 shows the updated design of the MOSFET heat sink and Figure I.2.7.9 shows a thermal FEA analysis of the new design.
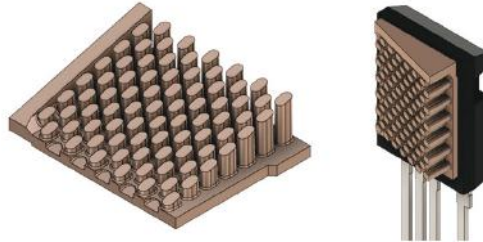
Figure I.2.7.8 Modified MOSFET heat sink design
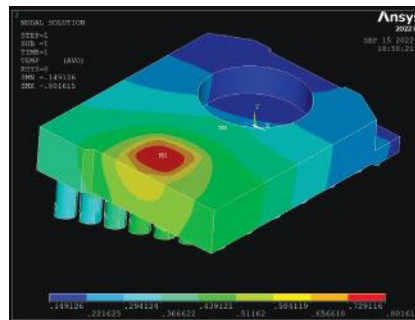
Figure I.2.7.9 Thermal FEA analysis of new heat sink

The new heat sink design was analyzed to confirm that its performance would meet the requirements of heat transfer from the MOSFET back plate to the cooling oil. Figure I.2.7.9 shows the thermal FEA analysis run on the new heat sink design, resulting in projected performance of 0.8 deg C/W, which is similar to that of the baseline design.

Stator and Rotor Fabrication

The stator and rotor components have been ordered. These are the longer lead items to be acquired for unit builds. Orders were placed with suppliers for the stator core lamination stamping, stator core winding, and wound stator injection molded encapsulation. Additionally, copper rotors were ordered in both insulated and non-insulated versions. Copper rotors are expected to be delivered in December 2022.

Over Molded Stator Fabrication

The over molded stator order was placed with the supplier and fabrication of the injection molding tooling was started based on the finalized design of the encapsulated stator. Before the tooling can be completed the supplier requires a completed wound stator for final dimensional checks. Shipment of stators to the over molder is expected to occur in December 2022.

Other Component Fabrication

A custom rotor position sensor is required for the motor only version of the EDU. This is due to the need to flow the rotor oil in the reverse direction with the oil inlet on the inverter end of the shaft instead of the gear box end. Without a gearbox connected there is no way to flow oil into the rotor shaft at the gearbox end. The position sensor is located on the inverter end of the shaft in the fully integrated EDU but with the need to flow

oil into the inverter end of the shaft the position sensor must be moved. The new custom rotor position sensor will be mounted external to the EDU on the empty gearbox housing.

The 650V ring inverter needed a design modification to meet the creepage and clearance requirements to operate at this voltage. To facilitate the needed space in the design, the number of MOSFETs were reduced from 5 devices per switch bank to 4. Additionally, since the required phase current of the selected motor design is 350Arms, which is 100Arms lower than the baseline design, the number of MOSFETs could be reduced without affecting the system performance and aiding in a cost reduction. This necessitated the need for redesigning the MOSFET heat sink. Additionally, the new spacing of the MOSFETs required a change to the inverter gate drive board. Figure I.2.7.10 shows the assembled ring inverter (left) with updated MOSFET spacing and the new gate driver board (right).

Figure I.2.7.10 Assembled ring inverter with updated design (left) & gate drive board (right)

Task 2.2 – Build Prototype Motors & EDUs

Prototype builds of the motor only unit are expected to be completed in February 2023, and the build of the full EDU is expected to occur in March 2023.

Task 2.3 – Test High Speed Induction Motor

Test Plan and Test Results

An initial test plan for the motor only unit was drafted. The plan includes evaluation of the motor parameters, insulation system, spin losses, and motor performance across the operating envelope.

Task 2.4 – Estimated EDU Costs

A quote was received from a 3rd party supplier to provide full EDU cost estimating.

Conclusions

During FY 2022, the project team has expanded upon AAM's baseline technology by completing the design of a high-speed (30k RPM) induction motor (rotor and stator) operating with a 650VDC supply; successfully demonstrating a discrete MOSFET copper sintering attachment process; and developing a stator over molding design for improved thermal performance. Parts have been ordered to build and test the design. With the current trajectory of efforts to research, develop, and test a Heavy Rare Earth (HRE)-free 3-In-1 EDU that has class leading power density and cost, the project will meet or exceed the Department of Energy (DOE) targets of a cost less than $7/kilowatt, power density of less than 12 kW/liter, and an operating voltage of greater than 600 VDC.

I.2.8   Wound Field Synchronous Machine System Integration towards 8x Power Density and Commercialization (Magna Services of America, Inc.)

Lakshmi Varaha Iyer, Principal Investigator
Magna Services of America, Inc. (Magna R&D)
750 Tower Drive
Troy, MI 48098
E-mail: LakshmiVaraha.iyer@magna.com

Susan Rogers, DOE Technology Development Manager
U.S. Department of Energy
E-mail: susan.rogers@ee.doe.gov

Start Date: October 1, 2019   End Date: June 30, 2023
Project Funding (FY20): $875,00   DOE share: $700,000   Non-DOE share: $175,000

Project Introduction

In support of VTO's Electric Drive R&D activity, the Electric Drive Technologies (EDT) Consortium, a multi-disciplinary team of national labs and universities, coordinates and conducts a portfolio of research to advance the state-of-the-art in electric drive technologies. The Consortium has established the following strategic goal listed in the table below:

EDT Research Consortium Strategic Goal (compared to 2015 baseline)
A 125kW electric traction drive system:

- 8X power density improvement, or 1/10 the volume (33 kW/L)

- ½ the cost ($3.3/kW)

- 2X useful life (300,000 miles)

- 100 kW/L inverter and a <20,000 rpm, 50kW/L electric motor

Objectives

The objective of this project is to design a Wound Field Synchronous Machine (WFSM) with 8X power density improvement and cost below $3.3/kW.

Approach

The approach includes design and development of wound field synchronous machine, cooling system and wireless power transfer technology. The project is divided into three budget periods outlined below:

- BP 1 – Simulation to determine feasibility of achieving goal and concept design

- BP 2 – Design motor for build and prototype rotor excitation system

- BP 3 – Build and test motor relative to project goals

This report presents tasks pursued and results obtained in part of Budget Period (BP) 3. Budget period 3 includes tasks such as:

- Optimization of the electric motor, brushless excitation system and cooling system for

- automotive reliability and manufacturing

- Prototyping and integration of all the subsystems

- Testing the motor

Results

1. WFSM design, optimization and prototyping

Multiple WFSM variants were designed using a metamodeling optimization approach to achieve a power density of 50 kW/L while maximizing an overall drive cycle weighted efficiency subject to average torque, torque ripple, voltage, field ohmic loss, and stress constraints. Direct optimization of wound field synchronous machines for drive cycle efficiency is extremely computationally expensive. The computational expense of evaluating a wound field synchronous machine design is higher than a permanent magnet synchronous machine because of the variable field excitation. For this reason, a metamodeling optimization approach, which forms the metamodel from a reduced number of samples compared to a direct optimization, has been adopted. Once the metamodel is created it also allows the optimization to be rerun with different input parameters, constraints, or objectives without having to repeat the entire sampling or direct optimization. Each WFSM design during the metamodeling and optimization process has a full electromagnetic analysis and a 2D structural analysis. A representative metamodel for the maximum stress in the lamination during a 20% overspeed condition is shown in Figure I.2.8.1. Torque speed curves delivered by the designed motor at two different DC bus voltages is provided in Figure I.2.8.2.
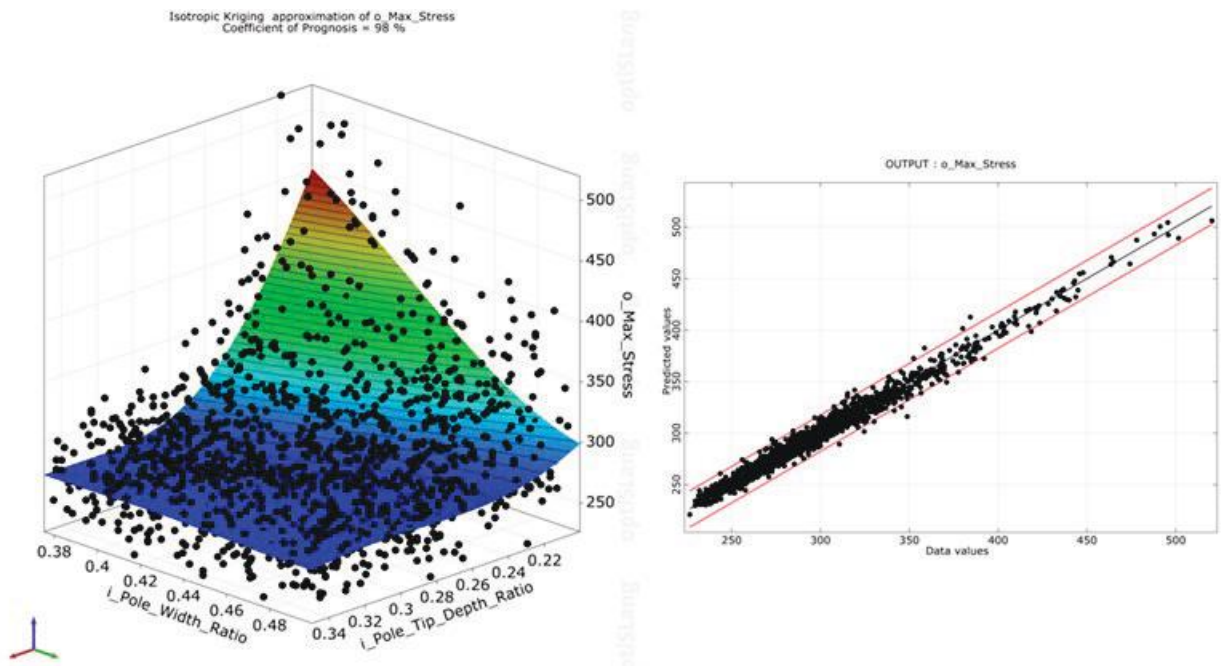
Figure I.2.8.1 Representative maximum stress in the lamination for 20% overspeed condition metamodel surface. Sampled designs are indicated by black dots for two input parameters in the figure on the left and a comparison between actual and predicted values is shown on the right.
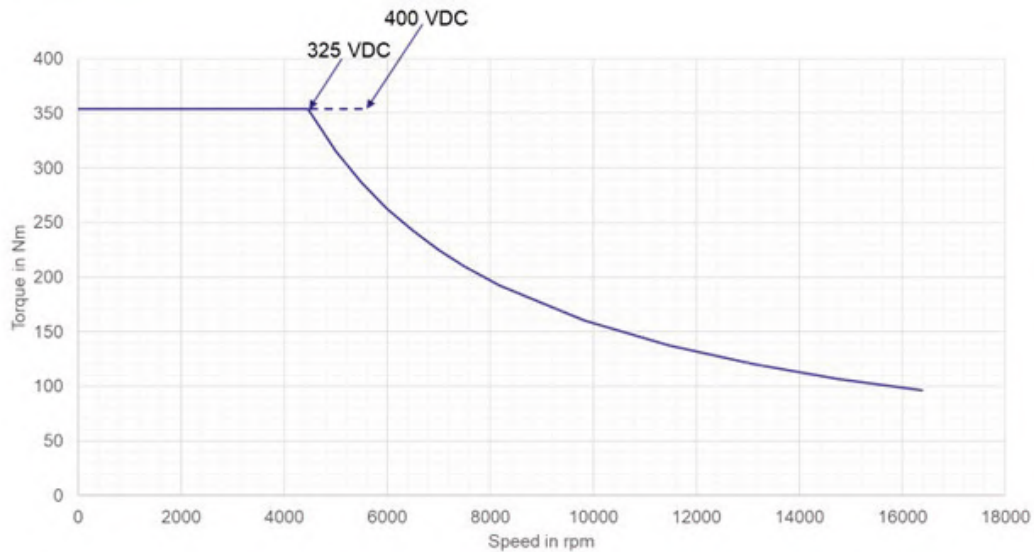
Figure I.2.8.2 Torque-speed envelope of the final prototype design

Down-selected designs for prototyping are expected to have a power density of 50 kW/L. The prototype design uses rectangular wire for the field winding. The winding layout was carried out with a particular focus paid to the design of the field winding endcaps. The design of the endcaps is critical for achieving a manufacturable winding with a high slot fill and retaining the winding at high speed. The mechanical CAD design of the housing and entire rotating assembly was also completed. The overall CAD model of the motor prototype and the rectangular wire rotor prototype are shown in Figure I.2.8.3. Prototyped shaft of the motor is shown in Figure I.2.8.4. During the prototyping stage multiple endcap designs were trialed and a custom winding process developed. Assembly of the prototype is well underway.
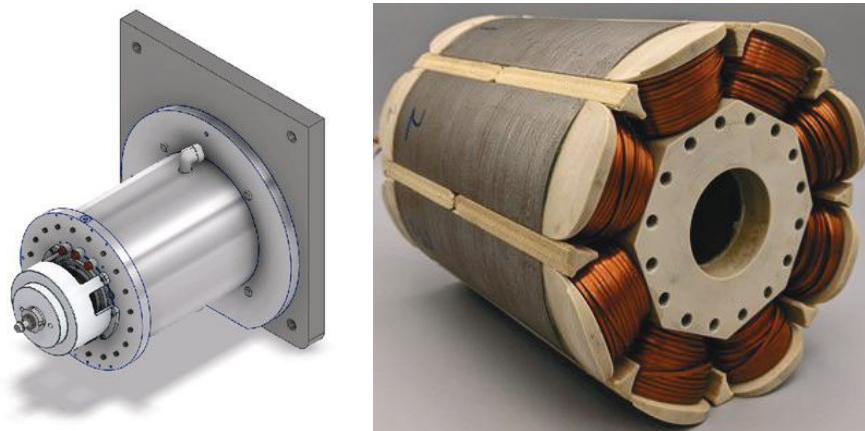
Figure I.2.8.3 WFSM CAD model including resolver and excitation system (left) and Prototype WFSM rotor with rectangular wire.

Figure I.2.8.4 Designed and prototyped shaft of the motor

2. Stator and Rotor Cooling

Oil jet cooling for the rotor was chosen as the preferred cooling solution after investigation of various cooling strategies. Factors such as cost, manufacturing simplicity and feasibility, coolant flow rate, pressure drop, type of gearbox, package dimensions, minimum coolant temperature, pump specifications, etc. were considered during the design optimization. Rotor temperature under the target of 180 deg C was achieved keeping class H insulation copper wires, maximum flow rate of 10L/min and minimum coolant temperature of 75 degC. Different nozzle shapes were investigated, and optimal nozzle diameter was chosen based jet velocity and pressure drop. The nozzles were designed to be placed on the end plates so that axial jet impingement could be carried out. The jets impinge on both sides of the rotor. Endplates were designed to carry the oil from the inlet pipe. Air valves were also investigated and optimally designed and placed on the package of motor. Moving mesh versus moving reference frame simulations were also carried out to understand the difference in results. Although, moving mesh simulation is computationally expensive, it provides lower temperatures. Oil outlet design at the base of the motor was also optimized considering reverse flow and heat transfer.
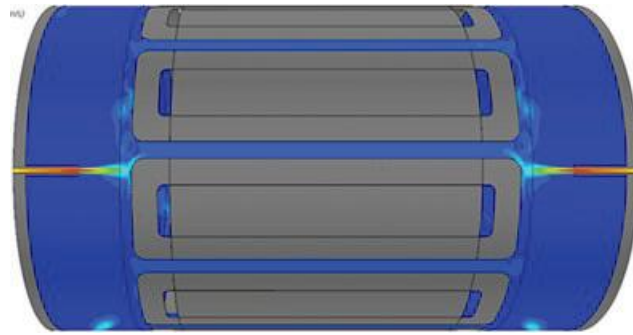
Figure I.2.8.5 Picture from CFD analysis that shows the oil jet impinging on the rotor
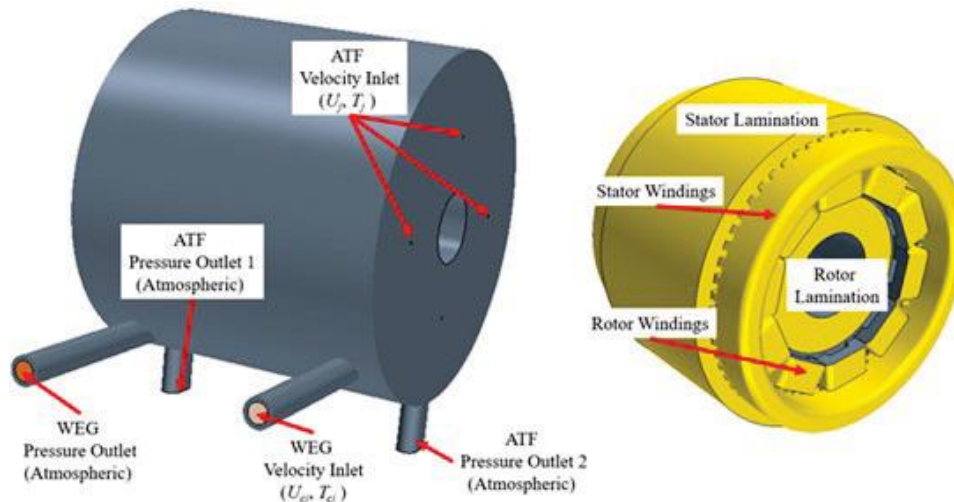
Figure I.2.8.6 Pictures showing various CAD parts of the motor, coolant inlets and outlets

After several design optimizations, a spiral jacket design was selected to cool the stator of the machine. 50/50 WEG is used to cool the stator. Factors such as coolant temperature, heat transfer, temperature rise, flow rate, pressure drop and manufacturing feasibility were considered in making the decision. Average stator temperature was maintained below 120 deg C with a minimum coolant temperature of 75 degC and maximum flow rate of 10L/min. External oil-WEG heat exchanger and pump will be used during testing. Currently the parts are being built and will be assembled for testing as a unit in 2023.
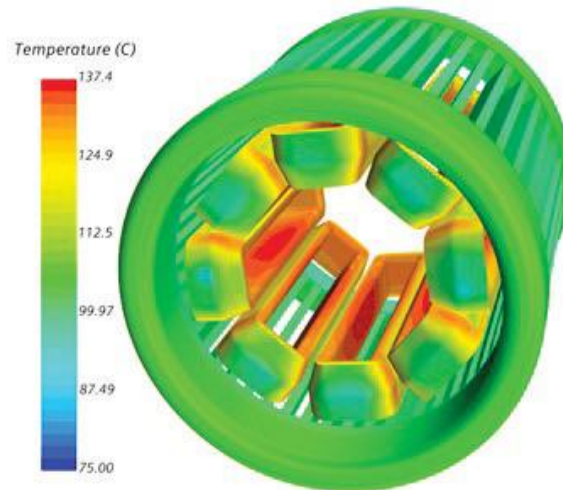
Figure I.2.8.7 The figure above shows sample result from CFD simulations on the stator and rotor. Maximum temperatures could be kept under 180 degC.

3. Design of a Brushless Excitation System design, optimization, and prototyping

The following are the highlights of the past year's efforts in brushless excitation system. An axial pot core geometry was chosen for the rotary transformer core. These cores are readily available from multiple sources, making them a good candidate for commercialization. The core dimensions were parameterized, then swept and evaluated both analytically and with finite element analysis to determine the optimal size and number of turns. Ultimately a brushless excitation system was designed to provided > 7kW of power transfer to the rotor.
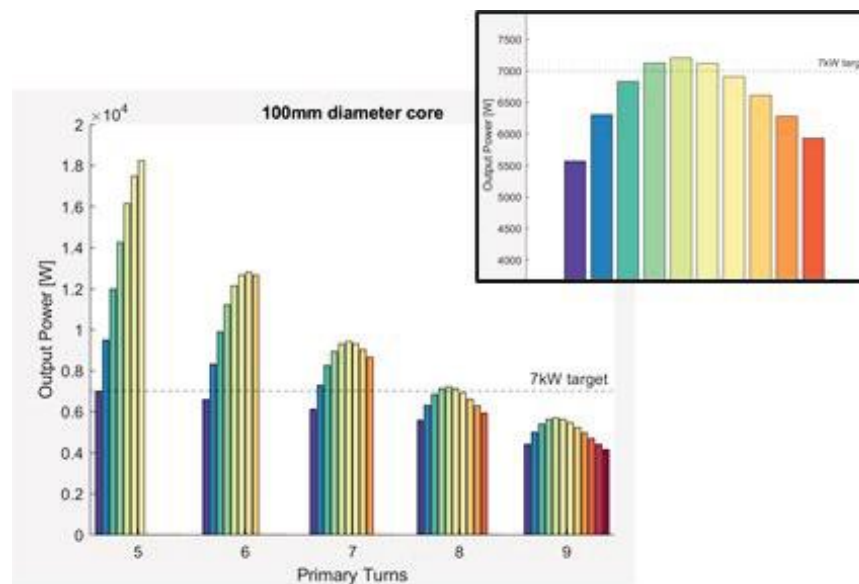
Figure I.2.8.8 Maxwell simulation results of transformer cores to select number of turns for desired power level.

The selected core design was machined from ferrite blocks, pictured below. Note the two holes for the winding leads to exit the transformer core without interfering with the air gap. The coils were wound on a separate bobbin/mandrel and then slid off into the ferrite core and potted.
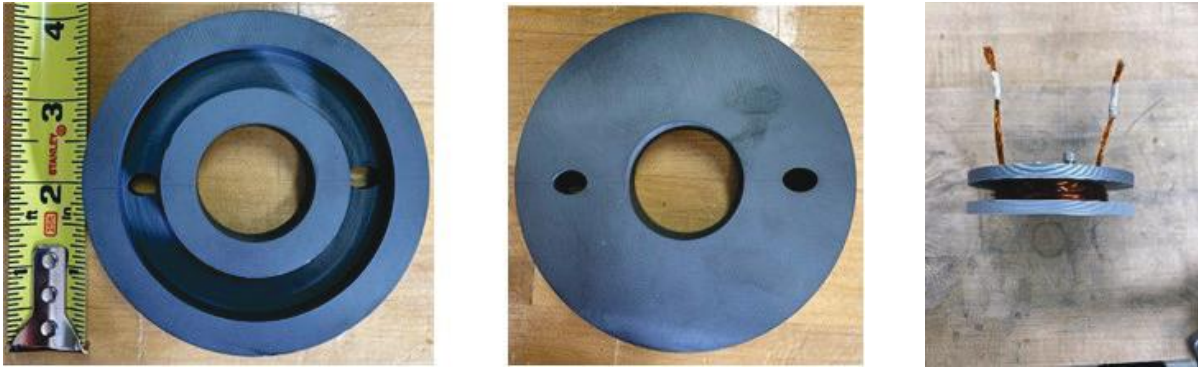
Figure I.2.8.9 Photos of IPT transformer cores and winding jig.

Since the core will rotate at high speeds, finite element analysis was conducted to ascertain the structural limits of the core at a speed of 20 krpm. Initial simulations revealed transformer core mechanical failure, ultimately leading to a carbon fiber wrapped approach, simulated below. With a carbon fiber wrap, the core has a margin of safety of 1.7 at high speeds. Next, the actual transformer assembly was carbon fiber wrapped using the pictured jig.
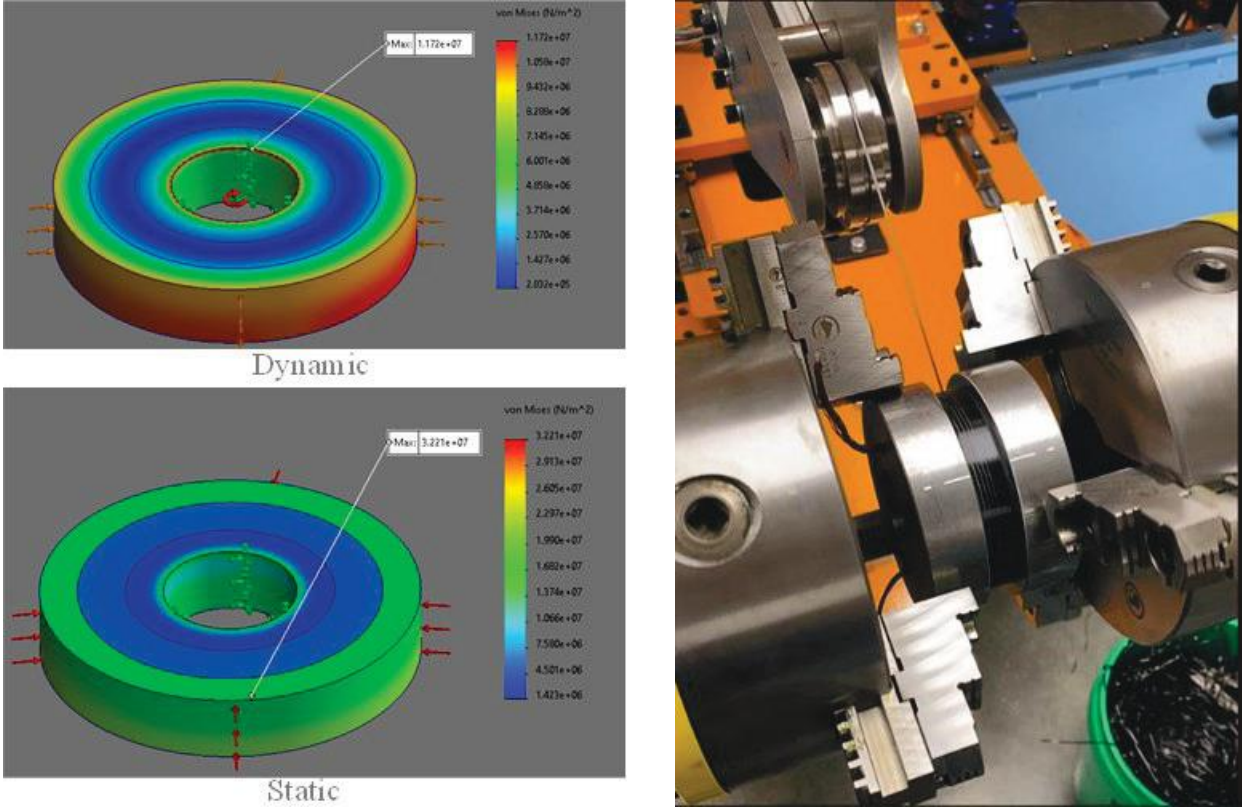
Figure I.2.8.10 Left – FEA of IPT system with a carbon fiber wrap, Right – carbon fiber wrapping of IPT transformer core.

Real-life physical components of the brushless excitation system is shown in the figure below. Immediate next steps are electrical bench testing at full power prior to installation on the wound field synchronous machine.
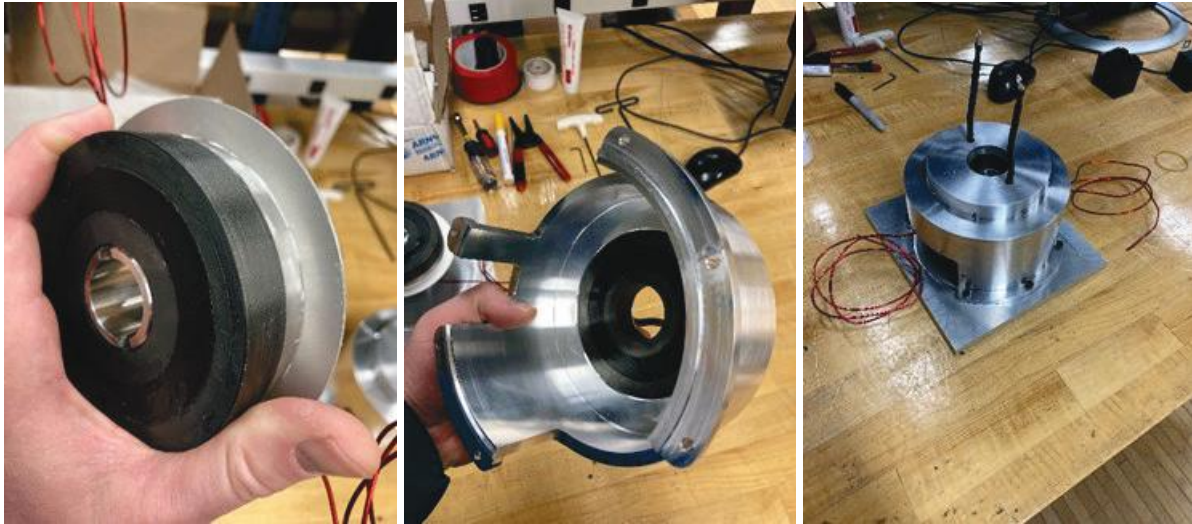
Figure I.2.8.11 Carbon fiber wrapped rotor core, stator core embedded in aluminum housing, IPT components assembled on mock motor plate.

Conclusions

Multiple wound field synchronous machines with a power density of 50 kW/L have been designed. Final down-selected design is being prototyped. Brushless power transfer system is also being prototyped. An integrated WFSM system will be tested in 2023.

II   Grid and Infrastructure

II.1   Industry Awards

II.1.1   Long-Range, Heavy-Duty Battery-Electric Vehicle with Megawatt Wireless Charging

Ryan Reed, Principal Investigator
Kenworth Truck Company
485 Houser Way N
Renton, WA 98057
E-mail: ryan.reed@paccar.com

Lee Slezak, DOE Technology Manager
U.S. Department of Energy
E-mail: lee.slezak@ee.doe.gov

Start Date: October 1, 2019	End Date: June 30, 2024	
Project Funding: $10,941,859	DOE share: $4,989,296	Non-DOE share: $5,952,563

Project Introduction

Most heavy-duty battery-electric trucks in operation today are designed for one shift per day and 100 miles or less operation, such as port drayage, due to the existing technology barriers of battery energy density and charging power capability. However, most truck operators prefer trucks that can achieve longer range without interrupting the daily delivery schedule to cover both intercity and regional hauling routes and to facilitate their dispatch efforts. For fleets where the diesel-powered trucks typically have a range of 350 to 500 miles, introducing trucks with shorter range presents a significant impact on operating cost, productivity, and schedule planning.

This project aims to demonstrate that 400 miles or more per day across two shifts can be achieved with little impact on a fleet's operations by developing a megawatt wireless charging technology that is capable of fully charging the battery pack during a driver's 30-minute required break. By applying the megawatt wireless charging technology, the daily operating range of the battery-electric truck-tractor can be extended without disrupting the delivery schedule and while keeping the required battery pack mass to a minimum.

Objectives

- Design and build a Class 8 Battery Electric Truck-Tractor with sufficient range to run from Seattle to Portland at 80,000 lbs. Gross Combination Weight.

- Design and build a wireless charging system capable of megawatt power transfer rate.

- Demonstrate the vehicle and charging system in commercial operations of at least 400 miles per day with a major shipping company.

- Collect and analyze data from commercial use over a period of up to three months, which will provide real-world feedback on how a large, electrified tractor-trailer might be used in freight operations.

Approach

During the project, Kenworth will leverage previously tested electric powertrain technology, and will design and build a Long-Range Battery-Electric Tractor (LRBET) specifically tailored for this application. Technical challenges that will be overcome during this project include mounting this quantity of battery capacity without adversely impacting the tractor's durability or vehicle dynamics, selecting appropriate battery chemistry and pack design to achieve high C-rate charging, providing adequate cooling for the batteries and power

electronics during vehicle operations and the extreme fast charging, and developing the controls code to manage the vehicle during vehicle operations and during charging.

Utah State University (USU) will leverage its core expertise in high C-rate battery charging, high power density grid-tied power electronics and wireless charging systems to design the megawatt inductive charging equipment circuitry and topology. The planned inductive wireless charging system will allow power to be transferred wirelessly between a primary (charging) pad embedded in the ground and a secondary (receiving) pad mounted on the bottom of the vehicle by using high frequency AC magnetic fields. Inductive charging is a mature and proven technology. However, it is seeing wider adoption today due to the availability of high-performance semiconductor devices, capacitors, and cables. The technology can operate in varying environmental conditions, including rain and snow, requires no operator interaction, and maximizes effective use of land with no above ground obstacles or components.
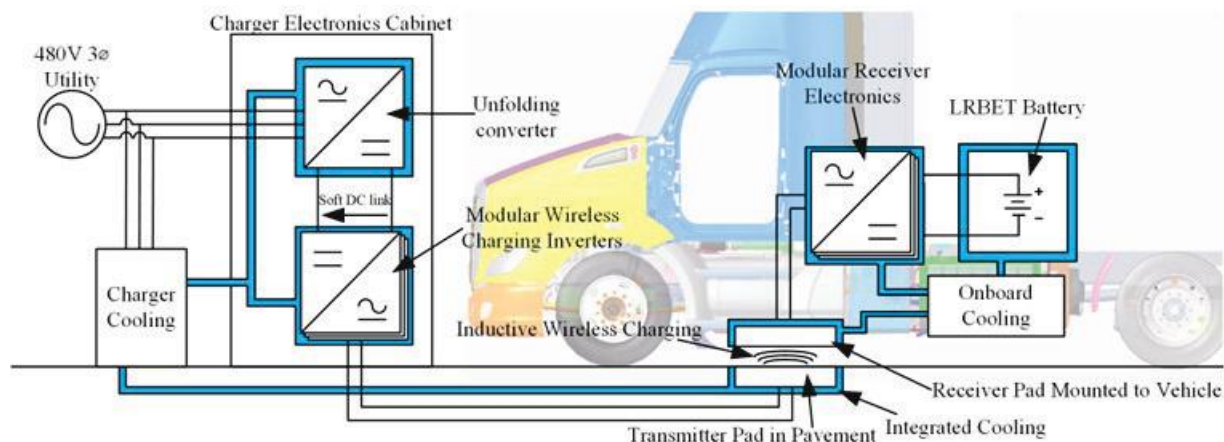
Figure II.1.1.1 System block diagram

WAVE has commercialized wireless charging systems capable of transferring up to 250 kW over an air gap of 10 inch and has obtained UL Field Certification. The maximum power that can be transferred with a wireless charging system is typically limited by the leakage magnetic fields that are generated since international standard bodies such as the International Commission on Non-Ionizing Radiation Protection (ICNIRP) regulate the maximum allowable leakage fields. USU has developed a charging pad configuration that utilizes multiple field shaping strategies as well as newly developed techniques to facilitate charging at power levels of one megawatt while maintaining leakage fields below ICNIRP regulations. USU's system has also considered other aspects of the system such as the power electronics design, thermal management, and tolerances.

Local electric utilities Seattle City Light and Portland General Electric will participate by providing installations of electrical grid connections and transformers to power the ground-based vehicle chargers at each location.

Results

A program time extension was submitted and approved with the following adjusted budget period dates:

- BP1: 10/1/2019 – 12/31/2020

- BP2: 1/1/2021 – 9/29/23

- BP3: 9/30/2023 – 6/28/2024

Directional effort towards Utility and End User Milestone 2.4 - Grid Electrical Power Supply

Portland facility drawings are complete, released by A&E firms and submitted for permit approval. Seattle facility drawings are in design review. UPS to make decision on electronics cabinet layout that is agreeable to engineering and operations. Primary concern is the impact on available space to adequately house the utility equipment, charger electronics and charge pad and allow adequate clearance for unobstructed tractor trailer operations around this equipment shown in Figure II.1.1.2 and Figure II.1.1.3.

A significant funding gap was identified for connecting power to the pad site at both facilities. UPS has pledged $140,000 to the program and has spent approximately $70,000 on site plans to date. In addition, Seattle City Light has pledged $162,000 for reimbursement after the Seattle site is up and running. Total unplanned cost of connecting power to both UPS facilities pad sites has been estimated at approximately $700k. A detailed estimate is under way which will be evaluated in mid-December.
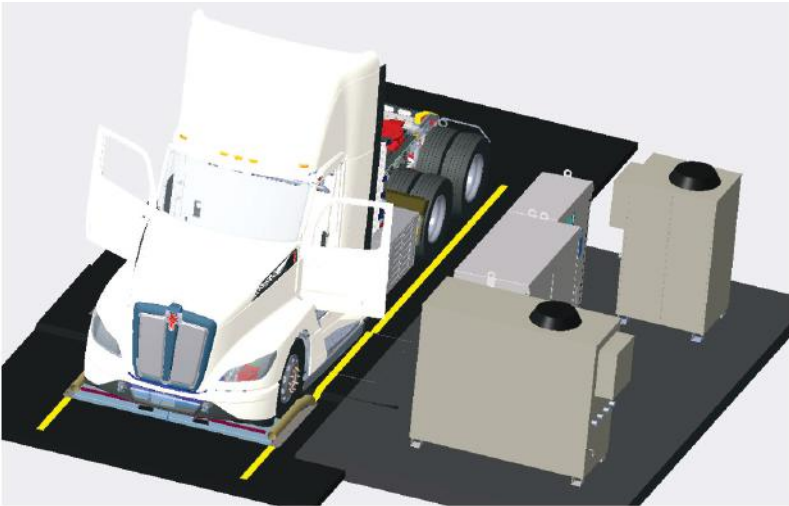
Figure II.1.1.2 Portland, Seattle facility drawings of electronics cabinet layout showing available space to adequately house the utility equipment, charger electronics and charge pad and allow adequate clearance for unobstructed tractor trailer operations around the equipment.

Figure II.1.1.3 Portland, Seattle facility drawings of electronics cabinet layout showing available space to adequately house the utility equipment, charger electronics and charge pad and allow adequate clearance for unobstructed tractor trailer operations around the equipment.

Directional effort towards Utah State University and WAVE Milestone 2.3

USU hosted UL representatives at their assembly lab with WAVE. The inspector conducted a preliminary review of the primary pad and electronics for this project. This is a necessary step and provides early critical design confirmation/direction to minimize schedule risks from the extended lead-times and market supply-chain issues.

USU hosted Kenworth and DOE representatives at their assembly lab in Utah State. They reviewed the progress and challenged faced with the development of the wireless charging system. This discussion resulted in the request submitted to the DOE for an overall project time extension for the program.

M2.3 - Key components of charging system characterized and validated

- Charge Pad

    o USU completed 500kW testing which resulted in the identification of a potting and isolation issue that required resolution before proceeding to greater power transfers.

    o The coolant plate simulations were completed and validated sufficiently cooling the charger electronics.

- Single stage AC-AC stage (Analyzed and Tested 95%):

    o Rated power test of individual T-type converter cells for a duration of 17 minutes, which validated the thermal performance of the T-type cells. Voltage map, creepage and clearance design numbers were reviewed. Further modifications will be required to comply with UL standards. Further design and testing of primary side resonant tank network components were conducted with significant volume and loss reductions. Achieved grid-to-battery efficiency of 95.1%. Validated T-type Cell operation over full operating conditions required for battery charging profile, including full range of battery voltages as shown in Figure II.1.1.4.

- Transmitter & Receiver Coils, Compensation Tanks, and Diode Bridge:

    o Rebuilt the primary transmitter coil, secondary receiver coils, and compensation tanks for the primary & secondary sides. The diode bridge and busbars have been designed and fabricated to perform final tuning for compensation tanks.

- Designs have been characterized and validated completing Milestone 2.3.

Battery profile of the Kenworth Electric Truck

Cell performance based on experimental measurements
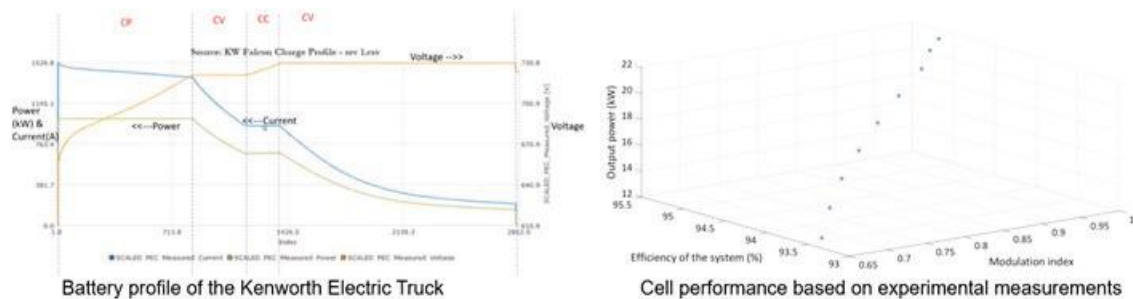
Figure II.1.1.4 (Left) Battery profile of the Kenworth Electruck Truck; (Right) Cell performance based on experimental measurements.

Directional effort towards Utah State University and WAVE Milestone 2.5

M2.5 - Demonstrate full-scale MW wireless charger in off-vehicle operation

- Cabinet designs are complete and internal equipment purchases are in process.

- 125kW module testing complete; electronics associated with building the two full systems of 125 kW modules in procurement.

- Chill plates for primary and secondary pad design are finalized. Models and partial drawings received from Wakefield on secondary chill plate.

- Primary chill plate is pending WAVE design completion and fabrication review. USU is working through design and procurement of sublevel components with long lead times. Design attempts are being made to replace devices with limited market availability and long lead times to support project partner procurement and project schedule. 3-phase Rectifiers and Unfolder modules were ordered and delivered to WAVE. UL validation tests pending.

- Critical path is procurement and approval for validation testing. Efforts continue with supply base to ensure dates do not continue to slip.

Directional effort towards Kenworth Milestone 3.1

All major components, with exception to the wireless charger assembly are received and installed on the chassis. The team has transitioned to the integration phase of the project. Individual components have completed LV testing and low power HV testing. The components are currently behaving as predicted except for the HV batteries.

HV Batteries
- The side packs and back of cab packs are assembled and installed. The supplier battery management system struggled with false current sensor BMS fault codes opening contactors at random intervals but was successfully resolved and firmware was written and uploaded.

Figure II.1.1.5 The side packs and back of cab packs.

- A final list of fault conditions was established allowing for safe fault management as reported by the BMS. The battery supplier released BMS software and made it available for testing. Chassis safe fault condition management code under development.The updated contract addendum is now under review by Kenworth and the battery supplier for final fault code management and responsibilities.

Controls
- WAVE received request from Kenworth to set up an external start/stop button away from the vehicle. USU completed simulations detailing the system is safe and a contingency plan to support a remote button will be enacted.

- Air and AC compressor contollers are now managed at the vehicle level to handle operation and purge timing direclty. HVAC controls are in process with cab heating functional based on user input. Cab AC under development with new hardware.

- The Motor transmission was commissioned for torque release and shifting. All necessary communications in place for propulsion and regeneration. First drive completed, subsequent test drives provided data for analysis and tuning. Multiple drive profiles were created to gauge driver satisfaction. Testing also exposed calibration issues in the shift tuning provided by the supplier prompting the replacement of the B0+ unit with a B2 sample.

- HVIL (High Voltage Interlock Loop) system functions are complete and verified. High Voltage will not be enabled if the HVIL system detects a fault. The Supervisory controller reports the fault and which component(s) is at fault.

- Wired DC fast Charging has been implemented and tested on multiple charge stations of different brands. Interfacing between charge controller and batteries is complete. Vehicle wake and shutdown upon initiation and completion of charging are still in process, waking the vehicle with the key is still required. Intended function is for the vehicle to wake at charger connection.

Motor-Transmission Assembly

- The B0+ was replaced with the B2 Traction Motor. Electrical connections have been verified and the HV system commissioned. The B2 Traction Motor was flashed with a slow shift L3A road release program. This temporary flash is required for road testing of other systems due to fast shift systems being delayed. All data shared with the supplier with no issues found. However, an open CAN test could not be performed due to chassis design and safety issues and is under review by supplier senior management. Resolution is expected mid-December.

Milestones

A significant responsibility transition has been implemented from USU to WAVE to minimize the program delays and clarify scope responsibility. The latest project schedule suggests the wireless charger will not be available for installation at the UPS facilities until August 2023, approximately one year behind schedule. Approval and procurement for the special equipment cabinet are critical path affecting MS#2.5 planned date.

Table II.1.1.1 Project Milestones

MS#	Milestone	Type	Date Planned	Date Achieved
2.3	Key components characterized and validated	Technical	10/31/2022	11/11/2022
2.4	Grid electrical power supply in place	Technical	9/23/2023	
2.5	Demonstrate full-scale megawatt wireless charger system in off-vehicle operation	Go-No-Go	10/25/2023	
3.1	Vehicle is Assembled and Operable	Technical	1/4/2024	

Major Accomplishments

- Completed facility and electrical drawings for Portland and Seattle UPS sites.

- Received the updated transition and deployment plan from USU/WAVE.

- Final battery BMS Release software received.

- Traction Motor installed, and communication established.

- Display screens functional for in cab data monitoring.

- First Drive of Vehicle.

- B2 00 Motor transmission assembly successfully tested at the PACCAR Technical Center.

- M2.3 achieved –BEV vehicle battery profile and T-type Cell operation verified over full operating conditions for battery charging profile. Grid-to-battery efficiency @ 95.1%.

Conclusions

At the end of FY2022, the conclusions of this program to date are:

- Fully integrated controls linking the vehicle systems and wireless charging for a road ready vehicle are extensive. Lower-level systems have competing needs which will have final arbitration by the upper-level requirements.

- Vehicle design and procurement is complete with the last remaining hardware the wireless module.

- The charge equipment designs are nearing completion. Schedule is not completely tied to the assembly processes as material shortages and lead times have become critical path.

- Facility designs and plans to the end user and utilities are a significant change to current systems. Costs can be difficult to establish without a full commitment to the process.

II.1.2   Development and Commercialization of Heavy-Duty Battery Electric Trucks Under Diverse Climate Conditions (Daimler Trucks North America LLC)

Marcus Malinosky, Principal Investigator
Daimler Trucks North America LLC
4555 N Channel Ave
Portland, OR 97217
E-mail: marcus.malinosky@daimler.com

Lee Slezak, DOE Technology Manager
U.S. Department of Energy
E-mail: lee.slezak@ee.doe.gov

Start Date: October 1, 2019   End Date: December 31, 2022
Project Funding: $3,195,00   DOE share: $1,095,000   Non-DOE share: $2,100,00

Project Introduction

Daimler Trucks North America LLC (DTNA) has developed and is in the process of demonstrating an electric Innovation Fleet eCascadia 2.0 to improve cost, reliability, and performance over DTNA's completed heavy-duty electric truck. Improving cost and performance characteristics will address immediate barriers to adoption and support growth for zero-emission truck technologies in freight applications. Range and performance factors can prevent heavy-duty fleets from adopting zero-emission technologies. Support from the Department of Energy (DOE) will allow DTNA to overcome this barrier developing and demonstrating a more fully integrated and capable, commercialized 116" day-cab electric tractor to serve freight and goods movement sectors having a daily travel profile of up to 250 miles.

Meijer and United Parcel Service (UPS) are participating as co-creation fleet partners and South Coast Air Quality Management District (SCAQMD) is providing guidance and expertise on incentives, regulations, and policies as they relate to the market potential for heavy-duty electric trucks. This project will advance state-of-the-art heavy-duty electric truck technologies to full commercialization, and in doing so, provide a platform for the market to reduce fleet operating costs, diesel consumption, and energy costs, as well as significant NOx, PM, and carbon emissions.

Objectives

The objective of the DTNA E-Mobility Group (EMG) Innovation eCascadia 2.0 project is to research, develop, and demonstrate, a fully commercialized Class 7/8 electric tractor with range and durability sufficient to meet the needs of 70% of freight movement in the United States. DTNA completed the design of the prototype eCascadia 1.0 test units in 2019, which were operated by Penske Truck Leasing and NFI Industries throughout Southern California in 2019 and 2020.

This project aims to improve performance over the baseline prototype eCascadia by increasing the range up to 250 miles, increasing the fuel efficiency of 2.0kWh/mile, increasing the battery capacity up to 550kWh, reducing the curb weight down to approximately 20,000 lbs., lighter battery packaging, and enhancing the motor design, software, telematics, weatherization, and diagnostic systems customer-designed for electric trucks.

Leveraging the significant investment, experience, and learning from eCascadia 1.0, this project will develop the next generation of this electric truck technology: the eCascadia 2.0, a commercialized electric truck product with significantly improved cost and operational performance capabilities.

Overall Technical Targets

- Develop and bring to market a fully commercialized, all-electric Class 7/8 day cab tractor.

- Increase range capabilities to 250 miles per charge and improve efficiency to achieve 2.0kWh/mile through a redesigned 500-550kWh battery back system and ultra-efficient integrated e-Axles.

- Provide a life-cycle cost-effective and zero-emission freight movement solution for more than 70% of use cases.

Approach

The project involves three (3) phases. During Phase 1a and 1b, the vehicles were developed for real world conditions expected of a Class 7/8 tractor. Vehicle designs were approved by co-creation fleet partners and the B-Sample vehicle assembly was completed during this phase. Performance tests were conducted to validate vehicle design and operational capabilities. The project is currently in Phase 2 and the C-Sample and D-Sample vehicle assembly and testing was completed. The finalized vehicles have been delivered to the fleets. Performance data and records will be continuously captured to assess vehicle performance and durability. Upon receiving certification demonstrating vehicle readiness, DTNA EMG will work with co-creation fleets to develop case study and other promotional materials.

Project Phases

- Phase 1a: Research, Design Building, and Commissioning: Vehicle Design and Specification

- Phase 1b: Research, Design Building, and Commissioning: Commercial Scale Production Model

- Phase 2: Deployment and Demonstration

DTNA EMG is leveraging global design, engineering, sourcing, and vertically integrated production capabilities to quickly achieve economies of scale and reduce product costs. Through a 'co-creation' approach with fleet partners, DTNA EMG will collect operator feedback and determine best practices for continuous improvement. To ensure a successful program, we review and track the status of the program at the end of each phase. Based on the go/no-go decision points, as shown in Table II.1.2.1, we evaluate the progress using the success criteria as shown in Table II.1.2.2. These are general success criteria that are associated with the Milestones as listed in the Milestone Log.

Technical Strategies

- Reengineer battery structure and develop proprietary design.

- Develop proprietary e-Axle integration.

- Simplify vehicle components and reduce the number of electric motors.

- Consolidate vehicle components and maximize assembly efficiency.

- Develop proprietary control software to improve overall power and enable peak performance.

- Vertically integrate design, development, and in-house production of batteries, transmission, and telematics systems.

Table II.1.2.1 Go/No-Go Milestones

Budget Period	Start/End Date	Milestone	Type	Description
1	10/1/2019-9/30/2020	B-Sample Vehicle Targets Achieved	Go/No-Go	Vehicle specifications for B-sample viable for operations of ≥250 miles per day
2	10/1/2020-09/30/2021	C-Sample Vehicle Targets Achieved	Go/No-Go	Vehicle specifications for C-sample viable for operations of ≥250 miles per day
3	10/1/2021-09/30/2022	Data Evaluation, Measurement & Verification	Technical	Record vehicle performance information including mileage, fuel-use, and cost information in collaboration with fleet partners

Results

During FY22, DTNA EMG achieved critical milestones and completed the reporting requirements in a timely manner. DTNA completed vehicle testing and conducted a final review for any bugs on the last software drop for each truck before signing off on the trucks for handoff to the customer. DTNA EMG completed financial reports for Quarter 1, Quarter 2, and Quarter 3 in 2022. DTNA EMG is keeping with bi-weekly meetings with DOE Project Officer. Data Validation Plan (DVP) of final data list to be collected/analyzed is complete. In Quarter 1 2022, DTNA hit one of the project milestones for Phase 2: Deployment and Demonstration when the Commercial Series Production began in January 2022. In Q2 2022 DTNA completed the Annual Merit Review Presentation. During Budget Period 3, DTNA achieved a critical milestone in Phase 2 by delivering the first vehicle to a customer. The Meijer infrastructure is ready with 1 ABB Terra 184 charger located in Lansing, Michigan. UPS infrastructure's In-Charge ICE-120 charger installations are in progress, 2 chargers will be installed at the Baldwin Park, CA facility and another charger will be installed at the Compton, CA facility. The charger installations are paused pending the construction of the make ready infrastructure by the local IOU, Southern California Edison. DTNA is on track to begin the Data Evaluation, Measurement, & Verification tasks during Budget Period 4 2022. In Table II.1.2.2, the project milestones are outlined as well as their date of completion.

Table II.1.2.2 Project Milestones

PHASE	DESCRIPTION	STATUS/COMPLETION DATE*
Phase 1a Research, Design, Building and Commissioning: Vehicle Design and Specification (Budget Period 1)	100% Finalization of Component Specifications	COMPLETE (July 2019)
	Feasibility Analysis of Series Development Confirmed (Go/No-Go)	COMPLETE (April 2020)
	Project Implementation Specifications Confirmed	COMPLETE (April 2020)
	Supplier Pre-Selection Confirmed	COMPLETE (June 2020)
	B-Sample Vehicle Specification Targets Achieved (Go/No-Go)	COMPLETE (September 2020)
Phase 1b Research, Design, Building and Commissioning: Commercial Scale Production Model (Budget Period 2)	Target Vehicle Metrics Achieved	COMPLETE (November 2020)
	Final Assembly of Test Vehicles Complete (C-sample)	COMPLETE June 2021
	Finalization of Data List to be Collected and Analyzed (DVP)	COMPLETE June 2021
	Finalization of Design Elements	COMPLETE June 2021
	C-Sample Vehicle Specifications Will Achieve Range Targets (range target 250miles/day)	COMPLETE September 2021
Phase 2 Deployment and Demonstration (Budget Period 3)	Start of Production Tests/ 100% of Parts are Customer Ready	COMPLETE November 2021
	Start of Commercial Series Production	COMPLETE January 2022
	Vehicle Delivery and Demonstration Initiation	COMPLETE June 2022
	Data Evaluation, Measurement and Verification	In Progress December 2022

The following tests were conducted prior to vehicle delivery so DTNA could make the necessary adjustments to ensure the vehicles were ready for clients.

During Phase 1A: Research, Design, Building and Commissioning, the following technical progress was accomplished:

Defrost test (B-sample Design)

- Thermal system passed defrost test for cold weather

- Defrosted windshield quicker than baseline diesel vehicle

- Meets FMVSS 103 requirements

- System (PTCs) bring air to temperature a lot quicker than a diesel (waiting for engine to heat up before blowing hot air).

Testing at Proving Grounds (B-sample Design)

- Testing Daimler High Dessert Proving Grounds (Madras, OR)

- Road load data acquisition for shaker tests and simulation

- Data collected can be used for shaker and accelerated testing to ensure vehicle and components meet B10 lifetime.

During Phase 1b: Commercial Scale Production Model, the following technical progress was accomplished:

Front Box Shaker (C-sample Design)

- Completed B10 lifetime – 10 years of service mileage

- Minor structural failures (brackets breaking at welds, incorrect torque, increase bolt size)

- Components sent back to suppliers for evaluation

- Changes being implemented for C-sample durability.

Battery Shaker (C-sample Design)

- In process – expected to complete 10 years of service mileage in 6 weeks

- Buck of battery and frame rail installation for component shaker

- Accelerated testing of higher risk components using RLDA inputs

- This amount of weight (batteries) has not been supported by our frame rails before.

Daily Software Testing (C-sample)

- Daily testing on-going with C-sample trucks

- 'Bugs' being identified and resolved for future software builds

- Global team works in unison to remove bugs and improve software for next release,

During Phase 1a and 1b the target vehicle metrics were achieved as well as the go/no-go milestones. The C-Sample and B-Sample vehicles achieved the range target of 250 miles/day.

During Phase 2: Deployment and Demonstration, the following technical progress was accomplished:

Winter Test (C-Sample Design)

- 750,000mi is the testing goal for total mileage of vehicles

- 3 of the trucks are running a mountain route at 100mi

- 1 vehicle (4x2) are running city route at 50mi

- A 5th vehicle is in Detroit running a highway route

- These trucks are fully loaded with larger trucks running 80k and smaller trucks running 65k

- Average efficiency is 2.1kWh/mi for the entire fleet.

Crash Test (C-Sample design)

- Physical crash test conducted on real C-Sample vehicle for high voltage (HV) Shutdown calibration.

- Side impact test conducted.

- Front underrun test conducted.

- C-Sample vehicle simulation is complete,

D-Sample Design

- Vehicle designs elements finalized

- Vehicle development supplier selection and procurement in progress

- Tooling supplier selection and procurement is in progress

- Vehicle development supplier selection to continue.

Vehicle Delivery

- First series production truck has been delivered to UPS, Penske

- Beginning to collect customer data from vehicles.

DTNA will continue to collect customer data to ensure the eCascadia's longevity in heavy-duty electrical vehicle market. The DTNA EMG initiated this project at TRL 4 and has progressed to TRL 8. The project team characterized the initial technology readiness at TRL 4 because the prototype vehicle was currently on the test bench undergoing validation of high-voltage components on both the battery and e-Axle.
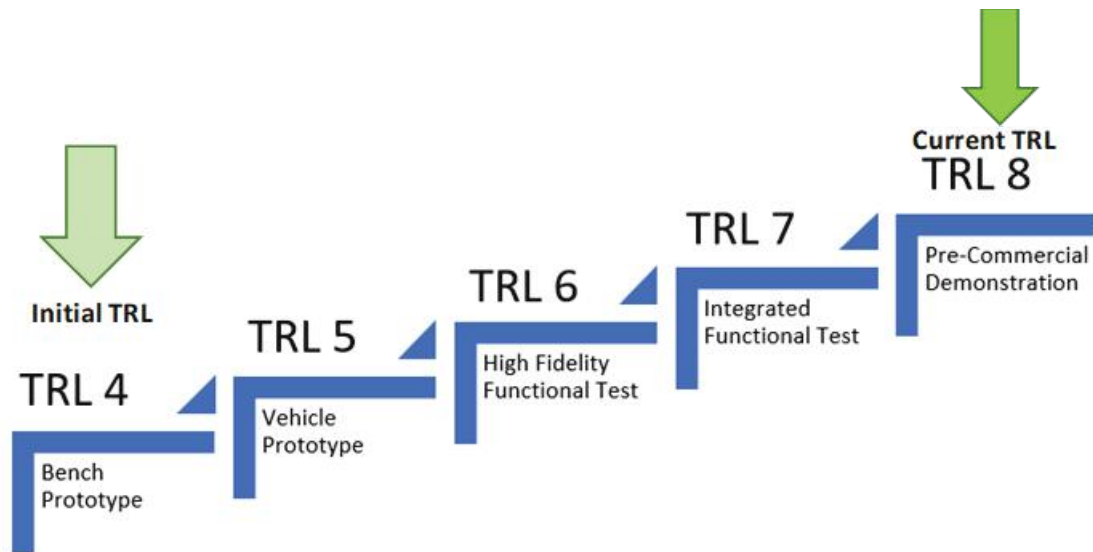
Figure II.1.2.1 Technology Readiness Level Advancement

During the project, social distancing took effect at DTNA EMG facilities which slightly delayed production of the B and C Sample builds but managed to avoid significant project delays and adhered to the project's original timeline. The COVID-19 public health crisis impacted the project team's ability to travel and meet with fleet partners, UPS and Meijer, and to access their infrastructure needs. Supply chain disruption and mandatory changes to standard vehicle assembly procedures slowed down production. To accommodate supply chain delays without revising the project schedule and timeline, compressed vehicle testing schedule was adopted. The compressed schedule led to increased wear and tear on the sample build vehicles which required additional maintenance prior to completing the tests. The vehicle testing was ultimately successful since DTNA was able to leverage its extensive resources as a leading global vehicle manufacturer to resolve supply issues and continue with modified production schedule to achieve critical project milestones.

Conclusions

The project team has completed Phase 1a: Research, Design, Building, and Commissioning and Phase 1b: Commercial Scale Production Model including production tests, commercial series production, and has finalized the design elements. The infrastructure installation and evaluations for Meijer are complete, the UPS infrastructure installation is in progress. The team made significant progress and achieved critical project milestones for Phase 2: Deployment and Demonstration, including delivering their first vehicle to their customer.

The advanced heavy-duty transportation technologies supplied by DTNA through this project have resulted in a heavy-duty vehicle platform that provides added flexibility, operational performance, efficiency, and maintenance cost savings to the end user. The all-electric Class 7/8 day cab tractor increased range capabilities to 250 miles/day and improved efficiency to achieve 2.0kWh/mile through a redesigned 500-550kWh battery back system and ultra-efficient integrated e-axles. For more than 70% of use cases, these all-electric cabs provide a life cycle and cost-effective zero-emission freight movement solution. The new eCascadia improves on the original design with innovative streamlined vehicle components, impressive range and efficiency, and completely redesigned electric drive train. Specific vehicle components innovations include reduced truck (battery) weight and thus increased payload, reduced wheelbase, increased battery capacity, decreased voltage, increased efficiency, strategic motor and battery placements, improved thermal efficiency and upgraded telematics and diagnostics. The larger outcome is an acceleration of the market transformation away from petroleum-based fuels. DTNA's comprehensive sales team, dealer network, customer network, and maintenance and support teams will ensure that this is not a standalone zero-emission truck, but rather one that

can be produced, marketed, and operated at scale to realize vast greenhouse gas and criteria pollutant emissions reductions, while also bringing zero-emission vehicles closer to cost parity.

While an all-electric Class 8 truck may be beneficial at low production scale to spread awareness, progress towards market transformation requires wider adoption. DTNA is a trusted, global OEM with the capabilities to commercialize, sell, and support entire fleets of the electric Class 8 trucks. Its global customer and dealer networks will be able to see that eCascadias are a success story for fleet operators whose businesses highly dependent on their trucks. A successful DTNA deployment has the power to create increased demand for heavy duty electrics and will drive innovation across the board. Through DTNA's 'co-creation' approach with its fleet partners, DTNA will continue to collect operator feedback and best practice information for continuous improvement activities and the development of best practice case studies for other future commercial vehicle operators.

Key Publications

1. DTNA EMG and the Freightliner Electric Vehicle council announced the Freightliner eCascadia 2.0 at the 2022 ACT Expo in Long Beach, CA. The announcement highlighted the 1 million customer tested miles and upgraded driver comfort.

II.1.3 Improving the Freight Productivity of a Heavy-Duty, Battery Electric Truck by Intelligent Energy Management

Teresa Taylor, Principal Investigator
Volvo Technology of America, LLC
7900 National Service Road
Greensboro, NC 27409
Email: teresa.taylor@volvo.com

William Northrop, Principal Investigator
University of Minnesota
200 Oak Street SE
Minneapolis, MN 55455
Email: wnorthro@umn.edu

Lee Slezak, DOE Technology Manager
U.S. Department of Energy
E-mail: lee.slezak@ee.doe.gov

Project Introduction

Battery electric Class 8 trucks, including those from Volvo, have made significant advancements in the past five years; however, high battery cost and vehicle weight restricts their ability to match the range and productivity of conventional diesel trucks. Although an electric tractor can be equipped with a larger battery to last for a large portion of a 250-mile daily route, vehicle cost increases non-linearly with increased battery energy and must be sized to last 8 to 10 years to provide a proper return on investment. Therefore, on-route fast charging is necessary to balance economics, functionality, and longevity. The objective of this project is to use vehicle and operations data to increase the vehicle range and lower the operating cost of battery electric Class 8 trucks that drive more than 250 miles per day using physics-based adaptive learning algorithms.

Objectives

The objective of the project is to use vehicle and operations data to increase the vehicle range and lower the operating cost of battery electric class 8 trucks that operate more than 250 miles per day using physics-aware machine learning algorithms. The project team will develop and implement an intelligent-Energy Management System (i-EMS) with vehicle-to-cloud (V2C) connectivity integrated with physics-aware spatial data analytics (PSDA). The i-EMS rule-based methods will use collected vehicle and operations data and calculated parameters as inputs into physics-based algorithms developed in the project to predict and reduce future energy consumption of the vehicle. The resulting i-EMS will increase the vehicle driving range and lower the operating cost of battery electric Class 8 freight movement trucks that drive ≥250 miles per day, demonstrating that Class 8 battery electric vehicles (BEVs) are capable of driving over 250 miles while carrying normal payloads and utilizing on-route opportunity charges.

Approach

Our approach is to understand our fleet partners' (HEB Companies and Murphy Logistics) baseline operations to be able to establish project duty cycles. In addition, we will combine physics-based truck model, battery information, utility demand charges and database parameters as inputs to a machine learning algorithm that will predict energy use, operational energy cost, and battery performance. The resulting i-EMS will be implemented on 2 Volvo VNR BEVs, using a low-distraction screen to display charging and routing recommendations to the operators. Charging stations will be installed at depot locations for both HEB Companies in Texas and Murphy Logistics in Minnesota, and an extra on-route charger will be installed in

Minnesota to allow the trucks to complete longer routes while operating from the Murphy Logistics depot. Finally, we will demonstrate the i-EMS in daily operations with HEB Companies in hot weather and Murphy Logistics in cold-weather conditions.

Results

The project has experienced several delays to date; supply chain bottlenecks have contributed to delays in the delivery and installation of chargers, maintenance of the first electric VNR, and the construction and repair of the second electric VNR truck. Even with these delays the team has continued to make progress on all tasks. A 6-month no-cost extension has been approved to allow the project team to sufficiently evaluate the i-EMS in hot and cold weather conditions once both electric VNRs are operating regularly with a fully integrated driver vehicle interface.

Task 2: Technology & Algorithm Development

Subtask 2.1 – Create physics-based, battery electric truck model
Develop the physics-based, battery electric truck model for use in the i-EMS.

The UMN team previously developed three separate vehicle models to help estimate vehicle energy consumption – one for each electric VNR (NME-6 with a smaller 256 kWh battery pack and NME-8 with a larger 564 kWh battery pack), and one for a physically-similar diesel-powered VNR internal combustion engine vehicle. Each model estimates the power required throughout a drive cycle based upon the vehicle velocity, acceleration, and road inclination. Vehicle parameters include the rolling resistance and drag coefficients, wheel radius and inertia, and the overall efficiency from engine or battery to wheels. Finally, the Volvo BEV models include an extra regenerative braking term with an associated efficiency parameter. The engine power is discounted for parasitic losses, and the battery power is a function of the current, internal resistance, and open-circuit voltage. The equations for the BEV model power computations are written below.

$$P_d\left(v, a, \theta, m\right) = P_{accel} + P_{ascent} + P_{drag} + P_{rr} + P_{inertia} + P_{regen} + P_{aux} = P_{bat}\eta_{bat-to-wheels}$$

The mass of the vehicle may vary over the course of a trip, which is addressed by a mass estimation method developed in Task 2.2. Driving data from the NME-6 electric VNR was collected periodically throughout 2022, though most trips were taken in Q2 and Q3 due to repairs being required through Q1.
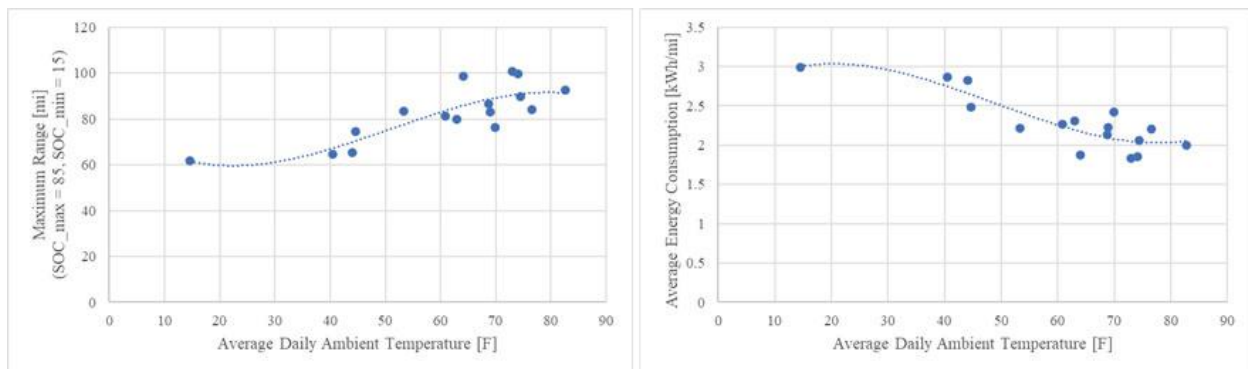
Figure II.1.3.1 Current trends for expected range (left) and average energy consumption (right)

An auxiliary power term was added to account for additional battery power used by auxiliary systems such as the HVAC and battery thermal management systems in extreme ambient conditions, and the overall trip efficiency term for the electric truck was adjusted based upon ambient conditions to capture the impact of the local weather on range. Figure II.1.3.1 and Figure II.1.3.2 show the results of progressive model tuning, accounting for temperature-related fluctuations in overall BEV efficiency and, consequently, range.
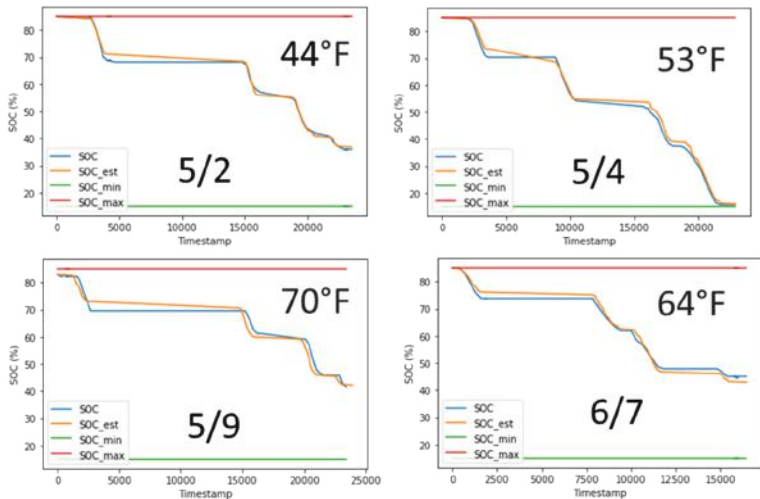
Figure II.1.3.2 Sample BEV model estimation results after tuning for temperature-related effects

Subtask 2.2 – Create initial machine learning algorithm

Combine the low-order physics model, battery information, utility demand charges and database parameters as inputs to a machine learning algorithm that will be used to predict energy use, operational energy cost, and battery performance for each duty cycle.

The project team has created machine learning algorithms to predict vehicle mass, energy use, remaining range, and the minimum charge required to complete a trip. The range and mass estimation techniques are discussed in detail in key publications [1] and [2], respectively. Formal methods of quantifying battery performance and operational energy cost have been explored as parts of Task 2.1 and Task 3.3, respectively, but machine learning algorithms have not been finalized to help solve these problems.

Subtask 2.3 – Develop energy-efficient routing and driving algorithms for use in demonstration

The project team has finished the design and development of an eco-toll physics-informed neural network (Eco-PiNN), a framework for fast and accurate eco-toll estimation (ETE) along the road network. The Eco-PiNN architecture is described by Figure II.1.3.3 and Figure II.1.3.4.
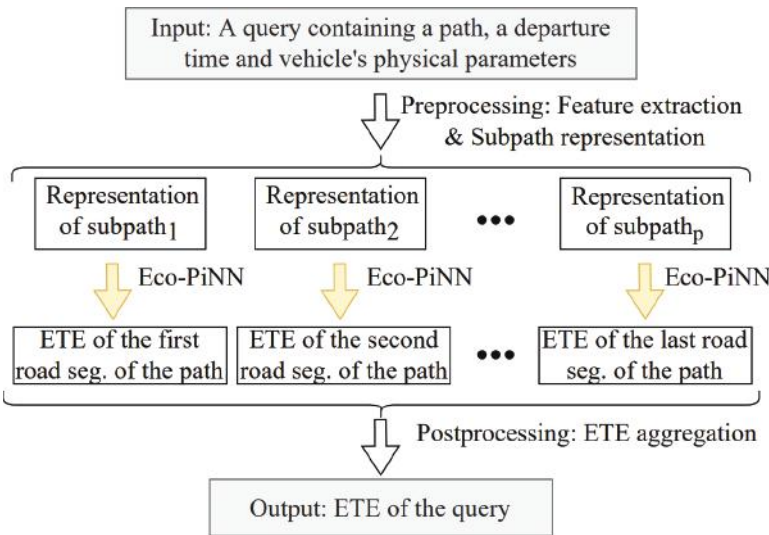
Figure II.1.3.3 Framework for energy-toll estimation (ETE) along the road network
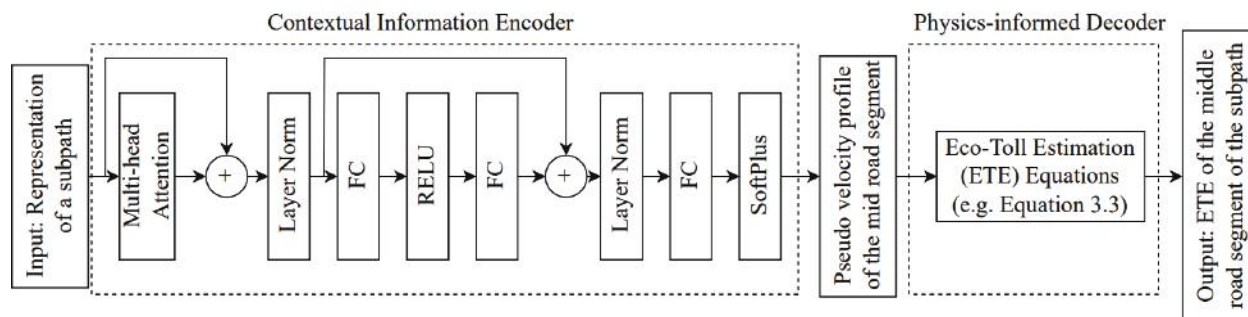
Figure II.1.3.4 Eco-PiNN architecture for analyzing subpaths

Figure II.1.3.3 shows the overall framework for finding the most energy-efficient route for a given origin-destination (OD) pair, using the Eco-PiNN to estimate the energy consumption (eco-toll) along shorter subpaths in the road network. The preprocessing step involves spatial proximity extraction to represent the similarity of different road segments and concatenating normalized numerical and embedded categorical input features that give the Eco-PiNN information about the road network (e.g., road type, endpoint types, speed limit, length, elevation change, etc.), vehicle (mass, historical OBD data if available), and query information (origin, destination, departure time). The Eco-PiNN architecture shown in Figure II.1.3.4 then makes ETEs for each road segment, which is used to find the most energy-efficient path from the origin to the destination. The Eco-PiNN architecture is also capable of using multi-task learning to estimate the travel time as well by using a second decoder dedicated to estimating travel time given the pseudo velocity profile from the encoder. This was done to compare the shortest-time path found by the Eco-PiNN framework with that from state-of-the-art methods for travel time estimation.

Table II.1.3.1 Eco-toll prediction accuracy

Mean Absolute Percentage Error (%): Mean (Standard deviation)						
Path length	1	10	20	50	100	200
Eco-PiNN	73.70 (2.37)	21.74 (1.26)	18.50 (1.36)	15.83 (1.72)	15.13 (1.68)	15.78 (1.79)
NREL	96.45 (6.31)	28.68 (3.07)	24.03 (2.92)	20.41 (3.30)	19.39 (3.65)	18.83 (3.93)
ConSTGAT	136.45 (8.04)	27.51 (1.44)	23.39 (0.90)	20.55 (0.89)	19.94 (1.74)	20.01 (2.81)

This method has been evaluated using available heavy-duty truck data collected by the Murphy fleet and outperformed two state-of-the-art methods initially developed by NREL (1) and Baidu Maps (ConSTGAT) (2) for energy and travel time estimation, respectively. The results are summarized in Table II.1.3.1 when just 5% of queries in the training and validation datasets had historical energy consumption information.

Subtask 2.4 – Define on-route charging locations for demonstration
Define on-route charging locations for demonstration. The established routes at each operator, and other information from Task 1.2 will be analyzed to determine demonstration phase charging locations. Chargers have been placed and commissioned at the Murphy and HEB depot locations in Minneapolis and San Antonio, respectively. A third charger has just been delivered to the UMN team, with plans to install the charger in Rochester, MN to serve as an on-route charging station that will make routes of greater than 250 miles to be feasible, even in winter conditions. A plan to choose test routes for final demonstration using the energy-efficient routing algorithm for Task 2.3, is being developed.

Subtask 2.5 – Determine optimal on-route charging locations for fleets

Determine optimal locations for on-route charging for the two participating fleet operators. The project team has continued to develop and refine new approaches to the charger placement problem. A framework for comparing different charger placement optimization methods was introduced in key publication [3], which used the previously suggested mixed-integer programming approach. Final results will soon be generated using all available data collected from Murphy and HEB operations.

Subtask 2.6 – Develop Driver-Vehicle Interface

A Driver-Vehicle Interface program application ("app") will be developed to send vehicle information to the team and to receive information from cloud-connected adaptive learning algorithms.

The Driver-Vehicle Interface has seen vast improvements in the past year and is nearly ready for deployment before the final testing phase. Development on the main screen is nearly complete, as the eco-routing algorithm has been fully integrated. Figure II.1.3.5 and Figure II.1.3.6 show the main screen and route-builder screen, respectively. The project team needs to finish implementing the charging screen that shows the driver how much to charge the vehicle to finish the desired route, as well as logic that uses the range prediction algorithm to make re-routing decisions regarding when to charge on-route.
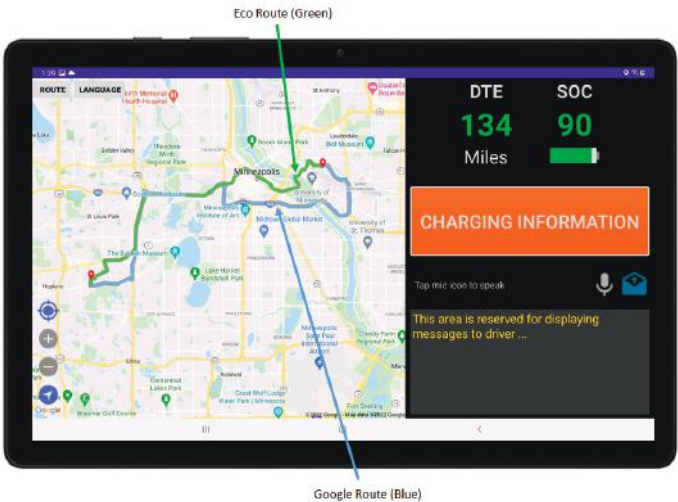
Figure II.1.3.5 Main screen showing the eco-route (green) and fastest path (blue) of a selected OD pair
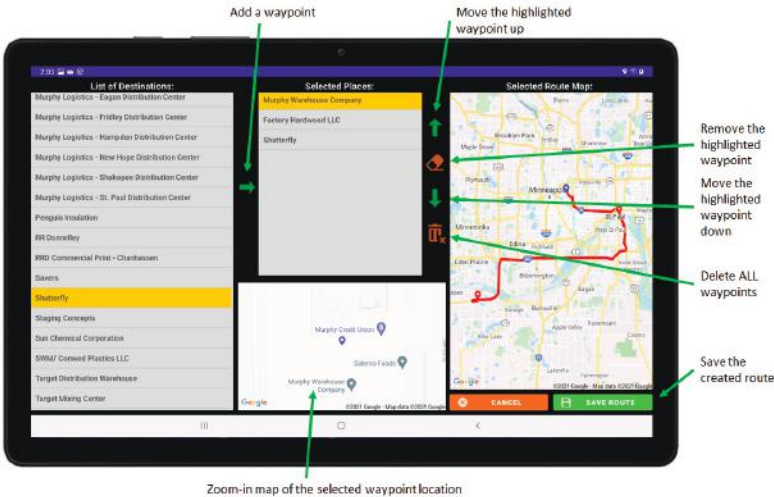
Figure II.1.3.6 The route builder screen helps users submit new routes to the eco-routing algorithm

Conclusions

The project team has made significant progress, despite numerous delays resulting from the Covid-19 pandemic. The second electric truck, NME-8, is almost ready to be delivered to Minnesota for winter testing. Final testing plans are being prepared to validate the developed models and test the eco-routing algorithm and driver-vehicle interface in operation. NME-6 is to remain in Texas through June of 2023 while NME-8 demonstrates the capability of Class 8 BEVs to travel more than 250 miles a day during normal regional haul delivery operations, even in extreme weather conditions.

Key Publications

1. Eagon, Matthew J., Daniel K. Kindem, Harish Panneer Selvam, and William F. Northrop. "Neural Network-Based Electric Vehicle Range Prediction for Smart Charging Optimization." Journal of Dynamic Systems, Measurement, and Control 144, no. 1 (January 1, 2022): 011110. https://doi.org/10.1115/1.4053306.

2. Eagon, Matthew, Setayesh Fakhimi, Adam Pernsteiner, and William F. Northrop. "Mass Detection for Heavy-Duty Vehicles Using Gaussian Belief Propagation." In 2022 IEEE Intelligent Vehicles Symposium (IV), 1655–61. Aachen, Germany: IEEE, 2022. https://doi.org/10.1109/IV51971.2022.9827370.

3. Eagon, Matthew, Setayesh Fakhimi, George Lyu, Audrey Yang, Brian Lin, and William F. Northrop. "Model-Based Framework to Optimize Charger Station Deployment for Battery Electric Vehicles." In 2022 IEEE Intelligent Vehicles Symposium (IV), 1639–48. Aachen, Germany: IEEE, 2022. https://doi.org/10.1109/IV51971.2022.9827442.

References

1. Holden, Jacob, Harrison Van Til, Eric Wood, Lei Zhu, Jeffrey Gonder, and Matthew Shirk. "Trip Energy Estimation Methodology and Model Based on Real-World Driving Data for Green-Routing Applications." Transportation Research Record: Journal of the Transportation Research Board 2672, no. 24 (December 2018): 41–48. https://doi.org/10.1177/0361198118798286.

2. Fang, Xiaomin, Jizhou Huang, Fan Wang, Lingke Zeng, Haijin Liang, and Haifeng Wang. "ConSTGAT: Contextual Spatial-Temporal Graph Attention Network for Travel Time Estimation at Baidu Maps." In Proceedings of the 26th ACM SIGKDD International Conference on Knowledge Discovery & Data Mining, 2697–2705. Virtual Event CA USA: ACM, 2020. https://doi.org/10.1145/3394486.3403320.

II.1.4 High Efficiency Powertrain for Heavy Duty Trucks using Silicon Carbide (SiC) Inverter - DE-EE0008806 (Ricardo)

Steve Peelman, Principal Investigator
Ricardo Inc.
40000 Ricardo Drive
Van Buren, MI 48111-1641
E-mail: steve.peelman@ricardo.com

Lee Slezak, DOE Technology Manager
U.S. Department of Energy
E-mail: Lee.slezak@ee.doe.gov

John J. Conley, NETL Project Manager
U.S. Department of Energy
Email: john.conley@netl.doe.gov

Start Date: October 1, 2019	End Date: June 30, 2023	
Project Funding: $7,140,067	DOE share: $4,605,398	Non-DOE share: $2,534,669

Project Introduction

The Ricardo led High Efficiency Propulsion (HEP) project will develop a high efficiency and compact 250kW continuous power SIC inverter designed to support the high continuous loads and challenging shock/vibration environment of heavy-duty trucks with an electrified axle specifically designed for high performance and efficiency in battery-electric Class 8 trucks used in medium range (~250 mile) distribution. The project is split into 3 budget periods, with the first two being design and development focused and the final one is a demonstration phase.

The HEP team is comprised of Ricardo as the prime and Transpower (Meritor) and NCSU as the subs with the primary project objective of developing a 250kW SiC continuous power inverter. An electrified axle with integrated 3-speed gearbox developed by Meritor will be utilized and integrated with a variant of the TransPower efficient EV architecture, which has been successfully utilized in numerous Class 8 truck and tractor models. This combination will provide an extremely compact, lightweight, robust and easy to integrate drive system for electric Class 8 trucks. It is expected that performance of the 250kW continuous power operation on an eAxle integrated into a vehicle with actual in-field use will be verified during the demonstration period.

Objectives

Budget Period 1: Development of Controls and Design of the Inverter (A-Sample) COMPLETED

Budget Period 2: System Integration and Evaluation of the Proposed Design

Task 2.1 – B-Sample Design

Results of testing from A-sample build will be reviewed and updates to the specification, electrical and mechanical design and testing methodology will be applied as learnings to the B-sample development effort. An updated system specification will be drafted based on the outcome of the reviews with all team members.

Task 2.2 – Mechanical Design

Thermal and detailed design will be updated along with drawings. FMEA review of mechanical design to ensure improvements include design for manufacturing and assembly (DFM/A), and the lower cost solution.

Task 2.3 – Electronic Design

Updates will be made to the HW requirements spec and design will commence. Schematic design, custom component calculations, specifications and quotation, and PCB design updates will all be performed. FMEA review of electronic design to ensure improvements include design for manufacturing and assembly (DFM/A), and the lower cost solution. Manufacturing data will be generated and checked.

Task 2.4 – Software Update

Software will be updated as required to optimize the design.

Task 2.5 – Prototype Build

Electronics manufacturing will be initiated, and mechanical components procured.

Task 2.6 – Hardware Test

The various electrical and mechanical parts will be assembled and tested first for basic electrical operation, then for functional performance. Additional controls work will be performed to test system functional operation, including early vehicle control interface debugging. Functional testing will be performed until desired specification levels are reached. Simulated load cycles will be performed to test for thermal and mechanical performance.

Task 2.7 – Hardware / Software Integration & Functional Testing

Motor-inverter characterization of hardware/software testing on back-to-back dyno testing continuous operation will be performed.

Task 2.8 – System Integration Testing

Testing of SiC inverter on early drive systems as well as communication testing with the Meritor eAxle and discrete control modules will begin.

Task 2.9 – Hardware Design Documentation Update

Results of testing from B-sample build will be reviewed and updates to the specification, electrical and mechanical design and testing methodology will be applied as learnings to the final development effort. The data pack will be compiled, and production recommendations provided.

Task 2.10 – Mechanical Design

The mechanical design will be updated, and the 3D design work will be readied for prototype manufacturing quotation and review.

Task 2.11 – Production-Ready Design Validation Performance Testing Complete

Acceptance testing will be completed.

Task 2.13 – eAxle Prototype Fabrication and Testing

Prototypes will be manufactured for in-house testing and for installation into the two demonstration trucks. The axle will be installed into one of the trucks. Powertrain Control Module (PCM) software will be developed to optimize performance of the tandem eAxle system using the new 3-speed gearbox.

Task 2.14 – Drive System Component Development

Assemble the subsystems required to equip the Class 8 demonstration trucks with the upgraded EV architecture featuring the 3-speed eAxle and SiC inverter.

Budget Period 3: Demonstration Vehicle Development

Task 3.1 – Demonstration Vehicle Development

The subsystems will be integrated and assembled into the two Class 8 demonstration trucks. Two Peterbilt 579 gliders will be acquired and drive system components and all high and low voltage wiring, and integration hardware will be installed.

Task 3.2 – Demonstration

The two demonstration trucks will be entered into operational service to demonstrate the performance of the integrated drive systems in Class 8 trucks under real-world operating conditions. Remote telematics will be used to continuously gather information on the performance of the trucks.

Approach

- Year 1: Design and Prototype Testing with the aim to demonstrate >92.5% SiC inverter efficiency
  COMPLETED

- Year 2: Inverter B-Sample Development and Drive System Component Development

    o   B-sample SiC inverter design and development go/no-go decision based on inverter design validation efficiency of 98.5%

    o   Optimization of gate driver and control board design

    o   Update mechanical design

    o   Build the inverter and perform functional tests

    o   Complete inverter performance testing

    o   Commence class 8 truck assembly and integrate electric drive system

    o   Go/no-go decision based on meeting 98.5% efficiency

- Year 3: Vehicle Integration and Demonstration of 2 class 8 Trucks

    o   Complete vehicle integration

    o   Complete vehicle verification testing

    o   Place class 8 trucks (x2) into demonstration service to accumulate miles

Results

The B-Sample inverter was developed during Budget Period 2. The updated B-Sample hardware (PCB and inverter assembly) was designed and built, undergoing a thorough bring-up functional testing, power switch double pulse testing, efficiency testing, and initial dyno testing, The Go/No-Go requirement to meet 98.5% efficiency was exceeded. The testing was done under the following conditions:

- Efficiency testing of B-Sample hardware conducted under nominal voltage (VDC 650 V), with static R-L load

- Current sensing using 100 kHz LEM Ultrastab closed loop high precision fluxgate current transducer

- Coolant flow rate controlled at 11 L/min

- Efficiency data captured for 10 kW to 250 kW

- Measured efficiency showed improvement over A-Sample design and met the target requirement at 98.5% efficiency

A summary highlighting completed B-Sample (Budget Period 2) activities follows:

PCBA Board Build and Test

PCB hardware construction was completed and EOL testing performed on the Gate driver, control and discharge boards shown in Figure II.1.4.1

Figure II.1.4.1 Control Board, Discharge Board and Gate Driver Board PCBA

Inverter Hardware Built and Functional Test

The inverter assembly hardware was built and went through the bring-up functional testing, power switch double pulse testing, the efficiency testing and dyno testing. Figure II.1.4.2 provides an isometric view of the design.
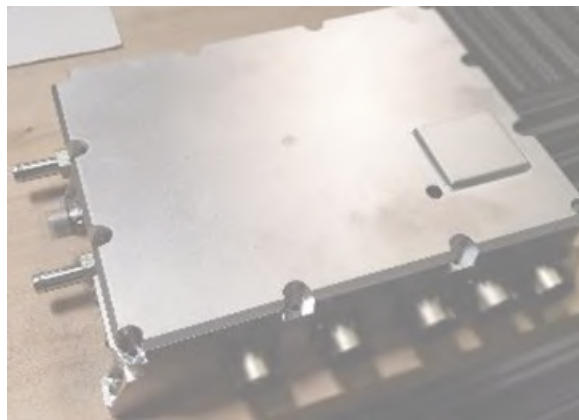
Figure II.1.4.2 Inverter Assembly

Software Development

Base software developed for the Aurix MCU with the application software adapted to the AUTOSAR architecture framework. The software was developed to allow functional and performance testing for the B-Sample inverter bring up, inverter efficiency testing and dyno tasks.

Inverter Testing

The inverter test execution was carried out at NCSU and Meritor facilities, as well as an external dyno lab. Following tests were conducted:

1. PCB and Inverter assembly End Of Line (EOL) and bring up tests (at Ricardo Carlsbad Lab, NCSU & Meritor)

2. Inverter functional tests (at NCSU)

3. Power switch double pulse test (at NCSU)

4. Inverter efficiency tests (at NCSU)

5. Inverter mechanical tests (at Trialon external test lab)

6. Motor characterization tests (at UTAC external dyno lab)

7. Inverter/Motor integration no load test (at Meritor)

8. Inverter sensor calibration tests (at Ricardo labs & NCSU)

9. Inverter dyno tests (at UTAC external dyno lab)

1. All inverters built passed EOL HiPot, leak tests

Figure II.1.4.3 HiPot and Leak Tests

2. All inverters went through high voltage bring up tests
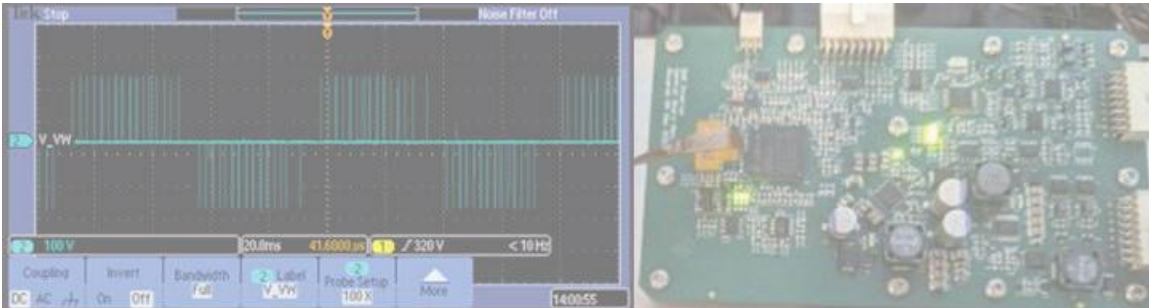
Figure II.1.4.4 HV Bring up Tests

3. Inverter Transient Double Pulse Testing Inverter

- Double-pulse test (DPT) conducted with 15 µH air core inductor under 650V, 430A condition for all 6 switches

- Overshot ranged from 103V to 153V (16% to 24%) vs observed at VDS = 600V → 912V (52% overshoot) for A-Sample inverter design→ attributed to the B-Sample revised DC/AC bus design with lower busbar inductance

- Extended DPT at 800V and 528A conducted to verify the inverter as designed capability in an overshoot of 100V (13%)
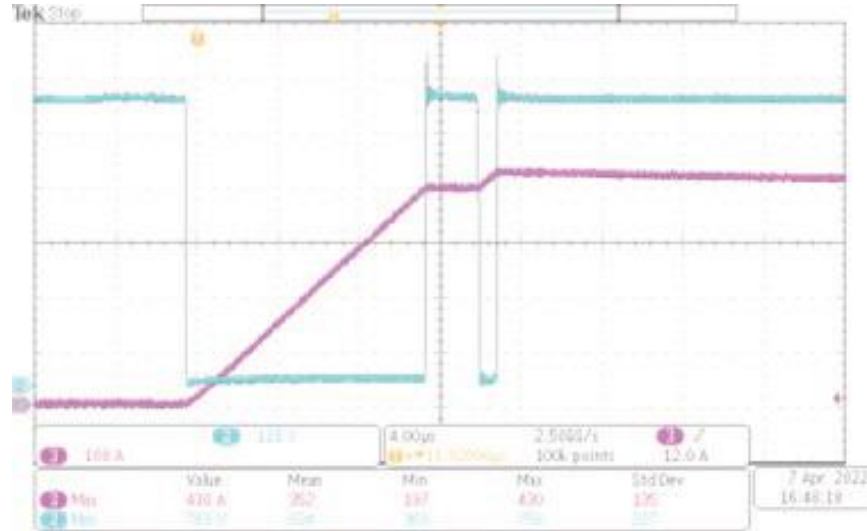
Figure II.1.4.5 DPT at 650Vdc

4. Inverter Power Performance Efficiency Test

- Power efficiency test conducted with B-Sample inverter with static (Resistive-Inductive) Load

- Maximum power reached 264 kW, 343 kVA with 600 V DC bus

- Phase current 480 Arms

- Fundamental frequency: 300 Hz

- Peak Efficiency 98.564% (@214 kW operation)
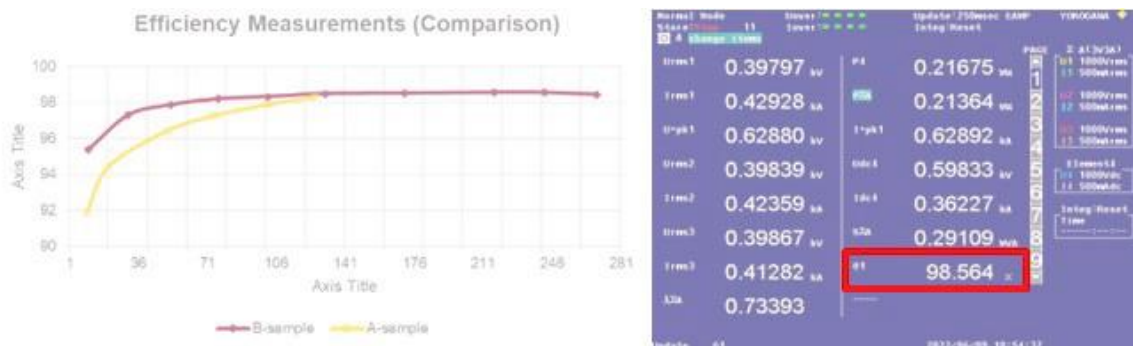
Figure II.1.4.6 Inverter Power Efficiency Test (A vs B-Sample) & Inverter Power Max Efficiency

5. *Inverter Mechanical Environmental Test*

- Completed inverter vibration test per ISO 16750 at Trialon test lab

- Completed inverter IP6x test

- No obvious damage observed at the end of each test

6. *Inverter Dyno Motor Characterization Test*

Motor parameters needed for the motor controller development work were tested in the external dyno lab at UTAC. Following test cases were successfully executed to obtain motor parameters used for the Meritor 14Xe eAxle project.

TEST ID	TEST NAME
3-MOT-01	Motor pole pairs
3-MOT-02	Determine resolver output signal format
3-MOT-03	Motor Commutation Offset Angle by DC voltage
3-MOT-04	Open Circuit Voltage (Back EMF)
3-MOT-05	Open Circuit Losses
3-MOT-06	Stator's Winding Resistance
3-MOT-07	Ld and Lq Measurement (Lock Rotor test)
3-MOT-08	Id/Iq Torque mapping

Figure II.1.4.7 Inverter Dyno Motor Characterization Test

7. *Inverter Dyno Closed Loop Controller Development and Performance Tests*

Inverter motor free spin closed loop speed controller development was conducted at Meritor Southern Cal facility with the 14Xe motor. Test data below shows the inverter motor closed loop controller testing at various commanded motor speed with the motor resolver position feedback closed loop control.
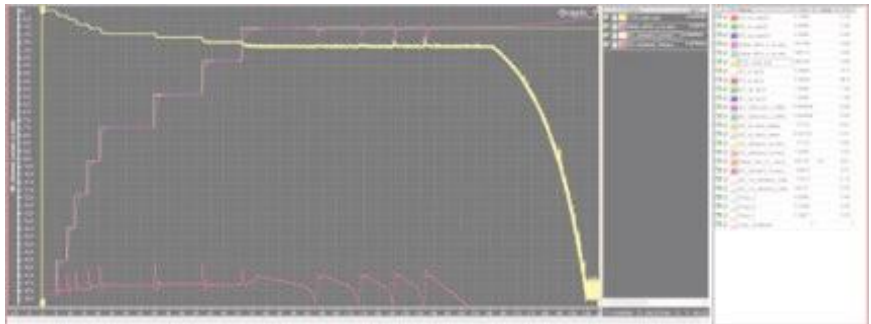
Figure II.1.4.8 Inverter Motor Closed Loop Speed Controller Development

8. *Inverter sensor calibration tests*

Following test result provides an example of the inverter sensing calibrations needed for the inverter closed loop feedback control, as well as inverter derating to ensure the inverter proper function. The inverter sensing calibrations include the current sensors, the motor resolver, the module temperature sensors, the motor temperature sensors and the HV DC calibration.
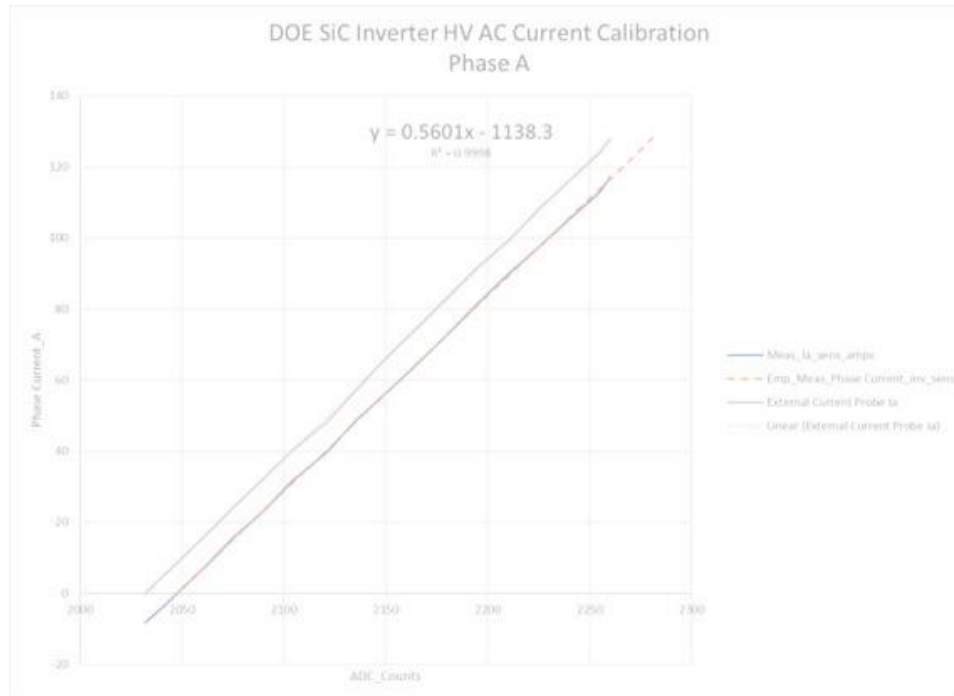
Figure II.1.4.9 Inverter Sensing Calibration (AC current sensor)

9. Inverter Dyno Tests

Inverter closed loop control and the inverter performance testing with the motor required use of a dyno. The inverter closed loop control include the torque controller (Current) tuning and the speed controller tuning, as well as the field weakening controller tuning. The torque controller was developed before the motor base speed as shown below, while field weakening controller tuning is needed for future development due to the dyno availability. Future work will also include the inverter motor speed torque tests.
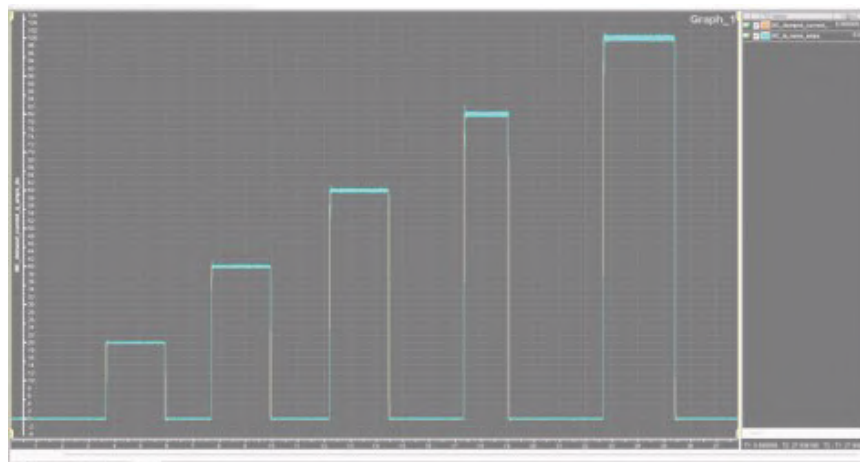
Figure II.1.4.10 Inverter Motor Dyno Torque Controller Development

NCSU Status

NCSU has continued to support inverter development by providing simulation analysis and providing testing capabilities for the B-Sample inverter development.

Meritor (TransPower) Status

Meritor has been actively progressing the BEV drive system confirmation via the ZANZEFF truck program. The two demo Class 8 Peterbilt 579 trucks integrated with BEV kits are now completed, with just the final integration activity required before vehicle commission and demo.
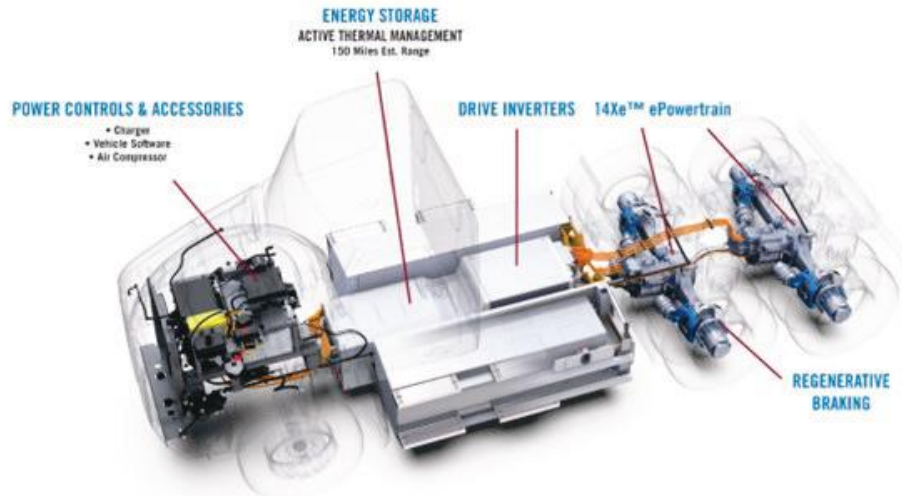
Figure II.1.4.11 Meritor Demo Truck Development

Conclusions

Overall, the B-Sample inverter development has been progressing well according to the Budget Period 2 project plan. The three project partners continue to collaborate on the inverter design, test plan development and vehicle integration.

The B-Sample inverters have been built and successfully tested on the bench through the EOL testing and functional testing, as well as mechanical environmental tests. The bench tests with RL load confirmed the inverter power efficiency of 98.5%+ efficiency. The Ricardo team commenced the inverter/motor dyno testing, with inverter closed loop speed and torque controller tuning completed. Future work is needed to complete the inverter field weakening PI controller tuning, and the inverter motor speed torque performance tests. Further software development using the AUTOSAR architecture is needed to complete the outstanding performance testing and vehicle communication.

Budget Period 3 will comprise of vehicle integration and commissioning ahead of mileage accumulation demo. Inverter control from vehicle needs to be tested and real road mileage accumulation will start thereafter.

Acknowledgements

NCSU's Dr. Iqbal Husain, Michael Kercher and Sodiq Agoro have been instrumental in supporting and progressing the inverter design. Tavin Tyler has managed all Meritor (Transpower) activities.

II.1.5 eMosaic: Electrification Mosaic Platform for Grid-Informed Smart Charging Management (ABB Inc.)

Alex Brissette, Principal Investigator
ABB E-mobility Inc.
1021 Main Campus Dr.
Raleigh, NC 27606
E-mail: alex.brissette@us.abb.com

Lee Slezak, DOE Technology Manager
U.S. Department of Energy
E-mail: lee.slezak@ee.doe.gov

Start Date: October 1, 2020   End Date: December 31, 2024
Project Funding: $7,666,953   DOE share: $4,933,028   Non-DOE share: $2,733,925

Project Introduction

Electric vehicle (EV) charging presents a new set of challenges and opportunities to a diverse group of stakeholders. Charging demand should be intelligently managed to reduce its impacts on grid operations but without sacrificing the experience of vehicle owners. Although smart technologies exist already in utility systems, charging networks, and EVs, no viable solution has been vetted to date that provides coordinated integration among them while providing benefits to and meeting the needs of all stakeholders. Most widely available solutions tend to focus on charging site control in isolation, while cloud platforms provide asset monitoring but lack control features. Preferred utilities load management approaches are "set-and-forget" policies and high-level communications and incentives for customers. The "eMosaic" project investigates technologies that enable closer coordination between grid operators and EV owners. New algorithms use prices as an incentive signal to influence EV charging behavior, while an edge+cloud architecture has been built to enable control and data exchange. The purpose of the project is to test and validate these concepts first in a lab setting, then again in a utility field demonstration.

Objectives

The goal of the eMosaic project is to enable and demonstrate the management of diverse EV site types via smart charging management functions, with a special focus on grid support functionality. Several applications have been developed: a reinforcement learning (RL) algorithm that sets real-time EV charging prices in response to grid conditions; a hierarchical, cost-saving optimization algorithm for scheduling the charging of public electric buses; a cloud-based optimization algorithm for aggregating EV charging to participate in grid services, such as demand response and frequency regulation; and a local, rules-based algorithm that controls individual charging sessions as a function of electricity price. A cybersecure communications architecture hosts the applications and enables the exchange of measurements, prices, and control commands between charging sites and back-end resources in the cloud. Supporting the effort to build these features in the lab, a major effort has been to develop real-time hardware-in-the-loop models that co-simulate EV charging and grid operation. Following the lab development, a field demonstration is planned for project partner Rocky Mountain Power's distribution system in the Salt Lake City, UT area. Ultimately, the goal is to test the feasibility of the various applications and technologies on real EV charging equipment and in a real grid operation scenario.

Approach

In the first two (of four) budget periods, laboratory setups have been created to test the performance and scalability of the eMosaic platform. Three teams have lab sites that host an eMosaic edge gateway device: the ABB E-mobility US Innovation Lab in Raleigh, NC, the Utah State University (USU) Electric Vehicle and Roadway (EVR) lab in Idaho Falls, ID, and the Idaho National Laboratory (INL) Electric Vehicle

Infrastructure Lab (EVIL) in Logan, UT. Each site is used for a different use case test. The edge devices exchange data with the cloud platform, and they also run the co-simulation of EV charging and grid operation.

After validating the applications and architecture in the labs, the second phase of the project, in the upcoming budget periods, will focus on a field demonstration with the project's utility team, Rocky Mountain Power (RMP). In this phase the project teams will apply the eMosaic solution to charging sites in the RMP territory and integrate applications into RMP's back-office systems. The field tests will be used to prove the benefit to the utility of a number of concepts: price-based regulation of EV charging, aggregated EV charging control for grid support, cloud-based control of EV charging, etc.

Results

Lab Configurations and Communications

Figure II.1.5.1 shows a high-level design of the eMosaic laboratory setup. Equipment and software have been installed in the three sites. The eMosaic cloud software is installed in the ABB lab as an on-site cloud solution. A cell modem-based wireless connection is established between this cloud and the USU and INL site equipment by establishing a secure VPN to the local site gateways and/or controller devices. Communications are also secured by applying TLS.
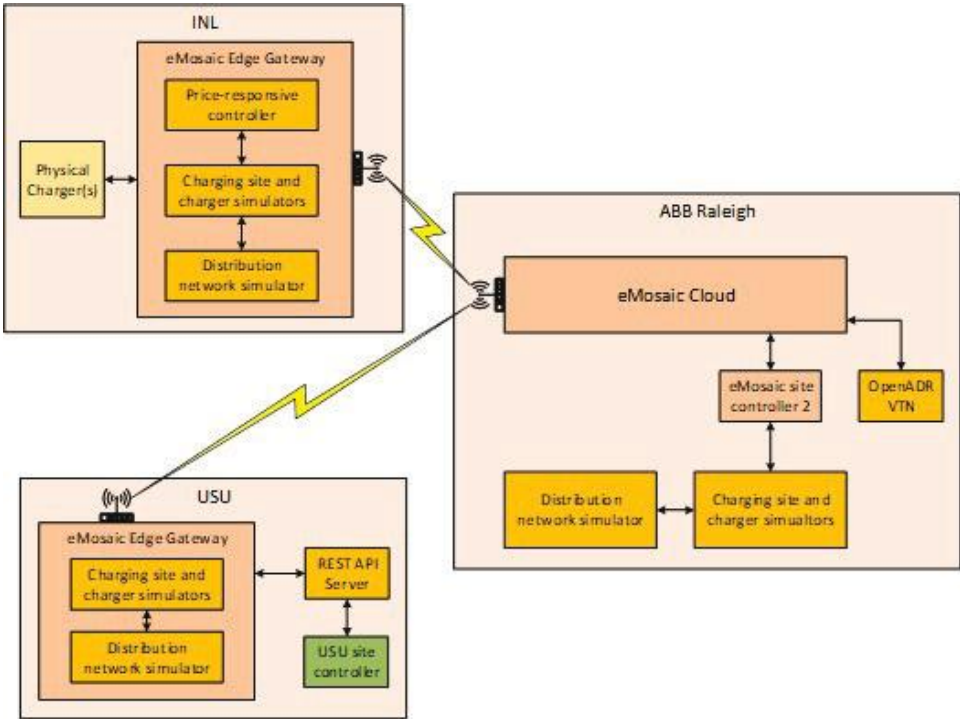
Figure II.1.5.1 Laboratory test setup

Communications Interfaces

Core Architecture

The communication architectures for each lab test were slightly different based on the needs of the demonstration case at the site. The edge platform is hosted on an industrial PC and includes a communications gateway, local resources such as charging control algorithms, communications to charging equipment, and, if necessary, an interface to 3rd party edge platforms. The cloud platform, in this phase of lab testing, is hosted on a single server PC in the ABB lab. Using Docker, the server is easily partitioned with a communication gateway and resources dedicated to each site. The containerized approach enables scalability by quickly deploying resources for multiple sites.

eMosaic Edge and Cloud Gateways

Communications between the eMosaic edge and cloud are bidirectional, but at the lab testing stage, there is a separate channel for each direction. Data sent from the cloud to the edge, including reinforcement learning (RL) price data, simulated charging sessions, and charging commands use a REST service, developed by the ABB team, hosted on the edge platform. The REST interface is intended for easier integration with 3rd party site controllers, such as the USU bus charging planner. The edge-side REST server maintains information about price, upcoming sessions, and detailed past charging sessions. The eMosaic cloud uses the interface to post this information to the REST server as it gets generated by the RL agent, and 3rd party systems can access it using an API.

Data sent from the edge to the cloud include distribution system voltage measurements and charging event updates. These payloads use the AMQP protocol, with a RabbitMQ broker hosted in the cloud platform. Each site has its own containerized RabbitMQ broker in the cloud. The broker receives data payloads from the edge and routes them to the applications (e.g. RL agent, database) that need them.

Modeling

EV Charging Models

Caldera is a tool developed by INL for simulating the power profiles of EV charging events. The tool can simulate dozens of sessions simultaneously, which is important for testing scalability of the control applications. In this project, new features have been added to Caldera that improve the tool's fidelity, scalability, communication capabilities, and co-simulation functionality. These include: dynamic insertion of new charging events during a simulation; dedicated OPC-UA servers that enable communications between simulated chargers and external systems; internal dynamic control strategies of real ABB chargers, such as first-in-first-out (FIFO) and equal share; a measurement bypass feature that allows other chargers, either real or simulated on other platforms, to be co-simulated with Caldera.

In addition to Caldera, the ABB lab uses Typhoon, a real-time hardware-in-the-loop platform, to model the electrical systems to a level of detail not available in Caldera. The Typhoon model can capture sub-cycle dynamics and other effects, while also providing the same OPC UA interface used by real chargers (and Caldera). Using the new bypass feature of Caldera, the Typhoon and Caldera models can run in parallel with the same connection to the OpenDSS grid model and to edge and cloud applications.

Grid Modeling

OpenDSS is a well-known tool for simulating distribution systems. Using the HELICS co-simulation framework [1], a closed loop is established between the grid model and the EV charging models in Caldera. For Typhoon, an OPC UA interface is used along with the Caldera bypass feature. The grid model includes externally controllable PQ loads on different nodes that receive their values from the EV charging simulations. At each time step, OpenDSS solves for the system voltages and sends them back to the EV charging simulations, which require voltage as an external input.

In its initial effort, the team used the IEEE 34 bus distribution system. Three nodes were assigned as EV charging sites using the Caldera co-simulation. The effect of heavy charging on one node was observed on adjacent as well as some remote nodes, and this complexity helped motivate the use of the RL approach. After initial development, the IEEE system was replaced by a model, provided by RMP, of the distribution system serving the area in and around downtown Salt Lake City.

Driver Behavior Modeling

One purpose of the Caldera/OpenDSS modeling is to create training and testing environments for the RL agent. The Caldera input is populated with charging event data generated from a driver behavior modeling function mapped to a 24-hour active power charging profile for each EV charging station. The 24-hour charging profile can be obtained based on past data. The driver behavior function is modeled as a function where the probability of a driver choosing to charge decreases as price increases.

To use the behavior model in the lab testing, upcoming charging sessions are generated in the eMosaic cloud, and they are posted to the edge using the REST interface. This emulates the behavior of a reservation system that allows drivers to indicate their intention to charge in the future based on the price of charging. Then, the upcoming sessions are retrieved from the REST server by Caldera/OpenDSS every 10 seconds and added to the simulation on the fly.

Preliminary Lab Demos and Outcomes

Following the initial effort to build the eMosaic platform, the team presented a live demonstration from the three lab sites. The main purposes of the demonstration were to show how the different algorithms are used in the platform and how data is exchanged between the various components. Each hosted a different demonstration use case.

INL Demo

Reinforcement Learning

The INL lab was used to demonstrate two applications interacting over the eMosaic edge+cloud infrastructure. The first, a charging price generation algorithm based on RL, is one of the key developments of the project. The purpose of the algorithm is to determine real-time electricity prices at charging stations that influence when and where EVs are charged in order to help regulate the health of the grid. The RL agent output is a multiplying factor, from 0.8 to 1.2, to the base cost of charging for each station, updated hourly. The input to the RL agent is a metric of the voltage deviation from its nominal value at each charging station, which represents the health of the grid.

The RL agent learns the relationship between prices and grid health through a simulation-based training process. To train the RL agent, hundreds of days of Caldera/OpenDSS simulations have been run. For a proof of concept, the IEEE 34 bus model has been simulated with two EV charging stations at different nodes. They are randomly assigned charging sessions over each day based on price-responsive customer behavior (see the Driver Behavior Modeling section). As the RL agent updates its prices, the simulation interacts with and responds to the RL agent, changing the charging events and the resulting grid voltage behavior. Figure II.1.5.2 shows the voltage deviation metric over 20 days on one EV charging station. The metric is an average of averages (average voltage every deviation every hour, based on voltage sampled every minute, averaged again over a day) and thus small improvements are significant. Figure II.1.5.2 shows that the average voltage deviation from the nominal 1 pu falls as the RL agent learns over 200 episodes, 400 episodes, and finally 900 episodes (i.e. simulated days). Compared to a fixed time-of-use rate, which is not grid responsive, the RL agent method gives a 10% to 20% improvement. Compared to a fixed price, the RL agent is 6% to 10% better.
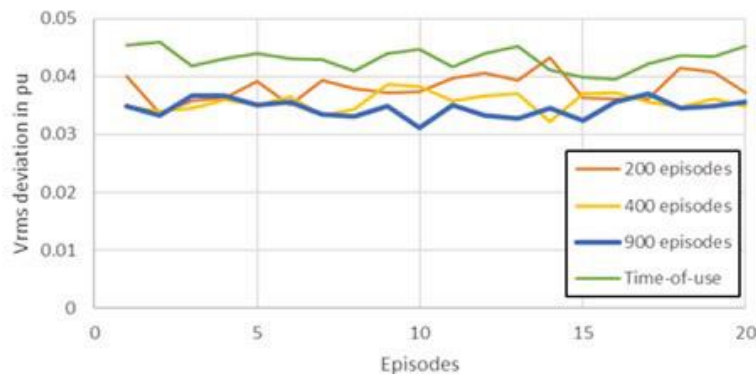
Figure II.1.5.2 Performance of RL agents using different training durations

Price-Responsive Controller

An algorithm was developed to handle price fluctuations sent from the RL agent. It was designed to be simple so it could be hosted directly in the eMosaic Edge platform, using site price info posted over the REST

interface. At a configured time interval, the algorithm collects operational data from the chargers and upcoming price info from the REST server to determine the power budget for each charger connector. First, the site-level power budget is determined as a piecewise linear function of the price. Next, the site level budget is evenly distributed among the chargers. Then, for each multi-outlet charger, the power budget is allocated to the outlets based on several factors: whether FIFO is used, the power limit of the EV, the power rating of the outlet, and the power budget allocated to the charger.

Demonstration

The INL EVIL facility hosts a fully controllable ABB Terra HP charger, which includes an OPC UA interface for exchanging measurements and control commands from the eMosaic edge device. In the live demonstration, varying prices were sent from the cloud to the edge, and the price-responsive control algorithm updated the charging budget according to its price-budget function. Using the OPC UA connection, the updated budgets were applied to a real charging session, and the charging power was observed to go up and down. Power measurements from the charger were received by the edge device and applied to the OpenDSS model using the Caldera bypass feature (see the EV Charging Models section), and the resulting node voltages calculated by OpenDSS were observed to be received by the eMosaic cloud gateway.

USU Demo

Bus Charging Planner

The USU team has developed a charging planner for Utah Transit Authority (UTA) electric buses. The algorithm attempts to find the least-cost bus charging plan using a two-level optimization hierarchy. The top-level planner finds the optimal charging plan for a 24-hour period based on perfect foreknowledge of the day ahead, including the station arrival and departure times for all buses, battery state of charge levels, the temporal profile of all non-bus related loads, and Rocky Mountain Power rate schedules. Figure II.1.5.3 illustrates the reduction in 15-minute average power achieved for the 24-hour planner (blue) as compared to a baseline of unplanned charging (red). Note the dramatic reduction in peak 15-minute average power during on-peak (shaded) and off-peak hours. This is responsible for significant cost reduction in real dollars. The planner achieves the reduction by simply shifting bus charging around in time and being aware of non-bus related loads and the rate schedule.
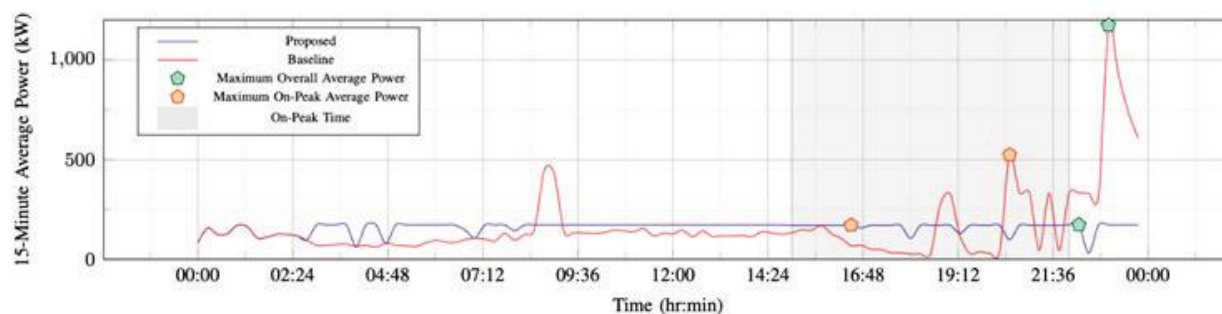
Figure II.1.5.3 Example results of the top-level bus charging planner

In addition to the top-level, 24-hour algorithm, a lower-level planner, referred to as the real-time planner, is needed to adapt to actual, unpredicted conditions observed during the day. The real-time planner looks ahead for one or two hours, leading to a much smaller optimization problem that can be solved more efficiently. It communicates with buses to get their location and SOC. It uses the same rate schedule to compute cost. Because the real-time planner only considers a small horizon into the future, it relies on the solution produced by the 24-hour planner for the desired end-state. Therefore, the objective of the real-time planner is to minimize the cost to move bus charging from its present state back to the optimal state provided by the 24-hour plan. Thus, the two-level architecture can achieve near-global optimality while adapting to unforeseen events.

Demonstration

The USU EVR lab has its own eMosaic edge device that communicates with the cloud back-end. The USU demo was similar to the INL demo, but the prices generated by the RL agent were used in the USU planner algorithm. The optimal charging schedule outputs were applied to simulated charging events in Caldera, and the resulting voltages calculated by OpenDSS were received in the cloud by the RL agent.

ABB Demo

Cloud-Based Grid Services Application

Similar to the USU Planner, a cloud-based optimal scheduler has been developed that can receive price signals from grid services markets. The optimizer runs periodically, getting updated charging event and price information to solve for new charging schedules. The cloud hosts three main components for this application: a database of charging reservations, an OpenADR virtual end node (VEN) for receiving price events, and the optimization algorithm. The database stores current and upcoming charging event data. Upcoming charging events were initially preconfigured data, but later they can come from a public-facing charging reservation tool, still to be developed. As charging events take place, the event database entries are updated with data measured at the charging equipment and sent from the edge.

The second key component of the MPC optimizer is the OpenADR VEN. OpenADR is a communication standard for automating the end user response to grid- and energy market-related events. A distribution system operator, frequency regulation market, or similar market managing entity can create an event in which the price of a grid service changes for a fixed period of time. Using OpenADR, the MPC optimizer receives the event data and updates its charging schedules to account for the fluctuation in price.

The core component of the MPC optimizer is the optimization algorithm itself. The algorithm is based on an ABB product that has a generalized framework for building optimization models. In this case, a model has been created that includes an arbitrary number of EV charging events, with electrical and financial connections to the grid and an energy services market. At regular intervals (e.g. every minute), the application gets updated vehicle data from the database and checks whether there is a new market event. Then it finds the least-cost solution of charging schedules for all the events. For in-progress events, the solution's current-time charging power command is sent to the edge gateway, which applies the command as a budget to the charger. Figure II.1.5.4 shows a five-hour frequency regulation event starting at the beginning of the 24-hour window. In the event, the market incentivizes stored energy, which would be released if activated by the four V2G-enabled vehicles in this example. The bottom plot shows the vehicle's SOC profiles resulting from the optimal charging schedules. As expected, because the vehicles are compensated for storing energy, they ramp up their SOC during the event. (They do not discharge because the actual call for reserves is not modeled.)
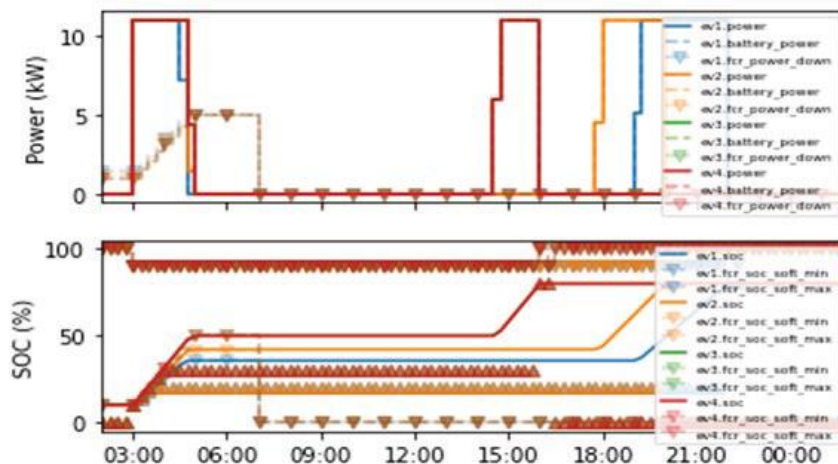
Figure II.1.5.4 Example charging schedules for four EVs with responses to a frequency regulation event

Demonstration

The main purposes of the demo in the ABB lab were to show the grid services algorithm and the Typhoon co-simulation with Caldera and OpenDSS. To create a grid services market request, a grid services market emulator was used to send OpenADR events. In the demo, the optimizer ran every 10 seconds, each time getting data from the cloud database, checking for new OpenADR events, and sending updated charging commands to the edge. On the edge side, the Caldera/OpenDSS co-simulation ran in connection with the Typhoon simulation. Both retrieved charging events from a database matching the one in the Cloud, and both used the edge gateway to send updated charging status and SOC values to the cloud. For in-progress events, the edge platform applied updated charging commands to the simulated chargers. In the demo, a new demand response event was created with its interval overlapping the current time, causing the optimizer to update the in-progress power commands, subsequently causing the simulated charging power in Typhoon to decrease.

Conclusions

As the market for EVs grows, there is a critical need to develop solutions for intelligent EV charging that supports, rather than strains, grid operations. The eMosaic project highlights the complexity of the problem and the array of technologies that need to be assembled into a complete solution: communications architectures, edge and cloud computing platforms, algorithms, standards-based interfaces, etc. At this stage, the eMosaic team has demonstrated a preliminary platform to meet these needs, validating it in a lab setting using various hardware-in-the-loop modeling tools. Based on these efforts, several price-based approaches to managing EV load show promise. In the second half of the project, the team will bring its solutions to the field, applying them to real EV charging and utility operations, with a goal to evaluate the real-world feasibility, drawbacks, and benefits of the new solutions.

References

1. B. Palmintier, D. Krishnamurthy, P. Top, S. Smith, J. Daily and J. Fuller, "Design of the HELICS high-performance transmission-distribution-communication-market co-simulation framework." *2017 Workshop on Modeling and Simulation of Cyber-Physical Energy Systems (MSCPES)*, 2017: 1-6. doi: 10.1109/MSCPES.2017.8064542.

Acknowledgements

II.1.6 Demonstration of Utility Managed Smart Charging for Multiple Benefit Streams

Stephanie Leach, Principal Investigator
BGE
110 W Fayette St
Baltimore, MD 21201
stephanie.leach@bge.com

Lee Slezak, DOE Technology Manager
U.S. Department of Energy
lee.slezak@ee.doe.gov

Start Date: October 1, 2020   End Date: December 31, 2024
Project Funding: $11,400,000   DOE share: $5,000,000   Non-DOE share: $6,400,000

Project Introduction

Exelon's mission is to be the leading diversified energy company by providing reliable, clean, affordable, and innovative energy products. Exelon believes that reliable, clean, and affordable energy is essential to a brighter, more sustainable future.

Exelon is already fully engaged with electric grid infrastructure planning processes to enable beneficial transportation electrification. Exelon's distribution utilities operating in Maryland include Potomac Electric Power (Pepco), Delmarva Power & Light Company (DPL) and Baltimore Gas and Electric (BGE) – collectively known as Exelon's Maryland Utilities. Maryland is a Zero Emission Vehicle (ZEV) state, and consequently, electric vehicle (EV) penetration is ramping up to meet the state's goal of reach 300,000 EVs on the road by 2025.

As part of their EVsmart® program that was approved in 2019, Exelon's Maryland Utilities have begun installing a network of utility-owned and operated public charging stations. This network, which will grow to 850 stations across Maryland by 2023, will complement other Exelon's Maryland Utilities' programs that provide charging equipment rebates and time-of-use rates to residential and multi-unit dwelling customers, amongst other program offerings.

Exelon understands the impact large-scale EV adoption will have on the electric transmission and distribution systems if customer charging behavior is not monitored or adjusted to avoid adding charging demand to the system during traditional peak loading times. If unchecked, EV charging load will increase the ratepayer capital investments required to ensure electric system reliability. This Smart Charge Management (SCM) project will show Exelon's commitment to the environment, beneficial electrification, and provide innovative solutions to customers by demonstrating how managed charging of EVs can provide grid relief that benefits both customers and Exelon's Maryland Utilities. This SCM project will also set the foundation for future scaleup projects throughout Exelon.

Objectives

The objective of the project is to research, design, and conduct a wide-scale demonstration of a utility Smart Charge Management (SCM) system to develop optimal managed charging structures for grid value as well as evaluate the impact of EV charging on local distribution utility operations, and the utilities' ability to control EV charging load based on grid conditions.

In collaboration with its partners, Exelon's Maryland Utilities are conducting a managed charging demonstration project where they serve roughly 2 million electric customers. The project will implement large-scale utility managed charging of electric vehicles and is expected to deliver a stack of benefit streams that will accrue to the local distribution utility, the Electric Vehicle Supply Equipment (EVSE) partner, EV owners, and

all customers. The project will enable Exelon to demonstrate multi-layer communication and coordination between the local electric distribution utilities (BGE, DPL, and Pepco), an EVSE partner (Shell Recharge Solutions, *formerly known as Greenlots*), an EV Telematics provider (WeaveGrid), a smart charge adapter provider (EVmatch), and EV owners participating in the pilot project.

The proposed project will be implemented in two phases to mitigate any inherent technical risks. In Phase One, Exelon will work with the partners to conduct tests and experiments at the Argonne National Laboratory (ANL) to inform and serve as the foundation for the large-scale demonstration. The goals in Phase One (BP1 2021 – BP2 2022) include:

- Demonstrating the integrity of the EVSE, vehicle telematics software and the communication network prior to public deployment through cybersecurity testing and validation at ANL's Smart Energy Plaza.

- Partnering with Smart Electric Power Alliance (SEPA) to conduct market research and perform industry interviews that will be used to develop managed charging program offerings for residential, fleet and public charging customers.

- Simulating the impact of EV charging on the grid in the next 10-15 years in Maryland using ANL's Agent-based Transportation Energy Analysis Model (ATEAM) tool. This will include analyzing customer charging behaviors in response to alternative EV charging incentive programs, simulating large-scale co-evolution of EV adoption, and charging deployment in the study area, and potential load impacts to the grid.

In Phase Two (BP3 2023 – BP4 2024), Exelon will carry out the large-scale Smart Charge Management (SCM) demonstration. The goals of the Phase Two demonstration include:

- Understanding EV owners' charging behavior in response to a portfolio of utility price signals and incentive structures across various customer categories to maximize future enrollment in utility-led managed charging programs.

- Simulating and evaluating the impact of EV charging on local distribution utility operations and evaluate the utilities' ability to actively control EV charging load based on grid conditions at the feeder and transformer level.

- Demonstrating the value streams from utility managed smart charging to the EV owner, the EVSE partner, and the local electric distribution utility and its customers.

- Demonstrating the ability for EV charging networks to provide frequency regulation and other electric grid services from EVs.

Approach

In Budget Period (BP) 1, Exelon's Maryland Utilities partnered with ANL, Shell Recharge Solutions and WeaveGrid to perform cybersecurity testing and validation of the electric vehicle supply equipment (EVSE), smart adapter and vehicle telematics-based software platform's ability to provide electric grid services. Exelon also partnered with SEPA to conduct market research and perform industry interviews to develop best practices and lessons learned that will guide the managed charging program design.

BP2 (2022) focused on grid impact simulation and customer engagement. ANL developed their Agent-based Transportation Energy Analysis Model (ATEAM) to begin simulating the impact of EV charging on the grid. Exelon also worked with SEPA to design innovative tactics that will maximize customer participation, flexible resource availability, and grid benefits. Exelon marketed the programs to customers and enrolled residential and commercial fleet customers into the managed charging programs. Exelon continued to install a utility-

owned charging network and purchased chargers to provide to fleet customers enrolling in the fleet managed charging program.

BP3 (2023) will consist of a wide-scale customer demonstration of managed charging across residential, commercial fleet and public charging assets. Exelon will conduct the first year of utility-managed charging program under a portfolio of tactics to test customer behavior and grid impact. Throughout BP3, Exelon will evaluate program impacts and adjust tactics to deliver more beneficial grid results and better drive customer behavior. Exelon will also work with ANL to collect results from the ATEAM model to use in the grid impact analysis.

BP4 (2024) will consist of the second year of the wide-scale customer demonstration of managed charging. Based on the results and learnings from the first year of the demonstration, Exelon will refine the design of the managed charging programs and adjust the program incentive structures to optimize the benefits for both customers and the utility. Upon the conclusion of the managed charging demonstration, Exelon and its project partners will perform analysis on customer behaviors, quantify the demonstration benefits, and produce and share a report of the project results.

Results

Task 2.1 – ATEAM tool simulation of EV charging on the grid

ANL defined the ATEAM simulation scope, analyzed the EV and EVSE data shared by Exelon and updated the input data for estimating total chargers in the study area, incorporating granular control over home-charging characteristics, and charging cost/incentives. ANL setup the ATEAM simulation environment and constructed baseline scenarios that will be used for the project. While some parts of this task have been delayed due to approvals ANL needed to obtain from Exelon IT Security, ANL is working to get back on track and will spend Q1 2023 translating smart charging scenarios into ATEAM inputs and running initial simulations of the co-evolution of charging infrastructure and EV adoption under different smart charging scenarios.
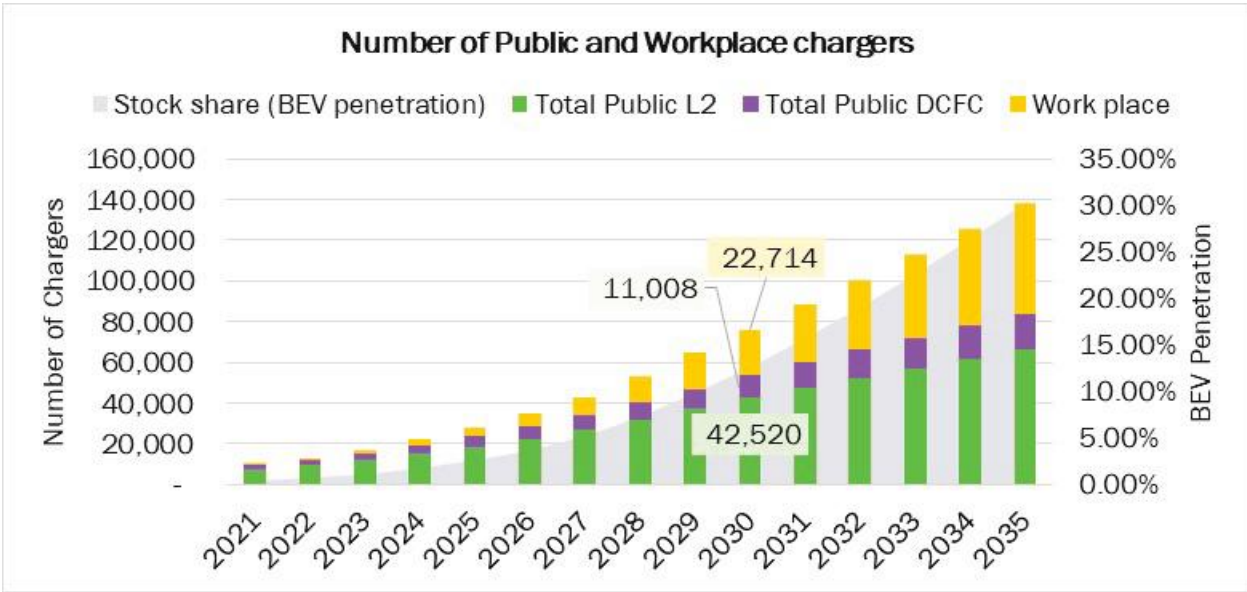
Figure II.1.6.1 Sample Results from ATEAM Study Area – Argonne National Laboratory

Task 2.2 – Customer Engagement

WeaveGrid completed an EV Detection Analysis that will help Exelon pinpoint EV drivers within Exelon's Maryland Utilities' service territory. WeaveGrid delivered EV Detection files to Exelon and presented them during weekly discussions with project leads. WeaveGrid's EV Detection Analysis identified 10,153

households likely to have an EV that Exelon can recruit to enroll in the Smart Charge Management residential program. Exelon's Maryland Utilities have added these households to their known EV driver lists. Exelon has also engaged SEPA to conduct customer research and outreach, which included customer interviews and an onboarding script upon initial engagement with commercial fleet customers. This research and outreach will help recruit and onboard commercial fleet customers and design the public charging program success metrics.

Task 2.3 – Install Utility-Owned Charging Network

Exelon's Maryland Utilities continued installing chargers at public facilities across BGE, Pepco and DPL's service territories, ensuring all counties have a fair number of chargers, including limited income communities.

Task 2.4 – Supply smart managed-charging devices to various customer profiles

Shell Recharge Solutions (SRS) continued supplying Level 2 and DC Fast Chargers to Exelon's Maryland Utilities for Exelon's public charging network, which will subsequently be used for the public program. SRS also provided hardware and software estimates to Exelon's Maryland Utilities for the Level 2 chargers that will be provided to fleet customers through the SCM program. For the Fleet program, SRS procured 200 EvoCharge L2 for Exelon's Maryland Utilities' fleet customers. Exelon has begun outreach to fleet customers and secured a list of customers to receive the initial batch of 100 chargers between Q4 2022- Q3 2023.

Task 2.5 – Enroll Customers in SCM Program

Exelon finalized the marketing recruitment materials for the residential and commercial programs and launched customer recruitment campaigns in November 2022. Additionally, WeaveGrid and the Exelon aligned on customer-facing materials that WeaveGrid will use for the Smart Charge Management program and pushed the enrollment website live in November 2022 to coincide with the completion of an Exelon IT project to automate the enrollment process for Exelon's Maryland Utilities. Exelon has completed the SCM program Terms & Conditions for both the residential and commercial programs along with the Master Service Agreement for the charging network software that commercial customers must review and sign to participate in the program. Exelon enrolled their first customers into the program in November 2022.
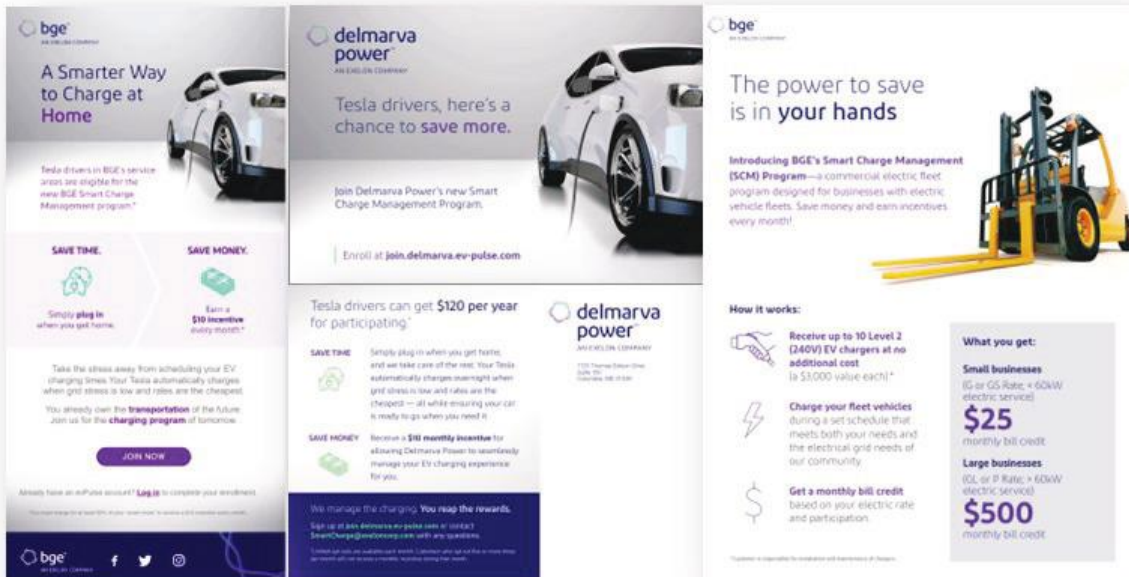
Figure II.1.6.2 Sample customer marketing collateral – Exelon Maryland Utilities

Task 2.6 – Collect data and develop system settings for economic impact analysis on the grid

ANL obtained Cyme data from Exelon's Maryland Utilities that will be used to complete the economic impact analysis. ANL compared service area of each dataset with ATEAM study area. ANL and Exelon determined the targeted study area, time and location for impact analysis and ANL is currently working on developing Cyme-OpenDSS conversion tool and model Exelon network in OpenDSS to make preparation for future impact analysis which will be completed in Q1 2023.
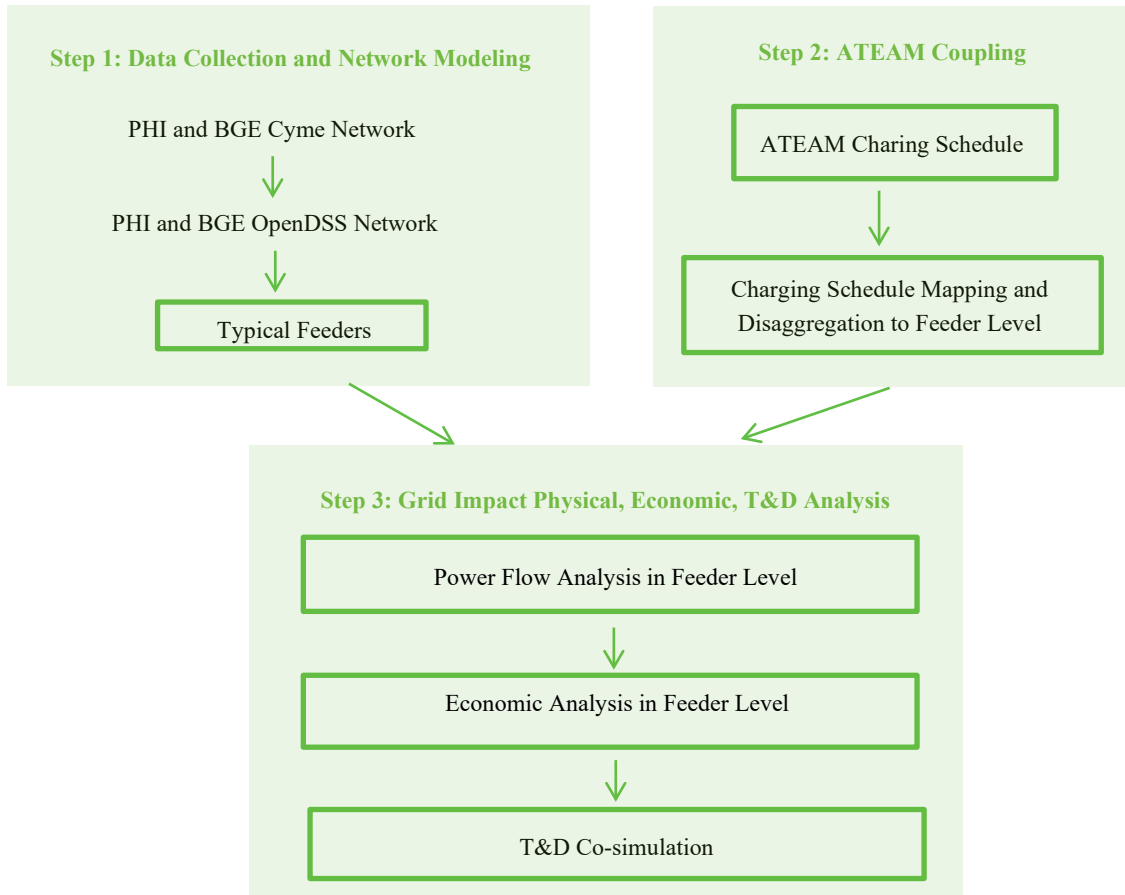
Figure II.1.6.3 Transmission & Distribution Co-Simulation – Argonne National Laboratory

Task 2.7 – Cyber vulnerability assessment across large scale distribution system with EV penetration

ANL analyzed and documented the cybersecurity challenges introduced by EV integration with particular emphasis on hardware, software, utility control system, and communications and delivered cyber vulnerability assessment report and slide deck to Exelon.

Task 2.8 – Product development to enable smart charging for Fleet and Public charging customers

Exelon and SRS completed design and development of the Smart Charing application and features for both fleet customers and Exelon-level of accesses. For the Public Program, the new demand response features and experience have been completed in preparation for the launch of demand response events on Exelon's public charging network in 2023.

Task 2.9 – Test Smart Charge Adapter

This task has been moved to Budget Period 3.

Task 2.10 – Cybersecurity Testing

The results of scanning were verified and synchronized with all vendor participants to complete their inclusion within security graphics and documentation. Triage plans were revisited and clarified to promote compliance. The finalized security report was completed, reviewed, and distributed to Exelon. WeaveGrid supported ANL in finalizing their cybersecurity report. SRS also reviewed the report and developed remediation strategies, where appropriate.

Task 2.11 – Test EVSE Platform's ability to provide Electric Grid Services

SRS implemented new functionalities such as load control by percentage, and group-based targeting per Exelon's requirements. SRS updated the test plan aligning with ANL and Exelon and received Exelon sign-off. SRS completed internal testing of the test plan. SRS received EVSE firmware version requirements from Exelon and communicated the required firmware versions to ANL. The suite of EVSE's has been revised to BTC L2, EvoCharge L2 (replacing NovaCharge L2), Tritium Veefil 50kW, BTCP HPC 200kW. Following the provided test plan from SRS, ANL completed functional testing of AC L2 EVSEs on the BTC L2 and EvoCharge L2. Compatibility issues arose in initial testing with BTC HPC 200kW, causing delays in ANL testing while BTC/SRS resolve firmware adjustments. ANL is looking to complete this testing by year-end.

Conclusions

Exelon's Maryland Utilities and its program partners are on track to launch year one of the smart charge demonstration in 2023 with all three of its target customer groups: residential, commercial fleet and public charging. The learnings that Exelon will gleam from managed charging will help the utilities as they continue to build out their EVsmart programs and other beneficial electrification offerings to customers. This pilot will also provide Exelon with the economic and grid impact research and results it needs to prepare for widescale EV adoption and plan for the any necessary grid infrastructure investments to keep up with electric demand.

Acknowledgements

II.1.7 EVs-at-RISC: A Secure and Resilient Interoperable Smart Charge Management Control System Architecture for EVs-at-Scale

Duncan Woodbury, Principal Investigator

Dream Team (renamed to Liberas)
6030 Marshalee Drive, Suite 565
Elkridge, MD 21075
Email: duncan@dtllc.io

Lee Slezak, DOE Technology Manager

U.S. Department of Energy
E-mail: lee.slezak@ee.doe.gov

Start Date: October 1, 2020   End Date: December 31, 2024
Project Funding: $7,047,628   DOE share: $4,762,949   Non-DOE share: $2,284,679

Project Introduction

Widespread deployment and grid integration of Electric Vehicles (EV), Electric Vehicle Supply Equipment (EVSE), and other Distributed Energy Resources (DER) will powerfully augment (1) today's patterns of electricity supply and demand, and (2) how utility operators interact with consumers, suppliers, service providers, and other energy market stakeholders. This growth will require widespread access to technology platforms that provide capabilities to address both (1) and (2), and these technology platforms must be scalable across millions of EV, EVSE, and DER, customer deployments, supplier accounts, and distribution areas.

EVs-at-RISC: A Secure and Resilient Interoperable Smart Charge Management Control System for EVs-at-Scale ("EVs-at-RISC") will create an open-source technology framework to address these requirements and enable future growth and extension of existing infrastructure to realize solutions for new business use cases and technology integration needs. This project will leverage existing R&D initiatives and solutions in communications interoperability and software portability at low TRL levels, and advance and combine them with additional novel research to create exemplar open-source hardware and software solutions that enable secure and resilient wide-scale supplier-managed EV Smart Charge Management (SCM).

Objectives

The primary objectives of EVs-at-RISC include: (1) reduce the cost and complexity of EV integration in the electric grid; (2) improve visibility and control at the grid edge; (3) improve interoperability between EV charging infrastructure, EVSE operators, and utility control systems; and (4) advance the adoption of interoperable open architectures for secure and resilient management and grid integration of EV charging infrastructure.

Approach

The objectives and vision of EVs-at-RISC will be realized through research, development, and demonstration of a Smart Charge Management system (SCM) that is ubiquitously interoperable with any EV and EVSE. DTLLC and our project team are developing a secure middleware framework for EV charging and distribution networks which embraces a decentralized communication architecture, and which achieves ubiquitous interoperability using scalable and extensible software-based protocol gateways positioned strategically throughout a power network. This framework leverages existing standards (IEC 61850, CIM, OCPP, and others) to standardize control patterns and interactions with EV charging infrastructure, operators, and other intermediary stakeholders, providing an powerfully simple abstraction which allows grid operators to interact with any EV and EVSE asset or intermediary stakeholder in a standardized way, and which can easily be implemented by OEMs and asset operators to shift the burden of third-party asset grid integration away from grid operators. EVs-at-RISC implements a secure design and defense-in-depth process to add layered security and Zero Trust to existing EV charging and distribution networks (where there is none currently), and to assure

that the EVs-at-RISC solution platform conforms with the security requirements of our project team and commercialization partners, and the relevant regulatory agencies.

To encourage adoption, refinement, and growth of the EVs-at-RISC technology platform, the core technologies developed in EVs-at-RISC will be released as open-source. We recognize and embrace the need to improve social equity through widespread access to security technologies, and the power of the global community to accelerate the development and widespread adoption of technology to secure critical energy infrastructure.

Results

Multi-Site SCM System Demonstration

As originally proposed, Budget Period 2 of the EVs-at-RISC program intended to produce a prototype zero-trust SCM system for EVSE and DER charge control, energy management, and grid services use cases in power distribution networks with improved capabilities for interoperability and system scalability. As of the end of FY22 (9/30/22), the project team has demonstrated a prototype SCM implementation fielded at multiple partner R&D sites using the EVs-at-RISC platform for interoperable SCM between multiple utility assets, metering assets, EVSE (conductive and inductive), and various DER including storage, PV, and conventional generator systems. These results are discussed in the subsections below.

While the project team has made significant progress during FY22, COVID-19 significantly delayed equipment sourcing, collaboration with commercial and national lab partners, and deployment of the EVs-at-RISC platform at partner field R&D sites. As the effects of COVID-19 continue to fluctuate, the project team is progressing as rapidly as possible increasing the TRL and functionality of the EVs-at-RISC platform to address a wide set of energy management use cases in real-world power distribution environments.

Multi-Site SCM System Demonstration – Topology

The EVs-at-RISC platform is intended to support wide-scale SCM of EVSE and DER in highly distributed and heterogeneous power distribution network environments comprised of traditional commercial and residential utility customers, residential and commercial prosumers, EVSE and DER aggregators, charging network operators, microgrid operators, and other relevant industry and market stakeholders. To achieve these design goals, it is critically necessary that the EVs-at-RISC platform is researched, developed, evaluated, and demonstrated across a diverse and geographically distributed set of real-world physical power distribution environments which enable Research, Development, and Demonstration (RD&D) scenarios that cannot be realistically enabled within laboratory test environments.

During FY22, the project team initiated deployment and evaluation of the EVs-at-RISC platform across five real-world test sites spanning Michigan, Maryland, and Pennsylvania. The deployment system topology is provided in Figure II.1.7.1. This multi-site deployment includes operational environments at an industrial 90MW microgrid, a distributed charging network of XFC and BESS, a university campus microgrid, a residential prosumer site, and a residential EVSE charging site, the collection of which span three power distribution utilities (DSO) and two interconnection system operators (ISO). This multi-site deployment enables RD&D of the EVs-at-RISC platform SCM implementation for a wide set of utility-centric, aggregator-centric, and ISO market-centric use cases, including and not limited to (a) interoperable SCM, (b) permissive curtailment, (c) emergency load shedding, (d) demand response, (e) disaster recovery, and (f) aggressive cybersecurity testing.
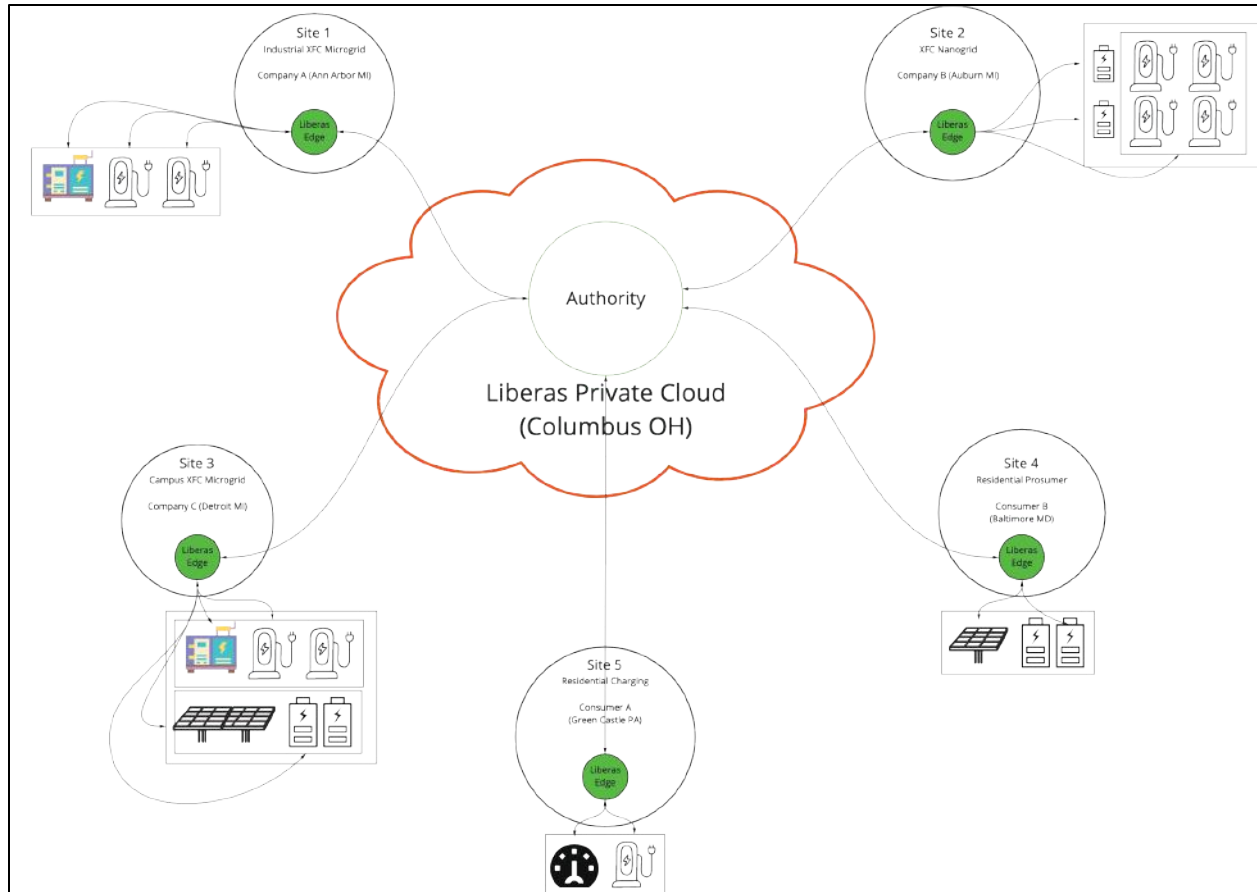
Figure II.1.7.1 Topology of 5-site EVs-at-RISC platform deployment for BP2 SCM demonstrations.

Multi-Site SCM System Demonstration – Interoperable SCM

Smart Charge Management (SCM) enables the use of manual and automated (e.g., algorithmic and model-based) control strategies for both system-level and granular local management of EVSE and DER operation to optimize the resilience and reliability of power distribution networks in near real-time. Fundamentally, SCM requires both (a) the underlying network, communications, protocol, and software infrastructure to enable the deployment of SCM control strategies, and (b) the SCM control strategies (algorithms and/or models) themselves. EVs-at-RISC approaches this problem by first solving (a), as creating the tools to deploy and scale the infrastructure needed for SCM control strategy deployment greatly simplifies achieving the latter (b) at-scale. For these reasons, initial efforts in FY21 and FY22 leveraged arbitrary SCM control strategies for the sake of maturing the EVs-at-RISC platform SCM infrastructure from proof-of-concept through prototype phase.

Initial SCM demonstrations using the EVs-at-RISC platform have successfully achieved basic control strategy deployment for managed charging at Sites 3, 4, and 5 shown in Figure II.1.7.1. EVs-at-RISC recognizes that commercial SCM systems will require cooperation from many stakeholders, including utilities, suppliers, aggregators, end customers, and others. For these reasons, the EVs-at-RISC SCM has been matured in FY22 to support multiple levels of hierarchical control, specifically: utility-managed SCM; aggregator and supplier-managed SCM; and site owner-managed SCM. The project team has collaborated with a wide variety of stakeholders during FY22 to elicit functional and business requirements, and has produced the front-end user interfaces for each of these user categories.

Figure II.1.7.2 provides the user interface developed for the distribution utility. Figure II.1.7.2(a) shows the use of this interface to perform manual smart charge management of all sites located in a specific distribution zone. Figure II.1.7.2(b) shows the resulting curtailment and change in the zonal load following issuance of the SCM commands. This functionality was tested across the deployment shown in Figure II.1.7.1.
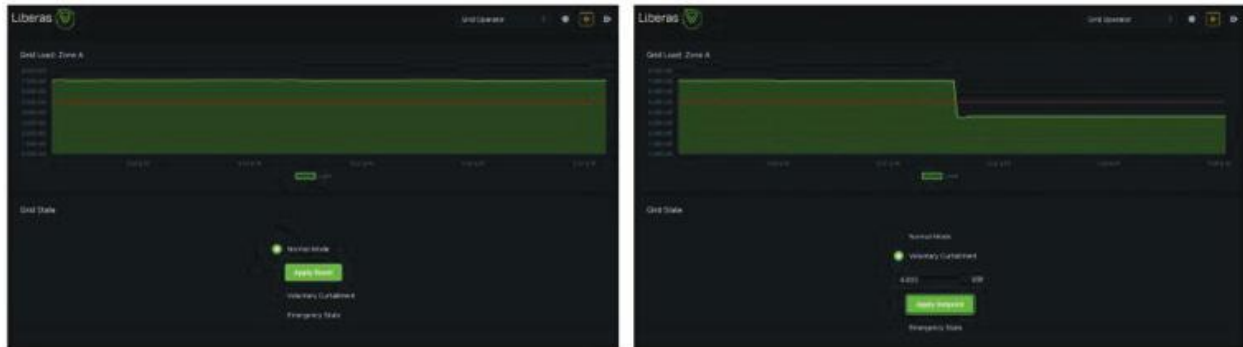
Figure II.1.7.2 EVs-at-RISC SCM distribution utility user interface for utility managed SCM. Right: Figure 2(a); Left: Figure 2(b)

Figure II.1.7.3 provides the user interface developed for the third-party aggregator or supplier. Figure II.1.7.3(a) shows the use of this interface to perform manual smart charge management of a bank of residential chargers located at an end customer site. Figure II.1.7.3(b) shows the resulting curtailment and change in state of the site load following issuance of the SCM commands. This functionality was tested across the deployment shown in Figure II.1.7.1.

Figure II.1.7.3 EVs-at-RISC SCM aggregator/supplier SCM user interface. Right: Figure 3(a); Left: Figure 3(b)

Figure II.1.7.4 provides the user interface developed for the site owner, or end customer. Figure II.1.7.4(a) shows the use of this interface by the site owner to manage charging at a customer-owned end site. Figure II.1.7.4(b) shows the resulting curtailment and change in state of the site load following issuance of the SCM commands to curtail in accordance with the output of a third-party site associated through a power purchase agreement. This functionality was tested across the deployment shown in Figure II.1.7.1.

Figure II.1.7.4 EVs-at-RISC SCM site owner (ratepayer) SCM user interface. Right: Figure 4(a); Left: Figure 4(b)

Multi-Site SCM System Demonstration – Load Shedding

Extending the SCM system shown in Figure II.1.7.2, Figure II.1.7.3, and Figure II.1.7.4, we have added functionality to allow the utility or supplier user to shed zonal load in an emergency scenario. Figure II.1.7.5 provides the user interface developed for this. Figure II.1.7.5(a) shows the selection of a load shed scenario using this interface. Figure II.1.7.5(b) shows the resultant zonal load shed following issuance of this command. This functionality was tested across the deployment shown in Figure II.1.7.1.

Figure II.1.7.5 EVs-at-RISC SCM distribution utility user interface for shedding zonal load. Right: Figure 5(a); Left: Figure 5(b)

Software Platform for SCM Control Strategy Development

Energy management algorithm design has been initiated with the addition of modules to Idaho National Laboratory's Caldera simulator. Modules developed and contributed to Caldera through EVs-at-RISC include distributed photovoltaic (PV) energy generation systems with programmable geographic, time, and weather-related constraints, battery energy storage systems (BESS) with real and reactive power control, high-power extreme fast charging (XFC) EV and EVSE models with adjustable ramp rates, and tools which enable the distribution of EV/EVSE charge events based on geographical data. These extensions provide the Caldera framework with commonly leveraged energy storage and generation assets that will be critical to the forthcoming distributed electric grid's demand response programs, volt-var control programs, and other energy optimization algorithms.

The Caldera simulation framework has also been extended to support the freely accessible EPRI OpenDSS Model ckt24 circuit model. This model (as opposed to any proprietary or simple example circuit model) allows for the widespread dissemination and use of our contributions to the Caldera framework, with the inclusion of several network segments, capacitor banks, substations, and bus coordinates, all of which are instrumental to energy control algorithm development. The tools and scripts generated to integrate the EPRI circuit model are extensible to other OpenDSS models and will support technology transfer when this tool suite is applied to other grid models.

These electric load and generation modules are being simulated with the EPRI ckt24 circuit model to support development of grid energy management and optimization programs on distributed grid architectures during Budget Period 2. Initial simulation cases have been completed and tooling providing data visualization capabilities have been developed by the project team. Additionally, simple energy control strategies have been scripted for module testing, validation, and verification. These initial simulations, visualizations, and control strategies are being used to inform the development of SCM energy algorithms.

Conclusions

The work performed to-date has validated the vision of the EVs-at-RISC program to enable interoperable metering, telemetry, and command-and-control capabilities across diverse, heterogeneous, and highly distributed EV charging/DER infrastructure assets and stakeholders within a zero-trust architecture leveraging free and open-source software technologies and minimal COTS components. We will continue to aggressively progress extending the EVs-at-RISC platform and SCM system implementation to provide broad support for integration and interoperability across power distribution networks, suppliers, service providers, and charging assets for utility-centric, supplier-centric, and ISO market-centric use cases throughout FY23.

Acknowledgements

II.1.8 Wireless Extreme Fast Charging for Electric Trucks

Ryan Calder, Principal Investigator
WAVE, Inc
4752 West California Ave, Suite B400
Salt Lake City, UT 84104
E-mail: michael@waveipt.com

John J. Conley, DOE Project Manager
U.S. Department of Energy
National Energy Technology Laboratory
E-mail: john.conley@netl.doe.gov

Lee Slezak, DOE Technology Manager
U.S. Department of Energy
E-mail: lee.slezak@ee.doe.gov

Start Date: August 1, 2018	End Date: December 31, 2023	
Project Funding: $9,838,241	DOE share: $4,292,137	Non-DOE share: $5,546,104

Project Introduction

The purpose of the wireless extreme fast charging (WXFC) truck project is to significantly accelerate the electrification of heavy-duty trucks, starting with shipping ports and expanding to regional delivery operations across the US. Charging time and range anxiety are major barriers to electric vehicle adoption, particularly for truck applications. Therefore, the major goal of this project is to demonstrate high efficiency, WXFC as applied to Class-8 trucks that have a typically higher gap and lower available space than, for example, transit buses.

Objectives

This project aims to develop and integrate a new 500kW WXFC system developed by WAVE into a Class 8 electric drayage truck developed by Cummins so that it can automatically and wirelessly charge at a high charging rate (C-rate) during its dwell times. The proposed wireless charger features a direct connection to the Medium Voltage (MV) 3-phase grid developed by Utah State University and Schneider Electric and the final prototype will be deployed at Total Transportation Services Inc. (TTSI), which is a truck operator at the Port of Los Angeles (POLA).

Approach

WAVE has assembled a strong and diverse team to develop, deploy, and operate two all-electric Class-8 drayage trucks with WXFC at the Port of Los Angeles (POLA).

The WXFC truck project leverages the active involvement of key partners on six major project tasks, as shown in Figure II.1.8.1 Project tasks include:

- Evaluation of a 250-kW wireless fast charging system in a Class 8 Truck field deployment.

- New development of 500 kW wireless power transmitter and receiver modules

- New battery pack and Class 8 truck powertrain development to support high C-rate charging

- New development of an MV grid-tied converter to improve safety and simplify grid integration of WXFC stations

- WXFC grid and vehicle-side system integration

- WXFC system deployment and evaluation at POLA
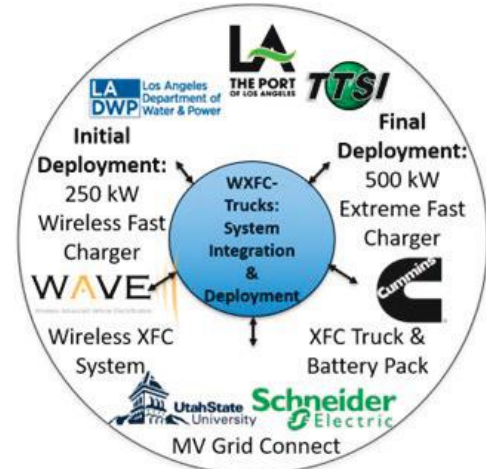
Figure II.1.8.1 WXFC project activities.

WXFC for electric trucks is a WAVE-led project with assistance from the following partners:

- The Port of Los Angeles – Deployment partner

- Los Angeles Department of Water and Power – Deployment partner

- Total Transportation Services Inc. – Port trucks partner

- Cummins – Truck integration and electric drivetrain partner

- Utah State University – A research partner

- Schneider Electric – Electrical supplier, industrialization partner

The general project approach for the MV AC-DC Converter, wireless charger, and the high c-rate Class 8 drayage truck development is outlined in Figure II.1.8.2.

Figure II.1.8.2 Project design and implementation approach.

The USU approach to the MV, grid-connected, AC/DC supply is:

- 3-phase unfolder with a soft DC bus two-level output

- Develop the 3-phase unfolder to achieve direct MV grid connection with switches commutating at the line frequency.

- Design the series of stacked isolated DC/DC converters to achieve the voltage step-down function from MV naturally with a near-unity conversion ratio to obtain high efficiency.

The WAVE approach to the 500kW wireless charger is:

- Deploy and simulate new magnetics design for the higher power density required at 500 kW.

- Build and categorize a 250-kW prototype pad set based on the new design.

- Leverage deployment experience with the 250kW charger to feed into design updates of the 500kW charger.

The Cummins approach to the extremely fast charging capable electric truck is:

- Investigate appropriate battery chemistry (LTO cells or NMC cells)

- Design custom thermal management for the cell to facilitate charging at 3C

- Select appropriate battery pack capacity and cell chemistry to integrate with the electric powertrain applicable to Class 8 drayage applications.

Results

The project team has worked together to define the requirements for the MV AC/DC supply, wireless charger, and Class 8 truck to deliver a solution that meets the needs of the deployment partner. A block diagram for the system is shown in Figure II.1.8.3.
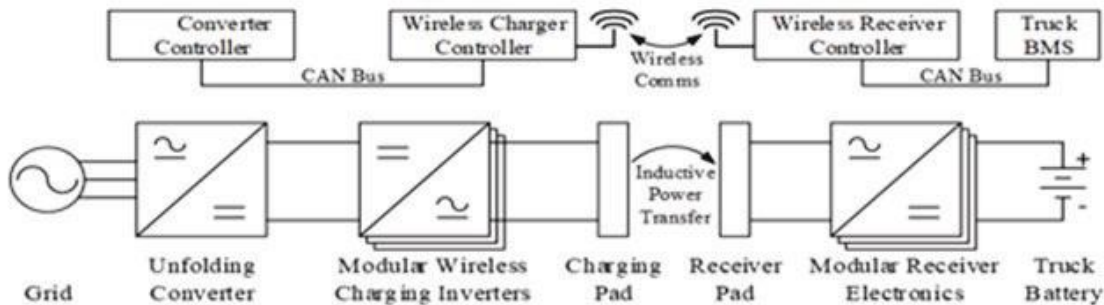
Figure II.1.8.3 System block diagram.

Key results and updates from each project partner are outlined below:

- WAVE - 500 kW Wireless Charger Development and Build

  o The project was significantly impacted by COVID-19 and WAVE and its partners have proposed to alter the course of the project. The supply chain issues have drastically extended the lead time to procure major electronic components necessary to build the MV equipment by almost 2 yrs. As a result, in the interest of the project without affecting the major goal of the project, WAVE has proposed to limit the MV system validation in the lab and deploy the wireless charger at the site using an alternate power supply equipment.

  o WAVE has procured the resonant power supply units required for the demonstration within a few months using its existing supplier base.

    o The BOM, drawings, software, and control scheme have all been updated to work with this new system design.

- o WAVE was able to test this configuration in 2021 during the Charge Testing event with Truck 1, thus confirming the feasibility of this concept.

- o Completed construction of the wireless charging equipment including the secondary pads, rectifier & LV control box for Truck 2.

- o Introduced a new inductor design to further improve the operating range. This design was tested, and validated and is ready to be used in one of the cabinets.

- o WAVE continued to develop and improve the efficiency of the overall system. In a lab setting, the team has achieved a system efficiency of 93.5% from the grid to the battery measured using calibrated equipment.

- o Finalized the tuning system for this application, which improved the harmonic suppression and the controllability of the system.

- o WAVE also had to develop a new control system to run the modular pads using just one control system that is fully automated and can start with just a push button.

  - o This new control system is a drop-in replacement for the old control system, allowing previously developed high-level controls to work with minimal effort.

  - o Power transfer with this new control system has been proven in the lab and will be tested with Truck 2.

Figure II.1.8.4 Primary Charging Pads

- Cummins – Truck Activities:

  - o Cummins completed builds and validation of the 2 Trucks.

    - o Truck 2 validation with WAVE wireless charging system is pending.

  - o Validation on test tracks and public roads: accumulated > 2500 miles.

    - o Including a 250-mile single-day round trip utilizing public CCS1 (125 kW) chargers.

  - o Cummins successfully had the inverter + motor combination certified by an authorized agency.

Figure II.1.8.5 Cummins Truck

- USU - Unfolder and Module Industrialization:

  o Schneider Electric has completed the MV Unfolder bare cabinet per UL specification and delivered it to USU.

  o USU has completed the mechanical assembly of the 8 DC-DC modules and the MV unfolder.

  o Completed the assembly of a 480V pre-charge circuit and system disconnects.

  o Fabricated and assembled all circuit boards required for control, communication, sensing, and protection.

  o Completed the cabinet assembly and wiring of potential transformers, current transducers, sensor boards, LV power supplies, blowers, and the HMI.

  o Due to a change in deployment plan, Motorpact and Custom 480V/120V AC Distribution Panel orders with Schneider Electric have been canceled.

  o Completed full controls testing with the low-power unfolder and three DC-DC Modules

  o Demonstrated close to 50% reduction in THD through modified control algorithms.

  o MV system test plan is completed and submitted for DOE's approval.

Figure II.1.8.6 DC – DC modules fitted inside the cabinet.

- Site deployment activities:

  o Application for Port Permit has been denied as the customs house building was found to have mold issues prohibiting initiating any new construction-related activities at the site.

  o WAVE and TTSI have started scouting for alternate locations for deployment in and around the port to maintain the same duty cycles earlier planned for the project demonstration.

  o As the deployment plan has changed, 480V is the new power requirement at the new location and the sites with this power will be selected for the demonstration to avoid further delays due to additional capacity addition and infrastructure development at the site to bring the required power.

Challenges

COVID-19 has severely impacted the supply chain of the components needed to build the equipment and other assemblies at WAVE, USU & Cummins. Significant measures are being taken to address these issues like procuring alternate parts, changing current designs, and adding more resources to reduce delays.

Conclusions

During this budget period, the WAVE team has completed the procurement of all the parts and systems need to run the wireless chargers. The validation of these systems is also complete in a lab setting and will be further validated once Truck 2 arrives at WAVE for 2nd charge testing event. Cummins completed the validation of the 2 trucks and got the motor and inverter combination certified. Truck 2 will undergo further validation through

charge testing at WAVE. USU had delays procuring the rest of the equipment needed for the final validation and was able to finish the procurement of all the required parts required to complete the build necessary for the MV system validation. Once the new site for the deployment is finalized, the trucks along with the charging system can be deployed and will undergo the demonstration in Budget Period 3. This is one of the crucial milestones that need to be accomplished for the effective deployment of the wireless charging equipment and truck.

This project is well positioned with the correct technical requirements to address the range anxiety and charging time restrictions, which are the key barriers to electric vehicle operation. With all the partners involved in the final stages of the validation testing, we are on track to deploy and operate the systems at the new location.

Key Publications

1. M. Masquelier, "Wireless Extreme Fast Charging for Electric Trucks." 2019 DOE VTO Annual Merit Review, Washington, DC, June 2019.

2. M. Masquelier, "Wireless Extreme Fast Charging for Electric Trucks." 2021 DOE VTO Annual Merit Review, Washington, DC, June 2021.

3. M. Masquelier, "Wireless Extreme Fast Charging for Electric Trucks." 2022 DOE VTO Annual Merit Review, Washington, DC, June 2022.

Acknowledgments

II.1.9 Development and Demonstration of Medium-Heavy Duty PHEV Work Trucks (Odyne Systems)

John R. Petras, Principal Investigator
Odyne Systems LLC
W237 N2878 Woodgate Road, Suite 2
Pewaukee, WI 53072
E-mail: john.petras@Odyne.com

Ken Kelly, Principal Investigator
National Renewable Energy Laboratory (NREL)
15013 Denver West Parkway
Golden, CO 80401
E-mail: kennith.kelly@nrel.gov

David Smith, Principal Investigator
Oak Ridge National Laboratory (ORNL)
2370 Cherahala Blvd
Knoxville, TN 37932
E-mail: smithde@ornl.gov

Steven Boyd, DOE Technology Development Manager
U.S. Department of Energy
E-mail: steven.Boyd@ee.doe.gov

Project Introduction

The heavy-duty vehicle market (Class 6-8) has been a difficult segment for the introduction of plug-in vehicles due to the large energy storage requirement (with corresponding cost), challenging duty cycles, and the diversity of vehicle configurations. The Work Truck market represents a significant opportunity for Heavy-Duty PHEV adoption. Odyne proposes development of a new class of PHEV Work Truck which will be modularized and customized to provide optimal ROI across multiple customers and applications. The proposed project will first demonstrate this technology as a Utility Work Truck variant:

- The usage cycle includes driving and stationary/worksite power requirements, ensuring full daily usage of the grid-charged battery (battery size: 15-30kWhr). Though daily driving can often be short (an average of 26 miles per day), worksite power includes substantial demand (hydraulics, exportable 110/220V power, 12V support, HVAC).

- Worksite power demands for conventional vehicles require continuous loaded engine operation, resulting in significant emissions, fuel consumption and noise impacts.

- These trucks serve an industry that is strongly incentivized to promote vehicle electrification, and which has publicly committed to spending a portion of their annual vehicle purchase budget on electrified vehicles (EEI press release of 11/18/14).

This project will develop and demonstrate a medium/heavy duty plug-in hybrid solution capable of meeting the needs of the work truck market while delivering fuel and emissions reductions of 50% when evaluated against the full-day work truck duty cycle.

Objectives

The project goal is to design, develop, and demonstrate a new generation of medium/heavy-duty plug-in hybrid electric work truck that achieves a 50% reduction in fuel consumption versus a conventional vehicle baseline when evaluated across a full day work cycle representative of the vocational work truck. The primary objectives are:

- To simulate, design and develop unique and innovative integrated powertrain, software, and calibrations which will optimize the complete diesel/transmission/hybrid powertrain and demonstrate the potential for driving fuel efficiency improvements greater than 40% with commensurate reductions in GHG emissions.

- To develop and validate a modular Lithium Ion battery system based on high volume lower cost cells and modules that are utilized in the light-duty sector which will meet the power, energy, and duty cycle requirements of the MD-HD vocational truck market at a cost approaching half that of currently available low volume solutions.

- To integrate fully electrified worksite functions and a daily duty cycle optimization function with the powertrain and battery solutions on an OEM class 6-7 chassis and demonstrate the capability of 50% reduction in total fuel used when measured against a full day duty cycle's and real world performance.

- To demonstrate ten optimized PHEV work trucks and validate the vehicle's operating performance, emissions, and full work cycle fuel reduction capability in excess of 50%.

Approach

The proposed solution incorporates a simple, parallel hybrid system that allows the torque of the electric motor to augment the torque output of the diesel engine, thus saving fuel. The motor speed is synchronized with the engine speed through the existing power take-off (PTO) unit. The traction motor drives the PTO, adding torque to the rear axle, or converts torque from the PTO into power to charge the PHEV batteries (see Figure II.1.9.1). Six patents have been granted, and other patents are pending prior to initiation of this project.

U.S. Patents 7,471,066 7,830,117 8,408,341 8,818,588 8,905,166 8,978,798
Other Patents Pending
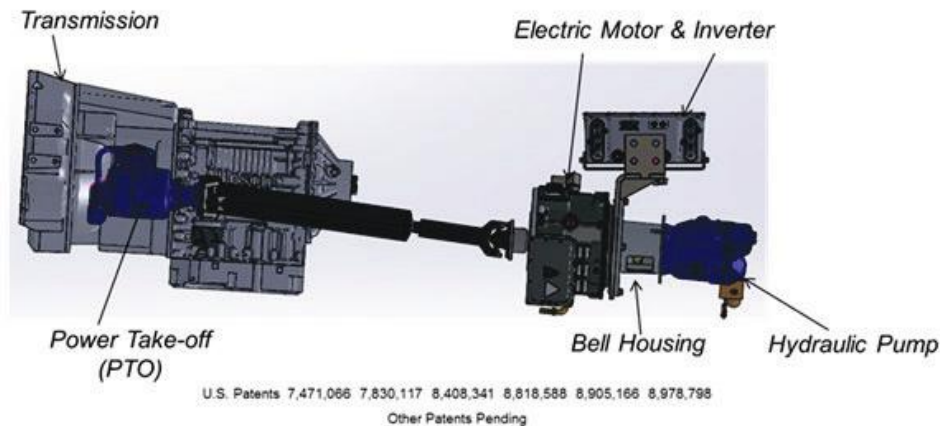
Figure II.1.9.1 Odyne powertrain configuration

The system is also designed to provide full jobsite engine off electrification utilizing power from the lithium ion battery system to provide 120/240 V exportable power, 12V chassis systems support, high efficiency electric heating and air conditioning along with the power to drive the primary work equipment (Figure II.1.9.2).
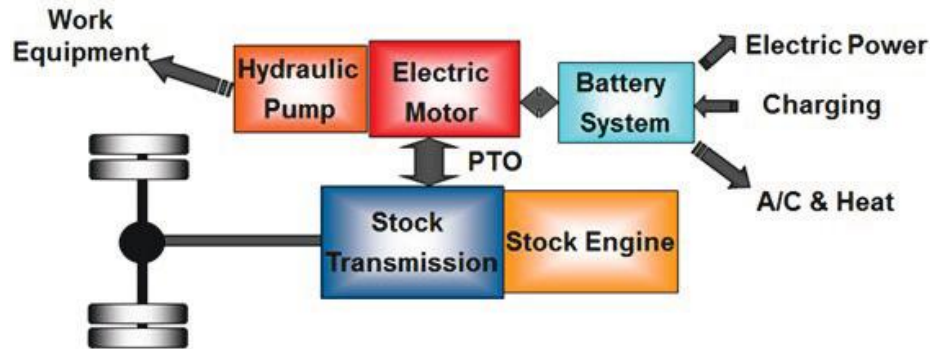
Figure II.1.9.2 Odyne hybrid architecture

The project will be conducted in three periods:

Period 1: System Design and Analysis: Analysis of existing fleet data will be performed and will be used for the establishment of baseline driving and full day usages cycles and current vehicle performance for system simulation, development and test. The project will create designs and systems which, when integrated, will produce a Medium-Heavy duty work truck capable of achieving requirements under real world conditions. The period will conclude with an analytical simulation verifying this performance improvement.

Period 2: System and Vehicle Verification: The subsystems will be verified and refined using prototype hardware and the full vehicle will undergo final development, functional and performance test. The prototype phase will conclude with test results confirming that the final design will provide a ≥50% reduction in fuel use under real world conditions. Approximately ten vehicles will be built to support field test and evaluation.

Period 3: Prototype Vehicle Demonstration: Ten vehicles will be put in regular service with telematics to measure performance. The Recipient will analyze the data along with customer feedback and will report the calculated real-world reduction in fuel use and customer acceptance of the technology.

The project will integrate three development streams into a final Prototype vehicle solution and 10 vehicle field demonstrations:

Powertrain Development and Optimization
- Odyne - Lead, Hybrid Powertrain development and design, Hybrid optimization and control strategies

- NREL – Duty cycle analysis, Dynamometer test, Full-year fuel use simulation and analysis

- Oak Ridge National Laboratory – Powertrain simulation and optimization, HIL Test

- Allison Transmission – Transmission control and optimization strategies

Battery Development
- Odyne – System Specifications and integration requirements, system integration test

- Odyne, Ricardo Strategic Consulting – Battery System supply chain evaluation

- Enerdel – Lithium Ion Module and BMS Supplier, Component System integration requirements

Chassis Development & Integration
- Odyne – System design, control, cost, and integration lead, Systems Efficiency & Sizing, System build

- Freightliner - OEM Chassis Integration improvements, Prototype chassis supplier

Results

In FY22, the project completed optimization of the combined driving and stationary hybrid strategies, secured a fleet demonstration partner (Tacoma Public Utilities), designed and assembled Hybrid ePTO systems for 15 demonstration chassis and assisted in the launching of the demonstration fleet at Tacoma.

Hybrid ePTO Optimization

Utilizing the full year duty cycles provided by NREL, along with the Drive and Stationary fuel savings results generated by the project test vehicle as tested on the NREL ReFUEL fuel and emissions dynamometer (FY2022), Odyne created a hybrid and stationary ePTO strategy which is predicted to reduce fuel consumption of a typical Hybrid ePTO utility vehicle by greater than 50%. Figure II.1.9.3 illustrates the predicted fuel savings on a daily basis when analyzed across the 1 year utility vehicle duty cycle provided by NREL.
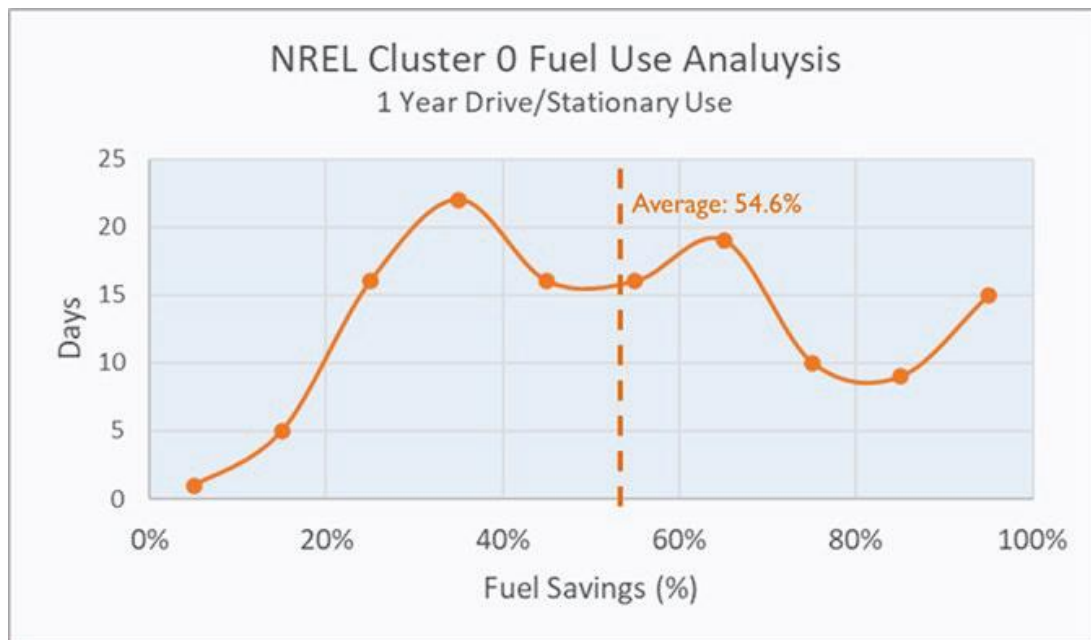
Figure II.1.9.3 Daily and Average Fuel Savings – 1 year Utility Truck Duty Cycle

Summary statements for the Hybrid Optimization:

- The Benefits of the Odyne System combine the fuel and emissions savings while driving with the Engine-Off benefits of hybrid jobsite operation.

- The benefits for All-electric Stationary work outweigh the driving benefits when looking at Gallons saved/kWh

- The system was optimized for available Battery energy by utilizing the Mild driving strategy, thus reserving more energy for Stationary work

- NREL Provided Full-year Drive/Stationary Duty Cycles for analysis

- From the Drive and Stationary Dyno data, full year fuel use reduction could be calculated

- **The Simulated Full Year Fuel Savings for the Odyne PHEV Work Truck was 54.6%**

Demonstration Fleet Design, Assembly, and Deployment

During FY22, the design team completed the packaging, subsystem and component layouts and drawings to efficiently install the hybrid electrification system on a fleet of demonstration vehicles ordered by Tacoma Public Utilities (TPU). Because of the compact size of the Enerdel battery, most of the freestanding power and control components were able to be attached within the footprint of the previous battery bracket, greatly reducing the system package space, number of sub-assemblies, and wiring complexity. Figure II.1.9.4 represents the new configuration with the hybrid components represented in green and Figure II.1.9.5 is the system on the updated test vehicle.
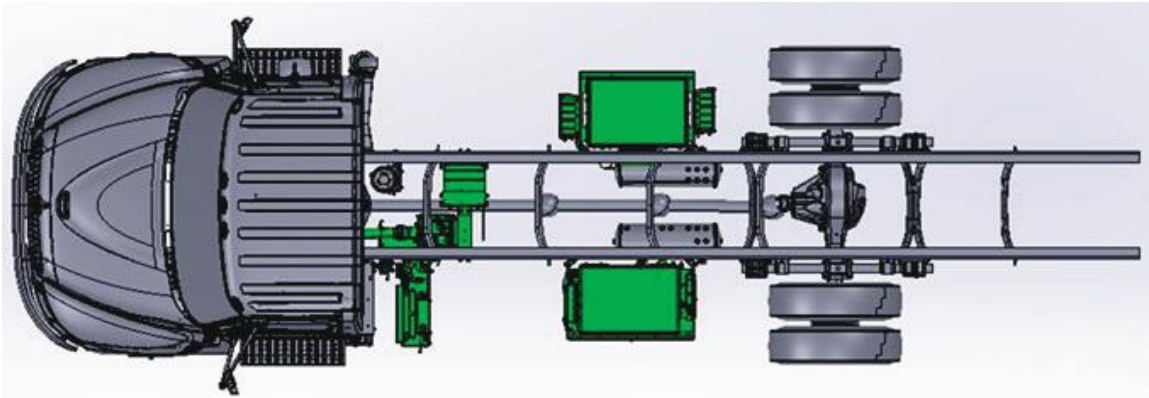
Figure II.1.9.4 Odyne Project System Layout

Figure II.1.9.5 Odyne Updated Test Vehicle

During the remainder of FY22, Odyne completed delivery, training and initial vehicle support for the Demonstration Fleet at Tacoma Public Utilities. Odyne will be gathering operator and fleet feedback and will be installing Telematics systems for objective feedback and refinement during the remainder of the project in FY23. Figure II.1.9.6 is one of the first units delivered to TPU.

Figure II.1.9.6 Tacoma Public Utilites Hybrid Step Van

Conclusions

In FY22, the project completed the test of the hybrid drive strategies and completed the system integration, layout and design to be utilized for the demonstration vehicles as well as future Odyne production. The drive testing demonstrated that the system is capable of delivering up to 75% fuel economy improvement, depending on duty cycle, although a lessor driving strategy was ultimately be utilized when considering battery cost and size, stationary energy needs, and the real-world duty cycle of the Medium/Heavy Duty work truck. The final goal of the project is to demonstrate the capability to reduce the full day fuel use of a Medium/Heavy Duty work truck by over 50% in field demonstration.

Acknowledgements

Odyne wishes to acknowledge the substantial contributions of Michael Ursic (NETL), Eric Miller, Peter Sindler, Jonathan Burton, Matt Thornton, (NREL), Adian Cook, Dean Deter (Oak Ridge National Laboratory), Greg Mann, Brent Maurer (Allison Transmission), Dan Purdy (Freightliner Trucks), and Mark Kuhn, Alan Munday (Ricardo Strategic Consulting), and Tacoma Public Utilities.

II.2 High-Power Charging (HPC) Enabling Technologies

II.2.1 Assessment and Validation of Next Generation EV High Power Charging Profiles (ANL)

Kevin Stutenberg, Principal Investigator
Argonne National Laboratory
9700 S. Cass Ave
Lemont, IL 60439
E-mail: kstutenberg@anl.gov

Lee Slezak, DOE Program Manager
U.S. Department of Energy
E-mail: lee.slezak@ee.doe.gov

Start Date: June 1, 2020   End Date: March 31, 2022
Project Funding: $300,000   DOE share: $300,000   Non-DOE share: $0

Project Introduction

The U.S. Department of Energy (DOE) Vehicle Technologies Office (VTO), along with national laboratories, performs research to advance vehicle powertrain technologies, including internal combustion engines, batteries, electric machines, light-weighting, fuels and lubricants.

To advance the understanding of direct current fast charging (DCFC) of recent electrified vehicles, this effort quantified the DC charging behavior and efficiencies of modern electric vehicles (EVs) and DCFC stations, providing a data driven understanding of operation, power flows, and energy consumption with four EV's: a 2020 Tesla Model 3, 2020 Nissan Leaf E-plus, and a 2017 and 2020 Chevrolet Bolt. These vehicles provided variability in vehicle type as well as DCFC standard, capturing insight into the CHAdeMo, CCS, and the Tesla Supercharger networks. Each vehicle was instrumented to provide data on vehicle operation during charging including HV battery voltage, current, temperature, power limits, and signals specific to thermal conditioning during the charge. Testing took place over a full calendar year in the US Midwest city of Chicago to capture a full range of ambient temperatures and charging conditions. During testing, the vehicles were discharged through a combination of on-road mileage accumulation and static operation and static discharging to provide a variety of starting conditions. The general metrics of vehicle preparation, including energy use and prior to the trip, and distance driven were noted. A total of over 120 DCFC events were captured for analysis across all vehicles to provide a distribution of the key variables of ambient temperature, battery temperature, starting SOC, and charge station.

Objectives

This project focuses on the following main objectives:

- Characterize DCFC power limitations on four vehicles across multiple charging stations with varying charge power levels (eg. Tesla SC: 72kW, 150kW,25kW)

- Develop a data management process for collecting, managing, and distributing DCFC datasets for internal review to public distribution

- Evaluate system operation during charging to determine power flows, aka how much power is used for charging vs thermal conditioning

Approach

This project focus had the following approach:

- Perform instrumentation of four research vehicle to capture key signals during charging including high voltage system power and current limits, SOC, battery temperature and other system temperatures.

- Capture vehicle data during DCFC events over the course of a year while ambient temperatures and conditions vary.

- Perform focused charging at public DCFC stations as well as the instrumented facility of the ANL SMART Energy Plaza to gain insight into DCFC efficiency.

- Analyze and distribute datasets publicly on Argonne's Downloadable Driving Database and Livewire to enable analysis beyond the scope of this project.

Results

Test Development and Vehicle Instrumentation

Research Vehicle Review

Vehicles were selected for this research effort to capture a vehicle DC fast charging from a range of vehicle manufacturers, and on the three main charging CHAdeMo, CCS, and the Tesla Supercharger networks. Historical Argonne research vehicles were used where possible to provide a baseline for vehicle instrumentation. From the Argonne research fleet, the four vehicles were selected as displayed in Figure II.2.1.1.

Figure II.2.1.1 Four research vehicles selected for investigation

Two research vehicles were selected which were equipped with a SAE-Combo style connector, a 2017 and 2020 Chevrolet Bolt. Though many aspects of these vehicle were similar such as manufacturer, charging standard, and liquid cooling system, the 2020 Bolt was equipped with an updated battery pack of a different chemistry with an increased overall capacity in addition to an updated DCFC profile. The 2020 Nissan Leaf selected provided a vehicle with an air-cooled HV battery which used the CHAdeMO system, and was intially stated as capable of DCFC at rates up to 100kW. The final vehicle selected was a 2020 Tesla Model 3 Long Range and All-Wheel drive packages, which offered a liquid cooled battery pack with a unique thermal control system, and a battery capacity of the 75kWh as stated by the manufacturer.

All vehicles entered use in the testing effort with between 3500-4500 miles, providing data from low-use HV battery packs with no noticeable degradation or charging limitations prior to testing.

Vehicle Instrumentation

Vehicles instrumentation focused on methods which were portable to allow for vehicles to be driven to and from public charging stations throughout the greater Chicagoland area. This allowed for a variety of Tesla Supercharger stations to used for charging over the course of the project, including the 72kW 'Urban'

supercharger, as well as 150kW (V2) , and 250kW (V3) stations. Additionally, as the vehicles were driven to charging station, processes for vehicle acclimation such as Tesla's 'Preconditioning battery for Supercharging' could be used in order to capture the impact on system thermal state and charging power.

Portable instrumentation was made possible by focused decoding of each research vehicle's communication (CAN) network. Key signals were determined prior to the start of testing, which included those that focused on:

- **Vehicle state:** Active systems (HVAC, screen, audio, etc) &

- **Environment:** (ambient temp / solar load)

- **High Voltage Battery:** Voltage, Current, SOC, Capacity, Temp, Limts

- **Charger (DCFC):** Voltage, Current, Limits, Status

- **Cooling system:** Temps, Flows, Set points, Status

- **Other Vehicle information:** Low voltage system metrics for power flow

An overview of the vehicle instrumentation and data colleciton pipleline can be seen in Figure II.2.1.2.

Figure II.2.1.2 Process for vehicle data collection used throughout process

This instrumentation process began with a review of each vehicles communication network to understand the pathways which key signal were broadcast between vehicle controllers. Networks of interest were then connected to, and the communication between these controllers monitored. Key signals were decoded from this communication with historical tools and processes developed within Argonne's Advanced Mobility Technology Research group, and the decoded signals validated against independent instrumentation and prior dynamometer testing results.

During testing, raw network traffic was recorded into a binary file on the communication networks of interest for each test vehicle. Following the testing, these binary files were then post processed with the decoded signal databases to create the final datasets for analysis and data sharing. By capturing full logs of network communication, rather than just specific signals, decoded signals could be later added or updated, and datasets created with the updated values. This was an important consideration with the Tesla Model 3 research vehicle which allowed for 'Over the Air' updates, where on multiple occasions, decoded signals needed to be revised (decoded again) following vehicle software updates. With this process testing was able to continue without delay while further decoding occurred.

Testing Process and Charge Metadata

While performing the charge testing, data outside of the time-series vehicle communication data was captured to document test conditions. To capture this information, a test operator created a test summary was created during each testing event which included:

- General operator test notes:

- o   Environment conditions,

- o   Noted vehicle state (mileage, firmware ver., etc),

- o   Surrounding vehicles notes (which may impact charge power at some charge stations)

- o   Additional general notes of anything insightful

- **'Since last charge' metrics:** Captured data about prior discharge cycle (vehicle dependent signal)

- **Pictures:** Charging station, vehicle, environment during charge, dash where useful, etc.

- **Station Data:** Charging data, such as cost, AC Energy, etc was captured from the Charging network where possible, including AC specific power data from Argonne's Smart Energy Plaza

The charge sessions were initiated with the vehicles starting at varying beginning HV battery state of charge levels to capture the effects of SOC on available charge power. Additionally, charge sessions were ended at different SOC setpoints to represent different charge durations. Following each charge session, research vehicles were discharged either with a static discharge from HVAC loads, or by on road operation. The metadata of vehicle mileage traveled prior to each charge session was recorded in each test file and could be used as an indicator for the type of discharge which occurred.

Following post processing of captured datasets to create the time series datasets, this text-based metadata was merged with the time series data to create a single file, of a .tdms file type. These datasets were then used for comparative analysis, postprocessing and later distribution to DOE partners and public.

Testing Process and Charge Metadata

To capture a variety of ambient conditions, the test vehicles were driven to charging locations across the Chicagoland. These tests were conducted at over 15 unique multiple Tesla Supercharger stations, A total of over 180 charge sessions were completed across the 4 research vehicles. 63 charge sessions occurred on the Tesla Model 3, 60 on the Nissan Leaf, and 60 sessions on the Chevrolet Bolt (MY20 and MY17 combined). Of these charge sessions, over 120 datasets were fully processed made available for comparative analysis. The test vehicles on charge at varying locations can be seen in Figure II.2.1.3.

Figure II.2.1.3 Test vehicles at varying locations and ambient conditions during charge events

Analysis of results and summary findings

The datasets captured provide opportunities for analysis on many aspects of DC fast charging including ambient temperature, component temperature, state of charge, charging station power, preconditioning, as well many others.

To provide an overview of the range of data captured, Figure II.2.1.4 lists all charge sessions for each research vehicle, showing the change in high voltage battery SOC and the peak charge power.
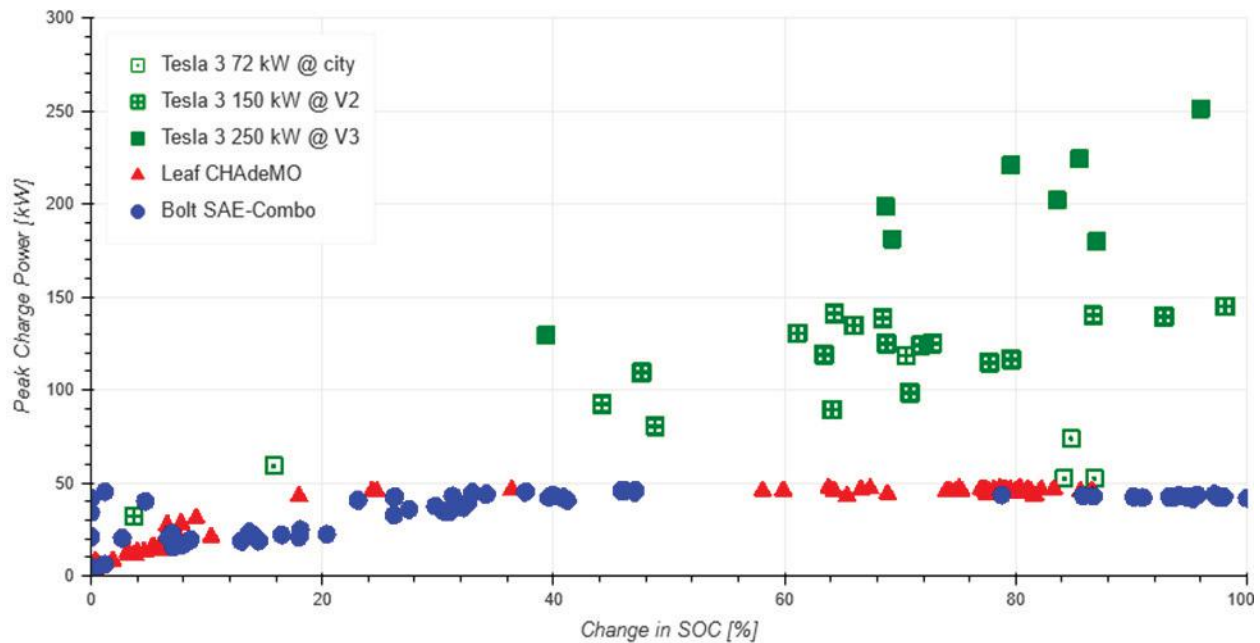
Figure II.2.1.4 Summary of Peak Charging Power vs Change in SOC for all charge sessions

This research effort captured a large number of comprehensive datasets on the charging characteristic, power flows during charging, and impacts of ambient temperature on several modern electrified vehicles. Several key findings were noted from this effort:

- The Tesla Model 3, though rated at a peak charge power of 250kW, was only found to reach this charge power on a single session at a Tesla V3 station. Other V3 charging sessions found peak powers over 150kW, though these high power levels were limited in duration.

- The Peak charge power of both the Nissan Leaf E+ and Chevrolet Bolt test vehicles was limited to less than 50kW of charge power

- Due to the limited duration which the Tesla charged at levels above 150kW, vehicle ambient conditions and beginning thermal conditions were found to have a larger impact on charge duration than the use of a higher power 250kW (Tesla V3) DCFC station.

The charge profile, and the impact to cell temperature during charge events at varying charge power levels can be seen in Figure II.2.1.5. As the Model 3 conditions the battery pack during supercharging, cell temperature was found to reach a control temperature of 52-53C on most charge sessions, where the temperature was then maintained for the duration of charge.
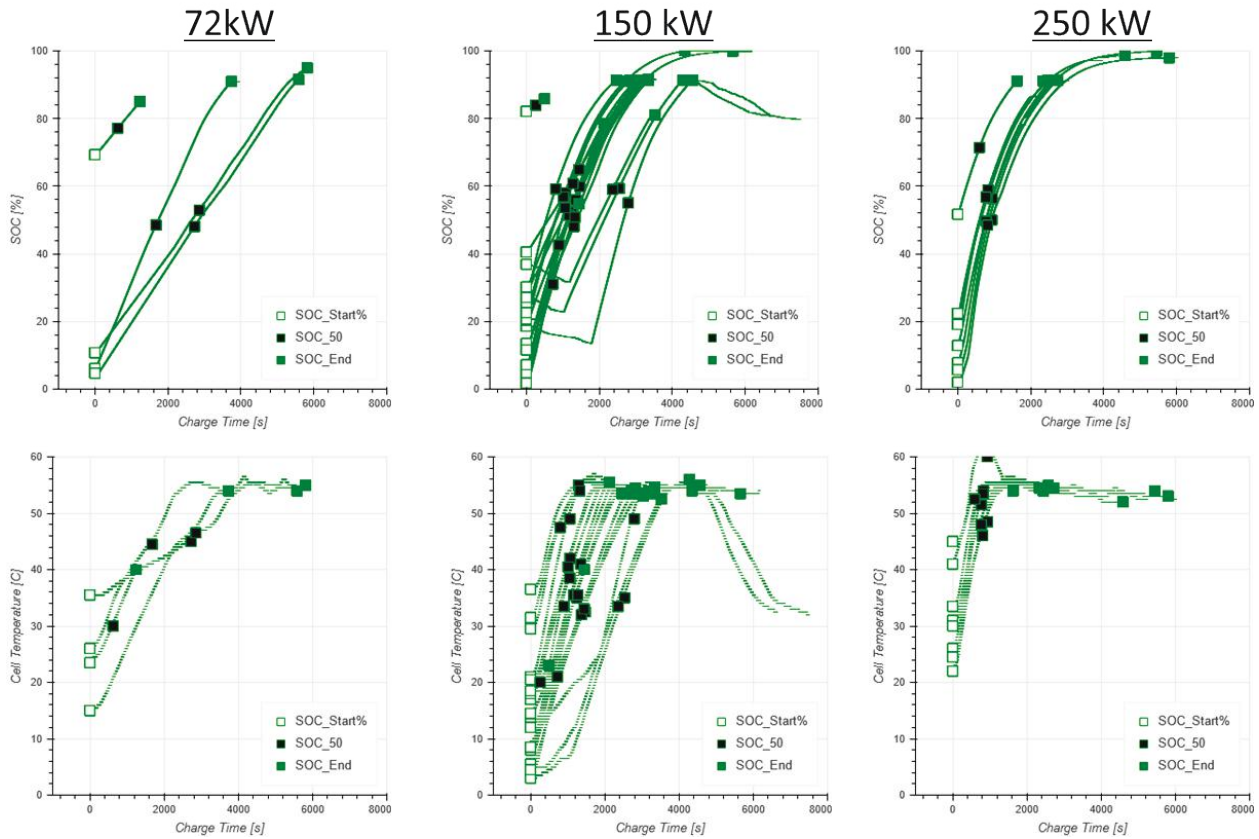
Figure II.2.1.5 Charge profiles and varying cell temperature during DCFC sessions on the 2020 Tesla Model 3

Only a small subset of the analysis possible with this dataset has been presented in this summary report. The datasets captured this research effort were made available through Argonne's Downloadable Dynamometer Database at www.anl.gov/d3, and linked to NREL's Livewire platform for wider access.

Conclusions

To advance the understanding of DC fast charging of recent electrified vehicles with data, a research effort was conducted to capture the DC charging behavior and efficiencies of four modern electric vehicles including a 2020 Tesla Model 3, 2020 Nissan Leaf E-plus, and a 2017 and 2020 Chevrolet Bolt. The experimental study provided data for analysis of over 120 charge sessions, from a wide variety of ambient conditions and public DCFC networks.

Acknowledgements

The project team would like to acknowledge the support in the instrumentation, experimentation, and analysis efforts. This team includes experimental technicians: Mike Kern, Geoff Amann, Tim Rutter, and Tony Wilcheski, and supporting Argonne researchers Toby Rockstroh, Noah Grom, Dan Dobrzynski, and Sam Thurston. Additionally, the project team would like to thank Thomas Wallner, Argonne experimental team group manager, for support and guidance through the duration of this effort.

II.2.2 Assessment and Validation of Next Generation Electric Vehicles High Power Charging Profiles (ANL, NREL, INL, ORNL)

Daniel Dobrzynski, Principal Investigator
Argonne National Laboratory
9700 S. Cass Ave.
Lemont, IL 60439
E-mail: ddobrzynski@anl.gov

Keith Davidson, Principal Investigator
National Renewable Energy Laboratory
15013 Denver West Parkway
Golden, CO 80401
E-mail: keith.davidson@nrel.gov

Barney Carlson, Principal Investigator
Idaho National Laboratory
2525 N. Fremont Ave.
Idaho Falls, ID
E-mail: richard.carlson@inl.gov

Omer Onar, Principal Investigator
Oak Ridge National Laboratory
1 Bethel Valley Road
Oak Ridge, TN 37830
E-mail: onaroc@ornl.gov

Lee Slezak, DOE Technology Manager
U.S. Department of Energy
E-mail: lee.slezak@ee.doe.gov

Start Date: October 1, 2020   End Date: September 30, 2023
Project Funding: $6,000,000   DOE share: $6,000,000   Non-DOE share: $0

Project Introduction

In both commercial and consumer electric vehicle (EV) segments there are concerted efforts by EV and Electric Vehicle Supply Equipment (EVSE) Original Equipment Manufacturers (OEMs) to increase charge energy delivered while simultaneously decreasing charging time. In order to accomplish these goals, innovations must be made to increase the peak charging power of EVs. As the first High Power Charging (HPC) systems, 200kW+, are emerging, it is apparent that HPC profiles can vary greatly by EV. In order to intelligently integrate HPC systems within the grid and among co-located loads and sources it is critical to quantify and characterize the charging profiles that these systems will present. This project leverages laboratory team capabilities, OEM stakeholder relationships, current HPC fleet deployments, and XCEL project outputs to quantify and characterize current and next generation HPC EV profiles and EVSE characteristics. The assessment performed in this project include both conductive and inductive charging topologies from a variation of vehicle classes including light, medium, and heavy duty. The output from this project will provide critical inputs to several ongoing efforts including modeling of electrified transportation systems, battery design, standardization best practices, and grid energy management systems.

Objectives

Develop Test Procedures – Collaboratively develop the test requirements, procedures, and measurement parameters for both conductive and wireless charging evaluation. These procedures to be used for laboratory

HPC profile capture and EVSE characterization. This objective also develops guidelines for data capture for fleet and in-field evaluations.

Capture HPC Profiles – Develop rich profile sets from each of the EV project assets. Assets constitute consumer and commercial EVs that include both conductive and inductive charging and span light, medium, and heavy duty EVs. The profiles are to be gathered through a combination of in-lab evaluations, field evaluations, and data gathering of in-use HPC EV fleets. Whenever possible, HPC profile sets include a nominal charging profile with subset profiles that are gathered during off-nominal conditions that include varied ambient temperatures, grid events, and/or managed charge control.

Characterize HPC EVSE – To fully quantify the charging load as seen by the grid, EVSE performance characterization of power transfer, efficiency, power quality, and harmonics injection, to be conducted for laboratory XFCs across the rated operating ranges and with next generation HPC profiles. These characterization measurements focus on quantifying the efficiency, power quality, harmonics, thermal management operation, etc. Characterization across the full operating range of XFC will eliminate the need for assumptions and extrapolation from the limited XFC operational data currently available.

Integrate, Analyze, and Report Data – Evaluation outputs and data collection to be shared publicly and among project partners. Throughout the project data analysis will be required to ensure all shared data is of requisite quality. Late-stage analysis will be conducted to report outcomes and findings of the resulting data. Results and data will be directly provided to modeling teams upon request.

Approach

Procedure Development – Collaborative develop of the test requirements, procedures, and measurement parameters for both conductive and wireless charging evaluation. This includes the definition of 'nominal' conditions as well as developing the factors for in-depth laboratory investigations. Prior to procedure execution, the project team will solidify the minimum measurement requirements and calculated parameters that will be generated from evaluations as a primary output from this project. Project collaborators and industry partners will be queried for input and feedback on the measurements, calculated parameters, procedures, and process of the characterization.

HPC Profile Capture and Characterization of HPC EVSE – The project team must align resources and leverage relationships in an effort to line up a wide breadth of HPC EV and EVSE assets; all capable of HPC (200kW+). These assets include partner laboratory resources, OEM partner share, OEM and laboratory field evaluations, in-use and planned fleet EV/EVSE, and use of XCEL research profiles. The project team has budgeted time and effort to continue outreach to emerging potential partners as the electric vehicle and infrastructure landscape changes.

Evaluation Methodology – Determine baseline HPC EV and EVSE equipment characteristics/charge profiles. Baseline datasets will be gathered during the procedure-defined nominal boundary conditions. Similar equipment characterization must follow utilizing factors identified in the procedure such as EV/battery conditions, ambient temperature, grid conditions, and charge management controls to observe how HPC profiles and equipment characteristics are affected by factors or factor combinations. These secondary evaluations will be referred to as off-nominal tests. The combination of these characterizations will allow evaluation of HPC EV and EVSE metrics that include; overall charging load profile, EV and EVSE thermal management loads, EV and EVSE charging efficiency, ramp rates, peak power, power quality, and external factor effects.

Dissemination and Reporting – Datasets and project outputs will be available for use by other research groups, grid planners, OEMs, and various other industry stakeholders. In order for the project results to be useful the datasets need to be clear, comprehensive, and consistent. The project team has planned budget to include regular data quality checks to ensure data from multiple sources are aggregated in identical formats using common labels. These practices will ensure that use of the datasets has low thresholds and can produce effective research and planning.

Results

Idaho National Laboratory Results

350kW EVSE Characterization

In support of the multi-national lab collaborative efforts in this project, INL completed the characterization of one 350kW Extreme Fast Charger (XFC) during nominal and off-nominal operating conditions. This testing was conducted in a laboratory environment using high-accuracy power analyzers and a data acquisition system. The testing was accomplished using a high-power EV emulator that consists of a DC load bank capable of 400kW (up to 900VDC and 500ADC) and a CCS communications module capable of emulating all of the necessary vehicle-side communication to enable a charge session.

Steady state EVSE characterization was completed for one 350kW XFC at 850VDC, 750VDC, 650VDC, 400VDC, and 300VDC across DC output currents ranging from 50ADC to 500ADC in 10A increments. These tests cover the wide range of operational conditions that are utilized by numerous vehicle classes, battery voltages, and battery charge acceptance rates. This steady state operational testing highlights the performance characteristics of the charging systems including AC to DC efficiency, AC power quality, stand-by power consumption, auxiliary power consumption while charging, and numerous other performance attributes.

OCPP curtailment response characterization was completed for one 350kW XFC using an open-source OCPP server running OCPP1.6J. The test cases completed include power transfer curtailment requests of 54kW AC and 65A AC at operational conditions of 400VDC and 850VDC for 150ADC and 500ADC. The OCPP curtailment requests evaluated at these eight test conditions included "ChargePointMaxProfile", "TxDefaultPofile", and "TxProfile" smart energy profile requests. The results from testing detail the latency between the time the request is initiated to the time the power curtailment begins as well as the latency from the end of the curtailment request until the XFC resume full power capable operation. Additionally, the difference between the curtailment requested current or power and the resulting power transfer by the XFC is determined to identify the offset or difference from the requested curtailment amount.

Results from testing, as shown in Figure II.2.2.1 show the average latency is 3.5 seconds from the curtailment request initiation to the initial ramp down in power by the XFC. The range of latency varies from 0.6 sec. to 4.6 sec. The ramp down rate is quite consistent for the various curtailment types with an average of 200A/sec. Additionally, the testing shows an accuracy by the XFC for the requested curtailments are 7% for the 65A curtailment requests and 5% accuracy for the 54kW DC power curtailment requests.
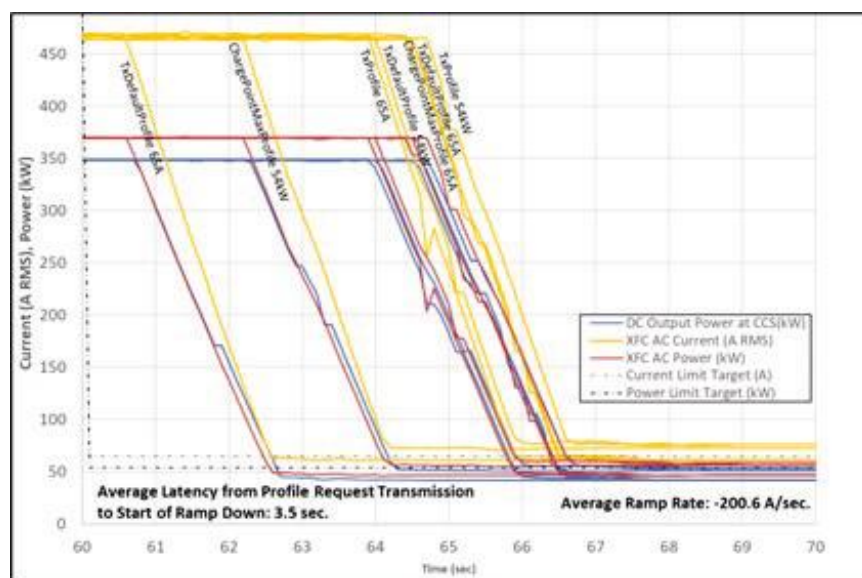
Figure II.2.2.1 - XFC characterization for OCPP curtailment request response and accuracy

High utilization testing at full power was conducted for one 350kW XFC for three consecutive high-power charge sessions. This test evaluated the XFC operational performance for a case when three EVs each require a 10-minute charge session at full power with minimal time between the charge events. This is representative of a highly utilized charge station along a travel corridor where vehicles stop for a short time and require fast charging to quickly replenish driving range.

The high utilization testing involved three 10-minute consecutive charge sessions, each at 750VDC at full power transfer with a five-minute rest time between each charge session. This rest time is appropriate for the time required for the first vehicle to unplug and drive away, and a second vehicle arrive and initiate a charge session. In total, the test is forty minutes in duration and highlights the XFC's thermal management system controls and capabilities. Results shown in Figure II.2.2.2 show the XFC is capable of providing 350kW for approximately 6 minutes prior to entering a state resulting in 90A DC output limitation. This appears to be the result of the liquid cooled CCS cable and connector reaching a thermal limit requiring reduced power operation. Of note, the XFC does not revert to full power capability until the XFC has been reset by cycling the 480VAC input.
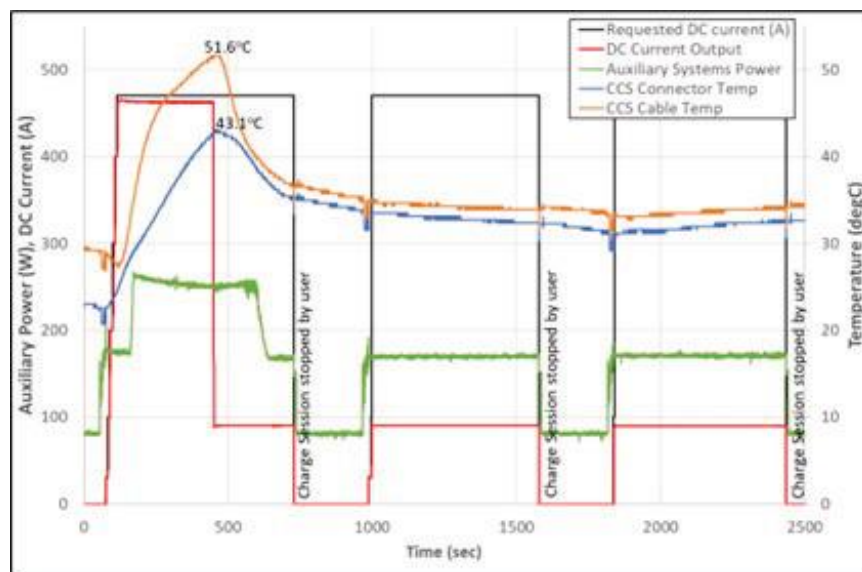
Figure II.2.2.2 - XFC characterization during consecutive, 10-minute, high-power charge sessions

Off-nominal gird input conditions testing was completed for one 350kW XFC. This testing evaluated the charge performance and resiliency during AC input deviations in voltage, frequency, and harmonics. Voltage deviation testing ranged from voltage swells up to 518VAC, to voltage sags of 426VAC. Frequency deviation testing ranged from a grid input frequency of 58.8 Hz to 61.2 Hz. Harmonics injection testing was conducted by introducing 5% THD harmonics to all three phases of the AC input to the XFC. The completed testing for the 350kW DC XFC includes testing at all of the above off-nominal conditions for 150A and 500A at 400VDC operation and 150A at 850VDC. The XFC operation continued without interruption through all test conditions during this off-nominal grid input testing. These highlight the 350kW DC XFC resiliency to deviations in the AC supply input voltage, frequency, and voltage harmonics.

Light duty EV Charge Profile

In support of the multi-national lab collaborative efforts in this project, INL completed charge profile testing of an advanced light-duty EV capable of up to 1.5C charge rate. Charge sessions were conducted for initial battery temperatures of -1°C, 21°C, 33°C, and 40°C. The vehicle was prepared for testing by reducing the battery State of Charge (SOC) to 10% displayed SOC. The vehicle battery temperature was prepared by either soaking the vehicle at ambient temperature below freezing or at 21°C for more than 12 hours, or the vehicle was driven in hot ambient temperature conditions to elevate the battery's average temperature to the prescribed charge session test condition. Once the vehicle battery was prepared, AC and DC measurements from the XFC

were collected before, during, and after the charge session from 10% to 100% displayed SOC. The results highlight the unique charge profile characteristics of this advanced light-duty EV and the impact of battery temperature on the charge profile. Figure II.2.2.3 shows the DC power charge profile versus the displayed battery SOC of this light-duty EV at various initial battery temperatures.
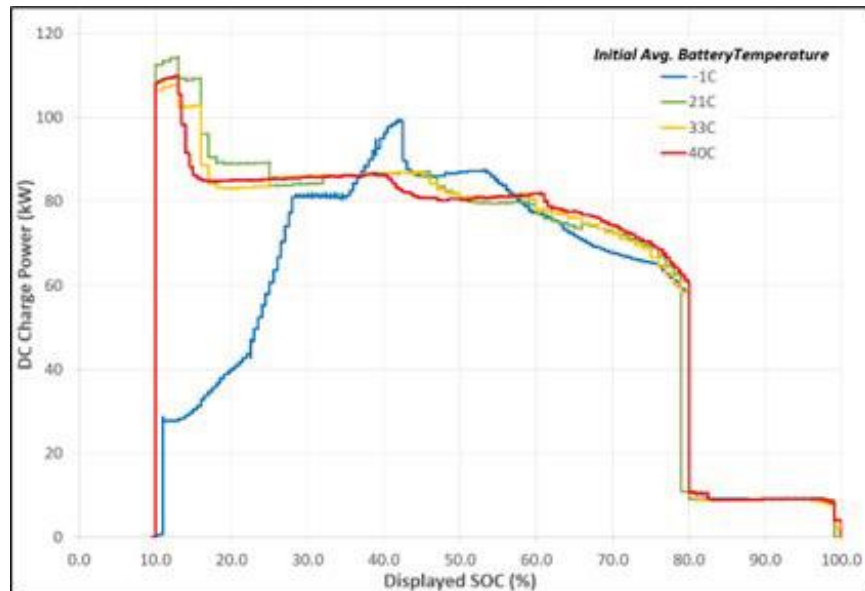
Figure II.2.2.3 - Light-duty EV charge profile at various initial battery temperatures

Argonne National Laboratory Results

OEM Collaboration & EV Characterization

ANL met with several OEMs to build relationships between research & industry partners throughout this project's timeline. The finite use of EV assets in exchange for in depth time-series feedback and analysis on charge performance has proven to be valuable for both parties and has aided in ANL conducting charge analysis for six different EV's, resulting in 24 unique charge profiles. ANL's continued outreach to industry partners has lined up several more EV deliveries scheduled for the winter months to conduct cold weather (-7°F) charge profiles. Different EV topologies of 400VDC and 800VDC battery systems have led ANL to explore unique charge profiles where charge time, thermal readings, system efficiencies, etc. have been quantified and compared. Figure II.2.2.4 shows the profile capture analysis of EVs LD1 and LD2 under the same starting conditions, but with drastically differing results based on OEM charge strategies, battery topologies, etc. This, and much more analysis is to come with further data acquisition of current and future EVs.
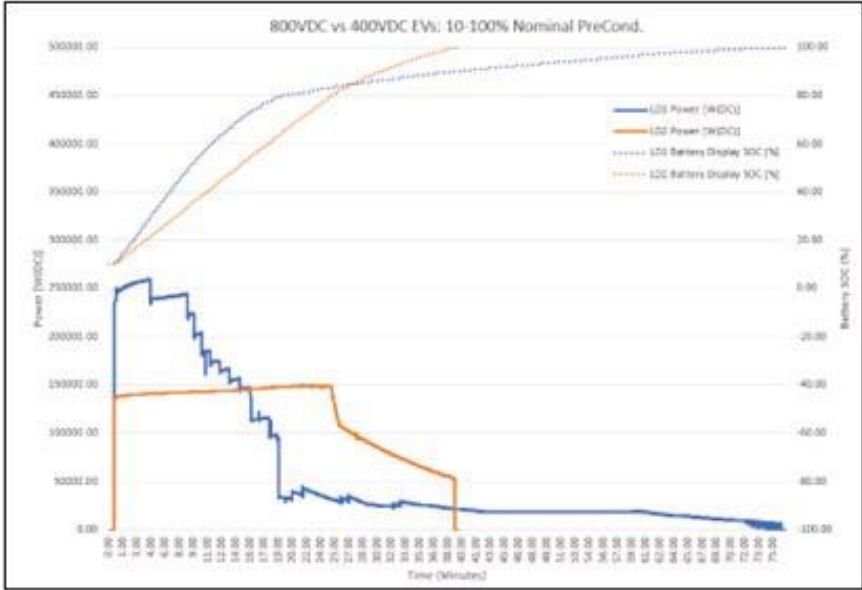
Figure II.2.2.4 Comparing charge profiles of different light-duty EVs under similar start conditions

Time-Sync'd Data, Graphical Analysis, & Reporting

ANL took lead on developing a post-processing strategy for EV characterization with the goal of standardizing EV profile formatting across all supporting national labs. This led to developing graphical analysis methods for our time-series data, conducting value assessment on the reportable data, and hosting technical reviews for final technical report formatting. Figure II.2.2.5 depicts a typical 10Hz time-series charge profile document that would be shared with collaborating OEMs. Discussions around what is to be included and the formatting of an anonymized public report have begun via technical discussions in a multi-national lab collaborative effort.
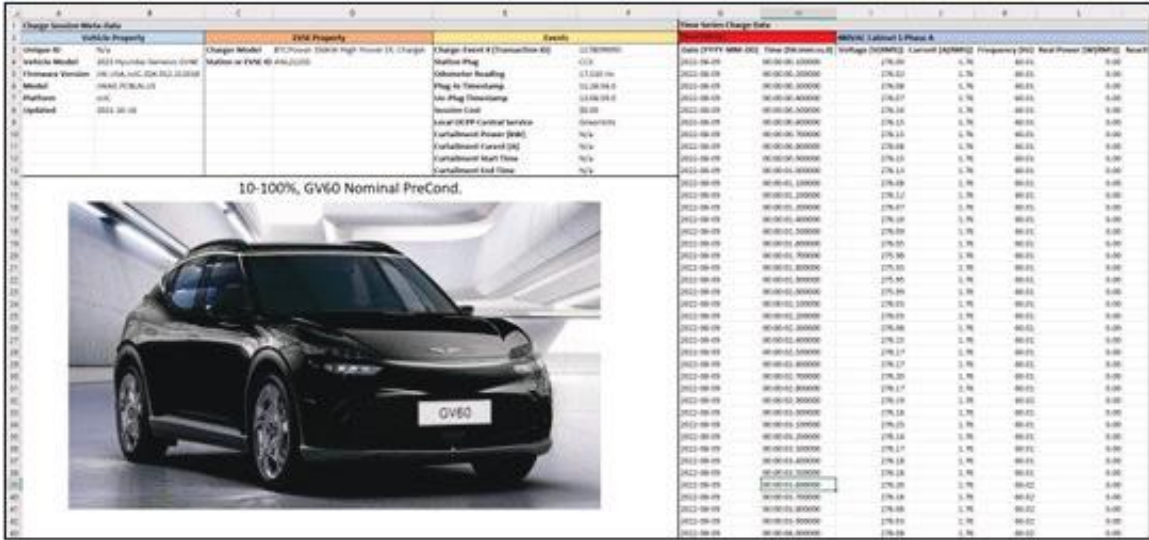
Figure II.2.2.5 - Time-Sync'd, 10Hz time-series data shared with OEM collaborators

Fleet Utilization Developments

Through the collaboration with Chicago Transit Authority (CTA) ANL gathered and quantified fleet utilization data on their newly launched line of Proterra electric transit busses. Given access to CTAs ViriCiti system that monitors/logs vehicle CAN-Bus data, ANL was able to export, filter, and review report utilization data on a

weekly, monthly, or yearly basis. This analysis was done under three sections: route analysis, charge analysis and time analysis. *Route Analysis* investigated average distance driven, net energy displaced, route start/end SOC, etc. to quantify usage seen by the fleet. *Charge Analysis* saw how often energy was being delivered, average start/end SOC, total charge time and energy, etc. to find fleet charging patterns, which could further be applied to city grid impacts, fleet optimization, etc. The third section *Time Analysis* is used to get a realistic understanding of how often these electric busses are being utilized in the field. Figure II.2.2.6 contains data from each of the three sections describes above in a report-style format.
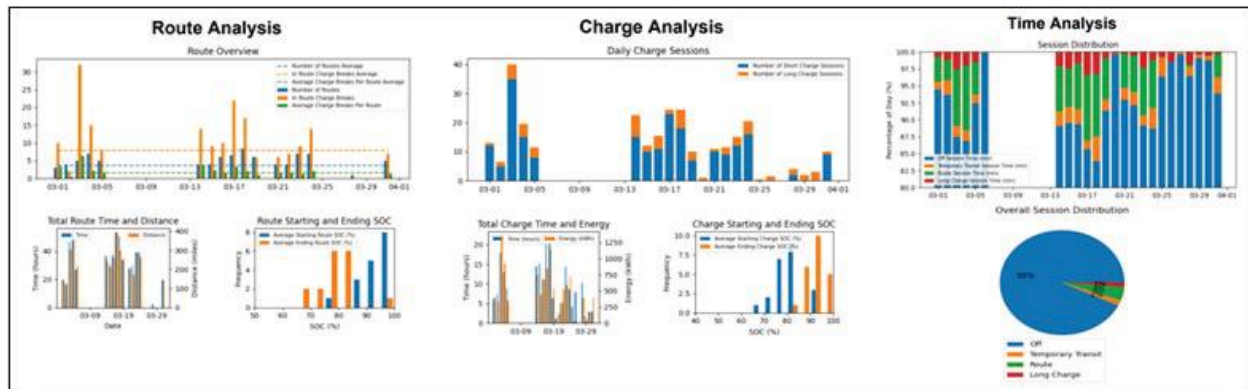
Figure II.2.2.6 - CTA Fleet Utilization Report from 03.01.2022 – 03.31.2022

Oak Ridge National Laboratory Results
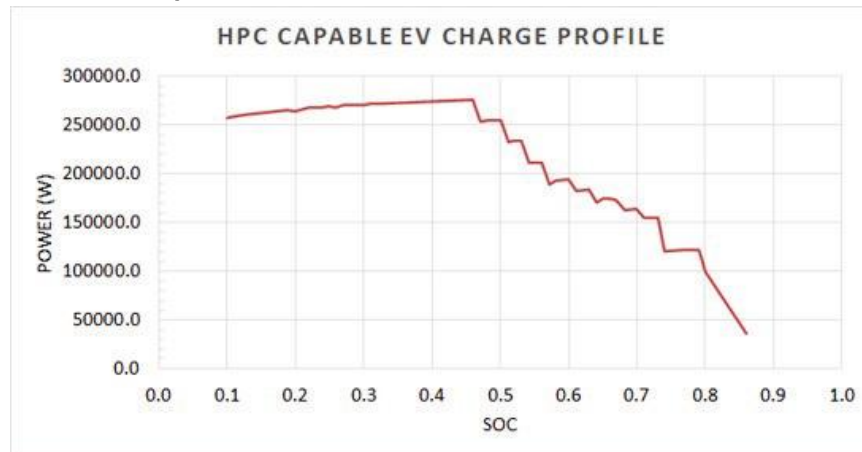
Figure II.2.2.7 - An HPC capable EV charge profile as a function of SOC.

Oak Ridge National Laboratory (ORNL) established and expanded relationships with automotive OEMs and utilized research vehicle assets for use in this project where an example of such data set is provided in Figure II.2.2.7. ORNL is working on standardized test procedures on wireless power transfer (WPT) based EV charging systems (wireless EVSEs) for nominal and off-nominal test conditions. The team will assess the performance of chargers (efficiency and power transfer level) for different z-airgap classes as outlined in SAE J2954 Standard as well as fully aligned and maximum possible x, y, and a combination of x and y-axis misalignment cases.

Performance evaluations will include dc-to-dc (high frequency inverter input-to-battery) efficiency of the system and ac-to-dc (grid-to-vehicle battery) efficiency at 10-20 kW increments for full power range characteristics, power factor, grid-side input AC current total harmonic distortions (THD), fundamental frequency on the resonant stage, load power, input power, electric and electromagnetic field emissions (at the door edge or 0.8 m away from the center of the secondary coil in laboratory setups without vehicle

integrations), and peak output power at nominal z airgap. Physical specifications of the couplers will also be identified such as transmitter and receiver coil mass, coil dimensions, surface power density (kW/m^2) and gravitational or volumetric power density (kW/kg or kW/liter).
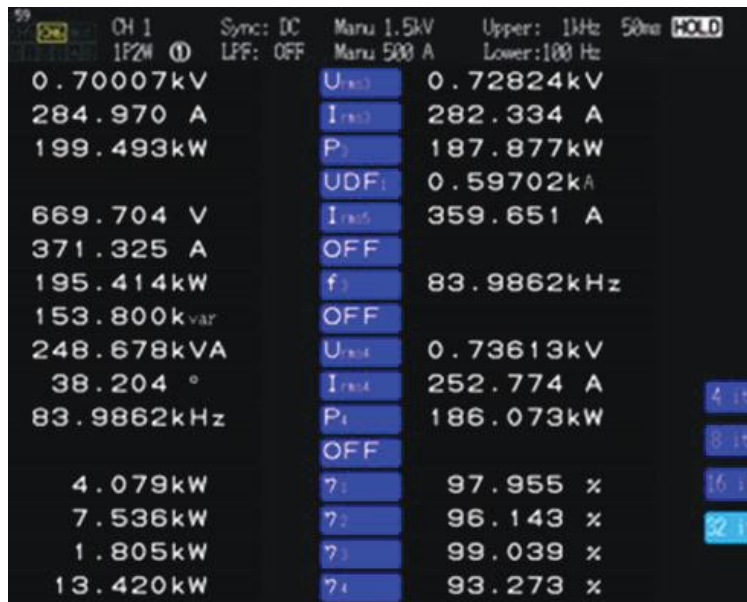
Figure II.2.2.8 - Power analyzer screenshot for 186 kW power transfer to test vehicle with 93.27% dc-to-dc efficiency over 9 inches of power transfer distance.

ORNL is currently working on a 100-kW wireless power transfer system using polyphase coils, a 200-kW wireless power transfer system with elongated double-D coils, and a 300-kW wireless power transfer system with polyphase coils. The wireless EVs performance characterizations will be completed on these systems with efficiencies and performance data recorded at 10-20 kW increments at each power level. An example power analyzer screenshot for 186-kW power transfer to the test vehicle (~199.4 kW input power) is presented in Figure II.2.2.8.

National Renewable Energy Laboratory Results

Lab-Based Hardware Testing

NREL team participated in regularly recurring project review meetings and provided input and feedback as needed on matters related to data collection, analysis, and presentation. NREL team invested significant time and energy engaging EVSE manufacturers to diagnose, troubleshoot, and repair material issues with XFC chargers that prevented full power charging operation and characterization testing. Both XFC chargers have been restored to full power operation as of September 2022. External control of both XFC EVSE by OCPP commands has been fully developed and demonstrated.

Work is ongoing to upgrade supporting equipment needed for EVSE characterization testing: in-house EV emulators will receive hardware that enables 500A simulation capability and upgrade enhanced compact real-time FPGA computational simulators that will emulate EV charging in a stand-alone electrical enclosure. Additionally, power conversion equipment is slated to receive hardware upgrades that increase impedance of the charging circuit to ground in early CY2023.

NREL team took delivery of a CCS-equipped vehicle in April 2022 and have developed the capability to utilize vehicle sensors to query and record charging telemetry utilizing the vehicle OBDII port. When combined with additional NGP-required instrumentation, NREL team is ready to characterize the EV charging envelope, which will begin for nominal and cold-weather testing in December 2022.

Fleet Data Collection

NREL team has signed an NDA with a charging network partner and have completed scripts for API data gathering. 400+ days of data have been collected on seven charging systems and 42 busses (three unique models). NREL team has selected and begun procurement of datalogging equipment and is planning an on-site data collection event with our charging network partner to verify accuracy of collected fleet data. NREL team engaged one potential partner to collect electrified drayage fleet data; this partner declined to participate in NGP fleet data collection and analysis effort.

Conclusions

During the past fiscal year, the NextGen Profiles project team has begun the key characterization work that was laid out in the first project year. With most project partners in place, the year began with the development of data acquisition systems and gathering the test device for characterization. All lab partners have begun the testing and characterization as outlined in our procedures, and some emphasis has been placed on the development of standardized reports, time-series data formats, and report-generation outputs. The data gathered this year and in the early parts of the next will be filtered and analyzed in the next year of the project.

The project group has successfully executed device characterizations that provide the key data required to deliver an initial industry charging performance report at the end of the next fiscal year. The aim of the analysis is to build a knowledge base and glean industry insights to intelligently integrate HPC systems within the grid and among co-located loads and sources. The characterization and dissemination work in the project is critical for understanding the emerging charge performance industry.

Key Publications

1. Dobrzynski, D. 2022. "Next Generation Profiles: High Power Charging Characterization" Presented at the U.S. Department of Energy Vehicle Technologies Office Annual Merit Review, June 22, 2022

Acknowledgements

II.2.3 High-Power Electric Vehicle Charging Hub Integration Platform (eCHIP) (EVs@Scale Consortium)

John Kisacikoglu, Principal Investigator

National Renewable Energy Laboratory
15013 Denver West Parkway
Golden, CO 80401
E-mail: john.kisacikoglu@nrel.gov

Jason Harper, Principal Investigator

Argonne National Laboratory
9700 South Cass Avenue
Lemont, IL 60439
E-mail: jharper@anl.gov

Prasad Kandula, Principal Investigator

Oak Ridge National Laboratory
2360 Cherahala Blvd., Knoxville, TN 37932
E-mail: kandular@ornl.gov

Lee Slezak, DOE Technology Manager

U.S. Department of Energy
E-mail: lee.slezak@ee.doe.gov

Project Introduction

Large-scale adoption of electric vehicles (EVs) will introduce new challenges for high-power charging (HPC), grid load management, and charging facility operations. This type of charging infrastructure is vital to charge the next generation of light-, medium-, and heavy-duty EVs fast enough to make them viable for all use cases. Megawatt-scale HPC stations today vary greatly in facility power usage and communication architecture construction. Three of the most common builds that are available for large HPC site design are shown in Figure II.2.3.1. The unit cost of the site varies based on the selected architecture, site electrical supply, number of ports, and port charging capacity, aside from the control policy implemented. The ability to connect on a common DC bus via a central inverter/rectifier (Figure II.2.3.1 (b) and (c)) reduces the unit cost, especially when the size of the site design increases [1]. Alternatively, having multiple inverters per each port (as with today's commercial off-the-shelf products-Figure II.2.3.1 (a)) would increase the size and number of components. Systems with a common AC bus come with disadvantages, including a higher number of power conversion stages, which lead to increased costs and reduced efficiency. Overall, the common DC bus approach provides heterogeneous port power ratings and upgrades during the lifetime of the station—supporting operation flexibility with minimal investment.

(a) Common AC-bus   (b) Common DC bus   (c) Direct MV SST based design
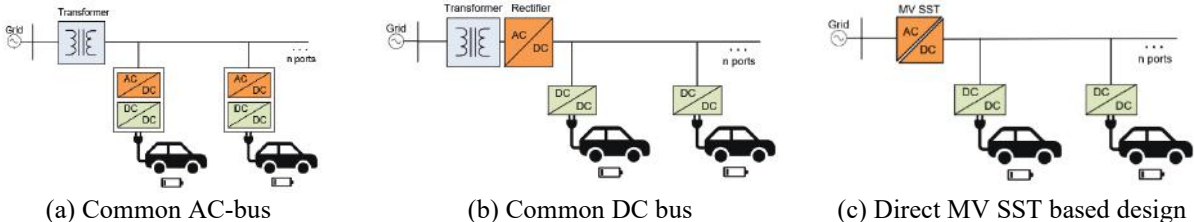
Figure II.2.3.1 Charging site architectures available today.

Today, the SAE J3271 megawatt charging system (MCS) describes the requirements for these types of high-power charging equipment, such as standards for charging connectors, chargers, DC distribution systems, DC protection, and grid interconnection. However, development and adoption of these high-power charging systems are still inadequate. There is a need to design and validate efficient, low-cost, interoperable hardware for high-power DC-hub charging, communication, and control architectures, which are crucial for accelerating adoption of EVs and their infrastructure.

Current initiatives that aim to standardize the operation of DC microgrids in different application areas were researched to develop our approach for the DC charging hub concept in this project. To the best of our knowledge, the following list overlaps with the focus of this project: Current OS protocol [2], Emerge Alliance [3], Open Direct Current Alliance [4], IEEE Standard for MVDC systems on Ships [5], and Electrical Systems Design Criteria and Practices for MVDC [6].

While these standardizations around a DC microgrid approach are promising, a unified approach in industry regarding development of high-power charging stations around this DC-hub concept is lacking. This project aims to fill this gap through developing and demonstrating the DC charging hub approach that leverages the developments made in different application areas. The project objective is to design a high-power, interoperable charging experimental platform to research, develop, and demonstrate integration approaches and technological solutions. The proposed work includes (1) interconnection and management of a grid-tied inverter; (2) development of a DC distribution system that is responsible for system energy management, interoperability, and DC protection; (3) modular DC-DC conversion for vehicle charging; (4) EV charging interface and DC-DC integration; and (5) smart charge control and vehicle-to-edge (vehicle-to-building [V2B], vehicle-to-everything [V2X]) capability.

Objectives

Addressing the challenges for high-power charging systems requires collaboration with industry segments, including the end users and station operators, vehicle manufacturers/partners, charging manufacturers, and utility partners. A successful approach will support 100+ kilowatt (kW) chargers at public light-duty (LD) and medium-duty (MD)/heavy-duty (HD) depots where many chargers are required, reaching 1 megawatt (MW) or more for the site and expand to support 1+ MW chargers where the dwell time for MD/HD vehicles is shorter, potentially resulting in 10 MW of combined load or more for the site.

The proposed plug-and-play solution allows a charging site to organically grow with additional chargers and distributed energy resources (DERs) through predefined compatibility with standards that will ensure interoperability and reduce upfront engineering expense. A common backbone that flexibly supports these use cases across all vocations will demonstrate integration approaches and solutions that overcome barriers for efficiency, cost, and power density. This project will establish existing state-of-the-art efficiency, equipment cost, and power density metrics and show an improvement through the proposed DC-connected site approach.

Overall goals of the project are listed below:

- Broadly identify limitations and gaps in DC distribution and protection systems that would allow for modular high-power charging systems.

- Develop and demonstrate solutions for efficient, low-cost, and high-power-density DC-DC for kW- and MW-scale charging.

- Determine interoperable hardware, communication, and control architectures for high-power charging facilities that support seamless grid integration and resilient operation.

Approach

We have designated four technical topic areas under which this project will develop: i) System power electronics architecture and development, ii) DC distribution bus design and protection, iii) Grid integration,

and iv) Site energy management. Regarding hub architecture, the system will include multiple isolated DC-DC converters connected to the common DC charging hub. One of these DC-DC converters will be developed in-house, while the rest of the converters will be acquired commercial off-the-shelf. The system will have a central grid connected inverter, which handles grid integration. A site energy management (SEM) system will control the operation of the individual system components.

Modeling and Control Hardware-in-the-loop (C-HIL) Evaluation Platform

The C-HIL platform is a critical development stage in this project that will provide a non-destructive real-time simulation environment to develop, test, and verify any DC hub operation and use case. The C-HIL development process comprises several steps, starting from component-level modeling and ending with system-level integration. Testing will be performed at the end to observe and validate the desired operations. The workflow of the CHIL development process is shown in. The completed and ongoing progress of each step in C-HIL are detailed in Phase-1 and Phase-2.
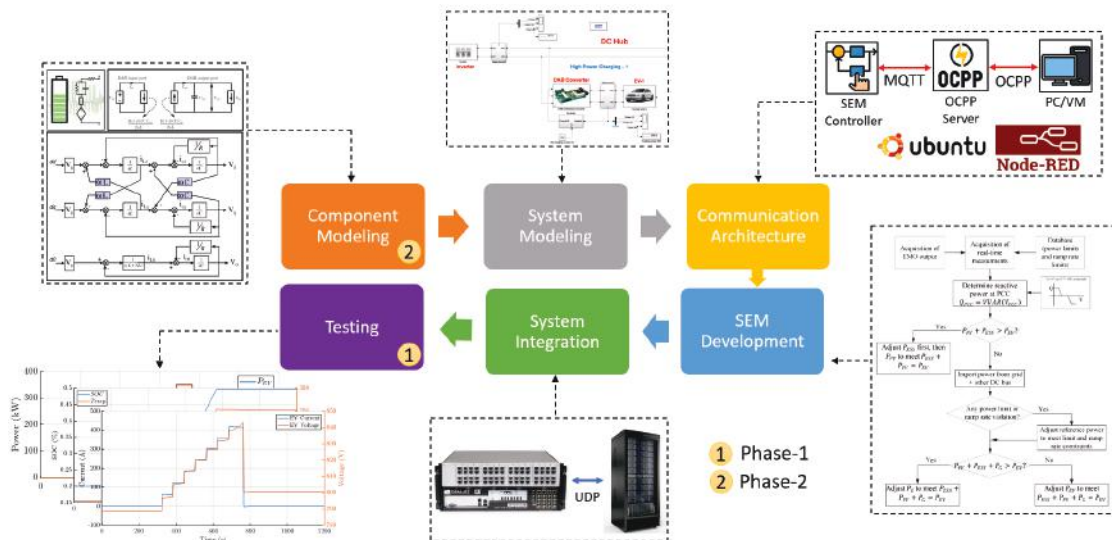
Figure II.2.3.2 C-HIL testbed development process.

The C-HIL Phase-1 has three main component models that are all simulated in real-time: grid-tied inverter, dual active bridge (DAB) bi-directional DC-DC converter, and EV battery. The average models of these components were developed and used for operational and multi-component simulation purposes. System architecture defines how different component models are connected through a DC distribution network. The system architecture for C-HIL Phase-1 is shown in Figure II.2.3.3. The three-phase grid-tied inverter with a DC bus voltage of 1000 V provides power to a DAB DC-DC charger that can provide up to 400 kW to an EV. The EV battery model was configured to represent the characteristics of a Hyundai IONIQ 5.
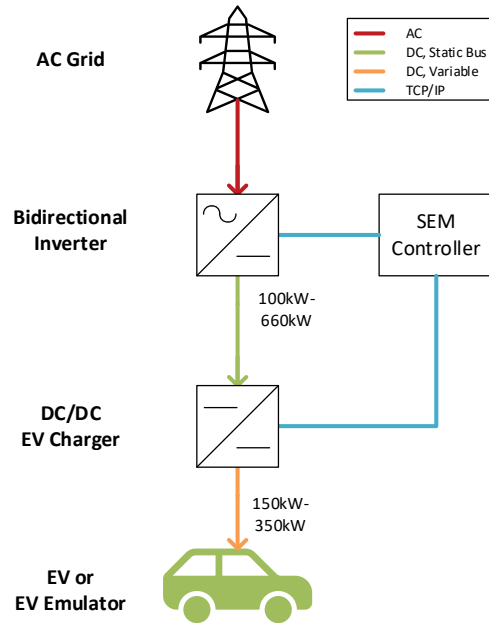
Figure II.2.3.3 System architecture of C-HIL Phase -1.

The communication architecture defines how system components communicate with the Site Energy Management (SEM) controller that runs on the server computer. The online communication between the real-time simulator and the server computer is performed through the user datagram protocol (UDP) connection. The SEM controller generates the real-time charging power commands (set points) and sends them to the EV charger through the Open Charge Point Protocol (OCPP) 1.6 protocol. All DC hub operations can be controlled, monitored, and recorded from the server computer. SEM development is an ongoing process where the objectives and needs of the controller operation are defined based on the system architecture. The SEM controller in C-HIL Phase -1 was designed to manipulate the EV's charging power in real time.

The developed models, systems, and controllers were integrated together using the OPAL-RT real-time simulator and a server computer. The system components and the DC hub were simulated on the OPAL-RT whereas the communication and charging protocols as well as the SEM controller were realized on the server computer. Finally, the integrated system was extensively tested, and the measurements were recorded for the validation of the expected controller operation. This marked the completion of C-HIL Phase-1, and its initial test results are presented in the Results section of this report. C-HIL Phase-2 is in the modeling stage since new components are required for Phase-2 use cases. Most of the components developed in C-HIL Phase-1 were also used in Phase-2 to avoid duplicating efforts.

DC-DC Universal Power Electronics Regulator (UPER)

The objective of this task is to develop the isolated DC-DC DAB converter, hereby referred to as UPER, interfacing the DC distribution bus and the vehicle. The first step is to identify the specifications and requirements for such a charger. In this context, a brief survey of various commercial chargers was conducted. The following observations were made after this initial search:

- Commercial DC-DC converter building blocks with medium frequency isolation are in the range of 50-125 kW.

- To achieve higher power, typically 350 kW, several of these building blocks are connected in parallel.

- A higher power building block (175 kW) is available but utilizes low frequency (60 Hz) isolation.

- Most of the chargers are unidirectional.

- In some of the charging systems, stationary storage is connected at the DC bus, to reduce peak demand charges.

- Chargers today can deliver charging voltage in the range of 250-950 V.

In terms of future charging requirements, the following observations were made:

- Off-road vehicles like battery locomotives may transition to 1500 V charging voltage, driven by increased battery capacity and thereby high charging power requirements.

- eVTOLs (electrical Vertical Take-off and Landing aircrafts) may transition to 1500 V charging voltage to reduce the charging time.

- Bi-directional power transfer will be required to enable V2X.

Considering the current state-of-the art (SOA) charger and future charging requirements, the requirements for the DC-DC converter to be developed in this project are identified below:

- A high-power modular building block (i.e., 350 kW) to enable 1+ MW charging

- An increased DC bus voltage (i.e., 2000 V) and increased vehicle battery voltage (i.e., 1500 V)

- Bi-directional power transfer

- Compact design to enable portability and plug-n-play capability

The requirements used to develop the specifications for a 1500 V class charger are shown in Table II.2.3.1. However, a 1500 V class vehicle does not exist today. To enable demonstration on a real vehicle, a 1000 V class charger is being built, and its specifications are listed in Table II.2.3.1 as well. The charger to be developed will involve Multi-Dimensional Improvement as shown in Figure II.2.3.4.

Table II.2.3.1 Charger Specifications

Parameters	1500 V class 350 kW charger	1000 V class 175 kW/350 kW charger
V_{in}	1500-2000 V	800-1200 V
V_{out}	500-1500 V	200-950 V
I_{max}	250 A	225 A/ 450 A
Efficiency	>99%	>98.5%
Temperature	-30°C to 50°C	-30°C to 50°C
Communication	CAN	CAN
Power flow	Bi-directional	Bi-directional
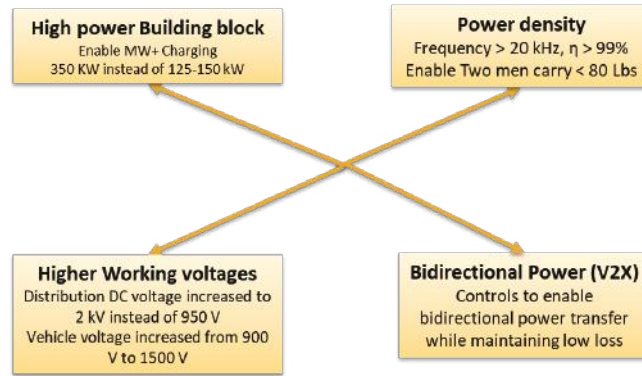
Figure II.2.3.4 Charger improvements compared to SOA.

As mentioned in the previous section, a major requirement for the DC-DC converter is the bi-directional charging capability. A literature review was performed to select the optimal topology for bi-directional power flow. The common topologies, LLC, CLLC, and DAB are compared in Table II.2.3.2. Each converter has merits and demerits. However, the concerns with DAB can be addressed through controls and was hence chosen as the choice for the charger.

Table II.2.3.2: DC-DC Converter Configuration: LLC, DAB, and CLLC Comparison.

	LLC	DAB	CLLC
Efficiency: ZVS range	Not good for wide voltage range	Not good for wide voltage range	Not good for wide voltage range
Controllability: Light load power regulation	Medium	High	Medium
DC bias currents-Transformer saturation	Caps block DC	Control based	Caps block DC
Voltage/Current Stress	Resonant cap has high voltage stress		
Bi-directionality	Not well suited		
Output current ripple	Large filter cap required		Large filter cap required
Leakage inductor		Relatively larger: high circulating reactive power	
Medium freq Xmr stress	Sinusoidal voltages	Square voltages	Sinusoidal voltages

* Green: Good, Yellow: Manageable, Red: Major constraint

Integration of UPER, Spec Module, and Site Energy Management

Three key components for implementing bi-directional charging in the eCHIP project are (1) hardware and firmware development of supply equipment communications controller (SECC), (2) developing communication protocol between the SECC and DC-DC UPER, and (3) designing and developing the software architecture as well as main applications for the SEM System.

Hardware and Firmware development

Leveraging Argonne National Laboratory's (ANL) previous work and experience with SECC development, the approach for this project was to integrate the ANL SpEC module with the ORNL UPER DC-DC power

electronics to create a bi-directional DC coupled charger. ANL researchers will utilize both the Gen I (Figure II.2.3.7 on the left) and Gen II (Figure II.2.3.7Figure II.2.3.7 on the right) SpEC modules in the development and demonstration phase of the project. Leveraging the DIN 70121 stack, researchers will update the firmware to implement the ISO 15118-20 standard to accomplish bi-directional DC charging. Custom firmware will be written to interface with the UPER and the SEM system.

Figure II.2.3.5 SpEC module Gen I (left) and Gen II (right)

Communication Interface Development

To ultimately demonstrate bi-directional DC charging with the Oak Ridge National Laboratory (ORNL) UPER, researchers must collaboratively define the interface requirements and protocols. ORNL and ANL researchers worked closely together to learn the intricacies of the UPER power electronics as well as the DIN/ISO charging standard requirements. Clearly defining communication protocol and logic will help the labs create emulators of the SECC or UPER controllers. Development of emulators will aid researchers in integration testing and reduce the risk of future integration issues when onsite testing occurs.

Site Energy Management System

One of the critical barriers to implementing a high-power charging facility is that interoperable hardware, communication, and control architectures do not exist to support seamless grid integration and resilient operation. Researchers will be tasked with defining requirements as well as development and deployment of a SEMS. The SEMS energy management scheme will flexibly handle the high-level control of the system, including DER management, vehicle charge scheduling, site load forecasting, and device onboarding. A modular open-source approach will allow scalable control across many use cases. This task will reduce barriers to integration by improving connectivity, defining communication and control approaches, and enabling a simplified integration approach with the distribution system (i.e., utilities).

Development of Power Hardware-in-the-loop Experimental Testbed

This work proposes the development of a power hardware-in-the-loop (P-HIL) testbed to support model validation, testing, and demonstration. The testbed will demonstrate high-power charging through a DC network. Multiple DC-DC chargers, distributed energy resources (DERs) and energy storage systems will be integrated into a common DC power distribution network. The implementation of the testbed is divided into three phases. The first two phases will be conducted in the Energy System Integration Facility (ESIF) at the National Renewable Energy Laboratory (NREL). P-HIL Phase-2 of the test bed is depicted in Figure II.2.3.6 where two EVs and two vehicle emulators are charged using a Tritium PKM150, UPER, and other available commercial-off-the-shelf (COTS) chargers (to be decided). In this setup, the SEM controller will accept feedback from the system nodes (i.e., chargers, DERs, grid-tied inverter, etc.) and direct their operation to optimally manage power and energy and react to grid fluctuations, dynamic charging demand, system faults, and other events. We will emulate the grid dynamics utilizing a grid simulator driven by models running on an OPAL-RT real-time simulator.
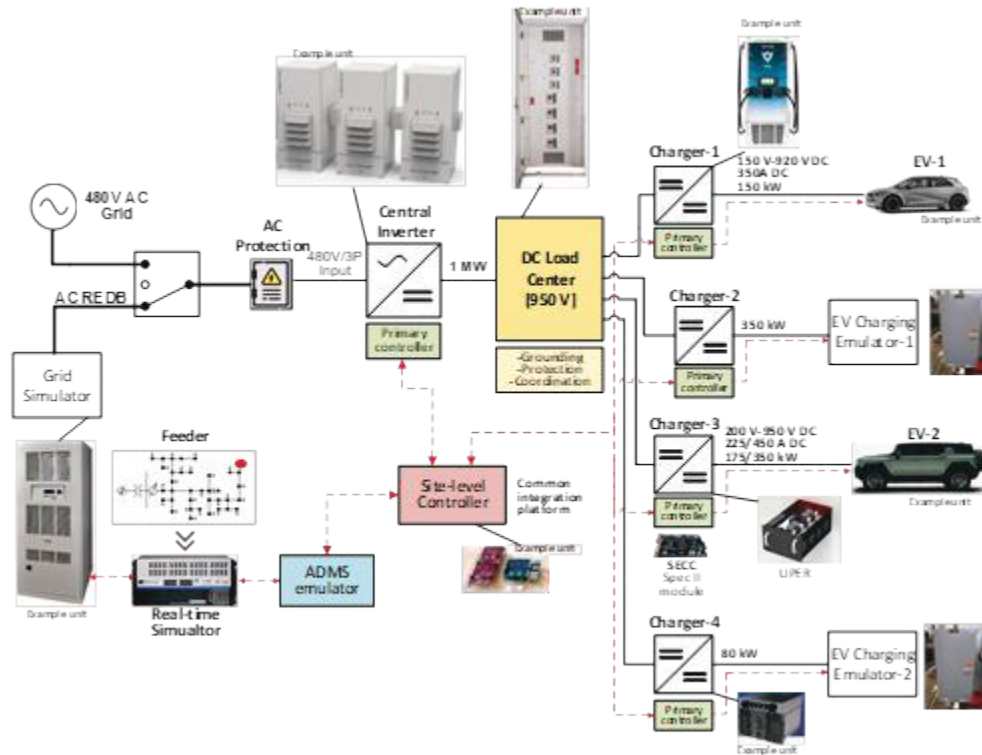
Figure II.2.3.6 100(+) kW Level DC Charging Hub Demonstration (P-HIL Phase-2).

To reach the P-HIL Phase-2 setup described above, an intermediary P-HIL Phase-1 testbed is constructed as depicted in Figure II.2.3.7. The P-HIL Phase-1 testbed accommodates the charging demonstration of an EV (E3) and an EV emulator (E5), charged through a Tritium PKM150. A grid-connected Anderson (E1) power conversion unit (PCU), capable of sourcing 660 kW, connects to the DC Research Electrical Distribution Bus (DC-REDB). DC-REDB (B1) is a highly configurable electrical power network rated at (+/-)500 VDC or 1000 VDC and 1600 A. The Tritium charger (E2) connects to the DC-REDB though the DC-braker (B1) which has established communication with the ESIF supervisory control and data acquisition (SCADA) system. The Tritium PKM150 is a DC-DC charger which is OCPP compliant and is designed to provide 150 kW maximum power. The EV, a Hyundai Ioniq 5, has an 800 V, 77.4 kWh battery pack capable of charging at a maximum power of 225 kW approximately.

The EV emulator (also known as charge control box-CCB) is an NREL-developed product which can emulate the charging dynamics of different vehicles and is rated to accommodate up to 350 kW charging. The vehicle models in the CCB are developed in OPAL-RT real time simulator platform. The EV emulator feeds the received power back to the grid through an AV900 (E6) PCU. The controller providing power reference to the charger is implemented in Python, hosted on CPU1. Data exchange between the controller and the OCPP Server is implemented with the Message Queuing Telemetry Transport (MQTT) protocol communicating with a local MQTT broker. OCPP is the application protocol which will be used to communicate with the charger. The OCPP Server is implemented on the NodeRed platform, hosted on CPU3, utilizing an ANL-developed OCPP server library [7].

The P-HIL Phase-1 demonstration platform has multiple data collection points identified as MP1-MP6 in Figure II.2.3.7. Of these data collection points, MP3, MP4 and MP5 are scoped; MP1 and MP6 are data collected from PCUs, and MP2 is obtained from the facility's DC-REDB monitoring system. The data collected from these measurement points will be analyzed to define the DC bus operating limitations and the effect of local controller dynamics on the system as a whole. In addition to this, data from the site level

controller (CPU1), MQTT Broker (CPU2), OCPP Server (CPU3) and EV emulator model in OPAL-RT (CPU4) are all logged and identified as LD1-LD5 in Figure II.2.3.7. These captured logs will enable the assessment of command/response latency which will define constraints and boundary conditions for the SEM controller development.
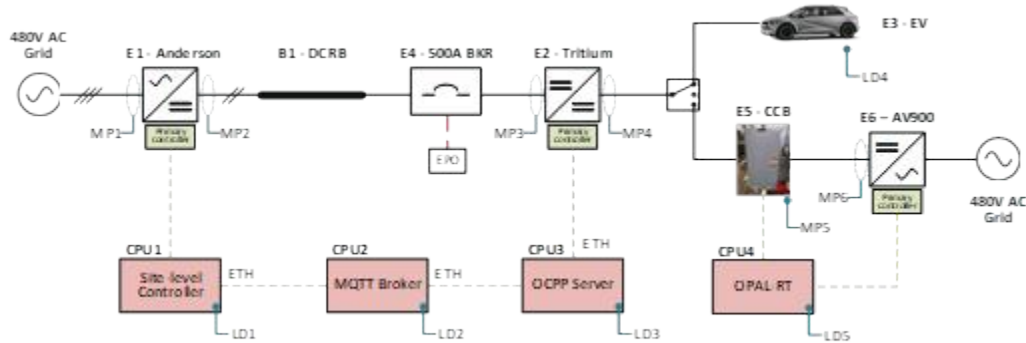
Figure II.2.3.7: 100(+)kW Level DC Charging Hub Demonstration (P-HIL Phase-1).

The Phase-1 demonstration platform and associated research activities will provide concrete insights into the capabilities and limitations of DC-REDB as a potential 950V DC load center for Phase-2. In parallel, a separate DC load center is under development which would serve as a one-stop interconnection for all the EV chargers as shown in Figure II.2.3.6. Experimentation and data collection in Phase-1 will also help define the parameters and limitations for the DC load center.

Results

Modeling and Control Hardware-in-the-loop (C-HIL) Evaluation Platform

The initial test performed in C-HIL Phase-1 involves manipulating the EV charger power within its operation range (0-350 kW) through the SEM controller running on the server computer. The goal of the test is to validate the successful communication and protocol implementation and observe the impacts of charging on the system components. There is currently no BMS implementation in the EV battery model. Therefore, the EV battery is charged at the charging power decided by the SEM. With the integration of the BMS, the EV will decide how much current will be requested from the charger based on its battery characteristics and limits. The test was performed for 895s during which the SEM controller periodically increased the power set point of the charger from 0 kW to 350 kW and stops the charging. Figure II.2.3.8 shows the electrical measurements of the critical system components resulting from the real-time simulation.

(a) Inverter DC current and voltage

(b) EV current and voltage

(c) EV reference power set point, actual power, and energy

(d) EV battery SOC and temperature.
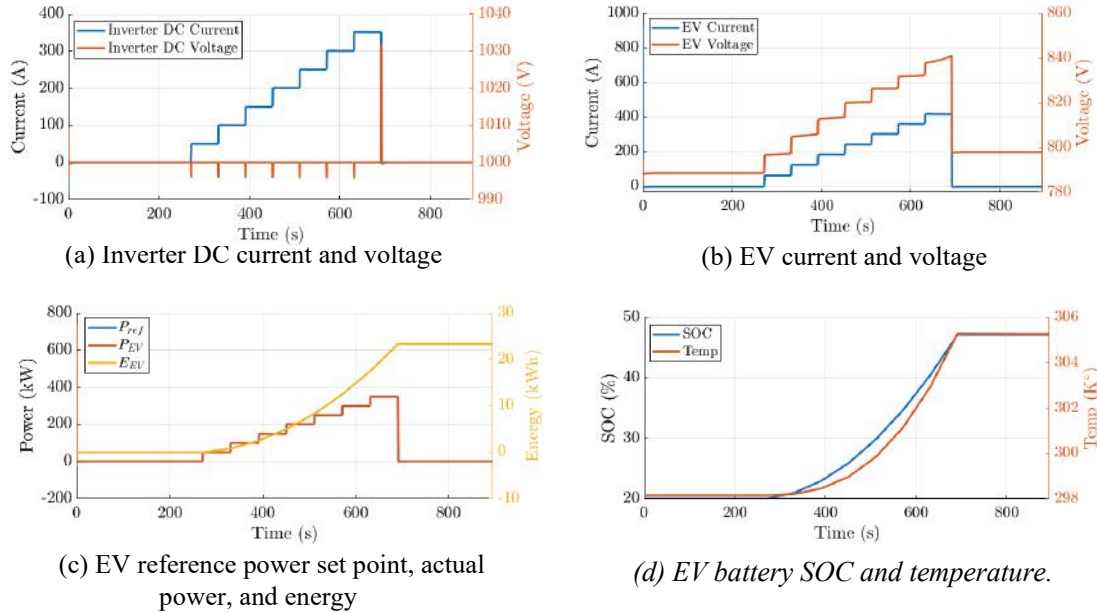
Figure II.2.3.8 Initial results obtained from C-HIL Phase-1.

It was observed that the EV charger followed the reference power set points generated by the SEM validating the successful communication protocol implementation (Figure II.2.3.8(b-c)). As a result of the charger operation, the EV battery was charged from 20% SOC to 47% SOC within around 408 s of charging, increasing the battery temperature from 298 K to 305 K (Figure II.2.3.8(d)). The impact of the EV charger actions is observed on the DC side voltage of the inverter (Figure II.2.3.8(a)). As the power set points increased, the DC bus voltage decreased for a very short duration (~0.5s), and it was quickly recovered by the inverter's primary controller. This test achieved its objective in terms of successful controller operation validation and charging impact observations.

DC-DC Universal Power Electronics Regulator (UPER)

In this task, first, a detailed design of the 1000 V charger was completed. The schematic and the parts are shown in Figure II.2.3.9, and the BOM is shown in Table II.2.3.3.
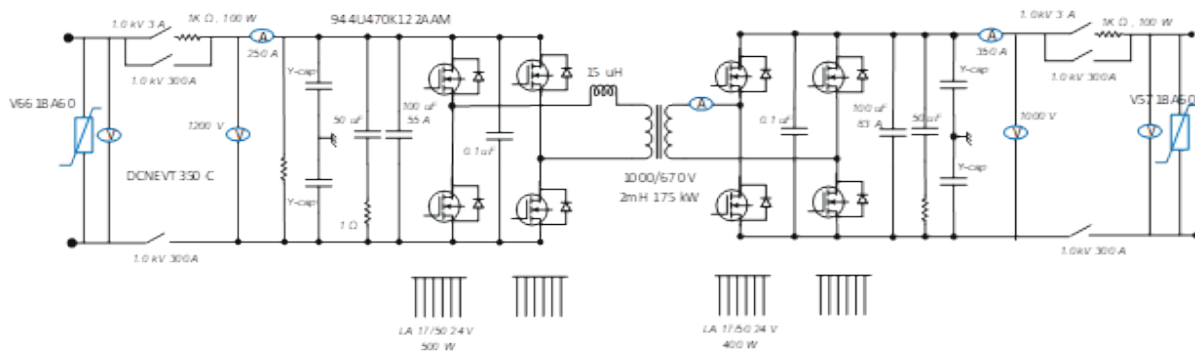
Figure II.2.3.9 1000 V class charger schematic.

Table II.2.3.3: 1000 V Class Charger BOM.

Item	Part No.	Qty
1700 V, 280 A, 5.8 mOhm, SiC devices	MSCSM170AM058CT6LIAG	4
1.7 kV Gate drives	Custom	8
Film caps 1400 V, 100 uF,	944U470K122AAM	2
Film caps 1400 V, 0.47 uF		4
LEM current sensor > 300 A	LF 310-s	2
1000 V, Voltage sensor,	ORNL sensor	2
20 kHz 175 kW Transformer	Custom	1
15 uH inductor	Custom	1
Heatsink	LA 17/100	4
Contactor 900 V, 10 A	DCNEVT350-C	2
Contactor 900 V, 300 A	DCNEVT350-C	2

Similarly, a detailed design of the 1500 V class charger was completed. The schematic and the parts are shown in Figure II.2.3.10, and the BOM is shown in Table II.2.3.4.
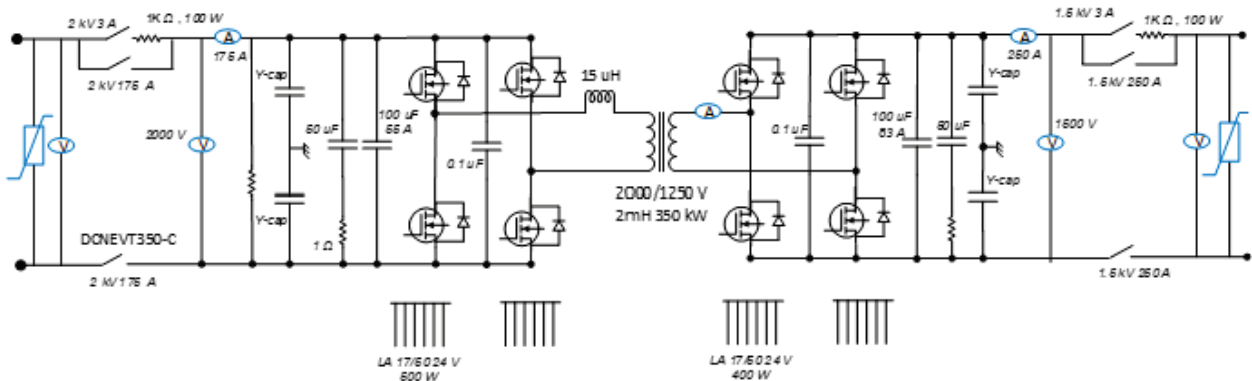
Figure II.2.3.10 1500 V class charger schematic.

Table II.2.3.4: 1500 V Class Charger BOM

Item	Part No.	Qty
3300 V, 500 A, SiC devices	5SNG 0500X330100/ ORNL Custom devices	4
3.3 kV Gate drives	Custom	8
Film caps 2000 V, 100 uF,	FFVE6N0356K7X	2
Film caps 1500 V, 35 uF	FFVE6N0356K7X	2
LEM current sensor > 300 A	LF 310-s	2

1000 V, Voltage sensor,	LV 100-1500/SP3	2
10/20 kHz 350 kW Transformer	Custom	1
15 uH inductor	Custom	1
Heatsink	LA 17/200	4
Contactor 900 V, 10 A	DCNEVT350-C	2
Contactor 900 V, 300 A	DCNEVT350-C	2

One of the issues with the DAB converter is that the soft switching can be easily achieved when the input/output voltage ratio is in unity and load is not too low. In charger applications, the voltage ratio will be non-unity and will vary greatly, especially when the same charger must be used with both 400 V class and 800 V class vehicles. Soft switching is necessary to maintain high efficiency and also to limit noise, which is especially important with SiC devices. Novel modulation was developed to achieve soft switching under the complete range (e.g., 250-950 V, 0 -225 A for the 1000 V class charger). The schematic and the simulation results are shown in Figure II.2.3.11.

(a) DAB schematic

(b) Charging current reference (yellow) and actual (blue)

(c) Leakage inductor current – Boost mode (Source: 800 V, Vehicle: 750 V, Xmr: 800 V:670V)

(d) Leakage inductor current – Buck mode (Source: 800 V, Vehicle: 600 V, Xmr: 800 V:670V)
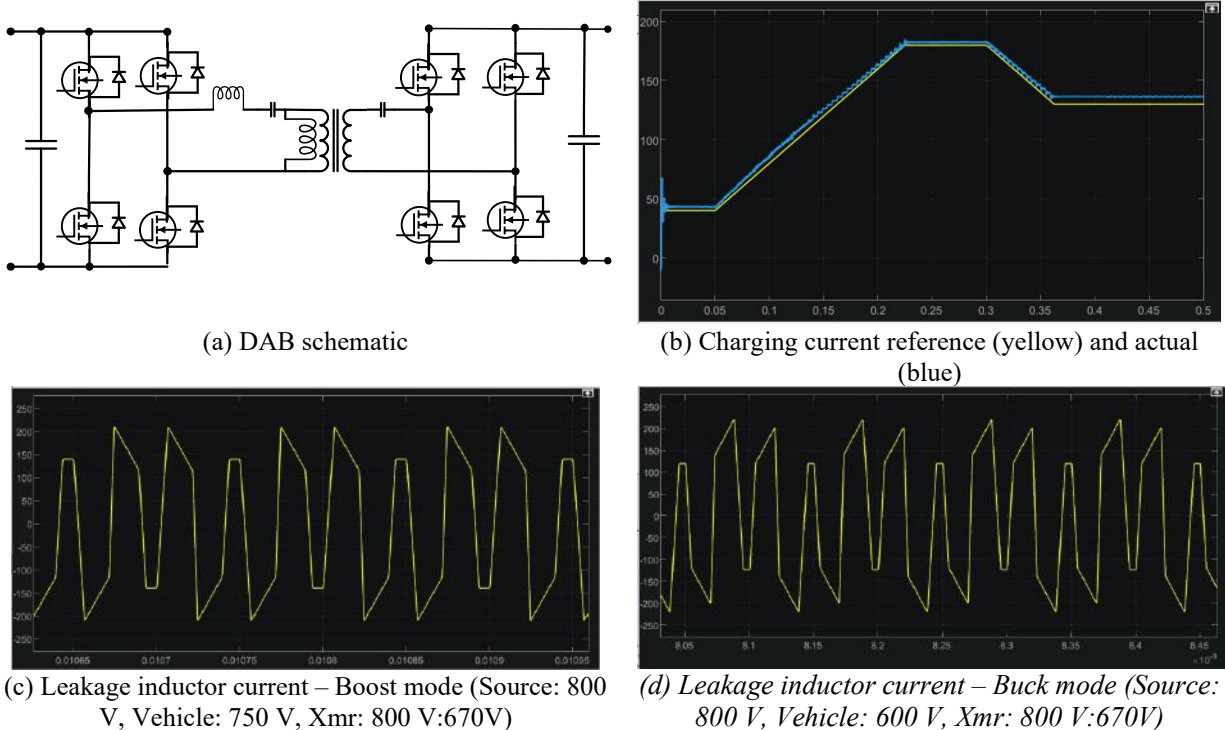
Figure II.2.3.11 DAB simulation results.

A custom gate driver for 1700 V SiC devices was developed. A test setup was built to characterize the 1700 V 280 A SiC devices, gate drives, 800 V/670 V 175 kVA, busplane, and thermal performance. The test setup is shown in Figure II.2.3.12. The custom gate drive is verified to have successfully turn on 1700 V, 280 A SiC devices up to 1200 V, 250 A, as shown in Figure II.2.3.13. Device turn-off tested successfully up to 1200 V, 250 A, as shown in Figure II.2.3.14. Device stress was limited to < 200 V verifying bus-plane design. Turn-off loss and dv/dt data was collected to estimate efficiency and noise performance.
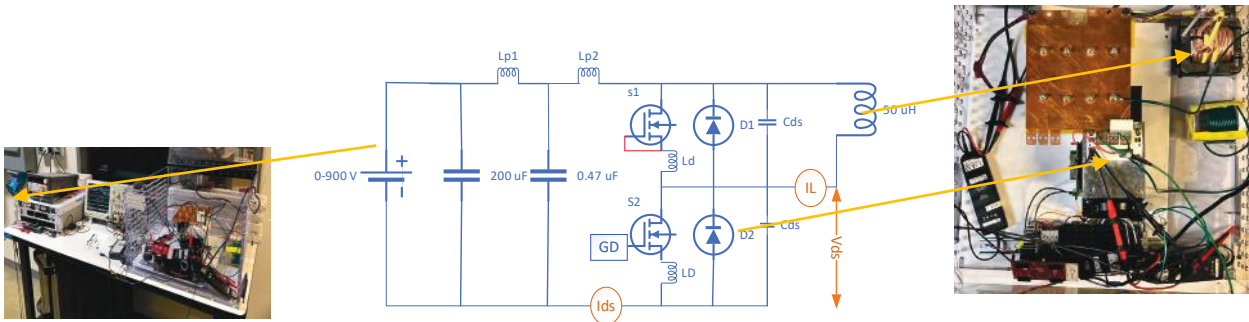
Figure II.2.3.12 Double pulse test circuit for 1700 V device.
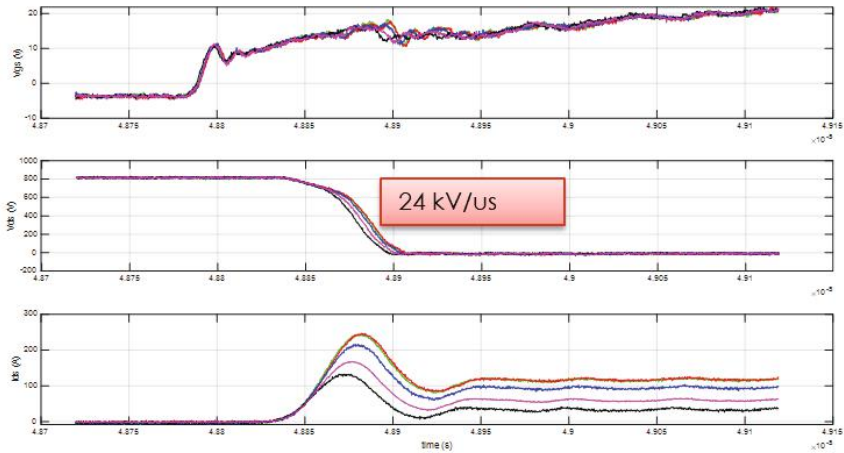
Figure II.2.3.13 Turn on results at 800 V, Rg_ext = 2 Ω.
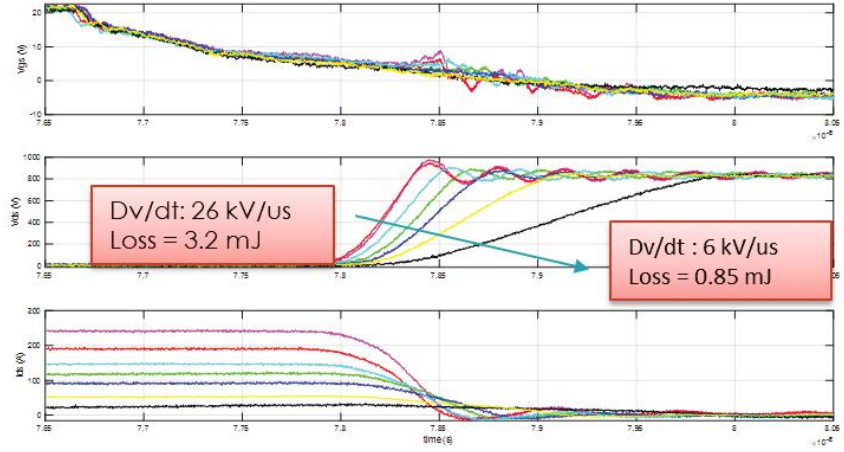
Figure II.2.3.14: Turn off results at 800 V, Rg_ext = 2 Ω

Data collected in the pulse test is used to estimate converter efficiency. Expecting a full-load efficiency of %98.5 (transformer efficiency ~%0.25).
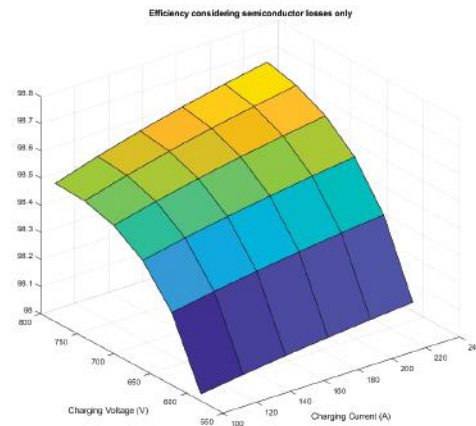
Figure II.2.3.15 1000 V class charger estimated efficiency.

The 175 kVA transformer has been designed and built as shown in Figure II.2.3.16.

Figure II.2.3.16: 175 kVA 1000V, 800 V Transformer based on Nanocrystalline core and Litz wire.

Integration of UPER, Spec Module Integration, and Site Energy Management

Hardware and Firmware development

Leveraging the custom DIN 70121 application written for the Gen I SpEC module, we modified this codebase to integrate with the UPER controller. We are taking a phased approach to this development and decided to first demonstrate DIN 70121 charging with SpEC/UPER EVSE. This first step will allow researchers to work out any integration bugs early in the integration process. Once DIN 70121 charging is demonstrated, ANL researchers will begin focusing on developing an ISO 15118-20 stack.

All CCS based high level communication (HLC) between the EVSE and EV requires an Efficient XML Interchange (EXI) codec (coder/decoder). Unlike the DIN 70121 or ISO 15118-2 codec, there are no open source 15118-20 codecs available and/or suitable for the embedded needs of our research. As such, other paid options are being explored.

Communication Interface Development

The SpEC module and UPER will communicate with each other using the Controller Area Network (CAN) protocol. For fiscal year 2022 (FY22), ANL focused on the development of a CAN message set between the UPER and SpEC modules which includes defining power requirements, limits, controls, status, along with defining individual message bytes, their timing considerations, scaling factors and what their corresponding

values signify. ANL also developed specifications of the wiring interface between the two modules, as well as necessary physical considerations. This was condensed into block diagrams for clarity, as shown in Figure II.2.3.17.
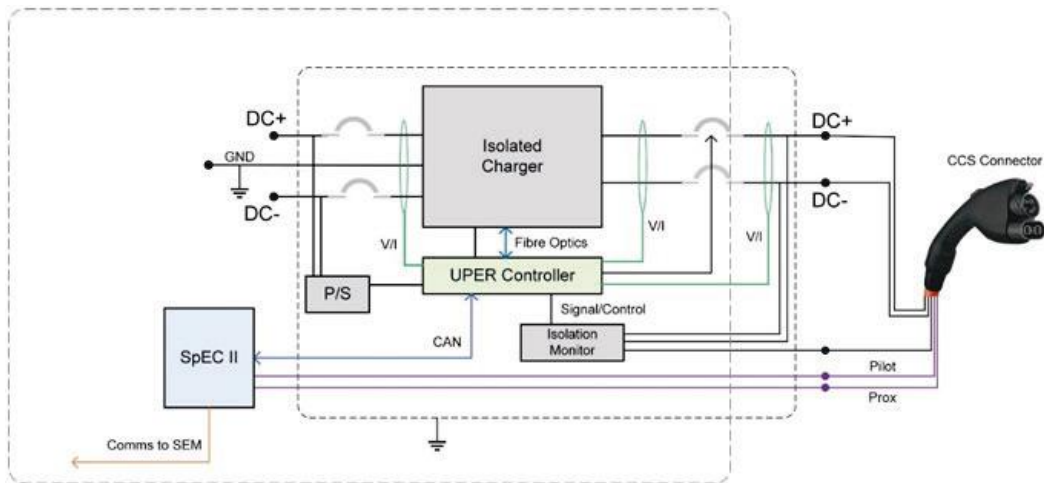
Figure II.2.3.17 Block Diagram of DC coupled bi-directional charger

ANL researchers implemented the UPER CAN messages in firmware on the SpEC I for testing. All of these CAN messages are also compiled into a database file (.dbc) using Vector CANdb++ as shown in Figure II.2.3.18. This is then used to actively develop a UPER emulator in Node-RED to allow rapid testing of simulated as well as actual charge sessions before the UPER power electronics hardware is ready.

Figure II.2.3.18 UPER CAN database file in Vector CANdb++

Site Energy Management System

Argonne and NREL researchers worked together early in the project's development to define the challenges, requirements, and possible approaches to site energy management of a high-power charging facility. The team is continuing discussions with respect to use case/control objectives, cyber security requirements, and measurement requirements. It was determined that the first approach to deploying a SEM system would leverage past research work at both ANL and NREL. However, in future years, other systems or applications will be explored. ANL and NREL will co-develop the SEM system platform which will be implemented onsite at NREL.

Given the need for defining the integration requirements of the DC-coupled bi-directional charger, it was decided that the charger will integrate into the SEM system OCPP and MQTT. OCPP 1.6j will first be utilized to handle charge session monitoring and management, while MQTT will be utilized to deploy non-standardized messages for control and monitoring. ANL developed the core profile as outlined in OCPP 1.6-J protocol, and this will be deployed for initial testing of the UPER/SpEC charger.

Development of Power Hardware-in-the-loop Experimental Testbed

The primary components of the P-HIL Phase-1 testbed was successfully acquired and integrated in the NREL ESIF facility. The facility's experiment readiness verification has been completed and full power flow has been achieved, delivering 150kW charging to a Hyundai Ioniq 5 EV as shown in Figure II.2.3.19. A data collection system was implemented to query and record diagnostic parameters directly from the EV using ISO 14229-3 (UDSonCAN) with the Vector Canalyzer platform.

Local current control was achieved on the Tritium PKM150 charger. The two charging sessions shown in Figure II.2.3.19 capture the results from this local charge control. During the first charging session, Session1 (t=0s to t=200s), the current is limited to 50A. It can be observed in Figure II.2.3.19 that the EV requests and is provided the full 50 A within this limit during this charging session. In the second charging session, Session2 (t=200s to t=550s), the local current limit has been removed and the charging is only limited by the Tritium PKM150's maximum power capability of 150 kW. During this period, it can be observed in that the vehicle is provided with 190 A approximately. Throughout both charge sessions, the EV battery voltage and SOC track within expected value ranges for these parameters.
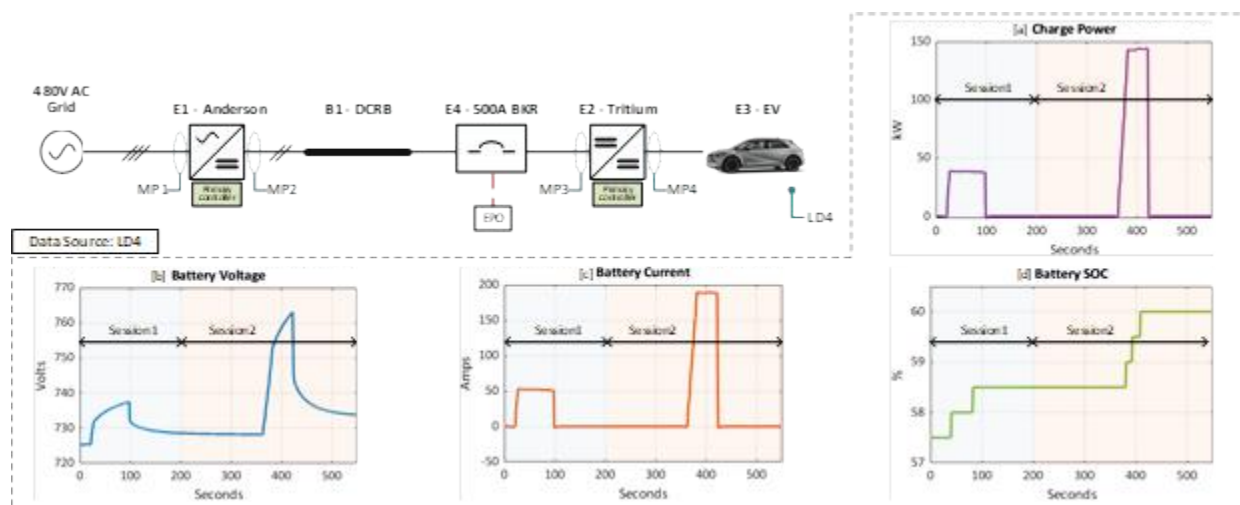
Figure II.2.3.19 100(+)kW Level DC Charging Hub Demonstration (phase-1) – Two charging sessions with local current control implemented to observe EV charging characteristics (a) Charging Power (b) Battery Voltage (c) Battery Current (d) Battery SOC.

These results show the latest status of the P-HIL Phase-1 testbed's incremental build up. The successful demonstration of power flow provided validation of the primary equipment specifications and the core strategy for the development of this testbed. Additional control and measurement capabilities can now be investigated and added to the existing capabilities. Implementing OCPP-based remote power control is the next target for the P-HIL Phase-1 testbed.

Conclusions

This project aims to develop a high-power, DC distribution-based, interoperable, grid-integrated charging hub platform that can scale to MW+ charging hardware development and testing. DC-hub approach has several advantages over the AC-hub including converter size and system efficiency, ease of control, and a single grid-integration point, i.e., a central inverter. The first year of the project focused on scoping the work to determine

the fundamental components of the system. We reviewed the available DC-based standards and specifications via outreach to the industry. The eCHIP team developed off-line and real-time station component models to test the first phase of the component operation in a non-destructive manner. The project team also determined the component software and hardware integration requirements. Finally, we designed a 350 kW DC-DC DAB converter hardware and started the hardware component testing to verify its suitability for the station operation.

Key Publications

1. A. Meintz, L. Slezak, M. J. Kisacikoglu, P. Kandula, T. Bohn, E. Ucer, J. D. Harper, M. Mohanpurkar, "Electric Vehicles at Scale (EVs@Scale) Laboratory Consortium Deep-Dive Technical Meetings: High Power Charging (HPC) Summary Report," NREL/PR-5400-84093. [Online]. Available: https://www.nrel.gov/docs/fy22osti/84093.pdf

References

1. H. Tu, H. Feng, S. Srdic and S. Lukic, "Extreme fast charging of electric vehicles: a tehcnology review," IEEE Tran. Transport. Electrific., vol. 5, no. 4, pp. 861-878, 2019.

2. "Current/OS based DC microgrids," Current OS Foundation, [Online]. Available: https://currentos.foundation/. [Accessed 18 11 2022].

3. "Open Industry Association," EMerge Alliance, [Online]. Available: https://www.emergealliance.org/. [Accessed 18 11 2022].

4. "Open Direct Current Alliance (ODCA) founded," DC-INDUSTRIE, [Online]. Available: https://dc-industrie.zvei.org/news/open-direct-current-alliance-odca-gegruendet. [Accessed 18 Nov. 2022].

5. "1709-2018 - IEEE Recommended Practice for 1 kV to 35 kV Medium-Voltage DC Power Systems on Ships," IEEE, 7 Dec. 2018. [Online]. Available: https://ieeexplore.ieee.org/document/8569023..

6. N. Doerry, H. Lopez and T. A. Barnard, "Preliminary Electrical Systems Design Criteria and Practices (Surface Ships) for Medium Voltage Direct Current (MVDC) Applications," NAVSEA, 2020.

7. Jason D. Harper, "node-red-contrib-ocpp," 16 Nov 2022. [Online]. Available: https://github.com/Argonne-National-Laboratory/node-red-contrib-ocpp.

II.3 Wireless Power Transfer (WPT) Enabling Technologies

II.3.1 High-Power and Dynamic Wireless Charging of Electric Vehicles (ORNL, INL, and NREL)

Veda Prakash Galigekere, Principal Investigator

Oak Ridge National Laboratory
2360 Cherahala Boulevard
Knoxville, TN 37932
Email: galigekerevn@ornl.gov

Richard Carlson, Principal Investigator

Idaho National Laboratory
2525 North Freemont Avenue
Idaho Falls, ID 83415
E-mail: richard.carlson@inl.gov

Andrew Meintz, Principal Investigator

National Renewable Energy Laboratory
2360 Denver West Parkway
Golden, CO 83415
E-mail: Andrew.meintz@nrel.gov

Lee Slezak, DOE Technology Manager

US Department of Energy
Email: lee.slezak@ee.doe.gov

Start Date: October 1, 2019   End Date: March 31, 2022
Project Funding: $4,000,000   DOE share: $4,000,000   Non-DOE share: $0

Project Introduction

High-power dynamic wireless charging is seen as an enabling technology to minimize range anxiety and reduce the onboard energy storage required for many electric vehicles. Previously, researchers determined that a high-power transfer level of 200 kW can significantly reduce the infrastructure cost compared with lower power solutions. A 200 kW dynamic wireless charging system, including the primary and secondary side power electronics, resonant network, and couplers, were designed, developed, and validated individually. The performance was deemed satisfactory for integration and evaluation as a system. This report focuses on the laboratory validation of a 200 kW dynamic charging system in stationary and dynamic charging modes.

Objectives

The overall goal of this project is to develop (design, model, simulate, and analyze) and validate a high-power static and dynamic wireless charging system that can be viably applied to roadway and traffic conditions in the United States.

The specific objectives are

1. to conduct experimental validation of power transfer capability of a dynamic wireless power transfer (DWPT) transmitter system embedded in concrete,

2. to conduct experimental validation of a dynamic wireless charging system in the laboratory prior to testing with couplers embedded in the roadway, and

3. to plan and lay out validation of a roadway-embedded 200 kW DWPT system at the American Center for Mobility (ACM).

Approach

Experimental Validation of Power Transfer Capability of DWPT Transmitter System Embedded in Concrete

The 200 kW DWPT system comprises the transmitter coil embedded in the roadway and will have the capability to transfer 200 kW efficiently and safely through the roadway material between the transmitter and the receiver. Some of the key requirements of the roadway related to the planned 200 kW DWPT demonstration are that it must

- retain structural integrity to enable safe movement of vehicle;

- not heat up at all or must heat up within safe limits because of the electromagnetic fields;

- not interfere with the power transfer, thereby enabling an efficient electrified roadway; and

- be easy to install and retrieve for structural analysis.

The computer-aided design (CAD) model of the 200 kW DWPT transmitter is shown in Figure II.3.1.1. The 200 kW transmitter has ferrite bars underneath the litz wire to enhance the mutual inductance and minimize leakage field, but the closely spaced ferrites encased in concrete create a challenge because the aggregate material will not be able to flow owing to limited space. Additionally, steel rebars cannot be used because they are ferromagnetic and would heat up, causing a potential safety issue in addition to losses.
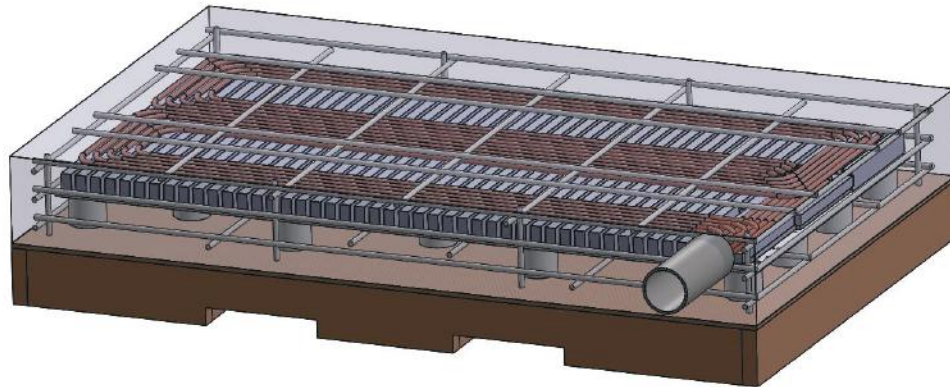
Figure II.3.1.1 CAD model of the 200 kW DWPT transmitter coupler.

Consequently, the coils were designed using fiberglass rebars as reinforcement. The design was created following standards from American Concrete Institute (ACI) 318 [1] and ACI 440 [2]. Owens Corning #4 fiberglass rebar with a diameter of 0.5 in. was added to improve the mechanical performance. The 200 kW DWPT system was first tested with the ground-side coupler not concretized to obtain the baseline data, and then the concretized ground-side coupler was tested to observe any changes in performance.

Figure II.3.1.2 Laboratory setup for characterization of 200 kW DWPT system prior to concretizing the ground coil.
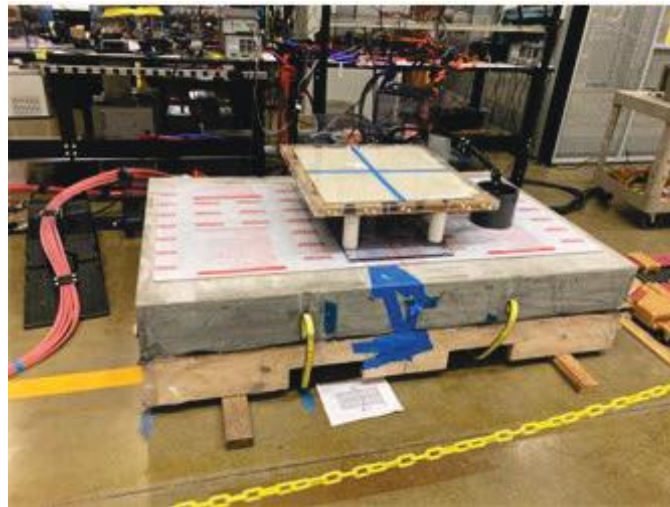
Figure II.3.1.3 Laboratory setup for characterization of 200 kW DWPT system with concretized ground coil.

High Power Dynamic Power Transfer Functionality Validation Using Dynamic Inductive Charging Emulator

To evaluate the 200 kW DWPT system, a dynamic inductive charging emulator (DICE) was set up in the laboratory and is shown in Figure II.3.1.4 and Figure II.3.1.5. This served as an intermediate step between stationary power transfer evaluation and the planned validation at ACM in Michigan. The main features of the DICE are the following:

- Track length: 18 m

- Payload capability: 100 kg

- Speed: approximately 9 m/s (20 miles per hour)

- x, y, and z coil misalignment capability

- Automated and programable operation modes

- Capability to incorporate with HIL software

Figure II.3.1.4 Top view of the ORNL DICE depicting the overall track length of 18 m.
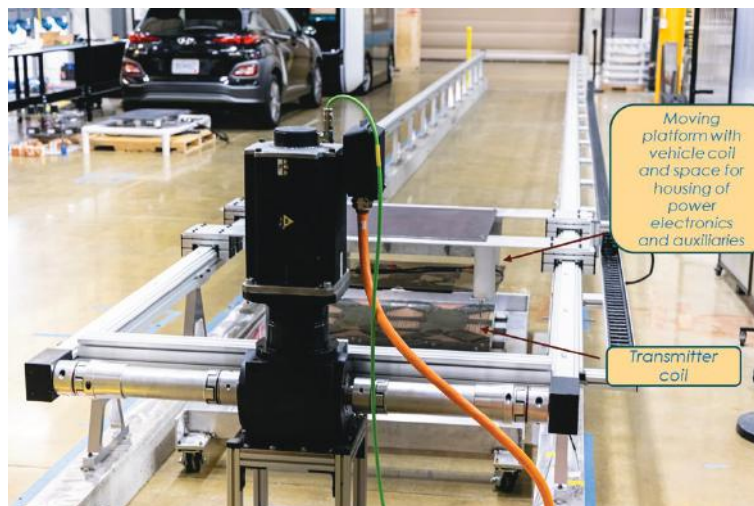
Figure II.3.1.5 ORNL 200 kW DICE.

The 200 KW transmitter was set between the dynamic rails, and the receiver and the vehicle-side power electronics were placed on the moving platform. The transmitter and the receiver were set up to mimic the planned layout at ACM. Figure II.3.1.6 shows the 200 kW dynamic wireless charging system integrated with the DICE. The transmitter and the receiver have a coil-to-coil distance of approximately 10 in., which accounts for the ground clearance of a Hyundai Kona and the 4 in. of concrete on top of the transmitter, mimicking the embedment process. The secondary-side receiving coil, resonant capacitors, high frequency rectifier, dc–dc converter, and the auxiliaries (cooling system and power supplies) were all securely mounted on the moving platform.

Figure II.3.1.6 ORNL 200 kW DICE.

Results

Experimental Validation of Power Transfer Capability of DWPT Transmitter System Embedded in Concrete

The 200 kW DWPT system was tested in stationary mode with the ground-side coil prior to and after being concretized. In both cases, the power transfer distance (coil-to-coil), the input voltage, and the load were the same. There was no noticeable difference in performance after the ground-side transmitter was concretized. The power analyzer results, measuring an output power of 186.8 kW with 93.775% efficiency, are shown in Figure II.3.1.7.

Figure II.3.1.7 Power transfer validation of 200 kW DWPT couplers with the transmitter embedded in 500 PSI epoxy grout. The output power was 186.8 kW, and efficiency was 93.775%.

Power Transfer Profile Evaluation

The 200-kW dynamic charging system was evaluated in 2 steps using the DICE.

- Stationary tests at discrete points were located along the length of the intended travel of the receiver coil. These points provide the power transfer profile before the vehicle is actively moving under electrified conditions and serve as an intermediate step.

- Dynamic tests involved the receiving system along with the moving platform moving continuously across the length at different speeds to mimic the movement of a vehicle.

Stationary Tests at Discrete Points

The 200 kW DWPT system was characterized at discrete points along the length of the transmitter. The variation of output power as a function of relative position along the transmitter is shown in Figure II.3.1.8, and Figure II.3.1.9 shows the efficiency as a function of relative position along the transmitter.
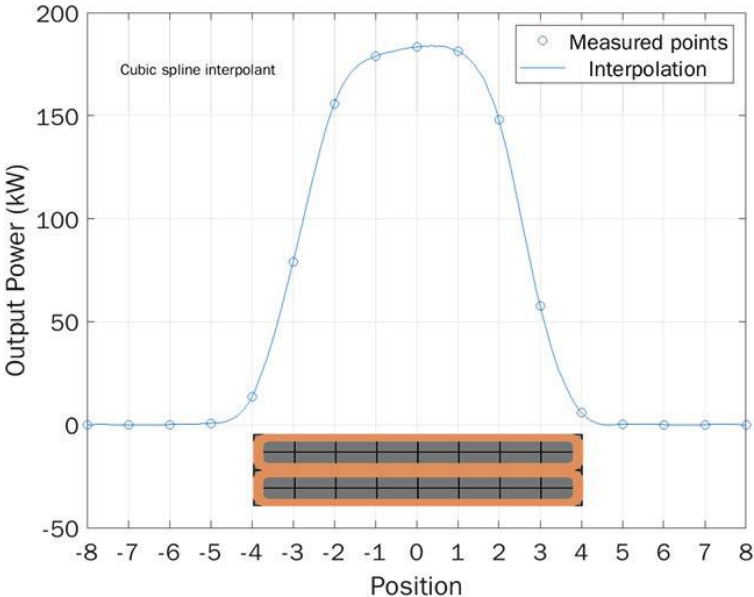
Figure II.3.1.8 Profile of measured output power of 200 kW dynamic charging system measured along the length of the transmitter.
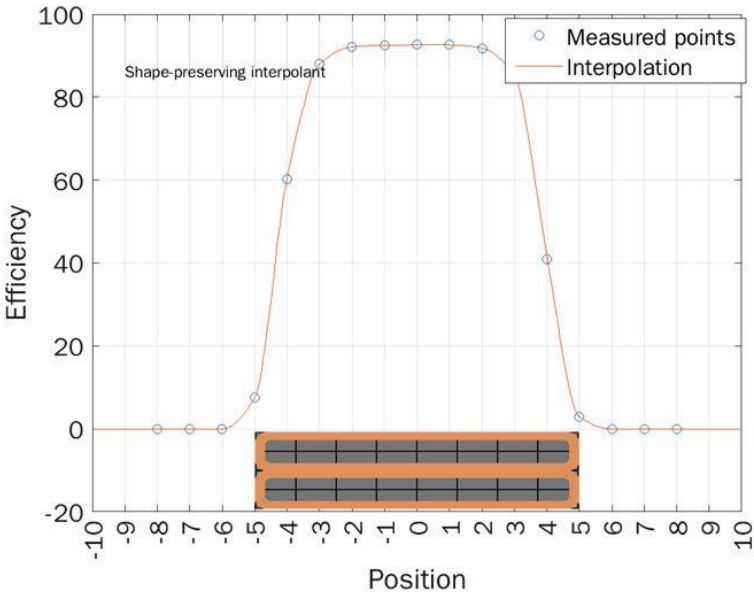
Figure II.3.1.9 Profile of measured efficiency of 200 kW dynamic charging system measured along the length of the transmitter.

This discrete step test corresponds to the vehicle being aligned along the horizontal, or *y*, axis of the transmitter at different positions along the *x* axis, or the axis in the driving direction of the vehicle. The input power of the system was limited to 200 kW owing to source limitations. Figure II.3.1.8 shows that the maximum power transfer reached 186 kW at position 0, which is the perfectly aligned condition. The output power was restricted to 186 kW because the input source was limited to 200 kW.

Dynamic Tests

The primary-side power electronics were energized when the receiver side was moved to position −10, which corresponds to the vehicle coil outside the coupling region of the transmitter. The receiver system was then moved to position +10 traversing the entire length of the transmitter. The power transfer profile was observed to be smooth, and all the parameters were observed to be like what was observed in the discrete step test, indicating smooth dynamic operation. The recorded output voltage and current for one of the dynamic tests conducted at 193 kW is shown in Figure II.3.1.10.
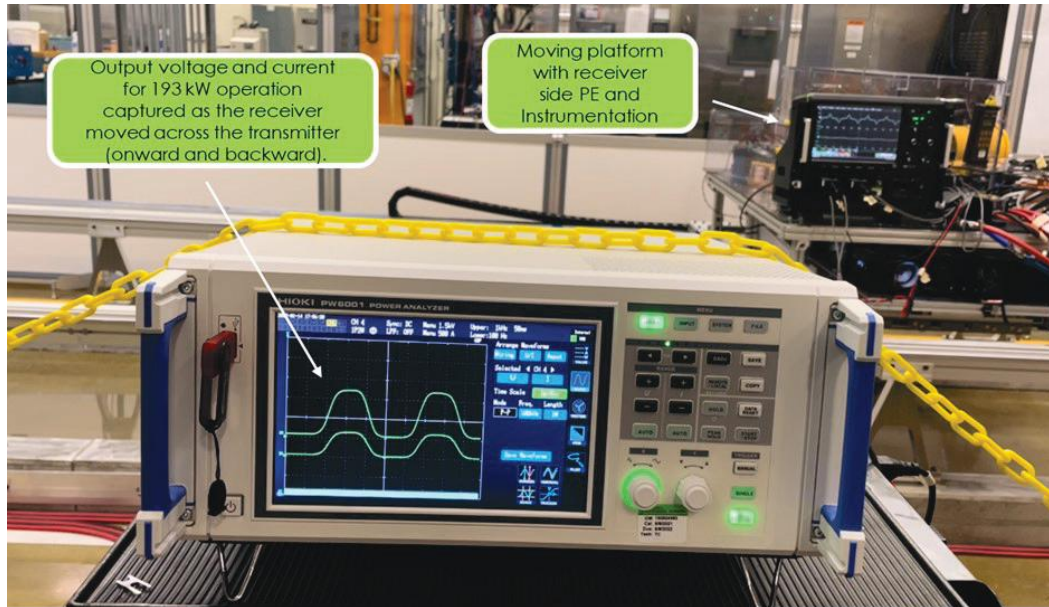
Figure II.3.1.10 The recorded output voltage and current for one of the dynamic tests conducted at 193 kW.

Conclusions

- Concretized coil was designed, and four-ground side units were built per the guidelines in References [1], [2], [3]. The electrical behavior was characterized before and after the concretization process, and the electrical behavior remained unchanged, suggesting the coil is suitable for deployment from the perspective of power transfer capability.

- Laboratory characterization of the 200 kW DWPT system was carried out in stationary and dynamic power transfer modes using the DICE. The rated power (200 kW input) tests indicated successful operation in both stationary and dynamic modes, thereby indicating viability of vehicle-integrated dynamic charging tests with couplers embedded in the roadway.

Key Publications

1. Xue, L., et al. "Design and Analysis of a 200 kW Dynamic Wireless Charging System for Electric Vehicles." 2022 IEEE Applied Power Electronics Conference and Exposition (APEC) (2022): 1096–1103. doi: 10.1109/APEC43599.2022.9773670.

References

1. American Concrete Institute Committee 318. Building Code Requirements for Structural Concrete (ACI 318-08) and Commentary. Farmington Hills, Michigan: American Concrete Institute, 2008.

2. American Concrete Institute Committee 440. ACI PRC-440-07 Report on Fiber-Reinforced Polymer (FRP) Reinforcement for Concrete Structures. Farmington Hills, Michigan: American Concrete Institute, 2007.

3. American Association of State Highway and Transportation Officials (AASHTO). AASHTO LRFD Bridge Design Specifications. AASHTO, 2017.

Acknowledgements

II.3.2 Misalignment Tolerant Three-phase Wireless Fast Charging System for EVs – (TCF: ORNL, Stellantis)

Veda Prakash Galigekere, Principal Investigator
Oak Ridge National Laboratory
2360 Cherahala Boulevard
Knoxville, TN 37932
Email: galigekerevn@ornl.gov

Richard Scholer, Manager
Charging Systems
Stellantis
Email:richard.scholer@stellantis.com

Lee Slezak, DOE Technology Manager
US Department of Energy
Email: lee.slezak@ee.doe.gov

Start Date: December 1, 2021	End Date: September 30, 2024	
Project Funding: $750,000	DOE share: $375,000	Non-DOE share: $375,000

Project Introduction

Wireless power transfer (WPT) based wireless electric vehicle (EV) charging offers the convenience of automated contactless charging which is suitable for autonomous EVs and automated charging procedure. High-power wireless charging is an attractive feature as the customer does not have to handle high power equipment. Current wireless EV charging systems being considered in SAE J2954 are limited to 20 kW in power level, but there is a need to scale up the power level to 50 kW to reduce the charging time particularly for light-duty EVs [1]. Conventional single phase wireless EV charging systems are limited in power density and specific power consequently limiting the wireless EV charging from realizing fast charging. Polyphase wireless charging systems offer significant power density and specific power compared to single phase systems owing to a more uniform electromagnetic field distribution and better utilization of allotted space and volume. Polyphase wireless EV charging technology has been validated at 50 kW in the laboratory as a benchtop system and the overall objective of this project is to develop a vehicle integrated 50 kW polyphase wireless charging system with sufficient tolerance to misalignment and interoperability.

This project is a team effort between Oak Ridge National Laboratory (ORNL) and Stellantis with ORNL the designated project lead. ORNL will develop the primary side and secondary side power electronics, couplers, and resonant network and Stellantis will provide the platform vehicle and support in vehicle integration and characterization.

Objectives

The objective of this project is to develop a prototype system and reference design for the DC-to-DC power conversion stages for a 50kW WEVC system including ground-side inverter, ground and vehicle electromagnetic couplers and resonant networks, and vehicle side rectifier. The prototype system will be used to compare efficiency and performance against existing WEVC systems. Interoperability performance of the three-phase system with the existing standard approaches (circular, DD) will be important since public locations may have a mix of products. The three-phase system has an advantage in this area because it can be made to be interoperable with both circular and DD systems in the naturally aligned case through a simple modification of the power electronics architecture. This contrasts with interoperability between single phase circular and DD, where the ground assembly and vehicle assembly must be purposefully misaligned to achieve the best magnetic coupling. This further exacerbates EMC issues but should not be the case with the three-phase system.

Approach

The overall approach is to design, develop, and perform benchtop validation of 50 kW wireless EV charging system based on the specifications provided by Stellantis in year 1. The system will then be integrated with a platform vehicle and characterized for performance and interoperability in year 2. The detailed approach in year 1 to develop the 50-kW wireless EV charging system is

- Design misalignment tolerant polyphase wireless charging couplers for different airgap zones, Z1, Z2, and Z3 targeting 50 kW output power.

- Conduct a comparative study of the following two resonant networks: (a) LCC for both ground and vehicle coils (LCC-LCC) and (b) LCC for the ground coil and LC parallel for the vehicle coil (LCC-LCP).

- Design and simulate resonant networks for the Z1, Z2, and Z3 coils with the same tuning network for the ground coils.

Design of 50 kW Polyphase Couplers

Three phase wireless charging system consists of three bipolar phase couplers to deliver 50 kW output power. The size of the transmitter pad is dominated by the required high misalignment tolerance and size of the receiver pad minimized to reduce the additional weight to the vehicle.

Table II.3.2.1 Target and Measured Primary Coil inductances of 4 Concretized 200 kW Transmitters

Z Class	Ground clearance (mm)
Z1	100 to 150
Z2	140 to 210
Z3	170 to 250

Design specification

Three different polyphase wireless charging systems are designed for three different Z-classes to deliver 50 kW output power. The ground clearance specifications for different vehicles are adopted from the SAE J2954 standard, as shown in Table II.3.2.1. While Table II.3.2.1 shows a range of ground clearance for each Z-class, the design considers the maximum gap, such as 150 mm for Z1, 210 mm for Z2 and 250 mm for Z3. The larger ground clearance reduces mutual flux between the transmitter and receiver pads. Therefore, either the transmitter pad or the receiver pad, or both needs to be increased to compensate the increased airgap. In this design approach, the transmitter is kept the same, and the receiver size is increased for the higher Z-classes. The specification of the misalignment tolerance is adopted from the SAE J2954, which requires 100mm misalignment tolerance along the side-to-side of the vehicle and 75 mm misalignment tolerance along the length of the vehicle. The inductance matrix obtained from the finite element analysis (FEA) based simulation is then utilized to perform resonant network analysis using circuit simulation package PLECS for preliminary validation of power transfer capability. Additionally, the component stresses can also be evaluated.

Results

The relative position of the receiver pad compared to the transmitter pad for aligned and misaligned pads are shown in Figure II.3.2.1. The relative positions and dimensions of the transmitter and receiver pad for different airgaps are shown in Figure II.3.2.2. The figure shows the receiver size increase with the increased airgap, while the transmitter size is kept the same.
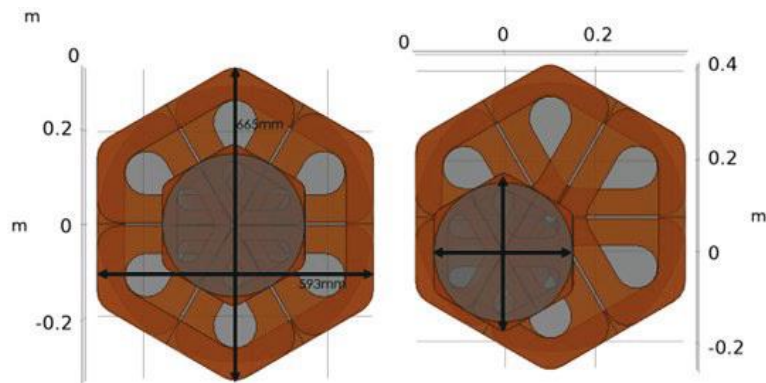
Figure II.3.2.1 Relative position of the receiver pad for aligned and maximum misaligned position.

Figure II.3.2.3 shows the detailed winding diagram for the receiver for Z1, Z2, and Z3 classes. The Z1 receiver is consists of the 4 turns with AWG6 litz wire, the Z2 and Z3 receivers are consisting of 4 turns of AWG4 Litz wire to accommodate higher current. The transmitter coil, which is common to all three charging pads, is made with 6 turns of two parallel AWG6 wire. All the litz wire are assumed to be made with AWG42 strands to minimize the ac resistance due to high frequency operation in high leakage magnetic flux.
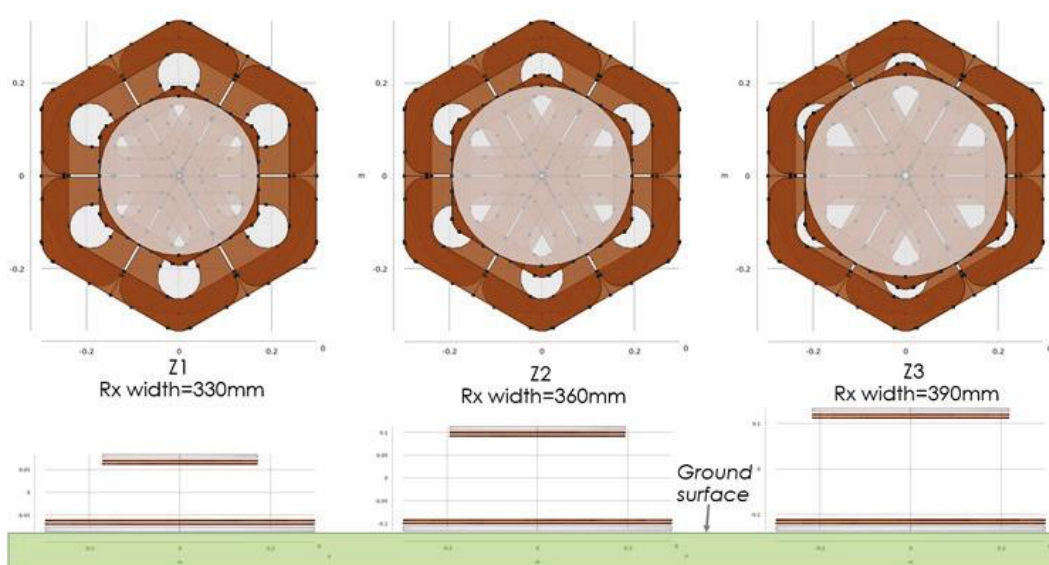
Figure II.3.2.2 Dimension of the transmitter and receiver pads for different Z-classes.
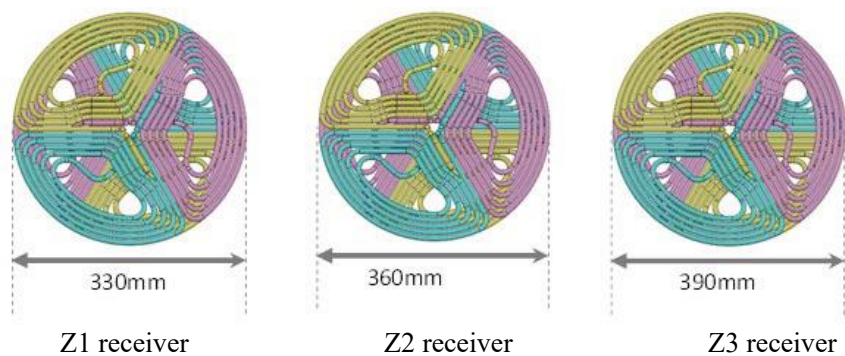
Figure II.3.2.3 Detailed receiver wire routing for three different Z-classes.

The inductance matrixes among the three phases of the transmitter and receiver pads can be defined as,

$$
L = \begin{bmatrix}
L_a & L_{ab} & L_{ac} & M_{ax} & M_{ay} & M_{az} \\
L_{ba} & L_b & L_{bc} & M_{bx} & M_{by} & M_{bz} \\
L_{ca} & L_{cb} & L_c & M_{cx} & M_{cy} & M_{cz} \\
M_{xa} & M_{xb} & M_{xc} & L_x & L_{xy} & L_{xz} \\
M_{ya} & M_{yb} & M_{yc} & L_{yx} & L_y & L_{yz} \\
M_{za} & M_{za} & M_{zc} & L_{zx} & L_{zy} & L_z
\end{bmatrix}
$$

where a, b, and c represent the three phases of the transmitter pad, and x, y, and z represent the three phases of the receiver pad. The inductance matrix from the FEA analysis for different Z-classes are given below.

$$
L_{z1} = \begin{bmatrix}
57.58 & -19.47 & -19.47 & 5.40 & -2.56 & -2.56 \\
-19.47 & 57.55 & -19.44 & -2.56 & 5.40 & -2.56 \\
-19.47 & -19.44 & 57.55 & -2.56 & -2.56 & 5.40 \\
5.40 & -2.56 & -2.56 & 11.56 & -3.80 & -3.81 \\
-2.56 & 5.40 & -2.56 & -3.80 & 11.56 & -3.81 \\
-2.56 & -2.56 & 5.40 & -3.81 & -3.81 & 11.56
\end{bmatrix} \mu H
$$

$$
L_{z2} = \begin{bmatrix}
55.04 & -18.23 & -18.23 & 3.55 & -1.73 & -1.73 \\
-18.23 & 55.01 & -18.20 & -1.73 & 3.56 & -1.73 \\
-18.23 & -18.20 & 55.01 & -1.73 & -1.73 & 3.56 \\
3.55 & -1.73 & -1.73 & 12.71 & -4.14 & -4.15 \\
-1.73 & 3.56 & -1.73 & -4.14 & 12.71 & -4.15 \\
-1.73 & -1.73 & 3.56 & -4.15 & -4.15 & 12.71
\end{bmatrix} \mu H
$$

$$
L_{z3} = \begin{bmatrix}
54.40 & -17.92 & -17.91 & 3.01 & -1.47 & -1.47 \\
-17.92 & 54.38 & -17.888 & -1.47 & 3.01 & -1.48 \\
-17.91 & -17.89 & 54.373 & -1.47 & -1.48 & 3.01 \\
3.01 & -1.47 & -1.4745 & 14.27 & -4.66 & -4.66 \\
-1.47 & 3.01 & -1.4787 & -4.66 & 14.27 & -4.66 \\
-1.47 & -1.48 & 3.013 & -4.66 & -4.66 & 14.27
\end{bmatrix} \mu H
$$

Comparative Study of LCC-LCC and LCCP Resonant Networks

Since both LCC and LCP tuning networks for the vehicle coil led to a current source behavior, a desirable feature for performing constant current charging over a wide range of battery voltage, they are chosen for a comparative study. Figure II.3.2.4 shows the PLECS model for the polyphase WPT system with LCC for the ground coil and LCC or LCP for the vehicle coil.
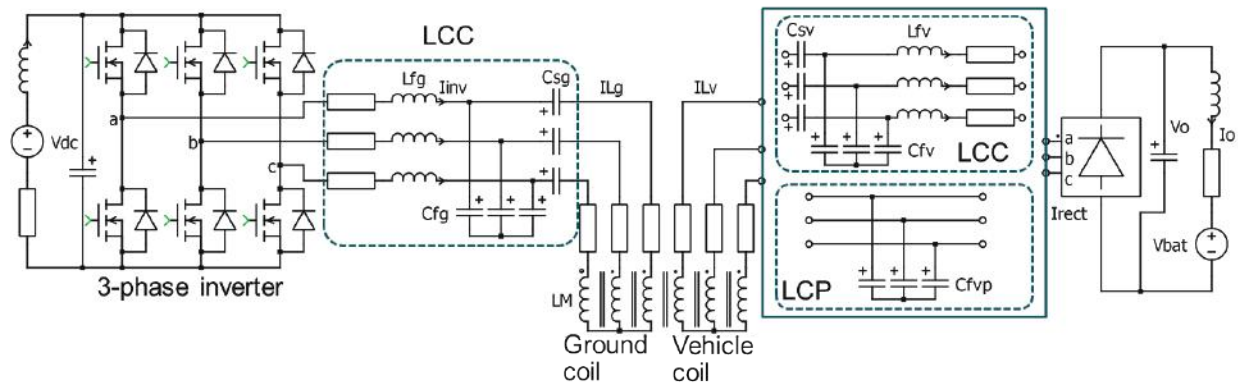
Figure II.3.2.4 PLECS model for the polyphase WPT system with LCC for the ground coil and LCC or LCP for the vehicle coil.

Figure II.3.2.5 show simulation results for charging at the rated power of 50kW, battery voltage of V_{bat}=400V, dc source voltage of V_{dc}=700V, and switching frequency of f_{sw}=85kHz, where (a) is for LCC-LCC tuning and (b) for LCC-LCP tuning; I_{invs}(a,b,c) are the inverter 3 phase output currents, I_{rect}(a,b,c) are the rectifier input currents, Vo charging voltage, Io charging current, and Po charging power. Table II.3.2.2 gives the tuning parameters and numerical values for the charging voltage, power, inverter, rectifier, ground and vehicle coil currents. Compared to the LCC tuning, the LCP tuning requires 5.2, 3.6, and 1.5 times higher inverter, ground coil, and vehicle coil currents, respectively. LCC-LCC is therefore chosen for hardware development.
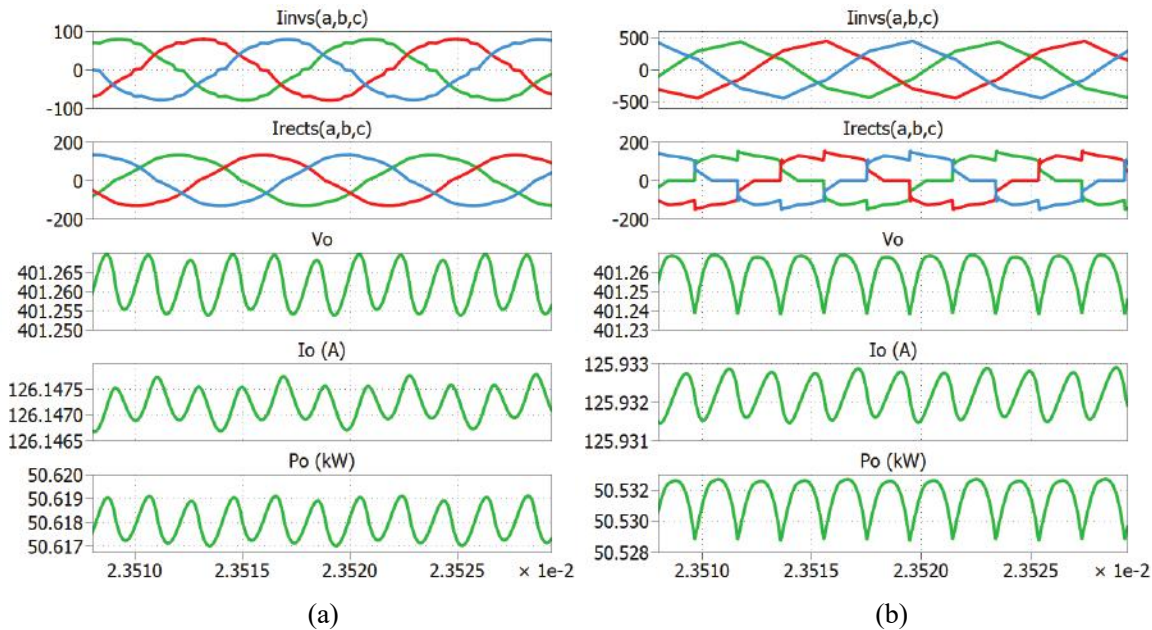
Figure II.3.2.5 Simulation results for charging power, Po=50kW, battery voltage, Vbat=400V, and switching frequency, fsw=85kHz, (a) with LCC-LCC tuning and (b) LCC-LCP tuning.

Table II.3.2.2 Comparison of LCC-LCC and LCC-LCP Tuning.

	Lfg (µH)	Cfg (µF)	Csg (nF)	Csv (µF)	Cfv (µF)	Lfv (µH)	Vo (V)	Po (kW)	Iinv (Arms)	Irect (Arms)	ILg (Arms)	ILv (Arms)
LCC-LCC	6.743	0.5199	52.72	0.292	0.7233	4.847	401.3	50.6	55.8	93.7	86.0	71.1
LCC-LCP	1.9	1.845	49.14		0.208		401.3	50.5	289.0	99.4	309.7	103.7

Design and Simulate Resonant Networks for the Z1, Z2, and Z3 Coils

The goal is to use the same ground coil and tuning network for all three clearance class vehicles. Table II.3.2.3 gives the resultant tuning parameters. Figure II.3.2.6, Figure II.3.2.7, and Figure II.3.2.8 show, respectively, simulation results for a full charging cycle at the Z1, Z2, and Z3 clearances, where (a) for constant current or power charging over the battery voltage range from 280V through 420V and (b) for constant voltage charging at battery voltage of 420V via inverter duty control. Numerical values for the voltage and current of the tuning components and the coils are listed in Table II.3.2.4, Table II.3.2.5, and Table II.3.2.6 for the three clearances.

Table II.3.2.3 Tuning Network Parameters for Z1, Z2, and Z3 Clearance.

	Ground Side: LCC			Vehicle Side: LCC			fsw (kHz)
	Lfg (uH)	Cfg (uF)	Csg (uF)	Csv (uF)	Cfv (uF)	Lfv (uH)	
Z1	6.27	0.55	0.05	0.43	0.5	7.11	84.43
Z2	6.27	0.55	0.05	0.3	0.7	5.06	84.6
Z3	6.27	0.55	0.05	0.25	0.8	4.51	83.83

(a)   (b)
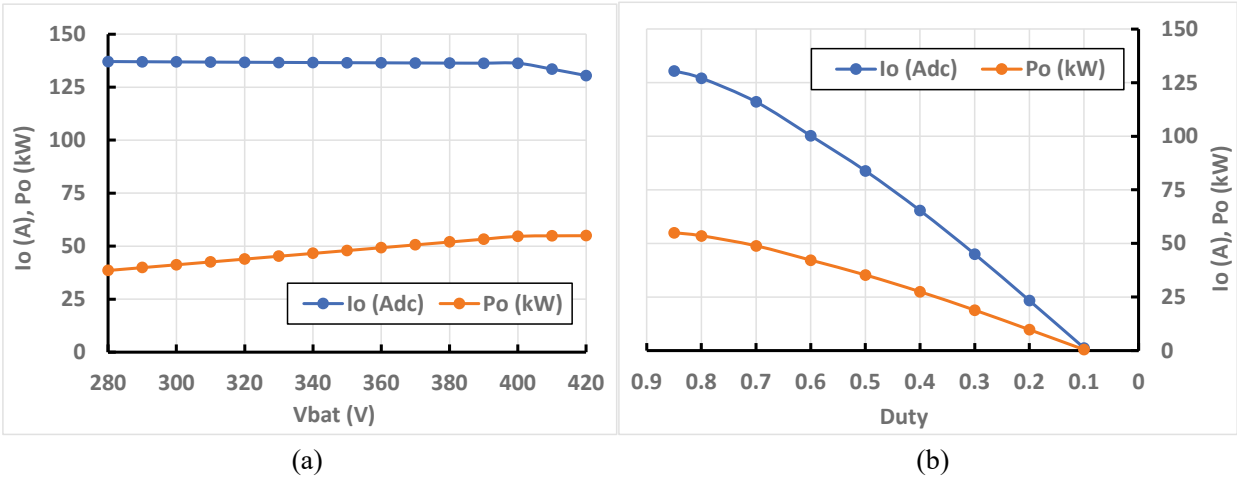
Figure II.3.2.6 Simulation results for a full charging cycle at the Z1 clearance, (a) Constant current or power charging over the battery voltage range from 280V through 420V and (b) Constant voltage charging at battery voltage of 420V.

(a)   (b)
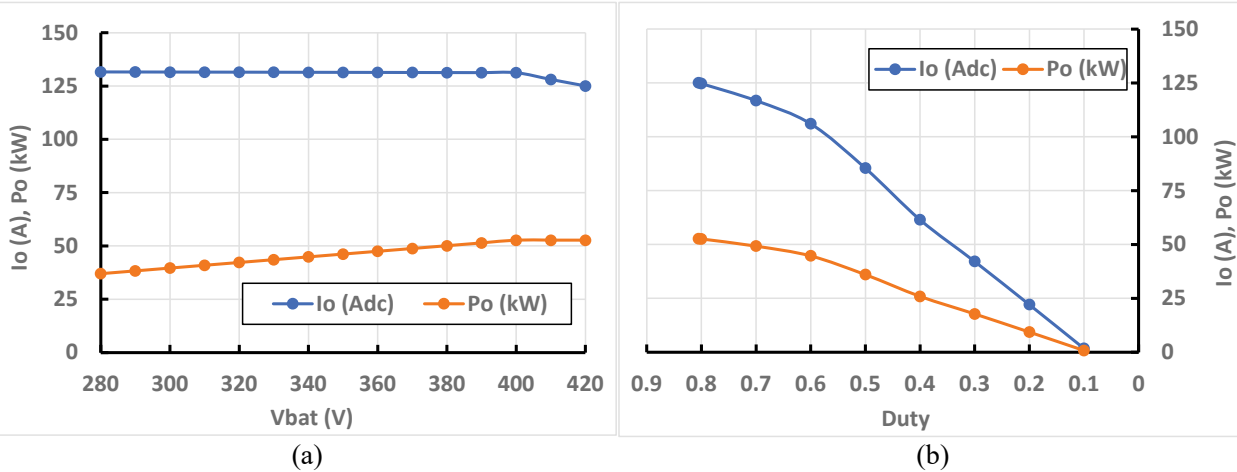
Figure II.3.2.7 Simulation results for a full charging cycle at the Z2 clearance, (a) Constant current or power charging over the battery voltage range from 280V through 420V and (b) Constant voltage charging at battery voltage of 420V.
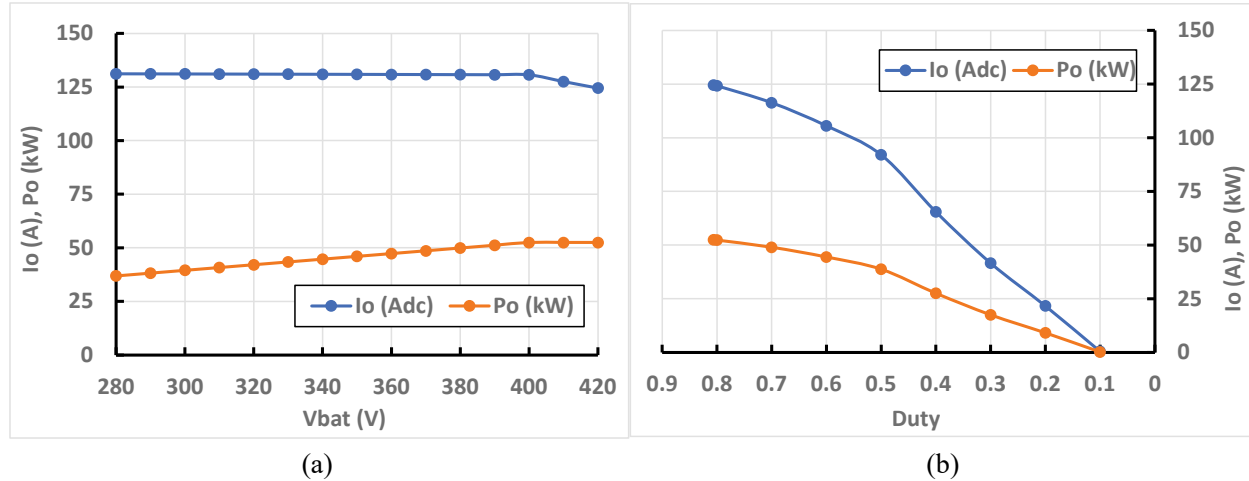
Figure II.3.2.8 Simulation results for a full charging cycle at the Z3 clearance, (a) Constant current or power charging over the battery voltage range from 280V through 420V and (b) Constant voltage charging at battery voltage of 420V.

Table II.3.2.4 Simulation Results for Z1 Clearance.

Vbat (Vdc)	duty	VCfg (Vrms)	ICfg (Arms)	VCsg (Vrms)	VCsv (Vrms)	VCfv (Vrms)	ICfv (Arms)	ILg (Arms)	VLg (Vrms)	ILv (Arms)	VLv (Vrms)
280	1	327.0	95.4	3419.0	151.5	408.7	108.4	90.7	3714.4	34.5	483.3
290	1	329.4	96.2	3416.9	156.7	410.3	108.8	90.6	3712.7	35.7	489.3
300	1	331.9	96.9	3415.0	161.9	411.8	109.3	90.6	3711.2	36.9	495.6
310	1	334.5	97.6	3413.2	167.2	413.5	109.7	90.5	3709.8	38.1	501.9
320	1	337.2	98.4	3411.4	172.4	415.2	110.2	90.5	3708.6	39.3	508.4
330	1	339.9	99.2	3409.8	177.6	417.0	110.6	90.4	3707.4	40.5	515.0
340	1	342.7	100.0	3408.3	182.9	418.8	111.1	90.4	3706.5	41.7	521.8
350	1	345.5	100.9	3406.9	188.1	420.7	111.6	90.4	3705.6	42.9	528.6
360	1	348.5	101.7	3405.5	193.3	422.7	112.1	90.3	3704.8	44.1	535.6
370	1	351.5	102.6	3404.1	198.5	424.7	112.7	90.3	3703.9	45.3	542.7
380	1	354.4	103.4	3402.1	203.8	426.7	113.2	90.2	3702.5	46.5	549.7
390	1	357.5	104.3	3401.0	209.0	428.8	113.7	90.2	3702.0	47.7	557.0
400	1	360.7	105.3	3400.4	214.2	431.0	114.3	90.2	3702.1	48.9	564.4
410	0.9	360.5	106.3	3331.9	219.4	426.5	113.1	88.4	3629.0	50.0	566.6
420	0.85	359.6	106.6	3256.8	224.5	421.5	111.8	86.4	3548.9	51.2	568.7
420	0.8	354.7	105.7	3172.5	224.4	413.3	109.7	84.2	3458.0	51.2	562.5
420	0.7	338.7	102.2	2896.6	224.1	386.9	102.7	76.8	3160.9	51.1	543.0
420	0.6	316.4	96.8	2503.6	223.6	350.4	93.0	66.4	2738.0	51.0	516.9
420	0.5	294.0	90.3	2097.3	223.1	314.9	83.6	55.6	2301.87	50.9	492.9
420	0.4	270.7	82.8	1637.5	222.53	278.2	73.8	43.4	1810.8	50.8	469.5
420	0.3	249.3	75.3	1134.9	221.9	244.3	64.9	30.1	1280.3	50.6	449.4
420	0.2	231.0	68.4	600.3	221.0	216.0	57.3	15.9	731.4	50.4	431.9
420	0.1	203.9	59.5	34.7	211.0	182.3	48.4	0.92	214.5	48.1	393.3

Table II.3.2.5 Simulation Results for Z2 Clearance.

Vbat (Vdc)	duty	VCfg (Vrms)	ICfg (Arms)	VCsg (Vrms)	VCsv (Vrms)	VCfv (Vrms)	ICfv (Arms)	ILg (Arms)	VLg (Vrms)	ILv (Arms)	VLv (Vrms)
280	1	188.1	55.2	3512.8	303.4	298.1	110.9	93.4	3645.4	48.4	517.3
290	1	191.8	56.2	3512.5	313.9	300.4	111.8	93.4	3645.6	50.1	530.6
300	1	195.5	57.3	3512.1	324.4	302.8	112.7	93.3	3645.9	51.7	544.1
310	1	199.3	58.5	3511.7	334.9	305.3	113.6	93.3	3646.2	53.4	557.6
320	1	203.2	59.6	3511.3	345.4	307.8	114.6	93.3	3646.4	55.1	571.3
330	1	207.1	60.7	3510.9	355.9	310.4	115.5	93.3	3646.8	56.8	585.0
340	1	211.1	61.9	3510.5	366.4	313.0	116.5	93.3	3647.1	58.4	598.8
350	1	215.1	63.0	3510.1	376.9	315.7	117.5	93.3	3647.4	60.1	612.7
360	1	219.1	64.2	3509.7	387.4	318.5	118.5	93.3	3647.8	61.8	626.7
370	1	223.1	65.4	3509.2	397.9	321.3	119.6	93.3	3648.2	63.4	640.7
380	1	227.2	66.6	3508.8	408.4	324.1	120.6	93.3	3648.6	65.1	654.8
390	1	231.4	67.8	3508.4	418.9	327.0	121.7	93.2	3649.0	66.8	669.0
400	1	235.5	69.0	3508.0	429.4	329.9	122.8	93.2	3649.4	68.5	683.2
410	0.861	239.4	71.2	3424.1	439.7	328.0	122.1	91.0	3564.1	70.1	694.8
420	0.805	243.2	73.3	3343.6	450.0	326.4	121.5	88.9	3482.3	71.8	706.8
420	0.8	243.1	73.3	3335.2	450.0	326.0	121.3	88.6	3473.7	71.8	706.6
420	0.7	241.5	74.7	3125.3	449.5	314.0	116.9	83.1	3258.0	71.7	700.5
420	0.6	238.5	75.1	2839.0	448.8	298.3	111.0	75.5	2964.1	71.6	692.8
420	0.5	230.6	72.9	2292.6	447.6	270.6	100.7	60.9	2404.5	71.4	679.8
420	0.4	221.6	69.4	1659.3	446.0	242.8	90.4	44.1	1759.9	71.1	667.2
420	0.3	214.5	65.6	1149.3	444.8	224.8	83.7	30.6	1247.8	70.9	658.8
420	0.2	205.1	61.1	611.7	441.2	205.3	76.4	16.3	709.5	70.4	643.3
420	0.1	189.7	55.5	49.2	422.8	182.0	67.7	1.3	205.9	67.4	604.8

Table II.3.2.6 Simulation Results for Z3 Clearance.

Vbat (Vdc)	duty	VCfg (Vrms)	ICfg (Arms)	VCsg (Vrms)	VCsv (Vrms)	VCfv (Vrms)	ICfv (Arms)	ILg (Arms)	VLg (Vrms)	ILv (Arms)	VLv (Vrms)
280	1	130.7	38.2	3710.0	416.0	270.9	114.2	97.7	3731.0	54.8	604.4
290	1	135.2	39.4	3709.5	430.4	273.5	115.3	97.7	3731.2	56.7	622.3
300	1	139.7	40.7	3709.0	444.8	276.1	116.4	97.7	3731.3	58.6	640.2
310	1	144.2	42.0	3708.5	459.2	278.8	117.5	97.7	3731.5	60.5	658.3
320	1	148.7	43.3	3707.9	473.6	281.6	118.7	97.7	3731.6	62.4	676.4
330	1	153.1	44.6	3707.4	488.0	284.4	119.9	97.6	3731.8	64.3	694.6
340	1	157.6	45.9	3706.8	502.4	287.3	121.1	97.6	3732.0	66.2	712.8
350	1	162.1	47.2	3706.2	516.8	290.2	122.3	97.6	3732.2	68.1	731.1
360	1	166.6	48.5	3705.6	531.2	293.2	123.6	97.6	3732.5	69.9	749.5
370	1	171.1	49.8	3705.0	545.6	296.2	124.9	97.6	3732.7	71.8	767.9
380	1	175.6	51.1	3704.4	560.0	299.3	126.2	97.6	3732.9	73.7	786.3

390	1	180.1	52.4	3703.8	574.4	302.4	127.5	97.5	3733.2	75.6	804.8
400	1	184.5	53.7	3703.2	588.8	305.6	128.8	97.5	3733.5	77.5	823.3
410	0.862	190.7	57.0	3615.6	602.9	304.8	128.5	95.2	3647.2	79.4	840.1
420	0.806	196.5	59.8	3530.9	617.1	304.2	128.3	93.0	3563.8	81.3	857.1
420	0.8	196.6	60.0	3520.3	617.0	303.8	128.1	92.7	3553.2	81.3	856.9
420	0.7	199.2	63.1	3298.6	616.4	293.8	123.9	86.9	3332.5	81.2	852.6
420	0.6	201.0	65.2	2996.4	615.5	280.8	118.4	78.9	3032.0	81.0	847.1
420	0.5	201.4	65.8	2617.0	614.4	265.5	111.9	68.9	2655.1	80.9	840.8
420	0.4	198.3	63.1	1876.1	612.3	239.5	101.0	49.4	1922.9	80.6	830.4
420	0.3	194.4	59.9	1208.7	610.0	220.0	92.8	31.8	1269.6	80.3	820.8
420	0.2	189.6	56.3	639.1	604.2	202.5	85.4	16.8	712.5	79.6	803.9
420	0.1	177.1	51.3	17.1	569.6	178.2	75.1	0.5	180.6	75.0	747.8

Conclusions

Simulation results show the LCP tuning for the vehicle coil requires much higher inverter, ground coil, and vehicle coil currents compared to the LCC tuning. LCC-LCC is therefore chosen for hardware development.

LCC-LCC based tuning networks are designed that can use the same ground coil for all three clearance class vehicles. Simulation results verify that the designs can perform a full charging cycle at the Z1, Z2, and Z3 clearances with constant current or power charging over the depleted battery voltage range and then with constant voltage charging at the end battery voltage via inverter duty control.

References

1. J2954 201904 Wireless Power Transfer for Light-Duty Plug-in/Electric Vehicles and Alignment Methodology, SAE, 2019.

2. J. Pries, V. P. N. Galigekere, O. C. Onar and G. -J. Su, "A 50-kW Three-Phase Wireless Power Transfer System Using Bipolar Windings and Series Resonant Networks for Rotating Magnetic Fields," in IEEE Transactions on Power Electronics, vol. 35, no. 5, pp. 4500-4517, May 2020, doi: 10.1109/TPEL.2019.2942065.

Acknowledgements

II.3.3 Integrating Dynamic Wireless Power Transfer Systems in Roadways (EVs@Scale Consortium)

Veda Prakash Galigekere, Principal Investigator

Oak Ridge National Laboratory
2360 Cherahala Boulevard
Knoxville, TN 37932
Email: galigekerevn@ornl.gov

Bo Zhang, Principal Investigator

Idaho National Laboratory
2525 North Freemont Avenue
Idaho Falls, ID 83415
E-mail: richard.carlson@inl.gov

Andrew Meintz, Principal Investigator

National Renewable Energy Laboratory
2360 Denver West Parkway
Golden, CO 83415
E-mail: andrew.meintz@nrel.gov

Lee Slezak, DOE Technology Manager

US Department of Energy
Email: lee.slezak@ee.doe.gov

Start Date: October 1, 2021　　　　End Date: September 30, 2022
Project Funding: $2,700,000　　　　DOE share: $2,700,000　　　Non-DOE share: $0

Project Introduction

High-power dynamic wireless (HPDW) charging has the potential to significantly alleviate range anxiety and reduce the onboard energy storage requirement across different classes of electric vehicles (EVs). It has been estimated that a dynamic power transfer level of 200 kW or more will be required to serve light duty, medium duty, and heavy duty EVs with reduced infrastructure cost. A proof-of-concept 200 kW dynamic wireless power transfer (DWPT) system has been developed and characterized in a laboratory setup, and it is being transitioned for real-world characterization with a roadway embedded transmitter and a vehicle integrated receiver system. The laboratory characterization indicated that high-power dynamic charging with a power transfer rate of 200 kW is possible with overall efficiency of more than 90%. This project addresses the challenges that must be met to transition HPDW charging from a proof-of-concept system to a practicable real-world system suitable for deployment at scale.

Several challenges need to be addressed for the adoption of wireless EV charging technology, including developing a safe electromagnetic (EM) shielding for the wireless power transfer system, detecting and preventing foreign object interaction with that EM field, and developing high-speed dynamic alignment and automated power transfer systems. Idaho National Laboratory (INL) will develop technologies, strategies, and solutions to conquer those challenges, thereby enabling safe and reliable wireless charging systems. The National Renewable Energy Laboratory (NREL) will perform broad use case analyses to evaluate the optimal applicability to medium duty and heavy duty EVs.

The project is envisaged to be a team effort leveraging the strengths and synergies of the US Department of Energy's (DOE's) Oak Ridge National Laboratory (ORNL), INL, NREL, Virginia Tech Transportation Institute (VTTI), and the American Center for Mobility in a collaborative manner to develop a practicable HPDW system suitable for integration in the real world.

Objectives

The overall goal of this project is to develop and validate technologies and solutions to transition HPDW charging of EVs from an early-stage, proof-of-concept system to a practical roadway-integrated DWPT system suitable for deployment at scale. The broad challenges to deploying high power DWPT systems are a lack of

1. practicable and verified methods of integrating DWPT transmitters in different types of roadways without compromising performance and safety,

2. comprehensive data on the performance of high-power DWPT systems under rigorous, real-world operating conditions, and

3. understanding of key system- and component-level barriers for roadway integration.

The objectives are as follows:

1. to perform thorough, real-world characterization of an HPDW charging system and identify the barriers to adoption of this technology at a deployable scale (including challenges to roadway integration);

2. to conduct research and develop the technology necessary across the domains (electrical, roadway, structural, and thermal) to overcome the barriers to deployment (installation, operation, serviceability, and performance); and

3. to conduct experimental and simulation studies to evaluate and map out the interoperability of HPDW systems (interoperability to stationary wireless charging, across vehicle classes, and coupler and system architectures).

INL's scope of work for this ORNL-led project focuses on advancing safe and high-power DWPT performance. The primary safety concern that INL is working on is the stray EM fields originating from the high-power DWPT system that can interact with people or foreign objects, resulting in potentially hazardous conditions. INL is also responsible for developing data collection systems and methodologies for evaluating and analyzing the advanced DWPT system demonstrated in this project.

Approach

Preliminary Design of 200 kW Ground Side Transmitters

A high-power dynamic charging transmitter was validated for electrical performance, including thermal mapping during operation at a rated power of 200 kW. The 200 kW ground-side transmitter validated for electrical performance was designed using fiberglass reinforcements and Ready Mix 5,000 pounds per square inch (psi) grout. The design was carried out using standards from American Concrete Institute (ACI) 318 [1] and ACI 440 [2]. Owens Corning #4 fiberglass rebar with a diameter of 0.5 in. was added to improve the mechanical performance. The computer-aided design (CAD) model of the modified 200 kW transmitter is shown in Figure II.3.3.1.
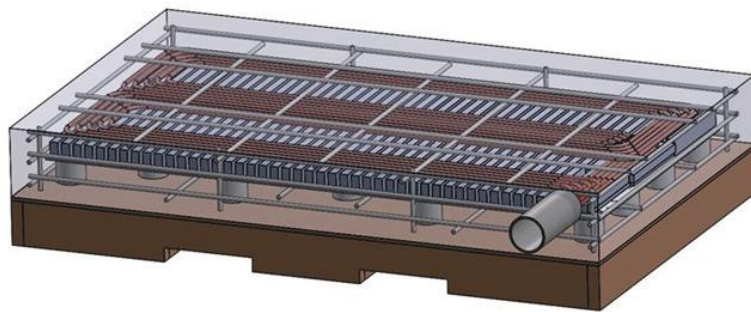
Figure II.3.3.1. CAD model of the 200 kW DWPT transmitter.

The following list contains the specifications for the equivalent design.

- Vehicle axle loads were considered to be 8,000–32,000 lb.

- The precast concrete shell was designed to be a buried box culvert (the coil provides no structural support).

- Loading scenarios were derived using the American Association of State Highway and Transportation Officials load and resistance factor design (LRFD) [3].

- The strength capacity of the top slab of the box culvert was calculated for a variety of reinforcement layouts using ACI 318 and ACI 440.

- The deflection (displacement) of the top slab was checked to ensure it remained under the limit to minimize the possibility of damage to the embedded wireless charger device.

Figure II.3.3.2 shows the 200 kW transmitter built using the Owens Corning #4 fiberglass rebar. The 200 kW transmitters was concretized using Ready Mix 5,000 psi grout. The grout was poured uniformly across the encasement, as shown in Figure II.3.3.3.

Figure II.3.3.2. The 200 kW DWPT transmitter.

Figure II.3.3.3. Grout poured uniformly across the encasement of the 200 kW DWPT transmitter.

Road Map of Activities Planned with VTTI to Transition Ground Side Transmitters from a Laboratory System to Roadworthy System

Real-world implementation of dynamic charging will require integrating high-power DWPT systems in different types of roadways and will need to be operable under various environmental conditions. The system will also have to withstand installing, servicing, and maintaining the DWPT system over the life cycle of a typical roadway. Important factors to consider before finalizing the embedment technique and structural analyses are listed below.

- DWPT slab materials and properties—the aggregate materials and dimension must be considered to meet the required operational limits (temperature and humidity) and strength (static and dynamic compression and tension). Durability must also be considered.

- An appropriate embedment technique—the depth at which the transmitter system needs to be embedded and the and the process of embedding it for different roadway types—needs to be identified. The type of reinforcement and treatment between different material interfaces will need to be identified.

- Identify compliance requirements per applicable agencies for highway installation and utility connection.

- Evaluate overground and underground installation implications of power electronics. This evaluation includes identifying suitable PE components available based on performance and suitability for deployment.

- Identify communication system requirements for integrating DWPT in existing and future highways including requirements of emergency vehicles and safety.

The civil engineering and structural evaluation of the ground-side unit is of utmost importance for safe and successful deployment of a HPDW charging system. A road map of collaborative research and development between ORNL and VTTI has been planned to transition the ground-side DWPT couplers to road-worthy. The ORNL-VTTI planned activity is summarized below.

- Perform system-level study and design review of 200 kW dynamic charging system from structural and mechanical viewpoint to develop a strategic road map to improve the reliability and suitability for deployment.

- Evaluate the instrumentation required to determine stress and strain during loading and changes in efficiency considering the following independent variables: (1) material, (2) temperature, (3) load, and (4) dry or flooded.

- Conduct characterization of roadway-embedded and vehicle-integrated 200 kW HPDW system. The characterization will include power transfer profiles and efficiency.

- Identify a set of viable coil encasement architectures, including options for materials, processes, and fabrication techniques, to meet the identified design targets to address roadway construction and installation challenges of the HPDW system. Additional independent variables for consideration include (1) electronic packaging, (2) installation methods, (3) testing temperature, (4) depth of installation, (5) road construction, (6) surface material, and (7) power and duty cycle of the charging system.

Laboratory Characterization of 200 kW Dynamic Wireless EV Charging System

The 200 kW dynamic wireless charging system, based on the transmitter shown in Figure II.3.3.2, was set up for validation in stationary mode. The objective of the test was to verify power transfer capability and establish baseline data. After the test in stationary mode, the dynamic power transfer profile emanating from the 200 kW transmitter and the DWPT system was characterized using the dynamic inductive charging emulator (shown in Figure II.3.3.4). The 200 kW transmitter concretized using Ready Mix 5,000 psi grout was set in the laboratory

for electrical power transfer validation (shown in Figure II.3.3.5). As shown in Figure II.3.3.5, the vehicle coil was placed at a distance of 10.5 in., which included the depth of installation and the ground clearance for the Hyundai Kona vehicle. The objective of this test was to verify that the concrete did not affect the wireless power transfer and also did not heat up owing to the presence of EM fields.
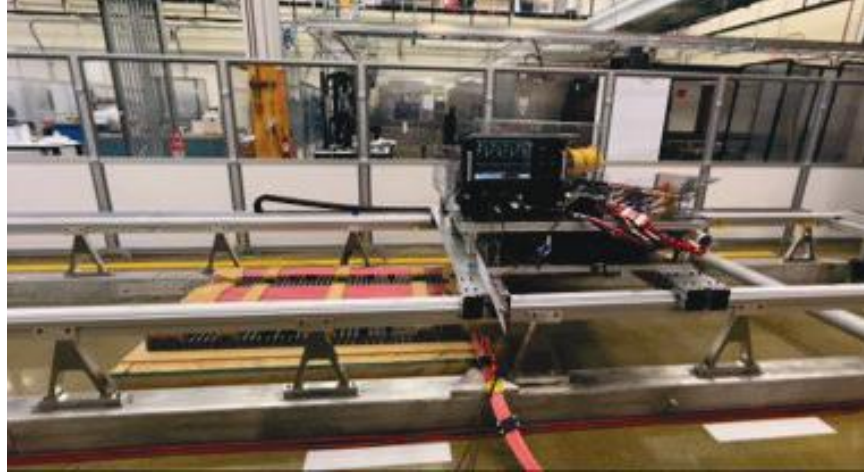
Figure II.3.3.4. Laboratory characterization of 200 kW DWPT system using dynamic inductive charging emulator.

Figure II.3.3.5. Concretized 200 kW transmitter setup for electrical characterization.

INL DAQ System Preparation and Verification Evaluation

- Assemble and verify operation of the multicomponent DAQ (complete).

    o   Ground-side measurements (e.g., electrical, EM field, coil alignment, vehicle speed)

    o   Vehicle-side measurements (e.g., electrical, EM field, backup data collection)

    o   LabVIEW data collection, merging of multiple data streams, and analysis for fast feedback of high-level results.

- Verify the functionality of the wireless trigger system (complete).

- Develop and evaluate the Driver's Alignment Aid (DAA) system for track testing (complete).

ORNL DWPT Evaluation in Preparation for Comprehensive Characterization Test

- Determine Y-alignment performance shoulder (i.e., misalignment threshold of declining performance with additional Y-misalignment); consider using quasi-static DWPT operation.

  o Evaluate this misalignment threshold for X-alignment of approach, alignment, and departure.

- Measure EM field during quasi-static DWPT operation with a Narda EHP probe to verify that EM field levels are well below the International Commission on Non-Ionizing Radiation Protection's (ICNIRP's) 2010 guidelines (i.e., no need for measurement during high-speed DWPT testing).

  o Optional steps: perform if possible, dependent upon ORNL test site progress and availability:

    o Verify INL DAQ equipment operation in conjunction with ORNL DWPT development, calibration, and testing at ORNL with its in-lab dynamic track system.

      □ Set up as much of the DAQ system as appropriate, and conduct measurements, data transfer, data merge, and data analysis for results display.

      □ Verify that the DAQ synchronization trigger properly functions near high-power DWPT.

      □ Determine the duration of the 1 MHz collection method (collect, transfer, merge, and analyze data).

      □ Determine the approximate range of EM field emissions at the edge of the lane during various misalignment and power transfer rates (i.e., the meter's 2 mT, 20 mT, and 200 mT ranges).

Results

Preliminary Design of 200 kW Ground Side Transmitters

The outcomes of the design study based on LRFD methodology are shown in Table II.3.3.1. The study included a small vehicle and a heavy truck. Data noted included the variation of required reinforcement size and spacing along the long and short directions as a function of top slab thickness. Of the ground-side units, 4 200 kW units were concretized and cured per specifications. The target and measured primary coil inductances are shown in Table II.3.3.2. Figure II.3.3.6 shows the power analyzer reading of the stationary wireless power transfer validation at an input of 200 kW. The input power was limited to 200 kW because it was limited from the power source. The output power was 186.8 kW at an end-to-end efficiency of 93.77%. Figure II.3.3.7 shows the output voltage and current recorded on the power analyzer for a dynamic power transfer test at 193 kW.

Table II.3.3.1. Outcome of the Design Study for Coil Design, including Fiberglass Rebar Thickness and Spacing

Vehicle	Axle load (lb)	Top slab thickness (in.)	Short direction	Long direction		
			Reinforcement size	Reinforcement spacing (in.)	Reinforcement size	Reinforcement spacing (in.)
Small vehicle	8,000	2.5	#5	4	#5	6
Small vehicle	8,000	2.5	#6	6	#5	6
Small vehicle	8,000	2.5	#8	12	#5	6
Small vehicle	8,000	3	#5	6	#5	6

Small vehicle	8,000	3	#7	12	#5	6
Small vehicle	8,000	4	#4	6	#5	6
Small vehicle	8,000	4	#6	12	#5	6
Heavy truck	32,000	3	#8	4	#5	6
Heavy truck	32,000	4	#6	4	#5	6
Heavy truck	32,000	4	#8	6	#5	6

Table II.3.3.2. Target and measured primary coil inductances of 4 concretized 200 kW transmitters

Coil	Concretized coil 1	Concretized coil 2	Concretized coil 3	Concretized coil 4
Primary inductance—target (μH)	7.15	7.15	7.15	7.15
Primary inductance—measured (μH)	7.288	7.292	7.166	7.399

Figure II.3.3.6. Power analyzer reading for operation of 200 kW DWPT system at 186.6 kW output operation at 93.7 % efficiency.
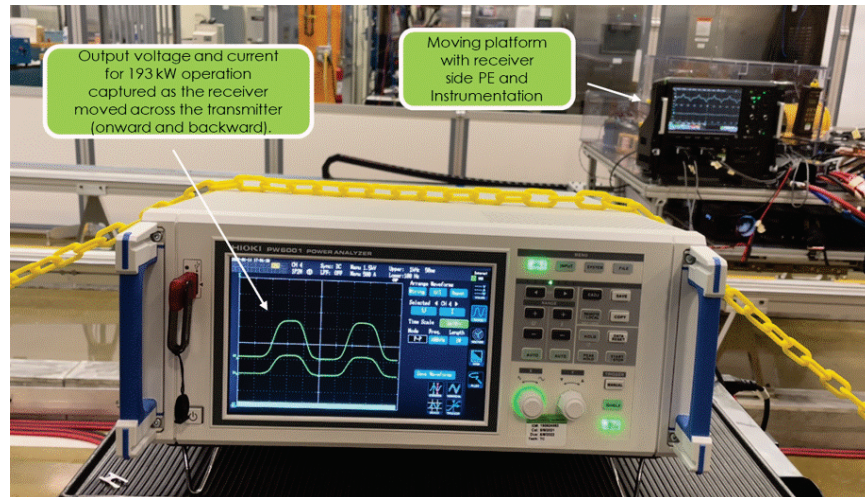
Figure II.3.3.7. Output voltage and current recorded using power analyzer
for dynamic wireless transfer of 193 kW.

Detailed Test Procedure for Comprehensive Characterization of 200 kW DWPT System

This section lists preparations conducted on the day before the testing day(s) as well as detailed descriptions of test procedures, including start-up, testing, and shutdown. Testing measures numerous characteristics of the DWPT system during high-speed driving on the closed test track.

Day Prior Preparations

- Set up the main DAQ components.

    o Ensure the Hioki power analyzers are equipped with current and voltage measurement probes and test leads.

    o Assemble the pop-up tent with the table, chairs, laptop, ac power strip, and other necessary items.

    o Install current and voltage measurement probes on the ground side and the vehicle side.

    o Set up the Y-alignment sensors.

        o Ensure the sensors are parallel and level.

            □ On-site height to be determined (730 mm in INL lab)

            □ Distance from lane center line equals 2,787.5 mm

            □ On-site interval between sensors to be determined (1,000 mm in INL lab)

                - Connector enclosures for up to six power and data connections

                - Wireless trigger system for the ground side and the vehicle side

- Set up the EM field probe locations.

    o Ensure the ground-side probe location is at the lane's edge (1,829 mm) in line with the center of DWPT coil 2.

    o Ensure the vehicle-side probe location is centered on the vehicle coil (X) close to the edge of the vehicle chassis (Y) at height (Z) on the opposite side of the Y-alignment measurement.

- Install the DAA into the vehicle.

    o Align the front license plate bracket sites.

    o Secure the camera with the suction cup.

        o Ensure the camera is centered on the vehicle axis and is aligned with the site's bracket.

    o Place the monitor on the dashboard.

    o Secure the 12 V power cable in the 12 V cigarette lighter port.

- Execute a dry run of the test procedure and the DAQ before DWPT evaluation.

    o Conduct a dry run with a vehicle of the same or similar make and model as the DWPT test vehicle. Conduct the dry run without DWPT power transfer to identify any issues with the DAQ setup or user familiarity.

        o Use the following steps for DAA accuracy verification.

            □ Employ Y-alignment testing to allow the driver to practice using the DAA system.

            □ Employ Y-alignment measurements to verify proper operation of the Y-alignment measurement subsystem.

        o Ensure the wireless trigger system is ready for use.

            □ Verify the wireless trigger system functions successfully for high-speed testing.

        o Ensure the test procedures are available for practice runs and ready for use.

            □ This step allows for the practice of test procedures, thus improving schedule efficiency during dynamic power transfer testing.

        o Use the following conditions to perform the dry run test cases.

            □ Aligned, 35 miles per hour (mph)

            □ Aligned, 65 mph

            □ +200 mm, 35 mph

            □ −200 mm, 50 mph

        o If dry run results are appropriate, mark the locations on the ground using paint, another nonerasable method, or with colored tape.

            □ Use tripod legs for the four Y-alignment sensors.

            □ Ensure the EM field probe stand is set up correctly.

            □ Mark the Hioki current and voltage cables with uniquely identifying colored tape on the back of the Hioki.

            □ Take photos of the entire setup, including the ground side and the vehicle side.

Start-up, Test, and Shutdown Procedures

Start-up Procedures

- Use the following start-up procedures:

  o Check the suction cups.

  o Ensure all connections are plugged in.

    o Check the ground-side components.

      □ Hioki (degauss and zero adj.)

      □ Y-alignment sensors (120 V input)

      □ Laptop power supplies

      □ Wi-Fi router

      □ Engage the trigger sender and receivers.

      □ Connect the Ethernet cables to the laptops and power analyzers.

      □ Turn on the Wi-Fi switch and router.

    o Check the vehicle-side components.

      □ Inverter

      □ EM field probe

      □ Hioki (degauss and zero adj.)

      □ Trigger sensor

    o Turn on both EM field probes.

      □ Set to MON.

      □ Set to R1 (up to 20 mT).

    o Start up both laptops (ground side and vehicle side).

    o Start up GPS logger (for backup data).

Test Procedures

For each test, conduct each of the following steps as specified in the test plan.

- Inform driver of test parameters.

  o Miles per hour target

  o Alignment target

- Inform DWPT operational staff of test parameters.

  o Target power transfer at miles per hour and alignment.

- Inform DAQ operational staff of the following.

  - 100 Hz or 1 MHz data collection—use the correct LabVIEW DAQ program

  - Ensure Hioki #1 channel 5 is properly connected (1 MHz trigger or 100 Hz dc bus voltage).

- Start LabVIEW program on both ground-side and vehicle-side laptops.

- Accelerate towards the DWPT road segment. Achieve miles per hour and alignment targets before the DWPT road segment.

- When the vehicle enters the DWPT road segment, the trigger automatically starts power analyzers recording (1 MHz only). For 100 Hz measurements, the trigger is recorded and used to align data during merge process.

- When the vehicle leaves dWPT road segment:

  - For 100 Hz only: Stop LabVIEW data collection for ground-side and vehicle-side.

  - RawData is saved on both laptops automatically via LabVIEW.

- When the vehicle stops, turns around, and returns to the starting point:

  - If applicable, park against wheel stop for GPS reference before the next test.

  - Data is transferred from vehicle-side laptop to ground-side laptop (wirelessly if within Wi-Fi range).

  - On the ground-side laptop, run LabVIEW Merge.vi, Calculate RMS.vi, and Analyze & Display.vi.

- Repeat test procedure for the next test case.

Shutdown Procedures
- Follow shutdown procedures at the conclusion of these tests.

  - Turn off the three Hioki power analyzers.

  - Unplug all current clamps and voltage sense test leads at the back of the Hioki.

  - Install the cover on the Hioki enclosures.

  - Turn off the three trigger senders and receivers.

  - Shut down (or sleep) both laptops (ground-side and vehicle-side).

  - Turn off both EM field probes.

  - Shut down the logger for backup data.

  - Unplug the following:

    - 120 VAC power to all components

    - Ethernet cables to laptops and power analyzers

  - Turn off the Wi-Fi switch.

DWPT Test Plan

DWPT Evaluation

This evaluation is the culmination of several years of research, development, planning, and preparation. The high-speed dynamic power transfer evaluation will focus on characterizing the operational and safety performance of the ORNL high-power DWPT. This evaluation includes measurement of the power transfer level, efficiency, EM field, and other characteristics. Testing and evaluation will focus on three primary interdependent test parameters. Additional testing will be conducted, as appropriate, to evaluate secondary test parameters. The three primary test factors include *Y*-misalignment (250 to −250 mm), driving speed (up to 65 mph), and requested power transfer (up to 200 kW). The nominal test case will be aligned (0 mm) at 200 kW power transfer when driving 5 mph. Secondary test factors will include *Z*-gap (±25 mm), nonconstant factors (e.g., acceleration and deceleration, swerving, lane change), and a second nearby vehicle (in front, adjacent lane, tailgating).

Primary Interdependent Test Parameters

- Y-alignment

    o 0, +150, +200, and +250 mm

    o −150, −200, and −250 mm

- Vehicle Speed (X)

    o 20, 35, 50, and 65 mph

- Power Transfer Target

    o 50, 100, 125, 150, 175, and 200 kW

Secondary Test Parameters

- Coil gap (Z)

    o 9, 10, and 11 in. (−25, 0, +25 mm)

- Adjacent second vehicle

    o Behind, in-front, side-by-side

- Variable primary parameters

    o Zig-zag Y-alignment

    o Accelerate and decelerate

    o Power ramping (if possible)

- Ambient temperature (if possible)

    o Hot, cold

DWPT Demonstration for VIPs

The purpose of this concise DWPT demonstration is to highlight the safety and performance characteristics of the high-power DWPT system. This demonstration should show the DWPT performance (e.g., power transfer, efficiency, EM field safety) at full power, high vehicle speed, and aligned or misaligned.

Demonstration Test Cases

- 50 mph, 200 kW, aligned (0 mm)

- 65 mph, 200 kW, aligned (0 mm)

- 50 mph, 200 kW, misaligned (200 mm)

Table II.3.3.2. Recommended Test Plan for Set-up and Debugging (before Commencing Full Testing)

Set-up and debug eval.	Power request (kW)	V_{eh} speed (mph)	Y-misalignment (mm)	Z coil gap (mm)	Second vehicle position
Debug	50	20	0	0	None
Debug	50	35	0	0	None
Debug	50	35	+200	0	None
Debug	50	35	−200	0	None
Debug	50	50	0	0	None
Debug	50	50	+200	0	None
Debug	50	50	−200	0	None
Debug	50	65	0	0	None
Debug	50	65	+200	0	None
Debug	50	65	−200	0	None

Table II.3.3.3. Primary Factor Tests (Single Factor)

Primary single factor testing	Power request (kW)	V_{eh} speed (mph)	Y-misalignment (mm)	Z coil gap (mm)	Second vehicle position
Power	50	50	0	0	None
Power	75	50	0	0	None
Power	100	50	0	0	None
Power	125	50	0	0	None
Power	150	50	0	0	None
Power	175	50	0	0	None
Nominal	200	50	0	0	None
Miles per hour	200	65	0	0	None
Miles per hour	200	35	0	0	None
Miles per hour	200	20	0	0	None
Nominal	200	50	0	0	None
Y-align	200	50	+150	0	None
Y-align	200	50	+200	0	None
Y-align	200	50	+250	0	None
Y-align	200	50	−150	0	None
Y-align	200	50	−200	0	None
Y-align	200	50	−250	0	None

Table II.3.3.4. Primary Factor Tests (Dual Factors)

Primary dual factor testing	Power request (kW)	V_{eh} speed (mph)	Y-misalignment (mm)	Z coil gap (mm)	Second vehicle position
Dual	125	35	−200	0	None
Dual	125	65	−200	0	None
Dual	125	35	+200	0	None
Dual	125	65	+200	0	None
Dual	50	35	−200	0	None
Dual	50	65	−200	0	None
Dual	50	35	+200	0	None
Dual	50	65	+200	0	None
Dual	200	35	−200	0	None
Dual	200	65	−200	0	None
Dual	200	35	+200	0	None
Dual	200	65	+200	0	None
Dual	125	50	−200	0	None
Dual	50	50	−200	0	None
Dual	125	50	+200	0	None
Dual	50	50	+200	0	None
Dual	125	35	0	0	None
Dual	50	35	0	0	None
Dual	125	65	0	0	None
Dual	50	65	0	0	None
Nominal	200	50	0	0	None

Conclusions

- Concretized coil was designed, and four ground-side units were built per the guidelines in References [1], [2], [3]. The electrical behavior was characterized before and after the concretization process, and it remained unchanged, suggesting that the coil is suitable for deployment from the perspective of power transfer capability. Notable outcomes of the design study are as follows:

  o The Ready Mix 5,000 psi epoxy grout used for concretizing the coil indicated sufficient compressive strength to withstand the vehicle loading, especially when provided adequate reinforcement.

  o Fiberglass reinforcement was required to meet the tensile stresses that occur during lift and vehicle drive-over.

  o As axle load increased from 8,000 to 32,000 lb, the required top slab thickness increased from 2.5 to 4 in.

  o To reduce top slab thickness, reinforcement spacing needed to be reduced, reinforcement thickness needed to be increased, or a combination of both needed to occur.

- A detailed road map was developed for collaborative work with VTTI to evaluate the roadworthiness of the 200 kW transmitters. Consequently, design changes and modifications will be conducted based on

this evaluation to make the coils roadworthy for installation, serviceability, and maintenance over a life cycle.

- The 200 kW transmitter was evaluated for 200 kW stationary and DWPT capability in the laboratory using the dynamic inducive charging emulator.

- A comprehensive characterization plan was developed and will be implemented after the 200 kW DWPT system has been installed and preliminary functionalities have been verified.

- A detailed data acquisition system was also developed for accurate characterization of the DWPT system.

References

1. American Concrete Institute Committee 318. *Building Code Requirements for Structural Concrete (ACI 318-08) and Commentary.* Farmington Hills, Michigan: American Concrete Institute, 2008.

2. American Concrete Institute Committee 440. *ACI PRC-440-07 Report on Fiber-Reinforced Polymer (FRP) Reinforcement for Concrete Structures.* Farmington Hills, Michigan: American Concrete Institute, 2007.

3. American Association of State Highway and Transportation Officials (AASHTO). *AASHTO LRFD Bridge Design Specifications.* AASHTO, 2017.

Acknowledgments

II.4 VGI & SCM

II.4.1 Charging Infrastructure Technologies: Smart Vehicle-Grid Integration (ANL)

Jason D. Harper, Principal Investigator
Argonne National Laboratory
9700 S. Cass Avenue
Lemont, IL 60439
E-mail: jharper@anl.gov

Keith Hardy, Principal Investigator
Argonne National Laboratory
9700 S. Cass Avenue
Lemont, IL 60439
E-mail: khardy@anl.gov

Lee Slezak, DOE Program Manager
U.S. Department of Energy
E-mail: lee.slezak@ee.doe.gov

Start Date October 1, 2018   End Date: March 31, 2022
Project Funding: $2,000,000   DOE share: $2,000,000   Non-DOE share: $0

Project Introduction

Problem Statement – The charging of grid connected vehicles must be managed and controlled or else the impacts of EVs at scale on the grid will be extremely disruptive, expensive, and will lead to the need for increased generating capacity. EVs at scale can contribute to grid resilience and reliability if charged intelligently. This will require controlled charge management that is coordinated with building and distribution network loads and requirements. Grid services previously identified in VTO-sponsored projects must be integrated into Smart Charge Management (SCM) schemes to maximize the potential benefit of EVs at scale to vehicle owners, building managers, charging network operators, grid services aggregators, and utilities.

Benefits of plug-in vehicles will be fully realized when the automotive, EVSE and utility industries cooperate, technically and programmatically, to ensure an integrated grid perspective and an implementation approach that supports sustainable business; the ultimate objective of vehicle-grid integration (VGI). This project takes a step in that direction by partnering with the Global Grid Integration Program, whose members are from US and European automotive, utilities, energy companies and research organizations. The intent is to collaborate on use cases/requirements for vehicle-grid integration and interim technology demonstrations, leading to a 'public' demonstration of smart energy management, where vehicles, buildings, renewable energy sources and energy storage are linked to meet the needs of customers as well as the electric power grid. This project will result in a managed network of devices at Argonne's Smart Energy Plaza capable of demonstrating the use cases/grid services specified by the GMLC and our industry partners.

Objectives

Primary goals – Demonstrate how smart charge management can be integrated with a network of building systems, renewables and energy storage, using an open source approach to:

- Respond to grid conditions/signals with minimal impact on local operations

- Identify potential benefits/impacts of EVs @ scale (controlled v. uncontrolled charging)

- Maximize the benefits of VGI on the customer-side of the meter

- Develop monetization scenarios of VGI for owners, utilities, and aggregators.

Achieving this goal necessitates several technical achievements: incorporating protocols for High-Level Communication (HLC) to enable 'smart' charging; control strategies that balance the needs on the customer-side of the meter with grid conditions; and enabling technologies (i.e., digital communication, tools to verify interoperability and perform diagnostics). The first three goals can be addressed in a laboratory environment such as the Argonne Energy Plaza, however the fourth requires collaboration with stakeholders such as utilities or aggregators. This was not possible due to the restrictions in place over the last three years.

FY 2021 was intended to be the final year of a 3-year project, with the objective of demonstrating a fully integrated 'grid of things' concept to illustrate the benefits of controlled versus uncontrolled charging using the energy plaza and a simulated grid. Field testing, technology transfer and commercialization studies would be initiated for the enabling technologies. And public demonstration projects with industry partners would be pursued.

Limited access to Argonne in FY 2020 due to COVID restrictions, as well as delays at vendors/subcontractors, impacted the schedule substantially, resulting in extending the project through Q2 FY 2022. The objectives of the third year were adjusted to demonstrate as many of the use cases and develop the enabling technologies as much as possible.

Approach

Argonne utilized its integrated network of devices at the Smart Energy Plaza to develop integrated control strategies for EV charging, building power demands, utilizing solar PV and interacting with the Argonne grid. This included demonstrating the flexibility/agility to manage loads and supply power from the customer side of the meter in addition to considering conditions on the grid side of the meter, as well as characteristics of a simulated distribution network.

In addition, the plaza is used to demonstrate enabling technologies that support smart energy management, including the Common Integration Platform (CIP.io), Smart Charge Adapter (SCA), the Diagnostic Electric Vehicle Adapter (DEVA), SpEC communication control modules, sub-metering, and test equipment to verify interoperability.

Tasks 1 and 2: Quantify benefits of smart charging

Barriers

- Lack of consensus on 'smart' VGI communication protocols (i.e., ISO 15118 or SEP2.0)

- Use cases demonstrated in the GMLC 062 project were implemented without the 'smart' protocols due to lack of commercially available compliant hardware (EVs and EVSE).

- GMLC use cases were originally specified before the ISO 15118 standard communication protocol was developed.

Solutions

Acquire EVs and EVSE with HLC, link to Argonne's common integration platform (CIP.io) and demonstrate the GMLC-defined use cases using 'smart' communication and control:

- Acquire ISO 15118-compliant EVs and EVSE and adapt ISO 15118 EVSE to CIP.io

- Demonstrate the GMLC uses cases utilizing the EVSE at the Energy Plaza (i.e., demand response, charge mitigation, frequency regulation, distribution upgrade deferral) as well as cases suggested by utility partners referred to as 'GMLC+' (i.e., Plug'n Charge, or PnC, and transactive energy trading using cryptocurrency).

Argonne acquired a 2018 Smart ED EV that is ISO 15118-2 compliant, but the message sampling rate is inadequate to demonstrate V1G frequency regulation and it is not capable of PnC. An alternative solution was chosen; to lease a Porsche Taycan that is equipped with ISO 15118. Two compliant EVSE were acquired as well, but both used proprietary communication protocols that did not allow external EVSE control, despite efforts to collaborate with the manufacturers. The alternative was to develop an ISO 15118-2-compliant EVSE for the smart charging studies.

Task 3: Optimized control for grid resiliency/reliability; impact of EVs @ scale

Barriers

- Unknown ability of multiple EVSE/workplace environment using SCM techniques to respond to grid conditions

- Lack of control strategies that consider the customer and the grid simultaneously

- Unknown impact of EVs @ scale.

Solution

Characterize the ability of the network of controlled devices on the customer side of the meter (at the Energy Plaza) to respond to grid conditions utilizing control strategies that support the customer and/or the grid. Translate the network response characteristics to node characteristics in the Argonne distributed network model (DNM) and link to the INL distribution and transmission models to identify potential impacts of controlled versus uncontrolled charging at a regional level.

Task 4. Early-stage R&D; Interoperability/grid integration components

Barriers

- Interoperability verification and diagnostics

- VGI solution for OEMs

- Integrated solutions for vehicle connectivity to local/workplace networks for energy management.

Solutions

Develop and demonstrate technologies to implement VGI in the workplace, e.g., smart interoperable AC L2 EVSE, containerized CIP.io, charge reservation system, charge scheduling based on smart communication (i.e., ISO 15118), and OCPP 1.6J client for Smart Charge Adapter.

Results

Tasks 1 and 2: Quantify benefits of smart charging

The current US electrical distribution grid cannot deliver an infinite amount of power to any receptacle on the grid. The distribution grid is physically constrained by the power ratings of substations, transformers, circuit breakers and wire gauge. Given that power is a finite resource and that most utilities oversubscribe distribution transformers, utilities' biggest fear is distribution transformer aging and/or failure due to EV load. The "clustering effect" occurs when one person buys an electric vehicle, which prompts the neighbor to buy an EV as well. If both neighbors charge their EV at the same time the peak demand as seen by the distribution transformer increases greatly. In order to combat EV charging during historical grid peak periods utilities have resorted to implementing Time-of-use (TOU) rates, in which energy becomes cheaper typically at night when grid demand is low. Other utilities have turned to utilizing demand response events to curtail specific EV driver's charging rate during peak demand and in return the EV driver receives a monetary reward. The issue with these approaches is that they are a form of controlled charging and do not take into account the needs of the EV driver. The EV is a form of transportation for the driver and each driver needs a minimum amount of energy at a specific departure time to make it to their next destination. TOU rates attempt to change the behavior of EV drivers by incentivizing them to charge during off peak hours and requires no communication

between the utility and EV/EVSE. Demand response events are more technically involved and require communication between the utility, charge station management system (CSMS) and the EVSE/EV.

The future of optimized smart charging is EV charge scheduling. In previous years of this project Argonne researchers implemented an ISO 15118 AC EVSE and charge scheduling application that utilized OCPP 2.0.1 smart charging messages. Demonstrated use-cases included load shaping, demand response, demand charge mitigation, distribution upgrade deferral and charging coordinated with PV. However, the true benefit of utilizing ISO 15118 smart charging messages lies in the ability of vehicle and grid to negotiate a charging schedule based on the maximum available power over a future duration (i.e., 8 hours). Even more powerful, the charge scheduling application or the EV can initiate a renegotiation allowing for redistribution of power levels when things change. The charge scheduling application can aggregate all EV charging loads and make decisions based on this load profile.

It is hard to quantify the benefits of true smart charging. It is beyond the scope of this research to get into a benefit-cost analysis of smart charging. Absent of upgrading all distribution transformers to allow for the aggregated load of EV charging, some form of controlled/smart charging will be needed in the future. What type of deployed program will be up to each utility. The goal of Argonne's research in this project was to develop and deploy a standard based approach to smart charging which is an alternative to current approaches today and to show the benefits of such an approach. EV charge scheduling meets the needs of the grid and EV driver and should be explored further as more EV models come to market that support ISO 15118 AC charging.

Task 3. Optimized control for grid resiliency/reliability; Impact of EVs @ scale

Building upon the linkage between the ANL distributed network model and INL's distribution and transmission models, experiments were performed with INL in FY22. The following text and figures are pulled from Wu, Z., et al. publication [1].

HIL Setup

More than 90 buildings, including different types of commercial and residential building loads, were modeled at 15 nodes in the ANL modified IEEE 37 nodes test feeder model (Figure II.4.1.1). A total of 460 EVs were distributed in the grid. These EVs include 2012 Nissan Leaf, 2015 Nissan Leaf, 2014 BMW i3, and 2012 Chevrolet Volt models.

Figure II.4.1.2 shows the HIL configuration of the frequency regulation use case. OPAL-RT performs real-time distribution network simulation, EV charging simulation, and distribution level energy management in real-time. The real-world SEP facilities are connected to node 775 as a microgrid of this distribution network. The rest of the EV charging processes are generated by EV charging simulation. An ISO 15118 EV Charge Scheduler System

Figure II.4.1.1 Topology of ANL modified IEEE 37 node test feeder model [1]

(EVCSS) is used to schedule and control the EV charging power for node 705. Other EVs are scheduled and controlled with the same method in OPAL-RT directly. The OPAL-RT receives the real-time SEP smart meter data, frequency, and EV charging load through the MQTT broker. Meanwhile, it performs all simulations and publishes EV charging requirements, grid conditions, and node consumption for the control of EVCSS. For a more detailed description of the setup and algorithms utilized refer to Wu, Z., et al. [1].

Figure II.4.1.2 Transmission and Distribution Grid Co-Simulation HIL setup [1]

HIL Frequency Regulation Use Case Results

A 24 hour simulation is performed through multiple subsystems with various timesteps. The distribution network simulation is run with a 200 μs timestep to achieve real-time grid analysis; the EV charging characteristic is updated every 5 seconds; the EMS and EVCSS are trigged every 1 minute. Figure II.4.1.3 shows the overall load profile of the distribution network. The substation capacity of the distribution network is set to 3 MW. If the EMS and EVCSS are disabled, all EVs will be charged with maximum power rate once they are connected. The charging durations are relatively short, but these will cause overloading during peak time and may cause damages. Once the EMS and EVCSS are enabled, the overall load is shifted smoothly and limited under the distribution network capacity.

Figure II.4.1.4 shows the frequency response from a transmission grid simulation. The transmission model is developed from a modified IEEE 39 bus system with 6 generators. The simulation is performed by Idaho National Laboratory (INL) and co-simulated through the cloud-based platform. The distribution network simulation by ANL is connected as one bus on the high voltage transmission line. The results in the uncontrolled scenario show a frequency violation occurs when the distribution network
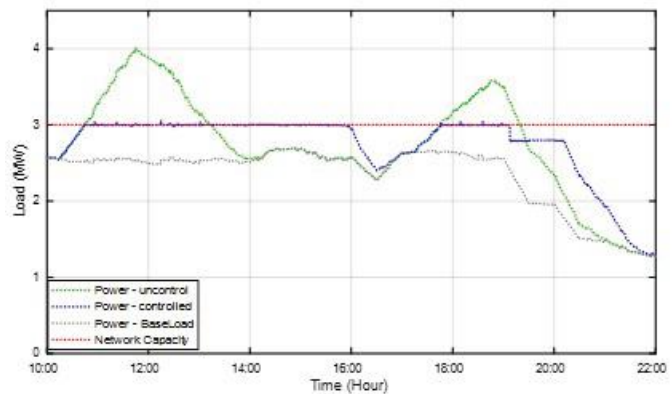
Figure II.4.1.3 Load Profile of the Distribution Network [1]
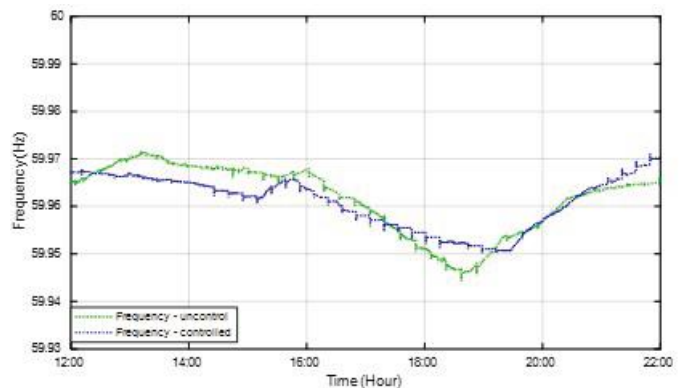
Figure II.4.1.4 Frequency Response from Transmission Simulation [1]

has a heavy EV charging load. The frequency drops below 59.95 Hz as defined in the dead-band due to the heavy EV charging load. In the controlled scenario, the distribution network capacity is defined by the substation limitation which is 3 MW initially. The EV charging loads are shifted smoothly and the frequency is saturated above the dead-band. At around 19:10, the frequency drops below the defined dead-band in EMS because of the increasing load in the transmission system. Therefore, the load-based frequency control is enabled to further curtail the network capacity from 3 MW to around 2.8 MW. The grid frequency then recovers back to the pre-defined dead-band.

Task 4. Early-stage R&D; Interoperability/grid integration components

Charge Reservation System

Argonne researchers saw a need to further explore ways to optimize the utility of charging ports at workplaces and other semi-public locations such as multi-unit dwellings (MUDs). Historically, workplaces and MUDs do not install a charging port for each EV driver, thus drivers must share the available ports. An online charge station reservation system with feedback from charge stations could greatly increase the utility of the charge stations as well as the satisfaction of EV drivers.

Leveraging the CSMS platform developed under the Smart Charge Adapter TCF project, Argonne began development of an EV driver reservation application termed EVrest. In addition to development of both an Android and iOS driver mobile app, further changes and features were added to the ANL CSMS platform to allow for setup and configuration of stations. The ANL CSMS platform allows station owners to group stations and define their mode of operation.

Figure II.4.1.5 EVrest Start Charge screen shot.

Currently there are three modes of operation for a group of stations:

- **Default:** Station is first come first serve. EVSE owners can enable or disable access control. By enabling access control drivers must utilize the EVrest app to begin a charge session.

- **Reservation:** Station requires the EV driver to reserve the station. This can be done in advanced or at the time of arrival if a port is available.

- **Waitlist:** Similar to the Default mode but when all ports of a Waitlist group are being utilized, drivers can add themselves to a waitlist and be notified when a port has become available.

Priority has been given to first developing the Reservation mode on the platform while focusing on integration of the following types of OCPP 1.6J stations:

- AC Single Port

- AC Dual Port

- DC Single Port

- DC Dual Port (1 session allowed at a time)

- DC Dual Port (2 sessions allowed simultaneously)

When stations are configured as reservation only, drivers will be required to reserve a timeslot. In order to reserve a charge port, the driver must input their desired start time, charge duration, electric miles needed and their vehicle (stored in their profile). This data can then be used in future research to calculate predictive analytics and aid in smart charging algorithms.

Once the reservation is made drivers will get push notifications at 15 minutes until reservation start and on reservation start. Drivers will have 15 minutes to start a charge session, or the reservation will be cancelled. Once the charge session starts, drivers will get push notifications if their charging ends. Drivers will also receive a notification once their reservation ends. Charging will automatically be stopped once the reservation end time occurs. The driver will then have 15 minutes to unplug their car. Each registered driver on the platform has a conduct score. This conduct score is a way to track and monitor habitual drivers that overstay their reservations or totally miss their reservation. Initially, there will be no penalty for low conduct scores but that could change in the future.

Containerized CIP.io

The Argonne Common Integration Platform or "CIP.io" is a framework of open-source applications and tools utilized to make monitoring, logging, and controlling of building and site energy an easier and more standardized task. In addition to the open-source applications which run on off the shelf hardware, even as minimal as a Raspberry Pi or Odroid single board computer, there are additional custom written open-source nodes to support specific protocols such as OCPP (Open Charge Point Protocol), OpenADR (Open Automated Demand Response), BACNet, and Modbus-TCP.

CIP.io mainly utilizes what is becoming a common framework stack in the IOT industry known as MING. MING stands for: MQTT, InfluxDB, Node-Red, Grafana. MQTT is utilized as the common communications protocol between both internal and external applications and entities. CIP.io relies on all communications being based on the TCP/IP stack. Entities which do not communicate via TCP may have an intermediary process or device which converts its communication to and from TCP / MQTT. InfluxDB is a time series database and is used to store historical data collected from devices and services. Grafana is an open-source graphing tool that makes graphing and analyzing data stored in time series (and other database formats) easy. Node-Red is an "Internet of Things" flow-based programming framework. The custom nodes mentioned above are all written as Node-Red custom nodes. In addition to the MING applications, CIP.io also utilizes a few other open-source programs such as MongoDB, etc.
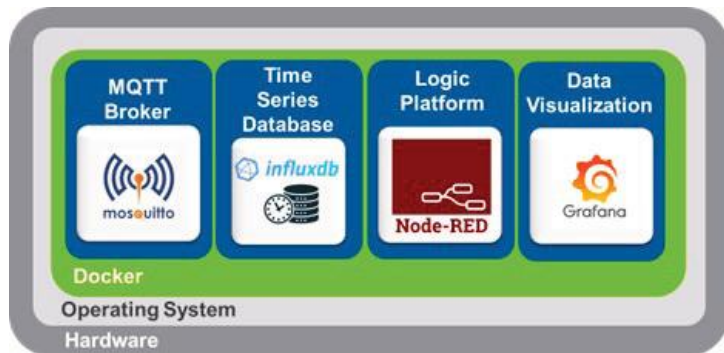
Figure II.4.1.6 Containerized CIP.io block diagram.

The initial implementation of CIP.io required that each application in the framework be installed individually. This required knowledge of:

- Where to obtain each application for installation on the chosen hardware

- How to configure it for proper use

- How to address (network wise) each application to communicate with the other pieces

- How to secure each application to prevent unwanted external access

- How to install the custom Node-Red nodes and examples.

All of the above made re-deploying of similar CIP.io setups a challenge to others outside of our organization.

To address each of these items a custom Linux script was developed. The custom script/installer accomplishes the following:

- Queries the user if they would like a default or custom installation of each application.

- Determines if the host system CIP.io is being installed on currently has a Docker environment installed and does the installation if needed

- Installs each of the CIP.io applications (MQTT, InfluxDB, Node-Red) into their own docker container

- Installs Node-Red container that includes the custom nodes (for OCPP, OpenADR, etc.) already installed for the user to use.

- Node-Red instance also provides pre-installed usage examples for the user's reference.

Besides the benefits of the script to automatically install the pieces of a CIP.io system, containerizing each component via a system such as Docker also addresses many of the issues listed above. Each container acts as a stand-alone installation, while groups of containers make networking easy and private amongst the containerized applications (unless the user chooses to expose those applications and ports). Upgrading individual applications within containers also has little impact on the rest of the applications. No need to reboot an entire system contained on a single host just to upgrade/update a single application. Utilizing multiple Docker hosts also makes redundancy easier and can reduce CPU load on a single host. Internally to the containerized network, each applications address on the network is simplified and standardized by the name of the container itself instead of a random IP address (for example http://influxdb instead of http://172.18.0.x)

OCPP 1.6J Client for Smart Charge Adapter

The Argonne Smart Charge Adapter (SCA) is a device that enables wireless communication, command, and control of non-networked or proprietary level 2 EVSEs. The SCA connects to the charging connector of the EVSE plugs into the EV. It uses Wi-Fi to communicate with a message broker, which in turn passes messages to and from a backend system. The current SCA firmware communicates with the message broker using the MQTT protocol.

The SCA currently has 2 single board computers (SBC) used for its operation. One of those SBCs job is to do all the local communication and metering of both the EVSE side and the EV side. It in turn passes information to the second SBC (an ESP32) whose job it is it relay messages to and from the wireless network to the backend control.

The "Proof of Concept" task was to replace the communications tasks done by the ESP32, passing command, control, and measurement via MQTT to a somewhat proprietary backend, and instead implement it as an Open Charge Point Protocol (OCPP) "Charge Point" (CP). The firmware on the ESP32 SBC was replaced with an open-source ESP OCPP implementation that was customized to continue to use the same internal communication between it and the main SBC firmware without change.

Figure II.4.1.7 Smart Charge Adapter with OCPP 1.6J client charging Chevrolet Bolt.

The POC OCPP SCA has been tested to now act as an OCPP 1.6 charge point station. The following are some of the OCPP communication capabilities tested:

- Boot Notification
- Heartbeat
- Status Notifications
- Authorize
- Start Transaction

- Stop Transaction
- Meter Values
- Get / Change Configuration
- Remote Start / Stop Transaction

Conclusions

The benefits of smart charging versus controlled and uncontrolled charging have been assessed. From a technical standpoint optimized smart charging via charge scheduling, although the most technically involved, has the greatest benefit to all actors in the SCM ecosystem. The goal of Argonne's research in this project was to develop and deploy a standard based approach to smart charging which is an alternative to current approaches today and to show the benefits of such an approach. EV charge scheduling meets the needs of the grid and EV driver and should be explored further as more EV models come to market that support ISO 15118 AC charging.

The real-time performance of the network of devices at the Energy Plaza has been linked to Argonne's distributed network model and regional distribution and transmission models at Idaho National Laboratory to enable analysis of grid impacts. A real-time HIL frequency regulation co-simulation was performed between the two laboratories and the results show that a hybrid approach of both smart and controlled charging can limit the frequency droop caused by aggregated EV load.

Argonne researchers have developed an EV driver charge station reservation system termed EVrest. The mobile app leverage previous development work and will allow EV drivers the ability to reserve both AC and DC EVSE, receive notifications and provide historical charging data to the driver. From a station owner's perspective, the platform will increase charge station utilization rates and alleviate driver complaints. From ANL researchers' perspective the EVrest platform will provide driver tagged charging data for future analysis and a platform to implement cutting edge EV smart charge management algorithms.

Argonne researchers have developed a method to easily deploy a basic CIP.io framework. This deployment method utilizes software containers to automate the rapid deployment and configuration of the ANL CIP.io platform. There are many benefits to utilizing software containers and with this new method of deployment will aid in extending Argonne's research with other outside partners.

Leveraging ANL's expertise with OCPP and the smart charge adapter hardware, ANL researchers have implemented a proof-of-concept OCPP 1.6J client that runs on the smart charge adapter hardware. With this new client, an SCA could be integrated into any commercial CSMS backend that is OCPP 1.6J compliant. This ability further extends the devices capabilities to integrate non-networked EVSE into the SCM ecosystem.

References

1. Wu, Z., Manne, N., Harper, J., Chen, B. et al., "A Cloud-Based Simulation and Testing Framework for Large-Scale EV Charging Energy Management and Charging Control," SAE Technical Paper 2022-01-0169, 2022, https://doi.org/10.4271/2022-01-0169.

Acknowledgements

II.4.2 Electric Vehicle Smart Charge Adapter TCF (ANL)

Jason D. Harper, Principal Investigator

Argonne National Laboratory
9700 South Cass Avenue
Lemont, IL 60439
E-mail: jharper@anl.gov

Lee Slezak, DOE Technology Manager

U.S. Department of Energy
E-mail: Lee.slezak@ee.doe.gov

Start Date October 1, 2018	End Date: May 30, 2022	
Project Funding: $1,180,698	DOE share: $590,349	Non-DOE share: $590,349

Project Introduction

Argonne National Laboratory (ANL) has invented and patented a universal smart charge adapter (SCA) that is connected between any AC charge station and plug-in electric vehicle. The smart charge adapter integrates legacy non-networked AC charge stations into a managed charging network that allows communication with grid operators. The smart charge adapter enables metering, monitoring and management control of charge sessions in response to local supply/demand levels. Qmulus, LLC (Chicago, IL) has an agreement with Argonne regarding the issued US patent and the EU patent application, with the intent to commercialize the technology.

The availability of the smart charge adapter will support the integration of EV charging as an additional grid resource, enabling grid operators to maintain supply/demand grid balance in part by controlling networked EV charging sessions as needed. As more EVs come under this level of control, it will support a reduction in the potential for brownouts, outages and voltage/frequency fluctuations that are caused by excess demand within a local or regional grid. Currently available charge stations (EVSE) are either not connected to the developing smart grid or are connected only through proprietary, insular platforms making it extremely difficult to interface charge sessions from large networks of diverse EVSE to monitor and control EV charging demand.

Figure II.4.2.1 The SCA is an in-line adapter for SAE J1772™ PEV charging (Mk III design)

Qmulus is the commercialization partner working with ANL. Final development of the Beta prototype and commercial smart charge adapter is underway on a contract basis with a contract-engineering firm. Zen Ecosystems (Newport Beach, CA) is providing access to its customer base for the full field trial. California Energy Commission (CEC) is providing advisory services for engagement with California utilities and for regional market and EV user information.

The primary goal of the project is to create a commercial SCA design that includes hardware, firmware, and software applications. The Beta prototypes will be tested at ANL in a controlled use setting and with end-users in Zen Ecosystems' coverage areas in California. Feedback from the current Beta device and our Beta pilot

programs will lead to a commercial SCA design. Additional pilot(s) are targeted for California utilities (and/or another regional utility) in cooperation with Zen and the California Energy Commission (CEC).

Objectives

Qmulus' commercialization strategy initially focuses on public and semi-public owners of EVSE who are interested in a low cost, single interface for their networked and non-networked EVSE. These users will be able to network all their AC EVSE, regardless of brand, under a single interface via the SCA's Wi-Fi communications and cloud platform. Qmulus' longer-term strategy will target utilities to support their grid management needs. Residential users are also considered in their planning, particularly to support the various utility energy savings programs in which an EV driver may enroll. The initial markets are guiding the development plan, since larger scale users desire a more rigorously tested and certified solution. Ultimately, Qmulus hopes to support utility-sponsored energy programs for both home and workplace charging, enabling utilities to realize increased potential for smart grid management.

Development of the Beta version of the SCA was not complete by the start of the TCF award period thus the TCF funds were used, in part, towards final development and testing at ANL during Phase 1 of the TCF project. Conformance to the specifications is being substantiated in testing by ANL. The SCA will satisfy all design requirements and conformance tests before being deployed in pilot programs. A successful Phase 1 will result in beta HW and software ready for pilot program deployment as well as the design of the commercial SCA.

In Phase 2, the Beta prototypes will be field tested in two separate pilot programs. Phase 2 will provide critical data and feedback on the Beta SCA that will guide the development of the commercial version. User surveys will be conducted throughout the pilot programs to understand users' perceptions of the device, applications and controlling software. The surveys will be revised and updated as new information is obtained. Qmulus will work with CEC to understand and target the needs of California consumers and utilities for a smart grid enabled SCA. Root cause failure analysis (RCFA) will be used to examine any devices that have failed in the field to identify the causes behind the failure. These findings will support any changes to the design package for a commercial SCA.

In Phase 3, the partnership will continue its ongoing efforts with CEC to engage one or more utilities to plan an EV Smart Charging Pilot. In addition, further collaborations with Zen will be developed. This will parallel Qmulus' commercial roll-out for public and semi-public users. Working independently of the TCF project, Qmulus will have completed all business development and marketing steps required for the short-term launch goals. Engagement with a utility and planning for a demonstration pilot will be important for the intermediate and long-term business strategy. A successful Phase 3 will result in identifying proactive utilities looking to implement EV smart charging programs and engaging them.

Approach

Phase 1: Finalize SCA Development and Testing

This phase began prior to TCF funding; however, it has carried into the TCF period. This phase involves finalizing all hardware (mechanical/electrical), software, firmware, and cloud platform. Design will focus first on a Beta SCA and web platform that are as close to commercial products as possible. Twenty Beta SCAs will be built for testing in the Phase 2 field trial. A user friendly, secure, and reliable Beta web platform will be developed. Testing will be performed in the laboratory and at ANL's interoperability center.

Phase 2: Beta Pilot Program

Qmulus, Zen and ANL would implement two small-scale EV Demand Response pilot projects, utilizing Zen's OpenADR 2.0a/b certified cloud which would enable the SCA to act as a Virtual End Node (VEN), providing automated Demand Response dispatch from utility Demand Response Automation Servers (DRAS). The first pilot (Pilot A) would be performed at ANL. Pilot B would focus on the integration of the ZEN's OpenADR cloud interface into the Qmulus Cloud Platform to add EV charging into an OpenADR demand response

program. Successful completion of Pilot B would result in the integration of the SCA/QCP into Zen's OpenADR system for 2 weeks with simulated DR events.

Phase 3: Utility Pilot Planning

Qmulus is partnering with Zen and the California Energy Commission (CEC) to identify California utilities willing to participate in an EV Smart Charging pilot. Prior to the TCF award, Qmulus and CEC will use their established contacts to engage partners and plan the pilot in California. Qmulus is also currently looking for potential partners in the Chicago, Denver, and Minneapolis metropolitan areas. Given the long planning periods of utilities, it is not expected that this Phase will be completed during the TCF project period, only that the engagement of partners, planning and development of the pilot will occur. If successful, the TCF project will lead to the EV Smart Charging pilot project, which will also support Qmulus' goal of identifying utilities that are potential customers for the SCA. Results of the EV Smart Charging Pilot may lead to further revisions to the design of the device, its software or firmware (if needed) or to a utility production package that ensures a reliable, rugged device and software that can be integrated into utility management systems or easily exchanged for utility-developed software.

Results

Unfortunately, this project was delayed due to Covid and the inability of Qmulus to raise sufficient funds to continue the commercialization of the Smart Charge Adapter. Given this news early in the fiscal year, development work on the adapter was paused until a new licensee was found. A suitable licensee was found late in FY 22. Argonne and EVmatch have entered into a licensing agreement to commercialize the Smart Charge Adapter. This is exciting news for the technology developed under this project but did affect the deliverables/results.

Smart Charge Adapter Hardware

From the extensive testing performed on the Mk III prototypes, the MK IV design was kicked off in FY21. The electrical bill of materials (BOM) was scrubbed for obsolescence and updated. The schematics and board layouts were updated with the new components and new printed board assemblies were manufactured for bench top testing. These printed circuit board assemblies required updated firmware. Unfortunately, the printed circuit board assemblies were not tested in updated Mk IV mechanical enclosures because tooling was put on hold due to the industry partner not being identified.

Figure II.4.2.2 Mk IV Commercial Beta Smart Charge Adapter: Portable, Robust and Easy to Use.

Since signing the licensing agreement ANL has worked with EVmatch and our development partners to derive a statement of work to utilize the remaining funds of the project to create 3D printed housings of the Mk IV design and utilize the printed circuit board assemblies to further test the Mk IV design.

Qmulus Cloud Platform and Mobile App Development

The cloud platform and mobile app development was finalized in FY21. Ongoing testing and debugging of the platform and mobile app occurred during this fiscal year.

Pilot Programs

The ANL pilot (Pilot A) began in Q1 of FY21 with deploying four Mk II beta SCA's at the ANL Smart Energy Plaza. The SCA's were locked onto a single port of four BTCP 40A L2 EVSE shown in Figure II.4.2.3. There are a total of 12 ports at the Smart Energy Plaza for employee EV charging. Argonne employees had the option to select a port with or without an SCA. This pilot continued through FY22. The platform was moved to new backend servers earlier in the fiscal year and unfortunately, the deployed SCA's were not

pointed to these new servers therefore, months of data was not recorded. However, 127 new sessions in FY22 were recorded, bringing the total number of sessions since deployment to 348 sessions resulting in 4.3 MWh of energy dispensed (Figure II.4.2.4). The Mk II prototypes held up well considering their exposure to the fall, winter, spring, and summer seasons. No mechanical failures occurred, though the white prototype housings turned yellow due to the lack of UV resistance in the plastic. This will be taken into consideration when choosing the commercial housing material.

Figure II.4.2.3 Mk II SCA deployment at ANL Smart Energy Plaza.

Figure II.4.2.4 Smart Energy Plaza SCA Pilot Data for FY22.

Multiple adapters were utilized by Argonne employees at their place of residence. Feedback from the employees has been positive. Data collection is still ongoing. In addition to Argonne employee deployment, Argonne has provided potential partners access to the MK II prototypes for testing in their own laboratories. The list of companies that have tested the MK II prototypes include BMW, Stellantis, Duke Energy, Ameren, Hilo Energie, and EVMatch.

Given the uncertainty with the commercialization partner, the Zen Ecoystems OpenADR pilot was put on hold for FY22. However, EVmatch is actively engaged with multiple utilities to setup an SCA pilot program.

Conclusions

Qmulus was able to meet the TCF cost share requirement but unfortunately was not able to raise additional funds to commercialize the SCA technology. Argonne is grateful to the Qmulus founders who believed in the technology early and provided significant time and effort to get the technology to the point where it is today.

The development of the hardware and software under this project helped garner a new industry partner (EVmatch). There still remains additional testing and debugging but the technology is very close to becoming a commercialized product.

Acknowledgements

II.4.3 Flexible charging to Unify the grid and transportation Sectors for EVs at scale (FUSE) (EVs@Scale Consortium)

Jesse Bennett, Principal Investigator

National Renewable Energy Laboratory

5013 Denver West Parkway

Golden, CO 80401

E-mail: Jesse.Bennett@nrel.gov

Jason Harper, Principal Investigator

Argonne National Laboratory

9700 South Cass Avenue

Lemont, IL 60439

E-mail: jharper@anl.gov

Manoj Kumar, Principal Investigator

Idaho National Laboratory

775 MK Simpson Boulevard

Idaho Falls, ID 83415

E-mail: ManojKumar.CebolSundarrajan@inl.gov

Andrea Mammoli, Principal Investigator

Sandia National Laboratories

7011 East Avenue

Livermore, CA 94550

E-mail: aamammo@sandia.gov

Lee Slezak, DOE Technology Manager

U.S. Department of Energy

E-mail: lee.slezak@ee.doe.gov

Start Date: January 1, 2022   End Date: December 31, 2026

Project Funding: $3,150,000   DOE share: $3,150,000   Non-DOE share: $0

Project Introduction

Electric vehicle (EV) adoption will greatly expand beyond light-duty (LD) vehicles capable of charging at single-family residences to now include LD, medium-duty (MD), and heavy-duty (HD) applications, with more powerful charging at additional public stations and private depots. The increasing power demand will challenge the electric grid in various ways, requiring mitigation through vehicle grid integration (VGI) and smart charge management (SCM) solutions designed to integrate with all vocations. There is also a lot of geographic and seasonal diversity in the electrical demand and generation across the United States. As EV adoption expands, the best VGI or SCM solutions to integrate EV charging will depend on several factors such as vehicle type and travel patterns, available charging infrastructure, and local grid characteristics, which may need to be selected on a case-by-case basis. To facilitate the electrification of these transportation sectors and ensure a maintained reliable and resilient electric grid, the following barriers must be addressed:

- Existing SCM strategies are effective for low adoption of LD EVs; however, a shift in charging locations, patterns, and charging power for EVs@Scale will impact efficacy

- MD and HD adoption will expand rapidly though grid planning for this new load, and SCM strategies that account for vocational needs and differences do not currently exist

- SCM and VGI benefits for consumers and utilities have not been demonstrated with EVs@Scale across the range of conditions (geographies and seasons) found in the US.

- There is a lack of enabling technologies for smart charging in a utility environment.

The EVs@Scale Laboratory Consortium has identified the SCM/VGI pillar to investigate barriers and develop solutions to mitigate these barriers. The Flexible charging to Unify the grid and transportation Sectors for EVs at scale (FUSE) Project Team is developing an adaptive ecosystem of SCM strategies and VGI tools that will be relevant to a wide geographic area and numerous vocations of electric vehicles across all class sizes. These solutions will both be analyzed in a simulation environment and developed in the lab with newly developed prototypes and market available solutions. These Solutions will be developed through a coupled grid and transportation approach, assessing the potential transportation energy needs of these vehicles and their charging power demands throughout the grid. This two-pronged approach will resolve practical implementation challenges for communication, control, and hardware deployment and work directly with utility partners and travel data providers to analyze the effectiveness of these SCM and VGI solutions for EVs@Scale.

Analysis of these solutions will focus on transportation in the state of Virginia and charging demands throughout the utility partner service territory. Building on past efforts [1], [2], this project will develop travel patterns for local MD vehicle travel, HD travel throughout the state including the port of Newport News, and LD vehicles with and without access to home charging in both urban and suburban settings. Applying realistic SCM strategies will require a detailed understanding of EV, charger, and grid communication standards to ensure proper assessment of grid impacts and SCM efficacy. Early-stage R&D for the development of enabling technologies will expand on the analysis efforts to demonstrate the capabilities of these technologies in a lab environment and generate adequate real-world data on the performance of these new technologies. These analysis and demonstration efforts will assess the effectiveness of SCM and VGI solutions at mitigating the grid impacts of EVs@Scale, while testing the performance of these technologies in a lab environment to ensure these capabilities provide grid support for utilities while ensuring vehicles receive the energy they need.

Objectives

Travel and Charging Analysis

This task will assess the vehicle energy needs and charging requirements for EVs@Scale and will synthesize travel data that represents expanding EV adoption, vehicle travel patterns, and transportation energy needs. It will also identify charging session requirements to meet these energy needs throughout existing dwell periods. These charge session details will inform the grid impact analysis portion of this project and identify the charge flexibility, defined as the difference between charge session duration and dwell period length. This charging flexibility will be leveraged to implement SCM strategies on vehicle charge sessions to mitigate the grid impacts of charging EVs@Scale.

Broad SCM Analysis

This task will broadly assess gaps in SCM strategies across a wide range of conditions due to geographic and seasonal diversity in the electrical demand and generation across the United States. For example, the best SCM strategy in San Francisco given its solar adoption and moderate climate may be different than in Pheonix given its solar adoption and hot climate (high air conditioning loads) which may also be different than in the northeast United States given its wind adoption and cold winters. This task compliments and adds breadth to the detailed grid impact assessment in task 2.2. This task will study more scenarios than is possible in 2.2, but in much less detail. The focus of this task is to assess the ability and limitations of each SCM strategy to strategically shift PEV charging in time across a wide range of conditions. Performance of SCM strategies will be evaluated at the regional/utility level as well as at the site level for HPC.

SCM Development & Demonstration

There is a lack of open-source technologies for smart charging research in a utility environment. This task will develop enabling technologies for the smart charging ecosystem, including smart interoperable EVSE, parking sensors (for real-time charger availability), and interoperability diagnostics. The effort will leverage previous developments including CIP.io, the Smart Charge Adaptor (SCA), charge reservation system, and schedule optimization. The system will be integrated, tested, and demonstrated at the Energy Plaza, then transferred to the utility partner environment for the pilot program.

Approach

Travel and Charging Analysis

Passenger EV charging demands are simulated for aggressive 2040 electrification scenario to understand the energy requirements and smart charge management opportunities for EVs@Scale. Existing models and approaches for synthesizing spatially resolved passenger EV travel and charging data from in-vehicle telematics data are adapted and refined in this project. Specifically, a semi-Markovian stochastic trip chaining method, named Zone Entity Probabilities (ZEP), was leveraged to develop the EV travel itineraries needed to simulate charging. Expanding upon previous studies [1-2], this study simulates EV travel and charging activities for two new regions in Virginia (Richmond and Newport News) and considers higher EV adoption levels (>50% EV penetration). Key requirements and steps of this task are summarized in Figure II.4.3.1.

1. Trip Data Acquisition & Preprocessing
Representative LDV travel data for region(s) of study is joined with geographically determined locational characteristics obtained from multiple data sources.

2. EV Adoption Modeling
For a given analysis year (2040), assign PEVs to households by vehicle model (battery size, ECR, & max kW acceptance required for simulation).

3. Travel Itinerary Synthesis
Vehicle trips from data aggregators typically do not contain persistent vehicle identifiers enabling analysis of multi-trip travel itineraries. Thus, an approach for generating synthetic travel itineraries is leveraged.

4. EV Charging Demand Simulation
EV charging is simulated for synthetic travel itineraries considering: 1) EV adoption assumptions; 2) charging behaviors and location-specific EVSE availability; 3) home charging access assumptions.

5. EV Load Profile Generation
Charging demand for a given analysis year (2040) is assigned to specific locations (i.e., land parcels) by location type.

Figure II.4.3.1 Key requirements and steps of LDV travel analysis

Key requirements and steps for the LDV travel and charging analysis are now outlined:

1. Wejo (https://www.wejo.com) connected vehicle data collected during September 2021 and February 2022 throughout the state of Virginia was procured to represent real-world driving behaviors in the regions of study. September data represents summer month and February winter month, capturing seasonal travel patterns and grid conditions. As shown in Figure II.4.3.2, the two months are chosen based on the consideration of avoiding the impact of COVID-19 omicron surge on community mobility (per Google statewide COVID-19 Community Mobility Reports). Besides the trip data, other data including vehicle registration and land use data were also collected. Figure II.4.3.3 shows some sample land use data for the two Virginia cities of study, Newport News and Richmond. The acquired trip data was preprocessed and joined to land use data to infer trip purpose.
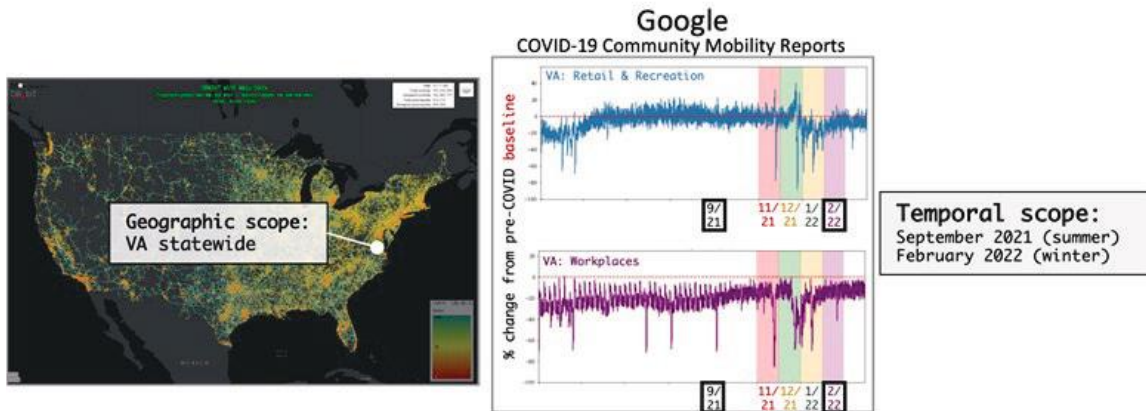
Figure II.4.3.2 (Spatial and temporal consideration of LDV trip data acquisition)
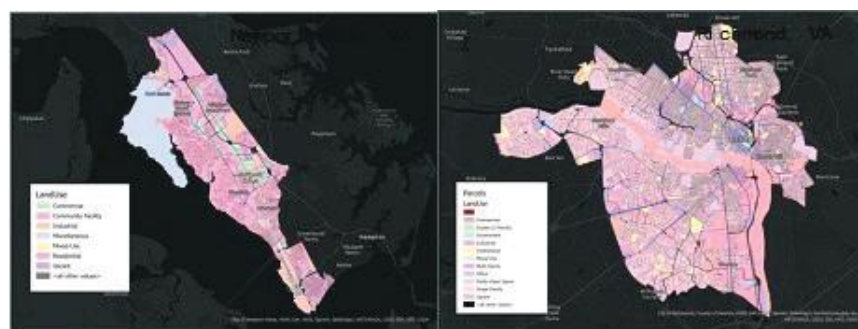
Figure II.4.3.3 (Land use data for Newport News and Richmond)

2. For scenario development and EV adoption modeling, we leverage NREL's TEMPO model. TEMPO is a transportation demand model that projects household-level vehicle ownership and technology choices based on consumer preferences. Here, we develop an aggressive passenger EV adoption scenario for 2040 where 50% of national sales are EVs by 2030 and 100% of sales are EVs by 2035. As shown in Figure II.4.3.4, this leads to a scenario where EVs represent ~52% of the total passenger vehicle stock in Virginia.
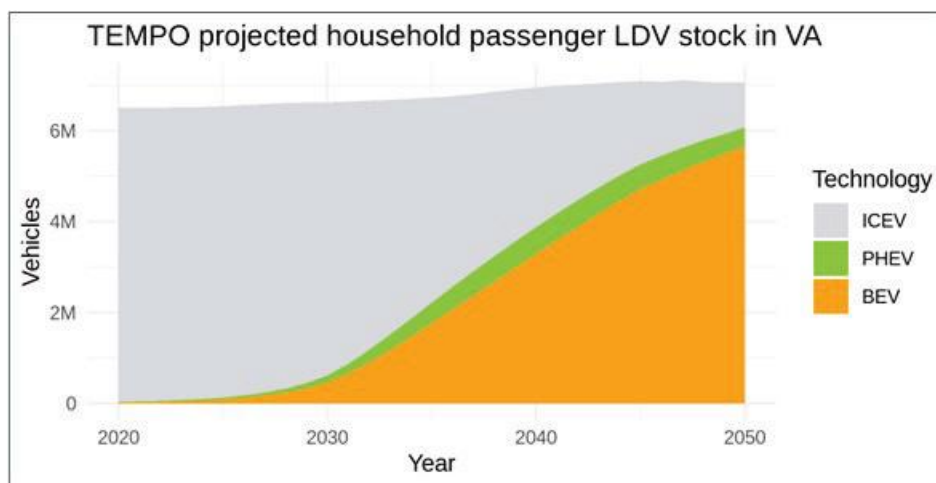
Figure II.4.3.4 (TEMPO projected household passenger LDV stock in Virginia)

3. Because the acquired Wejo trip data contained unlinked trips with no persistent vehicle identifier, the third step leverages the previously mentioned ZEP trip chaining method to generate synthetic vehicle travel itineraries from the unlinked Wejo trips data. Locational dwell distributions (from 2017 NHTS data) are used to infer vehicle dwells at each stop. Trips are chained based on spatiotemporal alignment of trip origins and destinations with consideration of dwells at each stop. Figure II.4.3.5 shows a trip chain example. In summary, the trip chaining process includes 5 steps: (1) select trips from the Wejo trip database; (2) determine the dwell time of a vehicle at the destination of a trip based on the distributions and land use; (3) determine the next trip that is in the some zone (census block groups are used in this project) and leaves within a small time period (15 minutes is used in this project) after the end of the previous dwell time; (4) the distance from previous end to next start is added to the daily sum, i.e., the red arrow in Figure II.4.3.5; and (5) at each location the expected departure time is compared against the required return home time to determine if the vehicle is sent to its home location. After finishing trip chaining, synthetic vehicle travel itineraries are validated against 2017 NHTS vehicle trip distributions.
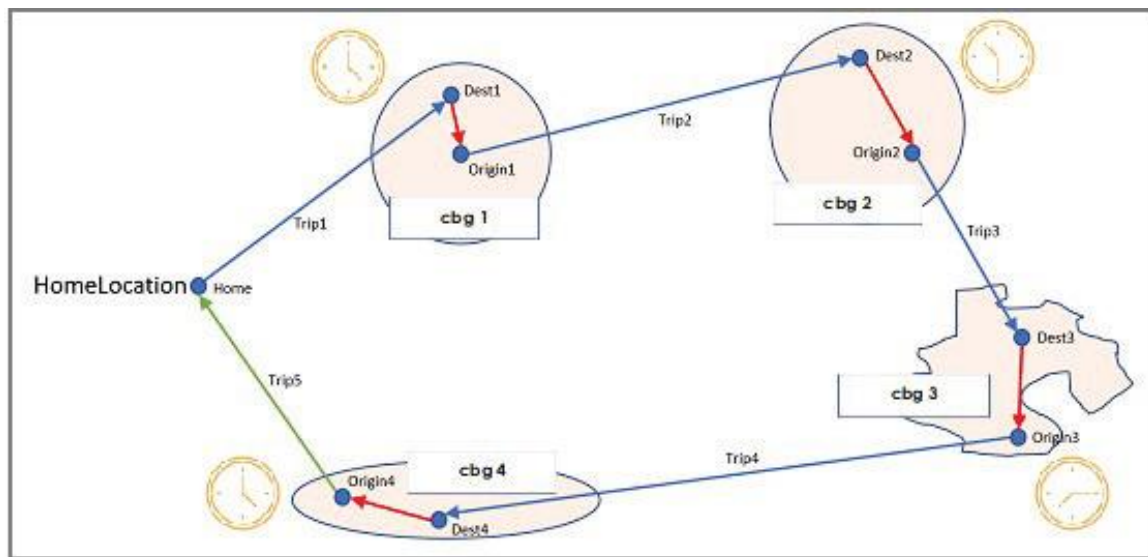
Figure II.4.3.5 (Trip chain example)

4. The EV charging simulation is conducted using NREL's EVI-Pro model. EVI-Pro takes a set of vehicle travel itineraries and simulates EV charging behaviors, energy demands, and infrastructure requirements. For this project, EV drivers are assumed to prioritize home charging, followed by workplace and public slow charging (increased opportunities for smart charging management and presumably lower charging cost). Home charging access is assumed to be 72% in year 2040 scenario, which is derived from previous modeling efforts [3].

5. EV charging demand is combined from two sources: (1) intra-regional charging demand is determined from EVI-Pro simulations; (2) inter-regional charging demand is determined by separately simulating charging for long-distance trips (>100 miles) that end within the region of interest. EV charging events are assigned spatial coordinates depending on their location type: (1) home charging locations are determined based on EV adoption projections and residential land use data; (2) workplace and public charging locations are based on census tract of charging demand and commercial land use data. EV charging events can be assigned to individual stations depending on EVSE type(s), station size, and port utilization assumptions.

SCM Development & Demonstration

Enabling Technology Development

To meet the EVs@Scale project objectives, researchers need access to technology platforms that are open and not reliant on proprietary implementations. In order to research and demonstrate VGI/SCM approaches to provide feedback and lessons learned to the broader industry, researchers set out to develop enabling technologies. These developed pieces of technology will then be demonstrated in future years of the EVs@Scale project.

EVrest: EV Driver Reservation System

Argonne National Laboratory operates an employee EV charging program. The program requires cost recovery per Federal Government rules, therefore ANL employees play a flat fee per month for unlimited charging during normal business hours. The Argonne Lemont, IL campus currently provides ~ 50 AC ports and ~8 DC ports with a mixture of networked and non-networked EVSE from multiple manufacturers. There are significantly more registered EV drivers than there are available charging ports across the lab, therefore the Argonne Sustainability group has implemented an online reservation form for each available port on campus. EV drivers are required to utilize the online reservation form to reserve a specific station/port on a specific day and time. Unfortunately, there is no feedback/communication between stations and this online reservation form. It should also be pointed out that both the networked and non-networked EVSE are configured to allow EV charging upon being plugged into an EV (i.e., no access control). One of the biggest issues with this current system is EV drivers utilizing reserved ports without making a reservation, which leads to upset employees who have reserved that specific port.

Leveraging Argonne's Open Charge Point Protocol (OCPP) Charge Station Management System (CSMS) developed in a previous DOE project, ANL researchers proposed developing an EV driver mobile application (Android and iOS) that could leverage the networked OCPP stations around campus and improve the current reservation system. The driver reservation mobile app is called EVrest which has multiple benefits and aims to aid in providing insight and data while providing researchers a platform to implement cutting edge VGI/SCM research.

EV Charge Scheduling

As more of the US light duty fleet transitions to electric vehicles, smart charge management will be key in integrating this new massive load into the US grid. The vast majority of EV charging is done at the workplace or at home. Argonne workplace charging data shows that the average charge session (plug-in to unplug) is ~4-5 hours, where only roughly half of that time is spent actually charging. This type of flexibility can be used when integrating a vast number of electric vehicles into the grid to help stabilize the load on the grid. Unfortunately, the currently deployed approaches for VGI only take into the account the needs of the EVSE owner, premise owner and/or grid operator and does not attempt to meet the needs of the driver (required energy by departure time). True smart charging takes into account the needs of all the actors in the ecosystem to meet the needs of the grid and the EV driver.

In order to get the needs of the EV driver there must be a standardized protocol across the industry for EV and EVSE manufacturers. Fortunately, the ISO 15118 standard establishes the high-level communication (HLC) protocol to enable digital information exchange between the EVSE and EV. One of the many features of the ISO 15118 protocol is the ability for the EV and grid to negotiate a charging schedule. This charging schedule is negotiated at the beginning of a charge session while both the grid and EV can initiate a renegotiation at any point during the session.

Leveraging previous work on developing a 15118 based EV charge scheduling application, Argonne proposed to continue developing a more robust version of the 15118 EV charge scheduling application while exploring possible deployment options for such a system.

OptiQ: Smart AC L2 EVSE

AC Level 1 (L1) or Level 2 (L2) charging does not require high-level communication to be accomplished. The majority of AC charging sessions today utilize the SAE J1772 or IEC 61851 standards which rely on analog based signaling to accomplish AC charging of the electric vehicle. This analog based signaling allows for controlled charging of the EV by limiting the maximum ampacity of the EVSE, thus curtailing the EV charging load as seen by the grid. Automotive OEM's have been slow to implement HLC for AC charging. However, the benefits of implementing HLC for AC charging has never been quantified or adequately explained to key industry stakeholders.

Therefore, Argonne has proposed to develop a Smart AC L2 EVSE, termed OptiQ. OptiQ incorporates both analog based AC charging (SAE J1772 PWM) as well as ISO 15118 HLC AC based charging. In addition, the OptiQ EVSE can establish HLC with all Tesla models. As of Q4 of 2021, Tesla had a 70% market share of all light duty electric vehicles in the US representing a significant portion of the US light duty electric fleet. The OptiQ EVSE allows Argonne researchers the ability to test new cutting edge SCM/VGI algorithms.

Results

Travel and Charging Analysis

Wejo trip data summary: In this project, two regions in Virginia are chosen for analysis: (1) Newport News region (includes four counties or unincorporated communities – Newport News, Hampton, York County, and James City County); (2) Richmond region (includes four counties or unincorporated communities – Richmond, Henrico County, Chesterfield County, and Hanover County). These regions were selected since they are well covered within Dominion Energy's (the utility the team is contracting with to provide models and data for subsequent distribution system impacts analysis). They were also selected for their diverse travel requirements, with Newport News containing a major freight terminal and Richmond being the third largest metropolitan area in Virginia and home to the state's capital. Table II.4.3.1 reports the total number of trips and total vehicle miles (VMT) traveled in the Wejo trip data for the two regions of Newport News and Richmond and two months of September and February. As reported by Wejo, these data represent ~3% of passenger vehicle population within each region.

Table II.4.3.1 Regional Trip Data Summaries

Region	Sep. Trips	Feb. Trips	Sep. VMT	Feb. VMT
Newport News, VA: Newport News Hampton York County James City County	920k	720k	4.3M	3.3M
Richmond, VA: Richmond Henrico County Chesterfield County Hanover County	1.5M	1.3M	8.9M	7.2M

EV Adoption Results: The TEMPO model projects EV adoption at the county-level broken out by powertrain technology, battery range, and body type. These projections are then translated to a set of 11 archetype vehicles (

Table II.4.3.2), developed in previous DOE studies (DirectXFC, ReCHARGE). These vehicle models contain additional attributes, such as average energy consumption rate (ECR, Wh/mi.) and DC charging acceptance rate (kW), that are required to simulate charging.

Table II.4.3.2 Archetype Vehicles for Simulation

Veh. Gen.	Vehicle Type	EV Range (mi.)	ECR (Wh/mi.)	DC Charge Accept. (kW)	2040 NN fleet share (%)	2040 Rich fleet share (%)
Gen 3	BEV SUV/truck	300	475	575	37.5%	39.5%
	BEV midsize car	300	325	400	7.8%	6.3%
Gen 2	BEV SUV/truck	250	475	350	10.8%	13.5%
	BEV midsize car	300	325	300	3.5%	3.7%
	BEV compact car	150	300	150	19.7%	17.8%
Gen 1	BEV SUV/truck	200	475	150	1.3%	2.2%
	BEV midsize car	275	300	150	0.6%	0.7%
	PHEV SUV/truck	50	475	N/A	10.8%	9.7%
	PHEV midsize car	50	310	N/A	3.2%	2.4%
Gen 0	BEV compact car	150	300	50	0.5%	0.8%
	PHEV midsize car	20	250	N/A	4.3%	3.2%

Results for Generating Synthetic Travel Itineraries: Using the trip chaining model ZEP described above, synthetic vehicle travel itineraries were generated and are validated against 2017 NHTS vehicle trip distributions. Figure II.4.3.6 shows the validation plots that comparing ZEP results with NHTS data. The top left figure compares the distributions of daily first trip starting times. The top right figure compares the distributions of daily return home times. The bottom left figure shows the comparison of daily vehicle distances traveled. Last, the bottom right figure shows the comparison of dwell time distribution for work and public stops. One can see from Figure II.4.3.6 that the synthetic vehicle travel itineraries from the ZEP model fit well to the 2017 NHTS survey data.
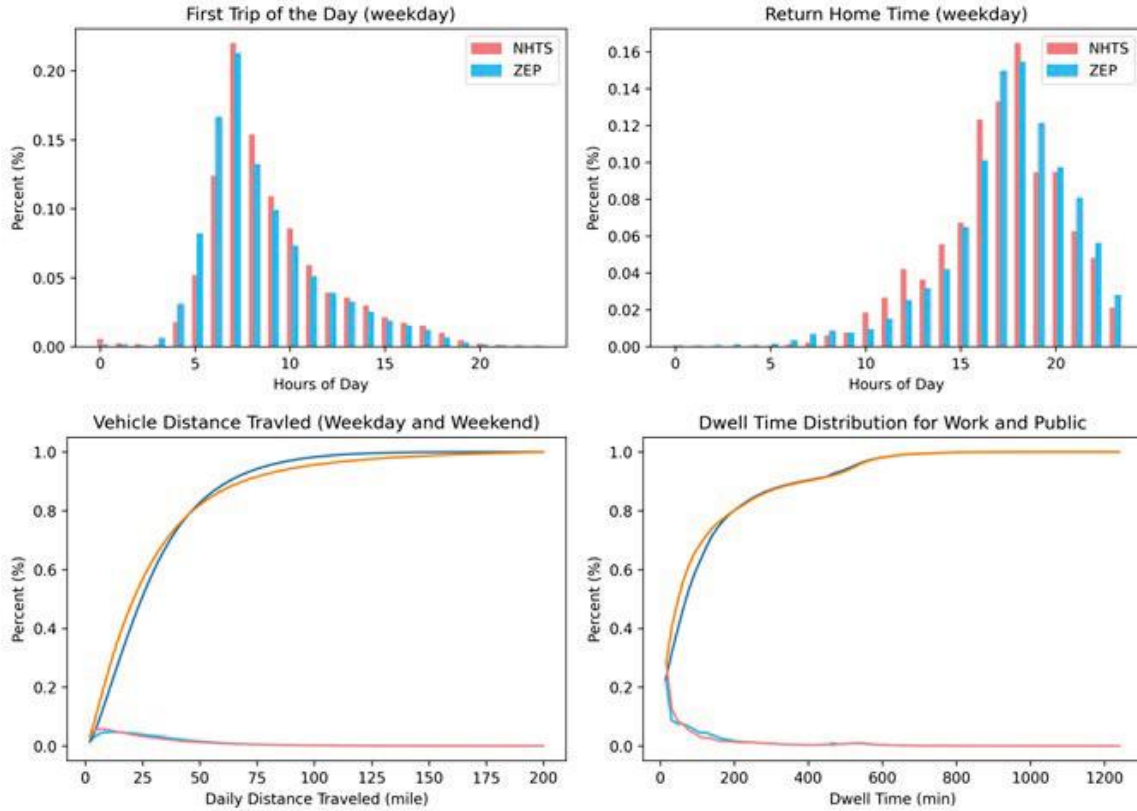
Figure II.4.3.6 (Validation plots for synthetic travel itineraries)

EV Charging Simulation and EV Load Profiles: reports high-level results from the EVI-Pro charging simulations for both Newport News and Richmond regions. Figure II.4.3.7 shows the charging event start time distributions for different charging locations (home, work, public), different days (weekday, weekend), and the two regions. Figure II.4.3.8 shows the charging demand by day of weeks for the two regions. From columns 1 and 2 one can observe that the total charging load over a week for the two regions are roughly proportional to the number of PEVs. From columns 3 and 4 in Table II.4.3.3 and Figure II.4.3.7 and Figure II.4.3.8 one can see that the two regions have similar EV charging patterns. Figure II.4.3.7 shows that work charging happens during early time of a day when people arrive at their work locations, home charging happens during late time of a day when people return to their homes from work, and public charging start time has a more uniform distribution during daytime. Figure II.4.3.8 shows that compared to weekdays, weekends have increased public charging and decreased home and work charging. Figure II.4.3.9 further shows the spatial distribution of charging demands for the core city of each region, i.e., Newport News city and Richmond city. From Figure II.4.3.9 one can observe that home charging and work charging have different spatial distributions for charging demands.

Table II.4.3.3 EV Charging Load Results Summary

Region	PEVs	1-wk kWh	% kWh - Location	% kWh – Flexible*
Newport News, VA: Newport News Hampton York county James City county	202,212	14,352,169	Home: 51%; Work: 9%; Public: 40%	Home: 81%; Work L2: 26%; Public L2: 13%; Public DC: 19%
Richmond, VA: Richmond Henrico county Chesterfield county Hanover county	470,114	39,745,324	Home: 53%; Work: 9%; Public: 38%	Home: 78%; Work L2: 23%; Public L2: 12%; Public DC: 21%

*In this scenario, EVs only charge when it is required to complete travel activities (i.e., they are not plugged in to provide grid services). Home charging is preferred over work and public use cases (see slide 11). Flexible kWh were determined from charging events where <6.2 kW is required to fulfill energy demands (with 5% time buffer) for home, work L2, and public L2 and <50 kW is required to fulfill energy demands (with 5% time buffer) for public DC charging.
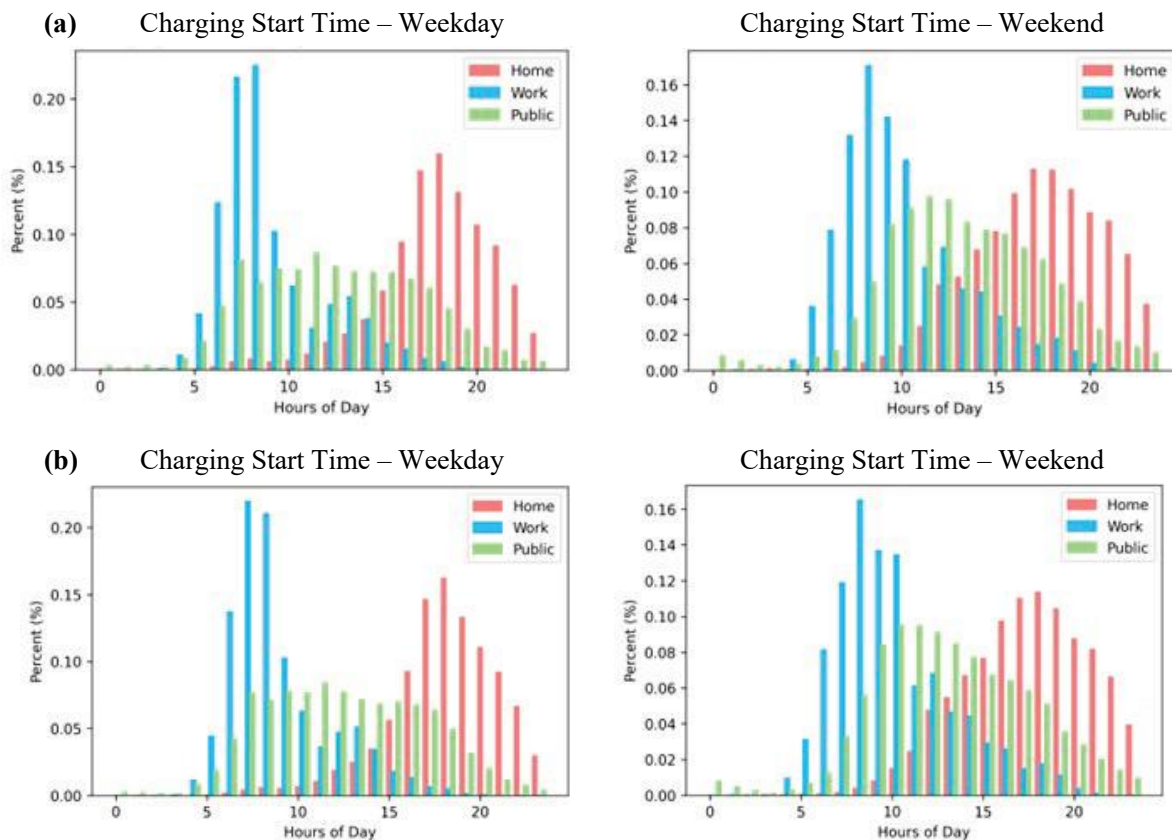
Figure II.4.3.7 (Charging start time distribution: (a) Newport News Region, (b) Richmond Region)

(a)   (b)
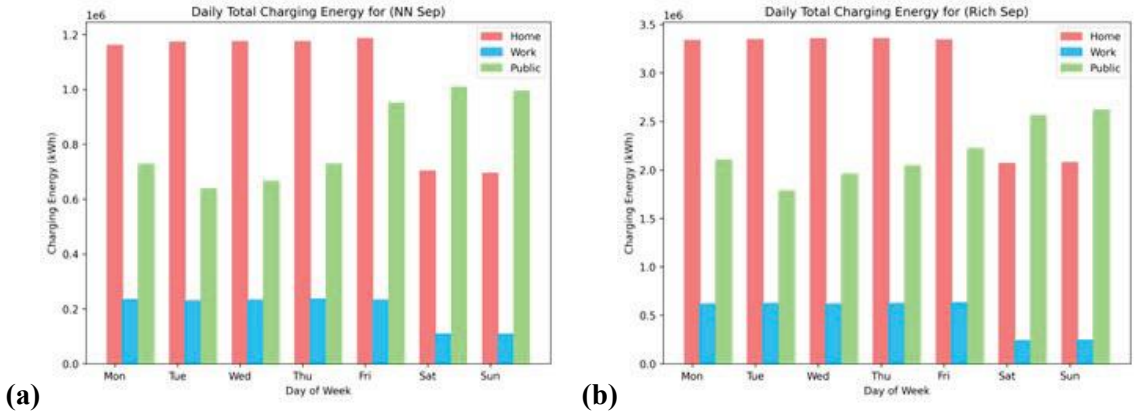
Figure II.4.3.8 (Charging demand by day of week: (a) Newport News Region, (b) Richmond Region)
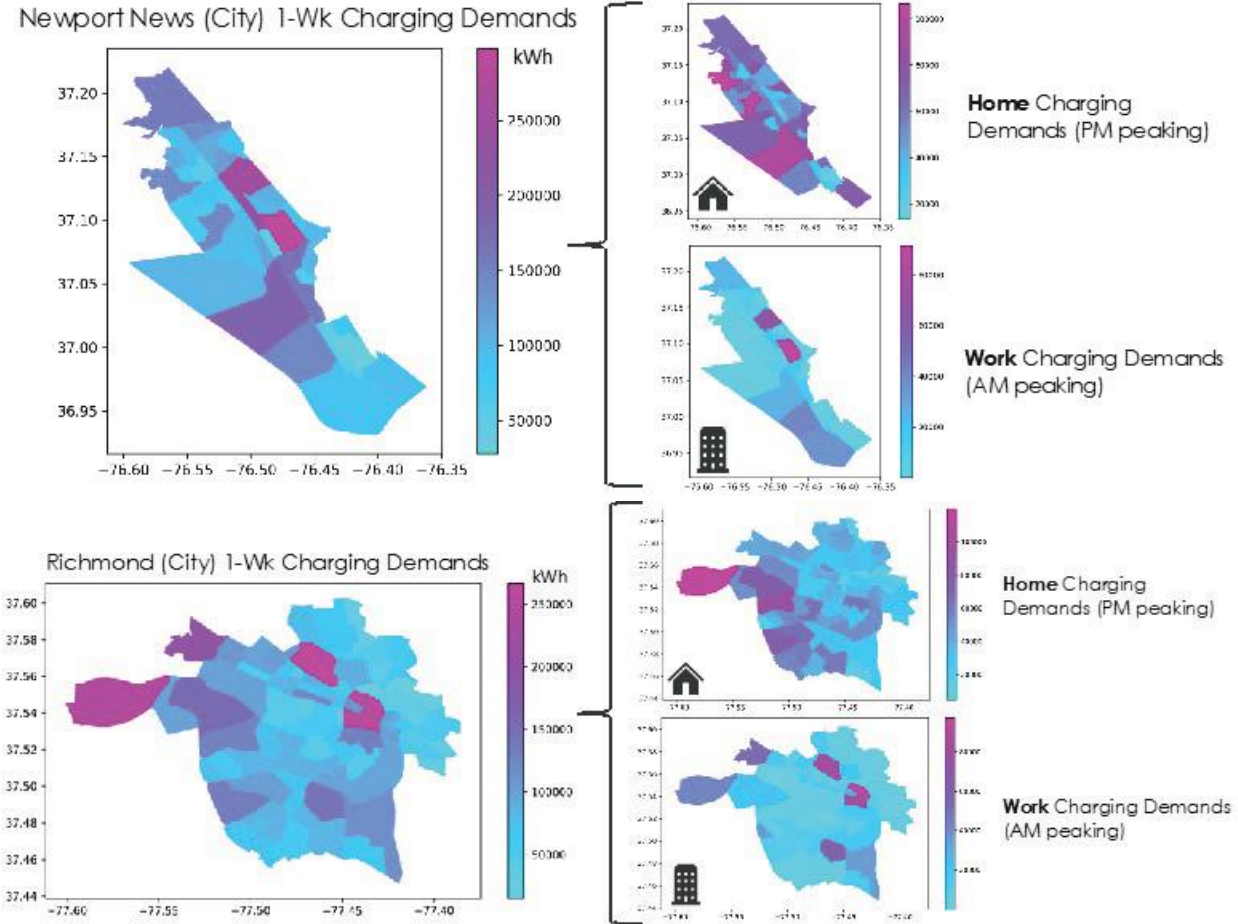
Figure II.4.3.9 (Spatial distribution of charging demands)

SCM Development & Demonstration

EVrest: EV Driver Reservation System

The majority of EVrest EV driver mobile app was developed under the DOE VTO Smart Vehicle-Grid Integration (SVGI) project. In addition to development of both an Android and iOS driver mobile app, further changes and features were added to the ANL CSMS platform to allow for setup and configuration of stations under this project. The ANL CSMS platform allows station owners to group stations and define their mode of operation.

Currently there are three modes of operation for a group of stations:

- **Default:** Station is first come first serve. EVSE owners can enable or disable access control. By enabling access control drivers must utilize the EVrest app to begin a charge session.

- **Reservation:** Station requires the EV driver to reserve the station. This can be done in advanced or at the time of arrival if a port is available.

- **Waitlist:** Similar to the Default mode but when all ports of a Waitlist group are being utilized, drivers can add themselves to a waitlist and be notified when a port has become available.

Priority has been given to first developing the Reservation mode on the platform while focusing on integration of the following types of OCPP 1.6J stations:

Figure II.4.3.10 EVrest Station Map screen shot.

- AC Single Port
- AC Dual Port
- DC Single Port
- DC Dual Port (1 session allowed at a time)
- DC Dual Port (2 sessions allowed simultaneously)

The platform utilizes the OCPP 1.6J *RemoteStartTransaction* and *RemoteStopTransaction* messages with custom business logic to send push notifications to the driver as well as handle pausing of a charge session, unplugging prematurely, ending a charge session before the reservation end time, as well as other edge cases. Argonne researchers are working with our developers to test all features of the mobile application to work out all of the bugs before deploying the beta application for use by Argonne employees.

EV Charge Scheduling

Building upon the proof of concept ISO 15118 charge scheduler developed under the DOE SVGI project, a more robust, deployable ISO 15118 charge scheduler was developed with additional features, termed the EV Charge Scheduler System (EVCSS). The EVCSS was written in the Go and Python programming languages. The goal of the EVCSS is to schedule EV charging so that the EV aggregated charge load profile does not exceed the Pmax profile (max capacity profile) provided by the grid. The optimal charge schedule of all the EVs is a version of the bin-packing problem. A heuristic algorithm was deployed to solve this problem. This algorithm is triggered upon the plugin of a new electric vehicle. Inputs into the algorithm include the grid Pmax profile, the existing vehicle charge schedule(s) and the newly negotiated charge schedule of the plugged in EV. Each EV participating in the EVCSS has an energy demand, max charge rate and a departure time. Some EVs are more flexible (low energy request with long departure time) than others. The algorithm is designed to minimize the number of renegotiations that must occur upon PEV plugin. The most flexible EV/EVSE pair are the first to be renegotiated.
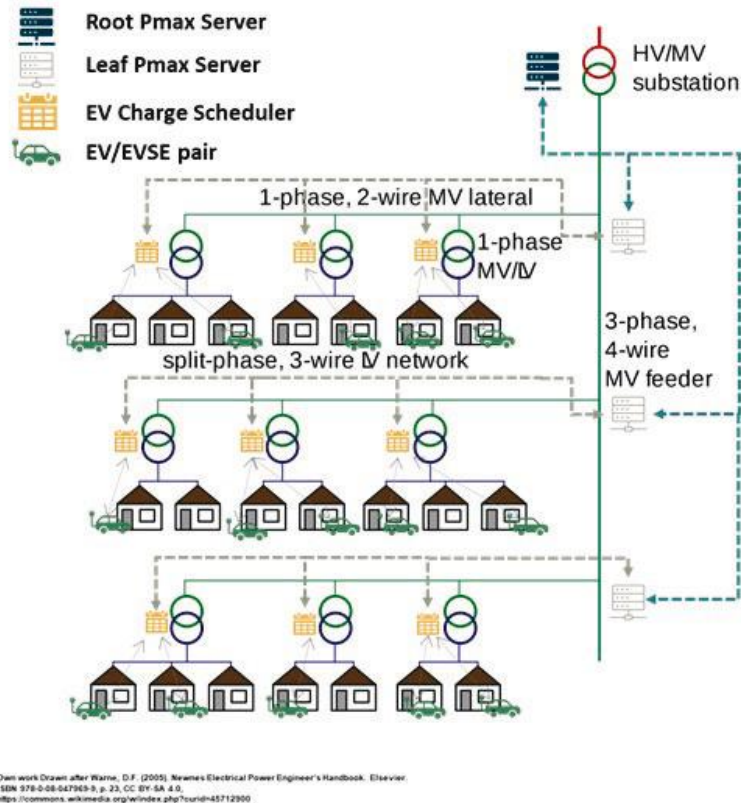
Figure II.4.3.11 Hierarchical distributed approach of the EVCCS on a distribution grid.

The newly developed EVCSS utilizes an MQTT based application programming interface (API) that is designed to communicate with an OCPP 2.0.1 CSMS. The EVCSS has been tested at scale with 1000's of simulated vehicles. The scheduler application utilizes a database to store EV and Pmax tables in a persistent manner, so if the application crashes and reloads no data is lost. In addition to accepting Pmax power tables, the EVCSS can also accept pricing tables from the grid, to allow for scheduling based on energy prices.

In addition to developing the EVCSS, Argonne engineers looked at possible deployment strategies. When talking to partner utilities, one of their largest concerns is overloading neighborhood distribution transformers due to multiple electric vehicles charging at the same time. One possible solution to alleviate this issue is the deployment of an EV charge scheduling system. Figure II.4.3.11 shows a possible hierarchical distributed approach to deploying a EVCSS on a distribution grid.

This approach utilizes Root and Leaf Pmax servers to negotiate available Pmax profiles for each MV feeder circuit. EV charge schedulers would be deployed for each distribution transformer and would receive their respective Pmax profiles from the feeder Leaf Pmax servers. Individual homes with EV/EVSE pair would then negotiate charge schedules with their respective distribution transformer based EV charge scheduler. This hierarchical distributed approach would ensure that load due to EV charging does not exceed a specific Pmax or capacity profile while still attempting to meet the needs of the EV driver.

The protocol utilized to communicate Pmax profiles from the Root Pmax servers to the Leaf Pmax servers and ultimately to the charge schedulers is not a defined standardized protocol. Therefore, Argonne researchers developed and documented the Recursive Pmax Distribution Protocol (RPDP). This protocol utilizes the WebSocket API to enable the distribution/negotiation of Pmax profiles.

Argonne researchers have also created a bridge to allow for non-ISO 15118 vehicles to participate in the EVCSS. The charge scheduler bridge deploys EV agents on behalf of the non-ISO 15118 EVs. The EV agent acts on behalf of the EV to interface with the EVCSS and negotiate a charge schedule. The EV agent emulates the ISO 15118 messages, therefore the EVCSS is unaware it is not communicating with an actual ISO 15118 EV/EVSE pair. This charge scheduler bridge is also useful to integrate simulated EV/EVSE pair and test how the scheduler performs in a real-time environment [4].

OptiQ: Smart AC L2 EVSE

The OptiQ AC L2 EVSE utilizes the Argonne SpEC II module to accomplish SAE J1772 PWM AC charging, ISO 15118 HLC AC charging and Tesla single wire can (SWCAN) HLC AC charging. An OCPP 1.6J compliant client was developed, tested and debugged during FY22 for the OptiQ EVSE. In addition, a custom application was written for the SpEC module to accomplish SAE J1772 PWM charging and integrate those charge sessions into OCPP 1.6J. Figure II.4.3.12 depicts the communication pathways for the OptiQ EVSE.
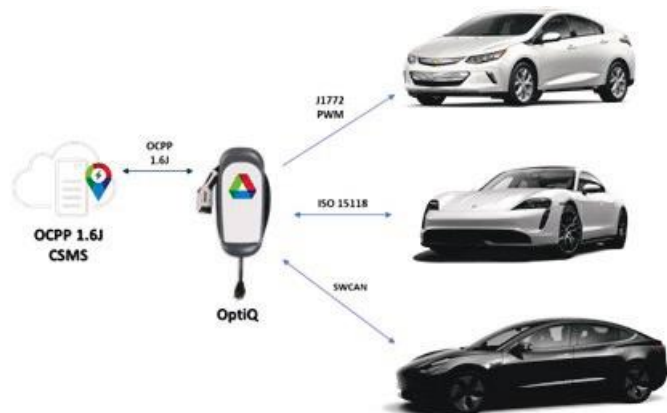
Figure II.4.3.12 OptiQ AC L2 EVSE communication pathways for charging and backend communication

Utilizing the commercial off the shelf ClipperCreek HCS-40P, three proof of concept OptiQ EVSE were constructed. The HCS-40P controller board was removed and the enclosure modified to utilize the Argonne SpEC II module. Figure II.4.3.13 left shows inside the HCS-40P enclosure and the SpEC II module.

In addition to a built-in AC submeter, the OptiQ EVSE has an integrated ground fault detection circuit that opens the contactors within milliseconds of detection of a ground fault. The current implementation relies on software based detection/mitigation which through extensive testing seems to be reliable. However, the next revision of the SpEC module will include hardware based mitigation.

The OptiQ EVSE communicates with the Argonne CSMS system via OCPP 1.6J. Custom logging has also been setup to allow for further debugging and testing. Two of the three proof of concept OptiQ EVSE were deployed in September for employee use at Argonne National Laboratory, shown in Figure II.4.3.13 right. This small deployment allows for Argonne researchers to discover possible bugs and issues, so that they can be fixed before moving onto the next phase of development work.

Figure II.4.3.13 Left: Argonne SpEC II module integrated into HCS-40P enclosure. Right: Two proof of concept OptiQ EVSE deployed for Argonne employee use at Argonne.

Conclusions

The first year of this project has expanded capabilities in transportation analysis, SCM assessments, and EVSE technologies to support EVs@Scale. EV charging loads have been developed across Virginia to represent electrification of 52% of the passenger vehicle stock. These loads represent the vehicle energy needs and charge flexibility, which will be critical in assessing grid impacts and SCM effectiveness throughout the utility partner grid models. The team is also expanding this analysis to include MD and HD vehicles across a wide range of vocations. Broad SCM analysis has begun to assess the effectiveness of various strategies across large regions. This will help to more rapidly determine the level of support various controls can provide the grid. The team is actively expanding these assessment capabilities and developing new SCM strategies to support a wide range of vehicle classes and vocations. Additionally, new EVSE technologies have been developed to support the reservation of EVSE, scheduling of charge sessions, and management of charging loads using modern standards and cutting-edge technology. These capabilities are crucial to support the most sophisticated SCM controls that are being developed and will support future laboratory demonstrations later in the project. Each of these developments furthers the understanding of EVs@Scale and the best solutions to integrate these new charging loads throughout the grid.

References

1. Meintz, A. and J. Bennett. 2020. "Smart Electric Vehicle Charging for a Reliable and Resilient Grid (NREL)." In Electrification:2019 Annual Progress Report, U.S. Department of Energy Office of Energy Efficiency and Renewable Energy Vehicle Technologies Office, 386–402. https://www.energy.gov/eere/vehicles/downloads/electrification-fy2019-annual-progress-report.

2. Bennett, J.etal. 2021."Charging Infrastructure Technologies:Smart Electric Vehicle Charging for a Reliable and Resilient Grid (RECHARGE)." Presented at the U.S. Department of EnergyVehicle Technologies Office Annual Merit Review, June 23, 2021.

3. Ge, Yanbo, Christina Simeone, Andrew Duvall, and Eric Wood. 2021. There's No Place Like Home: Residential Parking, Electrical Access, and Implications for the Future of Electric Vehicle Charging Infrastructure. Golden, CO: National Renewable Energy Laboratory. NREL/TP-5400-81065. https://www.nrel.gov/docs/fy22osti/81065.pdf.

4. Wu, Z., Manne, N., Harper, J., Chen, B. et al., "A Cloud-Based Simulation and Testing Framework for Large-Scale EV Charging Energy Management and Charging Control," SAE Technical Paper 2022-01-0169, 2022, https://doi.org/10.4271/2022-01-0169.

II.5 Cyber-Physical Security

II.5.1 Electric Vehicle Integrated Safety, Intelligence, Operations (eVision) - (Oak Ridge National Laboratory)

Madhu Chinthavali, Principal Investigator

Oak Ridge National Laboratory
1 Bethel Valley Road, Oak Ridge, TN 37830
E-mail: chinthavalim@ornl.gov

Thomas Carroll, Principal Investigator

Pacific Northwest National Laboratory
E-mail: Thomas.Carroll@pnnl.gov

Tim Pennington, Principal Investigator

Idaho National Laboratory
E-mail: Timothy.Pennington@inl.gov

Lee Slezak, DOE Technology Manager

U.S. Department of Energy
E-mail: lee.slezak@ee.doe.gov

Project Introduction

The U.S. adoption rate of electric vehicles (EVs) has risen in recent years. EV sales records show an increasing market share. While this potentially speaks to improved confidence in battery powered vehicles, range anxiety and charging infrastructure continue to be a concern for many would-be buyers. Level 3 and higher-class charging networks are considered crucial to reducing the concerns related to long distance travel and range anxiety associated with EVs. While these EV chargers may be seeing deployments in high numbers, the reliability of these systems may be in question. A recent study performed in California's Bay Area suggested that more than 25% of public DC charging stations were unusable [1]. The reasons include broken connectors (~1%), failed chargers with either non-working screens or error messages (~7.3%), connection errors (~1%), and charging failures (~6.6%). As presented in [2], these failures can be linked to challenges on the vehicle, charger, or interconnected grid system and speak to the resilience of these systems to ride through critical challenges.

System resilience has been defined in terms of the electric grid support as the "ability to withstand and recover from deliberate attacks, accidents, or naturally occurring threats or incidents [3]." In this work, the focus is on EV charging resilience or sustaining EV charging operation and/or recovering under a set of different anomalies.

In this work, EV charging resiliency has been categorized by three different target areas: 1) the EV charger and supporting communications and
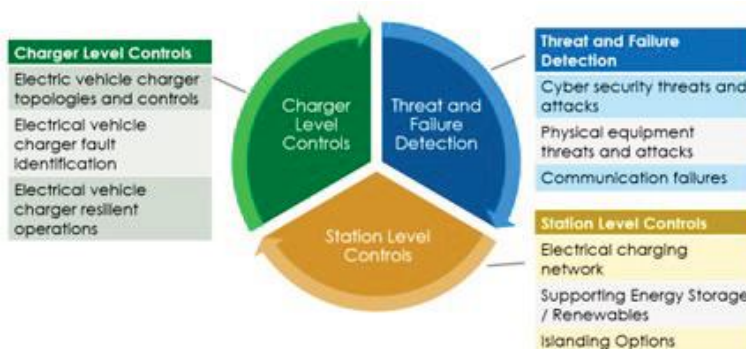
Figure II.5.1.1 Areas for resiliency improvement.

controls, 2) the station management controller (or site controller) with considerations on energy management response and coordination of resources, and 3) a detection system monitoring for potential threats and attacks. These areas of resiliency improvement are presented in Figure II.5.1.1. Within each domain, key technology areas are in development.

Objectives

In this work, the objective is to validate the electric vehicle (EV) charging anomaly detection methods and control strategies developed. These solutions must both mitigate impacts on charging infrastructure and the interconnected grid. The challenge is that EV charging stations can support different electrical topologies and EV types including heavy-duty (HD), medium-duty (MD), and light-duty (LD).

Approach

For reference, Figure II.5.1.2 presents a generalized electric system topology for an EV charging station (considering light duty (LD), medium duty (MD), and heavy duty (HD) EVs) and the potential challenges linked to resilience. In the presented topology, each EV charger is composed of power electronic systems (PES), software, and interface modules to provide the necessary communication and control to charge an EV. For MD/HD EV class charger systems (or MW class charging), a DC bus architecture is considered [4]. This design uses multiple parallel DC converter modules for EV charging. A high voltage DC bus architecture reduces the current, thus improving efficiency and lessening associated cable and equipment sizing challenges. For LD DC fast charging, systems include converter combinations that support AC-DC and DC-DC as presented in [5]. The second DC-DC conversation stage is utilized to directly couple the vehicle battery system with controlled charging.
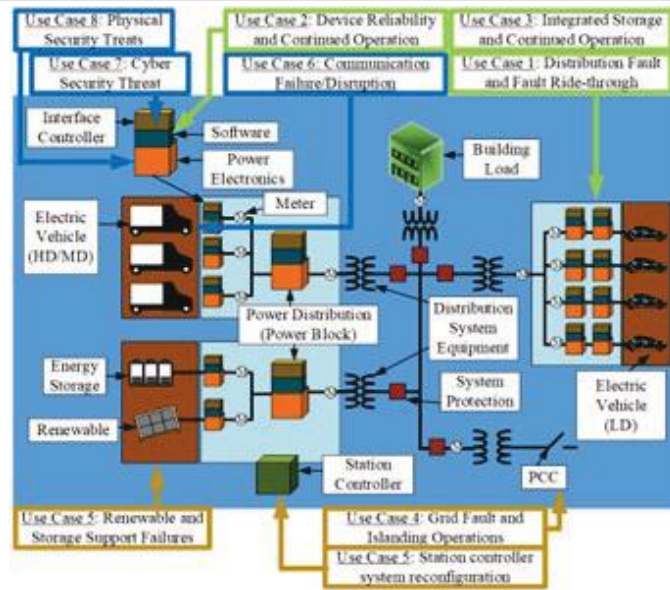
Figure II.5.1.2 Use cases for improving resilience of EV charging

Energy storage (ES) and photovoltaic (PV) systems have also been integrated into the charging station for this topology through the AC system network. The PV and ES systems can support energy management, power limiting control for the point of common coupling (PCC), and resiliency improvement during grid outage. Loads (such as a commercial building) have also been included into the topology to recognize other infrastructure beyond the EV chargers. System protection and transformers have been included for completion. The presented use cases were derived in the previous year and have been used to develop an overall system architecture to support resiliency and for the team to establish demonstratable improvements in resilience.

Results

Results in this year include the development of system and sub-system architectures and methods to support resiliency at the three target areas discussed.

Consolidated Architecture

In linking the three target opportunity areas identified for improving charging resiliency, a corresponding architecture has been developed as shown in Figure II.5.1.3. The architecture represents the different layers of an EV charging station (vehicle and resource layers, power electronics layer, interface layers, intermediate threat detection layer, station layer, and utility layer.) These are discussed in more detail.

The EV charger is represented by the PES and interface controller layers. The PES layer contains the power electronic converters with digital signal processors (DSPs) utilized for performing the closed-loop control of the converters. The interface layer or charger controller issues commands to the DSPs based on requests for charging by the interconnected EV or override requests by the station controller. The EV charger controllers presented in the proposed architecture use an approach as described in that ties power electronic resources and different protocols into a single system (including protocols for communicating to the EVs). For faults, the DSP is responsible for handling detection and ride-through capabilities and/or electrical isolation. The charger controller is responsible for reporting faulted systems to the station controller which can be reset on command. Failures within the PES are all handled by the DSP and reported to the charger controllers for decision.

The safety instrumented system (SIS) is complemented by a cyber-physical threat detection system (CPTDS) in Figure II.5.1.4, with both residing within the different layers of the EV charger and within an intermediate layer (Intermediate Threat Detection Layer). The integrated design provides a diverse recognition design, which includes an independent safety threshold monitor through the SIS, and an anomaly detection system with a physics-based correlation of residuals and an autoencoder deep neural network. This comprehensive, ensemble approach ensures that recognition of safety limits, both hard limits and recognized anomalous trends from normal, are considered in a robust fashion. Both the communications system and sensor data are evaluated to recognize malicious and non-malicious threat events associated with each charger or system. An SIS aggregator integrates the threat information to identify the potential for broader station wide attacks and reports these findings to the station controller. As an observing layer, these systems are designed to inform systems of potential problems but can also take direct action through isolation of EVs where short time scale safety responses are required.

Figure II.5.1.3 Proposed architecture for resiliency of EV charging stations.
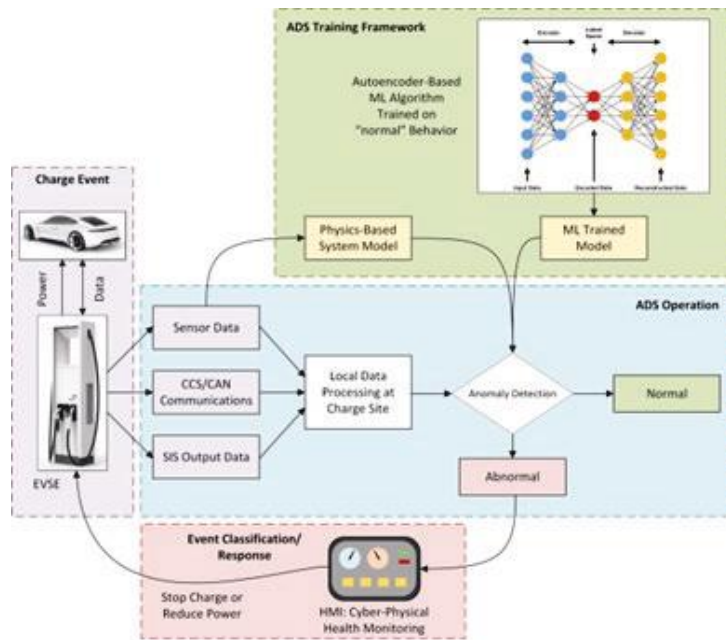
Figure II.5.1.4 Cyber-Physical Anomaly Detection System

The station controller, the top-level manager within the proposed architecture, coordinates with the interface controllers, providing intelligent supervisory control. The station controller collects data from the charging systems, integrated assets (such as PV and ES), ancillary components and SIS. The data is used by the controller to make informed and verified decisions. The decision-making process considers business and operational goals, objectives, and initiatives when selecting a consistent set of parameters, setpoints, and charge profiles. The lower-level controllers are then informed of the details of decisions for which they are responsible for implementing.

The station controller receives information, signals, and direction from higher order systems, such as utility systems—distributed energy management systems (DERMS) or advanced distribution management systems (ADMS)—and building- or facility-based energy management systems.

The controller interfaces with freight and fleet management systems so that vehicle and cargo operations are coordinated with depot charging operations and conditions. Influenced by the current and forecasted state of the charging operations, the freight and fleet management may designate a vehicle—charger association, retard or accelerate vehicle arrivals, prioritize cargo departures, or implement alternate vehicle charging strategies, such as incorporating en route and opportunistic charging, to augment depot capacity. Similarly, the station controller uses information from these management systems to influence operations, such as when to charge the ES.

The station controller is expected to perform customary energy management. This includes optimization of the EV charging stations and integrated assets to ensure the station peak (demand charge) and energy costs are minimized or that a facility constraint is observed. If the constraints are planned for and integrated assets are adequately resourced, the charging operation tempo need not slow. If not adequately resourced, a decision must be made to either accept the additional costs or adjust the charging profiles respective to potential costs.

The station controller does not respond to transient events in the sub-second timeframes; instead, the station controller orchestrates and prepares systems by selecting the necessary operational modes and informing the lower levels of the details. Details on the architecture and various levels of resiliency improvements are discussed in the next sections.

Use Cases: EV Charger Failures and Response to Faults

PES equipment reliability is a consideration in many applications. Challenges associated with bond wire cracking and liftoff and solder cracking due to quality issues, random events, or wear and tear often lead to power stack failures [6], [7]. While the lifetime of any single semiconductor device within the EV charger may be considered in a time frame of decades, the associated system life can be short (as low was several years) as discussed in analysis presented in [8]. Today, any AC-DC or DC-DC converter failure will result in an EV charging system outage and require system repair or replacement.

Beyond component failure, electrical interconnection faults can cause disruptions and are a common challenge in electrical infrastructure. Common causes are associated with animals, inclement weather (ice/lightning/wind), and vegetation [9]. An electrical fault within the charging station (or AC network) creates a transient undervoltage condition which will lead to an automatic trip in an EV DC fast charger without more advanced controls as presented in [5]. The fault-induced voltage drop reduces the maximum achievable energy withdrawal from the AC network to the intermediate DC bus. If the charging converter is attempting to charge the vehicle beyond the available energy from the fault, the intermediate DC bus voltage will sag, and the converter system will trip. This will lead to the deactivation of the charger potentially for an extended period without a reset.

Electrical faults within the charging station have historically led to EV charging tripping. One proposed solution to improving the resilience of EV chargers during an electrical fault is to ride-through the fault as proposed in [5]. The proposed method utilizes a DC droop control for the DC-DC converter stages supplying the EVs. This embedded control with the power electronics layer automatically reduces the delivered charging

power to match the available energy from the grid. In this way, the DC bus voltage does not sag, and the converters can continue to operate without tripping and needing to be reset. Post the ride-though event, information of the occurrence is propagated to the station controller.

The failure of a component in a conventional EV charger would traditionally lead to an out of service condition. However, new opportunities in modular system designs (multiple converters operating in parallel) and fault tolerant systems (multiple switches in a single converter operated in parallel) have introduced the potential for improved resilient operations of the EV charger. In these cases, systems are being designed to self-identify the occurrence of a failed component or converter in a system, remove these devices from operation, and adjust controls accordingly. In the proposed architecture, this occurs within the PES layer and is reported to the device controllers.

Beyond the inclusion of new control strategies in support of the EV charging, ES solutions are being investigated for integration at each charger. These ES solutions provide opportunities to also mitigate peak management at each charger and thereby at the station level. In the proposed architecture, these can either be integrated as a single system belonging to the charger or as a separate system managed by the station controller. These are already being modeled within the CHIL environment in support of continued operation under faults.

Use Cases: Cyber and Physical Security Threats

Threats associated with nefarious actors looking to perform harm or incur financial opportunities are growing [10]. These actors can attempt to intrude into various interface and software layers of the EV chargers within the charging station depot or other equipment. Recent studies have shown security issues with ChargePoint, Schneider EVlink, and Circontrol to name a few [11]. Spoofing, tampering, repudiation, denial of service, elevation of privilege are all methods for infiltrating and/or attacking EV charging systems and stations. Even beyond single charger attacks on equipment, systemic attacks and infiltration can impact the interconnected electric grid with potential larger impacts to the whole electric power grid [12]. This can lead both to long-term EV charger and EV station outages.

The hardware testbed consists of using vendor DC fast chargers interconnected to a power supply cabinet and 400kW EV emulator. Sensors have been placed throughout the system to provide data to the SIS system.

The SIS technology utilizes artificial intelligence-based techniques to identify relationships in complex systems of the EV chargers and EV station. The system monitors communication traffic and messages, electrical measurements (AC power and power quality, DC output to the EV, and auxiliary power such as CCS liquid chiller consumption), temperature (ambient and equipment such as the charging cable and cabinet), and component states and contactors. The data is collected as baseline information, trained in a machine learning (ML) platform, and used to evaluate data in real-time. The ML is iterative and must be optimized over time to ensure speed and accuracy are maintained. The system has already been tested on four different attack vectors: a) main AC contactors opening during high-power charging, b) internal controls and communications exploit disrupts power module coordination, c) and blocked air inlet for CCS cable thermal management, and d) disabled chiller & CCS cable temperatures spoofed during high-power charging. The SIS system has been able to achieve a 95% detection accuracy.

Use Cases: Grid Induced Challenges and Station Management

Conditions within the interconnected electrical system also induce challenges within the charging station. Electrical faults or outages on the primary grid will result in voltage transients and outages that trip equipment or create a station wide outage. A study from Sweden on EV charging station voltage showed that out of the more than 800 events recorded during the study window, 20% of the time voltage dips dropped below 70% per unit voltage [13].

 Furthermore, dynamic loading conditions from EVs can impact the distribution system voltage magnitude [14], balance [15], and equipment loading [16]. While optimization of the management of EV chargers has

been considered for many different use cases (minimization of power loss, electricity cost, peak load, voltage regulation, overloading in distribution transformer and lines [17]), considering frameworks for continued energy management under the loss of critical supporting infrastructure has not been as widely discussed.

The station controller evaluates inputs from the power system, individual vehicle charging sessions, and fleet management models. These inputs are used to determine supervisory control and setpoints to maintain the system operating conditions, such as maintaining vehicle charging throughput and keeping overall station energy demand below an administrative imposed level. While the actual controller utilizes the VOLLTRON [18] framework for implementation, the power system, vehicle arrivals, and vehicle charging are simulators coordinated in a simulation environment. GridLAB-D [19] (power systems) and Caldera [20] (vehicle charging) are coupled via the HELICS [21] cosimulation platform to the VOLLTRON-based controller to not only coordinate charging impacts on the power system, but also provide system inputs to the station controller and execute the output setpoints and control. It is important to reinforce that the station controller is providing a supervisory command, such as "energy storage - discharge at 5 MW." The individual devices still have their local controls to regulate to the desired voltage/power, as well as handle transient scenarios detailed earlier in the paper.

Per the description, the station controller manages the site/mission resilience by influencing not only the vehicle placement and charging parameters, but also by sending set point commands to other assets on the depot. For scenarios like a demand limitation due to a public-safety power-shutoff, the station controller coordinates the on-site energy storage to offset the power passing through the PCC. In the event an individual ES device is depleted, the station controller either redispatches other ES to cover that shortfall, commands a reduction in charger power, or will attempt to curtail other loads on the system (like building load).

For longer outages or islanded operation, the station controller would include information from the fleet management side to determine which vehicles have high priority charging needs and where they are located. This will help site the vehicle in an available charger at the depot, or potentially direct them to another depot or en route charging station if one is available. The overall goal is to manage the site mission resilience, in this case continued charging of vehicles that will need to deliver high priority cargo. As station resources are depleted (e.g., ES is drained), the station controller will reduce charger availability (avoid assigning vehicles to a charger) and curtail charging power to sustain operations as long as possible.

Conclusions

Architecture development and use cases for the different target areas have been developed. The architecture considers three distinct areas of an EV charging station: the EV charger, threats associated with nefarious actors, and the overall station and controller. Methods for improving resiliency are also introduced with discussion on testbeds and approaches for validation. Future work continues to examine the use cases in details and the consolidation of use cases into a single platform.

Key Publications

1. M. Starke, S. Bal, M. Chinthavali and N. Kim, "A Control Strategy for Improving Resiliency of an DC Fast Charging EV System," 2022 IEEE Transportation Electrification Conference & Expo (ITEC), 2022, pp. 947-952.

References

1. Cullen, David & Bryan, Mary & Cezar, Gustavo. (2022). Reliability of Open Public Electric Vehicle Direct Current Fast Chargers.

2. S. -Y. Wei, Q. Zhu, X. -M. Li and X. -H. Meng, "Research on Comprehensive Evaluation of Electric Vehicle Charging Failures," 2021 6th International Conference on Intelligent Computing and Signal Processing (ICSP), 2021, pp. 1255-1259.

3. Afzal, Suhail; Mokhlis, Hazlie; Illias, Hazlee Azil; Mansor, Nurulafiqah Nadzirah; Shareef, Hussain, State-of-the-art review on power system resilience and assessment techniques, IET Generation, Transmission & Distribution Journal, Vol. 14, No. 25, pp. 6107-6121, 2020.

4. M. Starke et al., "A MW scale charging architecture for supporting extreme fast charging of heavy-duty electric vehicles," 2022 IEEE Transportation Electrification Conference & Expo (ITEC), 2022, pp. 485-490.

5. M. Starke, S. Bal, M. Chinthavali and N. Kim, "A Control Strategy for Improving Resiliency of an DC Fast Charging EV System," 2022 IEEE Transportation Electrification Conference & Expo (ITEC), 2022, pp. 947-952.

6. Y. Song and B. Wang, "Survey on Reliability of Power Electronic Systems," in IEEE Transactions on Power Electronics, vol. 28, no. 1, pp. 591-604, Jan. 2013.

7. M. Ciappa, "Selected failure mechanism of modern power modules," Microelectron. Rel., vol. 42, nos. 4–5, pp. 653–667, Apr./May

8. J. Karunarathna, U. Madawala, C. Baguley, F. Blaabjerg and M. Sandelic, "Reliability Analysis of Fast Electric Vehicle Charging Systems," 2021 IEEE 12th Energy Conversion Congress & Exposition - Asia (ECCE-Asia), 2021, pp. 1607-1612.

9. C. A. Andresen, B. N. Torsæter, H. Haugdal and K. Uhlen, "Fault Detection and Prediction in Smart Grids," 2018 IEEE 9th International Workshop on Applied Measurements for Power Systems (AMPS), 2018, pp. 1-6.

10. A. N. Jaber and L. Fritsch, "COVID-19 and Global Increases in Cybersecurity Attacks: Review of Possible Adverse Artificial Intelligence Attacks," 2021 25th International Computer Science and Engineering Conference (ICSEC), 2021, pp. 434-442.

11. S. Acharya, Y. Dvorkin, H. Pandžić and R. Karri, "Cybersecurity of Smart Electric Vehicle Charging: A Power Grid Perspective," in IEEE Access, vol. 8, pp. 214434-214453, 2020.

12. S. Acharya, Y. Dvorkin and R. Karri, "Public Plug-in Electric Vehicles + Grid Data: Is a New Cyberattack Vector Viable?," in IEEE Transactions on Smart Grid, vol. 11, no. 6, pp. 5099-5113, Nov. 2020.

13. Shimi Sudha Letha, Math Bollen," Impact of Electric Vehicle Charging on The Power Grid," Luleå University of Technology, Report, January 2021.

14. A. Ihekwaba and C. Kim, "Analysis of electric vehicle charging impact on grid voltage regulation," 2017 North American Power Symposium (NAPS), 2017, pp. 1-6.

15. S. I. Ahmed, H. Salehfar and D. F. Selvaraj, "Impact of Electric Vehicle Charging on the Performance of Distribution Grid," 2021 IEEE 12th International Symposium on Power Electronics for Distributed Generation Systems (PEDG), 2021, pp. 1-8.

16. J. Ma, W. An, W. Ming, J. Du, W. Yin and J. Chen, "Coordinated Control Strategy for Electric Vehicle Charging Piles to Prevent Overload of Distribution Transformer," 2020 5th Asia Conference on Power and Electrical Engineering (ACPEE), 2020, pp. 684-688.

17. M. K. Das and S. K. Jain, "Review on Optimization Techniques used for Scheduling of Electric Vehicle Charging," 2021 International Conference on Control, Automation, Power and Signal Processing (CAPS), 2021, pp. 1-6.

18. VOLTTRON, online: https://volttron.org/.

19. GridLAB-D, online: https://www.gridlabd.org/

20. Caldera, EV Charging Simulation Platform, online:
    https://factsheets.inl.gov/FactSheets/Electric%20Vehicle%20Charging%20Simulation%20Platform20
    21.pdf

21. Hierarchical Engine for Large-scale Infrastructure Co-Simulation (HELICS), [Online], Available:
    https://helics.org. Accessed November 2, 2022.

II.5.2 Securing Vehicle Charging Infrastructure (SNL, PNNL, ANL)

Jay Johnson, Principal Investigator

Sandia National Laboratories
P.O. Box 5800 MS1033
Albuquerque, NM 87185-1033
E-mail: jjohns2@sandia.gov

Thomas E. Carroll, Principal Investigator

Pacific Northwest National Laboratory
PO Box 999 MS-IN J4-45
Richland, WA 99352
E-mail: Thomas.Carroll@pnnl.gov

Roland Varriale, Principal Investigator

Argonne National Laboratory
9700 South Cass Ave
Lemont, IL 60439
E-mail: rvarriale@anl.gov

Lee Slezak, DOE Technology Manager

U.S. Department of Energy
E-mail: Lee.slezak@ee.doe.gov

Start Date October 1, 2018	End Date: September 30, 2022	
Project Funding: $1,000,000	DOE share: $1,000,000	Non-DOE share: $0

Project Introduction

As the US electrifies the transportation sector, cyber-attacks targeting vehicle charging could bring consequences to electrical system infrastructure. This is a growing area of concern as charging stations increase power delivery and must communicate to a range of entities to authorize charging, sequence the charging process, and manage load (grid operators, vehicles, OEM vendors, charging network operators, etc.). The research challenges are numerous and are complicated because there are many end users, stakeholders, and software and equipment vendors interests involved. Poorly implemented electric vehicle supply equipment (EVSE), electric vehicle (EV), or grid communication system cybersecurity could be a significant risk to EV adoption because the political, social, and financial impact of cyberattacks—or public perception of such—ripples across the industry and has lasting and devastating effects. Unfortunately, there is no comprehensive EVSE cybersecurity approach and limited best practices have been adopted by the EV/EVSE industry. There is an incomplete industry understanding of the attack surface, interconnected assets, and unsecured interfaces. Thus, comprehensive cybersecurity recommendations founded on sound research are necessary to secure EV charging infrastructure. This project provided the power, security, and automotive industry with a strong technical basis for securing this infrastructure by developing threat models, determining technology gaps, and identifying or developing effective countermeasures. Specifically, the team created a cybersecurity threat model and performing a technical risk assessment of EVSE assets, so that automotive, charging, and utility stakeholders can better protect customers, vehicles, and power systems in the face of new cyber threats.

Objectives

The goal of the project was to protect US critical infrastructure and improve energy security through technical analysis of the risk landscape presented by the anticipated massive deployment of interoperable EV chargers. To improve the vehicle industry's cybersecurity posture, this project:

- conducted adversary-based assessments of charging equipment,

- created a threat model of EV charging, and

- analyzed power system impacts for different attack scenarios.

This provided DOE and automotive, EVSE vendors, and utility stakeholders with:

- clear documentation of gaps in EVSE cybersecurity and the path forward to address those weaknesses,

- a threat model for EVSEs and associated infrastructure and services,

- recommendations for the automotive industry based on EVSE penetration testing, and

- cyber attack impact analyses of the power system with remediation recommendations.

Approach

The team executed the following integrated cybersecurity R&D tasks:

1. Threat modelling to understand what potential cyber hazards exist with EVSE communications;

2. Assessing the current state-of-the-art cybersecurity posture of EVSE equipment using authorized, adversary-based assessment techniques (penetration testing and red teaming);

3. Establishing credible attack vectors based on the cybersecurity assessments and threat model;

4. Determining the impact of current and potential vulnerabilities on distribution and transmission power systems; and

5. Creating a risk matrix to prioritize mitigations that reduce the number of high-consequence/low-threat level attacks.

The task structure of the project is shown in Figure II.5.2.1, wherein the left side (blue) estimates the probability of different attack scenarios, and the right side (green) estimates the consequence of attack scenarios. The cybersecurity risk of a particular attack is the combination of the likelihood and impact of the attack. By studying a range of attack scenarios, optimal mitigations can be determined to prevent attacks at specific points in the attack kill chain (i.e., the steps to accomplish adversary goals).
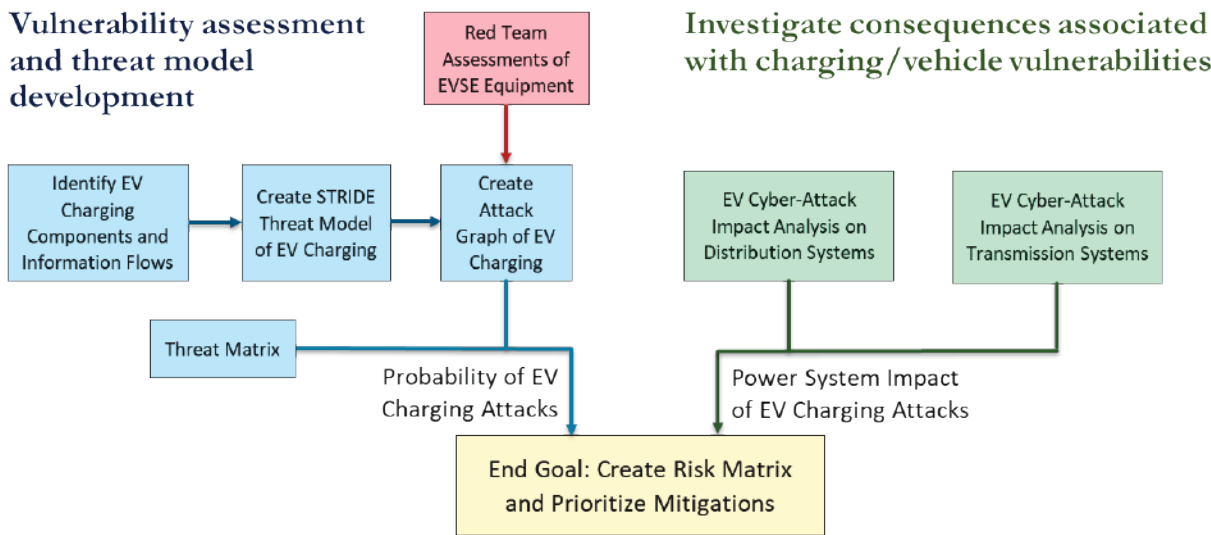
Figure II.5.2.1 Project tasking.

Results

The project team evaluated probable attacks based on hands-on cybersecurity assessments with partner organizations and evaluated the probability of success against the skill level required to conduct the attack. A detailed threat model was created for different EVSE chargers with connections to external entities. Attack graphs were developed and then revised based on penetration testing of multiple EVSEs. A distribution simulation of EVSE charging with and without vehicle-to-grid (V2G) functionality was conducted to determine if malicious control of EVSEs could cause high or low voltages on feeder circuits. Transmission simulations of coordinated charging control was modeled for the Western Electricity Coordinating Council (WECC) were also performed to understand bulk system impact from coordinated cyber attacks.

EVSE Penetration Testing

From the beginning of the project, the team worked closely with multiple EVSE vendors to better understand the vulnerabilities presented by EVSE equipment and associated networks. The project also studied vulnerabilities that affect supporting IT systems. This included assessing remote access controls, use of insecure protocols, and the ability to fingerprint devices from their online presence. This required working with the threat models and attack graphs and validating threat modelling approaches. Findings from network traffic analysis, forensic analysis, and open-source information gathering have led to vulnerability enumeration in both the EVSE as well as their supporting infrastructure. Use of insecure protocols, such as OCPP 1.6 and MQTT, on the globally routable Internet have resulted in several findings that were disseminated back to EVSE manufacturers for remediation. Additionally, the team was able to use their findings to create a generalized "fingerprint" for EVSE deployments, allowing the team to search for and enumerate similar systems that were Internet connected. From these similar systems, specific characteristics such as open ports, software versions, or reports of vulnerabilities were used to identify other instances of EVSE deployments. Some of these findings, enumerated through open-source intelligence (OSINT) means, were disseminated to EVSE manufacturers. These manufacturers confirmed our findings and advised that they indicate software or security misconfigurations. The hands-on assessments for EVSE equipment found many areas for improvement, e.g., failure to physically secure EVSE enclosures; default passwords for internal systems, or credentials posted inside enclosure; data not encrypted at rest and only financial data is encrypted in transit; unnecessary ports and services are enabled. A list of best practices was generated from these assessments [1], shown in Figure II.5.2.2. The project final report included an anonymized set of findings [2]. The assessment team also provided EVSE partners with the findings and potential mitigations for identified vulnerabilities. Some recommendations are included in Figure II.5.2.3. A large set of additional recommendations and areas for future R&D for this space was provided in [4].

Attack Graphs

Attack graphs show the steps an attacker must take to move from a system/network access point to a consequence or objective. The use of attack graphs simplifies the identification of key steps an attacker must take to achieve their objectives, allowing those actions to be detected or prevented. Figure II.5.2.4 illustrates access points, staging areas, and consequences of concern related to a generic EV charger network. In this figure, one of the attack paths involves an attacker using an initial compromise of an EVSE provider's business network to impact the bulk power system. By analyzing the steps in this attack path, detective or preventive controls – such as monitoring for unusual Network Time Protocol traffic or requiring code signing of EVSE updates – can be implemented. The team used the information gathered from their assessments, publicly available information regarding vulnerabilities, and knowledge regarding the tactics, techniques, and procedures used by attackers to advise the attack graph. In the case of coordinated EVSE attacks that disrupt the power system, there were two major questions:

- Can the attacker "pivot" between the components, systems, and networks in the EV/EVSE ecosystem to compromise the necessary information flows?

- Can an attacker synchronize their attack to affect large portions of the grid simultaneously?

From the assessment activities, it appears both are possible so an attacker *could* manipulate large networks of EVSEs and cause distribution and transmission impacts.

Figure II.5.2.2 EVSE Best Practices [1].

Figure II.5.2.3 EVSE vendor recommendations based on penetration tests of EVSE equipment and networks [1].

Threat Model Development

PNNL led the task to develop a threat model of high-power electric vehicle charging infrastructure and systemically analyze it for threats that have the potential to bring wide-ranging consequences to the electric grid and transportation systems. PNNL derived a novel consequence-centric variant of the STRIDE threat modeling methodology to: (i) discover consequences that potentially impact vehicles, the electric supply, and transportation; and (ii) focus subsequent modeling and analysis on threats that may precipitate the

consequence. STRIDE is an industry-accepted approach to threat modeling, first made popular for its application at Microsoft. Examples of the system models used for the threat modeling are depicted in Figure II.5.2.5, which show decomposition of chargers and vehicle into components, how information is exchanged among components, and the relationships of components to external entities. After the threats are enumerated, safeguards and countermeasures are identified to mitigate the vulnerabilities. By focusing on consequences, insights were gained into the security and resiliency of the EV charging ecosystem. Importantly, the threat model analysis suggests that no single entity (for example, charging station vendor or charging network operator) is ideally situated to secure the ecosystem, but instead, requires the concerted effort of the ecosystem. The threat model, analysis and results are detailed in [2].
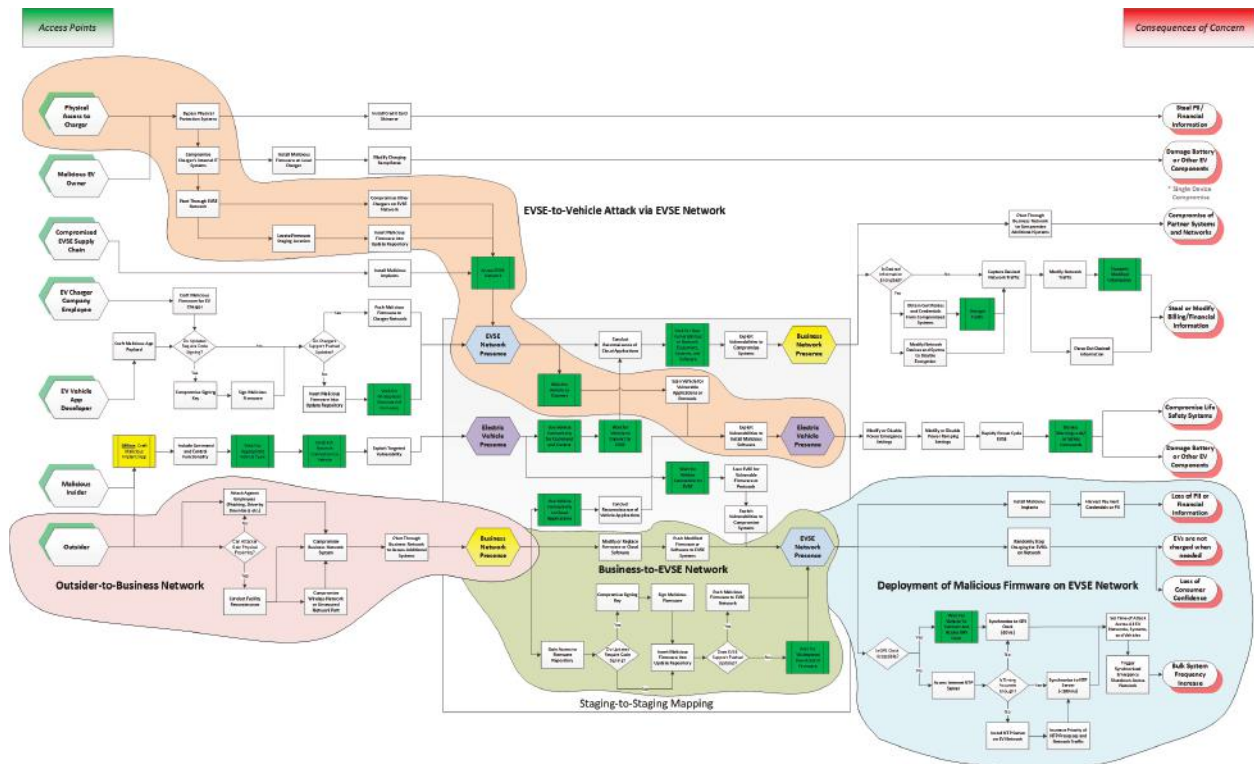
Figure II.5.2.4 Complete graph. Details presented in [3].
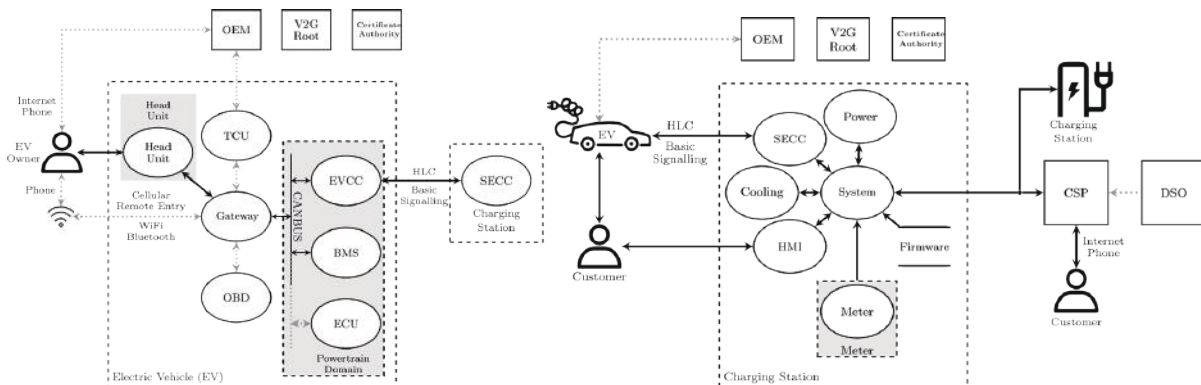
Figure II.5.2.5 The vehicle system model (left) depicts the components of the vehicle and their relationship to the charger. The charger system model (right) illustrates the relationship of the components and information flows.

Transmission System Consequence Analysis Simulations
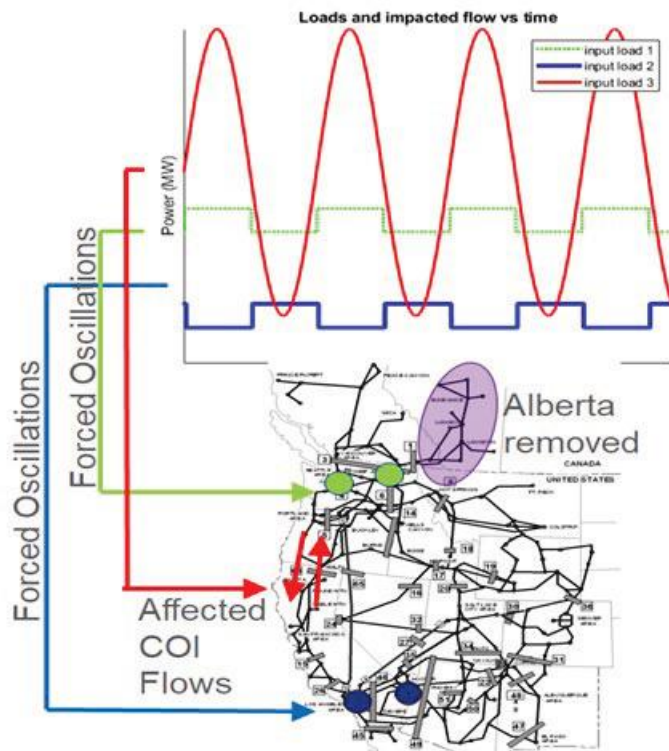
Figure II.5.2.6 Load oscillation simulation

PNNL's Consequence Analysis indicates that for the specific events studied in this work, the impact on the WECC system is concerning but generally manageable. Two different types of studies were simulated: a large discrete WECC-wide EV load drop across the region intended to raise frequency, and several smaller EV load modulation events intended to excite system inter-area oscillations along the California Oregon Intertie (COI). Figure II.5.2.6 illustrates this procedure. Here the green and blue dots indicate a distributed load to modulate on either side of the COI. The graph above the map shows that the loads are 180 degrees out of phase. Conceptually, if loads in the north are high and loads in the south are low, this will create a flow north along the COI. Similarly, when loads are low in the north and high in the south, this will tend to generate flows south along the COI. No significant adverse effects were observed in either set of simulations, however, COI flows of up to 3 times the oscillating load size were observed in the load modulation studies. Inter-area oscillations are of concern in that they put the grid in elevated state of risk during system events as well as making it difficult to achieve ideal transfer capacities and optimal power flows. Further details are presented in [2].

Conclusions

This project helped identify EV charger vulnerabilities and quantify the risk to critical infrastructure when vehicle chargers are maliciously controlled. This risk assessment is only an initial step in a continuous process of hardening charging infrastructure against cyber-attacks. There is much more work to secure charging infrastructure from cyber-attacks, including:

- Developing standardized policies for managing chargers and other assets in the charging ecosystem.

- Designing effective perimeter defenses to protect the assets including firewalls, access control mechanisms, data-in-flight requirements (encryption, authentication), etc.

- Creating situational awareness systems and intrusion detection/prevention systems in an ecosystem of diverse communication networks and systems.

- Providing search terms and key identifiers that can quickly identify potential misconfigurations and security gaps.

- Researching response mechanisms to prevent further adversary actions on the system, nonrepudiation technologies, and dynamic responses.

- Creating hardware- and software-based fallback and contingency operating modes.

References

1. J. Johnson, B. Anderson, B. Wright, J. Daley, R. Varriale, "Recommended Cybersecurity Practices for EV Charging Systems," Sandia National Laboratories, SAND2020-11401 D, doi.org/10.13140/RG.2.2.11141.37602.

2. J. Johnson et al., "Cybersecurity for Electric Vehicle Charging Infrastructure," SAND2022-9315, July 2022.

3. B. Anderson, "Securing Vehicle Charging Infrastructure Against Cybersecurity Threats," 2020 SAE Hybrid and Electric Vehicle Symposium, Pasadena, CA, 28-30 Jan 2020.

4. J. Johnson, T. Berg, B. Anderson, B. Wright, "Review of Electric Vehicle Charger Cybersecurity Vulnerabilities, Potential Impacts, and Defenses," Energies, vol. 15, no. 11, p. 3931, May 2022, https://doi.org/10.3390/en15113931.

5. Varriale, Roland, Ryan Crawford, and Michael Jaynes. "Risks of Electric Vehicle Supply Equipment Integration Within Building Energy Management System Environments: A Look at Remote Attack Surface and Implications." *National Cyber Summit*. Springer, Cham, 2021.

II.5.3 Cyber-physical Security Pillar for Unified National Lab Collaboration (CyberPUNC) (EVs@Scale Consortium)

Barney Carlson, Principal Investigator

Idaho National Laboratory
2525 N. Fremont Ave
Idaho Falls, ID
E-mail: richard.carlson@inl.gov

Jay Johnson, Principal Investigator

Sandia National Laboratories
P.O. Box 5800 MS1033
Albuquerque, NM 87185-1033
E-mail: jjohns2@sandia.gov

Tony Markel, Principal Investigator

National Renewable Energy Laboratory
15013 Denver West Parkway
Golden, CO 80401
E-mail: tony.markel@nrel.gov

Thomas E. Carroll, Principal Investigator

Pacific Northwest National Laboratory
PO Box 999, MS-IN J4-45
Richland, WA 99352
E-mail: Thomas.Carroll@pnnl.gov

Omer Onar, Principal Investigator

Oak Ridge National Laboratory
1 Bethel Valley Road
Oak Ridge, TN 37830
E-mail: onaroc@ornl.gov

Roland Varriale, Principal Investigator

Argonne National Laboratory
9700 S. Cass Ave.
Lemont, IL 60439
E-mail: rvarriale@anl.gov

Lee Slezak, DOE Program Manager

U.S. Department of Energy
E-mail: lee.slezak@ee.doe.gov

Project Introduction

Prior VTO-funded research discovered significant security gaps in high-power electric vehicle (EV) charging infrastructure, that if exploited, could cause significant harm to the grid and EV users. New research and outreach are needed to develop novel countermeasures, help industry deploy best practices, and train the nation's cyber workforce. With the increasing growth of electrified transportation and the charging infrastructure required to support its energy needs, cybersecurity of this infrastructure is critical to gain and

maintain consumer confidence through safe and reliable operation. Trust in the electric power system and transportation sectors must be built on secured communications between grid operators, electric vehicle supply equipment (EVSE) owners/operators, EVSE vendors, EVSEs, and EVs. If the collective power of these internet connected EVSE networks are manipulated in a coordinated attack, it will have a substantial impact on critical infrastructure and can potentially lead to cascading failure. This may disproportionally affect members of disadvantaged communities, where grid infrastructure is traditionally underbuilt and more susceptible to failure. The recent Colonial pipeline cyber-attack that disrupted the regional fuel supply chain is a stark reminder of the need for cybersecurity for energy infrastructure supporting transportation. Research and industry engagement are needed to ensure secure, safe, and reliable EV charging infrastructure operation that supports grid reliability and builds consumer confidence.

Objectives

The objective of the cybersecurity pillar of the Electric Vehicles at Scale Laboratory Consortium (EVs@Scale Lab Consortium) is to address and provide solutions to four key challenges and barriers to realizing secure and resilient high-power EV charging infrastructure:

1. *Industry implementation and utilization of latest security methods is not consistent* in legacy and new-product design, security configurations and operations. Examples observed range from the use of trivial passwords, outdated vulnerable software, adherence to insecure standards and protocols, and misinterpretation of secure standards. A means to assess and certify the EV charging infrastructure's security performance is currently missing and is needed to inform potential purchasing decisions and drive improvements.

2. *Lack of methods to identify, protect, detect, respond, and recover from cyber events* results in less secure communications, operations, and power transfer across the EV charging ecosystem. Novel countermeasures and safeguards are needed for integration with the charging infrastructure during component and system development to ensure reliable and secure EV charging.

3. *Unknown vulnerabilities in new, emerging features and standards* for advanced charging infrastructure compromise security. Due to increased features and complexity of controls across multiple components, vulnerabilities may be inadvertently introduced. Examples include Plug & Charge EV-to-EVSE communications, advanced energy management controls communications, wireless charging controls communications, and vehicle-to-grid (V2G) bi-directional power flow.

4. *Existing training for the EV charging infrastructure cybersecurity workforce*, which lacks sophistication and is limited to a narrow audience, is insufficient to combat the growing threats to electrified transportation and charging infrastructure. Through direct education and outreach, national lab staff can significantly enrich EV charging infrastructure cybersecurity training for a diverse workforce.

Approach

Six national labs are collaborating to address and provide solutions to the four key challenges and barriers identified in the objective of this EVs@Scale Lab Consortium pillar. The cybersecurity pillar is co-led by Idaho and Sandia National Laboratories in collaboration with NREL, Pacific Northwest, Oak Ridge, and Argonne National Laboratories.

Engagement with industry is leveraged to more effectively address several of the key challenges and barriers previously identified. Additionally, laboratory hardware and unique capabilities are leveraged to aid and accelerate these efforts to provide accurate, and insightful results and solutions to provide benefit to the Electric Vehicle Charging Infrastructure industry for improving cybersecurity and cyber-physical security attributes.

Results

PKI Adversarial Test Methods Support for SAE PKI Working Group

NREL has been a proving ground for a promising technique of securing the EV charging interface. Owing to the engagement of a global cohort of industry participants, the solution is well positioned for an accelerated transition to market. In 2020, the nonprofit SAE International launched an industry working group to understand the opportunities for implementing security features of international standard ISO 15118 that would utilize public key infrastructure (PKI) to enhance interoperability and security of transactions and controls between vehicles, chargers, and charge network operations. Industry leaders Eonti and DigiCert defined and developed an initial PKI architecture and prototype implementation, while NREL collaborated with the industry working group to define key testing methods that could validate new PKI system functionality. This resulted in a series of coordinated in-person pre-competitive testing sessions of new technology deployments.

This effort directly supports the first key challenge of assisting industry to test and deploy the latest standards-based security mechanisms applied to EV charging systems. PKI provides for the creation and distribution of public and private key pairs to authenticate end devices; encrypt the communications between entities; and automatically authenticate driver identity and authorize service. The technology provides end-to-end trust (integrity) and CIA (confidentiality, integrity, availability) for charging operations.

Initial testing events were hosted in April and September of 2022 with more than 30 participants using NREL's EV Research Infrastructure Laboratory in the Energy Systems Integration Facility. The focus thus far has been on interoperability and basic functions. The working group did successfully demonstrate PKI-based secure interoperable communications between vehicles and charging components, moving the implementation closer commercialization. The remainder of this project will focus on testing adversarial activities and the scalability of PKI systems to ensure operational availability for charging stations.

NREL and SNL researchers reviewed the PKI architecture documents and prior work on threat assessment to identify priority actions for with industry working group. The research team has identified several key functions for further exploration including understanding how to protect the system from a rogue Certificate Authority, methods for managing cross-root certification, trust lists, and revocation procedures. These efforts will help define the focus of the industry testing events in FY 2023.

In addition, the NREL-SNL team has expanded the scope of work to build an SAE-compliant PKI within a virtual simulation environment leveraging NREL and/or SNL high performance computing and cyber range resources. The virtual environment will allow researchers to evaluate potential PKI scaling issues and red-team strategies for engaging with PKI for EV charging systems.

Zero Trust Architecture for EV Charging Ecosystem

In this section, results from PNNL's efforts are detailed in context of three thrusts: "Build and Analyze Use Cases," "Design Architecture," and "Develop Prototype System." Even though discussed separately, the thrusts informed one another. The "Build and Analyze Use Cases" thrust identified requirements and objectives that influenced the architecture and implementation. These use cases were shared with external reviewers and enabled sharing implementation examples. External review and feedback from Cisco Talos and Seattle City Light were invaluable in identifying and understanding potential customers, preferred implementations, and the benefits and application of Zero Trust. Given how the marketplace has organized roles and responsibilities, it became evident that a Zero Trust architecture that strictly adheres to NIST SP 800-207 is not directly applicable to EV charging. NIST SP 800-207 couches Zero Trust in context of an organization's internal structure and operation. Zero Trust is positioned to tackle cybersecurity architecture for a complex organization, one in which "operate several internal networks, remote offices with their own local infrastructure, remote and/or mobile individuals, and cloud services." The organization has a direct relationship with users, systems, and devices and can institute policies that govern these elements. An organization utilizes device and user monitoring, network architecture, and strong authentication tokens so that

their cybersecurity operations have full visibility of the entities and the activities that are performed. When achieved, Zero Trust leads to highly effective cybersecurity. Interactions among organizations typically depend on mutual distrust. Critically, an organization does not have full visibility of external interactions. Unless imposed by a contractual obligation, the organization, for example, will not have state of health or a model of behavior for external devices and users. Even if data is made available, an organization should not trust it to the extent it trusts data collected from its own users and systems.

The market structure for EV charging operations is divided into two primary roles: *charging station operator* (CSO) and *charging network provider* (CNP). As defined in the National Electric Vehicle Infrastructure (NEVI) Formula Program notice of proposed rulemaking, CSO is "entity that operates and maintains the chargers and supporting equipment and facilities at one or more charging stations." CNP is the "entity that operates the digital communication network that remotely manages the chargers." CNP operates the *charging station management system* (CSMS), a system that manages the operations of chargers, billing, smart energy management, and other ancillary functions. Critically, these roles can be assigned to different organizations and their interactions will be classified as external. While we strive to enforce least privilege access in EV charging infrastructure, design patterns and architectures are to be adapted and tailored as customary practices and applications are insufficient. The insufficiency is caused by the orthogonality of the primary roles as one owns the chargers (CSO) but another operates them (CNP). This issue is illustrated with OCPP where chargers report security events to the CNP, but it is the CSO who will likely handle the cyber incident responses.

Build and Analyze Use Cases

Threat models were created to study the attack vectors triggering High Consequence Events (HCE). INL's *Consequence-driven Cybersecurity for High-Power EV Charging Infrastructure* (3C) project identified and prioritized thirty-three HCEs. A HCE is a potential result of cyber compromised high-power charging infrastructure. A system model developed by *Securing the Vehicle Charging Infrastructure* was modified and analyzed to identify and enumerate attack vectors that could provoke HCEs. A system model is an abstraction of a system that supports the generation and study of threats. Each HCE was likely associated with multiple vectors, which means that there are multiple ways to induce the result. By conceptualizing and abstracting away specific details, attack vectors became not unique to the HCE. The set of attack vectors were analyzed to discover commonalities among them. The distillation of the attack vector commonalities inspired the construction of six use cases. "Solving" the cybersecurity problem exemplified by the use cases should, in theory, reduce the likelihood that an attacker could induce an HCE. Zero Trust concepts were then studied in context of the use cases, which informed architecture and functional requirements.

To mitigate attack vectors leading to some HCE, non-customary zero trust concepts were explored and evaluated. In a scenario studied in 3C, we considered the case where fifteen chargers, attached to the same distribution system node, terminate charging at the same instant (less than or equal to 4ms). This induces a grid overvoltage/undervoltage on the distribution system. In Figure II.5.3.1, voltage rises above 1.05pu for 279ms, which exceeds the ranges of ANSI C84.1, a North American utility voltage tolerance standard. If such an event is prolonged or regular, equipment damage may result, such as insulation breakdown. While there are multiple vectors that could be used, the following focuses on the "inattentive" operator. The inattentive operator is an authorized user of the system, who carelessly performs their role and terminates the charging sessions. As the user is authorized to send the well-formed commands, identity and access controls alone are insufficient to dodge the outcome. Other policies were examined, such as metering OCPP `RemoteStopTransaction` request to one every 60ms. The result of the policy, shown as the red line in Figure II.5.3.1**Error! Reference source not found.**, is positive as the voltage remains below 1.04pu. Other policies and their implications are continued to be explored. For example, implementing stochastic "drops" of `RemoteStopTransaction` requests.
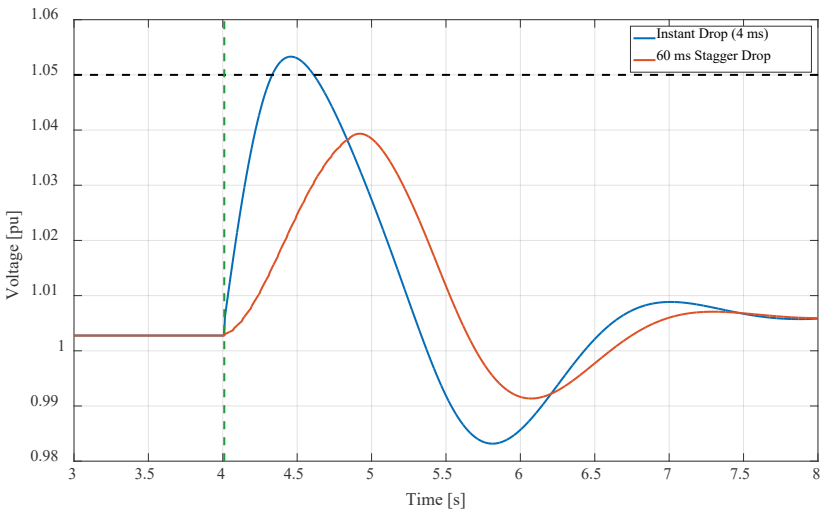
Figure II.5.3.1 Voltage overage when many chargers are commanded to terminate charging session

Design Architecture

Several notational architectures were designed, reviewed, and iterated. Early architecture suffered from imprecisely identifying the user of the resultant Zero Trust system. Cisco Talos, Cisco IoT Solutions, Cisco Transportation and Seattle City Light reviewed the at-that-moment architecture and use cases. They offered concurring feedback that the architecture and approaches were too intrusive, requiring too many significant changes, and that focus should be directed to an incremental approach which can be 'bolt on'. Seattle City Light further discussed the division between CSO and CNP and that the CSO would prefer to monitor the OCPP communications between the charging station and the CNP's charging station management system. The architecture and use cases were revised in response. The architecture was modified to focus on secure connectivity, ensuring access to services, and identity-based access controls.
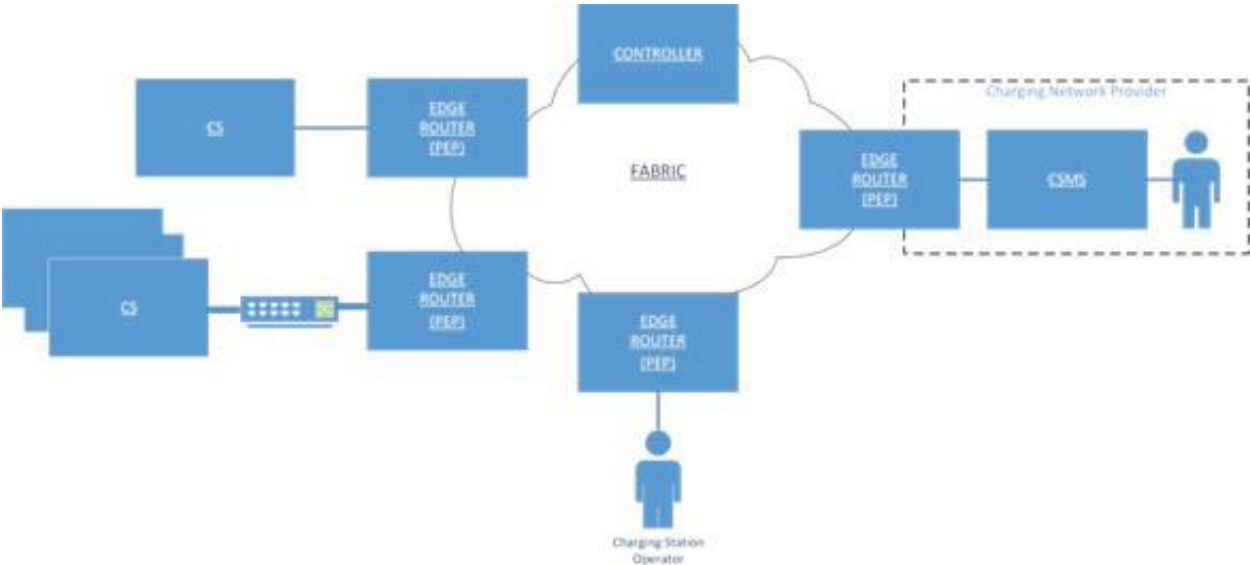
Figure II.5.3.2 The notional zero trust architecture for EV charging. The fabric interconnects edge routers. The edge routers, a policy enforcement point, host security services and enforce policy decisions. The controller manages and configures the components

The notional architecture is diagramed in Figure II.5.3.2. The *controller* is responsible for the control and management of the components. The *fabric* is an overlay mesh network that runs over standard internet transports. This overlay creates a private, encrypted network that securely interconnects the edge routers. The *edge routers* provide entry to the fabric and perform *policy enforcement point* (PEP) functions. The vital role of the PEP is that it enforces access controls, meaning it permits or denies access based on a policy decision. While a policy decision must fundamentally distill down to permit or deny, it may also include treatment directives. For example, a permit decision may also direct the PEP to delay or meter the flow.

Distinct security associations are established between every pair of edge routers, and every router and the controller. A *security association* is shared security attributes and secrets so that the pair can communicate securely. Within the fabric, *fabric routers* (not illustrated) assist getting edge routers communications to the correct destinations. Fabric routers never observe the traffic in plaintext. Network resiliency is ensured as the connections are *meshed,* meaning there are paths for communication to traverse.

Communications are permitted based on identity-based access controls. Because of the deny by default posture, every communication must be individually authorized. Access controls for Open Charge Point Protocol (OCPP), a protocol used for the management of charging stations, are handled more granularly. Policies are applied to each request / response in a OCPP session. This allows messages to be treated differently, such as metering or stochastic drops of bursting `RemoteStopTransaction` requests.

Develop Prototype System

Open-source software network frameworks and service meshes were identified and their qualities catalogued. We conducted an assessment to determine which were most relevant to project objectives and were aligned with staff skills and expertise. The Envoy Proxy, an open-source edge and service proxy, was selected as the basis for the edge router. Envoy is widely used in services meshes and has been the foundation for many cloud-based applications. OCPP operates on the WebSocket protocol, a bidirectional communication protocol common to full-featured web applications. Envoy support for WebSockets was assessed to be basic as it handled WebSocket communications as a byte stream. Ongoing software development efforts are remediating this deficiency and adding features to support OCPP.

EV Charging Infrastructure Cyber-physical Security Technical Support for the 2022 CyberAuto Challenge

The CyberAuto Challenge is an annual event for college students to learn about cutting-edge cybersecurity and cyber-physical security with state-of-the-art plug-in vehicles and EV charging infrastructure. At the event, numerous tutorial sessions are presented by industry experts focusing on information, tools, and methodologies currently used by the cybersecurity industry. Several equipment manufacturers sponsor the event by providing state-of-the-art vehicles and EV charging infrastructure, enabling a rich learning experience as well as in-depth networking and recruiting opportunities of the next-generation cybersecurity work force. Advanced vehicles, EV charging infrastructure (AC EVSE and DC chargers), and software suites used by these systems are available during a 24-hour 'hands-on' assessment, evaluation, and exploit-attempts session at the challenge. The students are encouraged and challenged to assess the security posture of the systems and conduct exploit attempts on the identified potential vulnerabilities in the vehicle systems and charging infrastructure.

At the 2022 CyberAuto Challenge, INL staff provided cybersecurity expertise and technical support as well as instructed the EV charging infrastructure tutorial sessions. This effort directly supports the fourth key challenge of the EV@Scale Consortium Cybersecurity pillar. The support provided by INL contributed to a successful event in 2022 with approximately 50 students in attendance. The event had six advanced vehicles and EV charging infrastructure provided by the manufacturers. INL staff conducted three tutorial sessions teaching the students about EV charging infrastructure architecture, communications protocols, operational functionality, and areas of potential vulnerabilities for investigation during the 24hr. 'hands-on' event. Additionally, the tutorials also focused on EV charger architectures for power electronics, thermal management, communications between EVs, EVSE, smart energy management systems, and other manufacturer specific communications used for internal controls and remote software management.

During the 24hr. event, several students worked with EV charging infrastructure hardware and software. INL staff advised students on assessment and exploit attempts focused on the EV charging infrastructure at the event. Numerous exploits were attempted by the students, and a few were successful. These exploit efforts, both successful and unsuccessful, results in invaluable learning experiences in their pursuit of a careers in cybersecurity. These successful exploits also provided valuable information back to the industry sponsors that provide the EV charging systems for the event.

The CyberAuto Challenge is an excellent learning opportunity for the next generation of the cybersecurity work force as well as a great opportunity for the industry collaborators to utilize the independent assessment and exploit attempts of their equipment hardware and software that is provided to the event. To ensure business-sensitive information is not released from this event, all participants, organizations, visitors, and collaborators sign a non-disclosure agreement at the beginning of the event. All materials, findings, and notes that are created during the event are destroyed at the end of the event or secured by the owner of the system to which the information pertains.

Implementation of High-Power Charging System Power Electronics Architectures in Hardware-in-the-Loop (HIL) Real-Time Emulator Platform

In this task, the project team from ORNL first reviewed a typical power electronics architecture for a high-power EV charging station including all of the power conversion stages. In most high-power EV charging stations, there is an active front-end rectifier with power factor correction, then a high-frequency inverter and a high-frequency isolation transformer, and then a rectifier and an optional dc/dc converter. In some cases, a 60 Hz line frequency isolation transformer is used but that does not change the overall system operation from a cyber-physical system point of view. The control system and communication peripherals for EV charging stations were also reviewed and evaluated. This was followed by hardware-in-the-loop implementation of a known EV charging station to calibrate and fine tune the hardware-in-the-loop model. The digital twin model implementation of the EV charging system is illustrated in Figure II.5.3.3. In Figure II.5.3.4, operation of the real high-power EV charging system (experimental results) and the waveforms from the HIL implemented system are provided to demonstrate that the HIL model worked exactly same as the experimental system.
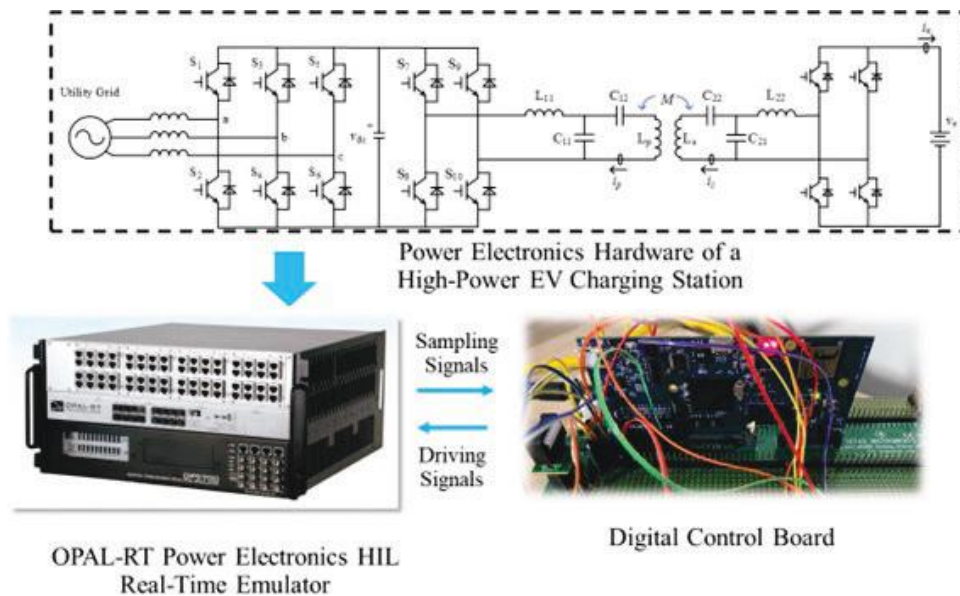
Figure II.5.3.3 Hardware in-the-loop implementation of a high-power EV charging station
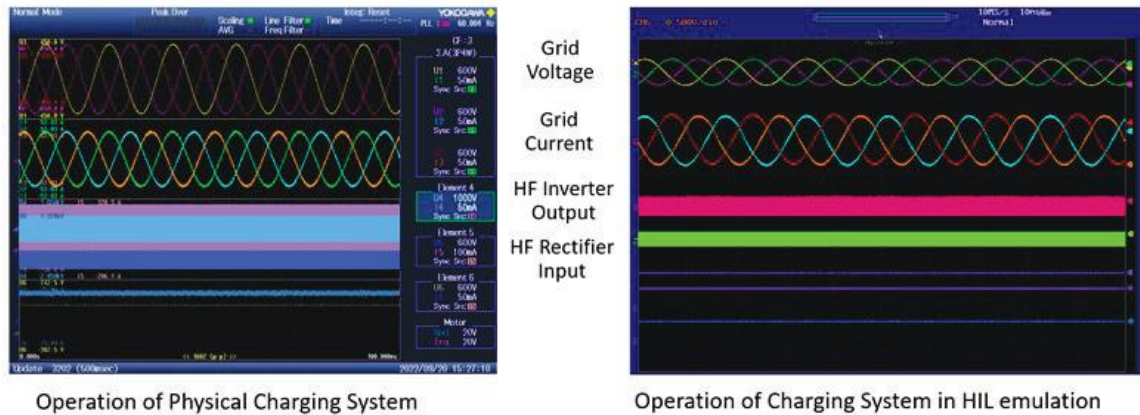
Figure II.5.3.4 Comparison of real hardware and the HIL implementation of a high-power EV charging station.

Next, the ORNL project team identified possible cyberattack scenarios with high consequences. These attack scenarios included DC shoot through which involves turning on the same phase-leg power devices simultaneously either on the grid-interface converter or on the high-frequency rectifier, AC phase-to-phase short-circuit which involves turning one of the switches ON in the grid interface converter, and the sudden disconnection of the battery load during high-power charging. For each of the attack scenarios analyzed here, team ran the simulations as well as the HIL implemented digital twin model. The consequences of the cyberattacks were evaluated on the abnormal operating conditions in terms of the voltage and current amplitudes and fault energies to assess the potential damage to the high-power charging equipment. Due to space limitations, results of only one cyberattack scenario is included here in Figure II.5.3.5 that is the DC shoot through. In this example, before the grid interface converters' fast fuses disconnect the system from the grid due to an overcurrent, the grid current increases by five times with a damage to grid interface converter. With the high discharge current from the DC bus bar capacitors to the fault, the short-circuited phase-leg modules is also damaged. The example results of this condition is presented in Figure II.5.3.5.
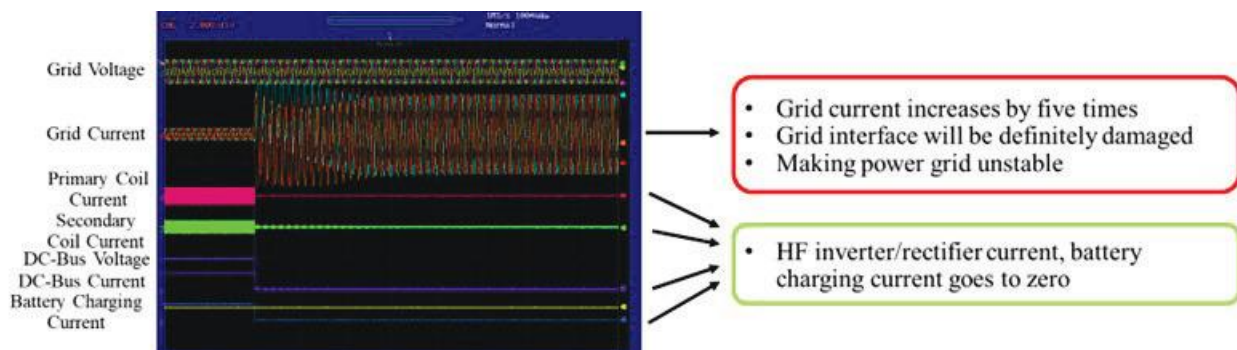
Figure II.5.3.5 DC shoot through / DC bus short-circuit HIL results.

Conclusions

As part of the EVs@Scale Consortium, the multi-lab team within the cybersecurity pillar have initiated a portfolio of work to address key challenges including:

- *Industry implementation and utilization of latest security methods is not consistent*

   o Testing the SAE PKI at NREL has given us a chance to participate with industry on identifying myriad gaps, ambiguities, and errors in the ISO 15118-2 standard that have made interoperability very difficult to achieve. These issues relate specifically to the Plug-and-Charge functionality and the associated PKI requirements.

o   We have proposed a dialogue between National Labs and industry (e.g. a PKI operating entity emerging from the SAE PKI development/prototype project) to explore technical and organizational remedies to the inconsistencies noted above.

- *Lack of methods to identify, protect, detect, respond, and recover from cyber events*

    o   Subsequent years of this project will build upon the insights and learnings from this first year of the project effort to develop and evaluate methods and mitigation solutions to improve the security and resilience of high-power EV charging infrastructure.

- *Unknown vulnerabilities in new, emerging features and standards*

    o   As part of our SAE PKI evaluation and simulation work, the NREL-SNL-UNM team is analyzing the cybersecurity and PKI provisions of the ISO 15118-20 standard, which is in early stages of adoption. We will focus on the kinds of issues that hampered the adoption of ISO 15118-2 (see above).

    o   Several new functionalities introduced in ISO 15118-20, including bi-directional power flow, dynamic pricing, and wireless communication, pose serious challenges regarding both interoperability and cybersecurity. We could extend the PKI modeling and simulation platform we're developing for current functionality (limited to Plug-and-Charge, CSP operations, and inter-CSP roaming) to facilitate the evaluation of these new features.

- *Existing training for the EV charging infrastructure cybersecurity workforce.*

    o   The CyberAuto Challenge was supported and enhanced for electrified vehicle technology cybersecurity hands-on training. This learning is focused on EV charging infrastructure cyber-physical security for a wide range of internal and external communications vulnerabilities. The enrichment to the CyberAuto Challenge training to include EV charging infrastructure technologies greatly enriches the learning experiences by the next generation of cybersecurity work force.

Key Publications

1. "Electric Vehicle Manufacturers Mobilize Behind Charging Cybersecurity at NREL." April 29, 2022. https://www.nrel.gov/news/program/2022/ev-manufacturers-mobilize-behind-charging-cybersecurity-at-nrel.html

2. "Electric Vehicle Cyber Testing Event at NREL Expands to More Participants, Wider Validation." September, 2022. https://www.nrel.gov/esif/esi-news-202209.html#:~:text=Electric%20Vehicle%20Cyber%20Testing%20Event%20at%20NREL%20Expands%20to%20More%20Participants%2C%20Wider%20Validation

3. Markel, Tony. "PKI Vulnerability Test Methods." Presented at CyperPUNC Deep Dive Session. Sept 20-21, 2022.

4. Overview of the US DOE EV SALaD demonstration https://www.youtube.com/watch?v=2BCPDiFhSds October 2022.

Acknowledgements

II.6 Codes and Standards

II.6.1 Electrified Vehicles Test Procedure Development (ANL)

Michael Duoba, Principal Investigator
Argonne National Laboratory
9700 South Cass Ave., Bldg. 362
Lemont, IL 60439
E-mail: mduoba@anl.gov

Lee Slezak, DOE Program Manager
U.S. Department of Energy
E-mail: lee.slezak@ee.doe.gov

Start Date: June 1, 2020	End Date: March 31, 2022	
Project Funding (FY21&22): $400,000	DOE share: $400,000	Non-DOE share: $0

Project Introduction

All the anticipated gains electrified vehicles are poised to make (and thus the entire thrust behind DOE's focus on facilitating electric vehicles at scale) are based upon metrics that come from standardized testing. These standards are carefully crafted dynamometer test procedures aimed at capturing the true performance of electrified vehicles which consider their unique operation and energy consumption. The potential for error in characterizing efficiency and performance is catastrophic: if EV test procedures miss reality by providing overly optimistic results, consumers and DOE will be disappointed in their substantial investments, if results are biased in the other direction (overly pessimistic), opportunities would be lost. This project to refine and further develop EV test procedures provides a risk management function to ensure efficiency, range, and performance results are a true representation of the technology upon which DOE builds its vehicle technology research portfolio. The national labs are the perfect 3rd party entity leading (working with regulatory bodies and OEMs) the development of improved procedures and making honest assessments of standardized procedures. ANL staff have nearly 30 years of experience creating and validating electrified vehicle dynamometer testing standards.

Objectives

The objective of this work is to update, refine and improve performance and efficiency test procedure standards for hybrid-electric vehicles (HEVs), plug-in hybrid electric vehicles (PHEVs), and battery electric vehicles (BEVs). The aim is to address the needs of certification authorities, OEMs, and researchers as electrified vehicles are now rapidly moving from niche production to mainstream OEM products. DOE-funded electrified vehicle standards work has a long history of many developments, in this project cycle, the test procedure revision goals were:

- reduce testing burden while maintaining better results (reducing OEM, EPA, and CARB costs)

- higher accuracy

- less restrictive test tolerances allowing more design optimization and ultimately higher efficiency

- Providing direct performance comparisons between electrified and conventional vehicles.

How these goals were reached will be detailed later in the Results section.

Approach

Acceptance of standardized vehicle test procedures is typically facilitated by SAE International (among other standards organizations). Whereas EPA and CARB have the authority to certify vehicles as they see fit, much of what is found in the CFR and California regulations refer specifically to SAE documents. The approach involved the support of three SAE standards task forces and documents:

- **SAE J1634 (Testing efficiency and range of BEVs)**
  Support the SAE committee revising SAE J1634 and serve as a subject matter expert on SAE testing procedures for California Air Resources Board. This approach ensures J1634 results are a true representation of BEV performance and ensure sound integration of procedures with regulation.

- **SAE J1711 (Testing fuel/electricity consumption and range of HEVs and PHEVs)**
  Serve as the task force chair, develop the agenda, do the analysis, propose changes, and edit document to reflect the changes. This approach generated new ideas and through tight collaboration with industry and regulatory staff, the significant new functions and calculations were added to J1711 and a new revision document brought through SAE balloting.

- **SAE J2908 (Testing peak power for propulsion of HEVs, PHEVs, BEVs, and FCEVs)**
  Serve as task force chair, develop a new power rating approach that allows direct comparisons with traditional engine ratings. Do the analysis, propose recommendations, edit J2908 document and bring to ballot.

In addition to the document development above, a multitude of other activities are supported. This effort includes providing data and feedback for a host of other SAE tasks force committees and serving as subject matter experts for CARB, ISO and UN-related committees.

Results

SAE J1634 (BEVs)

This was a relatively small portion of the project. This project started near the end of the latest J1634 revision. However, from early 2021 until the end of FY22, the activity focused on working with regulators in California as they finalized their Advanced Clean Cars II program. Many of their rules leverage SAE J1634 test results.

SAE J1711 (HEVs and PHEVs)

Legacy testing standards uniquely developed for conventional ICE vehicles date back to the early 1970s. Testing electrified vehicles using these approaches is like the preverbal "square peg in a round hole." HEVs have the added dimension of drawing from either, or both of two energy sources at any given time. After recharging, the PHEV operates as an electric vehicle first, and after a time, then behaves as a conventional hybrid. All these added complexities required deep consideration of how HEVs and PHEVs are used and how they should be compared to conventional vehicle counterparts.

The previous revision of J1711 first came out in 2010. This 2022 revision addresses too many specific refinements to list here, it rectifies issues that have accumulated by the test community over the years since 2010. Typically, the number one priority in EV procedure refinements is reducing test burden. To properly characterize BEVs, HEVs, and PHEVs, much more testing is required compared to a conventional vehicle. Any way to ease the burdens on the automakers in producing new electrified vehicles will have a direct impact on how electrified vehicles are integrated into product portfolio decisions.

The biggest change in the revised J1711 document was introducing a new method of testing that simultaneously reduces testing burden, loosens restrictive tolerances, and provides better accuracy. The battery energy state in HEVs and PHEVs are always changing while driving and this can cause high variability in consumption test results. The solution has always been to only accept tests where the battery state (termed "Net Energy Change"[NEC]) at test end is very close to its beginning. This can be restrictive, especially for

PHEVs which can have significant on-board electric power and energy available for electric propulsion. The new J1711 feature is an implementation of the concept of "NEC Corrections." This allows for a 2x to 3x wider range of allowable changes in NEC, while correcting the fuel consumption results back to zero NEC using correction factors. This factor is called the "S-factor" and it is depicted in Figure II.6.1.1. A test result that is charge-gaining falls on the 2-dimensional plot as the gray triangle. The consumption result is slightly too high, however, by using the established J1711 S-factor the result can be corrected to a new, synthesized result that represents the vehicle's true, charge-balanced consumption result for the test.

Wh of Fuel

$$\frac{\Delta Wh_{fuel}}{\Delta Wh_{NEC}}$$

△ CST result
▲ NEC-corrected CST result

$$S = -\frac{\Delta Wh_{fuel}}{\Delta Wh_{NEC}}$$

← (-)NEC in Wh   0   (+)NEC in Wh →
charge gaining   *charge depleting*
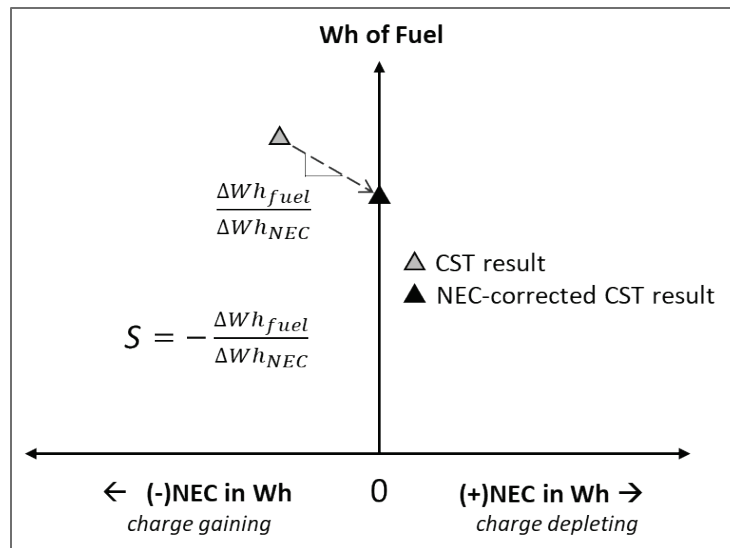
Figure II.6.1.1 Using new "S-factor" method to correct HEV/PHEV charge-sustaining results to zero net battery energy change in SAE J1711 (*Source: ANL*)

The new S-factor method allows automakers to open up control restraints and design more flexibility in the electric operation of HEVs and PHEVs. It also provides more accurate results because all charge-sustaining tests are now corrected for changes in NEC while in the past, the tolerance window, while small, introduced noticeable errors.

SAE J1711 was successfully balloted and is expected to be published by SAE early 2023.

SAE J2908 (testing for power rating for all electrified vehicles)

Defining power ratings for electrified vehicles has always been a point of contention. While conventional ICE power ratings are based a specific dynamometer test of the engine, electrified vehicles operate as a system and this requires a different approach. With such a diversity of electrified powertrain layouts (one or more electric motors) and system architecture complexity (e.g., series vs. power-split etc.), no agreed upon definition of electrified vehicle power has emerged to make fair comparisons across all powertrain types. The first edition of J2908 came out in 2017 and its scope was originally limited to testing procedures that quantify the maximum system power rating where the system boundary was at the wheels. Although this system test (wheel power) allows fair and unbiased comparisons among any and all types of vehicles (electrified powertrains and conventional vehicles), what about legacy engine power test ratings? Comparisons could only be made if conventional vehicles are all subjected to the same special wheel power test. This turned out to be an impractical expectation. So, at the request of the automakers, J2908 was reopened in 2020 to add in a methodology allowing comparisons of electrified vehicles to legacy conventional vehicle engine power ratings.

The J2908 revision maintains the original (hub) dynamometer testing approach, but presents a specific definition of "rated system power" along with a number of options detailing how the data collected from the test (and subsequent tests) can be processed to determine rated system power for any electrified vehicle. The

new definition of rated system power for J2908 is: "*The sum of mechanical shaft power outputs of all components contributing to the propulsion of the vehicle at the condition of rated wheel power (maximum power).*"

Four general options are presented to determine the sum of the system's mechanical shaft power outputs. The options make accommodations for the fact that both automakers and independent labs have different levels of access to powertrain data and controls. Automakers can leverage component-level data and system-level bench testing while 3rd party labs can rely on real-time reported component data or install in-situ sensors. The general process in depicted in Figure II.6.1.2.
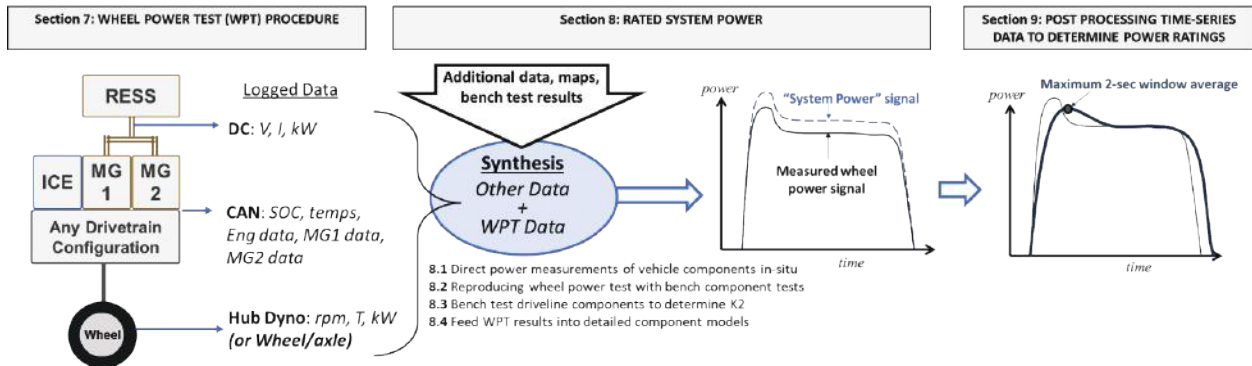
Figure II.6.1.2 Procedure to determine rated system power in SAE J2908 (*Source: ANL*)

For any of the options, the common goal is to synthesize a system power signal which is then filtered in such a way that it represents the final 2-second and optional 10-second system power ratings.

Conclusions

All electrified vehicle performance and efficiency metrics used throughout industry, the DOE labs, and regulatory agencies are based upon metrics that come from standardized tests. In this two-year program, two important documents were successfully revised and well-received by the testing community. Testing burden was reduced, and accuracy improved for HEV and PHEV testing. With these changes, HEVs, and especially PHEVs can be designed with more control flexibility and opportunities for optimization. The expectation is small but noticeable increases in efficiency for future HEVs and PHEVs.

With this work, there is now a way for all electrified vehicle types to be rated for power alongside their conventional vehicle counterparts. Advancements such as this help smooth the transition from known vehicle technologies to new and unfamiliar ones. Note that Volkswagen AG is currently providing J2908 ratings in their BEV product specifications, with other automakers likely to follow.

Mainstream adoption of electrified vehicle technology still has many challenges from many varied aspects. This effort in developing and maintaining accurate and representative test procedures provides a robust foundation upon which critical performance and efficiency metrics are analyzed and compared in the research and development community. This work is a critical part of DOE VTO's research portfolio that address challenges and help mitigate risks of rolling out EVs at scale.

Key Publications

1. SAE J1711-XXXXXX (pending publication date), "Recommended Practice for Measuring the Exhaust Emissions and Fuel Economy of Hybrid-Electric Vehicles, Including Plug-in Hybrid Vehicles"

2. SAE J2908-XXXXXX (pending publication date), "Vehicle Power and Rated System Power Test for Electrified Powertrains"

References

1. SAE J1634_202104, "Battery Electric Vehicle Energy Consumption and Range Test Procedure,"
    https://www.sae.org/standards/content/j1634_202104/

2. SAE J1349®, "Engine Power Test Code - Spark Ignition and Compression Ignition - As Installed Net
    Power Rating," https://www.sae.org/standards/development/about-saej1349-certified-power/

Acknowledgements

II.6.2 Composite Pillar Oversight, Reporting, Subcontracting and Standards Development Tasks (EVs@Scale Consortium - ANL)

Theodore Bohn, Principal Investigator
Argonne National Laboratory
9700 S. Cass Avenue
Lemont, IL 60439
E-mail: tbohn@anl.gov

Lee Slezak, DOE Technology Manager
U.S. Department of Energy
E-mail: lee.slezak@ee.doe.gov

Start Date: January 1, 2022　　　　End Date: December 30, 2022
Project Funding: $585,000　　　　DOE share: $585,000　　　　Non-DOE share: $0

Project Introduction

Problem Statement – The EVs at Scale lab call program is divided into 5 pillars (Grid integration, High power charging, Wireless power transfer charging, cybersecurity and Codes & Standards) plus consortium management. This progress report covers Codes & Standards tasks explicitly, when in fact all five pillars have Codes & Standards implications on EVs at Scale. Deep dive meetings of each of the other pillars have had updates and presentations from the Codes & Standards activities that support the other pillars.

Economic benefits, system level efficiency, and system reliability of 'EVs at Scale' are directly impacted by the quality and detail of standards that prescribe operating parameters as well as interoperability requirements. Codes are similar but different from standards, where codes and regulations are based on details in standards but can be more flexible in interpretation of which standards apply to a particular EV charging system attribute. Codes and regulations are most often enforcement mechanisms for the details contained in standards.

In legal terms there are two main types of standards; de jure and de facto; https://www.upcounsel.com/de-jure-facto. De jure facto and de facto are commonly confused to mean the same thing. While they are often used in the same contexts, they are distinctly different concepts. De jure standards refer to standards that are established by law, while de facto standards are standards that are based on facts but not formally recognized. These terms can be applied to a wide range of contexts, but they are most often used to describe certain business, legal, or political situations. Standards Defining Organizations (SDOs) are the focus of this work, leveraging international recognition of EV charging standards, with legal application of standards in each region while focusing on harmonization of standards between SDOs and regions.

The Codes and Standards pillar crosses the boundaries of codes, standards (developing de jure standards while acknowledging fact based de facto standards) and creating maps of the progress and/or gaps for each EV charging standards area that is covered in the scope of the project. There are insufficient resources from stakeholder participants in standards defining organizations since most are non-for-profit and rely on donated time and effort of subject matter experts. DOE support via national lab participants fills some of the gaps to define, create and refine EV charging related standards.

The group of 5 national labs engaged in FY22 Codes and Standards pillars for EVs at Scale include, ANL, INL, NREL, ORNL and PNNL. ANL is the lead lab coordinating tasks overall and leading the reporting tasks.

ANL assumed responsibility to support the largest variety of standards and leadership roles within the EVs at Scale Codes and Standards pillar. ORNL has focused on Wireless Power Transfer (WPT) standards, INL on WPT and Distributed Energy Resources (DER), NREL on Megawatt Charging System (MCS)-DER, and PNNL works on EV charging roadmap, DER and MCS tasks.

The EVs at Scale Codes and Standards Lab Call proposal scope, collectively submitted by all five labs, was based on consensus of the top 10 standards areas supporting EV charging, at scale, with respect to gaps in the impact on wider EV deployments that rely on standards. In shorthand, these include conductive and wireless charging, grid interconnection, grid integration/DER, safety, and high power (MCS) charging methods. Codes are mainly connected to safety testing of components/systems and commercial transactions for dispensing electricity as a fuel (NIST Handbook 44-3.40).

Mapping of existing EV charging standards is one of the key mechanisms to both track the status of existing EV charging standards. DOE sponsored the ANSI EV Standards Panel (EVSP) roadmap document last published in 2013. https://www.ansi.org/standards-coordination/collaboratives-activities/electric-vehicles Creating a 2023 version of the roadmap with identified gaps is a tool that will be used by groups that are accelerating EVs at Scale.

Objectives

Primary goals – Address challenges and barriers for high-power EV charging standards by identifying and filling gaps in charging equipment as well as grid impacts, interoperability, and safety topics. ANL led tasks have the goal to

- Facilitate creation and improvement of codes and standards enabling 'EVs at scale' charging

- Engage with industry stakeholders to create a consensus based EV standards roadmap

- Create interoperability guidelines and criteria to evaluate standards compliance/implementation

- Supply validation test data with industry partners to support standards refinement.

Achieving this goal is facilitated via research at the lab as part of providing validation data to standards development organizations along with direct creation of standards details and documents.

Approach

Argonne leveraged DOE Labcall for MW Charging requirements studies from FY2018 to FY2021 and the two decades of involvement with SAE, IEEE, IEC, ISO and other charging standards to align industry partners to complete the tasks in the FY2021 Codes and Standards pillar of EVs at Scale. The monthly industry engagement meetings with ANL led presentations has spanned over four years leading to a distribution mailing list of 800 members, covering stakeholders for a diverse array of industry perspective and standards partners.

The task numbers in this section are references to the DOE Annual Operating Plan (AOP), specifically for ANL tasks in this area of the annual report. Tasks for INL, NREL, ORNL and PNNL are listed in subsequent sections of the annual report. The barriers and solutions for each of the tasks are similar since the standards process is iterative and at times unending with 5 year document reviews and updates to all active standards as part of the renewal process.

Task 1.1 Supporting SAE J29254-2 and SWIFT Charge standard development activities to cover recent technological developments in power electronics and electromagnetics.

Barriers:
- SAE J2954 has been published for wireless charging of light duty vehicles; a similar standard does not exist for heavy duty vehicle wireless charging, necessitating SAE J2954-2 that reflects 2022 technologies

- SWIFT Charge wireless vehicle charging consortium was formed by member companies that are anonymous as of 2022 while the recommended practice documents are drafted, with an end goal of adoption by a standards defining organization after field validation and testing. National lab participants bring independent perspectives to objectively assess the goals and methods of the SWIFT Charge consortium. This consortium seeks to overcome fundamental limitations of the SAE J2954 methods of

coupling fields, EMC limitations and higher power density while meeting EMF limits. The consortium is not unlike the phone/consumer device Wireless Power Consortium; https://www.wirelesspowerconsortium.com/.

Solution:

ANL staff have participated in monthly SAE J2954 meetings and testing since the standard work area was launched in 2010. Supporting SAE J2954-2 for heavy duty applications is an extension of past activities. J2954-2 has expanded to include dynamic power transfer for electrified roadways and leverages state/federally funded demonstration projects. These projects include ASPIRE, based at the Utah State University facility, including 4 NSF funded universities. https://aspire.usu.edu/presentations/enabling-technologies-for-dynamic-wpt-vehicle-automation/ The SAE J2954 committee has several subcommittees that also meet each month, focused on EMC compliance/assessment, alignment-interoperability, and testing activities.

The SWIFT Charge consortium is led by Momentum Dynamics of Malvern PA that recently changed their name to InductEV (https://inductev.com/). The authors of the SWIFT Charge technical specifications committee met monthly to review document drafts and gather input from national lab participants (ANL, NREL, INL, ORNL).

Funding for task 1.1 is limited to participation in monthly meetings and document review/feedback/input.

Task 1.8 SAE J3271: Launch new work area on end-to-end specification for Megawatt Charging System

Barriers:

- The SAE J1772 and equivalent IEC62196 combined charging system (CCS) is widely deployed for light and heavy duty vehicles, with current iterations supplying up to 920vdc/500Adc. There is no standard for higher power human operated charging systems up to or above 1 MW power levels.

- The CharIN consortium requirements for a megawatt charging system (MCS) coupler/inlet were developed from 2018-2022 by industry stakeholders. The consortium needed to pass the requirements to a standards defining organization to develop into a de jure standard.

- Heavy duty electric truck manufacturers are on a short time line to have a standardized and NRTL listed charging solutions for the successful launch of their vehicles and customer needs. None exist.

- IEC and ISO standards for EV charging are broken into several documents and don't include utility interconnection, micro-siting of equipment/pull through access or use case details in one location.

Solution:

ANL engineers participated in the CharIN MCS requirements specification process since the launch of the 'High Power Charging for Commercial Vehicles-HPCCV' which was later shortened to MCS.

https://en.wikipedia.org/wiki/Megawatt_Charging_System

ANL drafted a scope and rationale text in 2021 to petition SAE to launch a new work area within the Hybrid-EV Committee. The scope of the document bins the technical requirements into five separate subsections

- 1 Electromechanical coupler/inlet

- 2 Physical/software layer communication

- 3 Cables/cooling, automated connection systems (ACS), cord handling

- 4 Use cases, DER integration, V2G, auxiliary power functions

- 5 Interoperability and testing requirements.

The end to end document covers point of utility interconnection to conversion/distribution to vehicle couplers to vehicle battery terminals. The coupler specification, leveraging the drawings/dimensions also included in IEC TS63379, is rated up to 1500vdc/3000A with adequate cooling, far above 920v/500A CCS levels. A very aggressive goal was set with 90 minute weekly meetings leading to a first technical information reference (TIR) SAE document draft to be released by the end of 2022. ANL engineers produced weekly Powerpoint presentation materials for decision making processes, with the goal of including text and graphics from the presentations into the standard document. Distribution/invitation lists were based on members of the CharIN MCS work group and the ANL led monthly MW+ Charging industry engagement forum. The initial group grew as awareness of the SAE J3271 document spread, leading to 300+ total participants in the newly launched SAE J3271 committee by the end of FY2022.

Task 2.3 SAE J3271 development of reference design connection detection safety circuits with superimposed communication

Barriers:

- Single ended powerline communication-over-pilot wire with earth return systems used in CCS charging have noise immunity and crosstalk limitations at 500A levels, even worse at 3000A

- SAE J3271 couplers have two pins for communication, and two for auxiliary or connection detection functions. A design solution is needed to compare and contrast superimposed connection detection on top of digital communication signals with a separate communication/connection detection scheme

- Safety circuits require a similar level of immunity of noise coupled from the high power DC conductors into connection detection wires. Filters and comparator levels need to be defined.

- Powerline communication (PLC) is a legacy physical layer; industry stakeholders are interested in 'multi-lingual' solutions that accommodate systems that use PLC, CAN or 10BaseT1S Ethernet.

Solution:

Work with industry partners and contractors to develop a reference design for connection detection safety circuits that immobilizes the EV while connected to the EV supply equipment (EVSE) as well as detects broken safety signal and protective earth conductors. The circuit board image in the results section shows the CAN based communication signals with superimposed connection detection circuits that has faster response than the four conductor (2 communication, 2 safety signaling) solution. Extensive real world conditions testing was conducted using CCS vehicles and EVSEs in/on an SAE J3271 specification twisted pair signaling cables adjacent to CCS conductors on a 17 meter charging cable. A test plan was developed and executed to collect noise and communication noise immunity data that will be used in the SAE J3271 MCS standard.

Task 3.1 Standards Identification- compile current list of standards applicable to EVs at Scale and document status, gaps and/or obstacles

Barriers:

- Standards are continually evolving with some becoming obsolete with changes in new technologies, market forces or standards that are slow/stalled in development.

- There is no single clearing house of standards status and applicability, specifically for EV charging.

- Standards Defining Organizations generally don't release work-in-progress documents, waiting until the document is completed and published. This leads to a gap in knowledge of the content and completion date of standards in development.

- Diverse perspectives from industry stakeholders and third party (national lab) participants are required for objective assessment of gaps and state-of-readiness of standards for EV charging.

Solution:

Work with American National Standards Institute (ANSI) as a contractor to ANL/DOE to convene the EV Standards Panel (EVSP) for regular work sessions to gather input and create and EV Charging Codes and Standards Roadmap. A similar DOE funded activity was completed in 2013 with input from ANL engineers and 100+ industry subject matter experts. Four subgroups were formed with bi-weekly meetings to develop the 2023 version of the roadmap. The participants range from national lab members, utilities, EVSE and vehicle manufacturers to academics. Many participants are members of active standards and can give 'insider' status inputs and subject matter expert level assessments on gaps in standards compared to needs.

Task 3.2 Standards Participation: Lab representatives actively participate in developing standards that support 'EVs at Scale' objectives to create, refine and bring the standards to a ballot for release.

Barriers:

- Standards defining organizations are generally not-for-profit with most of the standards development work conducted by volunteers, covered by their respective employers, not always with objective goals.

- There is a shortage of independent source participants that can keep standards perspectives objective .

Solution:

Using the 'top 10' standards areas defined in the Scope of Work EVs at Scale proposal, a divide and conquer approach was applied across the 5 national labs (ANL, INL, NREL, ORNL, PNNL) participating in the EVSE at Scale Codes and Standards pillar. The list of standards is diverse, with monthly meetings on most, leading and creating standards document materials on others. Liaison activities for information dissemination is also an important part of this task, giving presentations to 'other' SDO meetings to keep each SDO group up to date on evolving standards, the standards roadmap summary, adjacent industries/standards that may affect them (such as eVTOL electric aircraft, ships, rail, construction to on-road vehicles, and vice versa).

Results

The results here are specific to ANL activities including contractors funded under AOP guidance resource at ANL, for the tasks covered in this part of the Annual Report. Activities and results of other national labs in the EVs at Scale Codes and Standards pillar are covered later in this report.

Most of the results are part of a standards development 'team effort' focusing on ANL contributions on leading these particular standards in FY 2022.

The hardware results rely heavily on contractor and industry partners such as University of Delaware, BTCPower, 2G Engineering, Rema, and other component manufacturers. BTCPower provided production grade DC EVSEs, tied in parallel for 1000vdc/3000A testing and matching air cooled load banks in their lab space. Tesla engineers produced the first iteration of connection detection development circuit boards with test data.

Task 1.1 Supporting SAE J29254-2 and SWIFT Charge standard development activities to cover recent technological developments in power electronics and electromagnetics.

Figure below shows the functional wireless power transfer blocks covered in the published SAEJ2954. The work-in-progress J2954-2 for heavy duty electric vehicles have similar blocks, with higher power levels from 22kW to 500kW, and up to 1MW with parallel receivers matching ground assembly coils. The progress in the standards group moved the development of the document forward over the calendar year, not to publication, but monthly progress. The same goes for the SWIFT Charge consortium support with the technical requirements draft document monthly meetings to develop and review content but not yet released for external peer review.
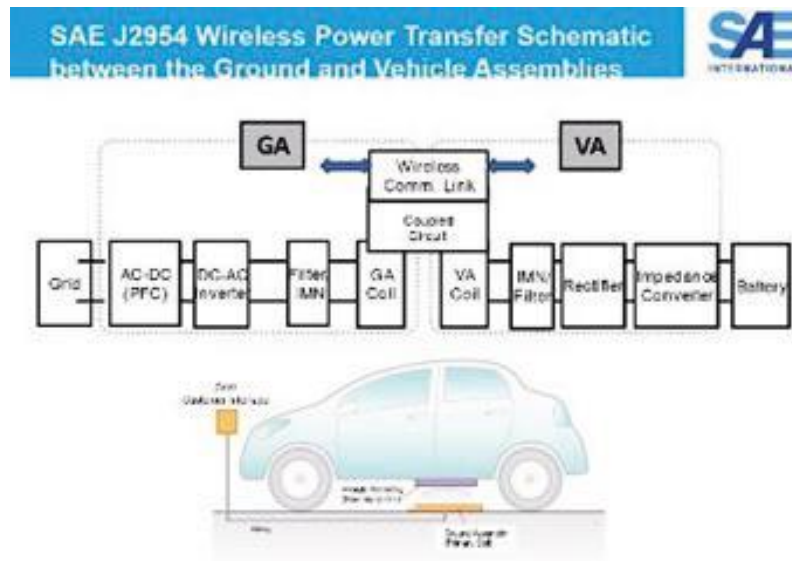
Figure II.6.2.1. Functional WPT blocks covered in SAE J2954

Task 1.8 SAE J3271: Launch new work area on end-to-end specification for Megawatt Charging System

As per the task description, the SAE J3271 new work area was launched in December of 2021. Weekly 90 minute meetings with up to 150 attendees were conducted for the entire calendar 2022 year resulting in the public release of the first draft Technical Information Reference level document by the end of 2022. The figure below shows the timeline for the SAE J3271 (and similar SAE AIR7357 aircraft MCS standard) development contrasted/complemented for IEC and ISO related standards. SAE J3271 is an end-to-end comprehensive charging standard from utility interconnection to vehicle battery terminals, for any large battery electric vehicle that 'rolls, flies, or floats'.
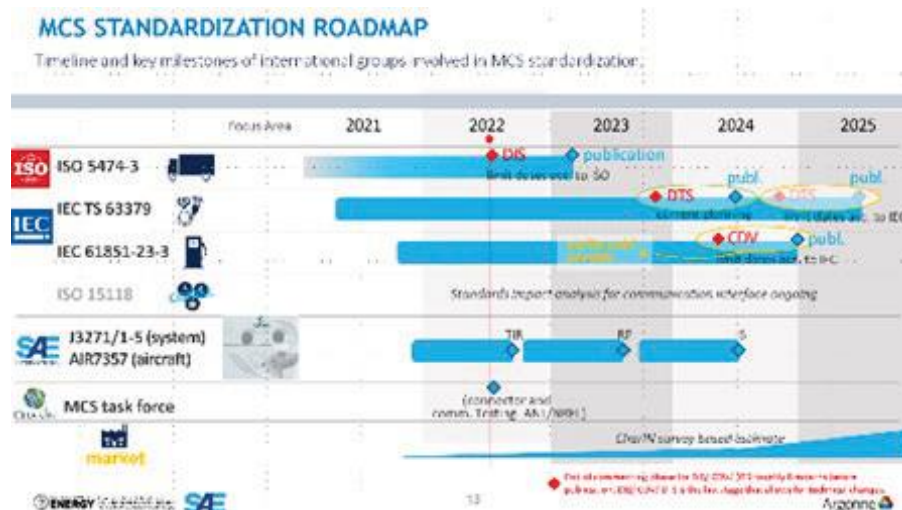
Figure II.6.2.2. Timeline of SAE J3271 MCS and other related standards

Figure II.6.2.3 shows the 1500v/3000A coupler included in the standard. Three MCS couplers were demonstrated at the October 2022 CharIN interoperability testing event at Electric Island in Portland OR, illustrating the progress made on SAE J3271 and the real world test data that will be included in future versions on the document. IEEE P2030.13 DC as a Service power distribution requirements are included in section 4, use cases of J3271covering utility interconnection and integration of distributed energy resources at a system integration level.

Figure II.6.2.3. SAE J3271 MCS coupler; pin functions, pre-production examples, Portand OR demonstration

Task 2.3 SAE J3271 development of reference design connection detection safety circuits with superimposed communication

The figure below shows the testing assets acquired for multi-lingual (CAN, PLC, 10BaseT1S Ethernet) differential digital communication over twisted pair conductors. The block diagram in the upper right corner is the scheme for connection detection safety signaling super imposed on the same twisted pair digital control lines, taking advantage of separating common mode (connection detect levels) from differential mode (physical layer communication).
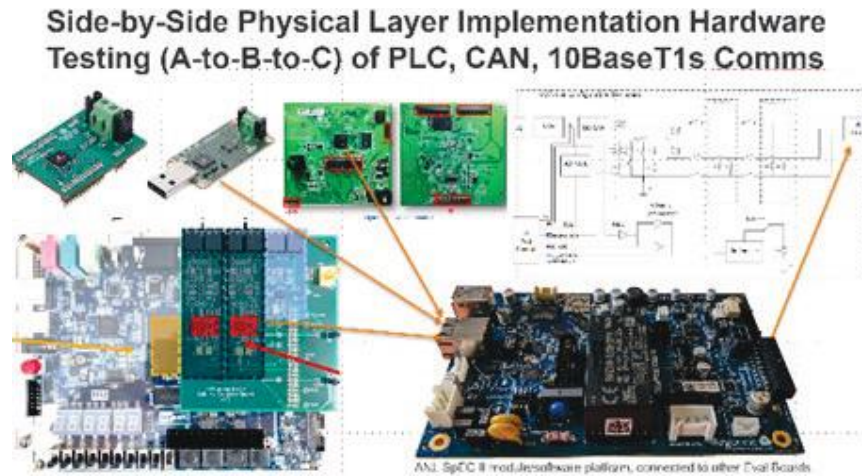
Figure II.6.2.4. Multi-lingual physical layer test articles; connection detection block diagram

The first connection detection circuit board was designed to accommodate differential CAN physical layer digital communication. A sensitivity analysis was performed impedance measurements were collected from the 17 meter test cable with SAE J1939 rated twisted pair signal wiring next to 3000A conductors and AWG#8 protective earth conductor. The connection detection circuit, when superimposed with physical layer communication signals, uses a pull-up and pull-down resistor on each of the differential signal wires for both terminator and broken wire detection.

CAN FD and CAN XL are able to run on the same conductors with different data rates. Likewise, the same signal wire terminating resistors, when properly sized, is able to support all three physical layer transceivers with the same terminator values.

Testing of the development board in the figure below yielded confirmation results on superimposed safety signaling response time, impact of component tolerances and noise immunity data that will be included in J3271. The tiled layout is the EVSE side on the left, EV side on the right.

Figure II.6.2.5. Tesla implementation of initial superimposed connection detection/comms board

Task 3.1 Standards Identification- compile current list of standards applicable to EVs at Scale and document status, gaps and/or obstacles

The figure below shows the 2013 and 2014 versions of the ANSI EVSP Standardization roadmap found at https://www.ansi.org/standards-coordination/collaboratives-activities/electric-vehicles .

https://www.ansi.org/news/standards-news/all-news/2013/05/updated-standardization-roadmap-for-us-electric-vehicle-deployment-released-14

The figure also shows the gap identification process and decision criteria about the state of EV charging standards. The four task groups met twice monthly and the document is on track for publication before the 2023 DOE VTO Annual Merit Review Meeting.
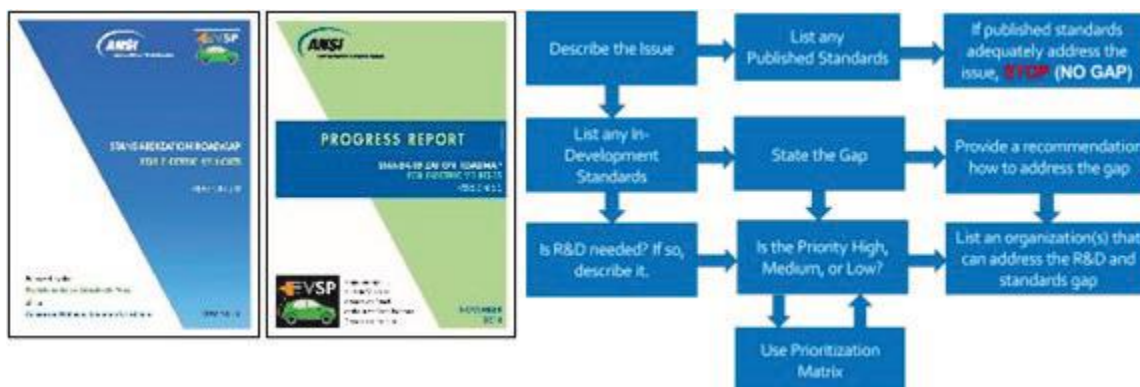
Figure II.6.2.6. ANL-ANSI EVSP Roadmap past documents; gap analysis process map

Task 3.2 Standards Participation: Lab representatives actively participate in developing standards that support 'EVs at Scale' objectives to create, refine and bring the standards to a ballot for release.

The figure below shows the work group names as an example of the SAE standards active participation areas. The Hybrid Communication task group hosts 23 standards shown in the matrix on the right; not all are presently active. The highest priority standard in this list is SAE J3271 MCS since it is new and has a big impact on EVs at Scale if it is completed ahead of expectations, with four years of specification development beforehand. The second highest priority is IEEE P2030.13 guide for functional specification of high power charging connected to distributed energy resources. An ANL representative is also the chair of this standard that was published in December 2022. Weights and Measures codes are not shown in these diagrams but have made measureable progress in 2022 under ANL leadership on testing procedure development (EPO30 in support of NIST Handbook 44-3.40 for commercial dispensing electricity as a fuel). Test fixtures based on

consumer off-the-shelf (COTS) digital bench meters connected to a purpose built Labview application was developed under ANL leadership and demonstrated at the CharIN Portland OR interoperability testing event on both CCS and MCS equipped EV charging stations. Sensors demonstrated with 3000A rating at 6 ppm accuracy as well. Training and education programs conducted state level weights and measures inspectors.
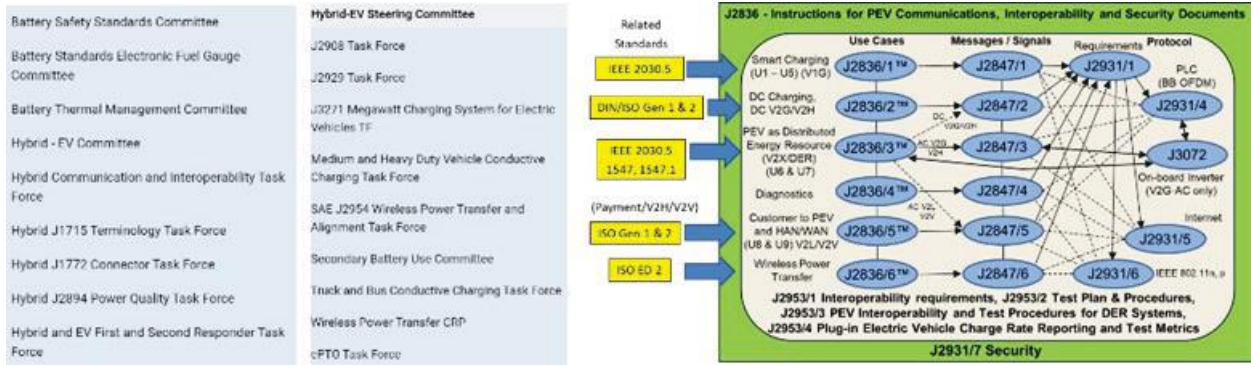
Figure II.6.2.7. SAE EV charging standards work groups; PEV communication matrix

Conclusions

ANL has the project lead role for the EVs at Scale Codes and Standards pillar activities. One of the tasks is hosting regular coordination meetings between the four national labs in this EVs at Scale pillar along with completing quarterly and annual reports. This section of the annual progress report covers ANL tasks in the scope of work.

The major thrust of this pillar is on supporting codes and standards development on the most impactful EV charging standards. SAE J3271 launch and release of the first TIR draft are major milestones. Weights and Measures codes as well as grid interconnection standards were developed and field tested in demonstrations. Wireless power transfer standards for commercial heavy duty vehicles were also advanced as part of SAE J2954/2 and the SWIFT Charge consortium.

II.6.3   Wireless Power Transfer, DER Standards Tasks (EVs@Scale Consortium – INL)

Timothy Pennington, Sr. Research Engineer
Idaho National Laboratory
1955 Fremont Ave.
Idaho Falls, ID 83415
E-mail: andrew.meintz@nrel.gov

Lee Slezak, DOE Program Manager
U.S. Department of Energy
E-mail: lee.slezak@ee.doe.gov

Start Date: January 1, 2022	End Date: December 30, 2022	
Project Funding: $65,000	DOE share: $65,000	Non-DOE share: $0

Project Introduction

Problem Statement – The EVs at Scale lab call program is divided into 5 pillars plus consortium management. This section covers INL Codes & Standards tasks. INL's tasks were performed in parallel and coordination with ANL's Codes and Standards project II.6.2.

Objectives

Primary goals – The INL portion of codes and standards pillar tasks focus wireless power transfer and IEEE P2030.13 'Guide for Electric Transportation Fast Charging Station Management System Functional Specification' interconnection standard. The goal is to create and improve codes and standards enabling 'EVs at scale' charging.

Approach

INL leveraged previous SAE standards testing and procedure development as well as grid modernization lab consortium (GMLC) work to support the IEEE P2030.13 to review definitions and block diagrams.

Tasks 1.5 and 1.6 Support SWIFTCharge Alliance and SAE J2954-2 wireless power transfer standard development and lab evaluation efforts in performance, interoperability, EM safety and communications.

Barriers:
- Same barriers as Task 1.1 of ANL project II.6.2.

Solution:

INL staff have participated in SAE J2954 monthly meetings and will continue to give input to the J2954-2 work group. The same with SWIFT Charge on the similar mission consortium.

Task 1.7 Support the IEEE 2030.13 Working Group

Barriers:
- Same barriers as Task 1.4, different lab activity.

Solution:

INL staff have participated in IEEE P2030.7 and P2030.8 microgrid standards meetings and will continue to give input to the P2030.13 work group based on other INL grid related research activities. The same with SWIFT Charge on the similar mission consortium.

II.6.4 SAE J3271 MCS Coupler Testing, DER Standards Tasks (EVs@Scale Consortium - NREL)

Andrew Meintz, Principal Investigator
National Renewable Energy Laboratory
15013 Denver W Pkwy
Golden, CO 80401
E-mail: Andrew.Meintz@nrel.gov

Lee Slezak, DOE Program Manager
U.S. Department of Energy
E-mail: lee.slezak@ee.doe.gov

Start Date: January 1, 2022   End Date: December 30, 2022
Project Funding: $400,000   DOE share: $400,000   Non-DOE share: $0

Project Introduction

Problem Statement – The EVs at Scale lab call program is divided into 5 pillars (Grid integration, High power charging, Wireless power transfer charging, cybersecurity and Codes & Standards) plus consortium management. This section covers NREL Codes & Standards tasks. NREL's Codes and Standards tasks were performed in parallel and coordination with ANL's Codes and Standards project II.6.2.

Objectives

Primary goals – The NREL portion of codes and standards pillar tasks focus solely on SAE J3271 MCS coupler testing and IEEE P2030.13 'Guide for Electric Transportation Fast Charging Station Management System Functional Specification' interconnection standard. The goals to create and improve codes and standards enabling 'EVs at scale' charging as well as supply validation test data with industry partners to support standards refinement are the same as the previous section for ANL.

Approach

NREL leveraged previous DOE funded activities under the CharIN MCS work group on previous MCS coupler designs for the latest pre-production prototype couplers. Likewise NREL leveraged grid modernization lab consortium (GMLC) work to support the IEEE P2030.13 to create definitions and block diagrams.

Task 1.3 Support of the CharIN MCS Connector thermal and mechanical interface evaluation activities to support connector safety workgroup activities.

Barriers:

- No standards based pin and sleeve (non-automated) couplers presently exist for megawatt level on-road vehicle charging.

- Test data is needed for standards validation and development of coupler testing procedures.

Solution:

NREL staff have participated in monthly CharIN MCS requirements defining meetings and hosted previous coupler testing events. More testing was planned and executed in FY2022 by NREL engineers. Data from this testing will be used for the CharIN MCS requirements white paper and SAE J3271 standard.

Task 1.4 Support standardization activities for site operation of DC interconnected charging systems to identify common pathways for site level integration of high power charging systems.

Barriers:

- Site level integration of DC coupled distributed energy resources (DER) is not common today.

- Assessment of topologies is needed for better diagrams in standards, iterating labels, functions

Solution:

NREL staff have actively participated in monthly IEEE P2030.13 meetings and the sub-tasks have been identified on assessing topologies, architectures and functional requirements of charging systems. Assessments were completed compiled in a summary report.

Results

Task 1.3 Support of the CharIN MCS Connector thermal and mechanical interface evaluation activities to support connector safety workgroup activities..

Testing event held at NREL-ESIF location on purpose built test fixture, evaluating all available MCS version 3.2 design couplers, both in production tooled molded parts and 3D printed parts. The results report is password protected and shared with the CharIN MCS work group members that have access to the report.

An anonymized version of the report is in the review process with an early 2023 anticipated release to non-CharIN members. The figure below shows the lab test setup and fixtures.

Figure II.6.4.1. MCS EV coupler testing at NREL

Task 1.4 Support standardization activities for site operation of DC interconnected charging systems to identify common pathways for site level integration of high power charging systems.

The following table lists the NREL sub-tasks and milestones coming up in 2023 as a work-in-progress in support of IEEE P2030.13.

Table II.6.4.1 2023 NREL Sub-Tasks and Milestones

TASK	RESULTS
Task 1: Assess and harmonize the topologies, architectures, and functional requirements of charging systems, BTM assets, and microgrids that are suitable for application to fast charging stations.	Two architectures (AC and DC) as described earlier are now included as part of the functional guide. They facilitate fast charging of EVs, DER integration, and will interface with DMS.
Task 2: Assess and develop interconnection requirements for fast charging microgrids under grid connected and isolated modes.	Core functional requirements that are being developed in the guide now include EMS and CSMS that facilitate managing overall power/energy availability and requirements against the EV charging needs.
Task 3: Evaluate and assess functional requirements of control systems to manage fast charging stations for multiple chargers and BTMS assets.	Three levels of functionalities are now included in the guide that include device level functions (level 1), core functions (level 2 with EMS and CSMS), and higher-level functions (level 3 for DMS or equivalent interface).

Task 4: Participate and contribute to the IEEE P2030.13 working group meetings and the development of the draft.	Ongoing monthly and any other working group meetings as required.
Deliverable: Functional requirements for a Fast-Charging Station with harmonized terms that are broadly applicable to high power charging of multiple EVs.	This deliverable is now complete and summarized above and included in the functional guide.
Milestone: Report summarizing the conceptual and functional requirements for operating a FCS as a microgrid with technical, simulation, and standardization gaps.	This report summarizes the conceptual and functional requirements for operating FCS as a microgrid leveraging the P2030.13 in conjunction with the existing IEEE 2030.7 and 2030.8 is provided. Relevant text and information are relayed to the functional guide as part of the main text or appendix.

II.6.5 Wireless Power Transfer, Medium Voltage Power Converter Standards Tasks (EVs@Scale Consortium - ORNL)

Omer Onar, Principal Investigator
Oak Ridge National Laboratory
National Transportation Research Center
PO Box: 2008 MS-6472
Oak Ridge, TN 37831
E-mail: Onaroc@ornl.gov

Lee Slezak, DOE Program Manager
U.S. Department of Energy
E-mail: Lee.slezak@ee.doe.gov

Start Date: January 1, 2022	End Date: December 30, 2022	
Project Funding: $130,000	DOE share: $130,000	Non-DOE share: $0

Project Introduction

Problem Statement – Same as previous stated in ANL project II.6.2. This section covers ORNL Codes & Standards tasks. ORNL's Codes and Standards tasks were performed in parallel and coordination with ANL Codes & Standards project II.6.2.

Objectives

Primary goals – The ORNL portion of codes and standards pillar tasks focus mostly on wireless power transfer topics, with liaison activities coordinating researchers on medium voltage power converters. The goal is to create and improve codes and standards enabling 'EVs at scale' charging.

Approach

ORNL leveraged previous and current DOE funded wireless power transfer activities to support WPT standards. The same with medium voltage power converter activities under a previous lab call.

Tasks 1.1 and 1.2 Support J2954, SWIFT Charge and IEEE PES Technical Committee 9 for WPT

Barriers:
- Same barriers listed for task 1.1 of ANL project II.6.2.

Solution:
ORNL staff have participated in past J2954 WPT work group meetings and SWIFT Charge consortium meetings and continued that activity in FY2022. The same for IEEE Power Electronics Society Technical committee #9 past and future meetings.

Task 2.1 Performing two-way interoperability work between ORNL polyphase coupler technology and circular and DD type couplers

Barriers:
- Same barriers listed for task 1.1 above.

Solution:
ORNL conducted interoperability assessment of the higher surface power density (ORNL designed) polyphaser WPT coupler compared to DD and circular couplers using a polyphase transmitter and DD-circular receivers and DD-circular transmitters with a polyphase receiver. Data used to support J2954 standards.

Task 2.2 Establishing industry/academia engagement on medium voltage solid state transformers

Barriers:

- Similar barriers listed for task 1.7 above.

Solution:

ORNL staff created industry and academia engagement for direct distribution level medium-voltage (MV) connected charging infrastructures with solid-state transformers or modular multilevel converters (MMC) for high-power charging plazas.

II.6.6 Wireless Power Transfer, Medium Voltage Power Converter Standards Tasks (EVs@Scale Consortium - PNNL)

Gregory Brian Dindlebeck, Principal Investigator
Pacific Northwest National Laboratory
902 Battelle Blvd
Richland, WA 99354
E-mail: gregory.dindlebeck@pnnl.gov

Lee Slezak, DOE Program Manager
U.S. Department of Energy
E-mail: lee.slezak@ee.doe.gov

Start Date: January 1, 2022	End Date: December 30, 2022	
Project Funding: $110,000	DOE share: $110,000	Non-DOE share: $0

Project Introduction

Problem Statement – Same as previously stated in project II.6.2. This section covers PNNL Codes & Standards tasks which were performed in parallel and coordination with ANL's Codes and Standards project II.6.2.

Objectives

Primary goals – The PNNL portion of codes and standards pillar tasks focus on SAE J3271 and EVSP roadmap tasks. The goal is to create and improve codes and standards enabling 'EVs at scale' charging.

Approach

PNNL leveraged previous and current DOE funded EWV charging research activities to support the development of the standards roadmap and write the text of the J3271 standard document.

Tasks 1.8, 3.1 and 3.2 Support J3271, EVSP standards roadmap and standards participation activities

Barriers:
- Same barriers listed for tasks 1.8, 3.1 and 3.2 of ANL project II.6.2.

Solution:

PNNL staff have participated in CharIN MCS work group meetings and EV Charging standards. Knowledge of cyber security, smart charging and other standards was utilized to draft wording in the EVSP standards roadmap augmenting the input from industry participants. I.e. perform the actual writing of the roadmap documents as well as SAE J3271 MCS standard first draft.

Key Publications/Presentations

1. Argonne National Laboratory contributions to CharIN Megawatt Charging System Requirements white paper; collectively developed from 2018-2022; published November 24, 2022.
   https://www.charin.global/technology/mcs/
   https://www.charin.global/media/pages/technology/knowledge-base/c708ba3361-1670238823/whitepaper_megawatt_charging_system_1.0.pdf

2. "Mega push for heavy duty EV charging" SAE newsletter, May 27, 2021
   https://www.sae.org/news/2021/05/megawatt-charging-for-electric-trucks

3. "Launch of SAE J3271-AIR7357 Megawatt Charging System Standards (MCS) for all large-battery vehicles that roll, fly, or float." SAE Updates Newsletter, June 2022
   https://www.nxtbook.com/smg/sae/22UPD07/index.php#/p/28

Acknowledgements

II.6.7   DC Meters for Commercial Charging Benchmark Study (ANL)

Theodore Bohn, Principal Investigator
Argonne National Laboratory
9700 S. Cass Avenue
Lemont, IL 60439
E-mail: tbohn@anl.gov

Lee Slezak, DOE Program Manager
U.S. Department of Energy
E-mail: lee.slezak@ee.doe.gov

Start Date: July 1, 2020   End Date: May 5, 2022
Project Funding: $75,000   DOE share: $75,000   Non-DOE share:$0

Project Introduction

Problem Statement – The EV Charger Metering and Testing project leverages the past decade of DOE research supporting development of the National Institute of Standards and Technology's Handbook 44 Section 3.40 (HB44-3.40) for commercial dispensing of electricity as a fuel. The NIST led EV charging national work group formed in 2012, published tentative requirements code in 2016, targeted for enforcement (starting with California) in 2020. Challenges in assessing and certifying Electric Vehicle Supply Equipment (EVSE) charging transactions as part of the type approval process led to deferral of the AC charging requirements enforcement to 2021 and DC systems in 2023. Part of the concern was a perceived lack of commercially available DC meter solutions capable of being integrated into a charging system to accurately indicate only energy dispensed to the vehicle eliminating sources of measurement error, such as charging cable losses.

DC charging systems have a range of power delivery capabilities within three current connector standards in the US (SAE J1772 CCS, Tesla SuperCharger, CHAdeMO). Cable lengths vary according to installation layout. Charging cable conductors are sized to balance conductive losses against cable mass and cost. Charging cable losses affect dispensed energy measurements if the losses are not properly addressed in meter sensing methods. This study addresses sensing methods and benchmark measurements of available charging cables. SAE J3271 Megawatt Charging System (MCS) requirements were a developing item in 2020 at the launch of this study. Conductors supporting 3000A charging currents are addressed in the study.

Lack of available traceable accuracy testing solutions for laboratory and field testing of DC EVSEs led to enforcement delays in NIST HB44-3.40. This gap led to engagement with Fluke, Agilent, Tesco and other test equipment manufacturers to address these gaps. An off-the-shelf components-based solution with a Labview user interface was developed and demonstrated as part of the benchmark study on both EVSE meters and equipment to evaluate DC meters.

Another complication is the lack of globally harmonized codes that establish requirements for charging equipment manufacturers and charging station operators. US and global EV charging industry stakeholders submitted a joint letter to DOE to request the Department of Energy's Argonne National Laboratory (ANL) to investigate methodologies needed to demonstrate electric vehicle (EV) direct current (DC) fast charger compliance with these codes. The project was launched in 2020 with the results and observations report being globally disseminated that led to collaboration of the Organisation Internationale de Métrologie Légale (OIML) member countries to further develop internationally harmonized charging system measurement requirements. A catalyst for these international collaborations was needed and the publicly available independently generated information from such a benchmark study was an essential part of those discussions.

At the time this project was launched there was no discrete DC meter standard that can be used by utilities or other energy distribution entities that use tariffs to transact DC energy sales to the charging sites. Subsequent to this study and engagement with Standards Defining Organizations (SDOs) such as ANSI, a DC meter standard was published in 2021 (ANSI C12.32).

Independent assessment and validation of meter manufacturer performance claims was needed to collect, compare and disseminate performance results side by side under identical test conditions. There was also no public forum for DC EV charging system stakeholders to ask specific questions or clarify code requirements as well as type approval testing procedure details. This project provided a clearing house of information references on requirements, available components, procedures and subject matter experts.

Another gap was an avenue of feedback from the EVSE manufacturers and charging system operators to meter manufacturers on features, pricing, performance and packaging expectations. Some EVSE manufacturers took the direct approach and designed their own meter solution for their DC EVSE products, which are not available to their competitors. Most of the available DC meters on the market in 2019 were targeted for photo voltaic system monitoring and battery storage management with lower quality and precision than is required for EV charging meeting NIST HB44-3.40 tolerances. This project provided a forum for EVSE equipment manufacturers to directly engage with meter manufacturers to refine requirements (and cost expectations) allowing meter manufacturers to refine their products to meet EV charging system application requirements.

Objectives

Primary goals – Acquire representative DC meters and cables for EV charging to be evaluated in the benchmark study, test components and disseminate results. As a constrained resource modestly sized project the study sample size and breadth of measurements was limited to fit the time and funding budget. The problem statement section details the scope of gaps that were to be addressed in this benchmark study. COVID19 impacted constraints on available testing locations along with NDA related procurement process steps that limited access to testing sample meters.

Developing the scope of what/why this equipment is to be evaluated is a primary goal along with testing and reporting the results. The range of evaluated meters started with the top 10 candidate samples constrained to those that are actually available for testing and potentially meet tolerance/power range requirements.

The industry engagement aspect of the study and dissemination of the project will likely have the largest impact in terms of getting all the stakeholders on the same page along with working as a team to refine codes and standards for EV charging measurements. One-on-one meetings with EVSE and meter manufacturers led to first hand information on the state of availability of existing solutions or gaps in some of the performance (price) criteria. A global audience web meeting facilitated direct interaction of stakeholders from multiple regions to fill in gaps of 'who is doing what and where' on measurement system requirements for energy dispensing commercial transactions.

Approach

Argonne utilized meter standards development hardware and test equipment from previous 10 years of projects to develop a test stand and test procedure to benchmark meter accuracy as well as other attributes.

The most time consuming portion of the benchmark testing study was acquiring test articles. The lowest performance lowest cost meters were generally available with short lead times.

Some imported meters had lead times under 30 days with normal procurement delays to place the order. Some meters were very challenging to get NDA paperwork approved by both sides before the purchase order was placed and then manufacturing/delivery lead times added to delays.

The last meters (2) arrived after the initial report was released, with only specification data in the benchmark study; test data added afterward. Procurement/deliver delays of meters for the benchmark study did not reflect

production quantity available of DC meters. Ordering a single quantity did not expedite the process whereas an order for hundreds of meters may have made the sample available sooner.

This effort included independent benchmark testing of DC meter accuracy and representative DC fast charger cables, from low power to high power as well as liquid cooled cables. DC fast charger meter accuracy and cable losses were evaluated to determine the overall accuracy of the energy measurement from the EVSE to EV. Figure II.6.7.1 shows the power flow path and location of the DC meter in the dispenser along with output charging cable that can be the source of measurement errors.
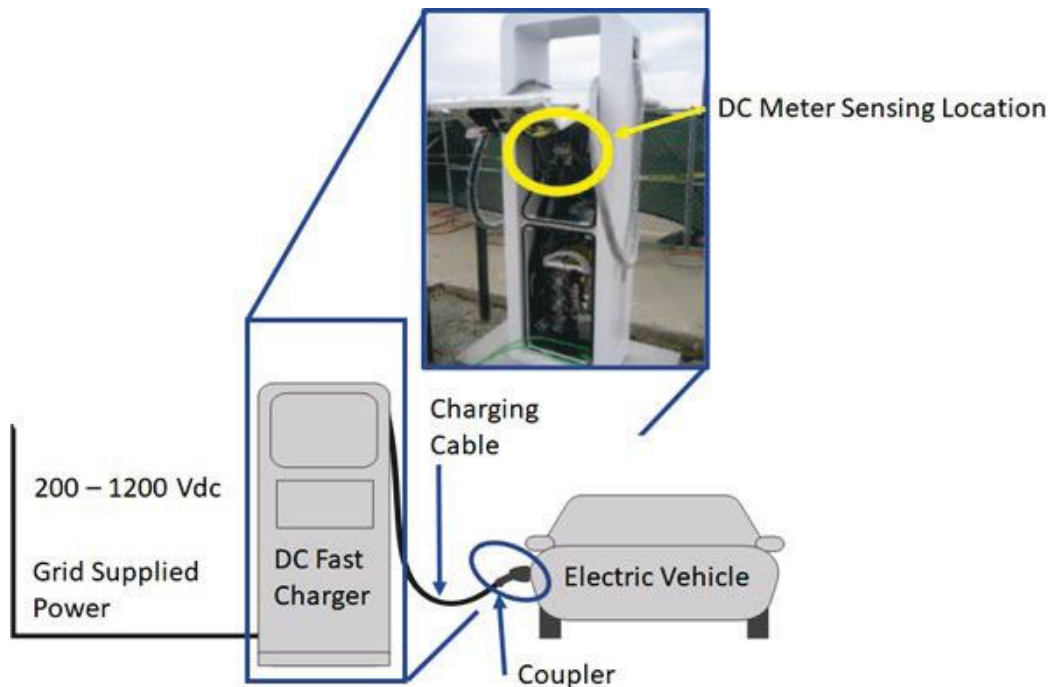

Figure II.6.7.1. Components of EV Charging System

Tasks 1: Identifying and Acquiring Sample DC Meters and Representative Charging Cables

Barriers:

- Perceived and actual lack of available DC meters due to immature commercial DC charging equipment market

- To date industrial grade measurement methods sufficed that met non-commercial transactions

- Cause and effect relationship on lack of market forces on DC meter manufacturers providing purpose built DC meters when EVSE manufacturers were not ready/willing to purchase more expensive meters than existing industrial grade (lower than 1% net measurement tolerance) sensing components in EVSEs.

Solution:

Direct approach was used to identify both the correct sales and technical representative at DC meter manufacturers or distributors to specify the correct model meter for the benchmark study. The same with NDA agreements to protect sensitive/secure data from the meters that cannot be publicly shared; case by case agreements needed in addition to purchasing sample meters. Figure II.6.7.2 shows the 10 meters included in the benchmark study, with information in Table II.6.7.1.

Figure II.6.7.2 Ten meter and current sensor benchmark test articles. (clockwise, top left); Rish, LEM, Tritium, Isabellenhuette, MeasurLogic, Lumel, EVoke, Porsche Engineering Services, Satec, and AccuEnergy (Source: ANL).

Table II.6.7.1. Tested Meters and their Manufacturers.

	Manufacturer	Model	Manufacturing Location
1	AccuEnergy	AcuDC 243	Canada
2	EVoke	EUMD6m	USA
3	Isabellenhuette	IEM-DCC	Germany
4	LEM	DCMB	Switzerland
5	Lumel	PH30	Poland
6	MeasurLogic	DTS DC	USA
7	Porsche Engineering Services	DCEM 100	Germany
8	Rish	Alpha EM DC	India
9	Satec	PM130-PLUS-DC	Israel
10	Tritium	integrated DC	Australia

Figure II.6.7.3 shows the liquid cooled and passively cooled cables evaluated in this benchmark study; models and manufacturers listed in table Table II.6.7.2. Active cooling was not needed to measure cable resistance and/or conductive losses. Cable resistance/losses were calculated from standard wire tables and confirmed with bench measurements in the lab. Cable resistance was measured at room temperature and elevated temperatures to confirm that percentage change in resistance is negligible total measurement error (well under 0.01% impact).

Figure II.6.7.3. Liquid cooled and conventional CCS-CHAdeMO charging cables evaluated in benchmark study (Source: ANL).

Table II.6.7.2. List of EV Charging Cable Test Articles.

Manufacturer	Model	Rated Current (Amperes)	Length (feet)
Rema	REV1-65C-DC	65A	14'
Rema	REV-C1-150C	150A	11'
Rema	REV-C1-200C	200A	14'
Rema	REV-C1-350C	350A	14'
Phoenix Contact	EV-T2M4CC-DC	125A	17'
Sumitomo	SEVD-02MU	80A	13'
Sumitomo	SEVD-01U	125A	13'
Liquid Cooled			
Huber+Suhner	RADOX HPC	500A	14'
Southwire	350mcm	1000A	12.5', 25'
Southwire	600mcm	3000A	12.5', 25'
Miller-ITW	WP-18	350A	12.5', 25'
Miller-ITW	WP-27	500A	12.5', 25'

Task 2. Develop Benchmark Test Procedure, Conduct Benchmark Accuracy Tests

Barriers:

- No existing DC meter standards existed at time of the benchmark study as a procedure foundation

- Obtaining a stable 100v to 1000vdc source, 30A to 500Adc source

- Constrained time budget to conduct tests for each meter; thermal stability/replicate tests limited

- Required 10x or better tolerance for reference measurements (+/-0.1% or better for 1% testing).

Solution:

The meter benchmark test procedure was developed based on OIML R46 draft templates and work-in-progress ANSI C12.32 meter standard. Figure II.6.7.4 shows the voltage/current sources (manually adjusted power supplies), Keithley-Hioki reference meter/LEM fluxgate magnetometer current sensor, logic power supply for meter under test and user interface laptop PC with software utility capable of accessing meter-under-test data. Charging cable resistance was measured with a Xitron milli-ohmmeter as well applied rated current, measuring voltage drop and resulting direct power loss measurements that impact EVSE measurement meter accuracy.
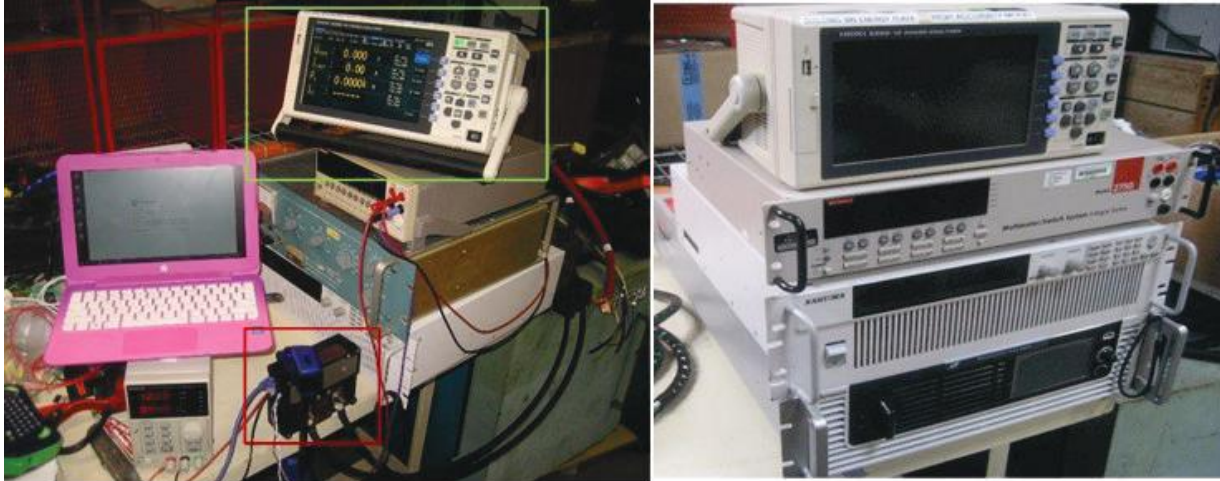

Figure II.6.7.4 Meter test stand components; Hioki 3390-10 (0.04%) meter/current sensor, Keithley 2700 DVM (10ppm), 600A current source, 3kV voltage source, application host PC (data collection), logic power supply and DUT meter. {ANL photos}

The same input voltage/current was applied to all meters at room temperature with selected meters tested at other than room temperature (nameplate temperature limits of meters; -30°C, +40°C). The cable loss measurements were performed using the same power supplies and meters shown in Figure II.6.7.4.

Task 4. Compiling Results and Information Dissemination

Barriers:

- Data collection method (access to meter data) is different for each meter

- No database/list of metering-EV charging stakeholders existed for US or global forums

- Industry engagement is an iterative process, introducing the problem/solution, feedback, retesting.

Solutions:

Learning curve for each meter data format was addressed to get through password locked registers, web accessed third-party service technician portals, and MODBUS registers in corresponding software tools to read meter registers. Data from cable and meter measurements compiled in a spreadsheet, including replicates to average pass-fail on meeting tolerance or other requirements. A 55-page report was generated and circulated to stakeholders along with 13 page section for the Report to Congress document covering metering needs to meet HB44-3.40 requirements that are soon to be enforced.

A spreadsheet was compiled with contact information for known state weights and measures agency members, EVSE and meter manufacturers, charging system operators and other international stakeholders involved in this topic. A webinar was hosted 9/23/2021 to review the results report and gather input on next steps for type approval programs for US and international segments. Over 300 people were invited with over 150 attendees from multiple time zones.

Results

A key objective of this study was to confirm availability of DC meter solutions suitable for EV charging that can meet HB44-3.40. At the end of FY22 all 10 meters are available for sale. Most of the meters that were tested met the stated accuracy on the published specification sheets. A listing of manufacturer-published meter specifications are available in the full ANL benchmark comparison study report. The cables measured for voltage drop matched the published conductor resistance table values within the resolution of the measurements. The calculated voltage drops on charging cables and corresponding power loss show manageable errors/magnitude for typical length/conductor area of charging cables. *Figure II*.6.7.5 shows the impact of cable losses as a function of amperage applied. Each cable tested was observed to impact measurement errors that are manageable via external voltage (kelvin point) sensing leads, calculated compensation (I^2R subtraction) or additive errors that remain within the tolerance specified by HB44-3.40.
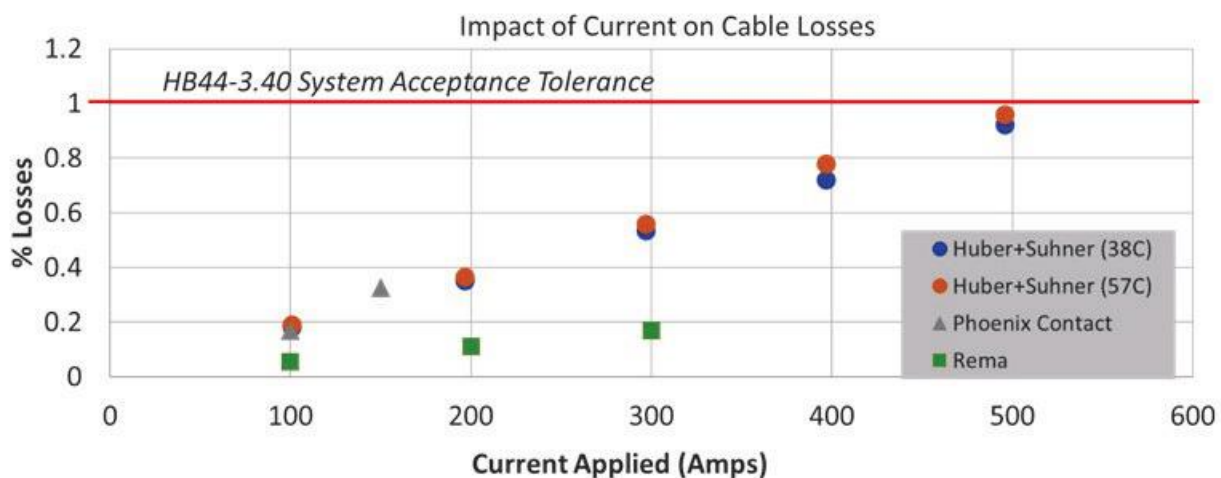

Figure II.6.7.5. Cable losses as a function of current.

Conclusions

To determine DC fast charger technologies compliance and calculation methods that help check the compliance with NIST's HB44-3.40, ANL conducted benchmark research on DC meters and cables. A conclusion from this benchmarking research is that manufacturers of EVSE DC fast charging equipment do not need to have a revenue grade meter in the coupler at the end of the cable to comply with HB44-3.40 specifications for measurement.

Other important conclusions from ANL's benchmark study include the following.

- 10 DC meters capable of measuring 1000 V/350 A with a less than 1% error are for sale today.

- 5 methods of managing/meeting HB44-3.40 accuracy with cable errors were identified.

- Charging cable voltage drop magnitude and resulting errors for several cables was characterized.

- The impact of temperature on conductor resistance minimally affects net voltage drop errors.

- Cable voltage drop matches calculated values from the standard resistance charts.

- For modest cable current density (cross section) voltage errors are 0.1%-0.55%, at 400 Vdc.

- ANL is working with EVSP/EVSE stakeholders and NCWM on NTEP testing.

Key Publications/Presentations

1. Interactive Webinar; Argonne National Laboratory. 9/23/2021. "An open discussion about Handbook 44-3.40 DC status, meter/cable loss benchmark study for EV Charging transactions"

2. Bohn, T. 2021. "Charging Infrastructure Technologies: Smart Vehicle-Grid Integration – ANL." Presented at the U.S. Department of Energy Vehicle Technologies Office Annual Merit Review, June 23, 2021

Acknowledgements

(This page intentionally left blank)

U.S. DEPARTMENT OF
ENERGY

Office of
**ENERGY EFFICIENCY &
RENEWABLE ENERGY**